The Seismic Performance of Coupled Reinforced Concrete Walls

Jacob A. Turgeon

A thesis submitted in partial fulfillment
of the requirements for the degree of

Master of Science in Civil Engineering

University of Washington

2011

Program Authorized to Offer Degree: Civil and Environmental Engineering

University of Washington
Graduate School

This is to certify that I have examined this copy of a master's thesis by

Jacob A. Turgeon

and have found that it is complete and satisfactory in all respects,
and that any and all revisions required by the final
examining committee have been made.

Committee Members:

Laura Lowes

Dawn Lehman

John Stanton

Date:

Signature____________________________

Date_______________________________

University of Washington

Abstract

The Seismic Performance of Coupled Reinforced Concrete Walls

Jacob A. Turgeon

Co-Chairs of the Supervisory Committee:
Professor Laura Lowes
Department of Civil and Environmental Engineering

Professor Dawn Lehman
Department of Civil and Environmental Engineering

Reinforced concrete core walls are used commonly in modern building construction as the primary lateral-load resisting system. Common core wall configurations include solid walls in one direction and walls with openings in the orthogonal direction to access elevators or to meet architectural requirements. Therefore, in the orthogonal direction, the walls are typically coupled together by reinforced concrete “coupling” beams. A significant amount of research has focused on the design of coupling beams to ensure that they exhibit ductile response through multiple cycles to large drift demands. However, only a few research studies have investigated the seismic behavior of coupled wall systems, and most of these previous studies have considered coupled-walls in low-rise structures. Most coupled walls are used in elevator cores, which are more typical in mid- to high-rise construction. A research study was undertaken by faculty and students at the Universities of Washington and Illinois to specifically investigate this category of structural system. The advanced testing capabilities of the NEES University of Illinois at Urbana-Champaign (UIUC) testing facility permitted unique experimental simulation of this system.

The coupled-wall test specimen simulated the bottom three stories of a ten-story building in a region of high seismicity designed with typical geometry and reinforcement.

Specialized load-and-boundary-condition boxes (LBCBs), which are part of the UIUC NEES laboratory, were used to simulate demands originating from the upper stories of a ten-story structure subjected to an ASCE 7-05 lateral load distribution and gravity load. Cyclic lateral loading was applied under displacement control until significant loss of lateral load carrying capacity was observed at 2.27% drift. Strength loss resulted from significant core crushing and longitudinal bar buckling in the compressive wall. Experimental data from this test, in combination with data from previous tests of coupled walls, to evaluate the performance of coupled wall systems including elastic and nonlinear modeling approaches as well as current design methods of coupled wall systems. This research indicates that, coupled wall behavior observed in laboratory testing as well as in nonlinear modeling, is inconsistent with current design assumptions and elastic analyses. For significant earthquake demands, current design approaches including elastic analysis tend to neglect the effects on the flexural strengths of the wall of the large compressive axial loads that develop in the compression piers as well as the redistribution of shear demand from the tension wall to the compression wall as a result of these axial loads. This behavior ultimately limits the ductility of the coupled wall system to the deformation capacity of the compression wall pier.

TABLE OF CONTENTS

Page

List of Figures v

List of Tables xiii

Chapter 1: Introduction 1

Chapter 2: Previous research to advance performance-based seismic design of coupled concrete walls 5
  2.1 Seismic Response of a Coupled wall 5
  2.2 Current Design Methods 6
  2.3 Research Addressing Earthquake/Seismic Design of Coupled Walls 9
  2.4 Summary of Previous Experimental Coupled Wall Components 13
  2.5 Review of Previous Experimental Tests of Coupled Walls 19
  2.6 Review of Previous Simulation Studies of Coupled Wall Systems 75
  2.7 Conclusions of Literature 84

Chapter 3: NEESR Coupled Wall Test Program 85
  3.1 Specimen Design 85
  3.2 Specimen Construction 103
  3.3 Experimental Test Setup 104
  3.4 Instrumentation 108
  3.5 Loading Protocol 119

Chapter 4: Experimental Observations 125
  4.1 Load–Displacement Data 125
  4.2 Description of Specimen Response 127

Chapter 5: Detailed Investigation of Behavior 177
5.1 Strain Guage Data 177
5.2 Coupling Beam Forces 185
5.3 Wall Pier Axial Forces 188
5.4 Wall Pier Axial Deformations 194
5.5 Wall Pier Axial Stiffness 198
5.6 Wall Pier Flexural Stiffness 203
5.7 Wall Pier Demands 208
5.8 Strain Fields 213
5.9 Deformation Components 231
5.10 Coupling Beam Rotations 242

Chapter 6: Coupled Wall Performance and Damage Evaluation 253
6.1 Performance Evaluation Parameters 253
6.2 Comparison of Coupled Wall Damage 259
6.3 Drift Capacity based on Damage States 272

Chapter 7: Elastic Analysis of Coupled Wall Experiments 273
7.1 Overview of Elastic Model in OpenSees 274
7.2 Review of Recommended Effective Stiffness values 275
7.3 Comparisons of Elastic Analysis Results 289

Chapter 8: Nonlinear Analysis of Coupled Walls 305
8.1 Overview of Nonlinear Model in OpenSees 306
8.2 Results and Comparisons of Nonlinear Analysis 312

Chapter 9: Design Recommendations 341
9.1 Initial Design of a Coupled Wall 342
9.2 Demand Analysis 346
9.3 Coupling beams 346
9.4 Wall Piers 347

Chapter 10: Summary and Conclusions 355
10.1 Summary 355

10.2 Conclusions 360
10.3 Future Work 364

Appendix A: List of Symbols 375

Appendix B: CW1 Experimental Information 377
B.1 CW1 Instrumentation Errors 377
B.2 CW1 Peak Drift Information 378
B.3 CW1 Testing Notes 379
B.4 CW1 Crack Widths 389

Appendix C: CW1 Data Analysis 395
C.1 Vertical Strain Fields 395

Appendix D: Elastic Analysis of Coupled Wall Experiments 401
D.1 Effective stiffness values used in each model 401

LIST OF FIGURES

Figure Number Page

2.1 Desired plastic mechanism 6
2.2 Distribution of moments in a typical coupled wall (Harries, 2001) 11
2.3 Coupling beam ductility demand versus degree of coupling from analysis 12
2.4 Test specimen geometry (Santhakumar, 1974) 22
2.5 Wall pier reinforcement detail (Santhakumar, 1974) 22
2.6 Coupling beam reinforcement detail (Santhakumar, 1974) 23
2.7 Test set up for walls tested by Santhakumar (1974) 24
2.8 Force-displacement response for Specimen WallA (Santhakumar, 1974) . 26
2.9 Force-displacement response for Specimen WallB (Santhakumar, 1974) . 28
2.10 Damage to specimens at end of test (Santhakumar, 1974) 29
2.11 Test specimen geometry (Shiu et al., 1981) 33
2.12 Wall pier reinforcement detail (Shiu et al., 1981) 33
2.13 Coupling beam reinforcement detail (Shiu et al., 1981) 34
2.14 Test set up for walls tested by Shiu et al. (1981) 35
2.15 Force-displacement response for Specimen CS1 (Shiu et al., 1981) 37
2.16 Crack pattern in CS1 at the end of test (Shiu et al., 1981) 38
2.17 Force-displacement response for Specimen RCS1 (Shiu et al., 1981) . . . 39
2.18 Crack pattern in RCS1 at the end of test (Shiu et al., 1981) 40
2.19 Damage to RCS1 at end of test (Shiu et al., 1981) 40
2.20 Test specimen geometry and wall pier reinforcement detail (Ozselcuk, 1989) 45
2.21 Wall pier reinforcement detail (Ozselcuk, 1989) 45
2.22 Coupling beam reinforcement detail (Ozselcuk, 1989) 46
2.23 Test set up for walls tested by Ozselcuk (1989) 47
2.24 Transfer relationship derived from 15-story prototype (Ozselcuk, 1989) . 48
2.25 Cyclic-load histories (Ozselcuk, 1989) 48
2.26 Force-displacement response for Specimen 1C (Ozselcuk, 1989) 50

2.27 Force-displacement response for Specimen 2C (Ozselcuk, 1989) 52
2.28 Damage to 1C at web crushing of left wall pier (-1.3% drift) (Ozselcuk, 1989) 53
2.29 Damage to 2C at the end of the test (Ozselcuk, 1989) 54
2.30 Test specimen geometry and reinforcement detail (Lequesne et al., 2010) 58
2.31 Coupling beam reinforcement detail for CW1 (Lequesne et al., 2009) . . . 62
2.32 Coupling beam reinforcement detail for CW2 (Lequesne et al., 2010) . . . 63
2.33 Test setup for walls tested by Lequesne et al. (2010) 63
2.34 Force-displacement response for Specimen CW1 (Lequesne, 2011) 64
2.35 Force-displacement response for Specimen CW2 (Lequesne, 2011) 64
2.36 Damage to wall piers at the end of each test (east wall pier is on the left) (Lequesne, 2011) 65
2.37 Damage to coupling beams at the end of each test (Lequesne, 2011) . . . 66
2.38 Comparison of coupled wall specimens and building inventory geometry . 68

3.1 Elevation of coupled wall specimen CW1 88
3.2 Specimen CW1 reinforcement layout (elevation view) 94
3.3 Coupling beam reinforcement detail 95
3.4 Cross-sectional view of wall pier reinforcement detail 96
3.5 Reinforcement stress-strain response with critical values 98
3.6 Axial-moment interaction diagram of CW1 wall piers 101
3.7 Moment verse curvature axial load interaction for CW1 102
3.8 Photo of LBCB 1 105
3.9 Coupled wall specimen test setup 106
3.10 Elevation view of LBCB and coupled wall specimen test setup 107
3.11 Metris system LED layout 109
3.12 Photogrammetry target layout 111
3.13 Non-contact instrumentation test setup 113
3.14 In-plane linear string potentiometers layout 114
3.15 LVDT layout, (north side of specimen) 115
3.16 Vertical strain gauge layout 116
3.17 Horizontal bar and confinement stirrup strain gauge layout 117
3.18 Coupling beam diagonal bar strain gauge layout 118
3.19 Definition of applied loads for 1/3 scale prototype and specimen 120

3.20 Degrees of freedom associated to the loading protocol 121

4.1 CW1 loading program: drift history 126
4.2 CW1 loading program: load history 126
4.3 CW1 load-drift repsonse 127
4.4 CW1 notation 129
4.5 Damage progression 142
4.6 CW1 initial cracking sequence 145
4.7 CW1 yielding sequence of longitudinal reinforcement 145
4.8 CW1 sequence of spalling concrete 146
4.9 CW1 sequence of transverse reinforcement yielding and bar buckling . . . 146
4.10 Axial-load vs. average vertical displacement 147
4.11 Damage following 0.128% drift level (Step 181), note very minor cracking in wall piers 148
4.12 EWP horizontal crack at -0.136% (0.192% D.C. (A), Step 205) approximately 30 inches above the foundation 149
4.13 Damage following 0.192% drift level (Step 247) 150
4.14 Cracking in CB3 (0.321% D.C. (B), Step 304) 151
4.15 Damage following 0.321% drift level (Step 337) 152
4.16 Damage following 0.50% drift level (Step 454) 153
4.17 Spacing of horizontal cracking along OBE of EWP (0.75% D.C. (A), Step 507), base of tape measure is approximantely 22 inches above foundation 154
4.18 Damage following 0.75% drift level (Step 600) 155
4.19 Spalling of EWP at E+ peak (1.00% D.C. (A), Step 623), bottom of spalling region 12 inches above base of wall 156
4.20 Close up of spalled region shown in Figure 4.19, tape measure referenced to base of wall 156
4.21 Cover damage of WWP at W- peak (1.00% D.C. (A), Step 802) 157
4.22 Spalling of EWP at E+ peak (1.00% D.C. (B), Step 710), top of spalling on far corner is 36 inches from wall base 157
4.23 Spalling of WWP at W- peak (1.00% D.C. (B), Step 754) 158
4.24 Damage following 1.00% drift level (Step 772) 159
4.25 Spalling of top corners on CB2 during the 1.50% drift level 160
4.26 Spalling of EWP at the end of the 1.50% drift level, top of spalling shown 28 inches above wall base 161

4.27 Spalling of WWP at the end of the 1.50% drift level, top of spalling 34 inches above wall base 161
4.28 Damage following 1.50% drift level (Step 932) 162
4.29 Spalling of TWC of CB1 during the 2.25% drift level 163
4.30 Spalling of EWP at 1.89% (2.25% D.C. (A), Step 951) 164
4.31 Backside of EWP at 2.20% (2.25% D.C. (A), Step 954) 164
4.32 Spalling of EWP at 2.20% (2.25% D.C. (A), Step 954) 165
4.33 Front corner of EWP at E+ peak (2.25% D.C. (A), Step 955) 166
4.34 Buckled rebar on south facing side of EWP at E+ peak 166
4.35 South facing side of EWP at E+ peak (2.25% D.C. (A), Step 955) 167
4.36 Backside of EWP at E+ peak (2.25% D.C. (A), Step 955) 167
4.37 Toe of WWP at W- peak (2.25% D.C. (A), Step 1003) 168
4.38 South facing side of WWP at W- peak 169
4.39 West facing edge of WWP at W- peak (2.25% D.C. (A), Step 1003) . . . 170
4.40 Close-up of WWP buckled rebar at W- peak (2.25% D.C. (A), Step 1003) 170
4.41 Failure sequence at 2.25% E+ peak 171
4.42 Failure sequence at -2.25% W- peak 172
4.43 Coupling beam damage at the end of the test (-2.25% Step 1003) 173
4.44 Wall pier damage at the end of the test (-2.25% Step 1003) 174
4.45 Damage to CW1 after axial loading to -1380 kips 175

5.1 Typical stress-strain behavior for CW1 reinforcement 178
5.2 Yielded strain gauges at the end of the 0.75% drift level 180
5.3 Yielded strain gauges at the end of the 1.00% drift level 181
5.4 Yielded strain gauges at the end of the 1.50% drift level 182
5.5 Yielded strain gauges at the end of the +2.25% drift half cycle 183
5.6 Yielded strain gauges at the end of the test 184
5.7 Coupling beam force equilibrium 186
5.8 East peak coupling beam shear demands using steel strain gauges 187
5.9 West peak coupling beam shear demands using steel strain gauges 187
5.10 West wall pier axial force demand during first east peaks 189
5.11 East wall pier axial force demand during first west peaks 189
5.12 West wall pier axial force demand during first west peaks 190
5.13 East wall pier axial force demand during first east peaks 190

5.14 CW1 P-M interaction and maximum measured axial forces for the compression wall piers 193
5.15 Measured degree of coupling (DOC) at the base of CW1 194
5.16 Axial deformations of west wall pier for increasing axial tension demand . 196
5.17 Axial deformations of east wall pier for increasing axial tension demand . 196
5.18 Axial deformations of west wall pier for increasing axial compressive demand 197
5.19 Axial deformations of east wall pier for increasing axial compressive demand 197
5.20 Definition for wall pier axial secant stiffness 198
5.21 Axial stiffness of west wall pier for increasing axial tension demand . . . 200
5.22 Axial stiffness of east wall pier for increasing axial tension demand 200
5.23 Axial stiffness of west wall pier for increasing axial compressive demand . 201
5.24 Axial stiffness of east wall pier for increasing axial compressive demand . 201
5.25 West wall pier compressive axial stiffness at peak cycles A and B 202
5.26 East wall pier compressive axial stiffness at peak cycles A and B 202
5.27 VecTor2 base shear distribution vs. drift results 203
5.28 VecTor2 base moment distribution vs. drift results 204
5.29 Flexural stiffness of wall piers plotted with TWP axial force (E+ Peaks) 206
5.30 Flexural stiffness of wall piers plotted with TWP axial force (W- peaks) . 206
5.31 Flexural stiffness of WWP for increasing axial compressive demand . . . 207
5.32 Flexural stiffness of EWP for increasing axial compressive demand 207
5.33 Equilibrium and the assumed linear strain profile used to determine the stress demands at the base of the compression pier 209
5.34 Vertical strain profile for the EWP at failure 210
5.35 Vertical strain profile for the WWP at failure 211
5.36 Example of five-node quadrilateral element used in strain calculation . . 214
5.37 ϵ_2 field at ± 0.321% (A) (diagonal cracking) 217
5.38 ϵ_2 field at ± 0.50% (A) (yielding) 218
5.39 ϵ_2 field at ± 1.00% (A) (initial spalling) 219
5.40 ϵ_2 field at ± 1.50% (A) (moderate spalling) 220
5.41 ϵ_2 field near failure of the east wall pier (2.25% E+ drift level) 221
5.42 γ field at ± 0.321% (A) (diagonal cracking) 222
5.43 γ field at ± 0.50% (A) (yielding) 223
5.44 γ field at ± 1.00% (A) (initial spalling) 224

5.45 γ field at ± 1.50% (A)(moderate spalling) 225
5.46 γ field near failure of the east wall pier (2.25% E+ drift level) 226
5.47 Location of WWP LEDs used to calculate vertical strain values 227
5.48 Variation of ϕ with net tensile strain, ϵ_t (ACI, 2008) 229
5.49 Lateral third story drift history for EWP 233
5.50 Lateral third story drift history for WWP 234
5.51 Layout of EWP instrumentation used to calculate drift contributions . . 235
5.52 Wall pier deformation mechanisms for a typical element 236
5.53 Contribution to total drift from different response mechanisms 238
5.54 Contributions to total drift during 0.321% drift level (diagonal cracking) 239
5.55 Contribution to total drift during 0.50% drift level (yielding) 239
5.56 Contribution to total drift during 1.00% drift level (initial spalling) . . . 240
5.57 Contribution to total drift during 1.50% drift level (moderate spalling) . 240
5.58 Contribution to total drift during 2.25% drift level (failure) 241
5.59 Definition of coupling beam end rotation 243
5.60 East peak coupling beam rotation 244
5.61 West peak coupling beam rotation 244
5.62 Wall pier and coupling beam rotation relationship 248
5.63 Ratio of wall pier and coupling beam rotations for east peaks 249
5.64 Ratio of wall pier and coupling beam rotations for west peaks 249
5.65 Hinge rotation instrumentation and notation for CB1 and CB2 250
5.66 Comparison between experimental end and hinge rotational measurements 251

6.1 Story height vs. axial compression demand (ACD) 256
6.2 Story height vs. axial demand capacity ratio of the tension wall, DCR_{axial} 256
6.3 Story height vs. plastic base shear stress demand, v_p 257
6.4 Story height vs. base shear demand capacity ratio, DCR_{shear} 257
6.5 Story height vs. degree of coupling (DOC) 258
6.6 Story height vs. coupling beam aspect ratio (AR) 258
6.7 Damage sequence chart for CW1 263
6.8 Damage sequence chart for Santhakumar WallA 264
6.9 Damage sequence chart for Santhakumar WallB 265
6.10 Damage sequence chart for Shiu CS1 266

6.11 Damage sequence chart for Shiu RCS1 267
6.12 Damage sequence chart for Ozselcuk 1C 268
6.13 Damage sequence chart for Lequesne CW1 269
6.14 Damage sequence chart for Lequesne CW2 270
6.15 Comparison of coupled wall damage states 271

7.1 Equivalent frame model for an elastic analysis of a coupled wall specimen 274
7.2 Effective stiffness values 277
7.3 Effective stiffness values derived from experimental results (Birely, 2011) 288
7.4 Predicted and measured responses for CW1 293
7.5 Predicted and measured responses for Ozselcuk 1C 293
7.6 Predicted and measured responses for Santhakumar WallA 294
7.7 Predicted and measured responses for Santhakumar WallB 294
7.8 Predicted and measured responses for Lequesne CW1 295
7.9 Predicted and measured responses for Lequesne CW2 295
7.10 Predicted and measured responses for Shiu CS1 296

8.1 Fiber cross-section for CW1 307
8.2 Steel and concrete constitutive models (“Hysteretic” and “Concrete01”) . 310
8.3 Nonlinear analysis CW1 force-drift response 314
8.4 Nonlinear analysis Ozselcuk 1C force-drift response 315
8.5 Nonlinear analysis Santhakumar WallA force-drift response 315
8.6 Nonlinear analysis Santhakumar WallB force-drift response 316
8.7 Nonlinear analysis Shiu CS1 force-drift response 316
8.8 LPM model distribution of shear at base of CW1 319
8.9 DPM model distribution of shear at base of CW1 319
8.10 LPM model distribution of shear at base of Ozselcuk 1C 320
8.11 DPM model distribution of shear at base of Ozselcuk 1C 320
8.12 LPM model distribution of shear at base of Santhakumar WallA 321
8.13 DPM model distribution of shear at base of Santhakumar WallA 321
8.14 LPM model distribution of shear at base of Santhakumar WallB 322
8.15 DPM model distribution of shear at base of Santhakumar WallB 322
8.16 LPM model distribution of shear at base of Shiu CS1 323
8.17 DPM model distribution of shear at base of Shiu CS1 323

8.18 LPM model distribution of moment at base of CW1 327
8.19 DPM model distribution of moment at base of CW1 327
8.20 LPM model distribution of moment at base of Ozselcuk 1C 328
8.21 DPM model distribution of moment at base of Ozselcuk 1C 328
8.22 LPM model distribution of moment at base of Santhakumar WallA . . . 329
8.23 DPM model distribution of moment at base of Santhakumar WallA . . . 329
8.24 LPM model distribution of moment at base of Santhakumar WallB . . . 330
8.25 DPM model distribution of moment at base of Santhakumar WallB . . . 330
8.26 LPM model distribution of moment at base of Shiu CS1 331
8.27 DPM model distribution of moment at base of Shiu CS1 331
8.28 Shear stress demand in CB2 for CW1 models 334
8.29 Tension wall pier axial load caparison, CW1 335
8.30 Compression wall pier axial load caparison, CW1 335
8.31 Tension wall pier axial load caparison, Santhakumar WallA 336
8.32 Compression wall pier axial load caparison, Santhakumar WallA 336
8.33 Tension wall pier axial load caparison, Santhakumar WallB 337
8.34 Compression wall pier axial load caparison, Santhakumar WallB 337
8.35 Tension wall pier axial load caparison, Ozselcuk 1C 338
8.36 Compression wall pier axial load caparison, Ozselcuk 1C 338
8.37 Tension wall pier axial load caparison, Shiu CS1 339
8.38 Compression wall pier axial load caparison, Shiu CS1 339

9.1 Drift capacity vs. degree of coupling (DOC) 343
9.2 Drift capacity vs. plastic base shear stress demand, v_p 344
9.3 Drift capacity vs. axial compression demand (ACD) 345
9.4 CW1 P-M interaction and analysis results for the compression wall pier . 353

C.1 ϵ_z field at ± 0.321% (A) (diagonal cracking) 396
C.2 ϵ_z field at ± 0.50% (A) (yielding) 397
C.3 ϵ_z field at ± 1.00% (A) (initial spalling) 398
C.4 ϵ_z field at ± 1.50% (A)(moderate spalling) 399
C.5 ϵ_z field near failure of the east wall pier (2.25% E+ drift level) 400

LIST OF TABLES

Table Number Page

1.1 NEESR Wall Specimen Test Matrix 2

2.1 Test matrix of planar wall experimental test program (Birely, 2011) . . . 15
2.2 Average coupling beam experimental results reviewed by Mohr (2007) . . 17
2.3 Average coupling beam experimental results conducted by Naish et al. (2009) 18
2.4 General information for previous coupled wall research programs 68
2.5 Coupled wall properties 69
2.6 Wall pier boundary element reinforcement properties 70
2.7 Wall pier web region reinforcement properties 71
2.8 Coupling beam reinforcement properties 72
2.9 Coupled wall experimental results 74

3.1 Concrete material properties 97
3.2 Steel material properties 97
3.3 Final loading protocol 124
3.4 Prescribed loading history 124

4.1 Maximum crack widths 139
4.2 Summary of Wall 5 damage 143

5.1 Axial load demands estimated at the base of each wall pier 191
5.2 Estimated demands in each wall pier at failure using Metris system . . . 212
5.3 Estimated demands in each wall pier at failure using moment-curvature . 212
5.4 Vertical strain, ϵ_z, measurements at base of each wall pier ($\mu\epsilon$) 228
5.5 Tension-controlled verification of compression wall piers 230
5.6 Tension-controlled verification of compression wall pier for design 231

6.1 Performance analysis results 254
6.2 Notation used in Figures 6.7 – 6.14 260

6.3 Wall pier damage states 261
6.4 Coupling beam damage states 262
6.5 Coupled wall experimental drift capacity comparison 272

7.1 Summary of effective stiffness values for coupled wall elements 276
7.2 ASCE/SEI 41-06 effective stiffness values for coupled wall components . . 278
7.3 NSZ 3101 effective second moment of inertia values for coupled walls . . 282
7.4 NZS stiffness reduction to account for diagonal cracking in beams 282
7.5 Summary of predicted drift at yield for linear elastic analyses 290
7.6 Summary of predicted base shear at yield for linear elastic analyses . . . 291
7.7 Summary of predicted secant stiffness at yield for linear elastic analyses . 292
7.8 Elastic analysis drift error at yield 299
7.9 Elastic analysis base shear error at yield 299
7.10 Elastic analysis secant stiffness error at yield 300
7.11 Wall pier analytical axial force results for CW1 301
7.12 Wall pier analytical axial force results for Ozselcuk 1C 302
7.13 Axial stiffness study for Mohr/Birely model (Case F) 303
7.14 Recommended effective stiffness values for coupled wall components . . . 304

8.1 Cracked flexural stiffness properties for LPM 308
8.2 Wall pier element quadrature point selection 311
8.3 Coupling beam element quadrature point selection 311
8.4 Drift results for LPM and DPM at critical limits states 313
8.5 Nonlinear analysis wall pier base shear stress demands 318
8.6 LPM wall pier base moment distributions 326
8.7 DPM wall pier base moment distributions 326
8.8 Tension wall pier axial results for LPM and DPM 332
8.9 Compression wall pier axial results for LPM and DPM 333

9.1 Recommended effective stiffness values for coupled wall components . . . 346
9.2 Percentage of total base shear resisted by CWP 348
9.3 Maximum experimental base shear demand capacity ratio assuming all shear is resisted by CWP 350
9.4 Compression wall pier axial results at yield and plastic strength 351

9.5 Ratio of CWP moment, M_{cw}, to total moment resisted by both wall piers, $M_{tw} + M_{cw}$ 352

B.1 Record of SimCor step numbers where instruments did not record data . 377
B.2 CW1 peak drift steps 378
B.3 Log of testing comments 379
B.4 Log of measured crack widths 390

D.1 CW1 effective stiffness values used in linear elastic analysis 402
D.2 Santhakumar WallA effective stiffness values used in linear elastic analysis 403
D.3 Santhakumar WallB effective stiffness values used in linear elastic analysis 404
D.4 Shiu CS1 effective stiffness values used in linear elastic analysis 405
D.5 Ozselcuk 1C effective stiffness values used in linear elastic analysis 406
D.6 Lequesne CW1 effective stiffness values used in linear elastic analysis . . 407
D.7 Lequesne CW2 effective stiffness values used in linear elastic analysis . . 408

ACKNOWLEDGMENTS

The author would like to acknowledge and thank professors Laura Lowes and Dawn Lehman for providing their guidance and assistance over the past two years. Additionally, professor John Stanton is also thanked for serving on this defense committee, providing advice and assistance. Professor Dan Kuchma from the University of Illinois, Urbana-Champaign is thanked for his help serving as a co-PI.

The author would also like to acknowledge the contributions of Professor Emeritus Neil Hawkins; Ron Klemencic and John Hooper of Magnusson Klemencic Associates, Seattle; Andrew Taylor, of KPFF, Seattle and Joe Maffei, of Rutherford & Chekene, San Francisco in advising the practical aspects of the research program. The research presented herein was funded by the National Science Foundation through the Network for Earthquake Engineering Simulation Research Program, grant CMS-042157, Joy Pauschke, program manager.

The author would like to acknowledge the contributions of graduate student researchers Anna Birely, Josh Pugh and Danya Mohr from the University of Washington as well as the contributions of graduate student researchers Chris Hart and Ken Marley from the University of Illinois, Urbana-Champaign.

Finally, the author would like to especially thank his wife Katelyn for her patience and support throughout thoughout this process.

Chapter 1

INTRODUCTION

Reinforced concrete structural walls are used commonly as the primary lateral-load resisting system for new and retrofit construction. However, despite the heavy reliance on wall systems by practicing engineers, recent efforts to develop performance-based earthquake engineering (PBEE) methods have not yet begun to address structural walls. Today engineers have few resources to consult regarding the simulation of wall response using practical linear and nonlinear numerical models or the prediction of wall damage (e.g., concrete crack width and concrete spalling) as a function of engineering demands (e.g., story drift). However, few previous experimental investigations provide data that characterize the earthquake response of walls with representative configurations, reinforcement layouts, base conditions and load patterns.

As a result the high-fidelity response and damage data that are required to support the development modern performance-based design tools is lacking. The research presented here represents part of a multi-year research effort to develop tools to enable performance-based design of structural walls. This effort includes (i) experimental testing of planar, coupled, and c-shaped wall components as well as a three-dimensional wall system to generate high-resolution response and damage data, (ii) development of model and modeling recommendations to enable simulation of earthquake response of wall structures and prediction of demands, and (iii) development of damage-prediction models for PBEE.

The first phase of this effort focuses on behavior, analysis and design of slender walls and includes a series of laboratory tests of slender wall sub-assemblages with design details representative of modern construction and load histories representative of those that develop in mid-rise buildings. Table 1.1 shows the proposed test matrix for the project, which includes planar, coupled, C-shaped walls. These categories of structural walls represent both individual walls found in seismic-resisting buildings as well as components of core-wall (typically elevator core) buildings.

Table 1.1: NEESR Wall Specimen Test Matrix

	Moment – Shear Ratio	**Design Details**
Unidirectional Loading	 Planar (2) 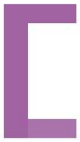 Flanged  Coupled	 Uniformly Distributed Long. Reinforcement  No Splice
Bidirectional Loading	 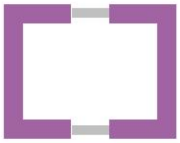 Core-Wall System	

To ensure that wall response is representative, it is necessary that wall subassemblages tested in the laboratory be relatively large scale with boundary conditions and reinforcement layouts that are representative of those that develop in the bottom stories of a mid-height building. The NEES "Multi-Axial Full-Scale Sub-Structured Testing and Simulation" (MUST-SIM) facility at the University of Illinois, Urbana-Champaign (UIUC) is being used. The MUST-SIM facility is a part of the George E. Brown Network for Earthquake Engineering Simulation (NEES), and it provides a testing, analysis and visualization-display environment that combines the ability to test large-scale subassemblies under complex loading and boundary conditions. Specifically, laboratory specimens were 1/3-scale models of the bottom three stories of a representative 10-story building.

The application of loads was achieved through using traditional ancillary actuators at each “floor” and load-and-boundary-condition boxes (LBCBs) to apply shear, moment, and axial load at the top of the specimen.

Common core wall configurations include solid walls in one direction and walls with openings in the orthogonal direction to accommodate required architectural openings for elevators or other access systems. Therefore, in the orthogonal direction, the walls are coupled together with heavily reinforced beams. Typically, these beams have lower aspect ratios and prior earthquake damage has proven they are susceptible to significant damage if not properly designed for the plastic shear demand or detailed to accommodate the required rotations to meet the system drifts. A significant amount of research has focused on individual coupling beams, and these results have dramatically improved the seismic performance of the beams. However, the few research programs have studied the seismic behavior of actual modern coupled walls systems, and most have focused on low-rise structures. Yet, most commonly coupled walls are used in elevator cores, which are more typical in mid-rise construction.

The research program described herein was undertaken to specifically study this category of structural system. The second phase of the experimental testing program included one test of a coupled wall specimen, CW1. High-resolution data was analyzed to thoroughly investigate the seismic behavior of the specimen. Performance-based design parameters as well as observed damage and specimen behavior were also compared to previous large-scale coupled wall experiments. Experimental data for a set of these coupling wall tests was then compared to linear and nonlinear equivalent frame analyses to validate the capabilities of these types of analyses for predicting the behavior of a coupled wall system. Finally design recommendations are given to improve the performance-based design of coupled wall systems.

Chapter 2

PREVIOUS RESEARCH TO ADVANCE PERFORMANCE-BASED SEISMIC DESIGN OF COUPLED CONCRETE WALLS

Current methods used in the design of coupled wall systems are discussed as a part of the following chapter. In addition to these design procedures, a review of research addressing the seismic design of coupled walls is discussed. A great deal of analytical and experimental research on coupled wall components such as wall piers and coupling beams have been undertaken in order to understand coupled wall behavior and develop design procedures. In this chapter, a small portion of this research is briefly summarized. While, a summary is provided of component research, a detailed review of previous coupled wall experiments are studied in order to verify component behavior and support the testing of a one-third coupled wall specimen as a part of this research program. Finally, simulations of coupled wall systems are reviewed in order to investigate analytical research techniques used for these systems.

2.1 Seismic Response of a Coupled wall

Primary goals of seismic design of a coupled wall are to design the wall such that during a seismic event energy is dissipated through yielding of coupling beams up the height of the wall as well as through flexural yielding of the wall piers. This response mechanism is idealized by the plastic mechanism shown in Figure 2.1. To ensure ductile response and significant energy dissipation from the system, the ACI 318 design code requires that i) coupling beam shear demands are limited, ii) coupling beams be capacity designed for shear, iii) coupling beams be designed with confining reinforcement to delay buckling of longitudinal reinforcement, and iv) wall pier boundary elements be confined by transverse steel. Also to ensure ductile response, the 2006 IBC Structural/Seismic Design Manual (ICC, 2007) recommends that pier walls be capacity designed for shear.

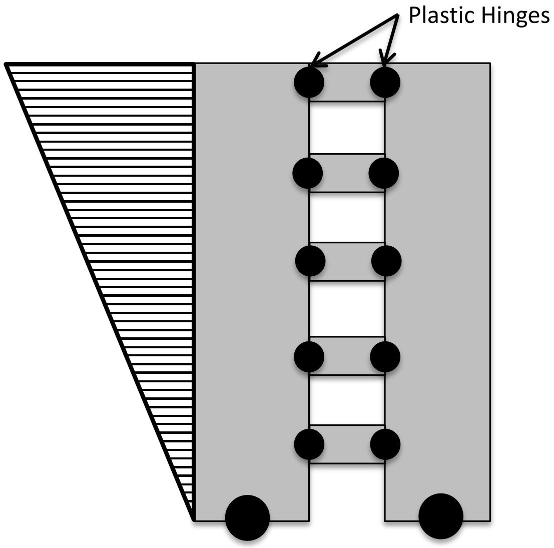

Figure 2.1: Desired plastic mechanism

2.2 Current Design Methods

The design of a coupled wall system is currently done following the 2006 International Building Code (IBC) (ICC, 2006). In particular, engineers are required to use ASCE 7-05 (ASCE, 2010) to determine appropriate design forces and ACI 318-08 (ACI, 2008) to design and detail the coupling beams and wall piers as well as other structural concrete components. The 2006 IBC Structural/Seismic Design Manual, Vol. 3 (ICC, 2007) was recently published by the International Code Council to provide engineers with a detailed design example for a reinforced concrete coupled shear wall that meet ACI 318 code requirements. The following is a summary of the recommended design procedure for a coupled wall.

1. Size wall piers and coupling beams on the basis of initial geometric requirements.

2. Calculate the factored vertical and lateral load combinations to be used in structural analysis following on the 2006 International Building Code (IBC) requirements, which are adopted from ASCE 7-05 (ASCE, 2010).
3. Perform an elastic analysis to determine the distribution of internal force demands within the coupled wall using the applied load combinations calculated above. Reinforced concrete coupled wall components are assigned effective elastic stiffness values, defined as a fraction of the gross section properties of the member, per the recommendations of ACI 318 or a reasonable alternative.
4. Using the controlling load combinations, design the coupling beams and wall piers following the ACI 318 strength based design requirements.
5. Perform a plastic analysis of the coupled wall using the recommended plastic mechanism (Figure 2.1).
6. Design the wall piers for either the factored shear demand resulting from the elastic analysis or the plastic shear demand calculated as a result of the recommended plastic analysis.
7. Detail the boundary elements of the wall piers in accordance to ACI 318
8. Detail the transverse reinforcement of the coupling beams in accordance to ACI 318

The design procedure recommended in the IBC Seismic Design Manual includes a plastic analysis to better predict design forces. The preferred IBC plastic mechanism is the same mechanism illustrated in Figure 2.1 and described in the section above where all the coupling beam ends form plastic hinges as well as the base of each wall pier. While a plastic analysis is not required by ASCE/SEI 7-05 or ACI 318, it is recommended in the Seismic Design Manual to estimate the shear demand corresponding to flexural strength of the wall piers and coupling beams as well as to identify potential plastic hinge regions where special detailing may be needed. In the design example, the plastic analysis is performed after preliminary design of the coupling beams and wall piers and includes the following steps.

1. Depending on the geometry/layout, lateral load distribution and relative strength between the wall piers and coupling beams, there may be multiple plastic mechanisms that form during an earthquake. Therefore, all the possible plastic mechanisms must be considered, and the one with the highest plastic base shear demand should be chosen. The coupled wall components should be proportioned so the preferred mechanism discussed above (i.e. Figure 2.1) controls.

2. The probable moment strength, M_{pr}, of the coupled wall components are then calculated per ACI 318-08 §21.0. This calculation assumes the tensile stress in the longitudinal reinforcement is $1.25f_y$ and the strength reduction factor, $\phi = 1.0$. The factor of 1.25 accounts for overstrength in the reinforcing steel as well as accounts for strain hardening in the steel at nominal moment strength of the section. The axial tension and compression effects due to overturning in the coupled wall are neglected in the calculation of the wall pier moment strength because the increase in moment strength due to axial compression in the compression pier will be canceled out by the reduction in moment strength due to axial tension in the tension pier.

3. The plastic shear demand at the base of the coupled wall is then predicted by equating the internal work and external work of the coupled wall and solving for the base shear demand. The external work at each story is calculated by multiplying the story force times the story displacement; this worked is summed for all the lateral external forces. The internal work is the sum of $M_{pr} \times \theta$ for all of the defined plastic hinge regions.

4. Calculate the shear amplification factor, ω_v, to account for inelastic dynamic effects

(if applicable lateral load distribution is used).

5. Shear reinforcement in the wall piers is designed to resist the plastic shear demand from the plastic analysis. The plastic shear demand at any given story is assumed to be equally distributed among all of the wall piers and must be less than or equal to the sum of all the wall piers shear strengths.

2.3 Research Addressing Earthquake/Seismic Design of Coupled Walls

Current design methods use procedures that are based primarily on strength design of coupling beams and wall piers, and the recommended plastic analysis allows the wall piers to be capacity designed against the demands associated with a plastic mechanism (Figure 2.1). In addition to these design procedures, a few recent research studies have addressed design of coupled wall to improve performance under seismic loading. Studies by Harries (2001) and Stringer (2007) are reviewed here.

2.3.1 Degree of Coupling, Harries (2001)

In a coupled wall system, the accumulation of shear from the coupling beams results in large axial loads in the wall piers. Because the compression wall pier becomes stiffer as a results increasing axial, the coupling beams endure greater ductility demands due to the much stiffer wall component. Harries (2001) reviewed the results of 30 previous coupled wall nonlinear analyses and compared the distribution of internal forces as well as component load and deformation demands with the the ductility capacities of 29 previously tested coupling beam specimens. The goal of his research was to determine whether coupling beams can be designed to provide the ductility and deformability necessary for a coupled wall system to achieve a desired plastic mechanism.

Most of the coupled wall models were two-pier coupled planar walls which were idealized designs or experimental specimens. However, two of the models were actual buildings subjected to ground motions which occurred nearby. On the other hand, a large portion of the models were subjected to the east-west component of the 1940 El Centro ground motion record. Additionally, four models were static pushovers. The peak values from each analysis were used to determine the ductility demands of the coupling beams and wall piers. The analytical degree of coupling (DOC) for each analyses was also included in their study and these results correspond to first yield of any coupling beam in the model. Because this is a review of several research projects, the peak ground motion parameters are not consistent. However, most of the models were subjected to ground motions which were representative of severe earthquakes.

Harries found that the average computed coupling beam ductility demand for all the analyses was approximately 10.1 with a standard deviation of 4.61. However, the average experimental coupling beam ductility capacity was approximately 4.1 with a standard deviation of 2.12. The ductility capacity of the coupling beams was determined when at least 80% of the ultimate shear capacity was reached. These tests were large-scale experiments of "reasonalby well detailed" coupling beams (19 of which contained diagonal reinforcemnt).

The author also computed the DOC of the system at first yield using analysis results. The degree of coupling defines the % of the total base moment transfered through the tension-compression couple (i.e. the coupling moment) and this mechanism is illistrated in Figure 2.2. The DOC is computed using the following equation:

$$DOC = \frac{TL}{M_{cw} + M_{tw} + TL} \tag{2.1}$$

where, T is the axial load in the wall due to the accumulation of coupling beam shear, L is the distance between the wall pier centriodal axes and M_{cw} and M_{tw} are the moments in the compression and tension wall piers, respectively. In general as the degree of coupling increases, a coupled wall will behave more like a punched wall and limits the energy dissipation mechanism to the base of the wall piers, which is not desirable. Other definitions of the degree of coupling which account for story height, nonlinearity and

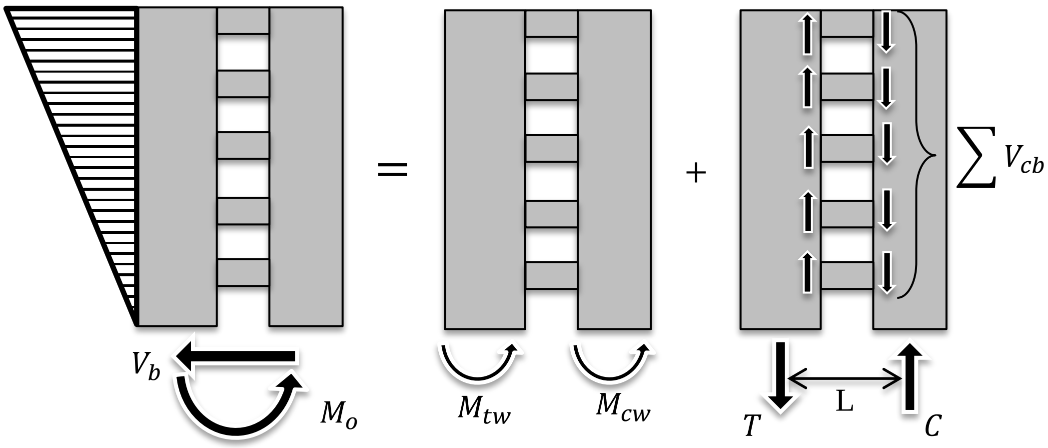

Figure 2.2: Distribution of moments in a typical coupled wall (Harries, 2001)

coupling beam geometry, are presented by Harries (2001).

Using the analysis results, the author compared the computed coupling beam ductility demands with the degree of coupling predicted from the analyses; this relationship is presented in Figure 2.3. The author concluded from these results that as the degree of coupling increases, the ductility demands on the coupling beams increase. This relationship is due to the interaction between the coupling action and the flexural behavior of the wall piers (i.e. stiffer and stronger coupling beams equal larger ductility demands). As a result, the author suggests limiting the strength of the coupling beam so the degree of coupling does not exceed 50% for a coupled wall system built with conventionally reinforced coupling beams and 55% for a coupled wall system built with diagonally reinforced coupling beams.

2.3.2 Seismic Performance of Coupled Shear Wall Buildings, Stringer (2007)

To investigate the performance of mid- to high-rise coupled wall buildings designed for construction on the West Coast of the United States, Stringer (2007) used the degree of coupling (Equation 2.1, Harries (2001)) as well as two other demand capacity ratios

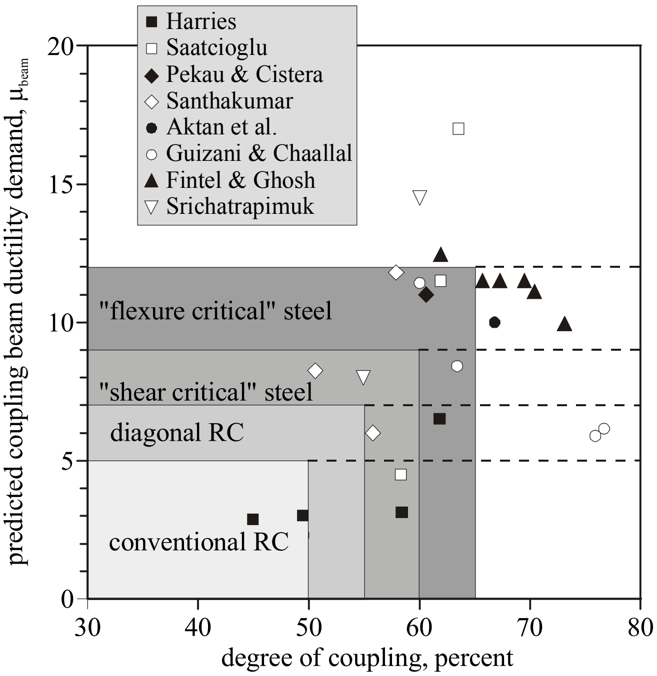

Figure 2.3: Coupling beam ductility demand versus degree of coupling from analysis (Harries, 1999). These data were determined from the coupled wall analyses

(DCRs) to evaluate 13 coupled wall buildings ranging from 10 to 60 stories, designed for construction in high seismic regions of Washington and California. All of the buildings considered included core wall systems in which the coupled walls form the elevator core. Wall configurations included planar, C and L shaped walls. The building inventory reviewed by Stringer (2007) is discussed in more detail in Chapter 3 as a part of the design of the coupled wall specimen, CW1.

As shown by Harries (2001), the degree of coupling is a simple but effective way to assess the extent to which frame action in a coupled wall system resists lateral forces. With higher degrees of coupling, there is a need to consider the axial force demand in the tension wall and the tensile capacity of the reinforcement in the tension pier. Stringer (2007) used Equation 2.2 to compute this demand-capacity ratio for the set of coupled wall buildings.

$$DCR_{axial} = \frac{N_{tw}}{\sum A_s f_y} \tag{2.2}$$

where, the axial force in the tension wall, N_{tw}, includes both the axial load in the wall piers due to the accumulation of coupling beam shear, $\sum V_{cb}$, as well as an gravity load present in the structure. The accumulation of coupling be shear is illustrated in Figure 2.2 for a typical coupled wall configuration. The tensile capacity of the wall is the total area of longitudinal steel, A_s, available to resist tension, including longitudinal reinforcement in the wall web and flanges, multiplied by the yield strength of the reinforcement, f_y. If the DCR_{axial} is less than one, the tensile yield capacity of the wall pier will be exceeded before the desired plastic mechanism is achieved.

The last evaluation measure used by Stringer to evaluate couple wall performance was the shear demand-capacity ratio of the wall piers:

$$DCR_{shear} = \frac{V_b}{V_{n,w}} \tag{2.3}$$

where, $V_{n,w}$ is the shear capacity at the base of the wall computed per ACI 318-08 and the shear demand, V_b, at the base of the wall computed from a plastic analysis using the mechanism shown in Figure 2.1.

2.4 Summary of Previous Experimental Coupled Wall Components

To verify and develop the design methods discussed in the previous sections, numerous experimental tests of coupled wall components including reinforced concrete walls and coupling beams, have been conducted the past ≈ 40 years. These tests are briefly summarized here. Birely (2011) provides a detailed review of multiple experimental test programs investigating the performance of slender wall specimens as well as results from four planar wall tests completed by researchers at the University of Washington and the University of Illinois Urbana-Champaign. Mohr (2007) provides a detailed review of multiple research programs investigating the performance of reinforced concrete coupling beams. In addition to these reviews, a summary of experimental coupling beam research conducted by researchers Naish et al. (2009) at the University of California Los Angeles is presented below.

2.4.1 Planar Walls

To evaluate the performance and design of slender reinforced concrete walls, data from laboratory tests of approximately 70 slender-wall specimens were reviewed by Birely (2011). These walls were selected from the literature using the following guidelines:

- Walls were conventionally reinforced, (i.e. with reinforcement placed horizontally and vertically)
- The shear-span-to-depth ratio was greater or equal to two,
- Walls did not have any openings,
- Walls were subjected to quasi-static loading, and
- Wall cross-sections were rectangular, barbell, C-shaped, I-shaped and T-shaped

Birely (2011) summarizes from these tests the purpose of the experimental research, the scope of the test program, damage progression and failure mode, and force-displacement behavior. Damage and response data were used to develop fragility functions defining the likelihood of a slender wall developing a specific damage state given a specific level of earthquake demand. In addition to the database of slender wall tests, Birely (2011) also reviewed earthquake reconnaissance reports and journal articles published after earthquakes in an effort to qualitatively determine reinforced concrete wall damage (i.e. boundary element compressive damage, web crushing, etc). As a results of this damage data synthesis, Birey, determined the most frequent type of observed damage in walls (more than 20% of all observed damage) was compressive damage in the form of concrete crushing and bar buckling.

Table 2.1: Test matrix of planar wall experimental test program (Birely, 2011)

Specimen	**Reinforcement**	**Lateral Load Distribution**	**Expected Shear Stress Demand**	**Splice?**
PW1	B.E.	ASCE 7	$2.75\sqrt{f'_c}$	Yes
PW2	B.E.	Uniform	$3.90\sqrt{f'_c}$	Yes
PW3	Uniform	Uniform	$3.90\sqrt{f'_c}$	Yes
PW4	B.E.	Uniform	$3.90\sqrt{f'_c}$	No

Birely (2011) also presented results of four planar wall tests conducted using the UIUC NEES Laboratory as apart of the NEESR "Design, Behavior and Analysis of Complex Walls" research project. These test specimens represented the bottom three stories of a modern 10-story planar wall, and specimens were subjected to load distributions representative of those that could be expected to develop in a mid-rise building subjected to earthquake loading. The parameters investigated in the test program included lateral load distribution and the associated shear demand, longitudinal reinforcement distribution, and the presence of a splice in the reinforcement at the base of the wall. Table 2.1 presents the test matrix for the planar wall test program where, f'_c is the concrete compressive strength.

Conclusions to the research conducted by Birely (2011) was as follows:

- Fragility functions calculated from observed laboratory test data suggest there is a high likelihood of cracking and steel yielding (DS1) occurring at a much earlier drift range than minor concrete spalling (DS2) (e.g. the drifts at 80% likelihood of achieving DS1 vs. DS2 are approximately 0.33% and 1.4%, respectively).

- However, the drift range for which more severe spalling occurs (i.e. spalling that exposes longitudinal reinforcement or DS3) closely relates to the previous damage state (e.g. approximately 1.6% drift at 80% likelihood of achieving DS3).

- Finally, DS4, which typically results in replacement of the wall pier (i.e. concrete crushing and bar buckling), occurred over a range from 0.75 to 4% drift and at 80% likelihood of achieving DS4, the drift was approximately 2.75%

- Based on previous experimental research, wall drift capacities has been shown to be sensitive to axial load, shear demand, confining reinforcement ratio and shear span ratio. The majority of damage patterns observed during wall tests was similar to post-earthquake damage (i.e. compressive damage in the form of concrete crushing and bar buckling).

- The following summarize the results of four planar wall tests conducted as a part of this research program: 1) shear demand (i.e. moment-to-shear ratio parameter in these tests) has an negative impact on drift capacity, 2) the presence of a splice at the base of a wall may result in a relocation of the critical section (e.g. from the base of the wall to the top of the splice) and 3) the wall with uniform layout of longitudinal reinforcement (PW3) experienced a lot of web crushing compared to the similar wall with reinforcement concentrated in the boundary elements.

2.4.2 Coupling Beams

Mohr (2007)

In an effort to evaluate the performance nonlinear finite element models of reinforced concrete coupling beams, Mohr (2007) assembled data from 22 coupling-beam tests conducted by three research groups between 1996 and 2007. The data included coupling beam geometries, material properties, experimental load-displacement results and observed damage. All specimens employed design details that were considered "modern" compared to a defined a range of design parameters included in a building inventory reviewed by Mohr. The building inventory used in Mohr's study was the same inventory discussed by Stringer (2007) in Section 2.3. Mohr (2007) selected coupling-beam test specimens for inclusion in his study on the basis of the following criteria:

- Only coupling beams typical of modern construction were used (i.e. coupling beam design parameters were within the range seen in the building inventory)
- Coupling-beam test specimens were tested under cyclic or monotonic, quasi-static loading
- Researchers provided sufficient data characterizing geometry, material properties and performance to enable creation and evaluation of numerical models.

The test specimens included in Mohr's dataset ranged in aspect ratio, reinforcement ratio, level of confinement and reinforcement layout. Table 2.2 provides details for the data set.

Table 2.2: Average coupling beam experimental results reviewed by Mohr (2007)

Reinforcement Layout	**# of Tests**	**Aspect Ratio**	$v_{y,cb}$ ($\sqrt{f'_c}$)	$v_{u,cb}$ ($\sqrt{f'_c}$)	$\theta_{u,cb}$ (%)
Conventional	15	1.48	3.24	3.82	6.14
Diagonal	7	1.41	3.53	4.23	6.34

where,

$v_{y,cb}$	coupling beam shear stress demand when reinforcement yields
$v_{u,cb}$	coupling beam ultimate shear stress demand specified by researcher
$\theta_{u,cb}$	coupling beam ultimate rotational drift capacity

Naish et al. (2009)

In a more recent coupling beam test program, Naish et al. (2009) tested seven diagonally reinforced coupling beams with aspect ratios (AR) of 2.4 and 3.33. These aspect ratios represent two common building configurations: residential (AR = 2.4) and office (AR =

3.33). The confining reinforcement for each specimen was either "diagonal confinement" designed according to ACI 318-05, "full-section confinement" designed according to ACI 318-08 or "full-section confinement" with the total volume of confining reinforcement reduced to half that is required by ACI 318-08 to study the impact of reduced confinement on performance. Three specimens were constructed with a four inch thick slab; in two of the cases, the slabs were post-tensioned and in the other case the slab was reinforced with mild steel. The average results of these tests for the two different aspect ratios are presented in Table 2.3.

Table 2.3: Average coupling beam experimental results conducted by Naish et al. (2009)

Reinforcement Layout	**# of Tests**	**Aspect Ratio**	$v_{y,cb}$ ($\sqrt{f'_c}$)	$v_{u,cb}$ ($\sqrt{f'_c}$)	$\theta_{u,cb}$ (%)
Diagonal	5	2.4	9.50	12.2	8
Diagonal	2	3.33	5.70	6.84	6

where,

$v_{y,cb}$	coupling beam shear stress demand when reinforcement yields
$v_{u,cb}$	coupling beam ultimate shear stress demand specified by researcher
$\theta_{u,cb}$	coupling beam ultimate rotational drift capacity

Naish et al. (2009) concluded that beams detailed with full-section confinement (ACI 318-08) perform better than beams with diagonal confinement (ACI 318-05) with respect to ductility; they note also that full-section confinement details eliminates congestion in the coupling beam. In this study, the beam built continuous with the reinforced concrete slab was 17% stronger than the beam without, and the beam with the post-tensioned slab was 25% stronger than the beam without a slab. This increase in strength was attributed to the additional flexural strength provided by the slab and the applied axial load of the post-tensioning.

2.5 Review of Previous Experimental Tests of Coupled Walls

A significant amount of research has focused on individual coupling beams, and these results have dramatically improved the seismic performance of the beams. However, few research programs have studied the seismic behavior of coupled wall systems, and most of these previous studies have considered coupled-walls in low-rise structures. Most coupled walls are used in elevator cores, which are more typical in mid- to high-rise construction. The following reviews and summarizes eight coupled-wall tests conducted by four research teams; the results of these tests are used throughout the current study to improve understanding of the behavior of coupled walls and develop recommendations for analysis and design of coupled walls. These experiments were selected using the following criteria:

1. Specimens were subjected to quasi-static, cyclic loading
2. Specimens were at least 1/4-scale
3. Repairs of structural components were limited to the coupling beams
4. Specimens were coupled walls, comprising of two wall piers coupled by coupling beams, not pierced or punched cantilever walls

* Note that details of specimen design (e.g. specimen geometries, reinforcement ratios and material properties) as well as computed response quantities (e.g. shear stress demand at max load) are presented in Section 2.5.5 following the discussion of individual specimens.

2.5.1 Santhakumar (1974) – Ductility of coupled shear walls

Research Objectives

Researchers at the University of Canterbury (Santhakumar, 1974) tested two reinforced concrete coupled wall specimens to study the impact of coupling beam reinforcement detailing on system response. Previous experimental research conducted by Paulay (1971) on conventionally reinforced coupling beams showed that even with an increase in transverse stirrup reinforcement, there was a significant loss in ductility and strength due sliding shear along the ends of the beams. This led to research conducted by Paulay and Binney (1974) in which it was observed that coupling beams detailed with diagonal reinforcement exhibited increased ductility and performance over conventionally reinforced beams. The researchers used the results of the coupling beam tests as a basis for designing two coupled wall systems, one with diagonally reinforced and one with conventionally reinforced coupling beams.

Test Program

Two 1/4-scale, seven-story reinforced concrete coupled-wall specimens (Figure 2.4) were tested. The specimen was 5 ft - 3 in long and 18 feet tall. The wall piers were 24 inches long by 4 inches thick and were quite slender with an aspect ratio of 9. On the other hand, the coupling beams were much stockier with an aspect ratio of 1.25; this design was typical of New Zealand practice at that time where coupled walls were designed to to have higher degrees of coupling. Both specimens had wall piers with the same reinforcing details (Figure 2.5). Note that the wall piers were not designed with a symmetric longitudinal reinforcement layout, but instead have much heavier longitudinal reinforcement in the outer boundary element. The coupling beams in WallA were conventionally reinforced; the coupling beams in WallB were diagonally reinforced. The difference in coupling beam reinforcement details are shown in Figure 2.6. While the strengths of the wall piers for both specimens were approximately the same, the coupling beams in specimen WallB were 10% stronger than the coupling beams in WallA.

The specimens were subjected to cyclic lateral loading and constant gravity loading. A triangular lateral load distribution was assumed, and loads consistent with this distribution were applied to the specimen at the third, fifth and seventh floors. A Gravity load equal to $0.06f'_cA_g$ (25 kips) was applied via one ungrouted prestressing cable for each wall pier; the stress in the prestressing cable was adjusted throughout the test to maintain a constant gravity load. For convenience each specimen was tested horizontally using the testing apparatus shown in Figure 2.7. The double cantilever loading system utilizes a steel truss that remains elastic and through symmetry provides the required base fixity for the specimen.

Specimens were subjected to reverse-cyclic loading under force control. The cyclic lateral-force history for Specimen WallA consisted of two cycles to a max force of 70% the specified theoretical ultimate load ($P_u^* = 52.5$ kips), which was based on a plastic analysis. Then the specimen was subjected to two "elastic" cylces to a max force of $0.30P_u^*$. The maximum load achieved in these four cycles was not large enough to yield the wall piers. The specimen was then loaded in seven high-inensity cycles each to a maximum load of $1.1P_u^*$. During a preliminary phase of testing, intended to verify the test setup, WallA was accidentally loaded to approximately $0.85P_u^*$. As a consequence, the steel in the second floor coupling beam was estimated to have yielded.

The cyclic lateral-force history for Specimen WallB consisted of two cycles to a max force of $0.15P_u^*$ followed by two cycles to a max force of $0.4P_u^*$ where, P_u^* was equal to 56.6 kips in the case of WallB. These cycles were then followed by two cycles to $0.75P_u^*$ and two "elastic" cycles to a max force $0.40P_u^*$. The maximum load achieved in these 8 cycles was not large enough to yield the wall piers. Eight high-intensty cycles were then executed to a max force of $1.1P_u^*$.

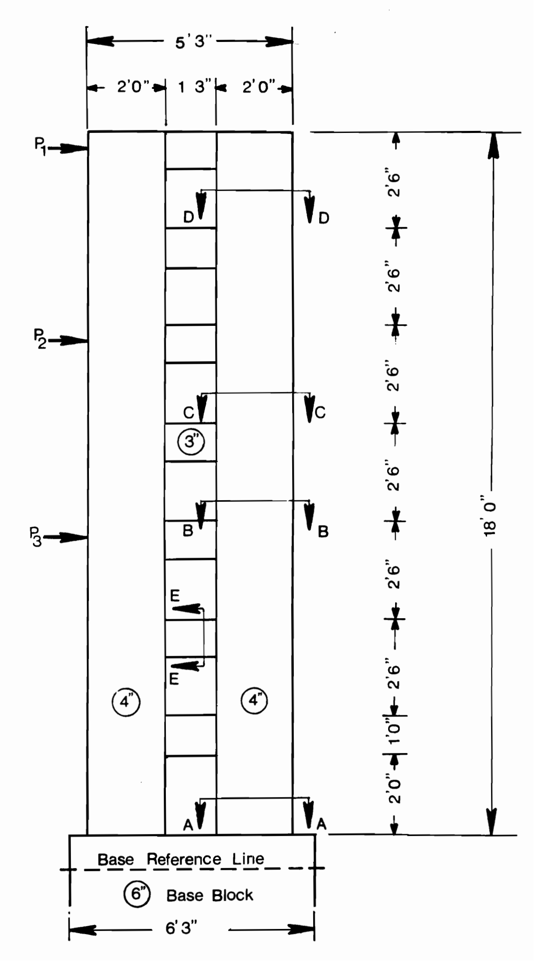

Figure 2.4: Test specimen geometry (Santhakumar, 1974)

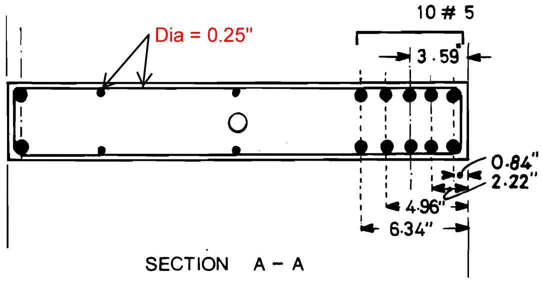

Figure 2.5: Wall pier reinforcement detail (Santhakumar, 1974)

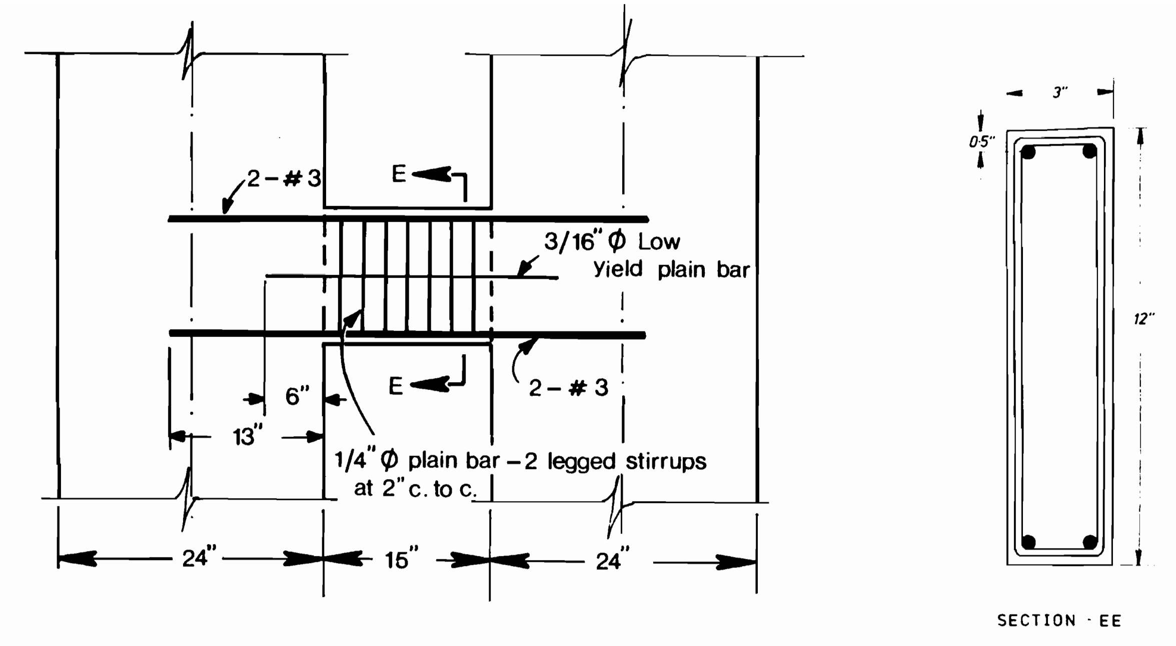

(a) WallA

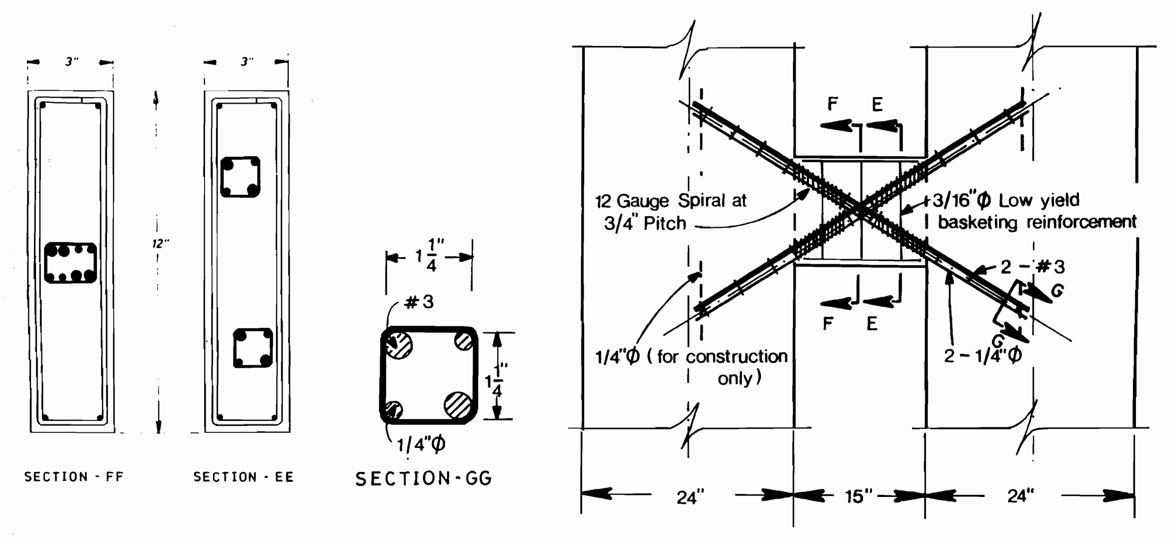

(b) WallB

Figure 2.6: Coupling beam reinforcement detail (Santhakumar, 1974)

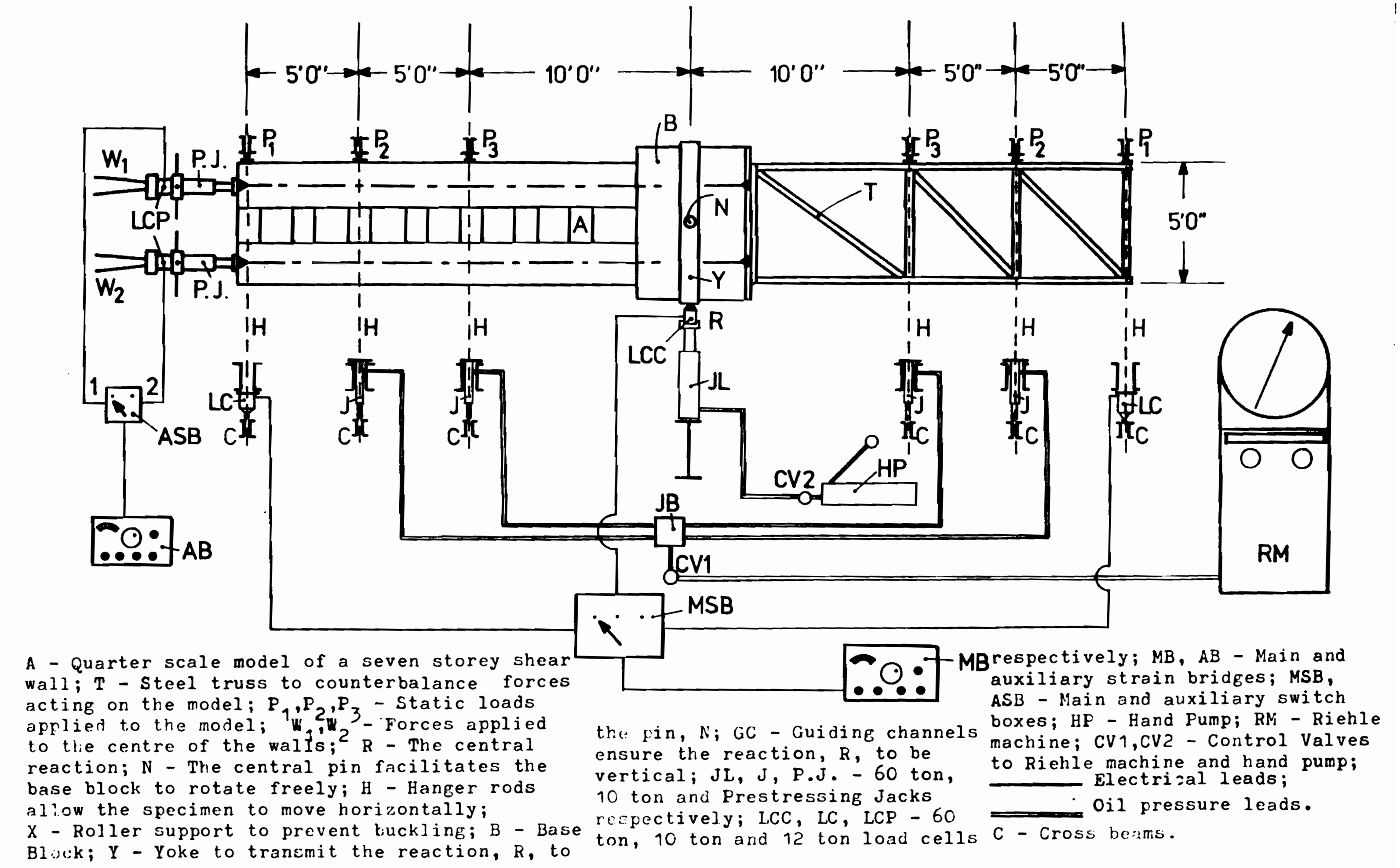

A - Quarter scale model of a seven storey shear wall; T - Steel truss to counterbalance forces acting on the model; P_1, P_2, P_3 - Static loads applied to the model; W_1, W_2 - Forces applied to the centre of the walls; R - The central reaction; N - The central pin facilitates the base block to rotate freely; H - Hanger rods allow the specimen to move horizontally; X - Roller support to prevent buckling; B - Base Block; Y - Yoke to transmit the reaction, R, to the pin, N; GC - Guiding channels ensure the reaction, R, to be vertical; JL, J, P.J. - 60 ton, 10 ton and Prestressing Jacks respectively; LCC, LC, LCP - 60 ton, 10 ton and 12 ton load cells respectively; MB, AB - Main and auxiliary strain bridges; MSB, ASB - Main and auxiliary switch boxes; HP - Hand Pump; RM - Riehle machine; CV1,CV2 - Control Valves to Riehle machine and hand pump;

——— Electrical leads;

═══ Oil pressure leads.

C - Cross beams.

Figure 2.7: Test set up for walls tested by Santhakumar (1974)

Experimental Test Results

For WallA the base shear verss roof displacement response is shown in Figure 2.8. The following summarizes the behavior and damage progression of Specimen WallA.

- The second story coupling beam yielded during the first cycle to 0.35% drift (low-inesity cycle).
- The coupling beams on the first, third, fourth and fifth floors yielded during the second drift cycle to -0.38% drift (low-inesity cycle).
- During the first two high-intensity cycles (i.e. cycles 5: max drift of 0.70% and 6: max drift of -1.0%), yielding in the left and right wall pier occurred when the walls were in tension at approximately at +0.44 and -0.45% drift, respectively.
- The sixth and seven floor coupling beams yielded at the peak drift in cycle 5 (0.70% drift).
- Throughout all the high-intensity cycles, the force-displacement response of WallA was pinched in nature.
- The load capacity dropped approximately 20% during the last loading cycle and was attributed to a loss in coupling beam capacity.
- At approximately 2.0% drift, the concrete on the inside corner of the tension wall (left wall pier) started to crush. This damage was then followed by horizontal slipping along the base which led to buckling of the two inside vertical reinforcement (2.0 - 2.4% drift).
- At the end of the test (cycles 11 and 12), the coupling beams had deteriorated substantially at the beam-to-wall interface, and test specimen formed a distinct

sliding shear failure mechanism along a diagonal crack in the tension pier and along the along the weakest sections in the coupling beams.

- The damage to the wall piers and the second story coupling beam at the end of the test is shown in Figure 2.10.

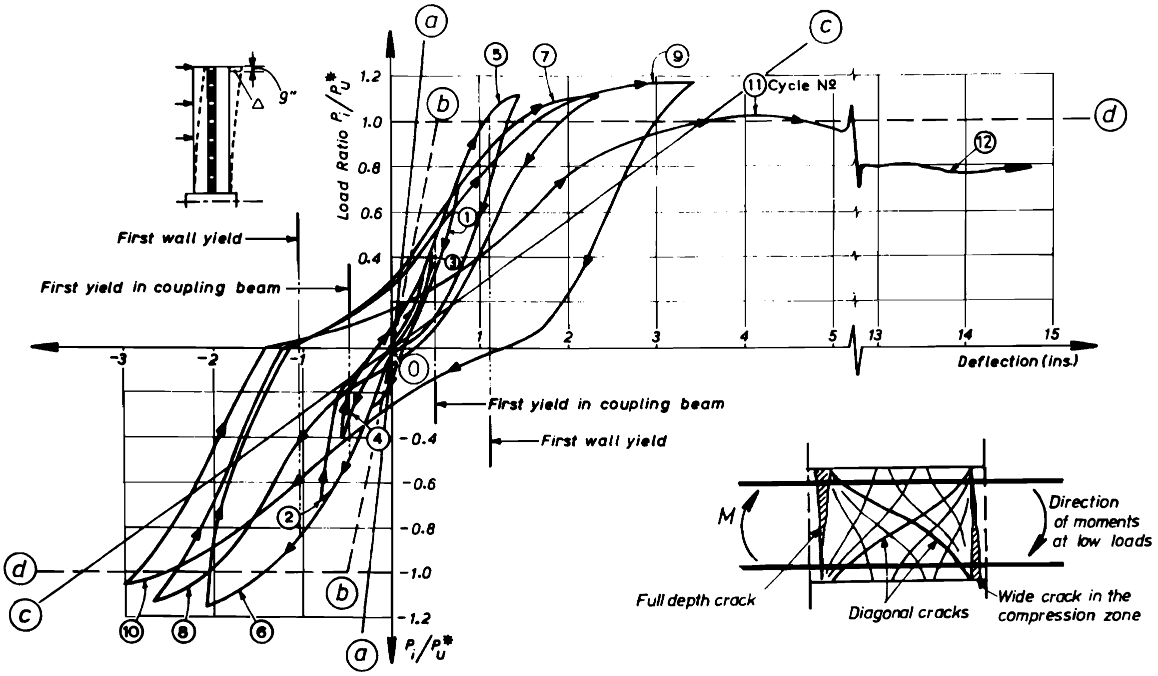

Figure 2.8: Force-displacement response for Specimen WallA (Santhakumar, 1974)

For WallB the base shear verse roof displacement response is shown in Figure 2.9. The following summarizes the behavior and damage progression of Specimen WallB.

- The second and first floor coupling beams yielded at 0.15% and 0.18% drift, respecitively during the low-inesity cycle 5 to a max drift of 0.22%.

- The third story coupling beam yielded during the next cycle at a peak drift of -0.23% (low intensity cycle).

- The coupling beams on the fourth, fifth and sixth floor yielded at the peak drift of 0.54% during the first high-intensity cycle (i.e. cycle 9).

- The outer vertical reinforcement in the left wall pier and inner vertical reinforcement in the right wall pier yielded simultaneously at 1.1% drift when WallB was subjected to loading in the positive direction (to the right).

- Unlike WallA, the force-displacement response of WallB did not exhibit any pinching in the hystereses loops.

- Less than 5% loss of load capacity was observed in the force-displacement response during all but the last loading cycle when failure of the specimen occured.

- The specimen failed at approximately 3.5% drift (cycle 16) when the compression wall (left pier) buckled out of plane. Buckling occured due to an initial imperfection in the wall caused by a misalignment in the concrete formwork.

- At failure, damage in the specimen was limited to minor spalling in the coupling beams and diagonal cracking extending from the top corners to the bottom corners of the coupling beams; however no sliding was observed in this beams. The base of the tension wall pier only sustained minor concrete spalling damage to the outer bottom corner of the wall.

- Unlike the previous specimen, the diagonally reinforced coupling beams in WallB endured large deformation demands while maintaining adequate strength, stiffness and energy dissipation.

- The damage to the wall piers and the second story coupling beam at the end of the test is shown in Figure 2.10.

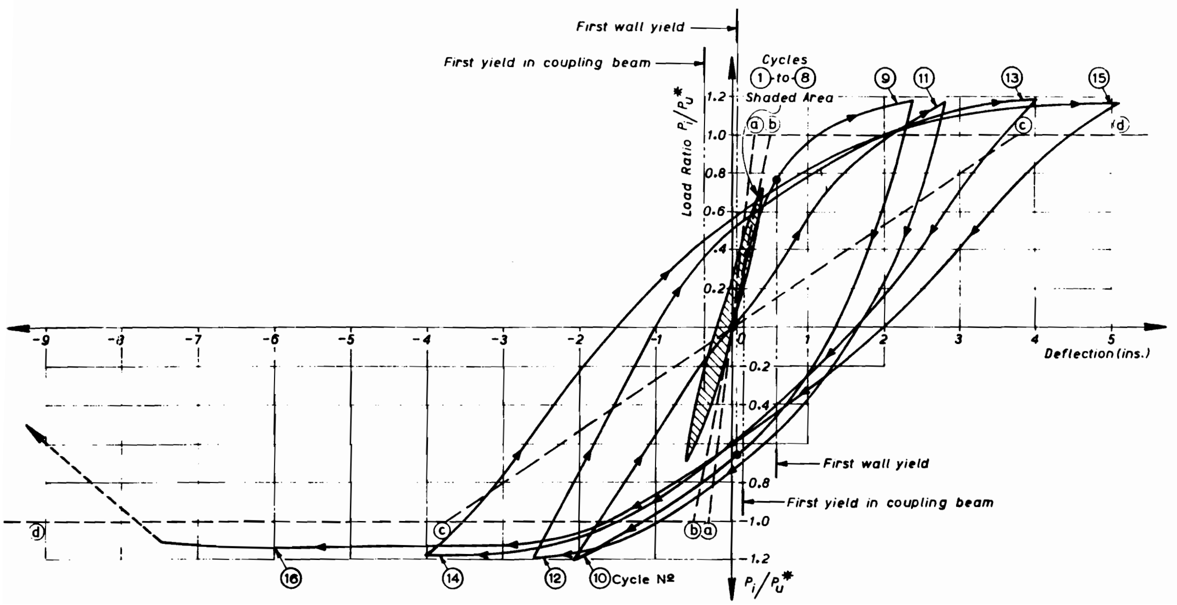

Figure 2.9: Force-displacement response for Specimen WallB (Santhakumar, 1974)

Research Conclusions

Santhakumar concluded that both WallA and WallB performed well when subjected to earthquake demands; however, WallB with diagonally reinforced coupling beams performed significantly better than WallA with conventionally reinforced coupling beams. The energy dissipated by WallB was approximately twice the energy dissipated by WallA under similar loading histories and WallB demonstrated higher drift capacity, relative to WallA. WallB failed due to out-of-plane buckling caused by a construction error; while WallA failed due to crushing of concrete and buckling of longitudinal reinforcement in the inner portion of the left wall pier as well as the development of a sliding shear mechanism throughout the tension wall and all the coupling beams. The overall sequence of yielding was similar for both specimens, and the concrete damage and steel yielding at the ends of the coupling beams and wall piers (Figure 2.10) suggest the desired plastic mechanism from Section 2.2 did form during the high intensity load cycles. During high intensity cycles, a significant percent of the shear was transferred from the tension wall to

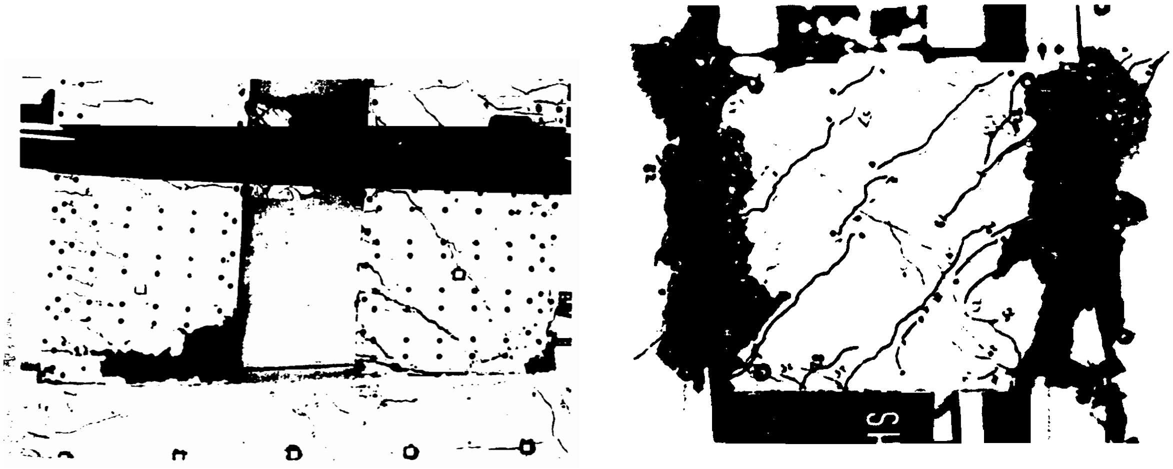

(a) Base of WallA

(b) Second floor coupling beam in Wall A

(c) Base of WallB

(d) Second floor coupling beam in Wall B

Figure 2.10: Damage to specimens at end of test (Santhakumar, 1974)

the compression wall, and at the time of failure it was estimated that almost 75% of the total shear force was being resisted by the compression wall. This shows the importance of the compression pier to the performance and stability of the system.

2.5.2 Shiu et al. (1981) – Earthquake Resistant Structural Walls - Coupled Wall Tests

Research Objectives

Shiu et al. (1981) of the Construction Technology Laboratories, a division of the Portland Cement Association, built and tested essentially, two 1/3-scale coupled-wall structures. A coupled wall specimen, CS1, was constructed with weak coupling beams and tested. Damage was concentrated in the coupling beams and coupling beams failure determined failure of the system. Following testing of CS1, the coupling beams were rebuilt to be much stiffer, and the wall was retested as specimen RCS1. The primary objective of the research program was to investigate nonlinear behavior of coupled wall structures under cyclic in-plane loading. Secondary objectives included:

- Identify the effect of beam strength (i.e. degree of coupling) on the behavior of the coupled wall system,
- Investigate the influence of axial loads, induced by coupling beams, on the strength and ductility of the wall piers,
- Investigate redistribution of shear and moment in coupled wall systems, and
- Determine critical design parameters for structural walls built with weak and strong coupling beams.

Test Program

The coupled wall system was 13 ft - 10⅔ in long and six stories tall (18 feet in height). Unlike the Santhakumar (1974) test specimens, the wall piers were symmetrically reinforced and included a 2.5 inch thick and 7 ft - 4 in wide reinforced concrete slab at each floor level. The wall piers were 6 ft - 3 in long and 4 inches thick and the coupling beam aspect ratios for CS1 and RCS1 were 2.46 and 2.05, respectively. Specimens were designed per ACI 318-71. Wall piers were heavily reinforced; the vertical reinforcement ratio for each boundary element was approximately 5.6%. The wall piers were designed to resist the base shear demand resulting from the plastic mechanism shown in Section 2.2 though strain-hardening in the coupling beams was not considered in computing the expected base shear. Figures 2.11 and 2.12 show the geometry of the test Specimen CS1 and the reinforcement detail for half of the wall pier, respectively. Researchers designed the coupling beams to investigate the effects of coupling action on the strength and stiffness of the wall piers. The predicted degree of coupling was reported as 13% for CS1 (lower coupling beam strength) and 30% for RCS1 (higher coupling beams strength). The coupling beam reinforcement details for CS1 and RCS1 are shown in Figure 2.13.

After the completion of the CS1 test, the coupling beams were replaced using the following construction sequence:

1. The concrete portion of the coupling beam slabs were removed leaving the longitudinal reinforcement in place.

2. All the coupling beams were removed and the longitudinal reinforcement was cut at the beam-to-wall interface.

3. The residual horizontal wall pier displacements were corrected by adjusting the cross-head.

4. Wall pier concrete near the coupling beams was removed from the edge of the wall pier up to the web region ($\approx$ 10 inches) and holes were drilled into the web region of the wall, so the new coupling beam longitudinal reinforcement could be bent and anchored around the boundary element reinforcement.

5. Concrete formwork was placed around the coupling beams and then concrete was cast.

The test setup is shown in Figure 2.14. Each wall pier was loaded through the top floor slab with equal lateral shear forces and no axial loads. Specimens were subjected to reverse-cyclic loading under force control. CS1 was subjected to six complete load cycles; the first three load cycles were loaded to max forces of $0.2V_y$, $^1/_3V_y$ and $0.2V_y$, respectively where, V_y is the computed yield load of the system. The third cycle was a half cycle where the load was only applied in the positive direction (i.e. to the right). Cycles 4 through 6 were applied to max forces of $1.2V_y$, $1.1V_y$ and $1.0V_y$, respectively. These high-intensity load reversals were expected to yield all the coupling beams and both wall piers.

For RCS1 the loading history described for CS1 was repeated except cycles 4 through 6 were all repeated at a max force to $1.2V_y$. Three cycles were then executed to a max force of $1.45V_y$ followed by one cycle to $1.65V_y$. The next cycle (11) was a half cycle loaded in the positive direction to $1.2V_y$. This was followed by another two full cycles to a max force of $1.65V_y$ and the last cycle (14) to $1.75V_y$. The RCS1 loading history was designed to yield the stronger coupling beams and develop the ultimate load capacity of the system.

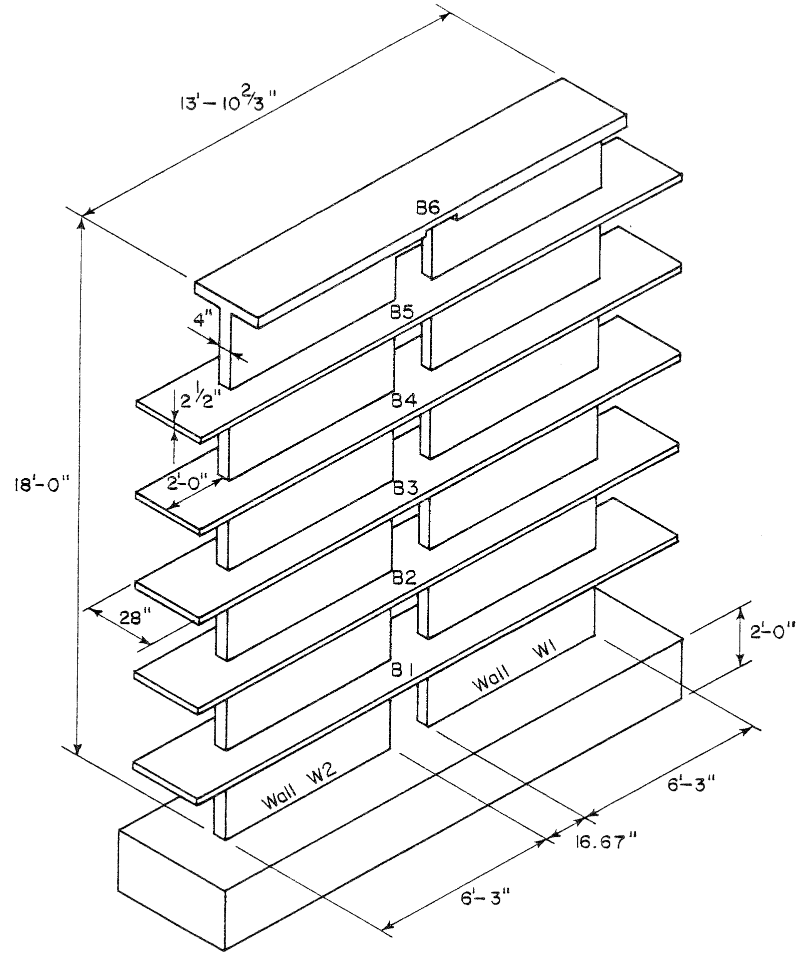

Figure 2.11: Test specimen geometry (Shiu et al., 1981)

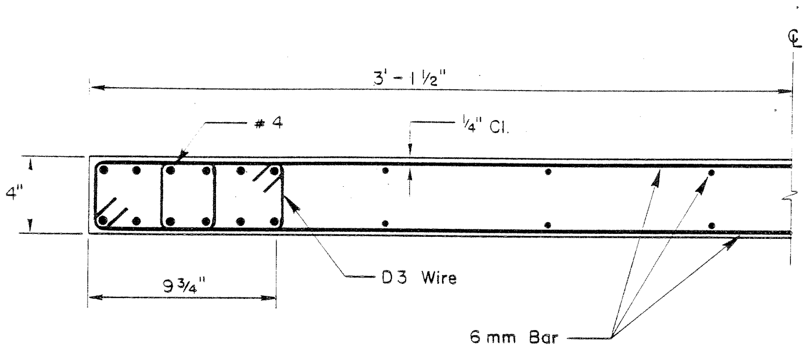

Figure 2.12: Wall pier reinforcement detail (Shiu et al., 1981)

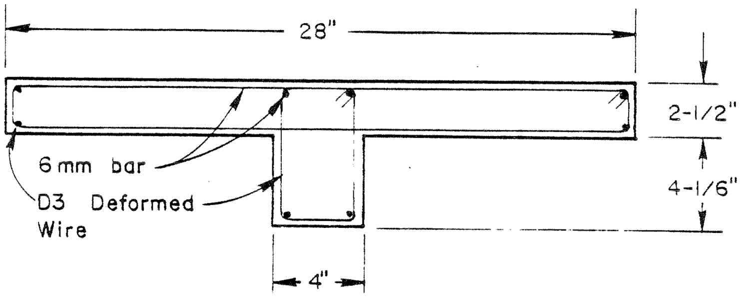

(a) CS1

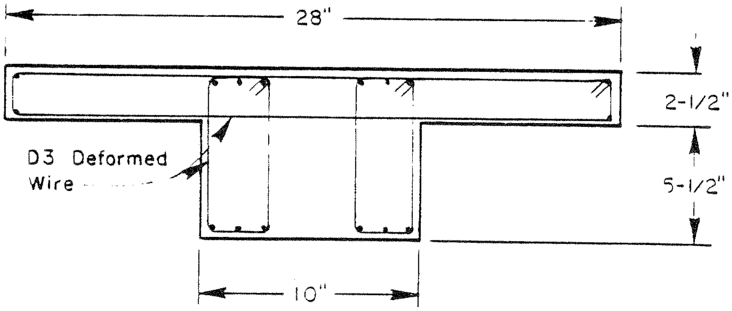

(b) RCS1

Figure 2.13: Coupling beam reinforcement detail (Shiu et al., 1981)

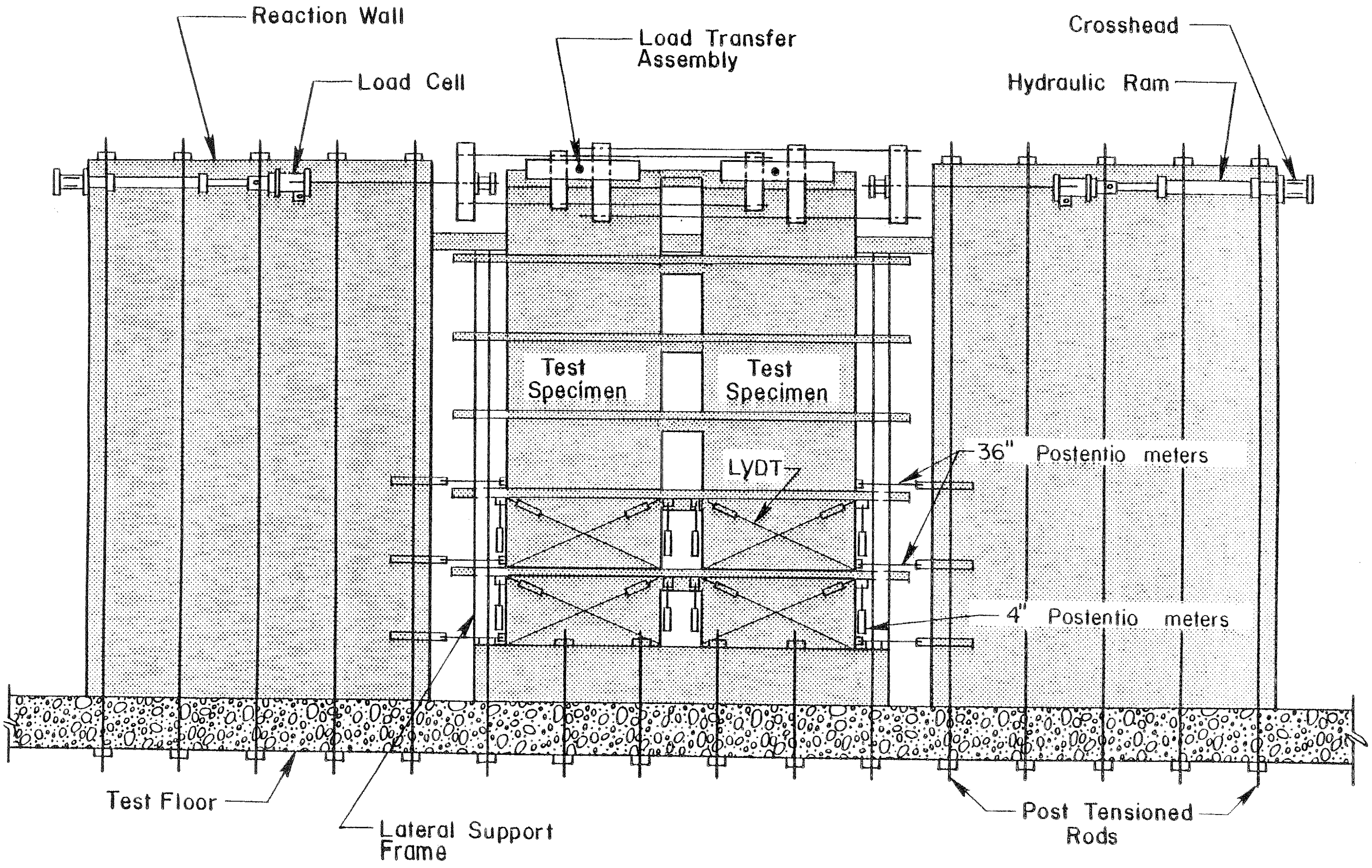

Figure 2.14: Test set up for walls tested by Shiu et al. (1981)

Experimental Test Results

For CS1, the base shear verse roof displacement response is shown in Figure 2.15 and observed response was as follows:

- During the cycles to max drifts of 0.03%, 0.09% and 0.08% no significant damage was observed

- During the fourth loading cycle which entailed loading to drift of 0.84% yielding of the top four coupling beams was reported at a drift of 0.1%

- Yielding of the second and first floor coupling beams were reported during cycle four at 0.18% and 0.34%, respectively.

- Both wall piers also yielded during cycle 4 at approximately 0.60% drift. This yielding occurred in the outer boundary element of each wall pier when the respective pier was subjected to a tension wall loading behavior.

- Yielding of the wall piers was, approximately, accompanied by opening of wide vertical cracks and spalling of the concrete cover at the coupling beam ends. This damage was reported to cause severe loss of shear in the coupling beams; the authors refer to this loss in capacity as "uncoupling" of the wall piers, which results in the wall piers behaving as two independent shear walls.

- Testing of CS1 was concluded following a sixth load cycle to 1.1% drift. At the end of the test, minor damamage to the wall piers was reported including minor cracking and yielding of some longitudinal steel; Figure 2.16 shows the crack patterns at the end of the test.

- The extent of damage to the coupling beams at the end of the test is not reported.

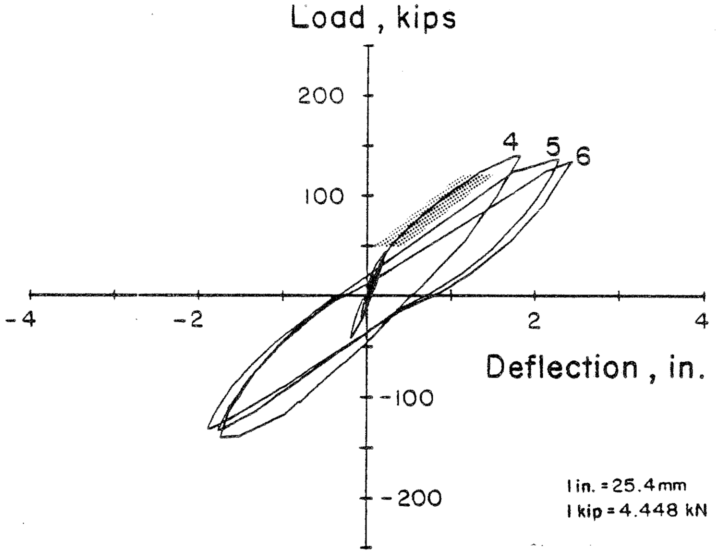

Figure 2.15: Force-displacement response for Specimen CS1 (Shiu et al., 1981). Note: the shaded area indicates the region over which yielding occurred.

Following replacement of the coupling beams, specimen CS1 was retested as RCS1. Figure 2.17 shows the force-displacement response and the observed response was as follows:

- During the first cycles to max drifts of 0.10%, 0.23% and 0.20% no significant damage was observed
- During the fourth loading cycle to a max drift of 0.58% the wall pier longitudinal reinforcement in the outer boundary element of each wall pier yielded at 0.46% drift. In the CS1 test, wall pier longitudinal reinforcement yielded at 0.6% drift; the lower drift at yield for RSC1 is attributed to increased axial tension demand in the wall piers due to increased coupling beam strength and stiffness.
- The fourth floor coupling beam yielded at 0.48% drift during the fourth load cycle.
- Yielding in the coupling beams at the third and fifth floors occurred during the

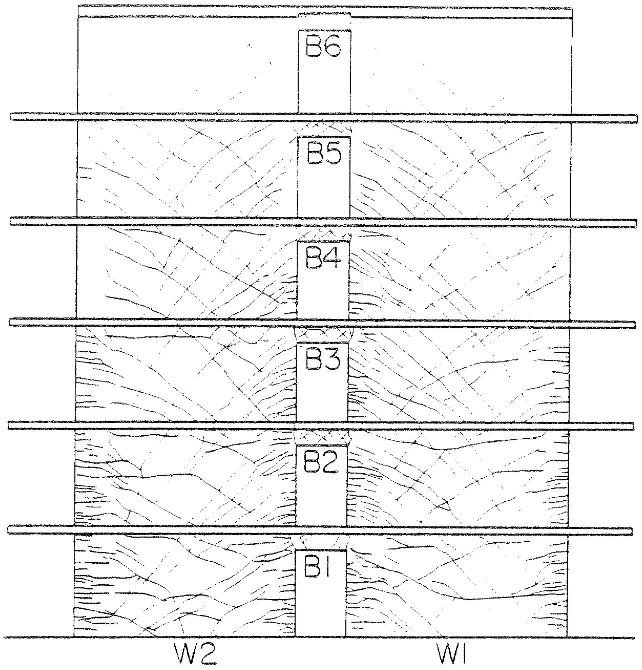

Figure 2.16: Crack pattern in CS1 at the end of test (Shiu et al., 1981)

fourth cycle at 0.52% drift.

- The sixth floor coupling beam yielded at a drift of 0.68% during the seventh load cycle to a max drift of 0.82% drift
- The coupling beams at the second and first yielded at approximately 0.9% and 1.05% drift, respectively during the tenth load cycle to a drift of 1.2% drift.
- Diagonal cracking observed during the test was more indicative of a coupled wall system in the sense that these cracks initiated in the tension wall and extended through the coupling beams into the compression wall. The crack pattern for the positive loading direction at the end of the test is shown in Figure 2.18.
- Throughout the entire loading history up to failure of the compression pier, the

specimen continued to increase in strength which was attributed to hardening of the reinforcing steel predominantly in the tension wall.

- During the last load cycle (i.e. cycle 14), at a drift of approximately 1.8%, the left wall pier failed in compression due to crushing of the web concrete. The specimen continued to be loaded up to 2.8% drift as it failed through sliding shear along the base of the wall piers. Figure 2.19 shows the extent of damage to the base of each wall pier at the end of the test.

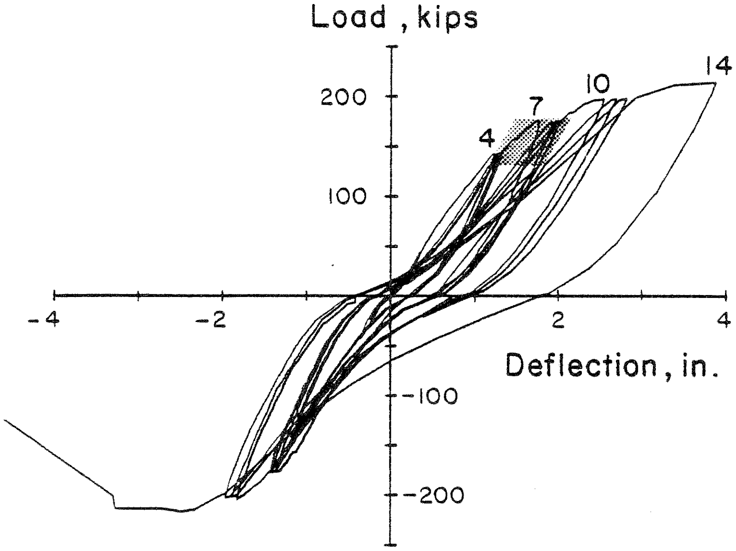

Figure 2.17: Force-displacement response for Specimen CS1 (Shiu et al., 1981). Note: the shaded area indicates the region over which yielding occurred.

Research Conclusions

On the basis of the experimental results discussed above, the researchers concluded the following:

- The specimen with weak coupling beams (CS1) displayed global force-displacement behavior similar to two isolated wall piers following the third load cycles to a

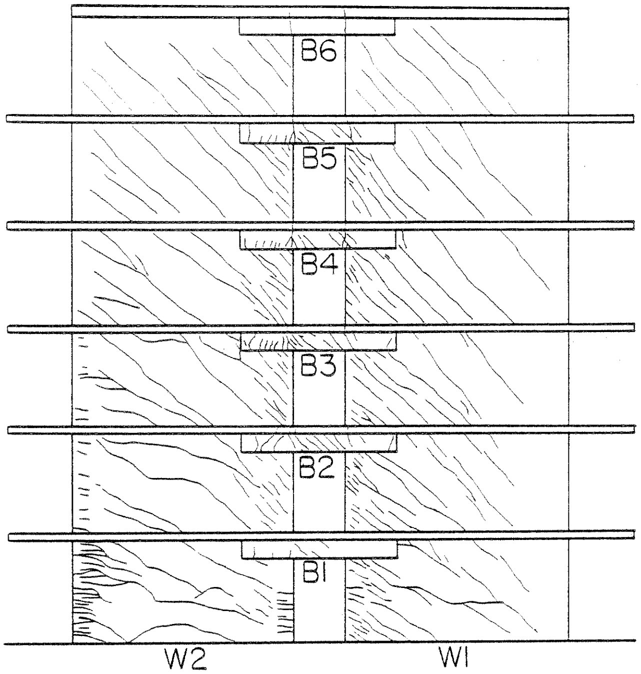

Figure 2.18: Crack pattern in RCS1 at the end of test (Shiu et al., 1981). Note: cracking is only drawn for positive loading.

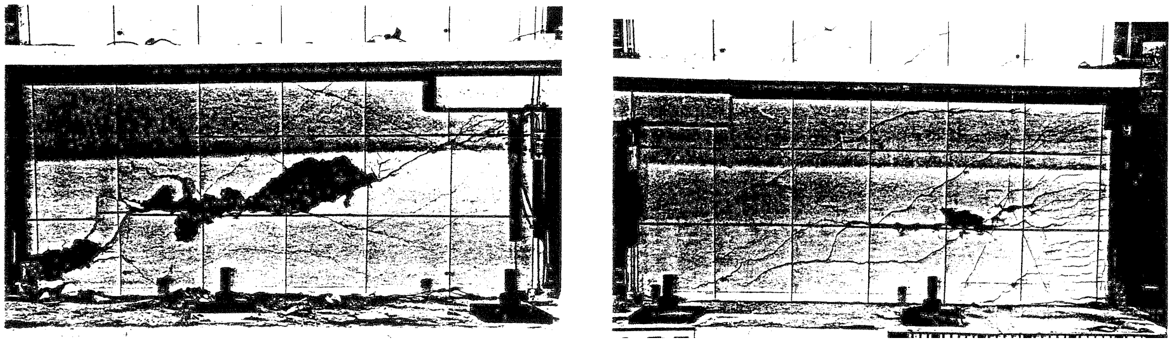

(a) Base of left pier

(b) Base of right pier

Figure 2.19: Damage to RCS1 at end of test (Shiu et al., 1981)

max load of $0.3V_y$. On the other hand, the deformation characteristics of repaired specimen were more representative of a coupled wall were an increase in the global strength and stiffness is attributed to an increase in coupling beam strength and stiffness relative to the wall pier (i.e. increased DOC)

- Both CS1 and RCS1 appeared to develop the expected yield mechanism consisting of yielding of all coupling beams and both wall piers, at the base.
- For both CS1 and RCS1, the compression pier carried a higher moment and shear than did the tension wall. The authors came to this conclusion by comparing the measured deformation characteristics (i.e. rotation and shear deformation) between the compression wall and the tension wall.
- An increase in wall pier axial load as a result of coupling action, greatly affects the behavior and deformation capacity of compression and tension wall piers. The design of "heavily" (e.g. DOC $\geq 30\%$) coupled wall systems is not recommended by the researchers because the system does not achieve the full energy dissipation capacities of the coupling beams and may lead to damage at the base of the wall piers that may not be repairable. The design of "lighly" coupled wall systems must include detailing to ensure coupling beam deformation capacities are adequate to achieve yielding of the wall piers.

2.5.3 Ozselcuk (1989) – Experimental and Analytical Studies of Coupled Wall Structures

Research Objectives

Researchers at the University of California, Berkeley investigated the seismic performance of reinforced concrete coupled walls through an extensive analytical and experimental study. A portion of their research program was dedicated to testing two 4-story subassemblages from a 15-story prototype coupled wall system; tests are documented in

Ozselcuk (1989) and summarized here. One unique aspect of their research was that two wall piers plus coupling beams tub components were connected at mid-span of the coupling beams by sophisticated load transducers. This enabled measurement of coupling internal forces and, as a result, resolution of the applied forces in this indeterminate system. The objectives of their research was to 1) collect quantitative data to provide a better understanding of the shear resisting mechanisms of barbell shaped walls with effectively confined edge columns that were typical of current building design, 2) investigate the shear and shear-flexural capacity of edge columns subjected to varying axial load as well as study the web-crushing phenomena typical of barbell walls under cyclic loading, 3) explore the effects of coupling action on the strength and stiffness of the wall piers by reducing the axial demand applied to one of the specimens, and 4) directly quantify the amount of shear and moment redistribution between the two walls piers and study this result as a function of the coupling moment variation.

Test Program

A full-scale 15-story prototype specimen was designed in accordance with the 1973 Uniform Building Code (UBC) and was designed with respect to a full-scale geometry. Plastic analysis of this code-based design was performed assuming plastic mechanism similar to that described in Section 2.2. The plastic analysis results were used to estimate the ultimate capacity of the system and determine a suitable load pattern for use in laboratory tesing of reduced-scale, 4-story subassemblages. Two test specimens, 1C and 2C, were constructed; specimens were 1/3-scale models of the bottom 4 stories of the 15-story prototype.

The test specimen geometry and reinforcement layout are shown in Figure 2.20, and the reinforcement layout for the wall pier cross-section are shown in Figure 2.21. Both specimens were 20 ft - 4 in long and 16 feet tall. The wall piers were barbel in shape and 7 ft - 10 in wide with 10 in square edge-columns and a 4 inch thick web panel. A 3 inch thick by 6 ft - 8 in wide reinforced concrete slab was located at each floor level.

The coupling beam aspect ratio was 3.50. Note that to maintain coupling beam loads and merely enable determineation of the load distribtuion within the structure, load cells (transducers) wre placed in the middle of each coupling beam. Figure 2.21 shows details of the transducer. The transducers due pose a discontinuity in the design, but they were fabricated with a strength and stiffness matching that of the actual coupling beams. The barbell wall reinforcement details are much different than the planar wall details used by Shiu et al. (1981) and Santhakumar (1974). Unlike the typical boundary elements of a planar wall, the boundary elements of this barbell wall are columns with spiral reinforcement used to confine the concrete core. The web panel zone was detailed to resist the total shear demand associated code design forces.

Three types of coupling beam designs were used in the prototype design and are identified as Type I, II and III. This was done to match the distribution of coupling beam shear demands along the height of the structure. Coupling beam demands were estimated from linear analysis of the 15-story prototype subjected to the code design forces. The first and second floor coupling beams were constructed with scaled designs of the Type I and II designs, and the third and fourth floor coupling beams were constructed with scaled designs of the Type III design. The scaled coupling beam designs used in the test specimen are shown in Figure 2.22.

A total of six actuators were used to apply shears, moments and axial forces to the top of the 4-story specimens. To determine an appropriate load distribution for the specimens, Aktan et al. (1982) performed a series of nonlinear time-history analyses of the 15-story prototype model and determined the base moment-to-shear ratio of the system, M/V, varied between 0.5H and 0.75H, where H is the total height of the prototype. For Specimen 1C, an average effective height of 0.6H was used for the base shear; using this and assuming the plastic mechanism shown in Figure 2.1, resulted in the load pattern at the top of the specimen shown in Figure 2.24.

To investigate the impact on performance of wall pier axial load resulting from coupling beam action, a different approach was used to determine the M-V load pattern for

Specimen 2C. For this specimen, the same analysis process as was used for Specimen 1C was used to compute the load pattern at the top of the specimen; however, for Specimen 2C, the coupling beams in the prototype structure were assumed to have a minimum capacity. Thus, axial loads applied to the wall piers to replicate coupling beams shears were greatly reduced in Specimen 2C. Figure 2.24 shows the load pattern used for testing Specimen 2C. It should be noted that despite the lower coupling beam strengths assumed in developing the load pattern for 2C, Specimen 2C was constructed nominally identical to 1C. Axial loads were applied to the wall piers through the edge columns. Inner and outer column loads differed to represent the different tributary areas of the inner and outer columns. 150 kips was applied to the interior column and 100 kips was applied to the exterior column. As a results, the total gravity force applied to one wall pier was approximately $0.09f'_cA_g$.

For Specimen 1C, the loading protocol consisted initially of six force-controlled cycles each to a max base shear demand of 1.4 times the serviceability lateral load level defined by UBC. Following thesis load-controlled cycles, the specimens was subjected to loading under displacement control. Because the loading history was so unique for the displacement-controlled region, it is shown in Figure 2.25. For Specimen 2C, initially, each wall pier was loaded independently, under load-control up to 80% of the predicted yield load; specifically, two cycles each to max base shear demands of 100 and 175 kips were applied. Subsequently, the wall piers were connceted by the coupling beam load cells, and loading of the coupled wall system was accomplished under displacement control, using the displacement history shown in Figure 2.25.

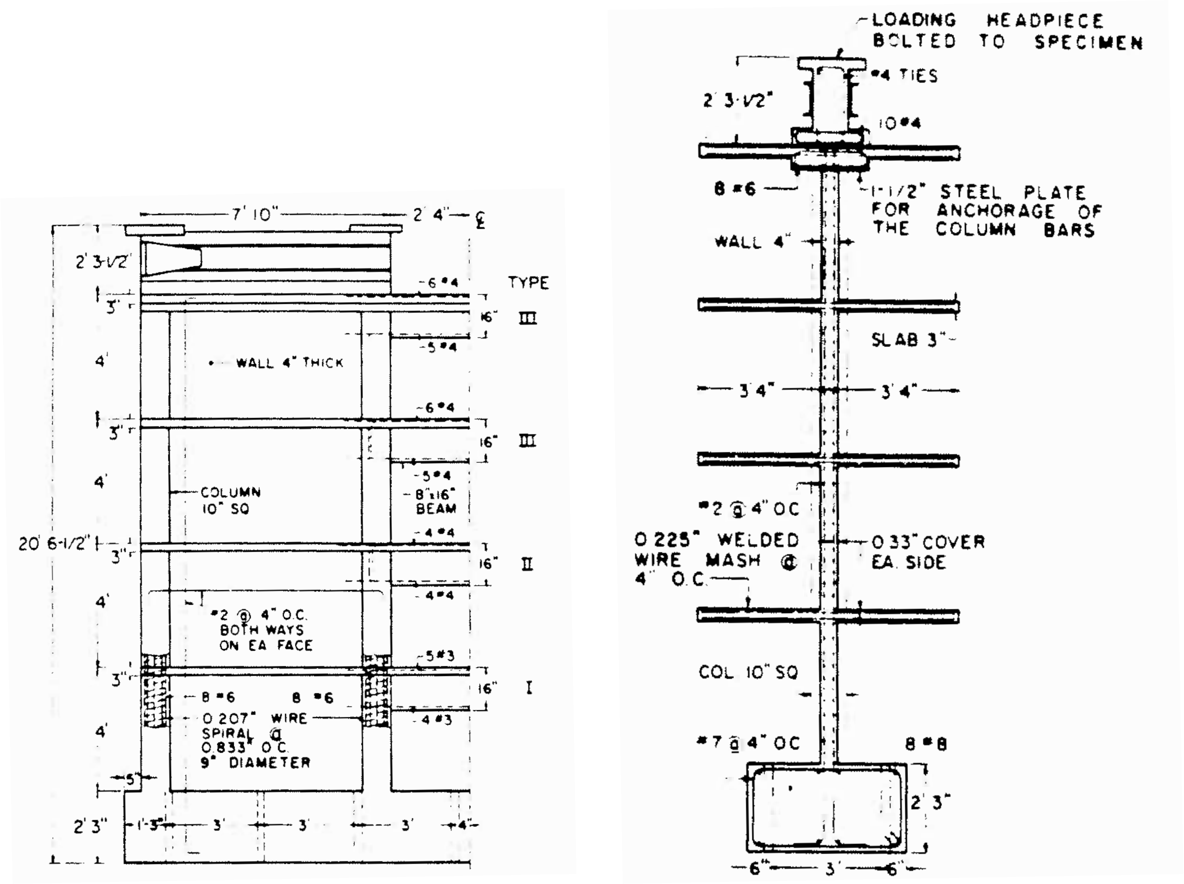

(a) Front view

(b) Side view

Figure 2.20: Test specimen geometry and wall pier reinforcement detail (Ozselcuk, 1989)

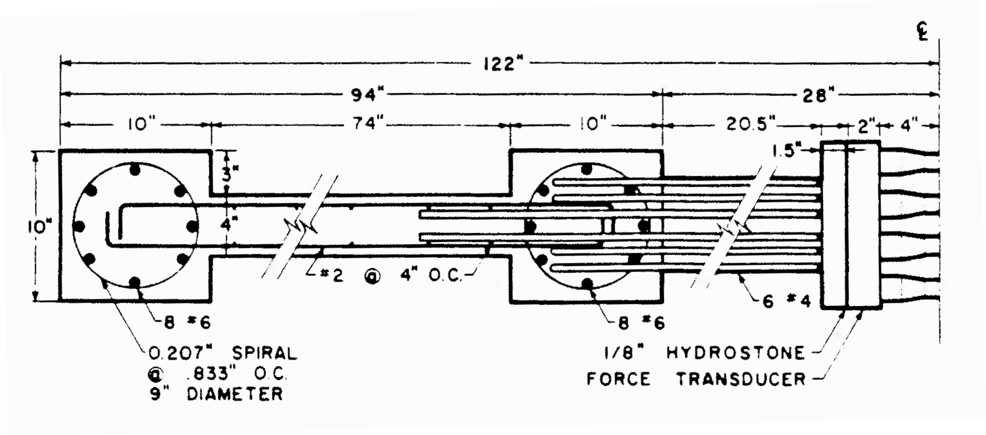

Figure 2.21: Wall pier reinforcement detail (Ozselcuk, 1989)

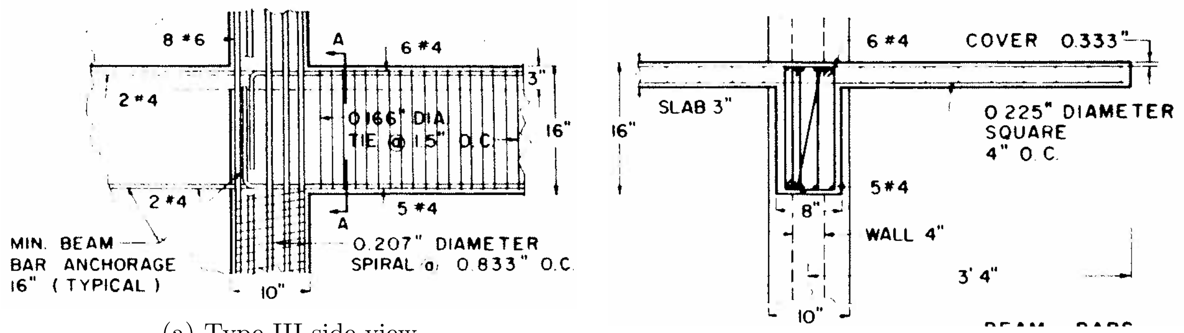

(a) Type III side view

(b) Type III section view

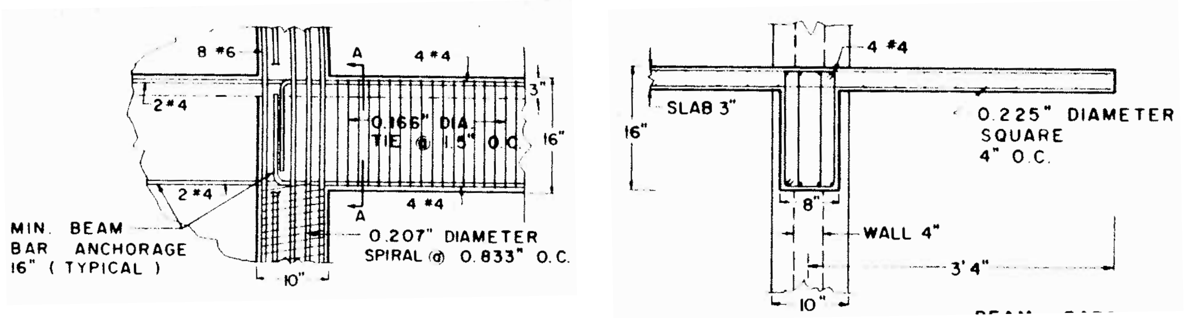

(c) Type II side view

(d) Type II section view

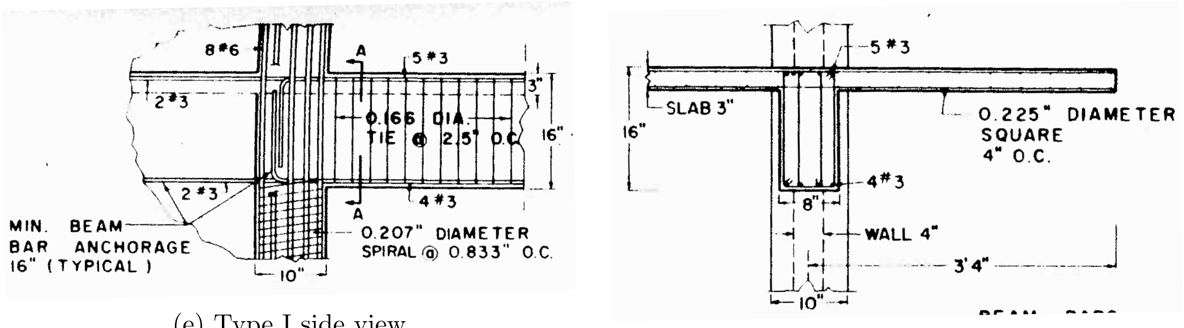

(e) Type I side view

(f) Type I section view

Figure 2.22: Coupling beam reinforcement detail (Ozselcuk, 1989)

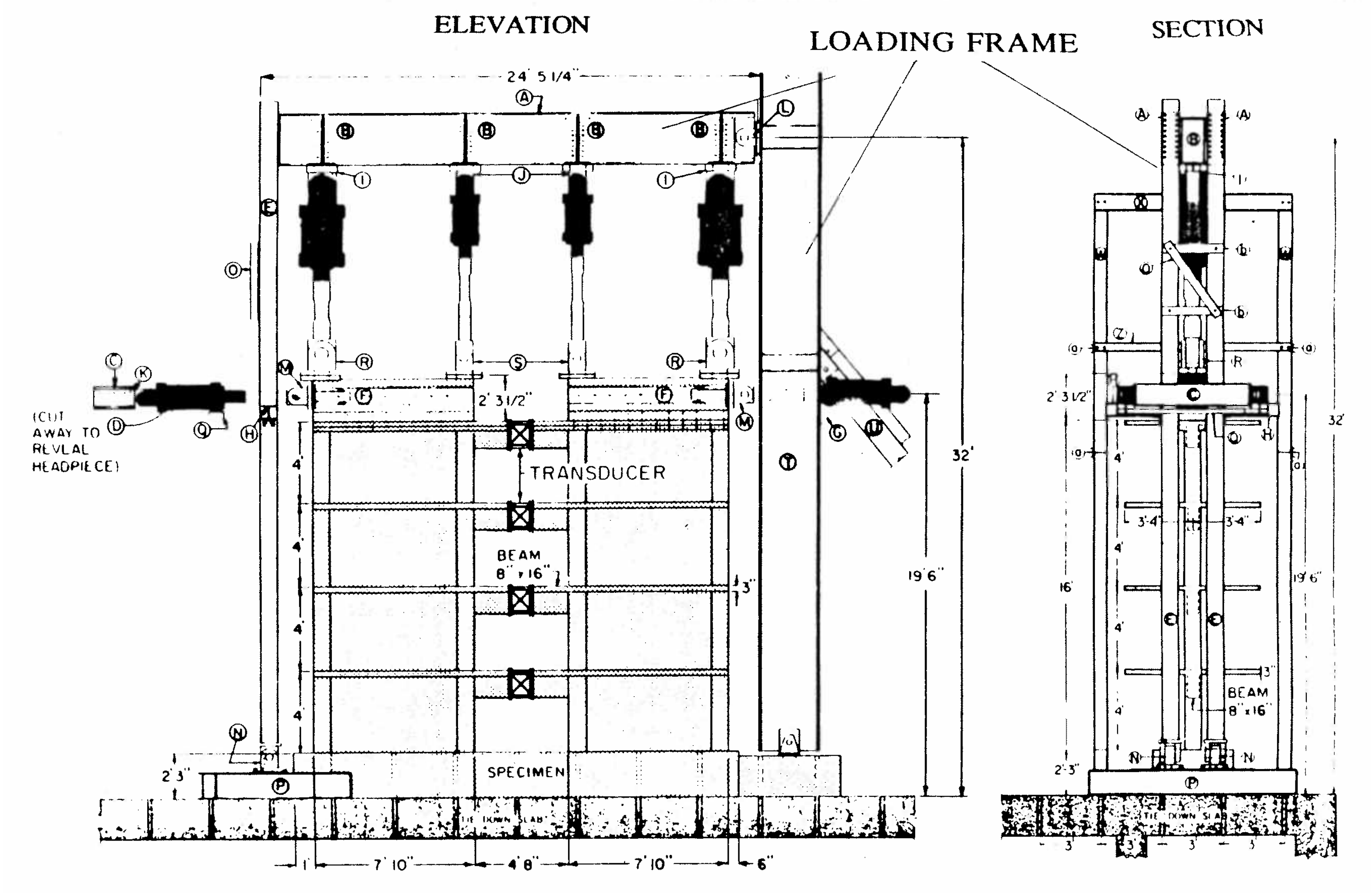

Figure 2.23: Test set up for walls tested by Ozselcuk (1989)

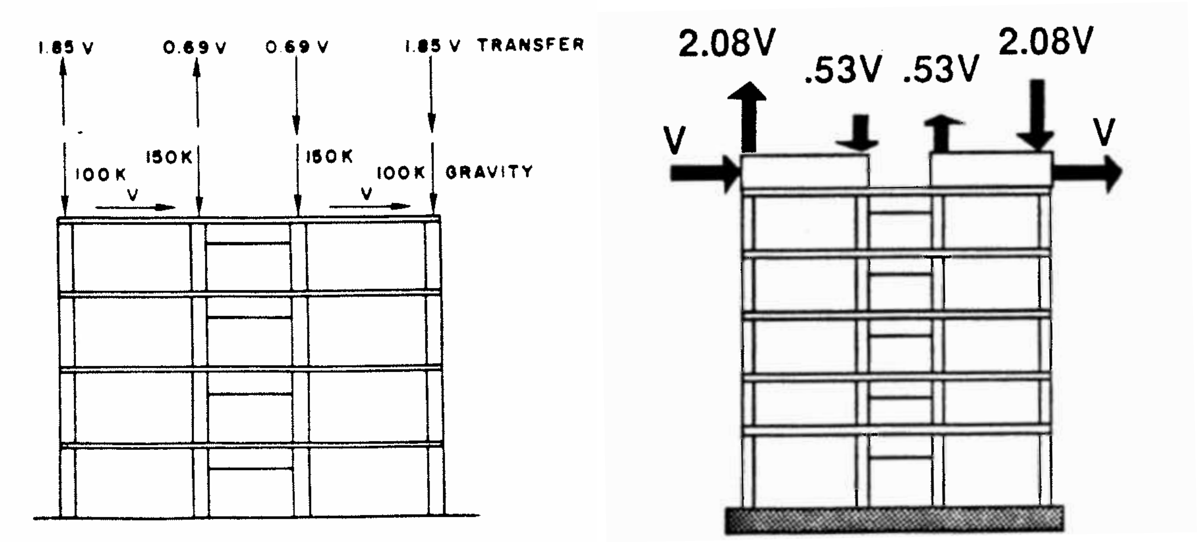

(a) 1C (b) 2C

Figure 2.24: Transfer relationship derived from 15-story prototype (Ozselcuk, 1989)

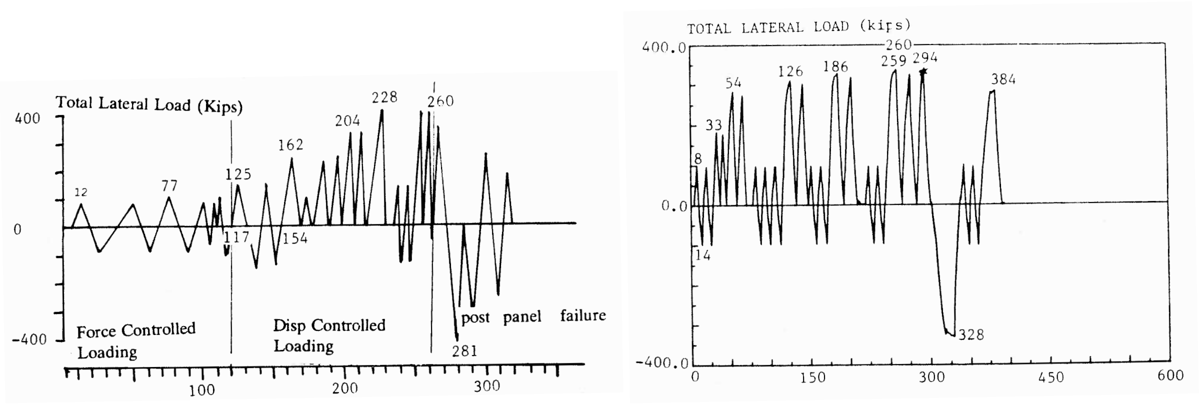

(a) 1C (b) 2C

Figure 2.25: Cyclic-load histories (Ozselcuk, 1989)

Experimental Test Results

In the first experiment, the base shear verse fourth-story displacement response is shown in Figure 2.26 and observed response was as follows:

- The top two coupling beams were reported to have yielded at a max drift of 0.24% (cycle 9).

- Yielding in the second floor coupling beam at approximately 0.35% drift occurred during the thirteenth load cycle to a max drift of 0.52%.

- At the peak drift of load cycle 13, the reinforcement in the first floor coupling beam as well as the reinforcement in the outer edge column of the left wall pier yielded at a drift of 0.48%. During the next positive cycle (0.63% max drift), the reinforcement in the inner edge column reached yield at a drift of approximately 0.57%. At this point in the loading the tension wall was only resisting 9% of the total lateral load; whereas 91% of the lateral load was resisted by the compression wall.

- Initially after load cycle 13, the force-displacement behavior of the specimen began to flatten out and at the peak before failure (cycle 15, 1.0% drift) a lateral load of 404 kips ($7.13\sqrt{f'_c}A_{cv}$) was reached. It was reported at this step the axial forces in the compression and tension piers had reached 80% of the balanced load and 85% of the axial yield capacity, respectively. The nominal shear stresses in the compression and tension piers were calculated as $16.2\ \sqrt{f'_c}$ and $1.55\ \sqrt{f'_c}$.

- At a drift of 1.23% (cycle 16), web crushing was observed in the right wall pier. The loading was reversed and the specimen was loaded to -1.3% drift where web crushing of the left wall pier was observed. The extent of damage at this damage state is shown in Figure 2.29 for the bottom two stories of the specimen.

- Testing was continued with two cycles up to 1.6% drift where the concrete confined in the outer edge columns severely crushed and the vertical reinforcement buckled.

- Damage to the coupling beams at the end of the test was concentrated to the ends of the beams in the form of vertical cracking and some minor spalling. No clear photographs of this damage were presented in Ozselcuk (1989).

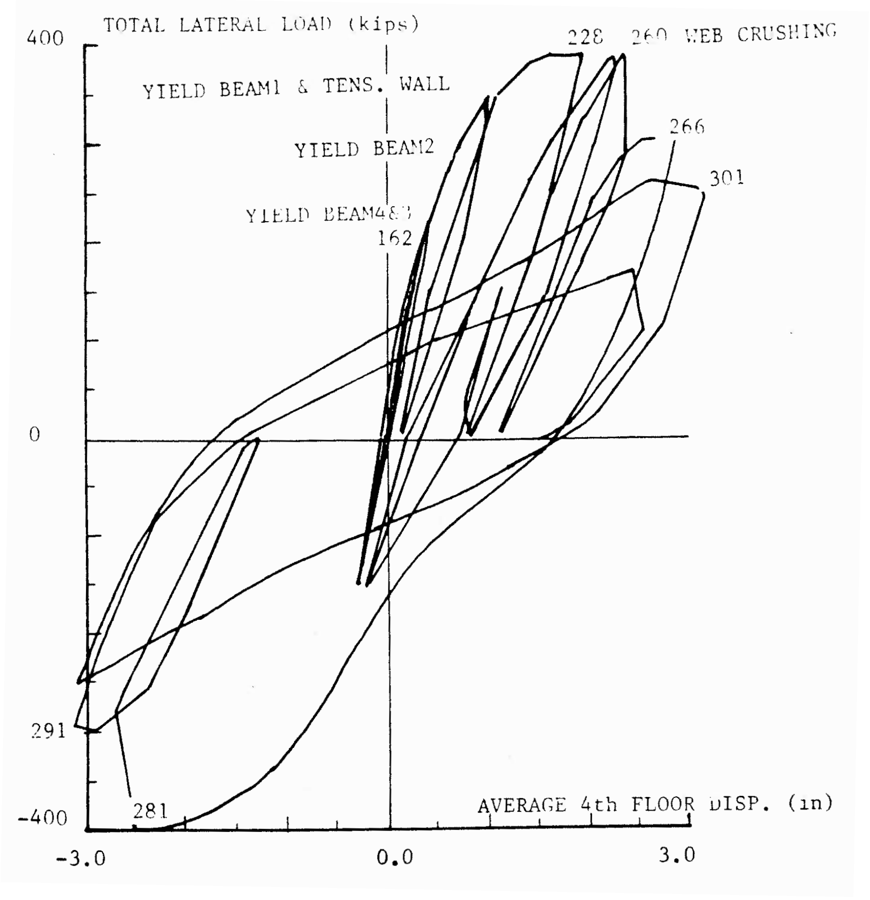

Figure 2.26: Force-displacement response for Specimen 1C (Ozselcuk, 1989)

As mentioned in the test program section, both wall piers of Specimen 2C were tested separately and then connected together via the force transducers. For 2C, the base shear verse fourth-story displacement response is shown in Figure 2.27 and observed response was as follows:

- During the fifth loading cycling to a max drift of 0.52% it was reported that the top story coupling beam yielded at approximately 0.36%.
- A the peak step of cycle 5, the bottom three coupling beams all yielded.
- Yielding of the compression and tension wall was observed at a peak drift of 0.71% during the tenth loading cycle. At this step the shear force calculated at the base of the compression wall was 82% of the total lateral load at this step.
- Crushing of the right wall pier web panel was initially observed at the peak drift of cycle 18 (1.24% drift), and the axial forces in the compression and tension wall had reached 65% of the balanced load and 50% of the axial yield capacity, respectively.
- During load cycle 20 the right wall pier crushed severely (i.e. observed core crushing and bar buckling in the edge-column) at 1.35% drift and the lateral capacity of the specimen dropped by 33%.
- At the negative peak in cycle 20 (-1.2% drift), a shear failure occurred in the second floor coupling beam, but no photos of this damage are present in their report.
- Figure 2.29 shows the damage to the outer edges of the wall piers after the 1.85% drift level. Note there is little damage to the left wall pier, but it should be noted this wall never endured multiple cycles of high axial compression due to the loading protocol.

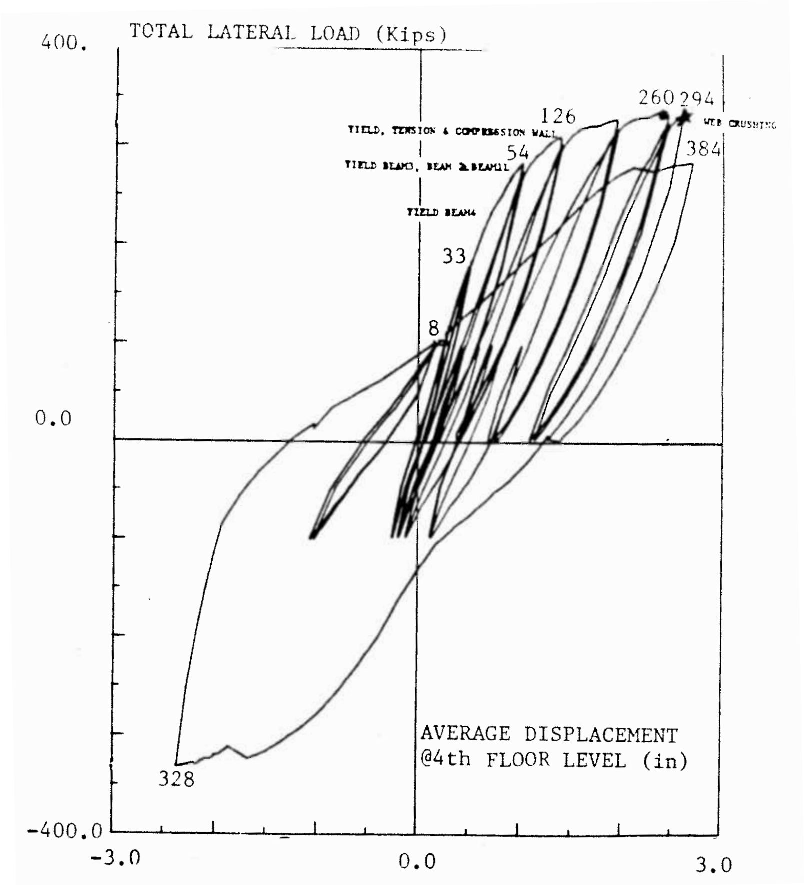

Figure 2.27: Force-displacement response for Specimen 2C (Ozselcuk, 1989)

Research Conclusions

In summary, two specimens were loaded to bound the possible range of demands originating from the upper stories of the prototype. This resulted in a degree of coupling in specimen 1C equal to 60% of the overturning moment and 50% of the overturning moment for 2C. The yield progression for both specimens matched the assumed plastic mechanism, in which the specimens loading protocol originated from. Measured deformations and observed damage for both specimens was quite similar. Overall, the redistribution of shear from the tension wall to the compression wall was slightly greater in 1C. This is most likely the result of higher axial tensile loads in the tension pier, which

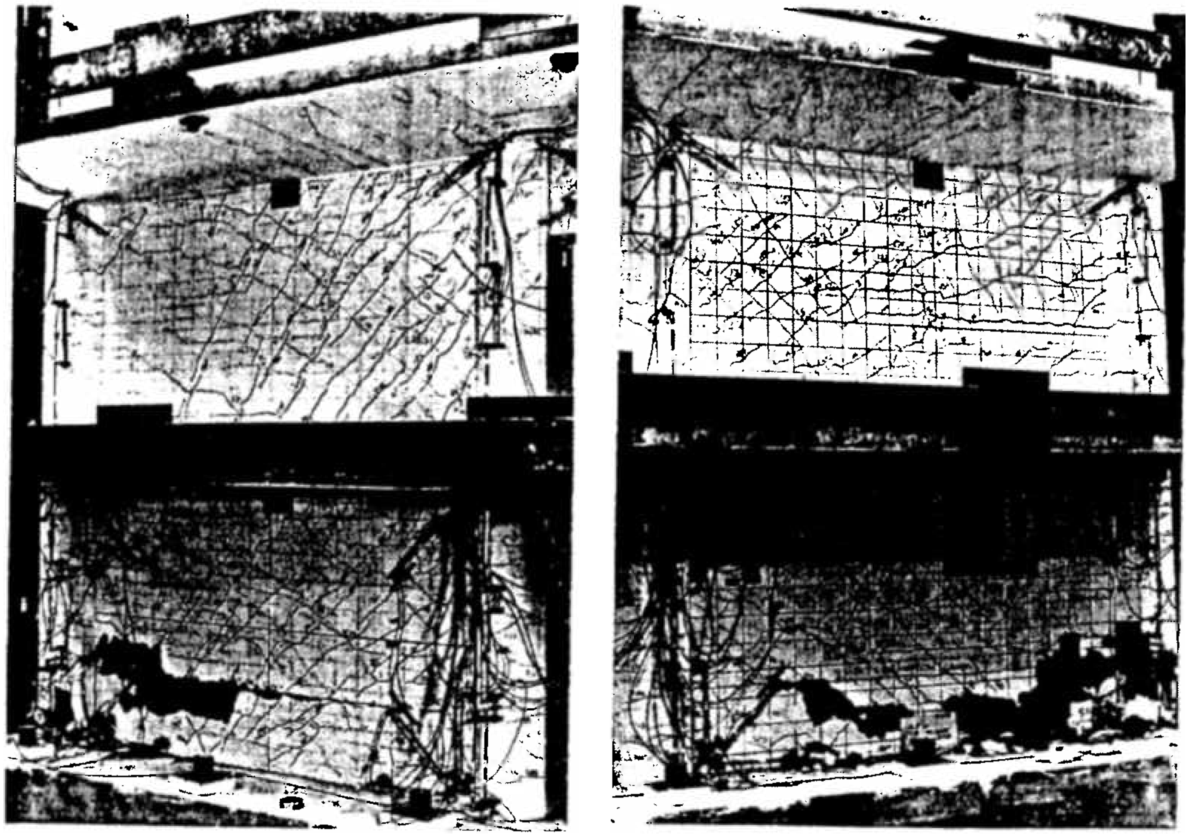

(a) Base of left pier

(b) Base of right pier

Figure 2.28: Damage to 1C at web crushing of left wall pier (-1.3% drift) (Ozselcuk, 1989)

degrades the flexural and shear stiffness of the wall. The results of these two experiments plus two other investigations using repaired specimens 1CR and 1CRR allowed the researchers to quantify the internal force-stiffness and internal force-strength interaction present in a coupled wall. Based on these results, the researchers made the following conclusions/recommendations regarding coupled-wall behavior and design.

- To predict the strength and stiffness of coupled walls piers, the effects of the axial forces on the flexural and shear stiffnesses need to be carefully considered.

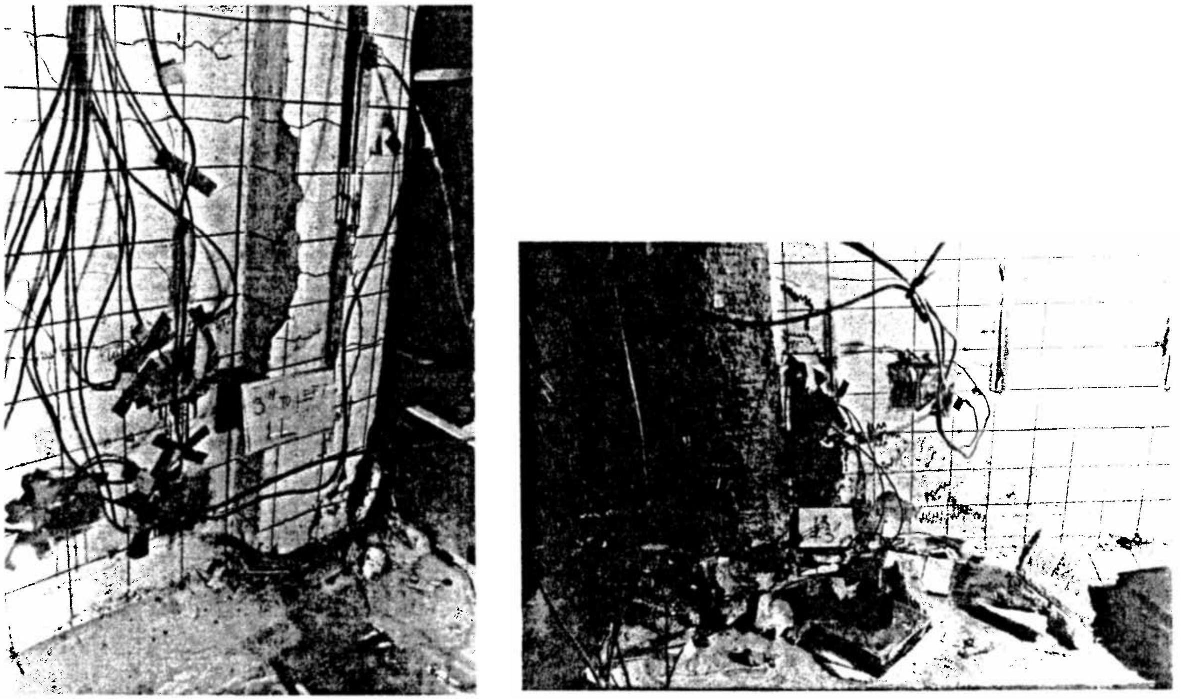

(a) Base of left pier (rear view)

(b) Base of right pier (rear view)

Figure 2.29: Damage to 2C at the end of the test (Ozselcuk, 1989)

- Results suggest there is a link between the reduced ductility of the compression wall and the increased axial compression caused by this wall; furthermore, the high axial tensile force in the tension wall leads to significant loss in flexural stiffness and strength.

- Differences in the energy dissipation capacities between the specimens suggests increasing coupling action in the system leads to increasing damage in the wall piers rather than the coupling beams.

- Coupling beams should be designed using the most accurate properties (i.e. design for strain-hardening, concrete confinement and contribution of slab steel in negative bending) so the degree of coupling does not exceed 50%.

- The wall piers should be designed so that the axial compressive stress demands at the ultimate limit state do not exceed $0.2f'_c$ and the axial force in the tension wall at the ultimate limit state does not overcome the gravity forces.

2.5.4 Lequesne (2011) – Design and Behavior of High-Performance Fiber-Reinforced Concrete Coupling Beams and Coupled-Wall Systems

Research Objectives

Two 1/3-scale, 4-story concrete coupled-wall specimens were tested under quasi-static lateral loading by Lequesne (2011) at the University of Michigan. For each specimen, the majority of the specimen was constructed of normal weight concrete and reinforced with mild reinforcing steel. Critical regions in the each specimen were identified and constructed of strain-hardening, fiber reinforced concrete (FRC); FRC was used to delay concrete cover damage and increase the ductility of the system under cyclic loading. Additionally, some coupling beams were precast using FRC and mild reinforcement. Previous large-scale experimental tests conducted by Canbolat et al. (2005) demonstrated that precast coupling beams with FRC fail in a ductile fashion and that FRC adequately confines the diagonal reinforcement and significantly increases to the shear capacity of the coupling beam. The objectives established by the component tests of the study were (Lequesne et al., 2010).

- Demonstrate that precast coupling beams can be integrated with cast-in-place structural walls in a constructible and efficient manner

- Study the behavior of coupling beams with different reinforcement details in a coupled-wall system

- Investigate coupling beam, concrete slab and wall pier interaction under cyclic loading

- Evaluate the performance of FRC wall piers with reduced conventional boundary element confinement details

Test Program

Two 1/3-scale, 4-story, coupled walls were tested under quasi-static lateral loading and constant axial load. Figure 2.30 shows the configuration of the specimens. The specimens were 10 ft wide by 16 ft tall. The wall piers were T-shaped and designed per ACI 318-08. The wall piers were 4 ft long by 7 in thick and the dimensions of the flange were 21 in wide and 7 in thick. The wall piers were capacity-designed for shear using the results of a plastic analysis and an assumed mechanism similar to that is Figure 2.1. For each specimen the coupling beam aspect ratio equaled 1.71 and the design of the beams differed up the height of the wall. Coupling beams were constructed of normal concrete as well as FRC and also differed in reinforcement layout. Both specimens include reinforced concrete slabs on the second and fourth floor as a means of distributing the applied lateral loads to the specimen; however, these components were casted separately and assumed to behave in noncomposite action.

Figure 2.31 shows the coupling beam designs for CW1. For Specimen CW1, coupling beams were all precast; three were constructed using FRC while the coupling beam on the second floor level was constructed using conventional concrete. The coupling beams were designed for a shear stress demand of $7\sqrt{f'_c}$ psi (f'_c in psi), with half of this demand to be carried by the diagonal reinforcement and the other half to be carried by the stirrups. While this violates ACI 318-08 design requirements, component tests (Canbolat et al., 2005) demonstrated coupling beams designed using this approach adequately carried the shear demands associated with large cyclic displacements levels. A three inch portion of the longitudinal reinforcement in the third floor coupling beam (Figure 2.31b) was debonded in hopes of eliminating a single failure plane along the terminated ends of the longitudinal dowel bars. The "RC" coupling beam on the second story was of a similar design to the "bonded" FRC beams located on the first and fourth floors, with the exceptions that 1) the development length of the longitudinal dowel bars along the beam-to-wall interface was extended and 2) the transverse reinforcement was doubled.

The design details for the wall piers and the coupling beams of the second specimen, CW2, are shown in Figure 2.30 and 2.32. For the wall piers, the stirrup spacing in the boundary elements of the left and right wall piers was increased, respectively, to 1.5 and 3 times the spacing of Specimen CW1. This was done to investigate the effectiveness of the FRC in providing adequate ductility and confinement to the wall pier boundary elements. The coupling beam design for CW2 was similarly to that of CW1, with the exception that 1) the coupling beam reinforcement detail excluded the termination of the dowel bars three inches into the wall but rather extended into the wall piers as fully developed bars, and 2) for the third floor coupling beam design, all longitudinal bars were fully bonded into the wall pier and no-debonded length was provided as for CW1.

A photo of Specimen CW1 in the testing setup is shown in Figure 2.33. A reverse cyclic displacement history for a total of 13 cycles was used to control the specimen in displacement-control. Lateral loads were applied through the second and fourth floor slabs via horizontal actuators, and the ratio of the loads by the two actuators was such that the effect loading height was 81% of the specimen height. Each specimen was subjected to two cycles at 0.25%, 0.5% and 0 75% and 1.0% drift levels. Then from 1.0 to 2.0% drift one cycle at 0.25% drift increments was executed. After 2.0% drift each new cycle was increased by 0.5% drift. An axial load of $0.07f'_cA_g$ was applied to each wall pier via two prestressing strands anchored in the foundation and by a hydraulic jack located at the second story slab (Figure 2.33). A constant vertical load was maintained throughout the experiment (Lequesne et al., 2010).

Experimental Test Results

For Specimen CW1, the moment-drift response is shown in Figure 2.34 and observed behavior was as follows:

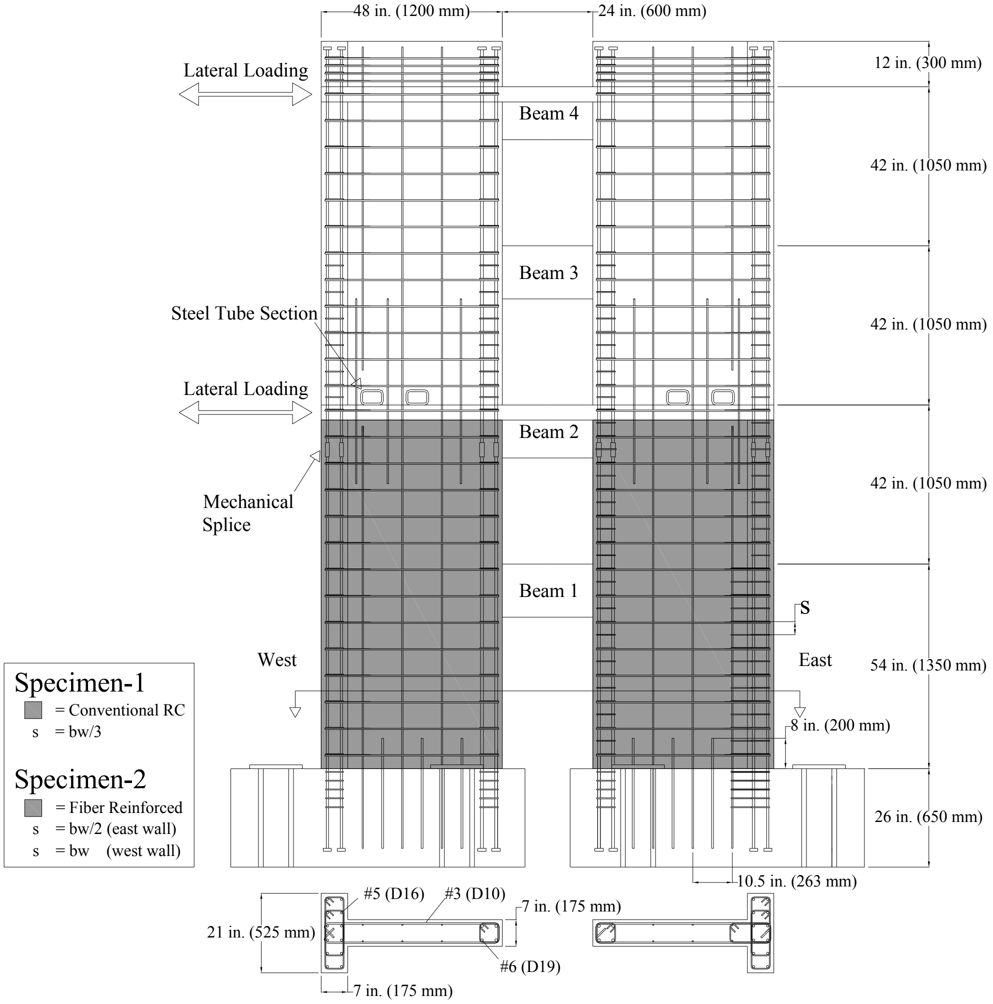

Figure 2.30: Test specimen geometry and reinforcement detail (Lequesne et al., 2010)

- Diagonal cracks in the wall piers of Specimen CW1 were observed at the end of the two drift cycles to 0.25% drift. This damage pattern transitioned to horizontall cracking in the boundary elements of the wall piers in the later cycles.

- It was reported that initial yielding of the diagonal reinforcement in all of the coupling beams occurred prior to the 0.5% drift (cycles 3 and 4)

- Yielding of vertical reinforcement located in the inner boundary element of each pier, when that pier was considered the compression pier, occurred prior to the 1.0% drift (cycles 7 and 8) (Lequesne, 2011).

- Following yielding in the wall piers, during the 1.25% drift cycles, the load-displacement behavior softened substantially compared to the initial stiffness. The system maintained 80% of its peak strength to a maximum drift demand of 2.5%.
- It was reported that the coupling beams in the second and third stories behaved predominately in a sliding shear fashion from 2.0% drift to the end of the test (cycles 12 and 13).
- During cycles to 2.5% drift, significant damage (i.e. cocrete cracking and spalling) was observed in the wall piers at the coupling beam-to-wall interface. This was attributed to the short anchorage length in the wall piers provided for the coupling beam longitudinal steel. This damage did not significantly affect the strength or stiffness of the system.
- During loading to 2.5% drift, reinforcing steel in the coupling beams and wall piers fractured and the test was terminated.
- The base of Specimen CW1 is shown Figure 2.36a at the end of the test and note this photo is taken from the rear for both specimens, so the nomenclature maintained (i.e. right and left wall pier) as a part of this review is flipped. Also note little damage in the form of concrete spalling occurred in the base of the wall piers. On the other hand, damage to the concrete in the wall pier at the coupling beam connections was much more severe (Figures 2.37c and 2.37a).

The response of CW2 was very similar to CW1, with the exception that an improved detail for anchorage of coupling beam horizontal steel in the wall piers reduced the damage and sliding at the coupling beam-to-wall interface. For Specimen CW2, the moment-drift response is shown in Figure 2.35 and observed behavior was as follows:

- Similar to CW1, diagonal cracks in the wall piers of Specimen CW2 were observed at 0.25% drift (cycles 1 and 2), This damage pattern transitioned to horizontall cracking in the boundary elements of the wall piers in the later cycles.
- It was reported that initial yielding of the diagonal reinforcement in all of the coupling beams occurred prior to the 0.5% drift (cycles 3 and 4)
- Yielding occurred prior to 1.0% drift in the inner boundary elements of both wall piers (cycles 7 and 8).
- The specimen maintained 80% of its peak strength beyond the 2.5% drift in the positive loading direction and beyond 3.5% drift in the negative loading direction. During the 2.5% drift cycle, diagonal cracks propagated into the flange of the compression wall (left pier in Figure 2.30); crushing of the web concrete as well as extensive spalling of the cover in the wall flange were observed at the 2.5% drift demand (cycle 13). On the reverse cycle, concrete crushing occurred in the flange of the compression pier at approximately -3.5% drift.

The base of Specimen CW2 is shown Figure 2.36b. There is more damage to the boundary element of the left wall pier. Recall this pier had half as much transverse reinforcing steel as the right wall pier. Damage to the coupling beams on the second and fourth floor are shown in Figures 2.37d and 2.37b. Unlike Specimen CW1, the coupling beams in CW2 had fully developed dowel bars and this detail focused damage in the precast beam away from the beam-to-wall interface leading to a better evaluation between the different coupling beam details. Additionally, no sliding behavior in the coupling beams was observed during this test.

Research Conclusions

Both specimens maintained lateral strength to drift demands in excess of 2.5%. The authors concluded that the use of precast coupling beams resulted in faster construction time than would have been the case if cast-in-place coupling beams with ACI code compliant reinforcement details had been used. The researchers also concluded that FRC significantly improved the damage tolerance of critical structural component regions in the coupled wall system and in combination with transverse reinforcement, provided adequate confinement to the boundary elements and diagonal reinforcement in the coupling beams. It was observed in the both experiments the progression of yielding led to the development of the desired and expected plastic hinge mechanism. Adequate shear reinforcement was provided to carry the demands associated this this mechanism.

The authors also used the experimental test results to make conclusions about the earthquake response of coupled walls. In general measured coupling beam chord rotations were generally less than what is predicted in design suggesting there is an additionally flexibility in the deformation mechanism assumed in design (i.e. the effective distance between the wall pier centers of rotation is smaller than traditionally assumed distance or the effective length of the coupling beam is longer than $l_n + h_b$). Additionally, diagonal cracks propagating from the tension wall through the coupling beam and into the compression wall observed throughout the test, and this distribution is typically indicative of shear redistribution from the tension wall to the compression wall due to changes in flexural stiffness of the tension wall.

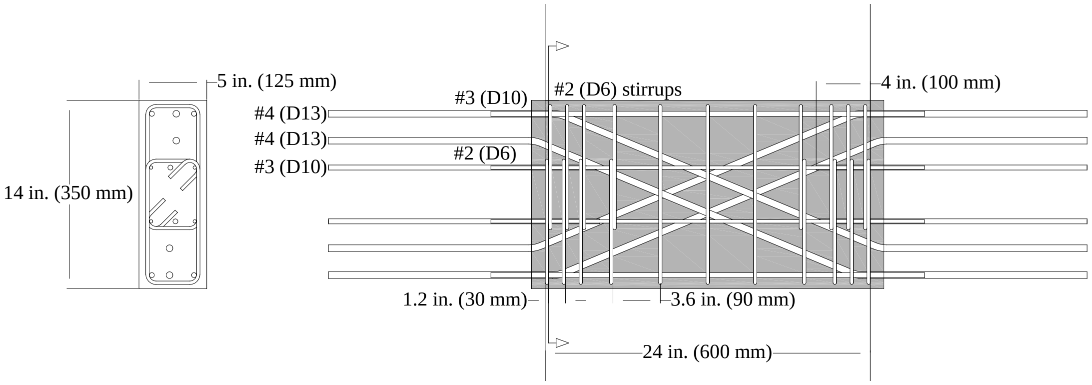

(a) Floor 1 and 4 (FRC-bonded)

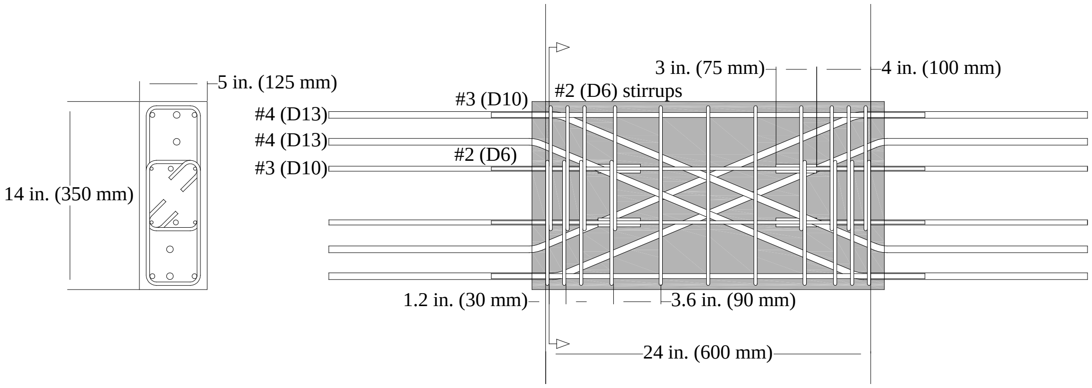

(b) Floor 3 (FRC-unbonded)

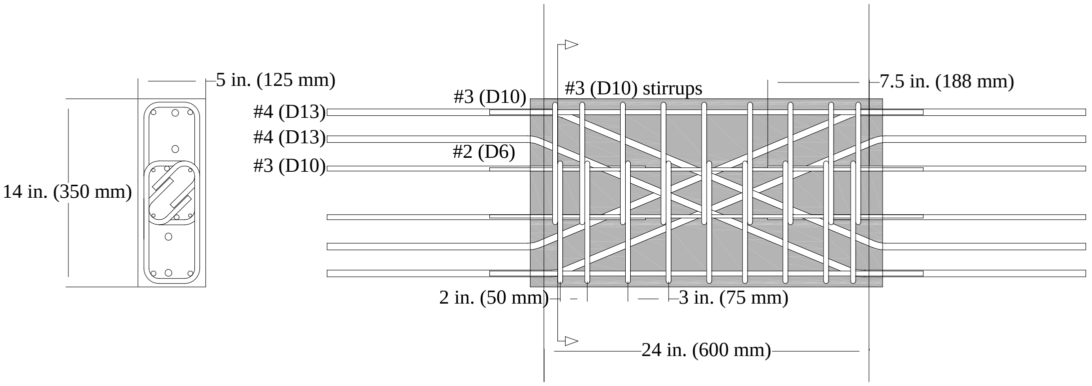

(c) Floor 2 (RC)

Figure 2.31: Coupling beam reinforcement detail for CW1 (Lequesne et al., 2009)

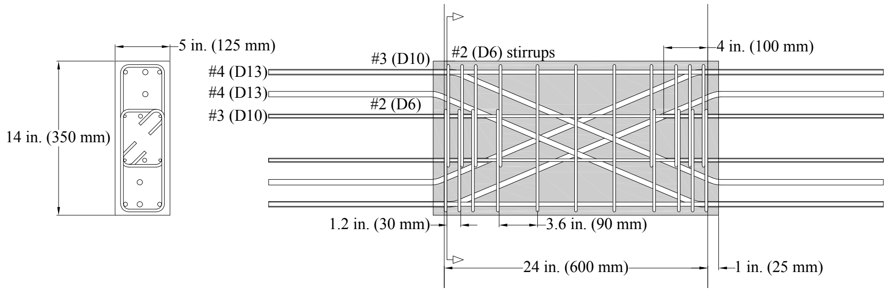

(a) Floor 1, 3 and 4 (FRC-bonded)

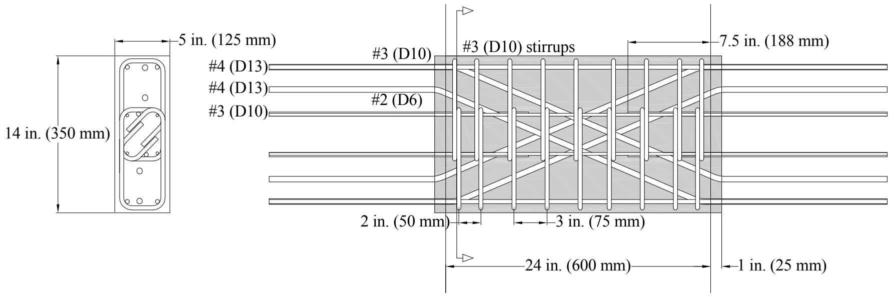

(b) Floor 2 (RC)

Figure 2.32: Coupling beam reinforcement detail for CW2 (Lequesne et al., 2010)

Figure 2.33: Test setup for walls tested by Lequesne et al. (2010)

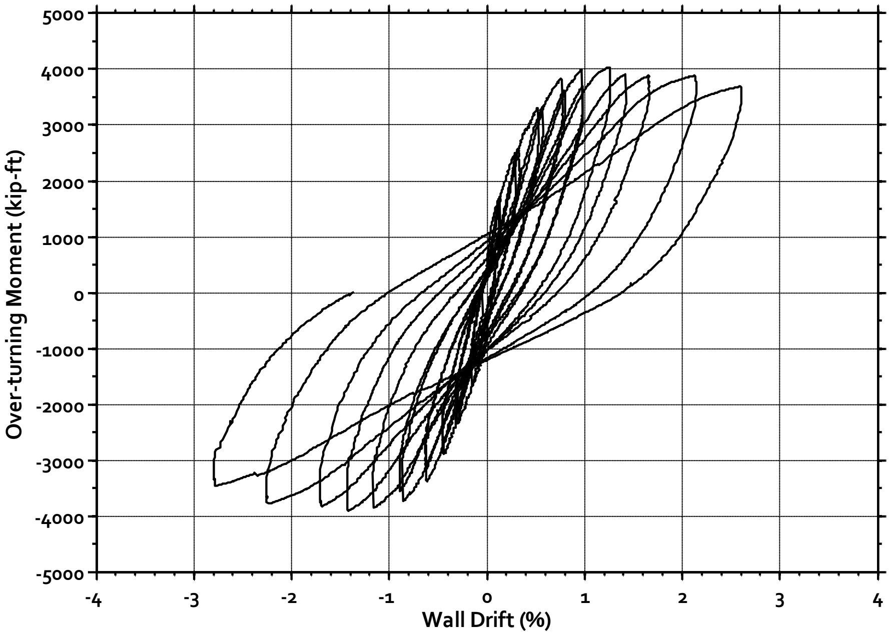

Figure 2.34: Force-displacement response for Specimen CW1 (Lequesne, 2011)

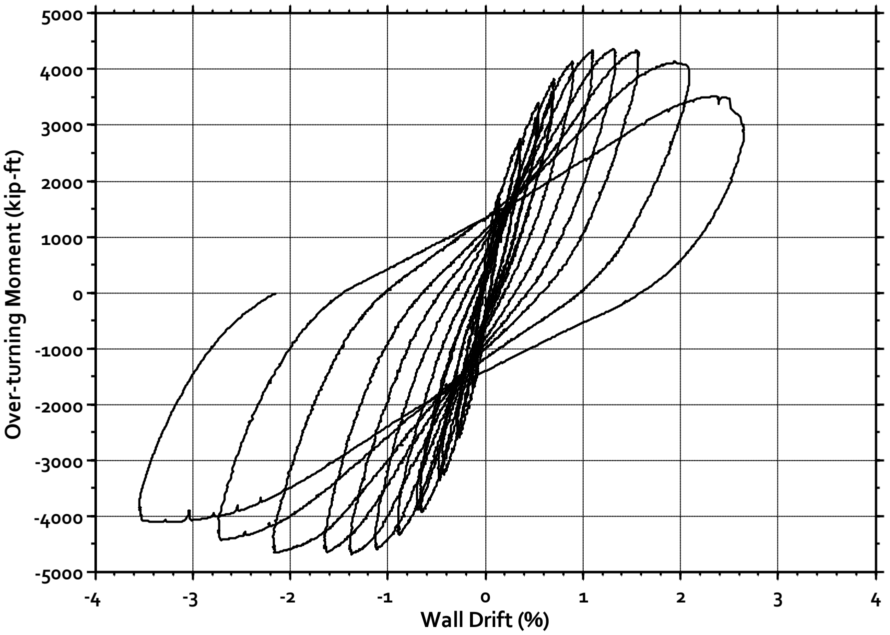

Figure 2.35: Force-displacement response for Specimen CW2 (Lequesne, 2011)

(a) Base of CW1 (rear view)

(b) Base of CW2 (rear view)

Figure 2.36: Damage to wall piers at the end of each test (east wall pier is on the left) (Lequesne, 2011)

(a) CW1 (fourth floor beam)

(b) CW2 (fourth floor beam)

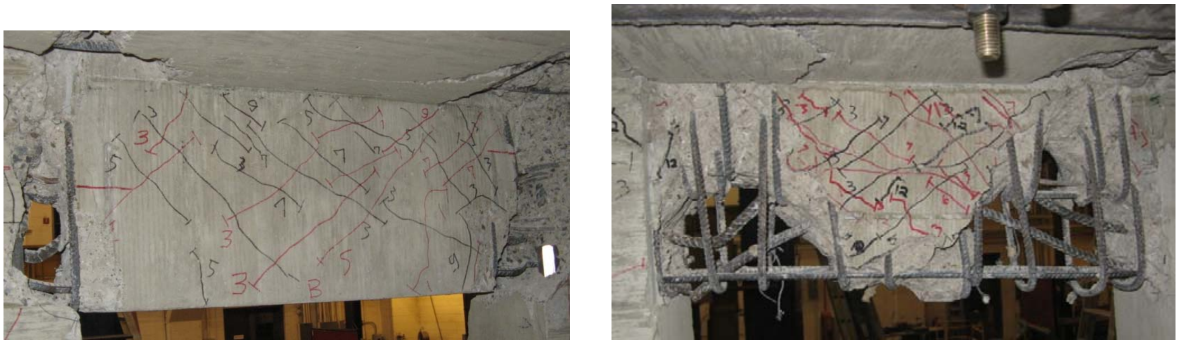

(c) CW1 (second floor beam)

(d) CW2 (second floor beam)

Figure 2.37: Damage to coupling beams at the end of each test (Lequesne, 2011)

2.5.5 Compiled Experimental Coupled Wall Data

These computed data are used to in combination with data from the NEESR CW1 test to support an evaluation of the impact of design parameters on coupled wall response (Chapter 6) and the evaluation of linear (7) and nonlinear (Chapter 8) response models.

Figure 2.38 and Table 2.4 provide a comparison of the previously tested large-scale coupled walls specimens and the NEESR CW1 specimen, which is the subject of this research. For comparison, a “typical” coupled wall found in mid- to high-rise buildings is included. This wall geometry was determined from a building inventory, which is discussed in the next chapter, and represents average values for wall length, wall height and coupling beam dimensions. For each test specimen, the dimensions, presented in the figure and table, were scaled using the experimental scale noted in each test program. Two primary findings are apparent from this figure:

1. In general, most coupled-walls tests simulate low-rise construction. Only three specimens (CW1 and Ozselcuk (1989) test series) simulate mid-rise construction. This is not surprising since simulation of mid- or high-rise construction requires very large forces, very small scale, or both.

2. There is significant variation among the tested specimens with respect to the pier length and coupling beam dimensions. For example, the walls tested by Shiu et al. (1981) have long wall pier lengths and shorter coupling beams, where the walls tested by Ozselcuk (1989) have long wall lengths and long coupling beams.

Table 2.5–Table 2.9 provide detailed design info and experimental data for the previously tested coupled-wall specimens discussed in this section. An overview of coupled wall properties are presented in Table 2.5. Reinforcement properties for the wall pier boundary elements, wall pier web region and the coupling beams are shown in Tables 2.6, 2.7 and 2.8, respectively. Finally, the experimental force displacement results are tabulated in Table 2.9.

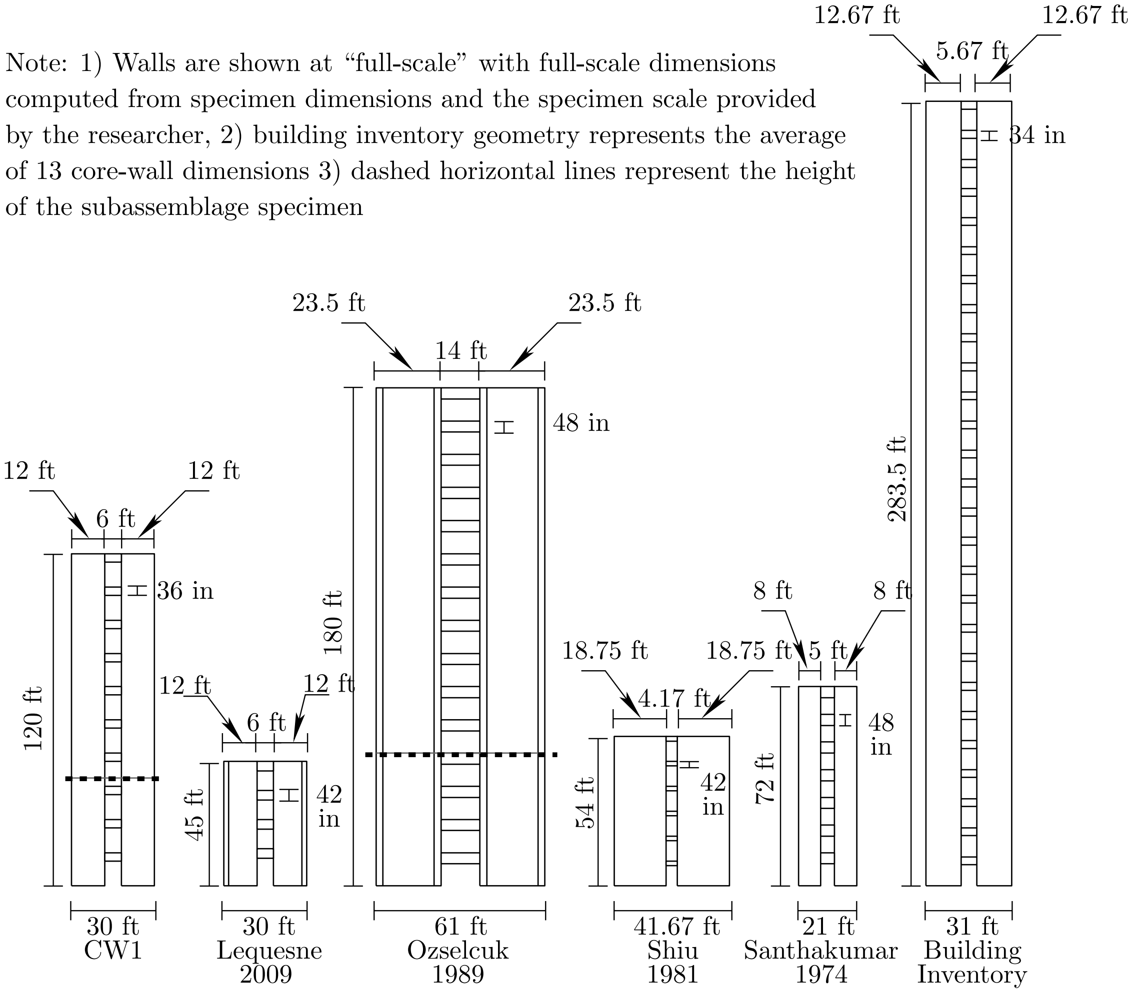

Note: 1) Walls are shown at "full-scale" with full-scale dimensions computed from specimen dimensions and the specimen scale provided by the researcher, 2) building inventory geometry represents the average of 13 core-wall dimensions 3) dashed horizontal lines represent the height of the subassemblage specimen

Figure 2.38: Comparison of coupled wall specimens and building inventory geometry

Table 2.4: General information for previous coupled wall research programs

Test Series	**Test Date**	**# Tests**	**Scale**	**Story Info**	l_n/h_b	l_w/t_w
CW1	2011	1	1/3	10@12 ft*	2.00	8.0
Lequesne	2009	2	1/3	4@10.5 ft	1.71	6.9
Ozselcuk	1989	2	1/3	15@12 ft*	3.50	23.5
Shiu	1981	2	1/3	6@9 ft	2.46	18.8
Santhakumar	1974	2	1/4	7@10 ft	1.25	6.0
Building Inventory	—	—	—	27@10.5 ft	1.91	5.51

* Actual experimental specimens are subassemblages of a taller prototype

Table 2.5: Coupled wall properties

Specimen	Wall Piers					Coupling Beams						
	Shape[1]	l_w/t_w	H/l_w	f'_c **(ksi)**	f_y **(ksi)**	**Slab?**	**# of Beams**	**R/F Layout**[4]	l_n/h_b	h_b/b_w	f'_c **(ksi)**	f_y **(ksi)**
Santhakumar WallA	R	6.00	9.00	4.58	44.2	N	7	C	1.25	4.00	4.58	45.7
Santhakumar WallB	R	6.00	9.00	4.35	44.2	N	7	D	1.25	4.00	4.35	45.7
Shiu CS1	R	18.75	2.88	4.43	63.0	Y	6	C	2.46	1.67	3.66	77.0
Shiu RCS1	R	18.75	2.88	4.43	63.0	Y	6	C	2.05	0.80	4.07	70.0
Ozselcuk 1C	B	23.50	7.66	5.80	58.9	Y	4/15**	C	3.50	2.00	5.20	80.0
Ozselcuk 2C	B	23.50	7.66	4.53	64.0	Y	4/15**	C	3.50	2.00	4.95	80.0
Lequesne CW1	T	6.86	3.75	7.00	68.0	Y*	4	D	1.71	2.80	10.4	76.9
Lequesne CW2	T	6.86	3.75	7.00	68.0	Y*	4	D	1.71	2.80	10.4	76.9

[1] R - Rectangular, B - Barbell, T - T-shaped

* Reinforced concrete slab only included on second and fourth floor

** Specimen is a subassemblage of a 15 story prototype

[4] C - Conventionally reinforced, D - Diagonally reinforced

where,

l_w	length of wall pier
t_w	thickness of wall pier
H	height of specimen or prototype (Ozselcuk 1C)
f'_c	compressive strength of concrete
f_y	yield strength of reinforcement
l_n	clear span length of coupling beam
h_b	depth of coupling beam
b_w	breadth of coupling beam web

Table 2.6: Wall pier boundary element reinforcement properties

	Outer Boundary Element					Inner Boundary Element				Confinement			
Specimen	**Bar Size**	**# of Bars**	f_y **(ksi)**	${f_u}^1$ **(ksi)**	ρ_{vert} (%)	**Bar Size**	**# of Bars**	f_y **(ksi)**	ρ_{vert} (%)	d_b **(in)**	f_y **(ksi)**	s_h **in**	ρ_s (%)
Santhakumar WallA	#5	10	44.2	68.4	3.49	#5	2	44.2	0.70	0.250	51.0	3.00	2.23**
Santhakumar WallB	#5	10	44.2	68.4	3.49	#5	2	44.2	0.70	0.250	51.0	3.00	2.23**
Shiu CS1	#4	12	63.0	101	5.63	#4	12	63.0	5.63	0.697	74.0	1.33	2.29
Shiu RCS1	#4	12	63.0	101	5.63	#4	12	63.0	5.63	0.697	74.0	1.33	2.29
Ozselcuk 1C	#6	8	58.9	97.0	3.52	#6	8	58.9	3.52	0.207	73.0	0.83*	1.80
Ozselcuk 2C	#6	8	64.0	74.0	3.52	#6	8	64.0	3.52	0.207	73.0	0.83*	1.80
Lequesne CW1	#5	12	67.2	109	2.53	#6	4	68.0	3.59	0.375	74.2	2.30	2.75
Lequesne CW2	#5	12	67.2	109	2.53	#6	4	68.0	3.59	0.375	74.2	7.00	1.56

[1] f_u is the same for inner boundary element

* Spiral reinforcement pitch

** No boundary elements, entire wall pier was confined

where,

f_y	yield strength of reinforcement
f_u	ultimate strength of reinforcement
ρ_{vert}	ratio of vertical reinforcement in the wall boundary over the cross-sectional area of the boundary element
d_b	diameter of reinforcement
s_h	spacing of confinement hoops or spirals
ρ_s	volumetric reinforcement ratio of confinement as defined by Mander et al. (1982)

Table 2.7: Wall pier web region reinforcement properties

Specimen	d_b **(in)**	f_y **(ksi)**	f_u **(ksi)**	**# of**[1] **Bars**	s_{vert} **(in)**	ρ_{vert} **(%)**	s_{horz} **(in)**	ρ_{horz} **(%)**
Santhakumar WallA	0.250	49.8	70.7	2	6.0	0.41	3.0	0.88
Santhakumar WallB	0.250	49.8	70.7	2	6.0	0.41	3.0	0.88
Shiu CS1	0.239	77.0	103.0	6	9.0	0.24	4.0	0.55
Shiu RCS1	0.239	77.0	103.0	6	9.0	0.24	4.0	0.55
Ozselcuk 1C	0.250	71.3	96.0	19	4.0	0.61	4.0	0.61
Ozselcuk 2C	0.25	74.0	102.0	19	4.0	0.61	4.0	0.61
Lequesne CW1	0.375	74.2	112.0	3	10.5	0.30	7.0	0.45
Lequesne CW2	0.375	74.2	112.0	3	10.5	0.30	7.0	0.45

[1] Number of vertical reinforcing bars in wall pier web region

where,

d_b	diameter of reinforcement
f_y	yield strength of reinforcement
f_u	ultimate strength of reinforcement
s_{vert}	horizontal spacing of vertical reinforcement in the web
ρ_{vert}	reinforcement ratio of vertical reinforcement in the web, $A_s/t_w s_{vert}$
s_{horz}	vertical spacing of horizontal reinforcement in the web
ρ_{vert}	reinforcement ratio of horizontal reinforcement in the web, $A_s/t_w s_{horz}$
&	all other variables are defined in Appendix A

Table 2.8: Coupling beam reinforcement properties

	Diagonal						Longitudinal						Transverse			
Beam Type	**Bar Size**	α_{cb} **(deg)**	**# of Bars**	f_y **(ksi)**	f_u **(ksi)**	ρ_d **(%)**	**Bar Size**	**# of Bars**	f_y **(ksi)**	f_u f_u	$\rho_l^{'}$ **(%)**	ρ_l **(%)**	d_b **(in)**	f_y **(ksi)**	s_v **(in)**	ρ_v **(%)**
Santhakumar WallA																
Typ.	–	–	–	–	–	–	#3	2/2	45.7	62.6	0.62	0.62	0.250	50.2	2.00	1.76
Santhakumar WallB																
Typ.	#3*	32.8	2/2	45.7	62.6	1.12	–	–	–	–	–	–	0.188	33.3	4.50	0.35
Shiu CS1																
Typ.	–	–	–	–	–	–	M6	2/2	77.0	103	0.36	0.36	0.697	74.0	1.33	1.13
Shiu RCS1																
Typ.	–	–	–	–	–	–	#3	6/6	70.0	103	0.91	0.91	0.697	74.0	0.83	1.00
Ozselcuk 1C & 2C																
B-1 (T1)	–	–	–	–	–	–	#3	5**/4	75.8	108	1.26	0.36	0.166	99.9	2.50	0.43
B-2 (T2)	–	–	–	–	–	–	#4	5**/4	80.0	106	1.28	0.66	0.166	99.9	1.50	0.72
B-3,4 (T3)	–	–	–	–	–	–	#4	6**/5	80.0	106	1.81	0.99	0.166	99.9	1.50	1.08
Lequesne CW1[1]																
B-1,4 (BF)	#4	22.6	2	76.9	115	0.67	#3	1/1	79.4	121	0.20	0.20	0.250	–	3.60	0.54
B-2 (RC)	#4	22.6	2	76.9	115	0.67	#3	1/1	79.4	121	0.20	0.20	0.375	79.4	3.00	0.65
B-3 (DF)	#4	22.6	2	76.9	115	0.67	#3	1/1	79.4	121	0.20	0.20	0.250	–	3.60	0.54
Lequesne CW2[1]																
B-1,3,4 (BF)	#4	22.6	2	76.9	115	0.67	#3	1/1	79.4	121	0.20	0.20	0.250	–	3.60	0.65
B-2 (RC)	#4	22.6	2	76.9	115	0.67	#3	1/1	79.4	121	0.20	0.20	0.375	79.4	3.00	0.54

[1] BF - Bonded R/F with Fiber Reinforced Concrete, DF - Debonded R/F with Fiber Reinforced Concrete, RC - Reinforced Concrete

* Diagonal bundle includes 2-#3 and 2-$\frac{1}{4}\phi$ bars, properties shown are for 2-#3

** Slab steel properties excluded, but ρ_l' includes 20 #2 bars from the slab

Note: variables are defined on the next page where,

α_{cb}	orientation of diagonal reinforcement
f_y	yield strength of reinforcement
f_u	ultimate strength of reinforcement
ρ_d	reinforcement ratio of diagonal reinforcement bundle, A_{vd}/bd
$\rho_l^{'}$	reinforcement ratio of the top longitudinal reinforcement, $A_s^{'}/bd$
ρ_l	reinforcement ratio of the bottom longitudinal reinforcement, A_s/bd
d_b	diameter of vertical reinforcement
s_v	horizontal spacing of vertical reinforcement in coupling beam
ρ_v	vertical reinforcement ratio, A_v/bs_v
&	all other variables are defined in Appendix A

Table 2.9: Coupled wall experimental results

Specimen	$^{M}/_{VH}$	λ_N	v_y ($\sqrt{f'_c}$)	D_y (%)	v_{max} ($\sqrt{f'_c}$)	$D_{V_{max}}$ (%)	v_{90} ($\sqrt{f'_c}$)	$D_{V_{90}}$ (%)	$\mu_{V_{90}}$
Santhakumar WallA	0.694	0.06	2.67	0.33	4.74	1.65	4.27	1.93	5.8
Santhakumar WallB	0.694	0.06	2.68	0.15	5.38	0.96	4.84	3.50	24
Shiu CS1	1.00	0.00	1.05	0.10	3.53	0.81	3.18	0.86	8.8
Shiu RCS1	1.00	0.00	3.00	0.47	5.34	1.51	4.81	1.60	3.4
Ozselcuk 1C	0.600	0.09	4.23	0.24	7.13	1.33	6.42	1.34	5.7
Ozselcuk 2C	0.600	0.09	4.60	0.36	6.68	1.24	6.01	1.38	3.8
Lequesne CW1	0.814	0.07	4.71	0.50	5.85	1.25	5.26	2.43	4.9
Lequesne CW2	0.814	0.07	4.71	0.50	6.75	2.15	6.07	1.87	3.7

where,

$^{M}/_{VH}$	effective loading height ratio of specimen
λ_N	wall pier applied gravity load ratio, $^{N_g}/_{f'_c A_g}$
v_y	measured base shear stress demand at yield of specimen, $^{V_{b,y}}/_{l_w t_w}$
D_y	measured total lateral drift at yield of specimen
v_{max}	maximum measured base shear stress demand, $^{V_{b,max}}/_{l_w t_w}$
$D_{V_{max}}$	measured total lateral drift at $V_{b,max}$
v_{90}	measured base shear stress demand at 90% of $V_{b,max}$, $^{0.9V_{b,max}}/_{l_w t_w}$
$D_{V_{90}}$	measured total lateral drift at $0.9V_{b,max}$
$\mu_{V_{90}}$	estimated ductility capacity of specimen, $^{D_{V_{90}}}/_{D_y}$
&	all other variables are defined in Appendix A

2.6 Review of Previous Simulation Studies of Coupled Wall Systems

As performance-based design of reinforced concrete structures becomes more common in practice, there is a need to predict system performance using nonlinear modeling techniques. A number of previous studies have sought to evaluate existing nonlinear analysis software for prediction of wall and coupling beam performance under earthquake loading. As part of the current NEESR project, Mohr (2007) evaluated VecTor2 (Wong and Vecchio, 2002), a 2D continuum software utilizing the modified compression field theory and disturbed stress field theory, for simulating the response of coupling beams with conventional and diagonal reinforcement using an experimental dataset comprising of 22 specimens. Oyen (2006) developed recommendations for simulating the response of concrete walls using nonlinear fiber-type beam-column elements in OpenSees (McKenna et al., 2000) and a set comprising of 60 walls. Additionally, Pugh (2012) has simulated shear wall components using nonlinear analysis software including OpenSees, VecTor2 and Abaqus and a dataset comprising of 70+ wall tests. The following section reviews studies addressing nonlinear analysis of mid- to high-rise coupled-wall systems fro prediction of earthquake performance.

2.6.1 Aktan et al. (1982) - Prediction of the Seismic Responses of R/C Frame-Coupled Wall Structures

To assess the 1973 UBC design provisions as well as state of the art simulation of coupled wall-frame buildings, Aktan et al. (1982) performed a series of linear and nonlinear time-history analyses of a 15-story coupled wall-frame system and an isolated 15-story coupled-wall system. The software package TABS (Wilson and Dovey, 1972) and DRAIN-2D (Powell, 1973) were used. The results of these analyses were used to support the design of a specimen to be tested in the laboratory by Ozselcuk (1989). The analytical models consisted of line elements located at the centroids of the wall piers and coupling beams; rigid links were used to offset the coupling beams from the centroid of the wall piers. In the nonlinear, DRAIN-2D model, elastic beam-column elements with nonlinear moment-rotation hinges were used to model the wall piers and coupling beams. Input parameters needed to define elastic element and rotational-hinge responses were defined using moment-curvature analysis results for all structural component cross-sections. The idealized planar coupled wall and coupled wall-frame models were first analyzed performing linear response-spectrum analyses using TABS. This was followed by nonlinear time-history using DRAIN-2D software. Both these analyses used the 1940 El Centro and 1971 Pacoima Dam ground motions.

A primary conclusion of the study addressed simulation of the gravity system. The results of the linear analysis suggested that the presence of the gravity frames in a dynamic analysis may increase the maximum dynamic base shear depending on the ground motion, and decrease the moment to shear ratio at the base of the coupled wall system. These results were compared with the static analysis results required by the 1973 UBC design standards, which did not include the gravity frame; the author concluded a coupled-wall design based on the static analysis procedure without modeling the gravity system does not result in a safer design than a design based on the results of a linear dynamic analysis in which the gravity frame is modeled.

Additionally, the results supported several conclusions regarding design and performance of coupled walls. Due to the uncertainty associated with defining basic strength, stiffness and nonlinear characteristics of the coupling beams and, especially, the wall piers, the researchers concluded that this form of nonlinear simulation was inadequate for predicting coupled wall-frame behavior. The 1973 UBC design procedure also led to a coupled wall design in which the shear strength of the coupled-wall system was not sufficient to resist the shear demands associated with the collapse limit state resulting from the two ground motions. Flexural overstrength of the system and a redistribution of shear demand from the tension wall to the compression wall caused the shear demand in the compression pier wall to be well above the level of shear the wall piers were designed to withstand. In addition to this demand, the moment to shear ratio at the base of the system at the time of the maximum base shear ranged from 0.30H to 0.46H, where H is the total height of the coupled wall. These results were for the coupled wall-frame model and depended on the input ground motion. This was significantly lower than the designed moment to shear ratio of 0.68H and most likely led to the high shear demand at the base of the wall.

2.6.2 McNeice and Harries (2004) – Performance-Based Design of a 30-Story Coupled Core Wall Structure

McNeice and Harries (2004) investigated the advantages of using a performance-based approach to design a 30-story coupled core-wall system over the strength-based approach used typically in design. The main differences between the two designs were as follows: i) unlike the code-based design, which assumes the wall piers and coupling beams yield simultaneously, the performance-based design (PBD) included more control over the non-linear behavior of certain structural components (i.e. the coupling beams were designed to yield at the Life Safety performance level and the wall piers were designed to yield at the Collapse Prevention performance level), ii) the coupling beams in the PBD were designed at each floor so the shear capacity was equal to the factored design shear force while in the code-based design only four coupling beam details were used over the height of the structure and iii) a performance objective in the PBD limited the coupling beams shear strength to a maximum of $6\sqrt{f'_c}$ (psi) where as the code-based design had to meet ACI requirements ($10\sqrt{f'_c}$).

The evaluation of the 30-story strength-based design was done using the results of three three sets of linear dynamic analyses performed using ETABS (CSI, 2001). Shell elements were used to model the wall piers and floors, and line elements were used to model the coupling beams. All the analyses were performed in the direction which coupling action would developed in the system, and the three sets of analyses included coupling beams modeled as conventionally reinforced, diagonally reinforced and linked coupling beams. The geometries and effective stiffness parameters differed between the conventional and diagonal beam designs. The linked coupling beams did not provide any additional stiffness or strength to the system so the overall model acted like two “linked” isolated wall piers.

The 30-story performance-based design was evaluated with static and dynamic nonlinear analyses using Ruaumoko (Carr, 2001). Rigid links were used to connect coupling beams and wall elements to offset the ends of the coupling beams from the centroids of the wall to the face of the wall. The wall piers were modeled using beam-column elements with axial load-moment interaction surfaces located at the wall centroids; while the coupling beams were modeled using line elements which do not account for axial load-moment interaction. A nonlinear pushover analysis was performed first; bilinear force-displacement response histories were used in the hinges at both ends of the wall pier and coupling beam elements to simulate nonlinear response. For the dynamic analyses, a more sophisticated hysteretic model, which accounts for stiffness and strength degradation due to cyclic loading was used for coupling beam and wall hinges. The dynamic model was subjected to five ground motions, two of which were artificially generated to represent design level and maximum credible ground accelerations.

The results of the linear dynamic study of the strength-designed coupled wall showed that the presence of the coupling action increased the stiffness of the structure significantly over that of two uncoupled walls. The degrees of coupling resulted in large coupling beams shear demands as well as large wall pier axial force demands for the two coupled-wall models. Additionally, a strength-based design approach may produce a coupled wall with a high degree of coupling and, as a result, coupling beam shear demands that exceed current code limits for which design is impractical. On the other hand, the nonlinear analysis results of the performance-based design coupled wall showed that reducing the effective stiffness of the coupling beams provided a reasonable procedure for determining the wall pier design forces. In the nonlinear pushover analysis, all of the coupling beams yielded before the wall piers yielded. The authors concluded from this that a certain level of care needs to be used in designing the coupling beams over the height of the structure because a single coupling beam detail used over the entire height will cause an undesirable progression of yielding. Higher mode effects in the all of the time-history analyses led to coupling beam yielding which in turn caused the period of the structure to elongate. Finally, the propagation of the nonlinear hinge region along the height the wall piers (i.e. inelastic action at the ends of each wall element for a number of elements up the height of the model) increased beam rotations in the middle of the structure.

2.6.3 Salas (2008) - Modeling of Tall Reinforced Concrete Wall Buildings

A parametric study of a 48-story, reinforced concrete coupled core-wall structure was performed by Salas (2008) to evaluate three different modeling approaches. and develop criteria to be used in performance-based design of tall buildings. A series of nonlinear time-history analyses using two input ground motions were completed using Perform-3D software (CSI, 2006). Both elastic shell elements and inelastic fiber shell elements were used to model the wall piers of the core-wall structure, and elastic beam-column elements with nonlinear shear hinges were used to model the coupling beams. Cyclic stress-strain relations were used to model the concrete (unconfined and confined) and steel fibers in the wall piers, and these relations are incorporated into model by user defined strain vs plastic rotation limit states. These limits states where defined using FEMA 356 sec 6.4.3.1. The wall pier elements were discretized such that their height was equal to half the wall length, as recommended from a previous study documented in the report that used data from experimental tests of planar walls. The shear hinge model was defined using a backbone curve with an elastic-perfectly plastic behavior up to a certain deformation, then the strength was reduced to 80% of its maximum strength and stayed at this strength to an ultimate deformation capacity. No guidence to how these limit states were defined was reported.

The case-study building had three different levels of model assumptions. The first five stories of the building were a basement, in which diaphragms were used to connect the core walls to perimeter basement structural walls at each floor. Nonlinear behavior of core and perimeter wall was not expected in the basement. The next six stories, which accounted for approximately 15% of the total core-wall height, were above the basement slab. These stories were assumed to be the plastic-hinge region of the building, and nonlinear action was expected in the core-wall in these stories. The remaining stories were not considered to be part of the plastic-hinge region and elastic reponse of the core wall was expected in these stories.

Three different modeling assumptions were investigated as part of this study. The first study was the effective elastic stiffness used to model the impact of effective shear stiffness on seismic performance; five models were created in which the elastic effective shear stiffness in the core-wall hinge region ranged from $0.25G_cA_cv$ to $0.50G_cA_{cv}$ where, G_c is the shear modules and A_{cv} is the shear area of the wall bounded by the thickness of the web and length of the wall. Other variation of effective shear stiffness for the other structural components are reported in Salas (2008). These properties were applied to elements inside and outside the plastic hinge zone as well as the basement walls and diaphragms. The models were subjected to a single ground motion. The results of this study showed how sensitive the response of a core-wall system is, especially to the moment and shear demands in the basement level, on the distribution of effective shear stiffness to different components in the system.

The second study investigated a typical modeling assumption made in design which allows for faster analysis preparation and run time. This assumption is to limit the amount of nonlinear elements to the plastic hinge region of the wall piers and provide elastic elements everywhere else. The other assumption is to provide nonlinear elements throughout the entire height of the wall piers in order to capture nonlinear behavior that could arise due to higher mode effects. The results of this parametric study showed the model using elastic and nonlinear elements grossly overestimated the moments in the upper stories and the shears in the bottom 10 stories while the model using all nonlinear elements over the entire height accommodates some yielding in the upper stories which reduced the demands on the structure. It was recommended that nonlinear elements be used over the entire height of the wall piers in order to accurately capture all the potential hinging regions.

The following two parameter studies only included results from one input ground motion, the 1994 Northridge earthquake, so in order to capture variation in response with respect to ground motion selection, an additional ground motion from the 1964 Niigata earthquake was used to excite a model using nonlinear elements up the entire height of the wall piers and gross shear stiffness properties for all structural components. In the analyses using the Northridge ground motion, high modes of vibration caused a second hinge zone at mid-height of the building. On the other hand, the analysis using the Niigata ground motion responded mainly in fundamental period of vibration and as a consequence limiting the yielding region to the base of the core-wall.

2.6.4 Case Studies of Tall Core Wall Buildings

The following review includes two case study designs of a 40-story tall reinforced concrete coupled core wall building system as a part of an evaluation of the Los Angeles Tall Buildings Structural Design Council's Alternative Design Procedure for Tall Buildings (LATBSDC Alt. Design Procedure)(LATBSDC, 2005). In addition to these case studies, two more case study designs of a 42-story tall coupled core wall tower using two design methodologies (i.e. code-based and performance-based designs (PBD)) were completed as a part of the Pacific Earthquake Engineering Research Center (PEER) Tall Building Initiative and the California Seismic Safety Commission. The code-based design of the core wall systems was performed using modal analysis procedures as prescribed by the 2006 International Building Code (ICC, 2006). On the other hand, the second design follows the recommendations by LATBSDC (2008) which utilizes a 3D modal response spectrum analysis for service level design and a recommended seven 3D nonlinear time-history analyses for collapse prevention design under a maximum considered seismic event (MCE). The design of the two case-studies of the 40-story building using the LATBSDC (2005) recommendations was similar to the design procedures discussed above using the

LATBSDC (2008) recommendations; however, before the new version of this document was published it was recommended engineers design a tall building for a code level design based earthquake (DBE) using a linear dynamic procedure.

Klemencic et al. (2007) and Zekioglu et al. (2007) each performed a 3D modal response spectrum analysis using ETABS for a DBE in order to design a 40-story core wall building. This design was then verified for a MCE by completing seven 3D nonlinear time-history analyses using CSI Perform3D software. Nonlinear behavior of the wall piers were accounted for using fiber shell elements strategically distributed up the height of the building in order to capture spreading of inelastic material behavior while still maintain computational efficiency. Shear deformations in the wall piers were modeled assuming these components to remain elastic. While both research teams used nonlinear elements to model the coupling beams, no details regarding the type of element was given by Klemencic et al. (2007). However, Zekioglu et al. (2007) modeled the coupling beams using linear beam-column elements with nonlinear moment-rotation hinges at the beam ends, and these elements were connected to the wall piers using rigid link elements at the floor level. The results of both studies highlight the importance of verifying the life safety performance of a tall core wall structure using nonlinear analysis procedures. The modal response spectrum analysis is inadequate capturing the dynamic amplifications and as a result the average shear demand from the nonlinear analysis (MCE) was anywhere from 4 to 6 times greater than the DBE results at the base of the wall piers. Additional nonlinear analysis results presented by Klemencic et al. (2007) noted higher mode effects were present in the upper stories of the core wall resulting in larger moments demands as well as a reduction in the moment-to-shear ratio.

In the second set of case studies, ETABS was used to design the 42-story core wall tower for both the code-level design and performance-based design procedure. Fry et al. (2010) and Ghodsi and Flores Ruiz (2010) then performed seven 3D nonlinear time-history analyses to evaluate the performance of the core system under the MCE hazard level. These analyses were carried out using the CSI Perform3D software. Similar to the last set of studies, the wall piers were modeled using nonlinear fiber shell elements that account for inelastic behavior of the reinforcing steel and concrete, and the shear-deformation behavior was modeled as elastic. The coupling beams were modeled using elastic beam elements with nonlinear shear hinges, and the shear hinge parameters were defined by both research teams according to coupling beam tests performed by Naish et al. (2009). A summary of the nonlinear analysis results are as follows:

- The mean coupling beam chord rotations for both case studies were less than half the set acceptance criteria of 0.06 radians
- The mean story drifts for both case studies were less than half the set acceptance criteria of 3% except for the x direction design by Fry et al. (2010) which approximately reached 2.1% drift in the upper-stories.
- Average wall pier shear stress demands times 1.5 (brittle action) ranged from approximately $8\sqrt{f'_c}$ to $10\sqrt{f'_c}$ for the Ghodsi and Flores Ruiz (2010) design and $9.5\sqrt{f'_c}$ to $11\sqrt{f'_c}$ for the Fry et al. (2010) design at the base of the structure.
- The overturning moment profiles in all analyses resulted in a maximum overturning moment at the ground level.

The performance based design of the core wall system for both case studies was different than the code base design. The PBD by Fry et al. (2010) led considerably thicker pier walls than the IBC design and the author anticipates the IBC design would lead to a shear failure under a MCE-level event. The wall thickness does not change between the two designs from Ghodsi and Flores Ruiz (2010), but the design concrete compressive strength is increased from 6000 psi to 8000 psi in the first 20 stories to account for the increase in demand estimated using the PBD procedure.

2.7 Conclusions of Literature

Typical coupled wall systems are currently designed using strength-based design procedures to protect structural components against forces from resulting elastic analyses. In an elastic analysis, the literature concludes coupled wall internal force and deformation distributions are sensitive to the effective stiffness parameters which are manually assigned by the designer, and these analyses tend to be inadequate at predicting ultimate capacity of a coupled wall system compared to a more complex nonlinear analysis. Recommended plastic analysis procedures allow engineers to design the wall piers against higher shear demands as a result of a flexural mechanism. However, it is unclear whether this yielding mechanism actual behaves the way the designers assume or if only a percentage of coupling beams yield before the wall piers are exhausted of their capacity due to large redistributions of shear stress to the compression wall and large axial force demands in the compression wall due to a high degree of coupling. If the latter is true, it would show there is indeed a misconception between the ductile energy dissipating coupled wall behavior which is assumed in design and the less ductile underachieved coupled wall system which is present due most impart to misunderstood nonlinear behavior.

A significant amount of research has focused on individual coupling beams, and these results have dramatically improved the seismic performance of the beams. While there is still a need to verify this performance in an actual coupled wall structure, their behavior is for the most part well understood. Few research programs have studied the seismic behavior of actual modern coupled walls systems, and with the exception of one, most have focused on low-rise structures. Yet, most commonly coupled walls are used in elevator cores, which are more typical in mid-rise construction. There is also an inconsistency among the tested specimens with respect to the pier length and coupling beam dimensions. In conclusion, there is still a need to quantify the performance of mid-rise coupled walls designed using details representative of modern construction.

Chapter 3

NEESR COUPLED WALL TEST PROGRAM

In the last chapter, three primary findings were apparent from the review of previously tested coupled wall specimens. First, most of the coupled walls tests simulated low-rise construction with the exception of the Ozselcuk (1989) test series, which was more representative of mid-rise construction. This is not surprising since simulation of mid- or high-rise construction requires very large forces, very small scale, or both. Second, there was an inconsistency among the tested specimens with respect to the pier length and coupling beam dimensions. For example, the specimens tested by Shiu et al. (1981) had long wall pier lengths and shorter coupling beams; whereas, the specimens tested by Ozselcuk (1989) had long wall pier lengths and long coupling beams. Finally, the previously tested specimens were constructed with geometries or reinforcing details that are not consistent with modern or conventional coupled wall construction.

On the other hand, the coupled wall test program discussed herein, investigates the seismic response of reinforced concrete coupled structural walls to simulate modern mid-rise building construction on the West Coast. The following chapter provides 1) an overview of the design process of the coupled wall specimen, 2) the specimen construction details including overall geometry, material properties and expected specimen strengths and 3) a summary of the test program (e.g. construction process, instrumentation layout, loading protocol and experimental setup).

3.1 Specimen Design

The coupled wall specimen was designed to simulate a “typical” coupled wall in a ten-story building. The objectives were to start the design process by 1) producing a specimen with a nominal shear strength that is determined by the ACI 318-08 minimum horizontal reinforcement ratio, 2) employ a performance-based plastic analysis of the flexural mechanisms in the wall, 3) utilize detailing methods that will reduce the congestion and simplify construction, 4) design a wall that will behave in a predictable and ductile manner.

3.1.1 Specimen Geometry and Assumptions

The test specimen was designed utilizing results from a building inventory review. The building inventory review consisted of 13 coupled wall buildings ranging from 10 to 60 stories in high seismic regions. All of the buildings included in the inventory were designed with core wall systems, where the coupled shear walls form the elevator core; therefore, only planar, C and L shaped walls were investigated. The primary objective of the inventory study was to determine a set of general design assumptions that are representative of current construction and uses these assumptions in the design of the coupled wall test specimen. In addition to the building inventory review, consultations with the Advisory Panel and the need for consistency with the planar wall tests specimens, led to the following design assumptions and specifications:

- Concrete compressive strength of 5000 psi
- Reinforcement yield strength of 60 ksi
- Wall pier axial load equal to 0.1Agf'c
- One-third scale wall geometry as shown in Figure 3.1

The test specimen designed as part of this program was one-third of full scale, in which the full-scale wall had 12 ft. story heights, 30 ft. length, 12 ft. long wall piers and 6 ft. long by 3 ft. deep coupling beams with an aspect ratio (i.e. the span-to-depth ratio) of 2.0. This coupling beam aspect ratio (AR) was chosen based on an average coupling beam aspect ratio computed from the building inventory (i.e. an average equal to 2.1 with a standard deviation of 0.41). The overall geometry of the coupled wall matched the planar wall specimens, as presented in prior papers Lowes et al. (2009). That is, the wall specimen was 10 ft in total length (two piers and a coupling beam) and 6 in. in thickness. Each floor was 4 ft in height.

3.1.2 Specimen Design Procedure

Using the prior assumptions and this geometry, the wall was designed following appropriate design documents, including the 2008 ACI Building Code (ACI, 2008) and the SEAOC Seismic Design Manual, Vol. III (2005 ASCE-7), which is now the 2006 IBC Structural/Seismic Design Manual, Volume III (ICC, 2007). A summary of this design process is as follows:

1. The wall flexural strength was designed to correspond to the shear capacity corresponding to the minimum allowable shear reinforcement, V_n per ACI 318-08. As a first step in the process, this shear capacity, V_n, was calculated.

2. The base shear corresponding to this strength was determined to solve the following inequality, $\phi V_n \geq V_u$ where, $\phi = 0.6$.

3. The base moment demand, M_u, was calculated using this shear demand and an equivalent lateral load distribution according to ASCE 7-05.

4. Using these loads, an equivalent elastic analysis was performed to determine the demands on the coupling beams. The coupling beams were then designed according to ACI 318-08, to meet the flexural and shear demands, including $\phi V_n > V_u$ where, $\phi = 0.85$.

5. Additional constraints were applied to the wall design including: 1) meeting a target longitudinal reinforcement ratio in the boundary elements of approximately

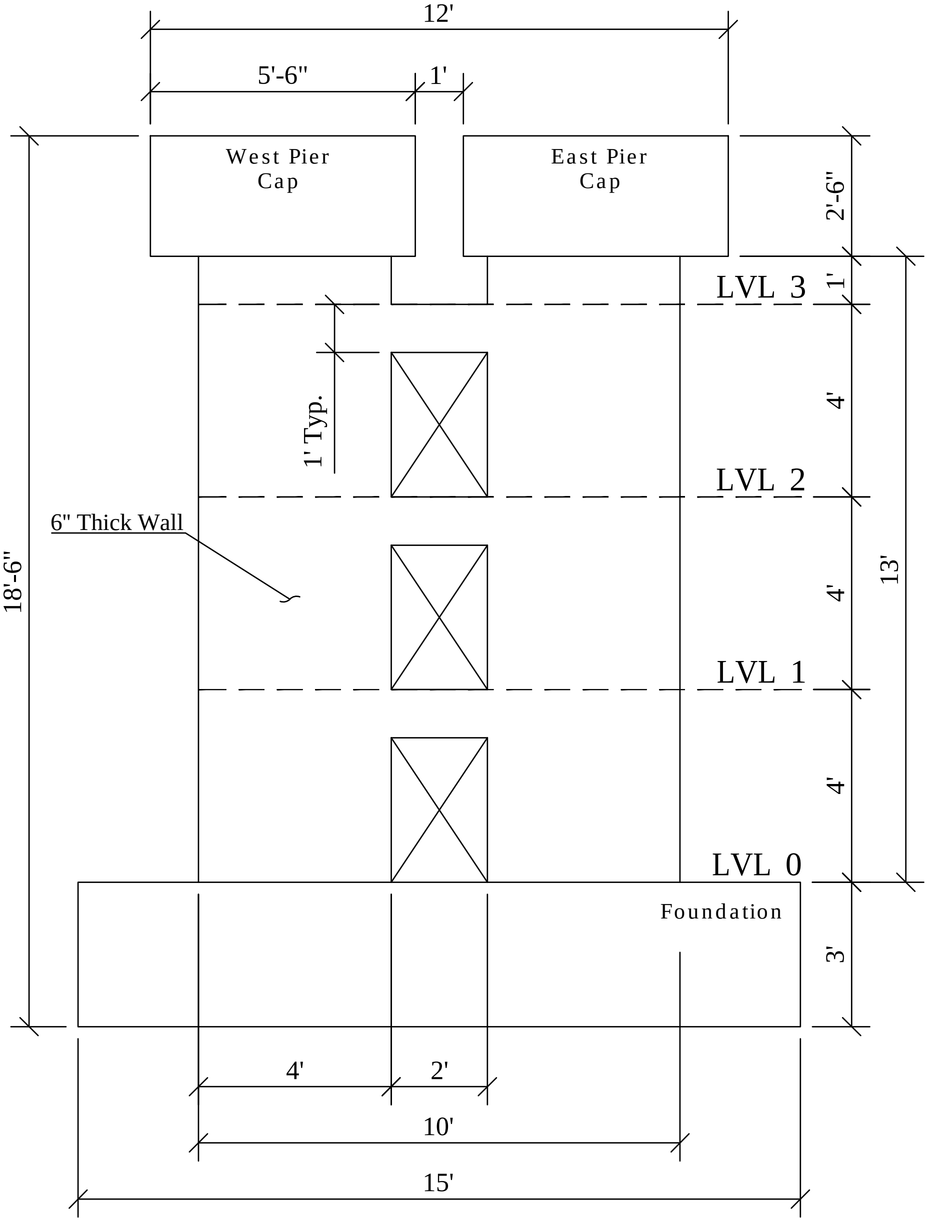

Figure 3.1: Elevation of coupled wall specimen CW1

3.5% and 2) achieve a degree of coupling less than 55% as recommended by Harries (2001).

6. Finally, the longitudinal reinforcement in the wall was designed to satisfy the ACI

318-08 (i.e. $\phi M_n > M_u$ where, $\phi = 0.90$).

This design process meets the current ACI and IBC building code requirements. However, it is solely based on elastic response with a prescribed loading pattern. To account for full plasticity in the coupled wall, the design was extended using a capacity-based design approach outlined in 2006 IBC Structural/Seismic Design Manual.

1. Initially, a plastic mechanism was assumed for the wall, which included plastic hinges developing at the base of the wall piers and at the ends of each coupling beam (total of ten coupling beams for ten-story building).

2. For the wall pier and coupling beams, the plastic moment strength, M_{pr}, at each plastic hinge location, as defined by ACI 318-08.

3. Using the principle of virtual work, the internal associated with development of the plastic mechanism was equated with the external work associate with the application of the lateral forces to determine the shear force demand at the base of the wall, V_p.

4. The wall shear reinforcement was designed to sustain this plastic shear demand, using $\phi = 0.75$, as appropriate for a plastic analysis (ACI 318-08). This design process resulting in a spacing of the horizontal reinforcement in the web that was half of the spacing resulting from the ACI procedure outlined above.

3.1.3 Preliminary Design

Mohr (2007) conducted a preliminary design of the coupled wall specimen using similar design assumptions and procedures presented above. One of his research objectives was to evaluate whether the assumed plastic mechanism will actually occur. As a result, nonlinear continuum analyses were conducted to simulate the plastic mechanism in the coupled wall and compare those results to the design assumptions. The author created a finite element model of the one-third scale ten-story coupled wall specimen using the nonlinear continuum software, VecTor2 (Wong and Vecchio, 2002). As a part of this study, the coupled wall specimen was modeled with the following three coupling beam reinforcement variations:

1. The coupling beams were designed to meet ACI 318-05, which required that each group of diagonal reinforcing bars be confined using stirrups.

2. The coupling beams were designed to meet ACI 318-08, which allows for confinement of the entire beam section rather around each group of diagonal bars. This coupling beam contained the same diagonal reinforcement as the previous design, thus the same design strength.

3. The coupling beams were designed to have a shear strength equal to 25% of the shear strength of the second coupling beam design (i.e. the coupling beam diagonal reinforcement was reduced by 75%).

The last model variation was chosen because results of the first two studies showed the assumed plastic mechanism did not fully develop in the coupled wall. Simulation of the first two models resulted in yielding of the wall piers and concrete crushing in the toe of the compression pier before any of the coupling beams reached yield. Therefore, to reduce the strength of the coupling beams relative to the wall piers, the area of diagonal reinforcement in one group was reduced from 0.80 in^2 to 0.20 in^2 so the coupling beams would yield when the wall piers reached the design level base shear, V_n. The VeTor2 results of the third design, led to the formation of the desire plastic mechanism with plastic hinging at the ends of all the coupling beams and hinging at the base of the wall piers.

3.1.4 Final Design

The analyses conducted by more Mohr (2007) prompted the research team iterate the design of the coupled wall specimen such that the coupling beam strengths were proportioned appropriately relative to the strength of the wall piers and would result in the desired plastic mechanism. The third coupling beam variation achieved this goal using one-quarter the reinforcement for the diagonal bars. However, in order to meet ACI 318 requirements which call for a minimum of four reinforcing bars in each diagonal group, the research team did not want to reduce the diagonal reinforcement in the coupling beams because it was already at the desired minimum bar size (No. 4). As a result the aspect ratio of the coupling beam was increased from 1.5 to 2.0. This resulted in a coupling beam diagonal reinforcement angle of 19 degrees which is approximately 60% less than the preliminary designed coupling beam (i.e. a reduction in shear strength of approximately 62%). Additionally, the change in coupling beam geometry led to a reduction in the coupling beam shear demands calculated using an elastic analysis, resulting in a code-compliant design which was not the case for the third variation of the VecTor2 model. VecTor2 analyses were performed on the new design and the desirable plastic mechanism was verified.

3.1.5 Design Strengths and Reinforcement Details

The reinforcement detail for the coupled wall specimen is shown in elevation in Figure 3.2. The details of the coupling beam reinforcement layout are shown in Figure 3.3. Two sets of of diagonal reinforcement groups angled at 19 degrees from the horizontal contained 4 – #4 reinforcing bars ($\rho_d = 1.25\%$). Using Equation 3.1 as defined by ACI 318-08, the nominal shear strength, V_n, of the coupling beams was equal to 31.3 kips ($6.1\sqrt{f'_c}A_{cw}$).

$$V_n = 2A_{vd}f_y sin(\alpha) \leq 10\sqrt{f'_c}A_{cw} \tag{3.1}$$

The total area of reinforcing steel for one diagonal group is defined as A_{cv}, and the yield strength of said group is f_y. Additionally, α is the diagonal reinforcement angle of inclination with respect to the horizontal axis of the beam. Finally, A_{cw} is the coupling beam area which is bounded by thickness of the coupling beam web and the height of the beam. The diagonal reinforcement was anchored into the wall piers a distance of 22 inches in order to develop 1.25 times the development length for f_y in tension, as required by ACI.

The coupling beam confinement utilizes the ACI 318-08 code detail for full section confinement. Closed vertical stirrups (No. 2) were spaced along the coupling beam length two inches on center (ρ_v=1.22%), and No. 2 transverse reinforcing ties were spaced vertically 2.5 inches on center. Finally, horizontal reinforcement (No. 2) was spaced vertically 2.5 inches on center. In order to not develop f_y in these horizontal bars, as required by ACI, the horizontal reinforcing bars were anchored two inches ($8d_b$) in the wall pier on each end of the coupling beam.

While the coupling beam design changed in the second iteration of design, wall piers contained the same reinforcement ratios and geometry that was specified in the preliminary design. The reinforcing detail for the cross-section of the wall piers is shown in Figure 3.4. Each wall pier boundary element contained 16 – #4 vertical reinforcing bars spaced horizontally at two inches on center (ρ_{vert} = 3.8%). The No. 2 confinement ties and hoops in the boundary elements were spaced vertically two inches on center, and the horizontal and transverse reinforcement ratio was 0.82% and 0.70%, respectively.

In the web region of the wall piers, vertical reinforcement (No. 2) was spaced at six inches on center corresponding to a reinforcement ratio of 0.27%. Recall, the spacing of the horizontal web reinforcement was reduced from six inches in the first floor to two inches. This was a result of the 2006 IBC Structural/Seismic Design Manual plastic analysis. The horizontal reinforcement ratio, ρ_t, in the first and upper stories equaled 0.54% and 0.27%, respectively.

The nominal moment and shear strengths of each wall pier were approximately 871 kip-ft and 150 kips ($7.3\sqrt{f_c'}A_{cv}$), respectively. A_{cv} is the area of the wall pier bounded by the length of the wall and the thickness of the web. The nominal moment strength was calculated using moment-curvature analysis with an axial load equal to $0.1f_c'A_g$. The axial-moment interaction for the wall piers is shown in Figure 3.6. ACI 318-08 defines the nominal shear strength of a reinforce concrete shear wall using the following equation:

$$V_n = A_{cv}\left(\alpha_c\sqrt{f_c'} + \rho_t f_y\right) \tag{3.2}$$

where, α_c is a coefficient that defines the relative contribution of concrete strength to the nominal shear strength of the wall ($\alpha_c = 2$ for $H/l_w \geq 4.0$).

3.1.6 As-Built Material Properties

Concrete Properties

On the first day of testing, compression tests were performed on three 4”x8” cylinders in order to determine the average concrete compressive strength, f_c', for Specimen CW1. The specimen was casted in one lift so, this measured strength is representative of both wall piers and all three coupling beams. The target strength was 5000 psi, and on the day of testing the average compressive strength was 5690 psi. Using the average compressive strength, the modulus of rupture (f_r), the elastic modulus (E_c) and the shear modulus (G_c) was estimated using the following three equations. These properties are reported in Table 3.1.

$$f_r = 7.5\sqrt{f_c'} \quad (psi) \tag{3.3}$$

$$E_c = 57000\sqrt{f_c'} \quad (psi) \tag{3.4}$$

$$G_c = \frac{E_c}{2(1+\nu)}, \quad \text{where} \quad \nu = 0.2 \tag{3.5}$$

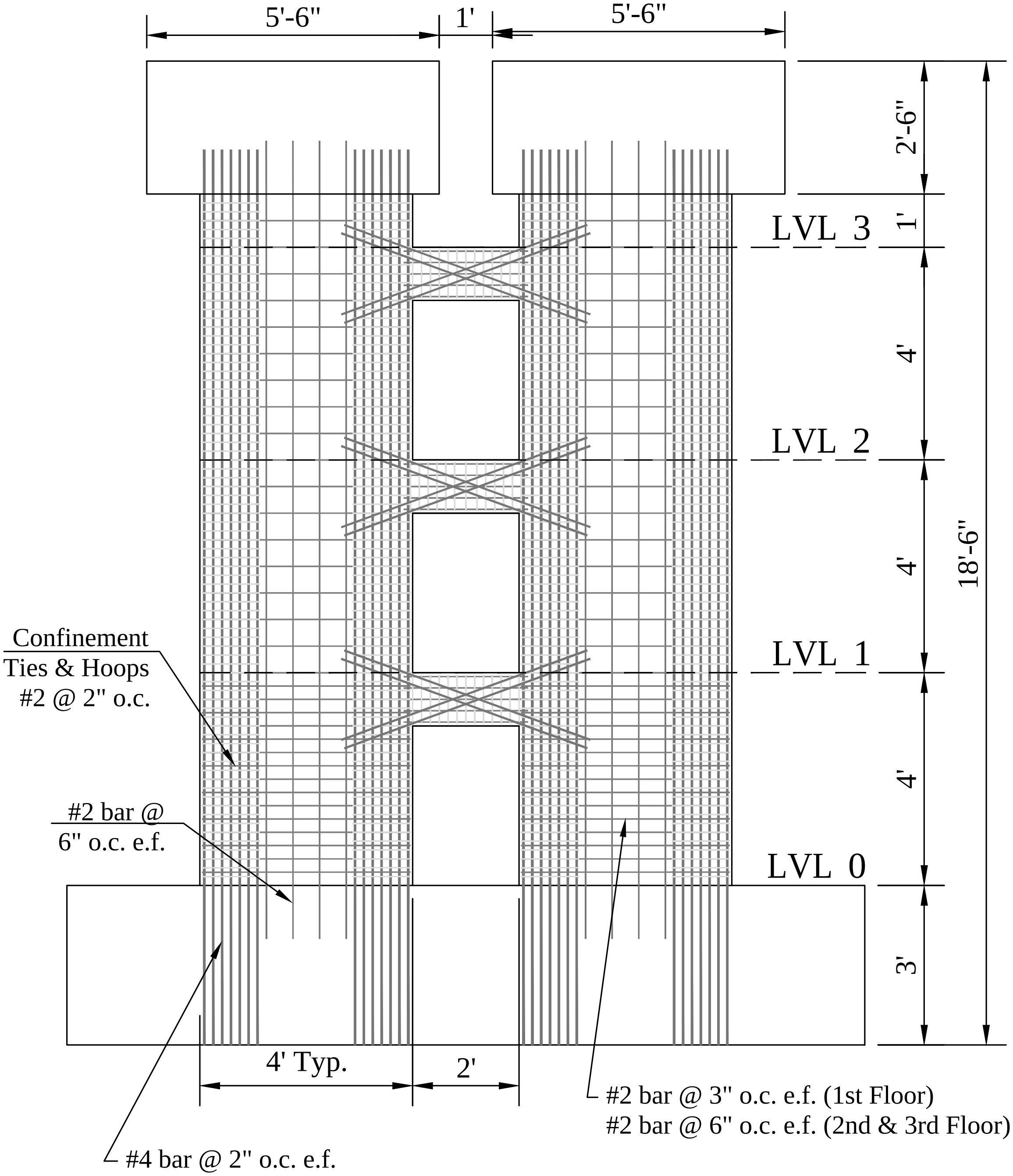

Figure 3.2: Specimen CW1 reinforcement layout (elevation view)

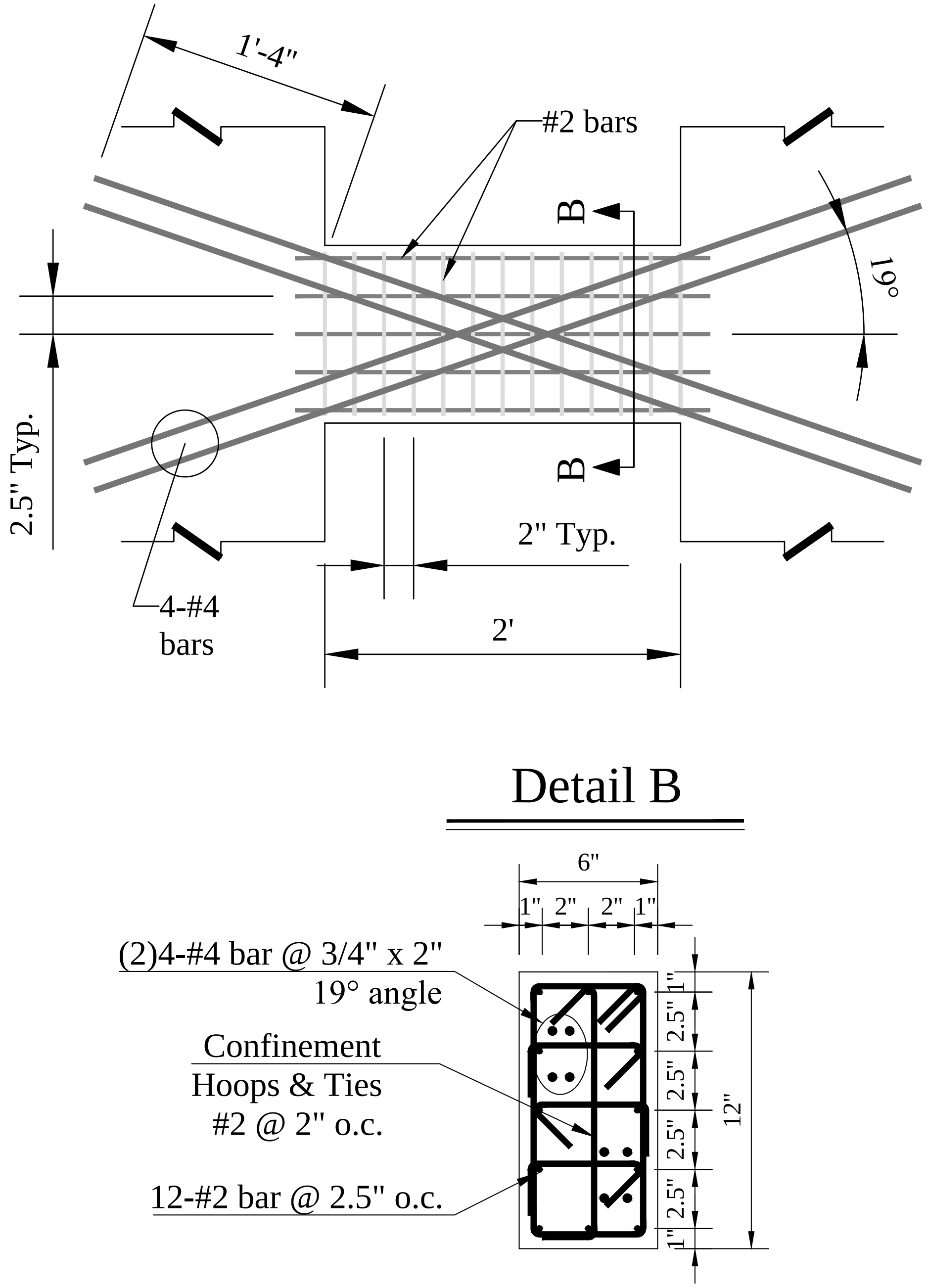

Figure 3.3: Coupling beam reinforcement detail

Steel Reinforcement Properties

Material properties of the steel reinforcement are presented in Table 3.2. No. 4 reinforcing bars were used as the vertical reinforcment in the boundary elements of the pier walls

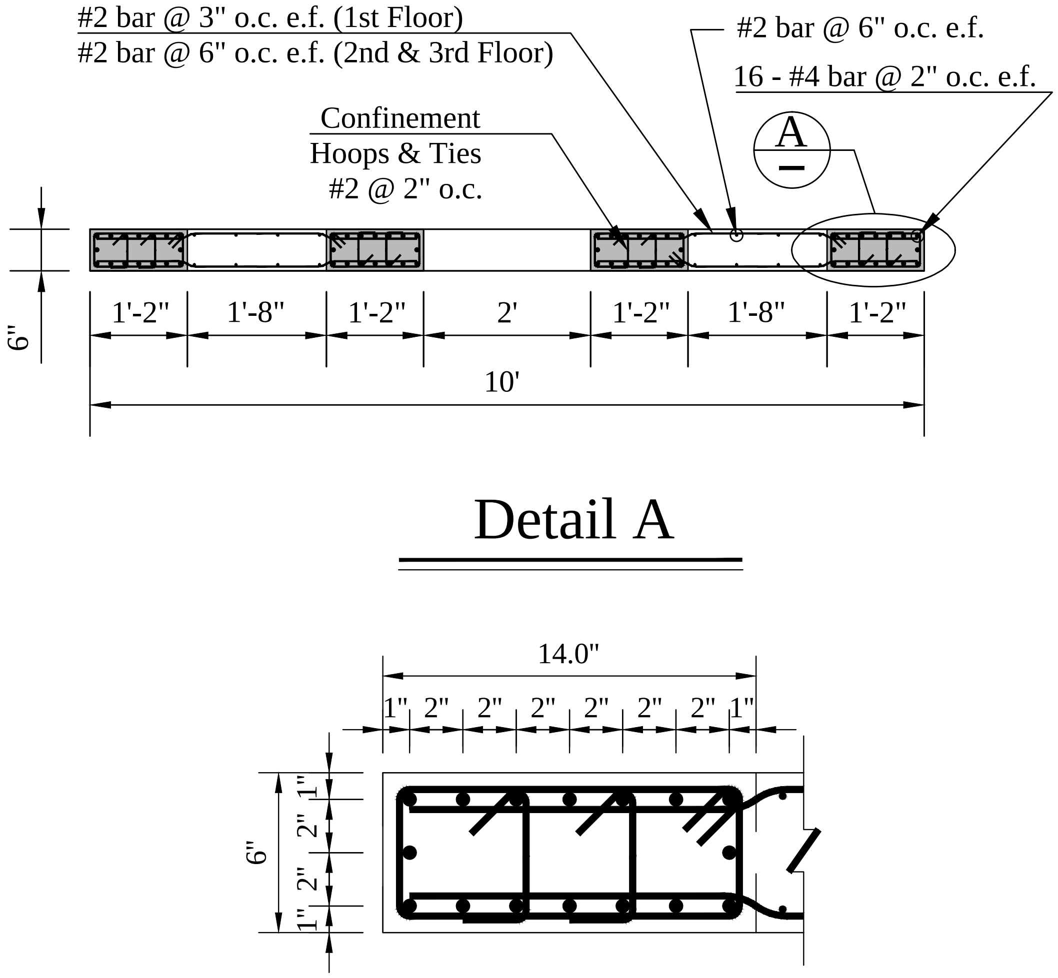

Figure 3.4: Cross-sectional view of wall pier reinforcement detail

and as the diagonal reinforcement of the coupling beams. No. 2 reinforcing bars were used as the horizontal and vertical reinforcement in the web of the pier walls, and as the horizontal and transverse reinforcement in the coupling beams. The No. 4 reinforcement was produced under the ASTM specification A615 with designated yield strength of 60 ksi. The No. 2 reinforcement was heat treated to match the target yield strength of 70 ksi.

Standard tension tests were performed on a sample of steel reinforcing bars to deter-

Table 3.1: Concrete material properties

f'_c **(ksi)**	f_r **(ksi)**	E_c **(ksi)**	G_c **(ksi)**
5690	566	4300	1720

mine the mechanical properties of the reinforcement. The experimental stress-strain data from these tests are shown in Figure 3.5. For each rebar specimen, the values corresponding to yield, strain hardening, maximum stress and ultimate strain were determined, and the average values were calculated for both batches (Table 3.2). An elastic modulus of E = 29,000 ksi was assumed for all reinforcement. The yield strength was determined using a typical offset line method. Using a plot of the stress-strain data, a line with slope E was offset from the origin by 0.2% strain, and the yield strength, f_y, was determined at the intersection of this offset line and the experimental stress-strain data. The corresponding yield strain was calculated as $\epsilon_y = f_y/E$. To capture the yield plateau behavior of a reinforcing bar, the strain at which strain-hardening initiates, ϵ_{sh}, was recorded using the experimental stress-strain data. The stress associated with strain-hardening, f_{sh}, was larger than the yield strength in order to create a slight slope in the yield plateau. This eliminated any potential issue associated with a "zero" tangent when performing a moment-curvature analysis using certain software. The maximum stress, f_{max}, was also recorded along with the strain associated with this maximum, ϵ_{max}. Finally, the ultimate strain, ϵ_u, was determined when the experimental stress data decreased to $0.90 f_{max}$.

Table 3.2: Steel material properties

Bar Size	f_y **(ksi)**	ϵ_y **(in/in)**	f_{sh} **(ksi)**	ϵ_{sh} **(in/in)**	f_{max} **(ksi)**	ϵ_{max} **(in/in)**	f_u **(ksi)**	ϵ_u **(in/in)**
#4	65.8	0.0023	66.4	0.0077	106.4	0.10	96.4	0.14
#2	75.7	0.0026	77.0	0.015	84.6	0.05	76.3	0.058

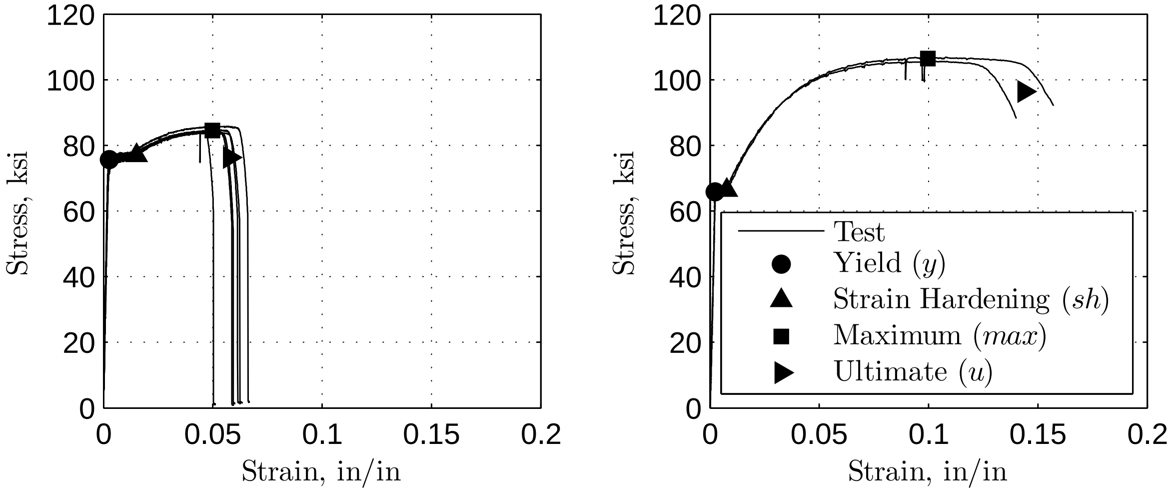

(a) #2 rebar (b) #4 rebar

Figure 3.5: Reinforcement stress-strain response with critical values

3.1.7 Expected Strengths

Expected coupling beam and wall pier capacities were calculated using the measured concrete and reinforcing steel material properties presented in Section 3.1.6. In addition to these component strengths, a set of coupled wall design evaluation parameter calculated. The details of these design methods were presented in Section 2.1 as a part of research conducted by Stringer (2007).

Expected Shear Strengths

The nominal shear strength, V_n, of the coupling beams and wall piers were calculated using Equations 3.1 and 3.2, respectively. The expected shear strength of each wall pier and a coupling beams are equal to 34.3 and 162 kips, respectively. Normalizing the nominal shear strengths by the coupling beam shear area (A_{cw}) or the wall pier shear area (A_{cv}) results in a stress capacity of $6.3\sqrt{f_c'}$ and $7.5\sqrt{f_c'}$, respectively.

Expected Moment Strengths

The cracking moment of a single wall pier, as defined by ACI 318-08, was approximately 109 kip-ft, and it was estimated using the following equation:

$$M_{cr} = \frac{f_r I_g}{y_t} \tag{3.6}$$

where, I_g is the gross wall pier second moment of inertia and y_t is the distance from the centroid of the wall pier to the extreme tensile fiber of the cross-section.

Both the nominal moment strength and the yield moment strength of the each wall pier was calculated using moment-curvature analyses with an axial load equal to $0.1f'_cA_g$. In general, the yield moment was calculated when a steel reinforcing fiber reached the yield strain as defined in Table 3.2. Additionally, the expected nominal moment strength of the wall pier was chosen when the strain in the extreme concrete fiber, ϵ_c reached -0.003. The expected yield and nominal moment strengths are equal to 741 and 945 kip-ft, respectively. Recall the design moment strength with the same axial load was equal to 871 kip-ft.

The axial-moment interaction diagram for the wall piers is shown in Figure 3.6 for the nominal design moment strength, the probable moment strength and the expected nominal moment strength. The “expect” strength interaction includes the effect of strain hardening in the steel reinforcement bars where the other diagrams to not. Additionally, results of a series of moment-curvature analyses are shown in Figure 3.7. The axial load for these analyses was varied to identify the performance of the wall pier under varying axial stress states. Critical points such as tension and compression yielding of the reinforcement are also shown. The point at which the extreme concrete fiber reach -0.003 (ACI nominal) along with the point at which the confined concrete core reaches its respective peak strain, $K\epsilon_{co}$, are also represented in the figure. Note the axial loads are normalized by either the gross cross-sectional properties or the yield capacity of the wall pier depending on the direction of the axial force.

Additional Design Parameters

Additional design parameters such as the degree of coupling (DOC) and the demand capacity ratios (DCRs) for the wall piers are calculated. The degree of coupling for the specimen was calculated using Equation 2.1 and was equal to 52.7%. This is satisfies the recommendation made by Harries (2001) to limit the DOC for a coupled wall designed with diagonally reinforced coupling beams to less than 55%. Furthermore, the demand capacity ratio for the tension wall axial load was calculated using Equation 2.2, and it was equal to 0.43. Because this values is well under one, the wall piers have been deisgn with enough tensile yield capcity that all the coupling beams can yield. Additionally, the shear demand capacity ratio was calculated using Equation 2.3, and it was 0.41. These parameters are all dependent on the strength of the coupling beams relative to the wall piers, and the coupled wall detials were carefully chosen based on those interactions, which is essential to the performance of the coupled wall.

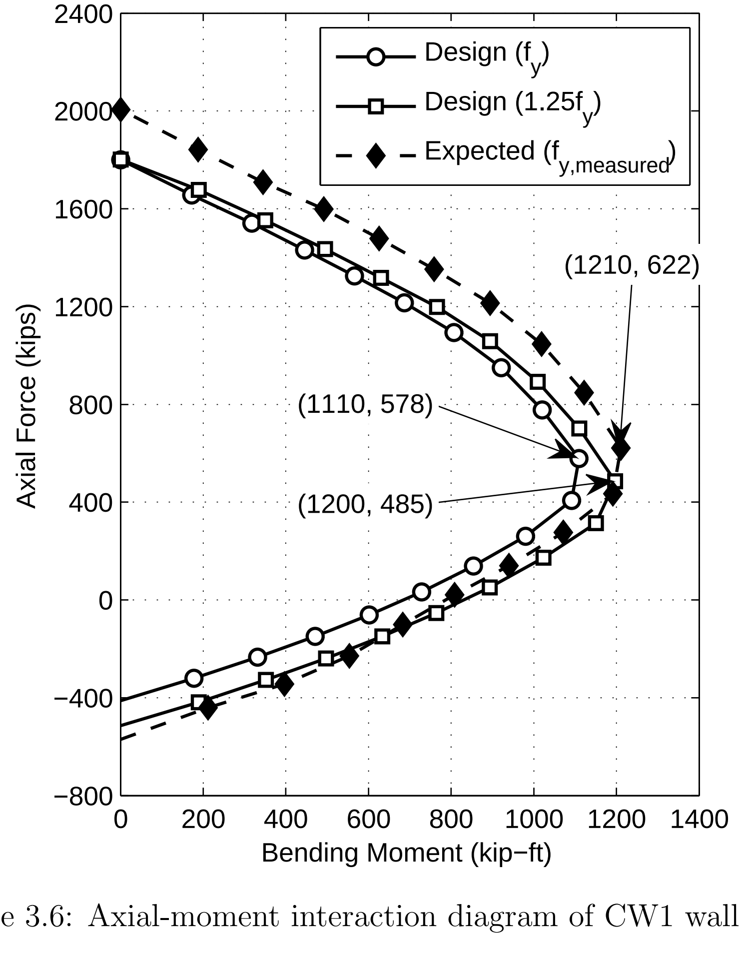

Figure 3.6: Axial-moment interaction diagram of CW1 wall piers

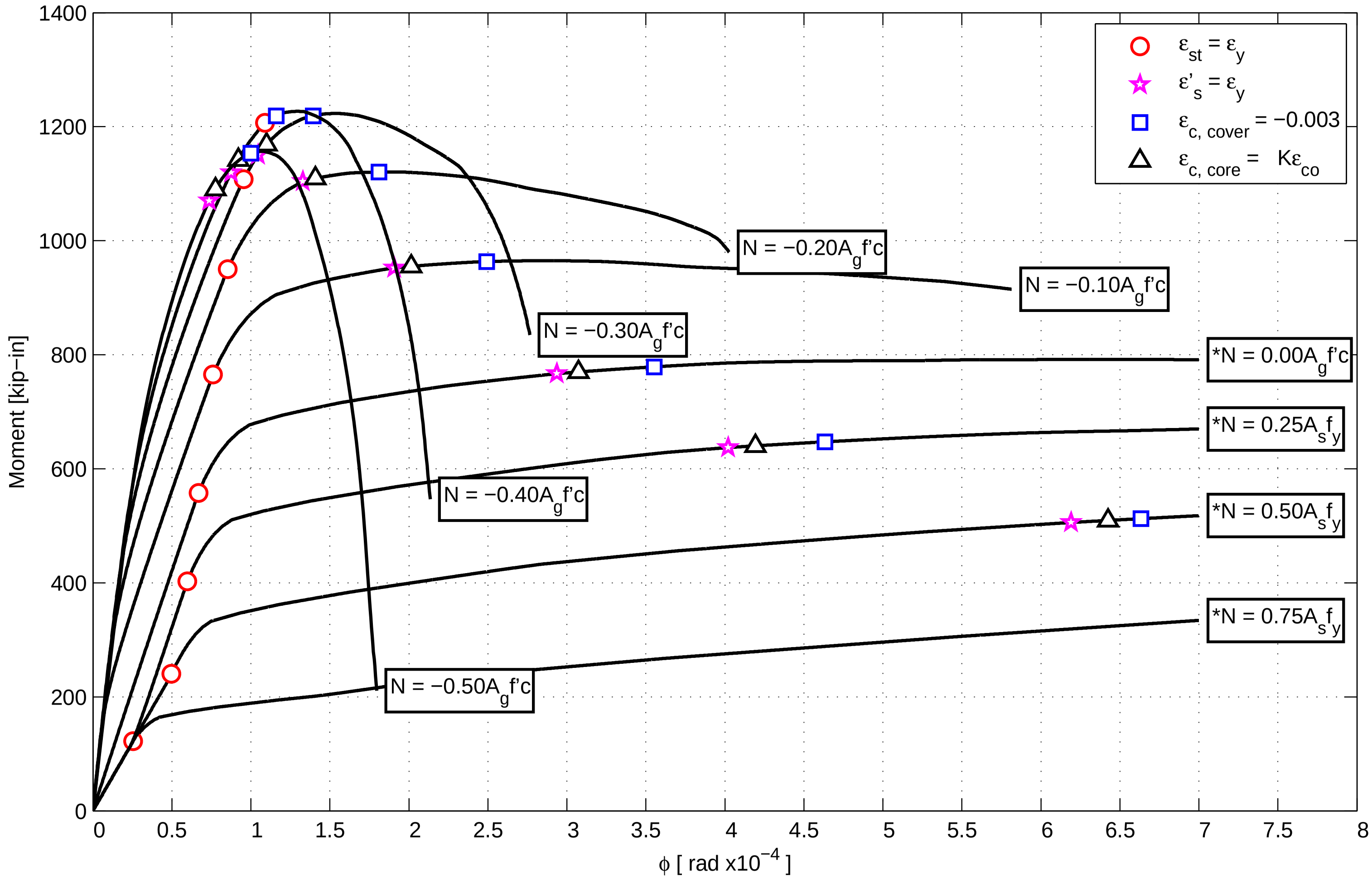

Figure 3.7: Moment verse curvature axial load interaction for CW1

3.2 Specimen Construction

The coupled wall specimen was constructed at the University of Illinois NEES MUST-SIM facility by the UIUC project team and lab technicians. A reinforced concrete foundation block and two reinforced concrete pier caps were designed and constructed in order to connect the specimen to the laboratory strong floor and the two LBCBs. These components were designed by the UIUC project team to ensure appropriate dimensions and strength, and details of this process are provided elsewhere (Hart, 2011).

The foundation block, wall specimen and pier caps were all casted separately using highly fluid self-consolidating concrete (SCC). Unlike conventional concrete which needs to be manually vibrated around tight reinforcing cages, SCC is a highly fluid, workable concrete. This was ideal for the concrete casting of the one-third scale specimen. A brief summary of the construction sequence is shown below, and more details regarding the construction of Specimen CW1 are reported by Hart (2011).

1. Tied reinforcing cage for foundation block and included the vertical reinforcement for the wall piers

2. Assembled foundation block formwork and casted concrete

3. Reinforcement hoops were placed over the boundary element vertical steel to provide horizontal confinement to the boundaries, transverse ties and horizontal reinforcement bars were then tied to this cage

4. Diagonal reinforcement was thread into the wall piers at each floor level and the respective horizontal and vertical coupling beam reinforcement was tied into place

5. Constructed specimen formwork and casted concrete

6. Tied reinforcement for each wall pier cap, applied formwork and casted concrete

3.3 Experimental Test Setup

To ensure that wall response is representative, it was necessary that wall subassemblages tested in the laboratory be relatively large scale with boundary conditions and reinforcement layouts that are representative of those that develop in the bottom stories of a mid-height building. The NEES "Multi-Axial Full-Scale Sub-Structured Testing and Simulation" (MUST-SIM) facility at the University of Illinois, Urbana-Champaign (UIUC) was used to achive this requirement. The MUST-SIM facility is a part of the George E. Brown Network for Earthquake Engineering Simulation (NEES), and it provides a testing, analysis and visualization-display environment that combines the ability to test large-scale subassemblies under complex loading and boundary conditions. Specifically, the coupled wall specimen was a 1/3-scale model of the bottom three stories of a representative 10-story building. The application of loads was achieved using Loading and Boundary Condition Boxes (LBCBs) to apply shear, moment, and axial load at the top of the specimen. The LBCBs are able to impose load and displacements in all six-DOFs using six-actuators affixed to a contact platform (Figure 3.8).

The test setup of the coupled wall specimen in the MUST-SIM Facility is shown in Figure 3.9. The coupled wall test utilized the LBCBs to apply axial load, moment, and shear to the top of the test specimen. Two LBCBs were used in this test, one attached to the top of each wall pier cap, to control each wall pier separately. While the DOFs of each wall pier are applied independently by the two LBCB platforms, the state-of-the art control software allowed global constraints to be controlled about fictitious control points shown in Figure 3.10. More details of the loading protocol are discussed later in Section 3.5.

In order to prevent slip of the LBCB relative to the strong wall, each LBCB was mounted and post-tensioned to the strong wall with 36 high strength 1.5 inch diameter threaded rods. To further prevent the boxes from moving upward under extreme applied downward force, simple shear keys were installed at the top of both LBCBs. External

Figure 3.8: Photo of LBCB 1

sensors were used to measure slip, and no significant movements were observed during the test. A W14x132 loading beam was used to connect the top cap beam of each wall pier to the LBCB (Figure 3.10). The beam was designed to remain elastic and evenly distribute the load from each LBCB to the wall pier concrete caps.

The foundation of the coupled wall specimen was post-tensioned to the strong floor using ten high-strength post-tensioning rods. The specimen was orientated along the long leg of the 5 foot thick L-shape strong wall (Figure 3.9). The in-plane direction of the coupled wall was aligned in the east-west direction of the laboratory. Additional details of the test set up are discussed by Hart (2011) and Marley (2011).

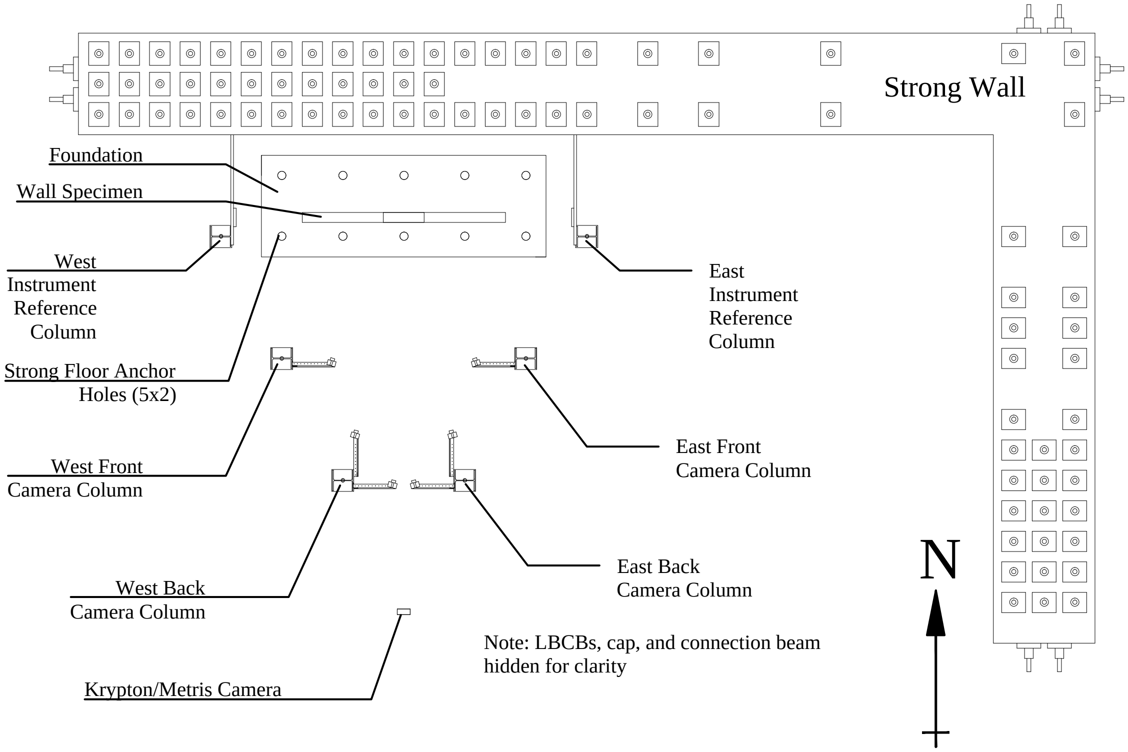

(a) Plan view

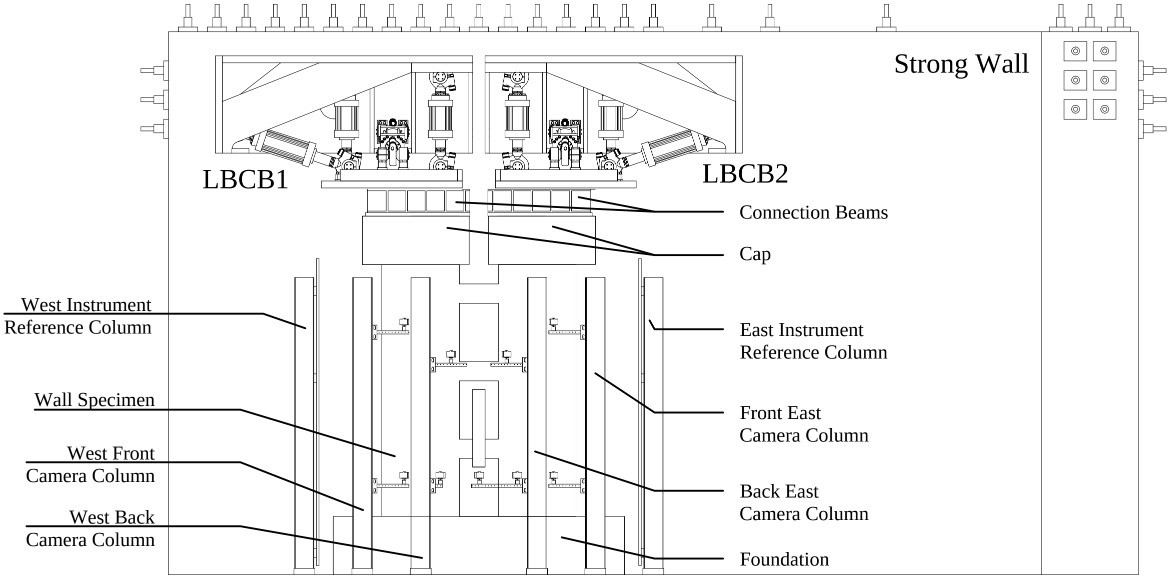

(b) Elevation view

Figure 3.9: Coupled wall specimen test setup

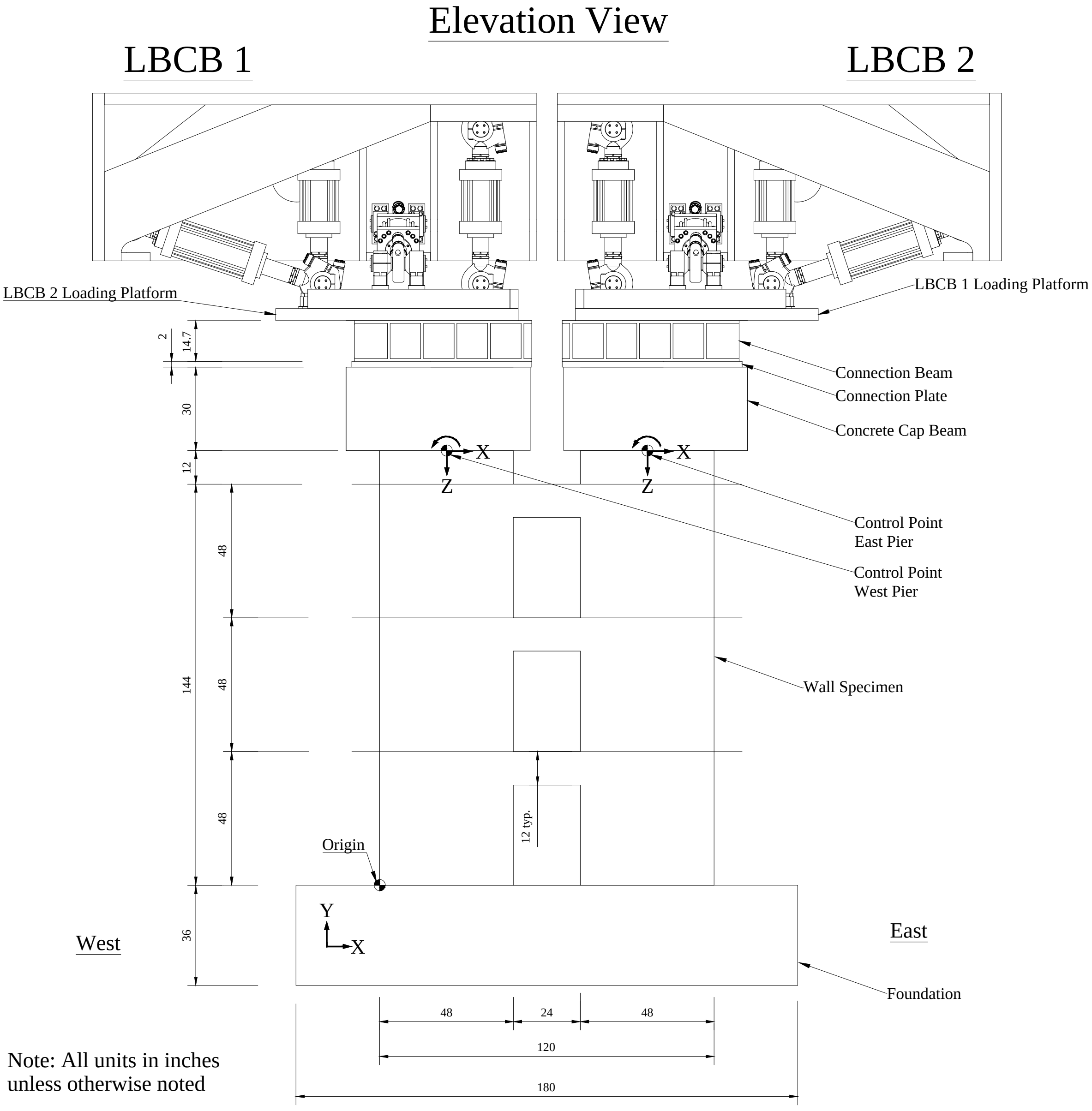

Figure A6-1: CW1 Test Setup

Figure 3.10: Elevation view of LBCB and coupled wall specimen test setup

3.4 Instrumentation

One of the unique features of the MUST-SIM facility is a wide range of instrumentation, including conventional and non-contact instrumentation systems (e.g. photogrammetric and Metris) were available. These instruments were used to meet the research objective of capturing local response mechanism to support design and analysis of modern walls. The coupled wall instrumentation plan called for over 450 channels of data and 11 strategically placed high-resolution cameras in order to successfully capture the specimen behavior. Continuous data was recorded at 1.5 Hz and was captured using all the conventional instrumentation as well as the Metris system (recorded at 1.0 Hz). Additionally, data was acquired for all the instrumentation systems, including the photogrammetry system, at the completion of each prescribed load/displacement step. This sophisticated acquisition was achievable due to the sophistication of the LBCB plugin control software developed by UIUC. Details of these instrumentation systems are discussed in more detail by Hart (2011); however, a brief summary of the instrumentation systems is discussed in the following section.

3.4.1 Non-Contact Instrumentation

The Metris system uses three linear charge-coupled devices (CCD) cameras to triangulate the location of small light emitting diode (LED) targets in three-dimensional space (Figure 3.13a). Targets were distributed in a grid pattern on the south face of each wall pier in the first two stories of the specimen (Figure 3.11). This grid was spaced approximately six inches horizontally and 12 inches vertically. Where rods were embedded in the wall to anchor LDVTs (Figure 3.15), targets were placed on the exposed ends of the rods; elsewhere targets were glued to the wall surface. An additional 6x8-inch grid of LEDs was attached to embedded rods on the first and second story coupling beams.

For the photogrammetric system, paper targets where glued in 16x12-inch and 6x6-inch grid patterns on the south face of each wall pier and coupling beam, respectively

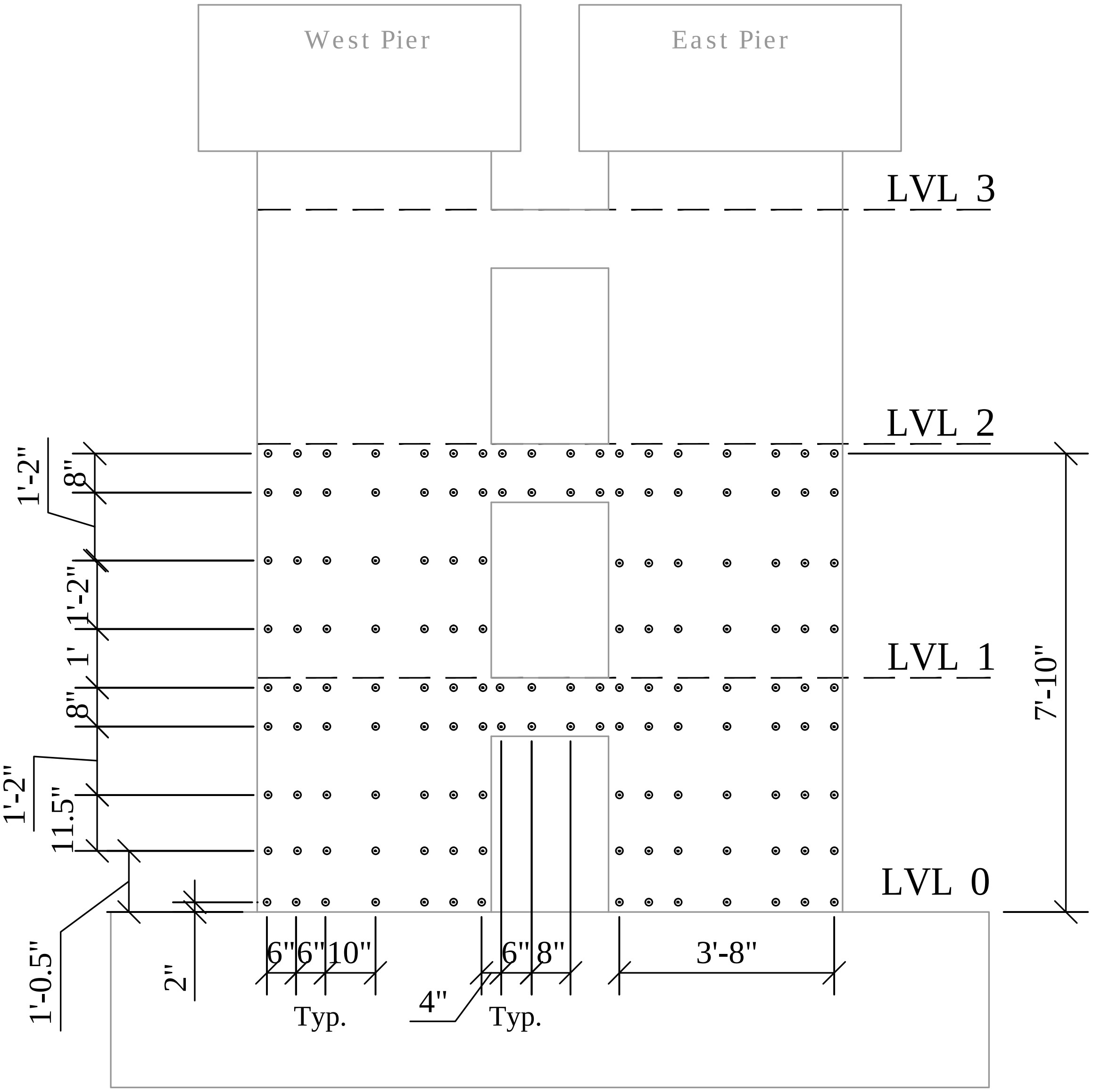

Figure 3.11: Metris system LED layout

(Figure 3.12). These paper targets are "tracked" using photogrammetry software, which employs a minimum of three high-resolution cameras. Triangulation of the paper target was calculated using a commercial software package PhotoModeler 6.

The layout of the 11 high-resolution cameras is shown in Figure 3.13b. These cameras were used as a part of the photogrammetry system, but also were used to take high-resolution still images of the coupled wall specimen at each load/displacement step. Four cameras were used to capture close up images of the top and bottom halves of the east and west wall piers. Five additional cameras located on the back reference towers provided images of the entire specimen. Additionally, two cameras were used on the back-east reference tower to provide close ups of the coupling beams (bottom-CB1 and top-CB2 and CB3). Finally, a high-resolution "roaming" camera was used to take picture of specific areas of interest throughout the test.

3.4.2 External Instrumentation

Absolute specimen displacements were measured at several locations along the specimen height using linear string potentiometers attached to a stationary reference frame and connected to rods embedded in ends of the wall piers (Figure 3.14). Two horizontal high-tension string pots were connected to center of each wall pier (154 inches above the foundation) in order measure horizontal displacements needed for the loading control logic (discussed in the Section 3.5). A string pot was also connected to the foundation block to measure its horizontal movement relative to the strong floor. Additional string potentiometers (not shown) were included to measure the out-of-plane movement of the wall piers and where anchored to the strong wall and connected to the north face of the specimen.

Local deformations including vertical, horizontal and diagonal movements of the instrumented segments of the wall piers and coupling beams were measured using linear voltage displacement transducers (LVDTs) located on the north face of the specimen (Figure 3.15). Because the viewing window of the Metris system did not include the third story, eight additional LVDTs were added to the ends of the top story coupling beam for redundancy. Two in-plane LVDTs located at each end of the foundation were used to measure uplift of the foundation relative to the foundation. Additionally, two out-of-plane LVDTs were used to measure slip and/or twist of the foundation relative to

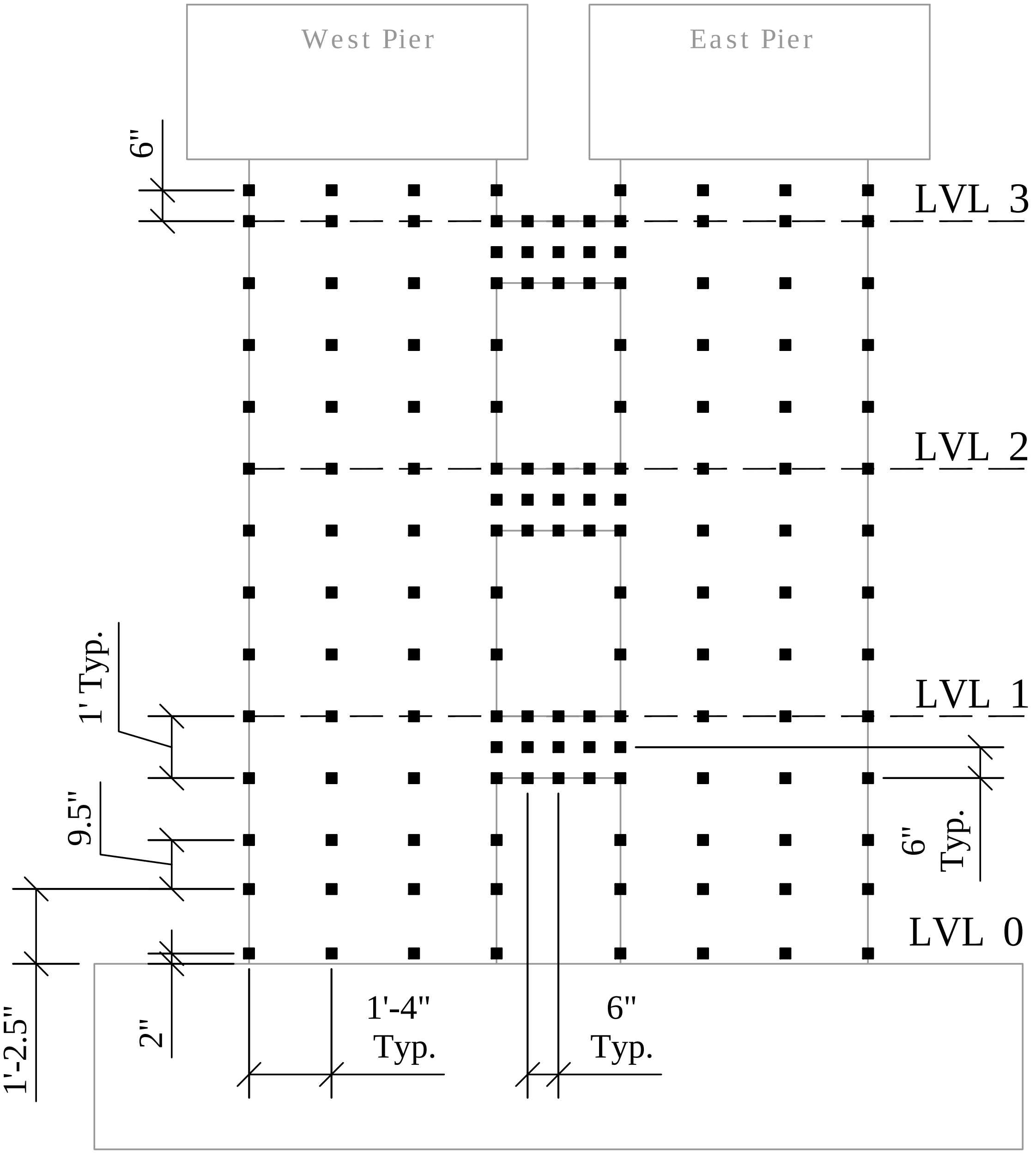

Figure 3.12: Photogrammetry target layout

the strong floor.

3.4.3 Internal Instrumentation

The coupled wall specimen was heavily instrumented with over 200 strain gauges located on the reinforcing bars embedded in the wall piers and coupling beams. These gauges were affixed to the vertical reinforcement in the boundary elements and web region of the specimen (14 inches into foundation (Figure 3.16)). The vertical spacing of these gauges tapered up the height of the specimen with a denser spacing of 6-8 inches near the base of the wall piers. Strain gauges located on the wall pier horizontal reinforcement were located in the center of the wall piers and spaced 12 inches in the first story and 18 inches in the second story (Figure 3.17). Strain gauges located on the confinement stirrups in the inner and outer boundary elements of the west wall pier were located seven inches in from the edge of the wall. The vertical spacing of these gauges was similar to the spacing used for the strain gauges on the horizontal reinforcing. Finally, the coupling beam diagonal reinforcement was instrumented with steel strain gauges spaced approximately 4-12 inches along the bar (Figure 3.18). At the corners of the beam, the spacing between the two adjacent gauges (i.e. one in the pier and one in the beam) was approximately four inches. Additionally, four gauges were located near the center of the beam. Unfortunately, a construction error led to all the strain gauges in the first floor coupling beam to be located in the west half of the specimen.

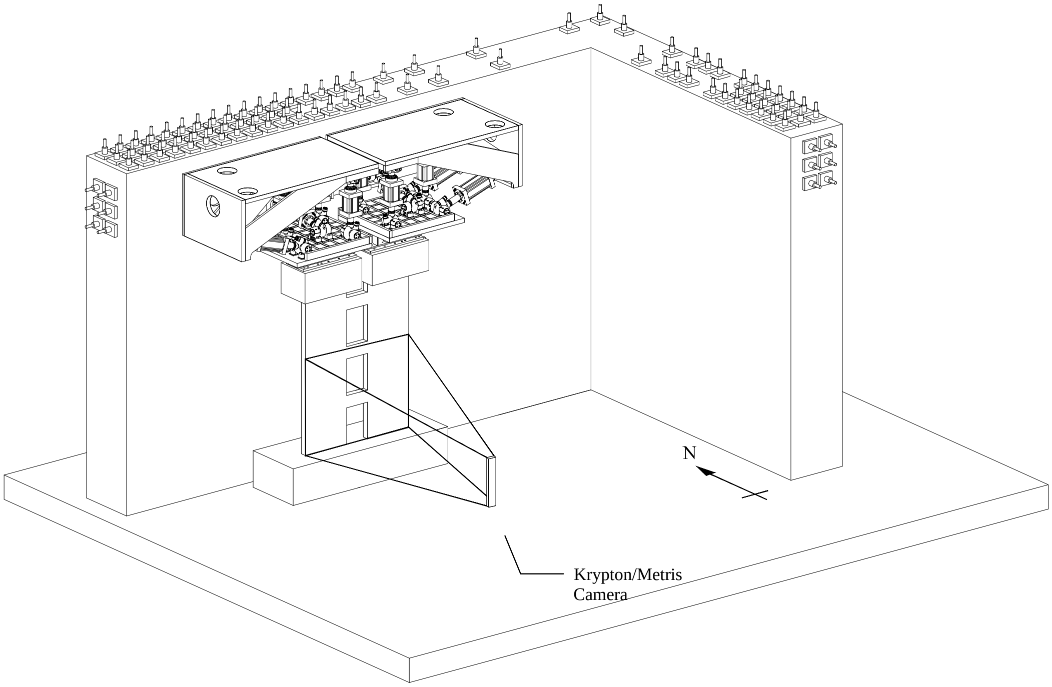

(a) Metris camera

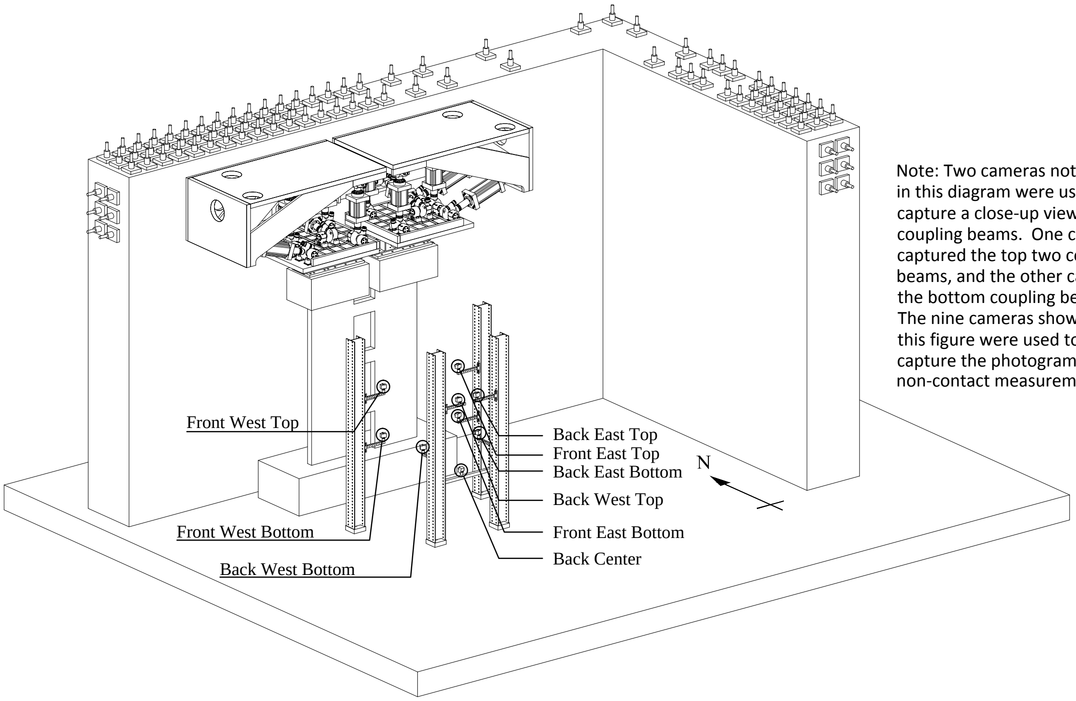

Note: Two cameras not shown in this diagram were used to capture a close-up view of the coupling beams. One camera captured the top two coupling beams, and the other captured the bottom coupling beam. The nine cameras shown in this figure were used to capture the photogrammetric non-contact measurements.

(b) High-resolution cameras

Figure 3.13: Non-contact instrumentation test setup

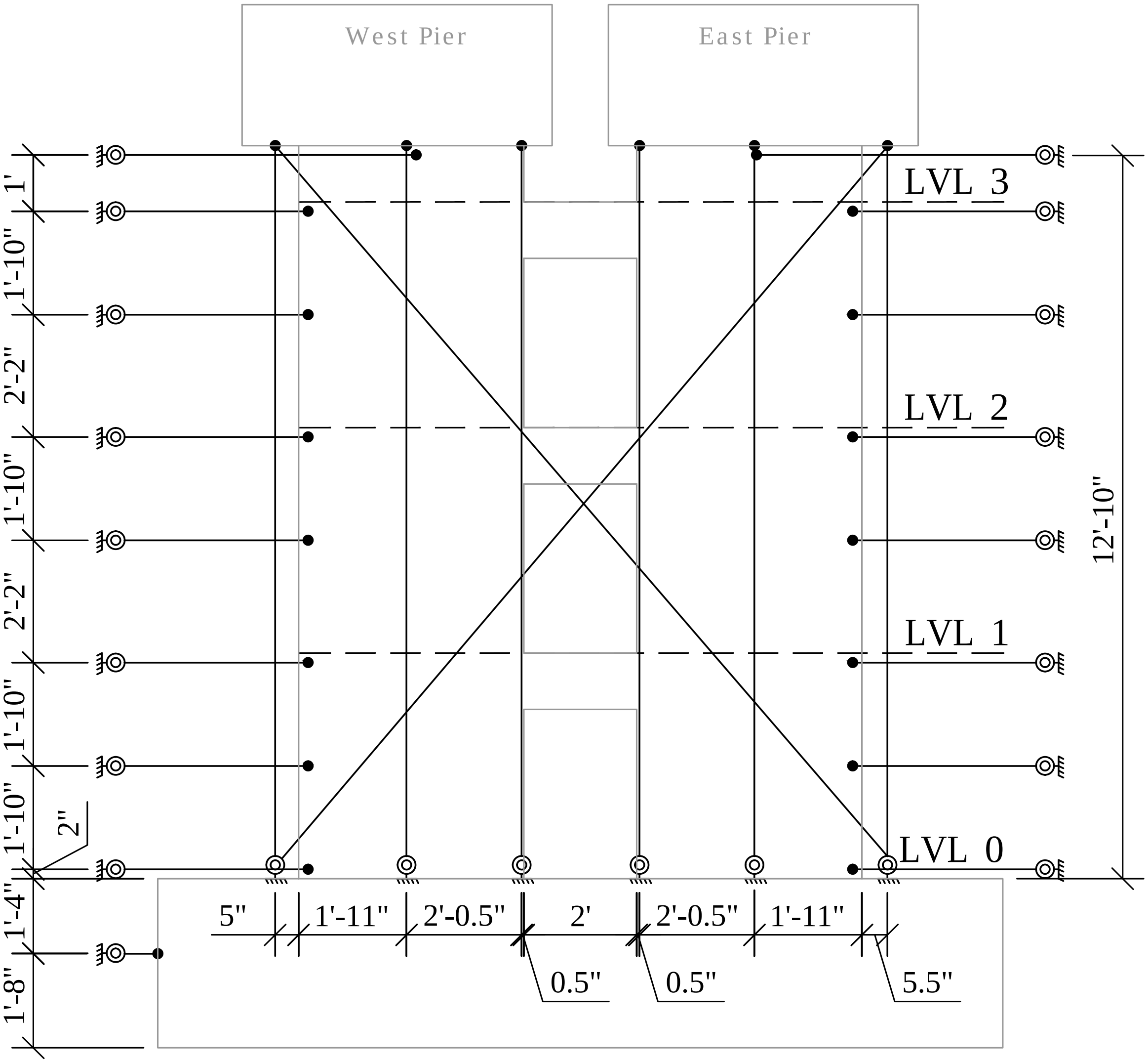

Figure 3.14: In-plane linear string potentiometers layout

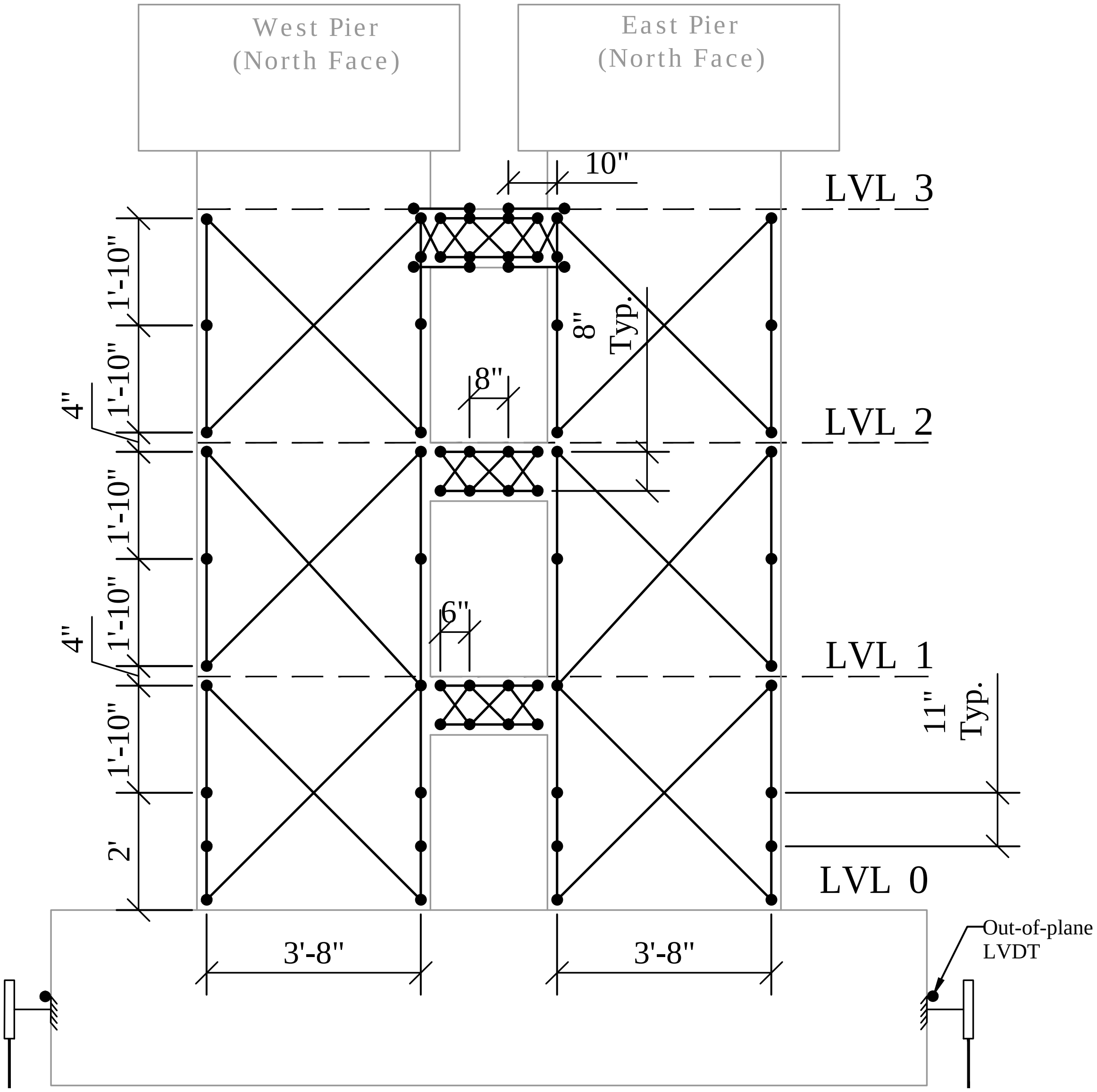

Figure 3.15: LVDT layout, (north side of specimen)

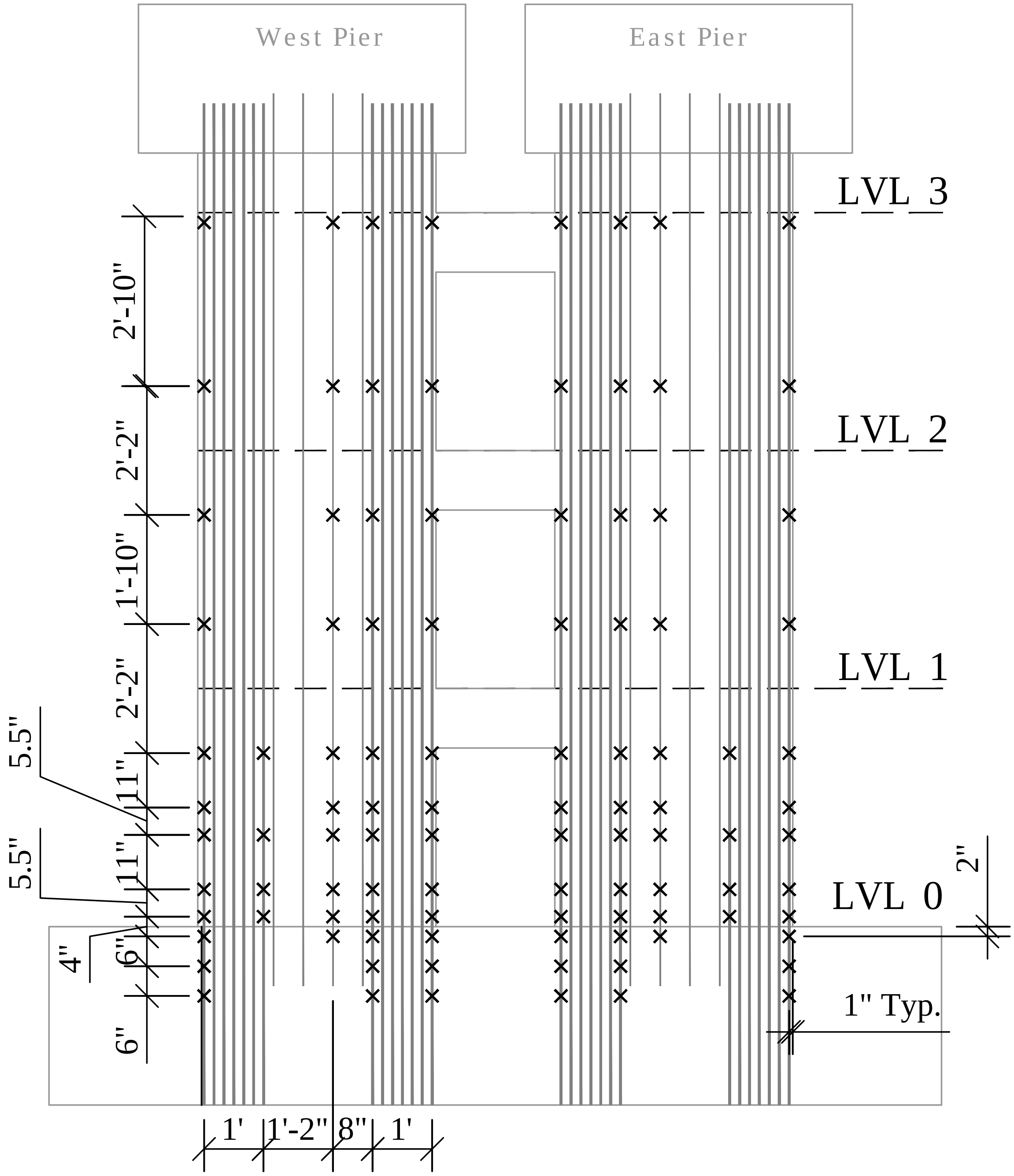

Figure 3.16: Vertical strain gauge layout

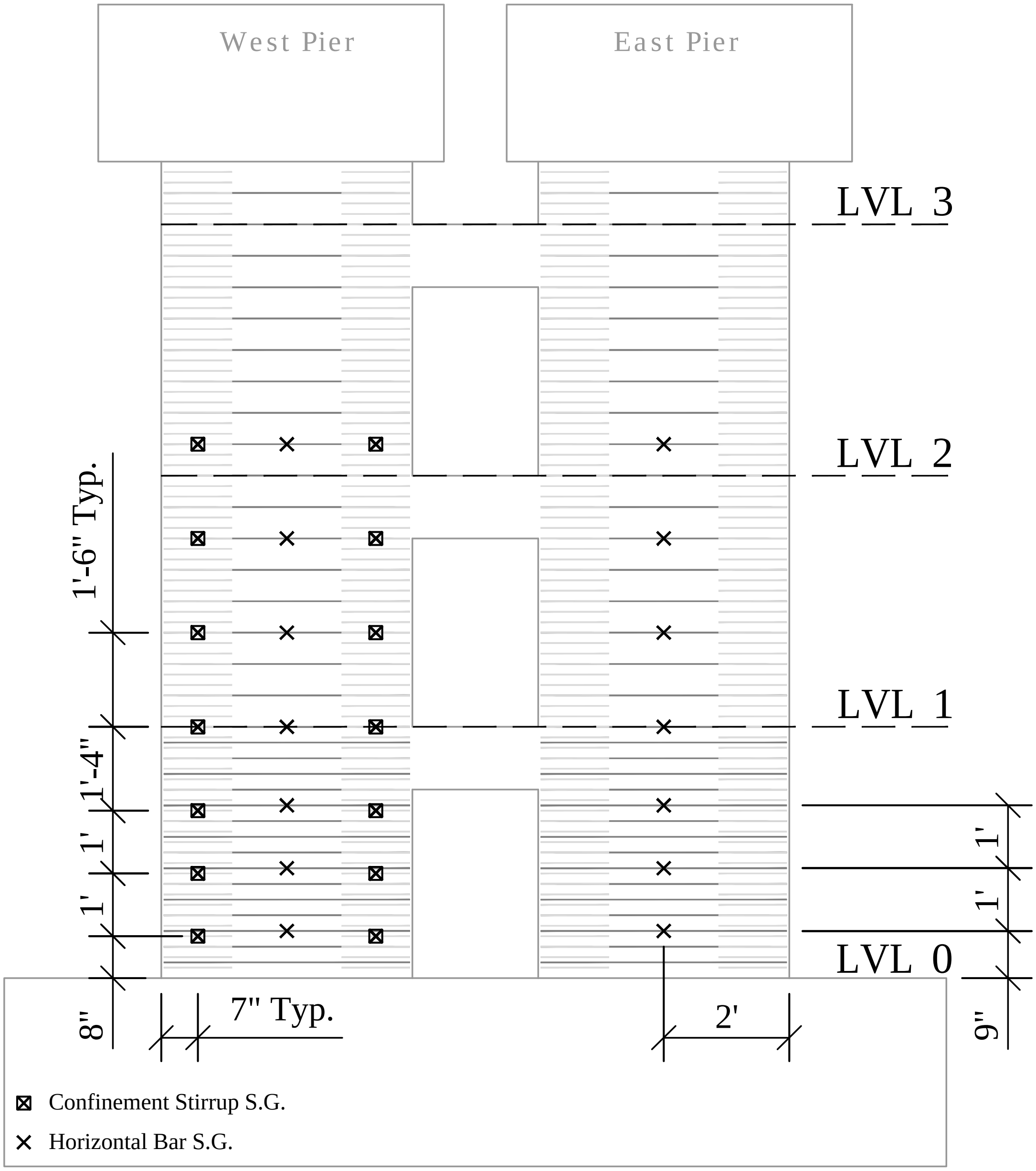

Figure 3.17: Horizontal bar and confinement stirrup strain gauge layout

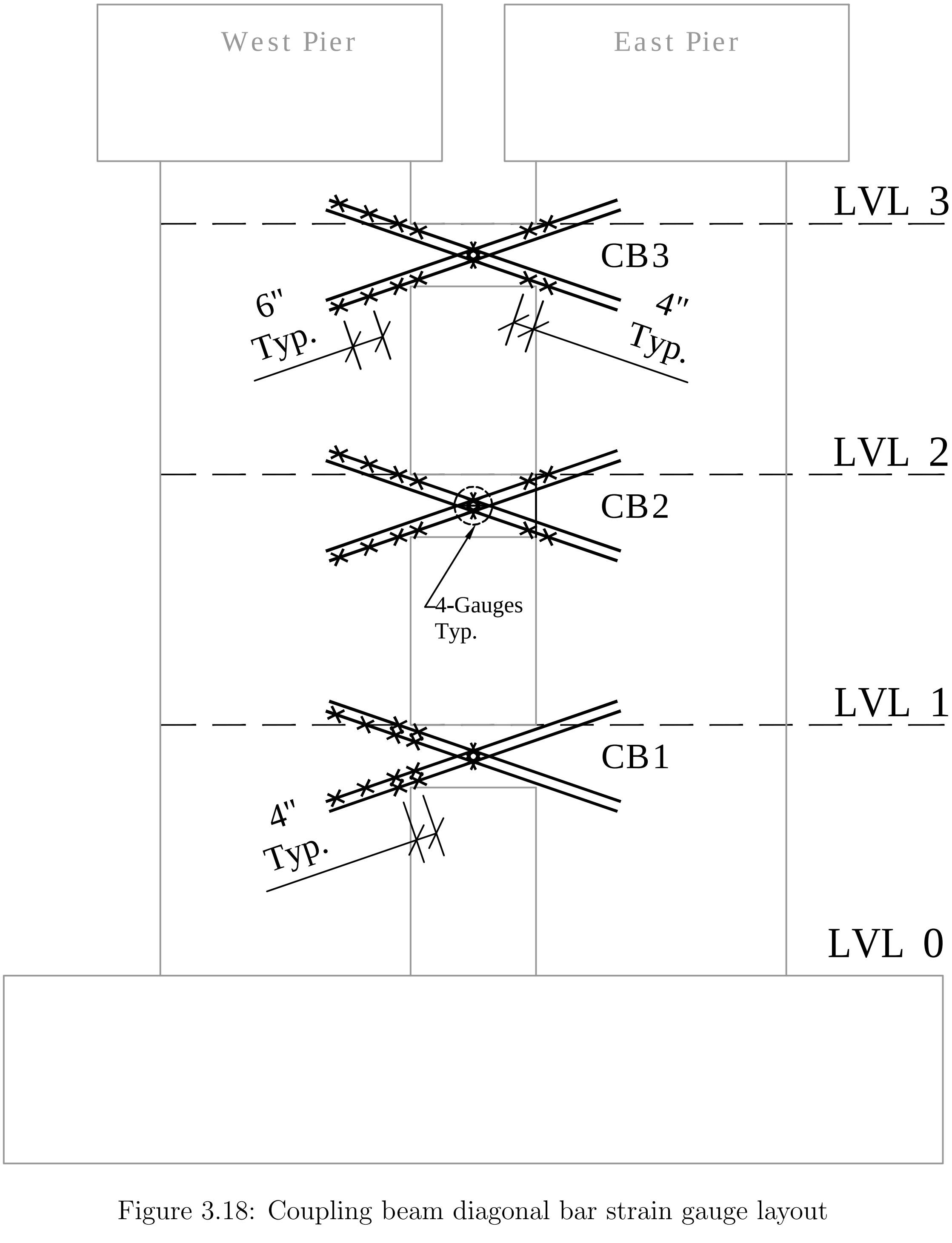

Figure 3.18: Coupling beam diagonal bar strain gauge layout

3.5 Loading Protocol

To maximize the specimen dimensions and focus on regions in which inelastic action occur, only the lower three stories of the ten-story prototype wall were modeled in the laboratory. The LBCBs were used to simulate demands originating from the upper stories of a 10-story structure subjected to an ASCE 7-05 lateral load distribution (Figure 3.19). The loading protocol was more complicated than the planar wall test loading protocol. For the planar wall tests, the relation between the shear and moment at the top of the walls was appropriately set to simulate the demand. In the coupled wall, both the overall loads (shear F_x, moment M_y, and axial F_z) and the local pier loads (pier shear, moment and axial) must simulate load that would be present in a coupled wall. As noted in Figure 3.20, the overall loads are designated with a subscript of *total*; the local demands at the top of the wall are designated with a subscript of *1* or *2*, for the west and east piers, respectively.

Of particular interest was the determination of the relative displacement of the two wall piers, and the relation to proportion the total moment applied to the top of the specimen to meet target individual pier moments and coupled moment ($F_z \times L$). Both of these relations were determined using the results of continuum analyses, which are summarized here. Additional information on the development of the loading protocol may be found in Marley (2011).

The loading protocol was developed to control the combination of displacements and forces in all six degrees of freedom at points of contact between the loading devices and the test structure. A critical aspect of test planning was to develop a test protocol that realistically simulates the demands on a coupled wall in an accurate manner. The constraints were as follows:

1. Because the coupled wall specimen was tested as a planar element, the associated inactive degrees of freedom (DOFs) were maintained to be zero for the entire test.

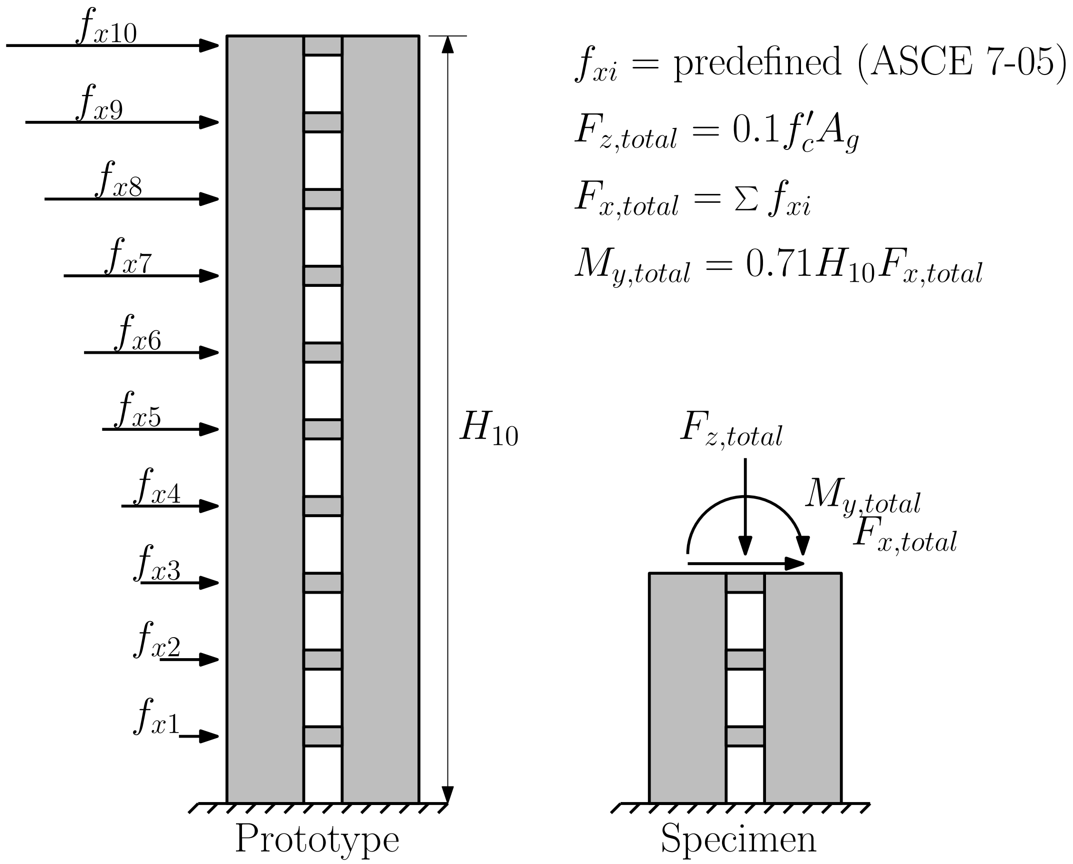

Figure 3.19: Definition of applied loads for 1/3 scale prototype and specimen

2. The free-body diagram from the load distribution provides constraints on the total axial load, total shear force, and total moment using the assumed gravity load and lateral load distributions.

3. The remaining loads and deformations must be defined including vertical (axial) displacement, horizontal (shear) displacement, and rotation (moment) for both LBCBs for a total of six active DOFs. Therefore, three additional constraints are required to fully define a viable loading protocol.

The coupled wall loading procedures were based on extensive analytical investigations of the 10-story prototype and the 3-story specimen model using VecTor2, a two-

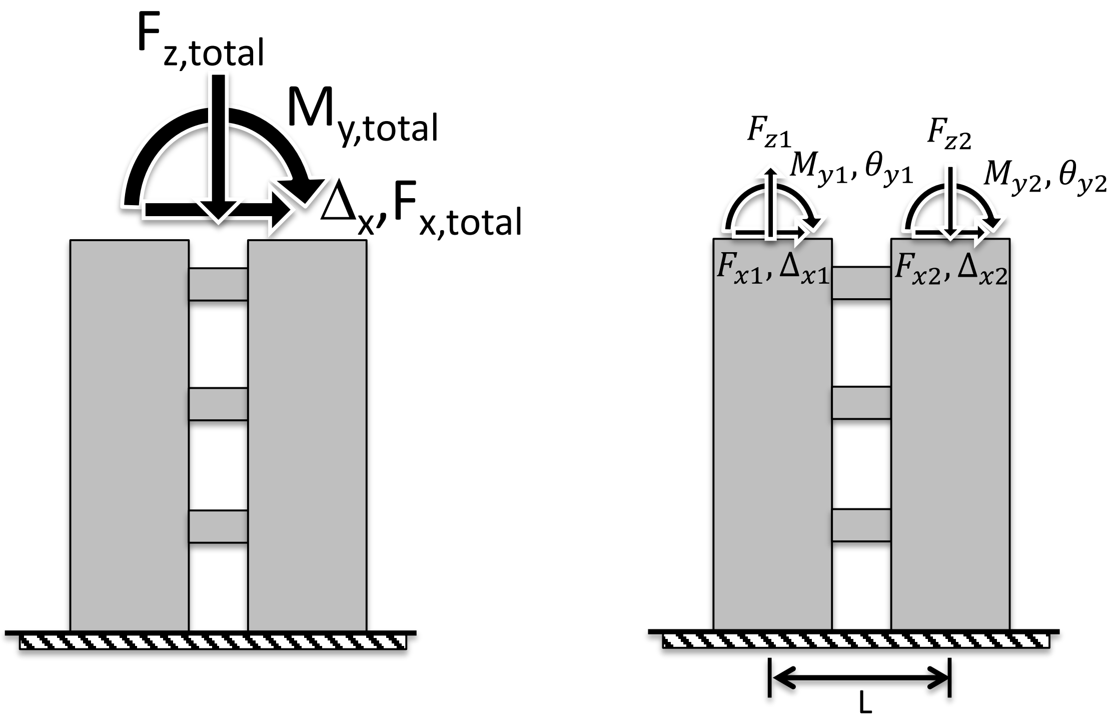

(a) Global DOFs (b) LBCB DOFs

Figure 3.20: Degrees of freedom associated to the loading protocol

dimensional nonlinear finite element program. The initial results for the analysis were developed to define the relations between the horizontal displacements of the wall piers and horizontal displacements and rotations. This resulted in the following constraints for the loading of the wall piers:

$$M_{y,total} = 0.71 H_{10} F_{x,total} \tag{3.7}$$

$$F_{z,total} = 0.10 f'_c A_g \tag{3.8}$$

$$\Delta_{x1} = \text{predefined} \tag{3.9}$$

$$\Delta_{x1} = \Delta_{x2} \tag{3.10}$$

$$\theta_{x1} = \alpha \times \Delta_{x1} \tag{3.11}$$

$$\theta_{x2} = \alpha \times \Delta_{x2} \tag{3.12}$$

where, the variable α was determined from the 10-story cyclic analysis. This loading regime constrains four of the six active degrees of freedom using displacement-control. Furthermore, the global loading objectives call for the total moment and axial load to be force-controlled, this requires iterating on individual pier axial loads using force control after applying their rotations to satisfy both requirements.

The proposed mix-mode control algorithm was implemented in VecTor2 to simulate the LBCBs control logic implemented in the laboratory control software. While the global results showed good correlation between the 10-story and 3-story models. There were important more local differences. In particular, the analyses indicated that the top (third-story) coupling beam was subjected to large normal strains (large compressive force in the top story beam) which resulted from the imposed lateral displacements of the wall piers.

Since using a predefine lateral displacement relation between the two wall piers resulted in erroneous demands in the coupling beam, the loading protocol was modified to include an iterative procedure of controlling the wall piers while satisfying a differential in shear force between each wall pier. This approach resulted in the following loading protocol constraints:

$$M_{y,total} = 0.71 H_{10} F_{x,total} \tag{3.13}$$

$$F_{z,total} = 0.10 f'_c A_g \tag{3.14}$$

$$\Delta_{x,total} = 0.5 \left(\Delta_{x1} + \Delta_{x2}\right) \tag{3.15}$$

$$F_{x2} - F_{x1} = f \left(F_{x,total}\right) \tag{3.16}$$

$$\theta_{x1} = \alpha \times \Delta_{x1} \tag{3.17}$$

$$\theta_{x2} = \alpha \times \Delta_{x2} \tag{3.18}$$

Compared to the first loading protocol, the new loading protocol had two significant differences. First, the average global lateral displacement of the wall system was defined using Equation 3.15. Second, a shear force differential, dF, (between the two piers) was defined as a function of the total force applied to the specimen. This revised loading protocol was implemented in VecTor2, and the results indicated an improvement in the stress distributions at the top floor while providing a good correlation between the 10-story and 3-story global results.

The algorithm was then implemented in the laboratory's control software, and the control algorithm was verified in the laboratory at very small cycles. However, implementing this algorithm at small elastic cycles resulted in convergence issues because the imposed rotation-displacement relationship could not be satisfied. The moments induced by a small change in rotation affected the ability for the other DOFs to converge appropriately (i.e. the shear differential and axial load due to coupling).

To troubleshoot the issue seen in the laboratory during verification, a third set of control procedures were developed to control the shear force differential, the relative coupled moment and applied pier moments in the tension and compression piers. The resulting algorithm is provided in Table 3.3. This final control algorithm improved the correlation between the results of both numerical models and provided a robust control logic for use in the laboratory. Three distinct testing phases were identified. Finally, the

Table 3.3: Final loading protocol

	Phase 1	**Phase 2**	**Phase 3**
Description	Pre-cracking	Cracking/yielding	Concrete damage
Lateral DOF	Force-controlled	Force-controlled; adjusted as needed to reach target displacements	Displacement-controlled; adjusted as needed to satisfy dF target
Shear Force Differential	$dF = 0$	$dF = 0.18\,(F_{x1} + F_{x2})$	
Rotational DOFs	Force-controlled		
Compression Pier Moment	$0.10M_{y,total}$	$0.15M_{y,total}$	
Tension Pier Moment	$0.10M_{y,total}$	$0.05M_{y,total}$	
Axial Forces	$F_{zi} = \pm\frac{0.80M_{y,total}}{L} - 0.1f'_cA_g$		

prescribed loading history for the experiment is shown in Table 3.4.

Table 3.4: Prescribed loading history

Cycles	**Target Force/Drift**	**Loading Phase**	**Description**
1-2	10 kips	1	Pre-cracking
3-4	20 kips	1	
5-6	0.128%	1*	Cracking
7-8	0.192%	2	Pre-yielding
9-10	0.321%	2	
11-12	0.50%	2	Yielding
13-14	0.75%	2	
15-16	1.00%	2	
17-18	1.50%	3	
19-20	2.25%	3	

* Loading phase modified during test (Section 4.2)

Chapter 4

EXPERIMENTAL OBSERVATIONS

The test specimen, CW1, was built at 1/3 scale and represents the bottom three stories of a ten story building. It was tested pseudo-statically in the test setup described in Section 3.5. In order to properly represent the moments, shears and axial forces at the top of the specimen, an extensive analytical study was undertaken to predict these demands. Using the developed loading protocol, the specimen was loading in three phases which represented pre-cracking, pre-yielding and post-yield drift levels. The following chapter provides an in depth presentation of the observed experimental results. Global force-displacement data, observed damage and a discussion of specimen failure are investigated in order to assess the seismic performance of coupled wall Specimen CW1.

4.1 Load–Displacement Data

As discussed in Section 3.5, the testing protocol used to control CW1 employed a force control logic up to the start of the 1.50% drift level and a displacement control for the remainder of the experiment. Figure 4.2 is the measured cyclic load history and Figure 4.1 is the measured third-story drift history.

In Figure 4.3 the measured base shear verse third-story drift response of the coupled wall is shown. The coupled wall reached a maximum third-story drift of ±2.27%, and the maximum base shear reached at the step prior to failure of the EWP measured 175 kips. At the last E+ peak, the coupled wall base shear capacity dropped 55%, and upon reverse loading to its maximum W- peak, the capacity dropped 52% of the maximum W-peak base shear (173 kips). The sudden drop in lateral load capacity at ±2.27% drift is easily seen in Figure 4.3.

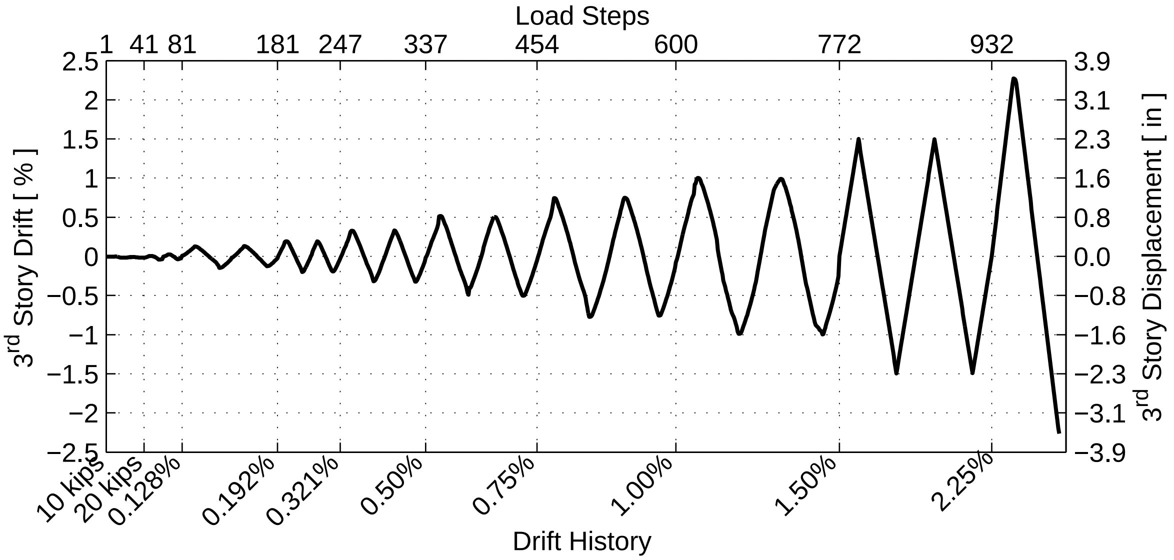

Figure 4.1: CW1 loading program: drift history

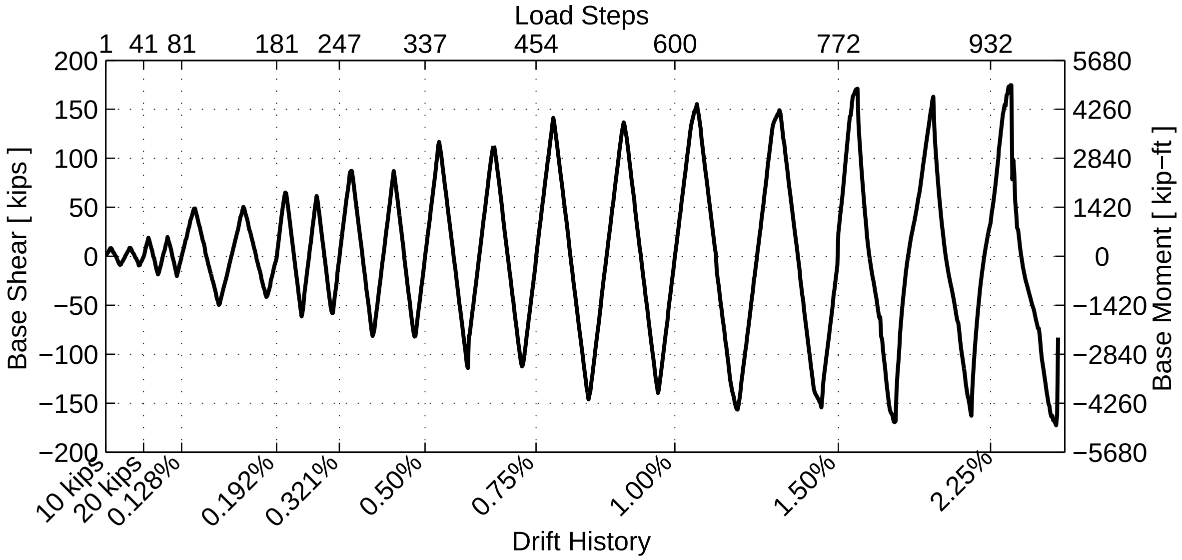

Figure 4.2: CW1 loading program: load history

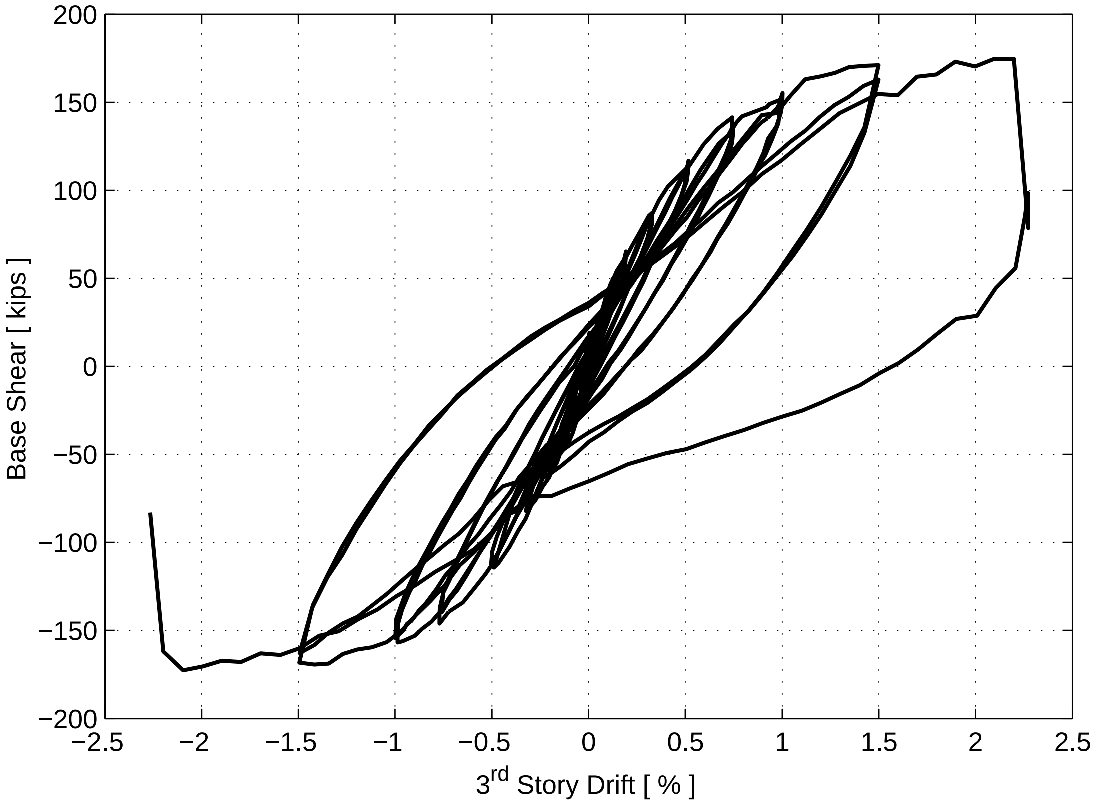

Figure 4.3: CW1 load-drift repsonse

4.2 *Description of Specimen Response*

In order to understand the behavior and performance of CW1, observations of damage were made throughout the test. The following section provides a detailed discussion of observed damage during the test. As mentioned in Section 3.4, the data acquisition system, Metris system and high resolution photographs were triggered at each step of the loading history. Throughout the test, detailed notes were recorded when unique specimen behavior was noticed, observations of damage were made or testing issues occurred. These notes are referenced to a particular step number and are reported in Table B.3 in Appendix B. During cycle A of the loading history, visible cracks were marked with colored pens at any step were new displacements were targeted; however, cracks were only marked at peaks during cycle B. Additionally, crack widths were measured throughout the experiment at the peak drift levels. Residual cracks widths were also measured at the end of each drift levels. These recorded crack measurements are reported in Table B.4 in Appendix B.4. Drift measurements described in the following refer to the average third story lateral drift measured using two string pots located 154 inches above the foundation as shown in Figure 3.14. Finally, steel strain gauge data was used to quantify initial yielding in the specimen. This behavior was observed when the measured strain value for a particular strain gauge exceeded the yield strain determined from the steel material properties discussed in Section 3.1.6.

Because the coupled wall specimen is made up of many different structural components, the following notation wad developed and is used regularly throughout this chapter. It should be noted coupling beams 1, 2 and 3 correspond to floor heights 1–3 and are abbreviated throughout this document as CB1, CB2 and CB3. Concrete damage such as cracking and spalling is classified to specific corners of coupling beams. Each beam is made up of the four following regions:

TWC Top west corner

TEC Top east corner

BWC Bottom west corner

BEC Bottom east corner

Additionally, the east and west wall piers are abbreviated EWP and WWP and each are divided into the following regions:

IBE Inner boundary element, 14 inches in length

OBE Outer boundary element, 14 inches in length

Web Web region of each wall pier, 20 inches in length

All of the following notation described above including the loading direction of CW1 is shown in Figure 4.4.

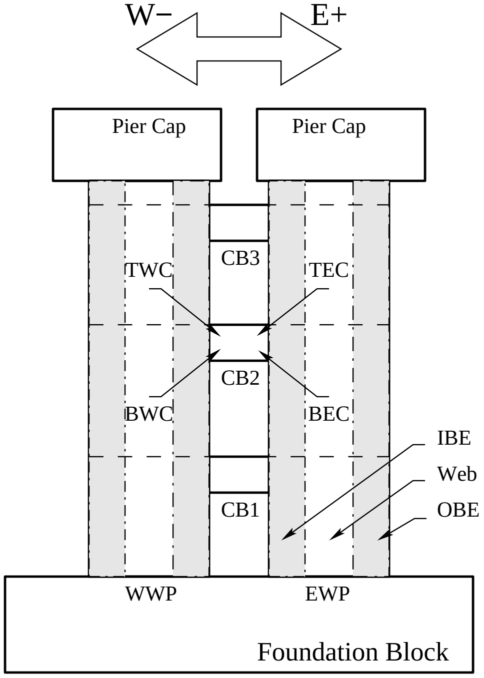

Figure 4.4: CW1 notation

4.2.1 Force Controlled Cycles

As explained in 3.5, the first four cycles of testing were completed under force control to circumvent the issues related to using displacement control at very small displacement targets. The specimen was subjected to cycles at 10 kips and 20 kips total shear and these peak data are shown in Table B.2. These cycles were used to soften the specimen and generate data which was used to verify the control algorithm. While no visible damage was recorded after the last 20 kip cycle, the secant stiffness of the specimen reduced by approximately 20% during the 20 kip load level. It was determined the specimen had softened enough to modify the Phase 1 loading protocol so the average third story displacement was targeted rather than an applied horizontal force. This transition is discussed in Section 3.5 but was not considered Phase 2 loading because the shear differential remained zero and the applied compression and tension pier moments remained equal to 10% of the total applied moment.

4.2.2 0.128% Drift, Initial Cracking in the Wall Piers and Coupling Beams

Vertical cracks were initially observed in the TEC of CB3 at 0.033% drift (Step 85), which was during the first E+ cycle to 0.128% drift. On the east end of CB3, four vertical cracks spaced at approximently two inches apart extended four or more inches into beam. Cracks running along the east end wall-to-beam interface extended down the entire depth of the beam. It is not until 0.103% (Step 92) when vertical cracks started to form in the BWC of CB3. Additionally, one diagonal crack formed during the same step and was approximately four inches long. Approaching the first W- peak at -0.028% (Step 112), vertical cracks formed in the BEC of CB3. At -0.059% (Step 115) a single three inch long crack was visible in the TWC of CB3. Diagonal cracks were visable at -0.102% (Step 118) at midspan of CB3, and the longest crack in CB3 extended diagonally from the TEC to the midspan and ends two inches from the bottom. More diagonal and vertical cracks in CB3 formed during Cycle B. The diagonal cracks were spaced at approximately two inches apart across the midspan of CB3.

In the TEC of CB2 vertical cracks were initially observed at 0.033% drift (Step 85) during the first E+ cycle to 0.128% drift. In the same location on CB2, one vertical crack extended approximately 90% of the coupling beam depth. At this same step the BWC of CB2 has one vertical crack extending roughly two inches into the beam's depth. Approaching the first W- peak at -0.028% (Step 112), vertical cracks formed in the BEC of CB2 and CB3, and on the next step, vertical cracks formed in the TWC of CB2 (-0.040% drift). Approaching the first W- peak at -0.028% (Step 112), vertical cracks formed in the BEC of CB2, and on the next step, vertical cracks formed in the TWC of CB2 (-0.040% drift). Diagonal cracks were observed at -0.148% drift (Step 120) at midspan of CB2. During cycle B, a diagonal crack in CB2 and additional vertical cracks were visible at the E+ peak.

Two four inch long vertical cracks in the TWC and BWC of CB1 initiated at 0.111% (Step 92) and 0.125% (Step 94), respectively. A crack six inches in length formed in the BEC of CB1 on the next step (-0.0696% drift). Unlike the top two coupling beams, no additional cracks formed during cycle B.

During the second cycle of loading, horizontal cracks spaced approximately 12 inches apart in the OBE of the WWP became visible at the E+ peak (0.129% drift, Step 146). These cracks only extend one inch into the boundary of each pier, but formed over the height of the first story.

At the W- peak (-0.125%, Step 170), horizontal cracks spaced four to 12 inches apart also formed in the OBE of the EWP. These cracks only extend one inch into the boundary of each pier, but formed over the height of the first story. While a majority of the cracking was concentrated in the second and third story coupling beams at the end of cycle the first cycle, vert few cracks actually formed during the second cycle. Figure 4.11 shows the specimen at the end of the two 0.128% drift cycles.

4.2.3 0.192% Drift, Continuation of Cracking

While very few new cracks were observed in the coupling beams throughout the entire drift level, loading to the first E+ peak (0.193%, Step 190) led to visible horizontal cracks in the second story of the WWP. One crack in the middle of the story apprixemately six feet above the foundation propagated 14 inhces in the wall pier. Two long horizontal cracks in the web of the WWP formed at the E+ peak (0.191% drift, Step 223). One crack was located approximately 24 inches above the foundation in the first story and the other was located approximately 80 inches above the foundation in the second story. Furthermore, a four inch horizontal crack in the OBE of the WWP was visible at the third floor elevation. It was also noticed at this step more new horizontal cracks spaced approximately 4 to six inches apart became visible in the lower two stories of the WWP. Throughout cycle B very few horizontal cracks in the WWP. Figure 4.13 shows the the specimen at the end of the two 0.192% drift cycles.

At -0.136% drift (Step 205) a long horizontal crack extending 16 inches into the web from the interface of the OBE in the EWP was visible (Figure 4.12). Two steps after this cracked formed significant cracking along the first twp storied in the OBE of the EWP were observed at the W- peak (-0.200% drift, Step 207). These horizontal cracks were spaced approximately four inches apart and extended into the wall pier in a range of six to 24 inches. It was noticed as the cracks in the web started to reach the IBE, the cracks appeared to be orientating to a flexure-shear behavior. At the subsequent W-peak (-0.191% drift, Step 239), one to two inch horizontal cracks had formed in the EWP third story OBE; however few new cracks formed elsewhere.

4.2.4 0.321% Drift, Diagonal Cracking in Wall Piers and CB1

Only a few newly formed vertical cracks were visible in the top coupling beam at the end of the first cycle. However, extensions of diagonal cracks towards the ends of CB3 did occur in this drift level. Cracking associated with development of diagonally reinforcing bars in the top coupling beam also became visible (Figure 4.14). No new cracks formed in CB3 during cycle B.

No new vertical cracks in CB2 were visible at the end of the first cycle. The extensions of diagonal cracks towards the ends of CB2 did occur in this drift level on the other hand. Cracking associated with development of diagonally reinforcing bars in the CB2 was also observed.

During the second cycle (cycle B), diagonal cracking was initially observed in CB1 at the W- peak (-0.324%, Step 326). Two cracks approximently five inches in length formed and vertical crack spacing was appoximently three inches at the end of the drift level.

New horizontal cracks were observed a -0.277% drift (Step 281) during the first cycle of the new drift level. At the W- peak, these cracks were spaced approximately 16 inches and extended approximently 1.5 inches into the IBE of the WWP. The spacing between horizontal cracks in the OBE decreased to approximately three inches in the first floor, two inches in the second floor and 6 inches in the thrid floor during cycle A. Additionally, diagonal cracks formed in the second story web region of the WWP at 0.264% drift (Step 257). During the second cycle, new horizontal cracks formed in the OBE and web region of the WWP, and the crack spacing in the web was approximately 12 inches.

During the first cycle of the new drift level, initial horizontal cracking was noticed in the IBE of the EWP at 0.224% (Step 256). At the E+ peak, these cracks had extended approximately eight inches into the boundary element of the EWP and where spaced at approximately 14 inches. The spacing between horizontal cracks in the OBE of the EWP was similar to the spacing the in WWP during cycle A. By the end of the first cycle, diagonal cracks and horizontal cracks were visible in both wall piers up the entire height of each wall. Additionally, diagonal cracks formed in the second story web region of the EWP at -0.237% drift (Step 280). During the second cycle, new horizontal cracks formed in the OBE and web region of the EWP, and the crack spacing in the web was approximately 12-16 inches.

The axial load applied to the third story of the tension wall during this drift level overcame the gravity force of $0.1f_c'A_g$. As a result, diagonal cracks formed in the upper stories, and this cracking is an indication that the loading had significantly changed the stiffness between the tension and compression walls. Consequently, the tension wall sheds shear and moments to the compression wall via the coupling beams to maintain global equilibrium, and this is a preliminary sign that coupling action in the specimen is indeed occurring at these lower drift levels. Figure 4.15 shows the the specimen at the end of the two 0.321% drift cycles.

4.2.5 0.50% Drift, Yielding of Wall Piers and Coupling Beams

At 0.364% drift (Step 349) the diagonal steel located in CB3 yielded (measured by strain gauges). On the reverse half cycle the diagonal steel located in CB3 yielded in tension at -0.263% drift (Step 376). The only cracking behavior observed during this drift level was a decrease in diagonal crack spacing to approximently four inches.

The diagonal steel in CB2 yielded in tension at 0.364% drift (Step 349). At -0.231% drift (Step 375) the other bundle of diagonal reinforcement in CB2 yielded in tension. Newly observed diagonal cracks in CB2 were spaced at appoximently four inches and were roughly nine inches in length.

New diagonal cracks associated with E+ loading were visible in CB1 and measured approximately five inches in length. New vertical cracks were not observed during this drift level in CB1.

The outermost vertical rebar as well as a web bar located 24 inches into the WWP reached the yield strain at the E+ peak (0.509%, Step 351). When the loading was reversed, diagonal cracking was initally observed in the WWP (compression wall) at -0.465% (Step 381). This is the first observed diagonal cracking in the WWP associated with this loading direction. At -0.484% drift (Step 438), the outermost reinforcing bar in the WWP reached the compressive yield strain two inches above the foundation.

At the same step where initial yielding was observed the in WWP (0.509% drift Step 351), diagonal cracks formed in the EWP when the wall was in compression. This was the first time diagonal cracking was observed in the compression wall. During the reverse loading, the outer bar in the EWP reached the yield strain at -0.465% drift (Step 381). During the cycle B, one vertical reinforcement strain gauge in EWP (10 feet above the foundation) reached the tensil yield strain at the W- peak (-0.503%, Step 439). Figure 4.16 shows the the specimen at the end of the two 0.50% drift cycles.

4.2.6 0.75% Drift, Yielding of CB1 and the IBE of each Wall Pier

Diagonal crack spacing in the top two coupling beams measured approximately three inches in CB3 and one to two inches in CB2 at the end of the 0.75% drift level. No new vertical cracks formed during this drift level; however, the existing vertical cracks along the CB3 beam-to-wall interface measured 1/16 of an inch at the first E+ peak.

Additionally, the diagonal reinforcment in CB1 yielded in tension at (0.666% drift, Step 471).

The outermost reinforcing bar reached the compressive yield strain at the base of the EWP at 0.595% drift (Step 470). In the EWP at 0.743% drift (Step 473) the innermost reinforcing bar yielded in tension two and 24 inches above the foundation. Additionally, the strain gauge on the innermost reinforcing bar, two inches above the foundation, yeilded in tension at -0.771% drift (Step 509).

Throughout these cycles diagonal cracks continued to form and extend into the web of the compression wall pier depending on loading direction. Again, this extensive diagonal cracking indicates strong coupling between the two wall piers. An approximately uniform crack spacing of two inches has developed along the outer edges of each wall pier, and this spacing is shown in Figure 4.17. Furthermore, Figure 4.18 shows the specimen at the end of the 0.75% drift level.

4.2.7 1.00% Drift, Spalling of Wall Pier and CB3 Cover

As the specimen approached the E+ peak (cycle B) the cracks in the TEC of CB3 reopened and concrete was removed, and it was determined that spalling occurred at the last W- peak (Step 666). Additionally, this behavior was noticed loading to the W- peak during cycle B, and it was determined that spalling of the TWC of CB3 occurred at the last E+ peak (Step 706). Spalling of CB3 can be seen in Figure 4.24c. The maximum recorded vertical cracks widths at the end of 1.00% drift level for CB1, CB2 and CB3 are 0.075, 0.150 and 0.188 inches, respectively.

While loading to the first E+ peak, a horizontal reinforcing bar in the WWP, 84 inches above the foundation, yielded in tension at 1.00% drift (Step 623). In the reverse loading direction at a drift equal to -0.988% drift (Step 666), the concrete cover on the back corner of the WWP spalled and extensive vertical splitting of the cover was visible (Figure 4.21). During the second 1.00% drift cycle, additional spalling of the concrete cover along the edges of the WWP occurred. Most of this spalling was observed at the

W- peak (-0.999% drift, Step 754) as shown in Figure 4.23.

Three steps prior to the first E+ peak (0.992% drift, Step 620), a horizontal reinforcing bar in the EWP, just above the second floor, yielded in tension. The concrete cover on the OBE of the EWP spalled at 1.00% drift which was the E+ peak (Figures 4.20 and 4.19). Note in the figure, the tape measure provides a vertical distance measured with respect to the top of the foundation. During the second 1.00% drift cycle, additional spalling of the concrete cover along the edges of the EWP occurred. Most of this spalling was observed at the E+ peak (0.988% drift, Step 710) as shown in Figure 4.23.

Cracks continued to form and extend in the web region of both wall piers only when the wall was loaded in compression. The angle of inclination for these cracks had orientated more vertical due to the influence of increasing compression demand (Figure 4.24).

4.2.8 1.50% Drift, Exposed Reinforcement in the Wall Piers and Spalling of CB2

At the end of the 1.50% drift cycle, the maximum recorded vertical cracks widths for CB1, CB2 and CB3 measured 0.15, 0.25 and 0.25 inches, respectively. On the other hand, residual crack widths at the ends of CB1, CB2 and CB3 measured 0.10, 0.15, and 0.15 inches, respectively. All other maximum and residual cracks widths reported up to this drift level, including the measurements taken in the wall piers, were less than 1/16 of an inch. Furthermore, the concrete cover in the TEC of CB2 spalled at -1.50% drift (Step 832) and additional loose concrete was removed at the next E+ peak (1.50% Step 872)(Figure 4.25a). At this peak the TWC of CB2 spalled (Figure 4.25b).

Moving towards the E+ peak led to an increase in cracking throughout OBE of the WWP. The horizontal crack spacing decreased during this cycle and was uniformly spaced at one inch. Similarly, spalling occurred at the base of the WWP during the reverse loading cycle to W- peak (-1.50% Step 832). During cycle B the WWP continued to spall as loading increased to the opposite W- peak (-1.49% drift, Step 912). At the end of the 1.50% drift level, spalling had progressed spalling extended roughly 34 inches up the height of the first story and approximently two inches into the OBE (Figure 4.27). Furthermore, the longitudinal reinforcement was exposed at the base of the WWP.

Spalling on the EWP extended 40 inches up the height of the first story at the end of the E+ peak (1.50% drift, Step 792). The outside of the EWP continued to spall, and this damage progressed roughly five inches into the OBE approximately 12 inches above the foundation (Figure 4.26). Note the longitudinal reinforcement was exposed at the base of the EWP. Additionally, Figure 4.28 shows the damage of the specimen at the end of the two cycles.

4.2.9 2.25% Drift, Spalling of CB1 and Compression Failure of Wall Piers

At 1.89% (Step 951), the TWC of CB1 spalled and details of the damage are shown in Figure 4.29. At the same step, the concrete cover along the east face of the EWP up to 27 inches above the foundation had completely spalled off. Additionally, the spalling had progressed eight inches into the OBE of the EWP approximately 14 inches above the foundation. This damage is shown in Figure 4.30.

At the step before the E+ peak (2.20% drift, Step 954), spalling on the south facing side of the EWP measured approximately 19 inches into the wall length (Figure 4.32). Furthermore, Figure 4.31 shows the minor extent of spalling on the backside of the EWP, and due to access constraints from instrumentation, the removal of spalled concrete was not performed.

A sudden loss of lateral load occurred at 2.27% (Step 955) when crushing of the EWP concrete core and buckling of the longitudinal reinforcement cause a sudden drop in 55% of the base shear. All the OBE longitudinal reinforcement buckled as well as two vertical bars in the web. Within the two foot region above the foundation, the toe of the wall shorted by 0.30 inches in one step (i.e. 0.11 inches of lateral movement). Photos of the compressive failure can be seen in Figures 4.33–4.36. In the negative direction, up until -1.59% drift (Step 996), concrete had only spalled on the outer west facing edge of the WWP, and moving from this drift to the W- peak, the south facing side of the pier spalled. As the specimen was displaced from Step 1002 (-2.20%) to the peak (-2.27% drift, Step 1003), extensive damamge was sustained in the OBE of the WWP where core crushing and bar buckling of all the OBE longitudinal reinforcement was observed. The toe region bounded by the foundation and 24 inches above the foundation shorted approximately 0.28 inches during this step. Figures 4.37 – 4.40 show the extended of the compressive damage at the peak drift.

4.2.10 Sequence of Wall Pier Compression Failure

The sudden progression of damage to the OBE of the EWP is shown Figure 4.41 for four displacement steps leading up to failure of the EWP. Additionally, the sudden progression of damage of the OBE of the WWP is captured in Figure 4.42 for four W- direction steps. It is interesting to note from these figures how little the specimen displaced before superficial spalling transitioned to severe damage of the core. Due to concerns for safety, spalled concrete was not removed during the negative loading cycle, so extent of damage was more difficult to detect until the peak was reached (Figure 4.42d).

4.2.11 Final Damage State

The last step of the test occurred at -2.27% drift (Step 1003). Final photographs of the damage to all the structural components was taken in order to assess damage in other locations other than the damaged wall piers. Figure 4.43 shows the extent of damage to the coupling beams at the last peak displacement (-2.27% drift). Most of the damage was localized to the beam ends while diagonal cracking in the middle of the span was relatively minor. These cracks at any beam did not measure over 1/16 of an inch at any portion of the test. No sliding along the wall-to-beam interface was observed during the test.

Additionally, the state of the wall piers can be seen in Figure 4.44 at the last peak displacement (-2.27% drift). Diagonal cracking in the second and third stories suggests

Table 4.1: Maximum measured peak and residual crack widths (in)

Crack Type	**Location**	**W-WP**	**E-WP**	**Crack Type**	**CB1**	**CB2**	**CB3**
Maximum Residual Crack Widths (Step 1072, start of 2.25% (A))							
Horizontal	**OBE**	closed	0.010	**Vertical**	0.100	0.150	0.150
Horizontal	**Web**	closed	0.015		—N/A—		
Diagonal	**Web**	0.015	0.020	**Diagonal**	0.005	0.005	0.005
Maximum Peak Crack Widths (Step 1117*)							
Horizontal	**OBE**	0.025	0.035	**Vertical**	0.150	0.400	0.300
Horizontal	**Web**	0.100	0.050		—N/A—		
Diagonal	**Web**	0.075	0.050	**Diagonal**	0.010	0.005	0.015

* Last Step of Recorded Crack Widths

a strong coupling action between wall piers as discussed previously. Furthermore, maximum residual and peak crack widths recorded throughout the experiment are summarized in Table 4.1, and more detailed cracking data is reported in Table B.4. Finally, a time-lapse movie showing the damage to the specimen for the entire cyclic loading histroy is located at `http://www.youtube.com/user/NEESRWallProject`.

4.2.12 Summary of CW1 Damage

Figure 4.5 provides an overview of damage at particular drift levels throughout the test. The initial yield and plastic behavior damage levels were used to distinguish reinforcement behavior. Using the steel strain gauge data, initial yielding was observed when the measured strain value for a particular strain gauge exceeded the yield strain determined from the steel material properties discussed in Section 3.1.6. Additionally, the plastic behavior damage state was quantified when these measured strain values exceed the strain-hardening strain determined from the same steel material tests. A more detailed investigation of steel reinforcement behavior is discussed later in Section 5.1. Furthermore, Table 4.2 provides a tabulated summary of observed damage throughout the experiment.

To illustrate the data provided in Table 4.2, Figures 4.6 – 4.9 plot the progression of damage for cracking, yielding, spalling and failure with respect to the global force-drift measurement. A typical annotation in these figures is explained below. *Element* defines the structural component where damage is located and *location* is the region within the element. *Damage* is used to distinguish between certain identifiers relating to damage. Finally, the *order* portion of the annotation indicates the sequence in which damage occurred within a set of damage.

$$\underbrace{WWP}_{\text{element}} : \overbrace{OBE}^{\text{location}} \underbrace{(E),}_{\text{damage}} \overbrace{\;8\;}^{\text{order}}$$

Finally, a brief summary of the observed damage for CW1 is as follows:

1. Vertical cracks were initially observed in the top corners of CB1, CB2 and CB3 at 0.111%, 0.033% and 0.033% drift, respectively.
2. Horizontal cracks were initially observed in the OBE of the WWP and EWP at drifts of 0.129% and -0.125%, respectively.
3. Diagonal cracks were initially observed in CB1, CB2 and CB3 at -0.324%, -0.148% and 0.103% drift, respectively.
4. Diagonal cracking occurred in the web of the WWP and EWP at drifts of 0.264% and -0.237%, respectively.
5. Horizontal cracks were initially observed in the IBE of the WWP and EWP at drifts of -0.227% and -0.224%, respectively.
6. CB2 and CB3 diagonal reinforcement initially yielded in tension at 0.364% drift in the first cycle to the 0.5% drift.

7. Both wall piers yielded in tension in the OBE at peaks of the 0.50% drift level
8. CB1 diagonal reinforcement initially yielded in tension at 0.666% drift during the 0.75% drift level
9. The horizontal reinforcement in the web region of the EWP and WWP yielded during the same cycle to 1.00% drift at drifts of 0.922% and 1.00%, respectively.
10. Initial spalling of concrete cover located on the OBE of the EWP and WWP occurred at the E+ and W- peaks during the first 1.00% drift cycle (Figures 4.22 and 4.23).
11. Initial spalling of concrete cover located at the top of CB1, CB2 and CB3 occurred at drifts of +1.89%, ±1.50% and ±0.988%, respectively (Figures 4.29, 4.25 and 4.24c).
12. Concrete cover spalling lead to the exposure of vertical reinforcement in the OBE of each wall pier at corresponding peaks during the second ±1.50% cycle (Figures 4.26 and 4.27).
13. At +2.27% drift the OBE in the EWP failed in compression resulting in extensive core crushing and buckling of all 16 vertical wall boundary bars (Figures 4.30–4.35).
14. Yielding of the steel confinement in the WWP OBE occurred at -1.69% (2.25% (A) drift)
15. At -2.27% drift the OBE in the WWP failed in compression resulting in extensive core crushing and buckling of all 16 vertical wall boundary bars (Figures 4.37–4.40).

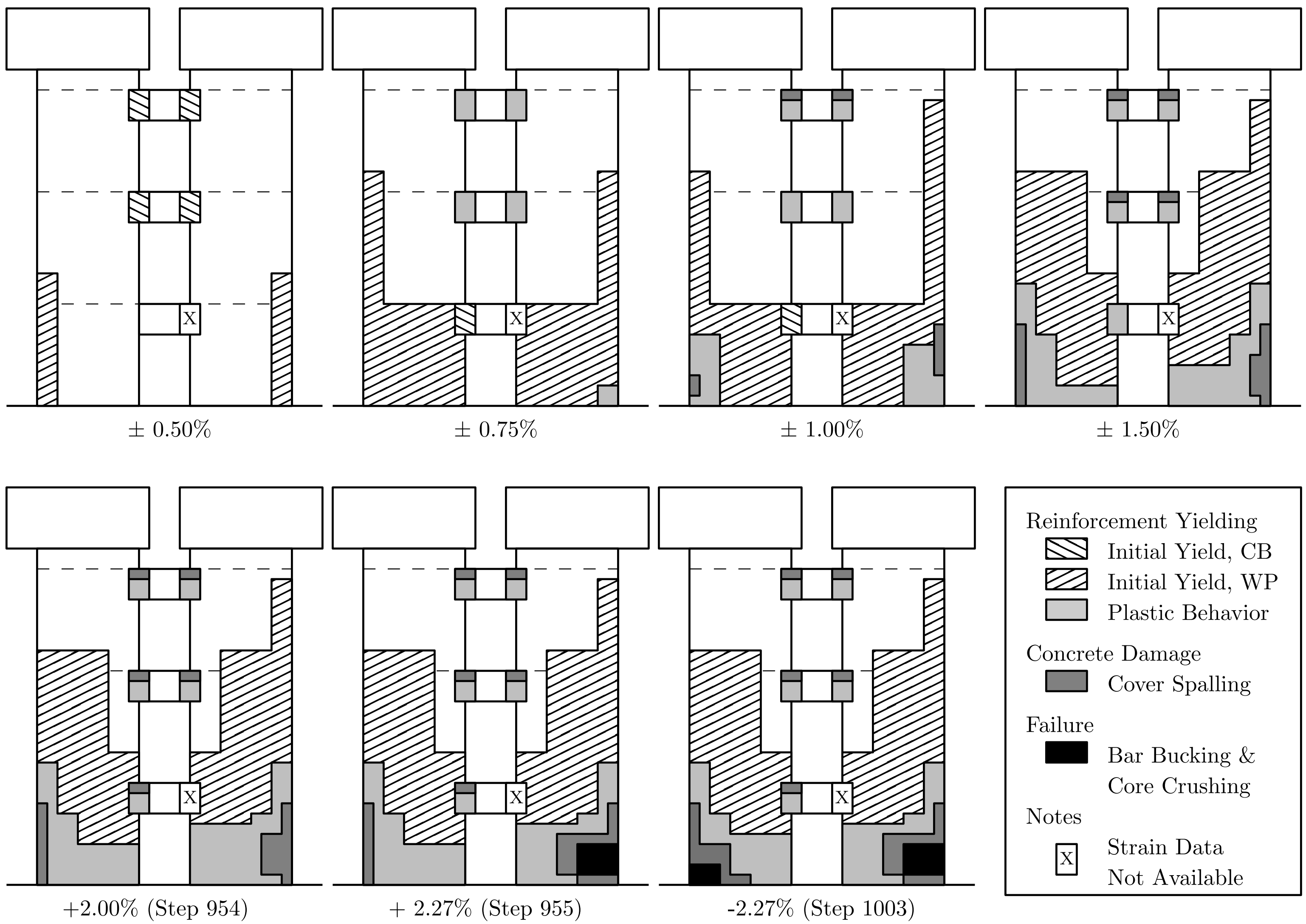

Figure 4.5: Damage progression

Table 4.2: Summary of Wall 5 damage

Load Step	**Damage**	**Element**	**Location**	**Cycle Drift**	**Drift (%)**	V_b **(kips)**
85	Vertical Cracking	CB2	TEC	0.128% (A)	0.033	16
85	Vertical Cracking	CB3	TEC	0.128% (A)	0.033	16
92	Vertical Cracking	CB1	TEC	0.128% (A)	0.103	42
92	Diagonal Cracking	CB3	—	0.128% (A)	0.103	42
112	Vertical Cracking	CB2	BEC	0.128% (A)	-0.028	-18
112	Vertical Cracking	CB3	BEC	0.128% (A)	-0.028	-18
116	Vertical Cracking	CB1	BEC	0.128% (A)	-0.070	-34
118	Diagonal Cracking	CB3	—	0.128% (A)	-0.102	-43
120	Diagonal Cracking	CB2	—	0.128% (A)	-0.148	-50
146	Horizontal Cracking	WWP	OBE	0.128% (B)	0.129	50
146	Diagonal Cracking	CB2	—	0.128% (B)	0.129	50
170	Horizontal Cracking	EWP	OBE	0.128% (B)	-0.125	-42
256	Horizontal Cracking	EWP	IBE	0.321% (A)	0.224	68
257	Diagonal Cracking	WWP	Web	0.321% (A)	0.264	76
280	Diagonal Cracking	EWP	Web	0.321% (A)	-0.237	-68
281	Horizontal Cracking	WWP	IBE	0.321% (A)	-0.277	-76
326	Diagonal Cracking	CB1	—	0.321% (B)	-0.324	-82
349	Diagonal Cracking	CB1	—	0.50% (A)	0.364	94
349	*Yielding in Tension*	CB2	Diagonal	0.50% (A)	0.364	94
349	*Yielding in Tension*	CB3	Diagonal	0.50% (A)	0.364	94
351	Diagonal Cracking	EWP	Web	0.50% (A)	0.509	113
351	*Yielding in Tension*	WWP	OBE	0.50% (A)	0.509	113
351	*Yielding in Tension*	WWP	Web	0.50% (A)	0.509	113
381	Diagonal Cracking	WWP	Web	0.50% (A)	-0.465	-112
381	*Yielding in Tension*	EWP	OBE	0.50% (A)	-0.465	-112
438	*Yielding in Compression*	WWP	OBE	0.50% (B)	-0.484	-109
439	*Yielding in Tension*	EWP	Web	0.50% (B)	-0.503	-112
470	*Yielding in Compression*	EWP	OBE	0.75% (A)	0.595	126
471	*Yielding in Tension*	CB1	Diagonal	0.75% (A)	0.666	135
472	*Yielding in Tension*	EWP	IBE	0.75% (A)	0.743	141
509	*Yielding in Tension*	WWP	IBE	0.75% (A)	-0.771	-146
620	*Yielding of Horizontal Reinforcement*	EWP	Web	1.00% (A)	0.922	147

* Longitudinal Reinforcement Exposed

Table 4.2: continued

Load Step	**Damage**	**Element**	**Location**	**Cycle Drift**	**Drift (%)**	V_b **(kips)**
623	*Yielding of Horizontal Reinforcement*	WWP	Web	1.00% (A)	1.00	155
623	**Concrete Spalling**	EWP	OBE	1.00% (A)	1.00	155
644	*Yielding in Compression*	WWP	Web	1.00% (A)	0.080	-15
666	**Concrete Spalling**	WWP	OBE	1.00% (A)	-0.988	-157
666	**Concrete Spalling**	CB3	TEC	1.00% (A)	-0.988	-157
710	**Concrete Spalling**	CB3	TWC	1.00% (B)	0.988	149
832	**Concrete Spalling**	CB2	TEC	1.50% (A)	-1.50	-168
849	*Yielding in Compression*	EWP	Web	1.50% (A)	-0.225	22
872	**Concrete Spalling***	EWP	OBE	1.50% (B)	1.50	163
872	**Concrete Spalling**	CB2	TWC	1.50% (B)	1.50	163
912	**Concrete Spalling***	WWP	OBE	1.50% (B)	-1.49	-163
951	**Concrete Spalling**	CB1	TWC	2.25% (A)	1.89	173
955	Bar Buckling & Core Crushing	EWP	OBE	2.25% (A)	2.27	79
997	*Yielding of Confining Reinforcement*	WWP	OBE	2.25% (A)	-1.69	-163
1003	Bar Buckling & Core Crushing	WWP	OBE	2.25% (A)	-2.27	-83

* Longitudinal Reinforcement Exposed

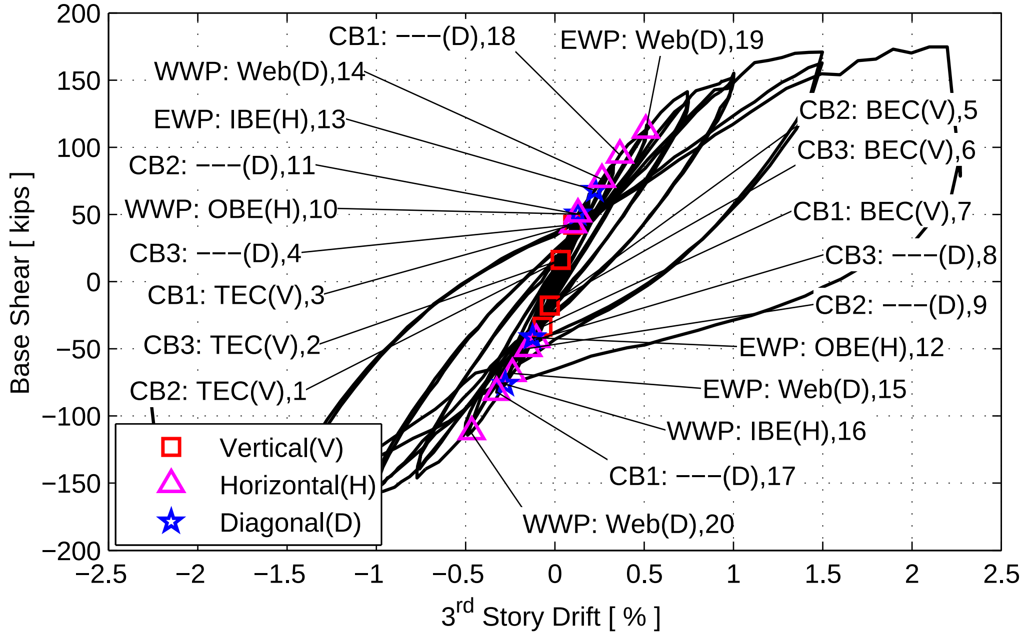

Figure 4.6: CW1 initial cracking sequence

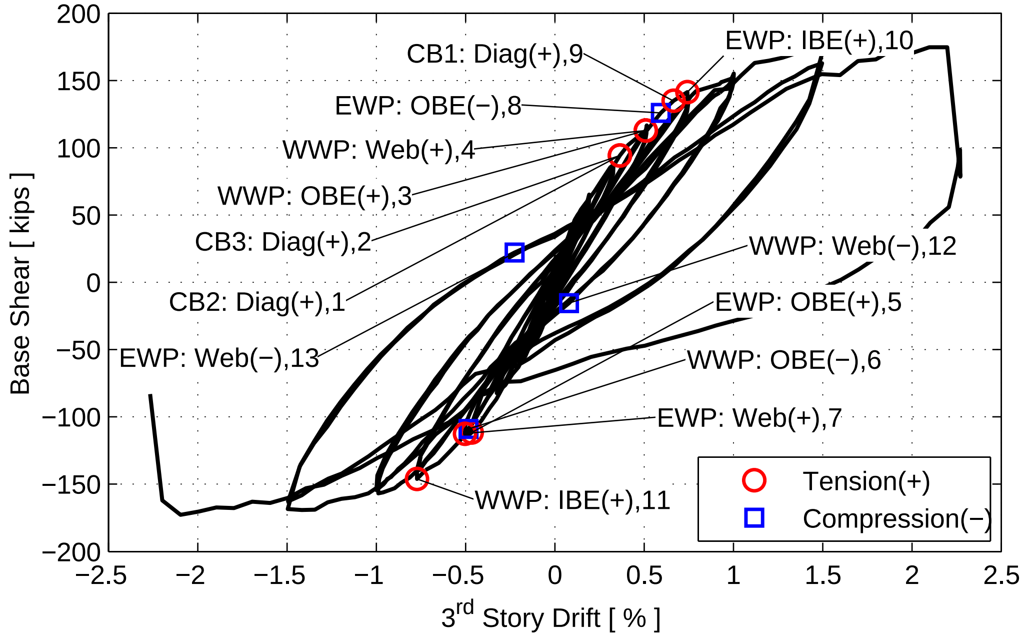

Figure 4.7: CW1 yielding sequence of longitudinal reinforcement

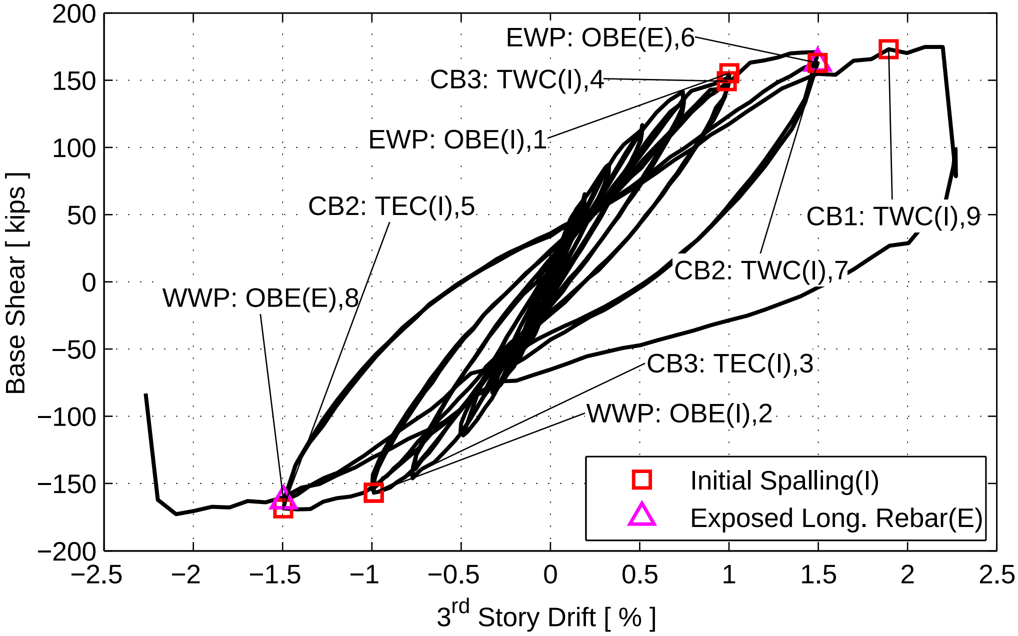

Figure 4.8: CW1 sequence of spalling concrete

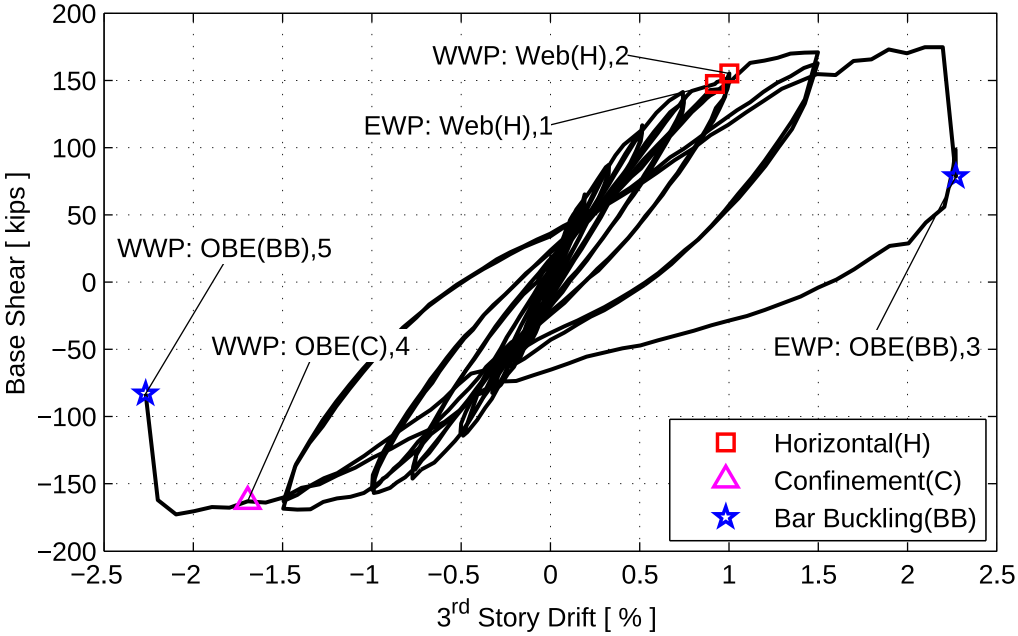

Figure 4.9: CW1 sequence of transverse reinforcement yielding and bar buckling

4.2.13 End of Test: Determination of Axial Capacity

After completion of the lateral load history, the damaged system was tested to determine the residual axial capacity. This quantification is important in examining the gravity load carrying capacity of damaged lateral load resisting systems. Therefore, axial load was applied to each wall pier until the applied axial force dropped significantly. Figure 4.10 shows the applied axial load verse the average axial deformation in both wall piers. The maximum axial load applied to the specimen was -1380 kips which equates to a demand on each wall pier of $0.42A_gf'_c$. Figure 4.45 shows the extent of the damage at the base of the specimen after the axial load test.

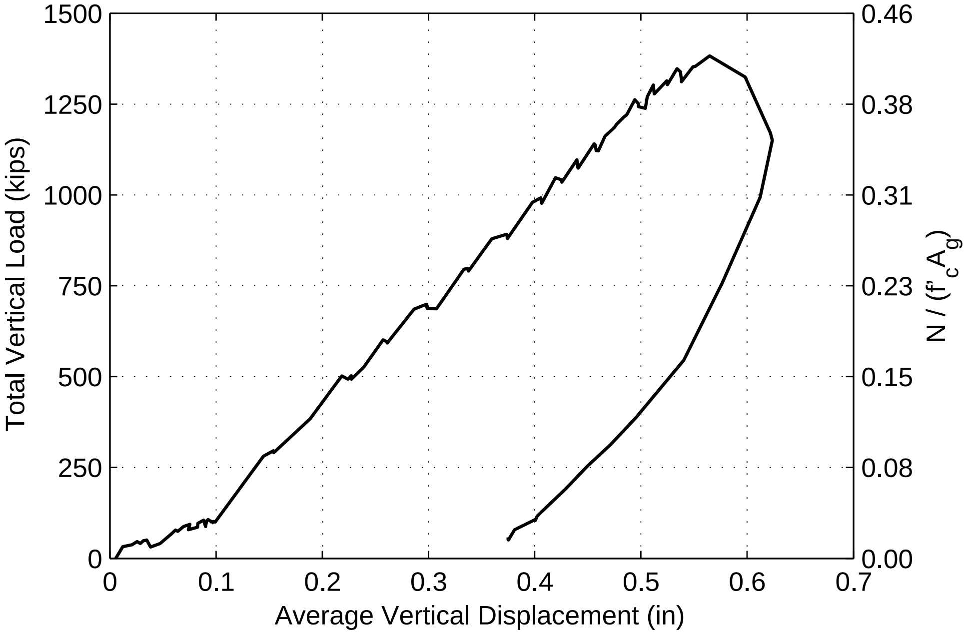

Figure 4.10: Axial-load vs. average vertical displacement

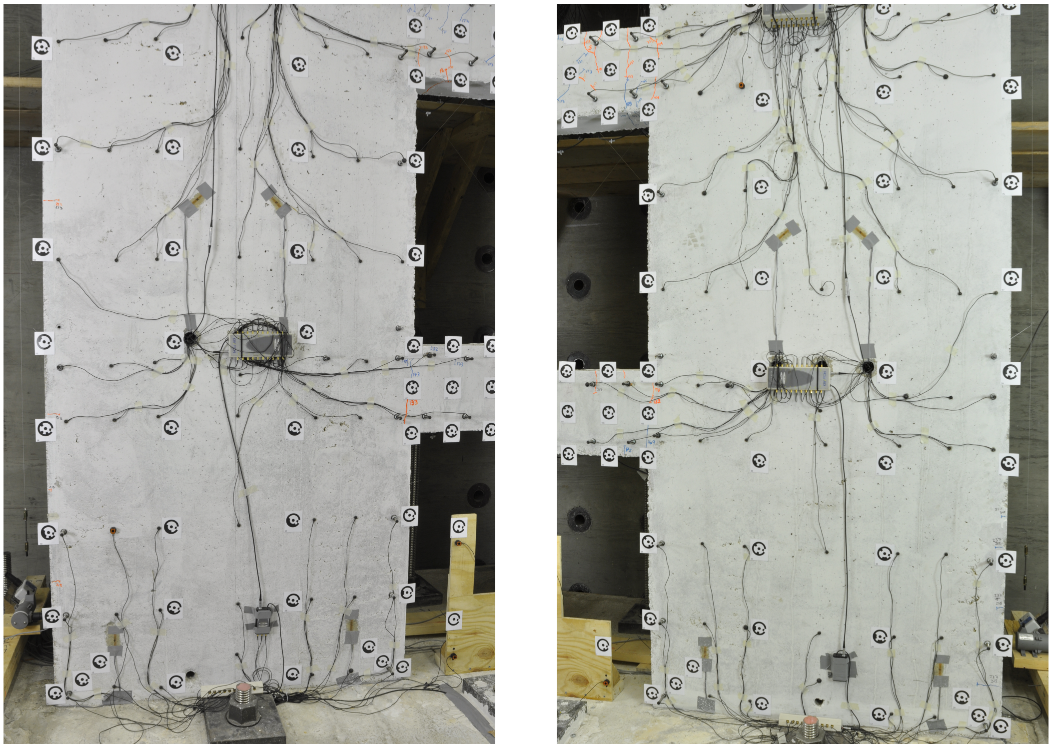

(a) West Wall Pier (b) East Wall Pier

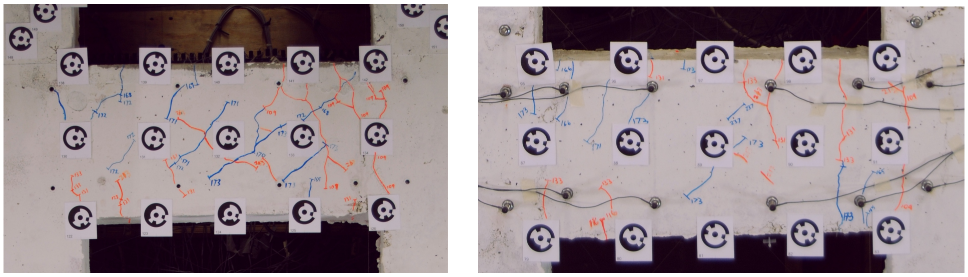

(c) Coupling Beam 3 (d) Coupling Beam 2

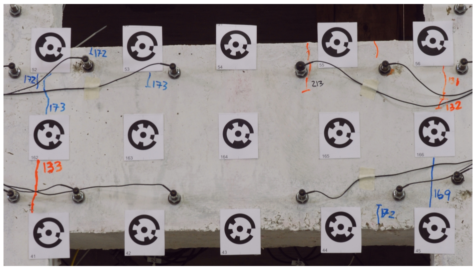

(e) Coupling Beam 1

Figure 4.11: Damage following 0.128% drift level (Step 181), note very minor cracking in wall piers

Figure 4.12: EWP horizontal crack at -0.136% (0.192% D.C. (A), Step 205) approximately 30 inches above the foundation

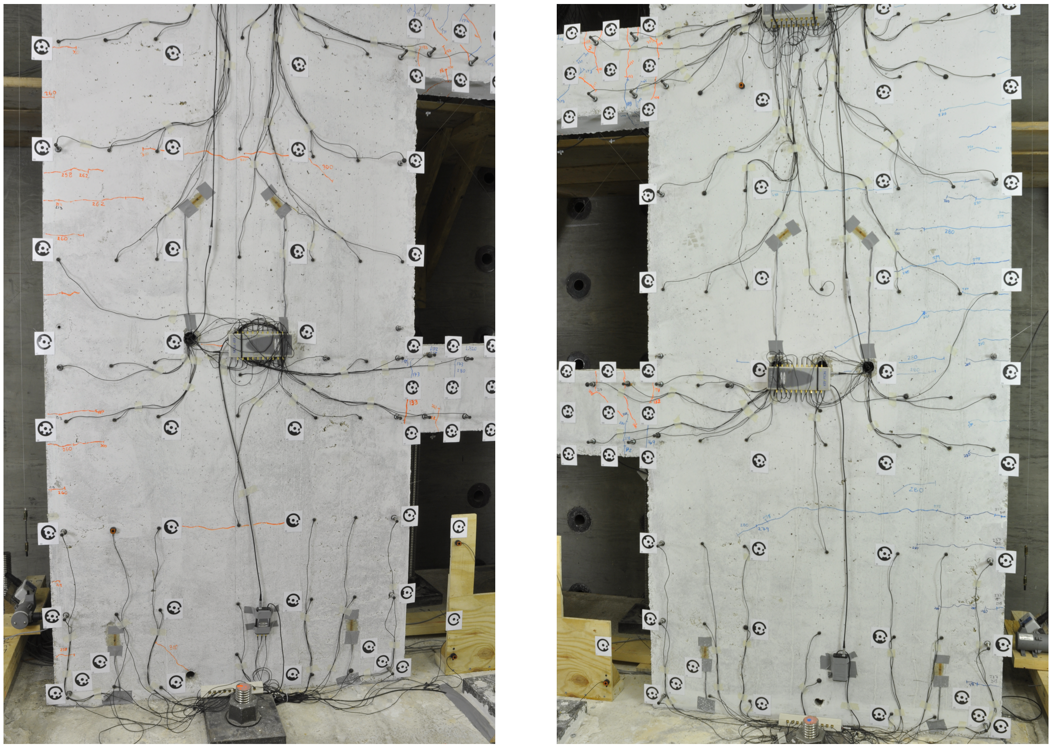

(a) West Wall Pier

(b) East Wall Pier

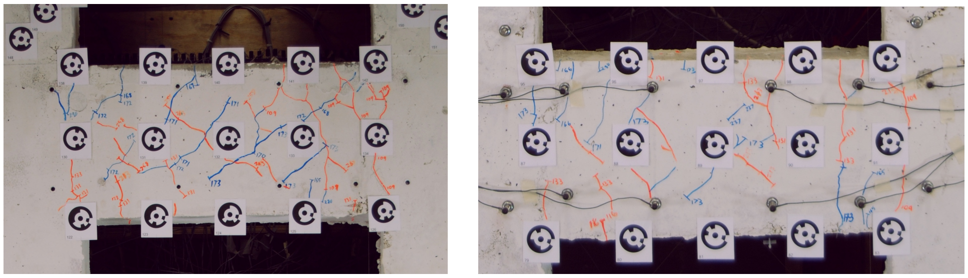

(c) Coupling Beam 3

(d) Coupling Beam 2

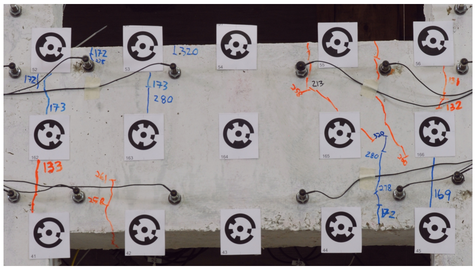

(e) Coupling Beam 1

Figure 4.13: Damage following 0.192% drift level (Step 247)

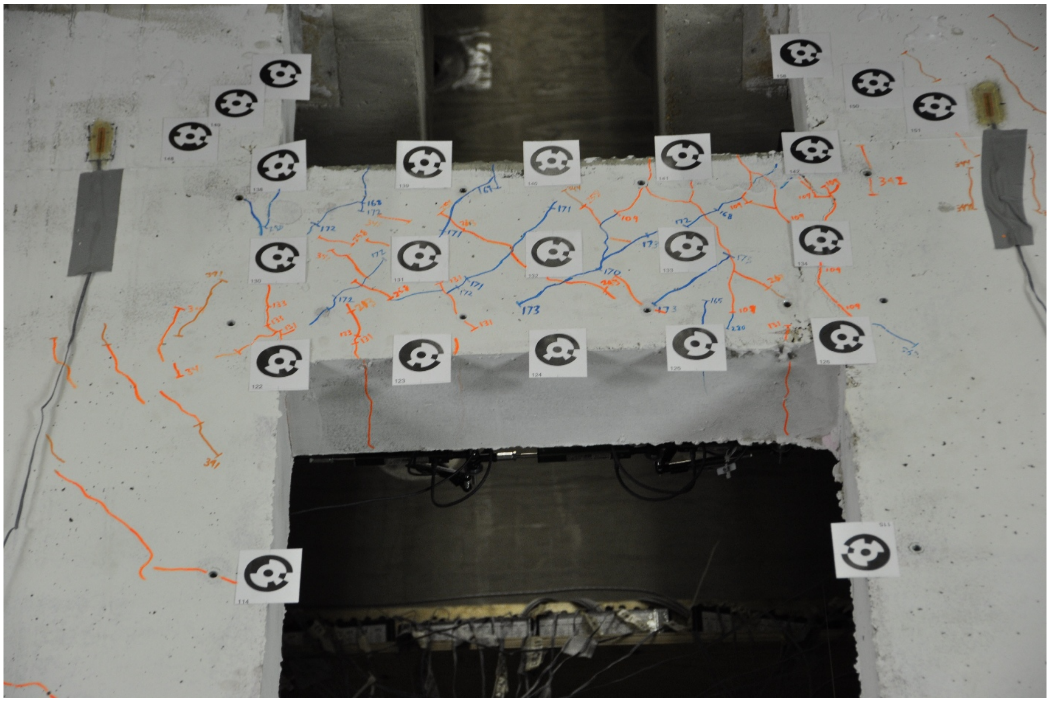

Figure 4.14: Cracking in CB3 (0.321% D.C. (B), Step 304)

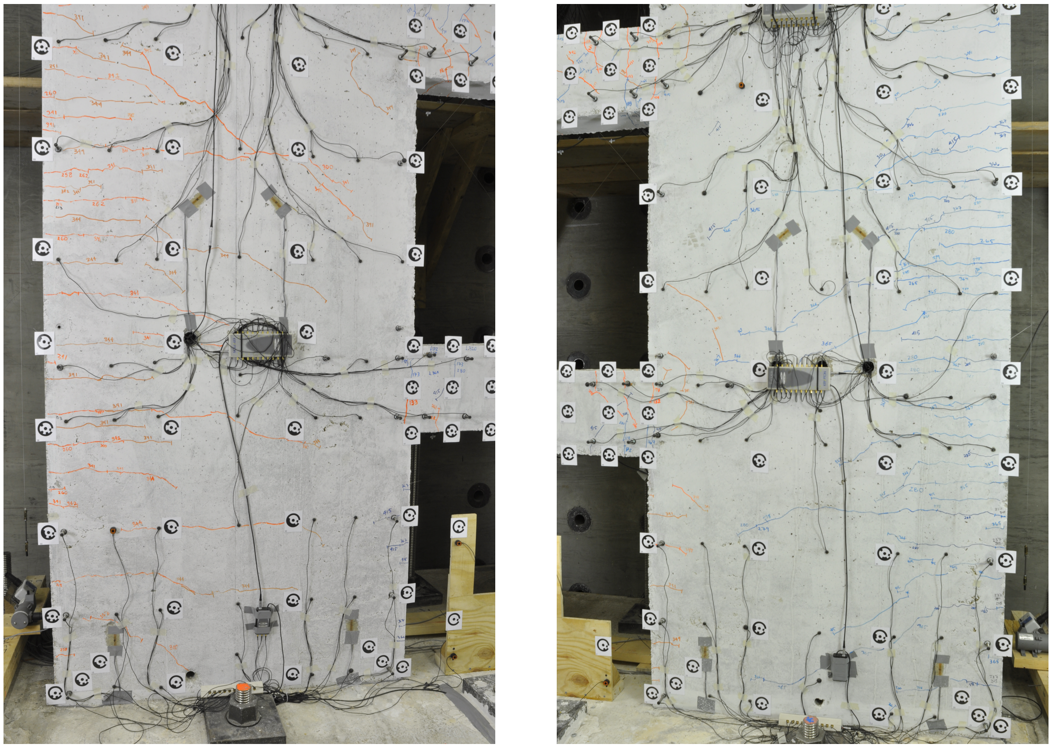

(a) West Wall Pier (b) East Wall Pier

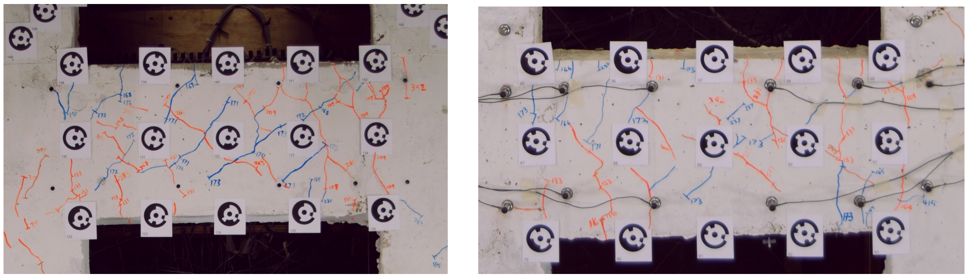

(c) Coupling Beam 3 (d) Coupling Beam 2

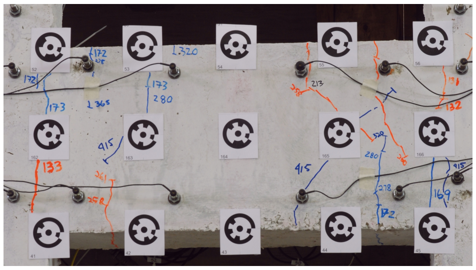

(e) Coupling Beam 1

Figure 4.15: Damage following 0.321% drift level (Step 337)

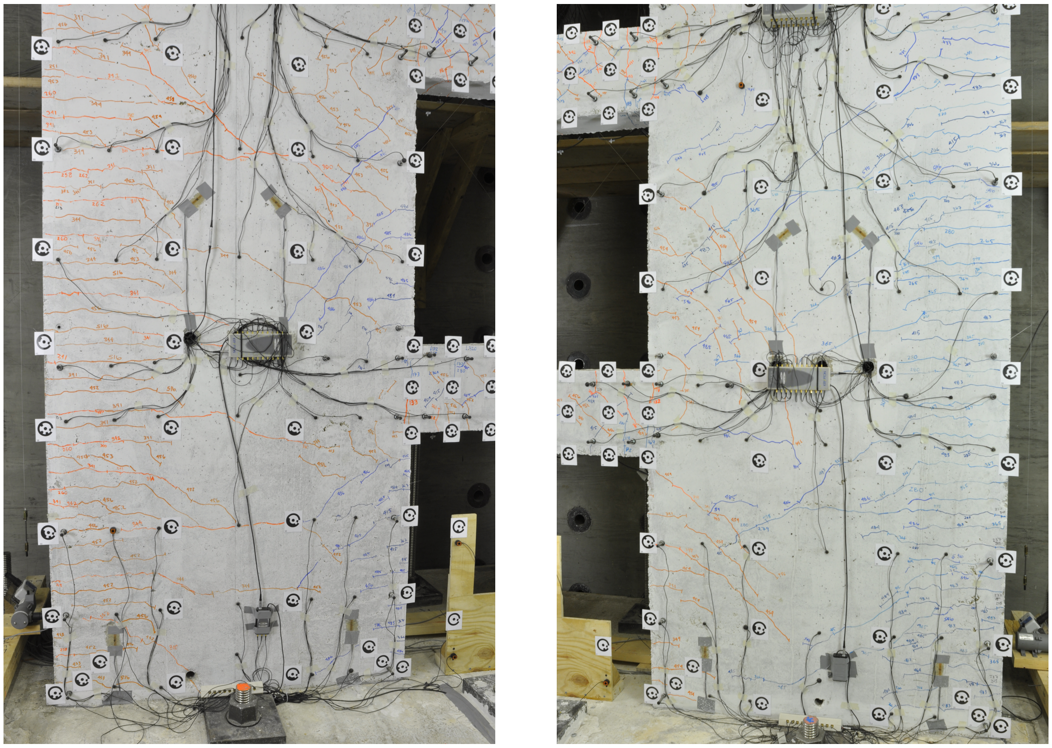

(a) West Wall Pier (b) East Wall Pier

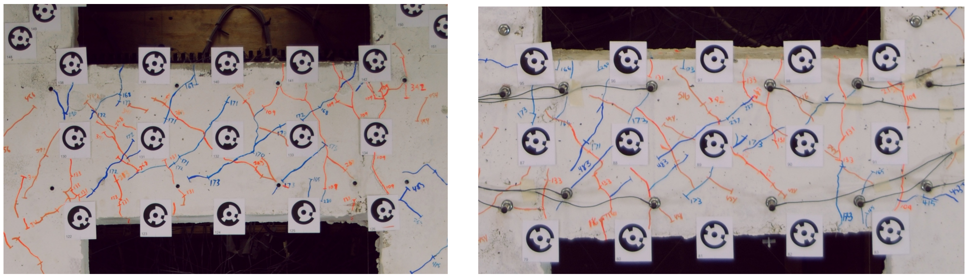

(c) Coupling Beam 3 (d) Coupling Beam 2

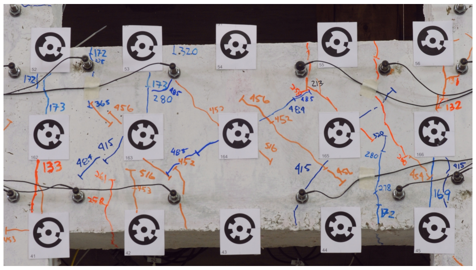

(e) Coupling Beam 1

Figure 4.16: Damage following 0.50% drift level (Step 454)

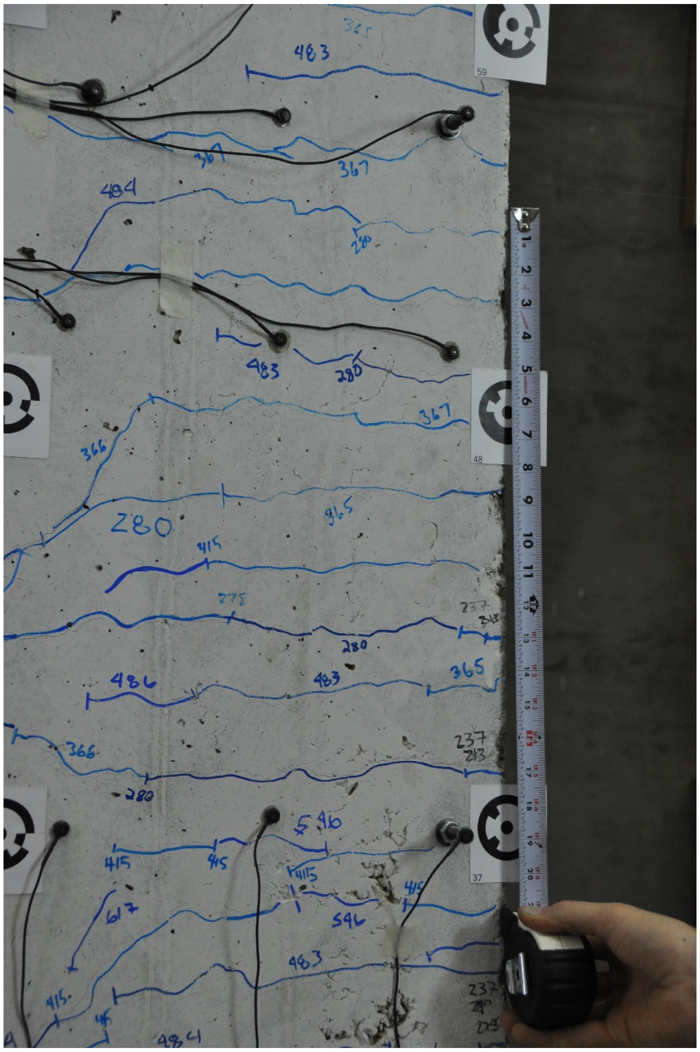

Figure 4.17: Spacing of horizontal cracking along OBE of EWP (0.75% D.C. (A), Step 507), base of tape measure is approximantely 22 inches above foundation

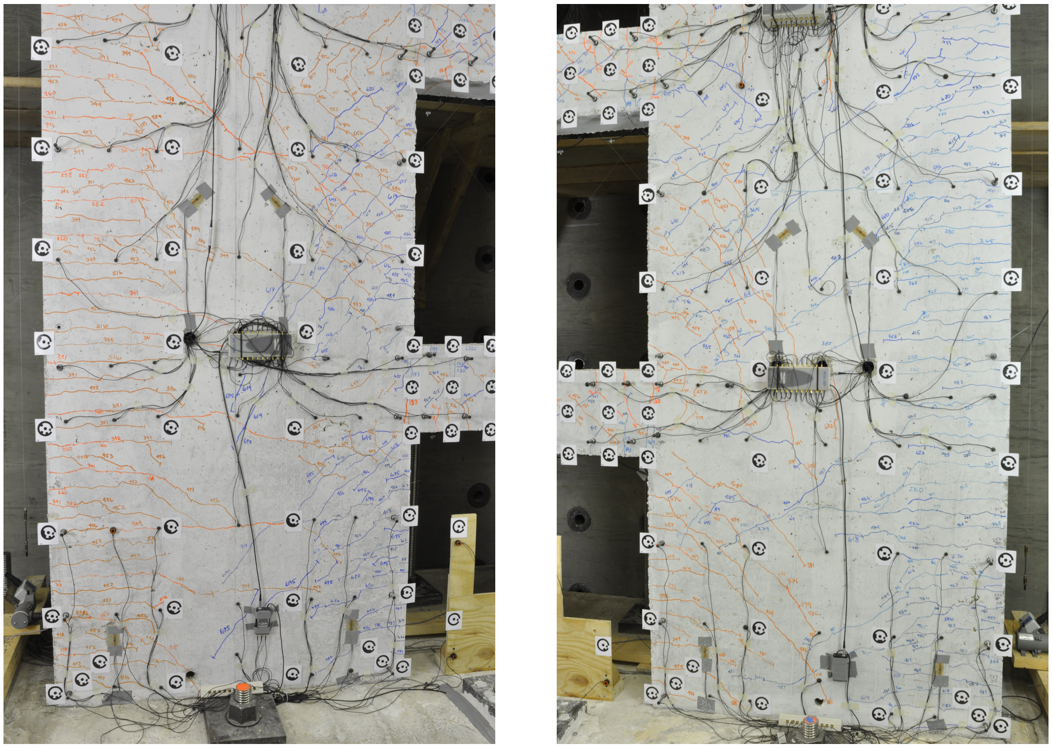

(a) West Wall Pier

(b) East Wall Pier

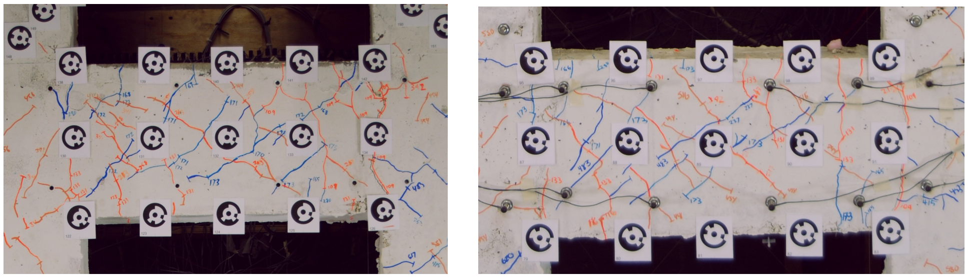

(c) Coupling Beam 3

(d) Coupling Beam 2

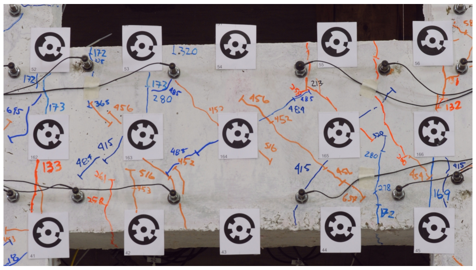

(e) Coupling Beam 1

Figure 4.18: Damage following 0.75% drift level (Step 600)

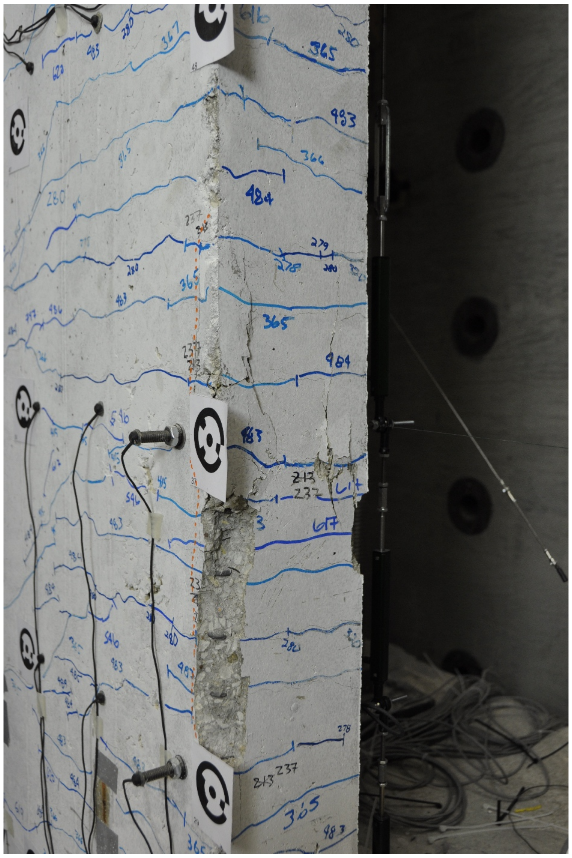

Figure 4.19: Spalling of EWP at E+ peak (1.00% D.C. (A), Step 623), bottom of spalling region 12 inches above base of wall

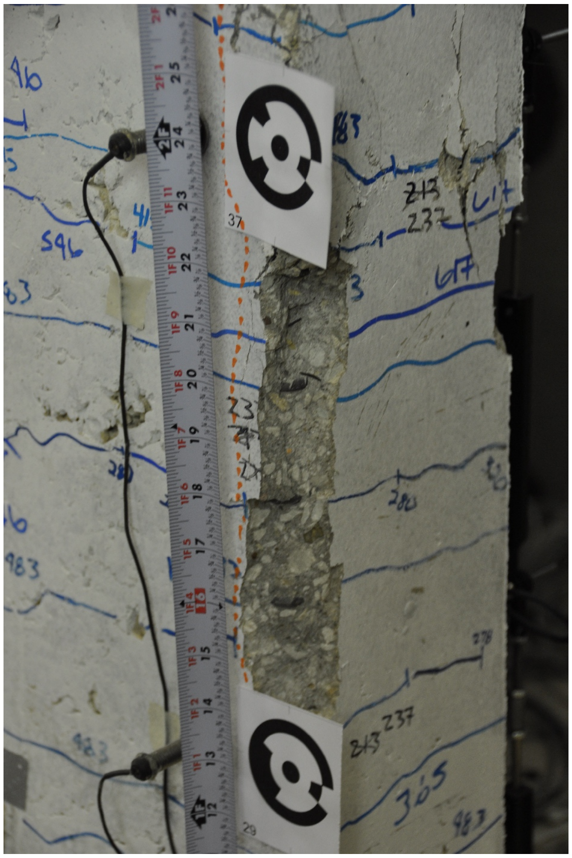

Figure 4.20: Close up of spalled region shown in Figure 4.19, tape measure referenced to base of wall

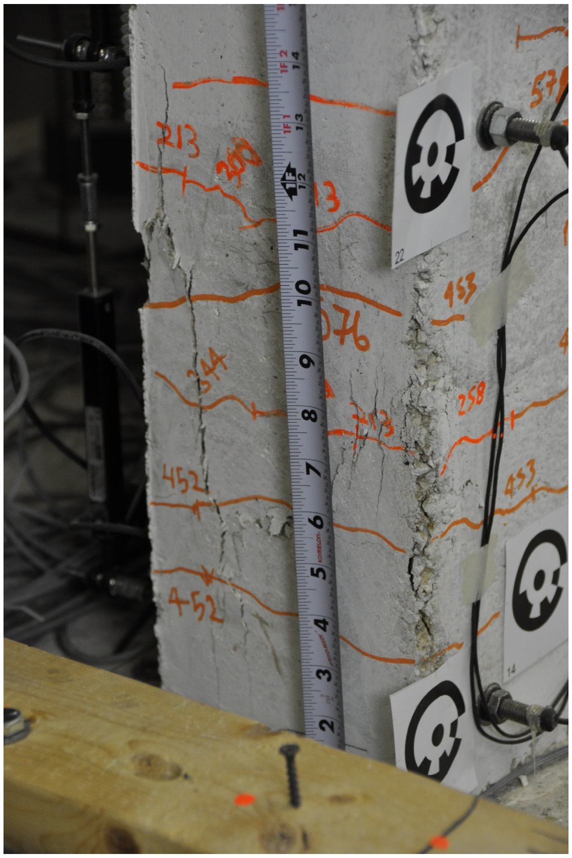

Figure 4.21: Cover damage of WWP at W- peak (1.00% D.C. (A), Step 802)

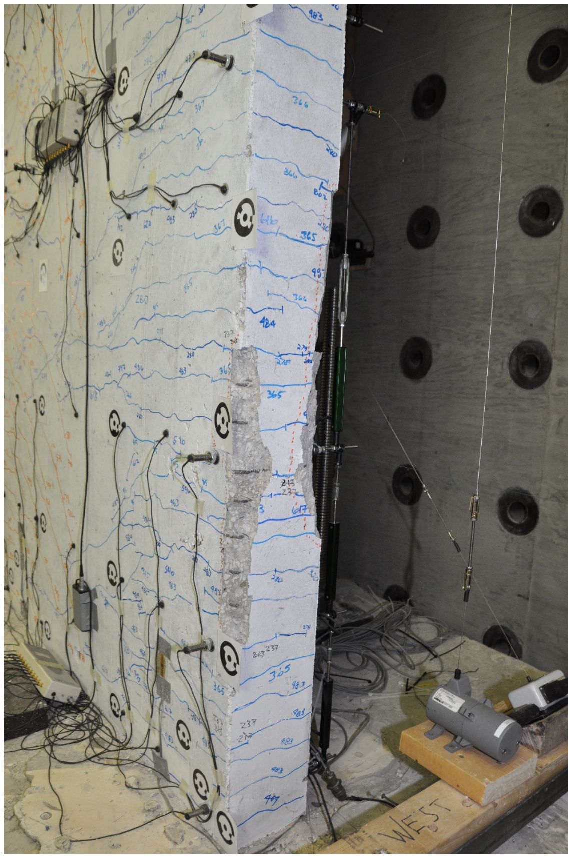

Figure 4.22: Spalling of EWP at E+ peak (1.00% D.C. (B), Step 710), top of spalling on far corner is 36 inches from wall base

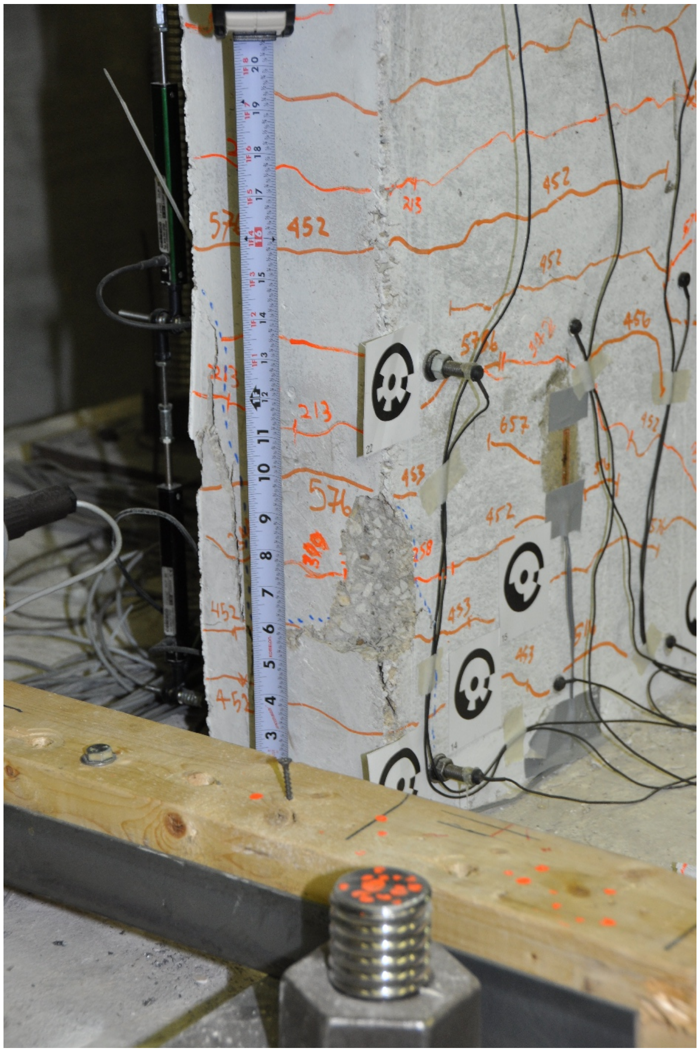

Figure 4.23: Spalling of WWP at W- peak (1.00% D.C. (B), Step 754)

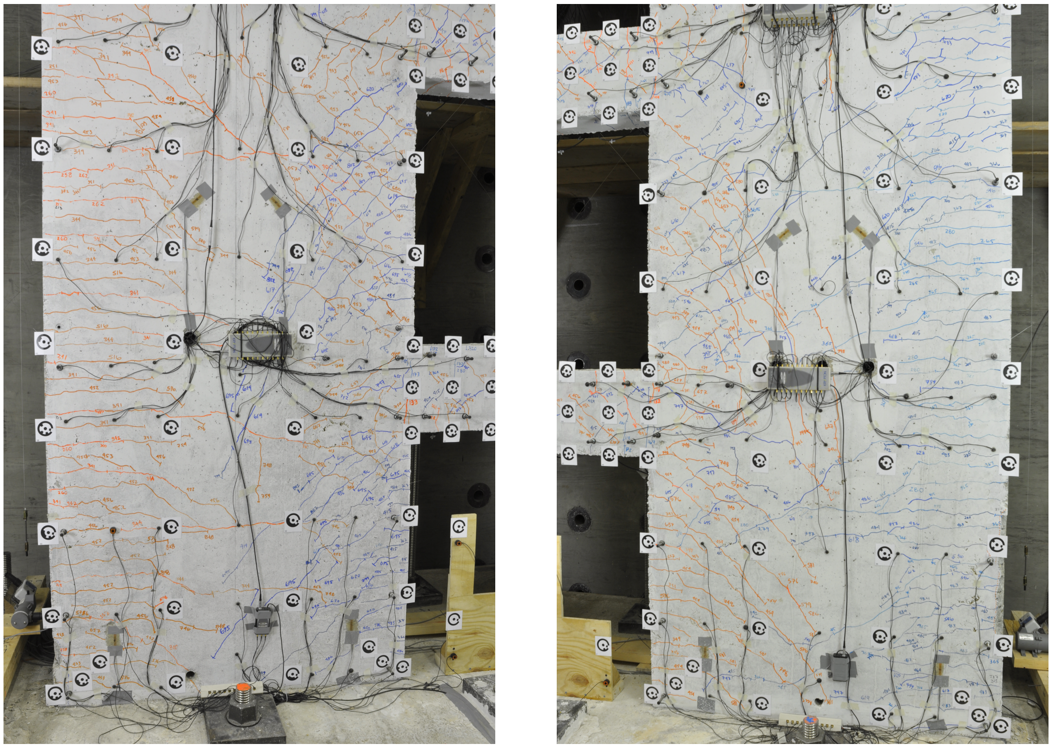

(a) West Wall Pier

(b) East Wall Pier

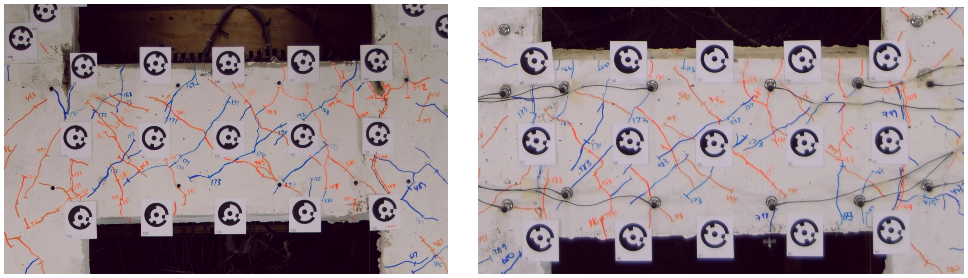

(c) Coupling Beam 3

(d) Coupling Beam 2

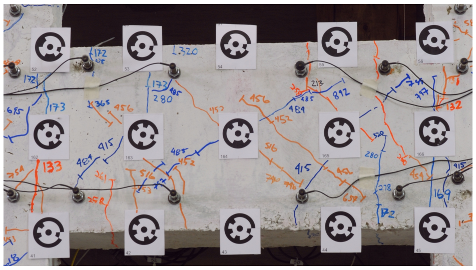

(e) Coupling Beam 1

Figure 4.24: Damage following 1.00% drift level (Step 772)


(a) TWC of CB2 (b) TEC of CB2

Figure 4.25: Spalling of top corners on CB2 during the 1.50% drift level

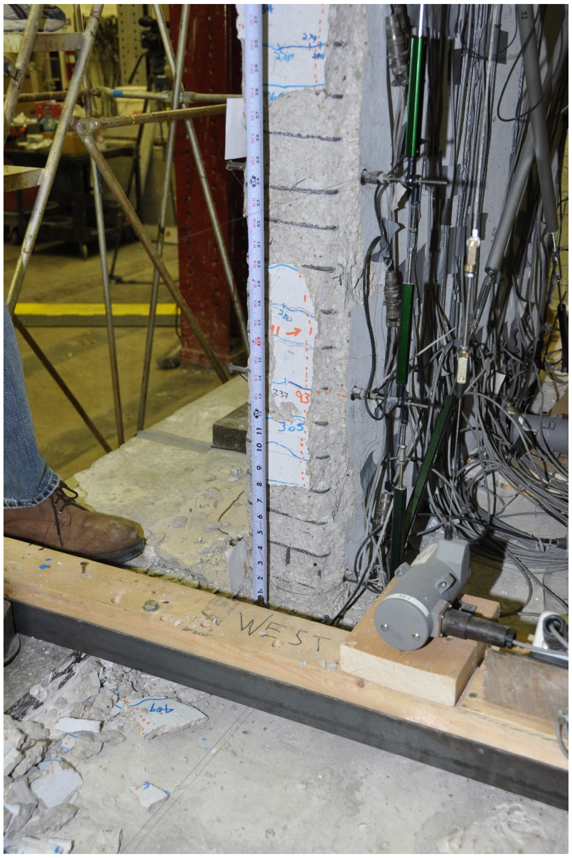

Figure 4.26: Spalling of EWP at the end of the 1.50% drift level, top of spalling shown 28 inches above wall base

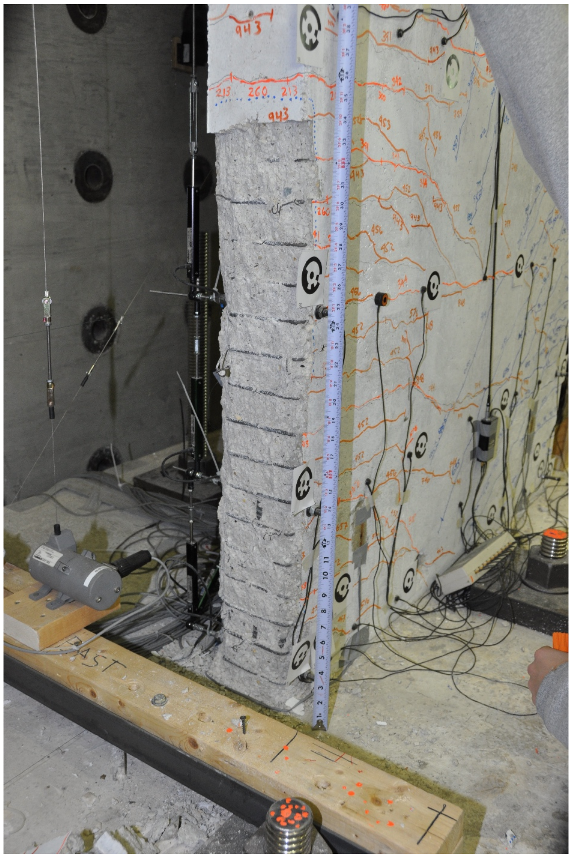

Figure 4.27: Spalling of WWP at the end of the 1.50% drift level, top of spalling 34 inches above wall base

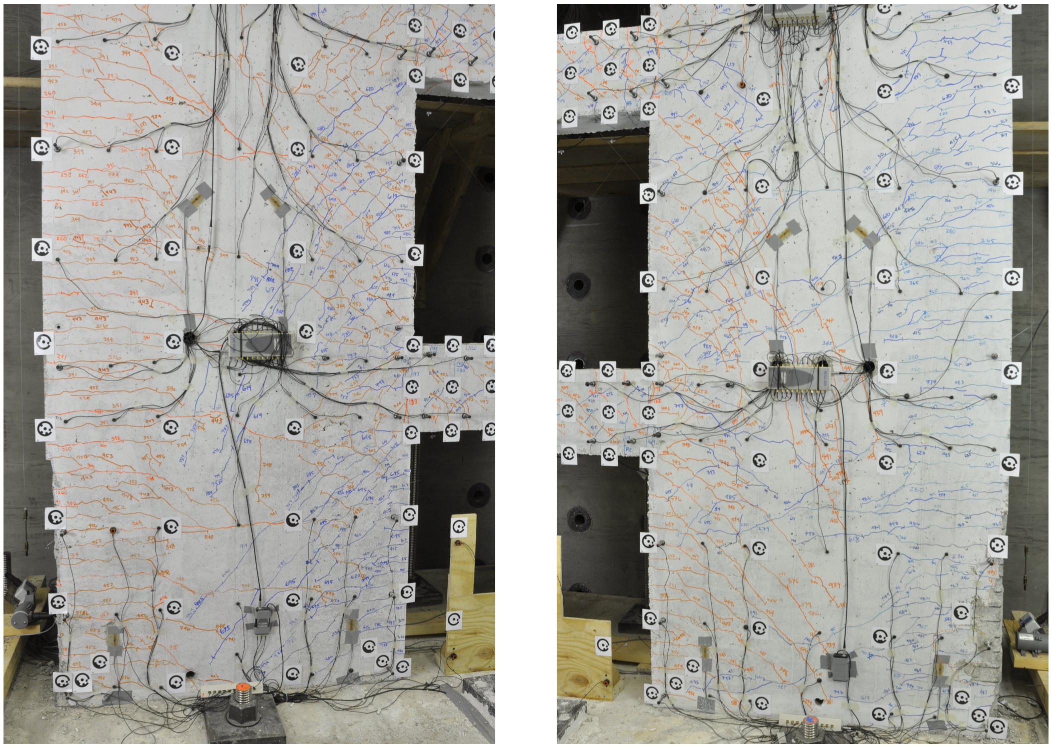

(a) West Wall Pier (b) East Wall Pier

(c) Coupling Beam 3 (d) Coupling Beam 2

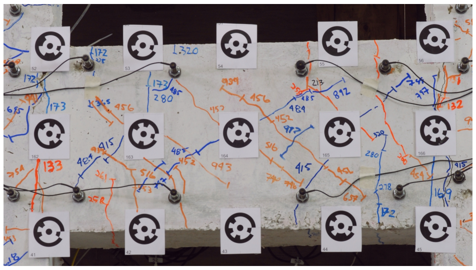

(e) Coupling Beam 1

Figure 4.28: Damage following 1.50% drift level (Step 932)

(a) E+ peak (Step 955)

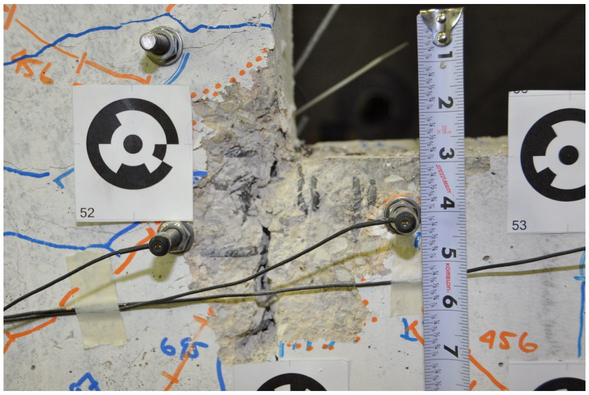

(b) W- peak (Step 1003)

Figure 4.29: Spalling of TWC of CB1 during the 2.25% drift level

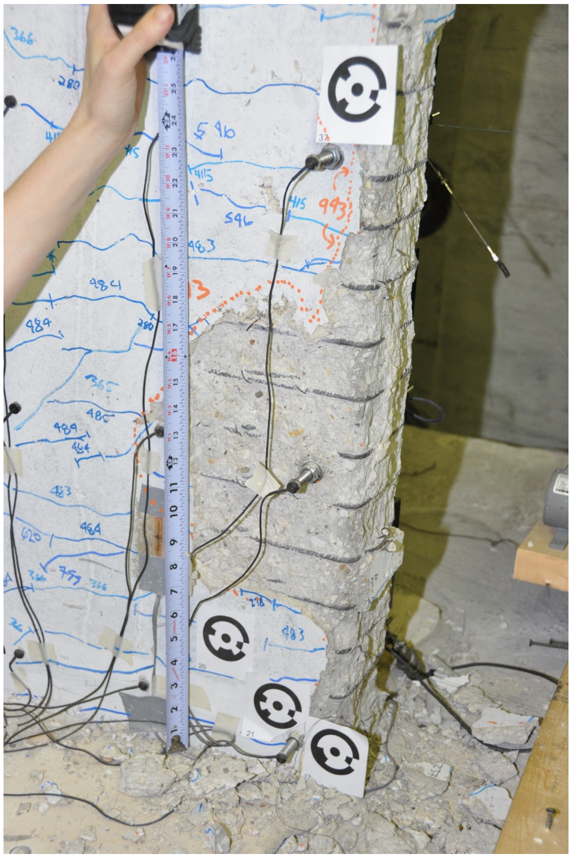

Figure 4.30: Spalling of EWP at 1.89% (2.25% D.C. (A), Step 951)

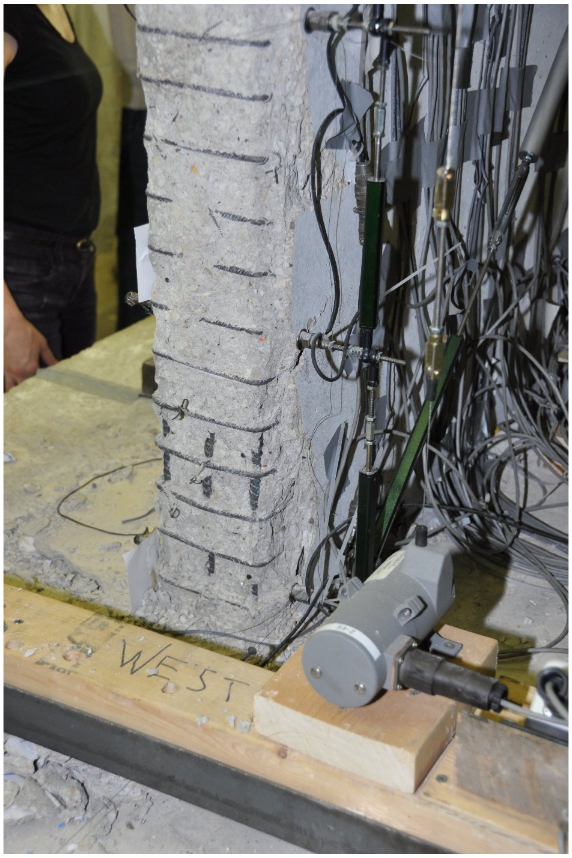

Figure 4.31: Backside of EWP at 2.20% (2.25% D.C. (A), Step 954)

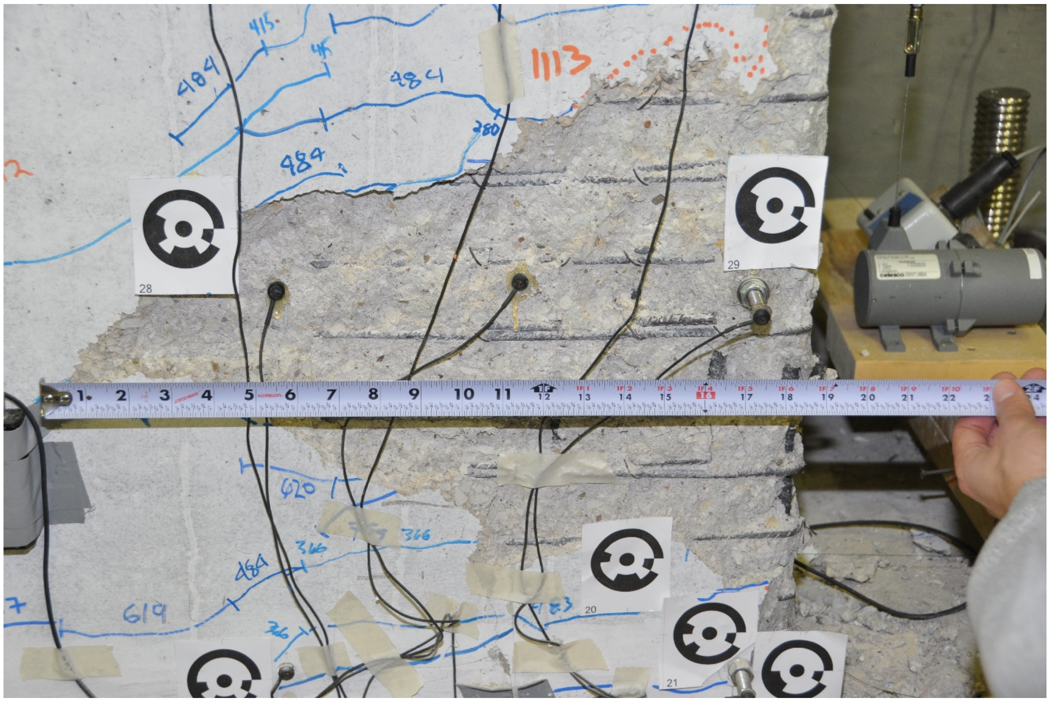

Figure 4.32: Spalling of EWP at 2.20% (2.25% D.C. (A), Step 954)

Figure 4.33: Front corner of EWP at E+ peak (2.25% D.C. (A), Step 955)

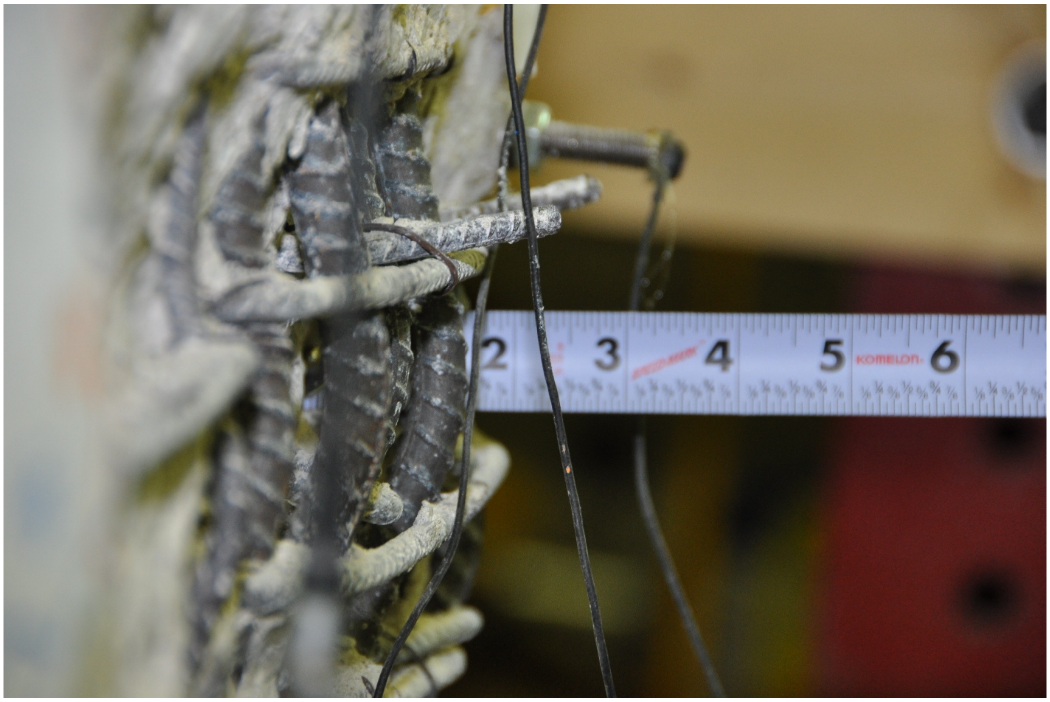

Figure 4.34: Buckled rebar on south facing side of EWP at E+ peak

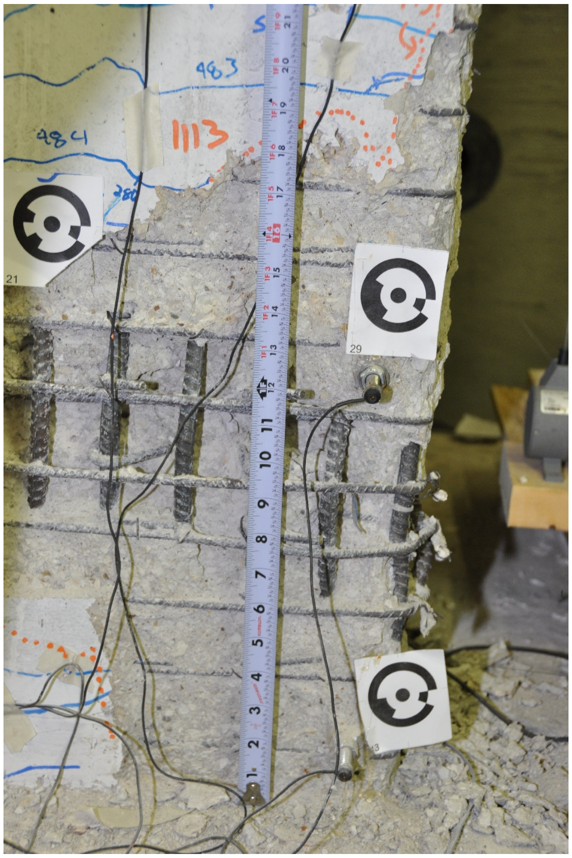

Figure 4.35: South facing side of EWP at E+ peak (2.25% D.C. (A), Step 955)

Figure 4.36: Backside of EWP at E+ peak (2.25% D.C. (A), Step 955)

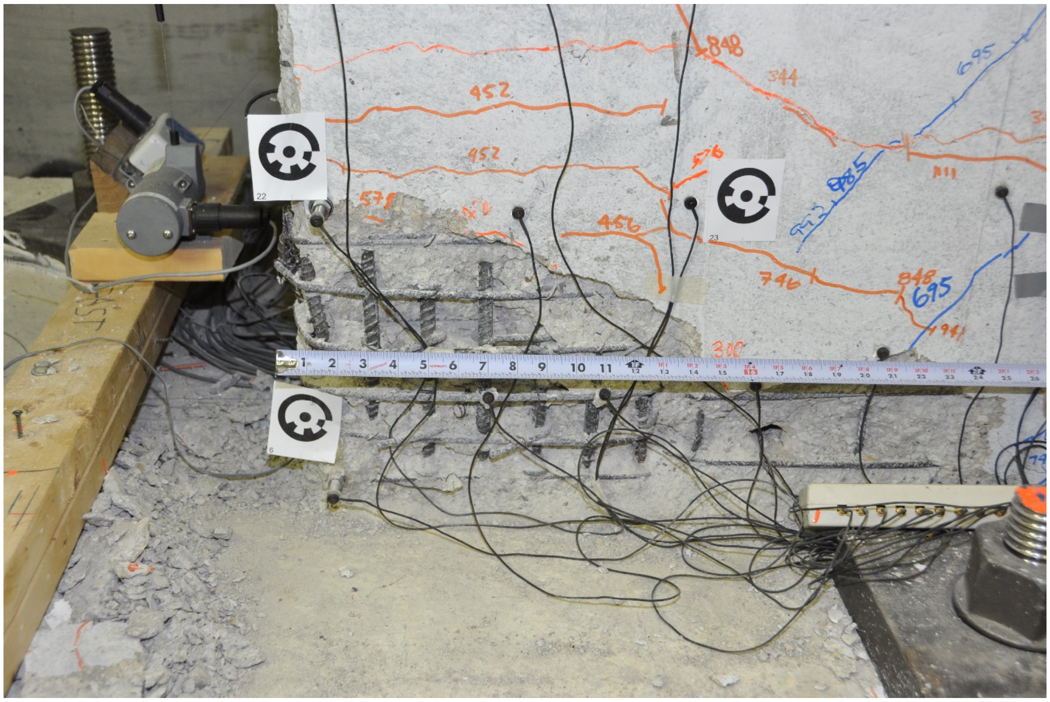

Figure 4.37: Toe of WWP at W- peak (2.25% D.C. (A), Step 1003)

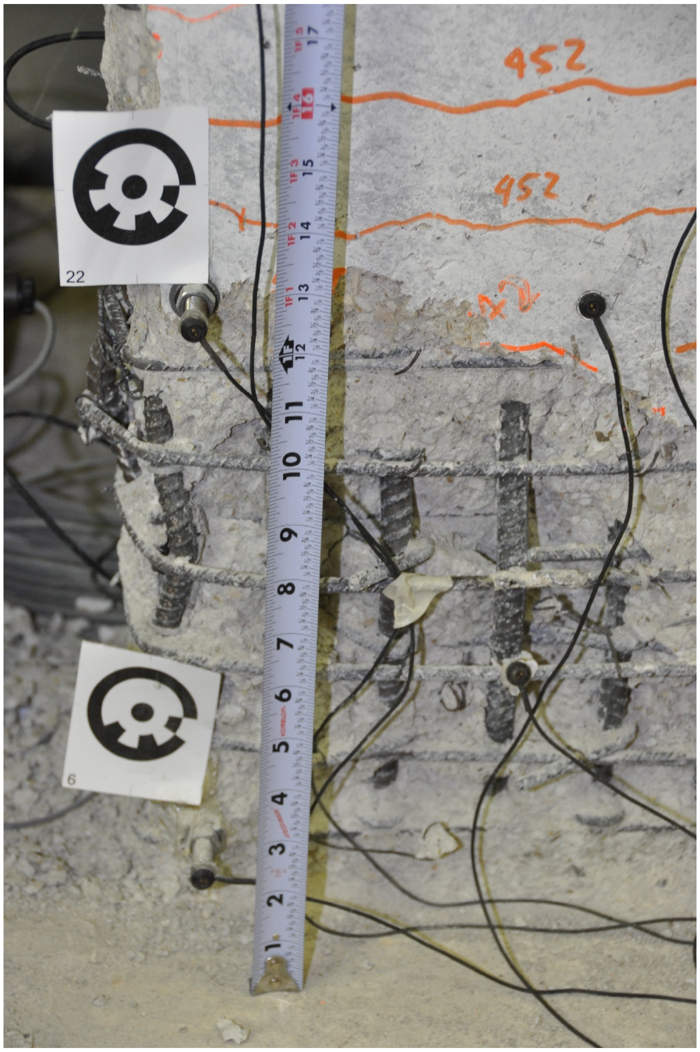

Figure 4.38: South facing side of WWP at W- peak

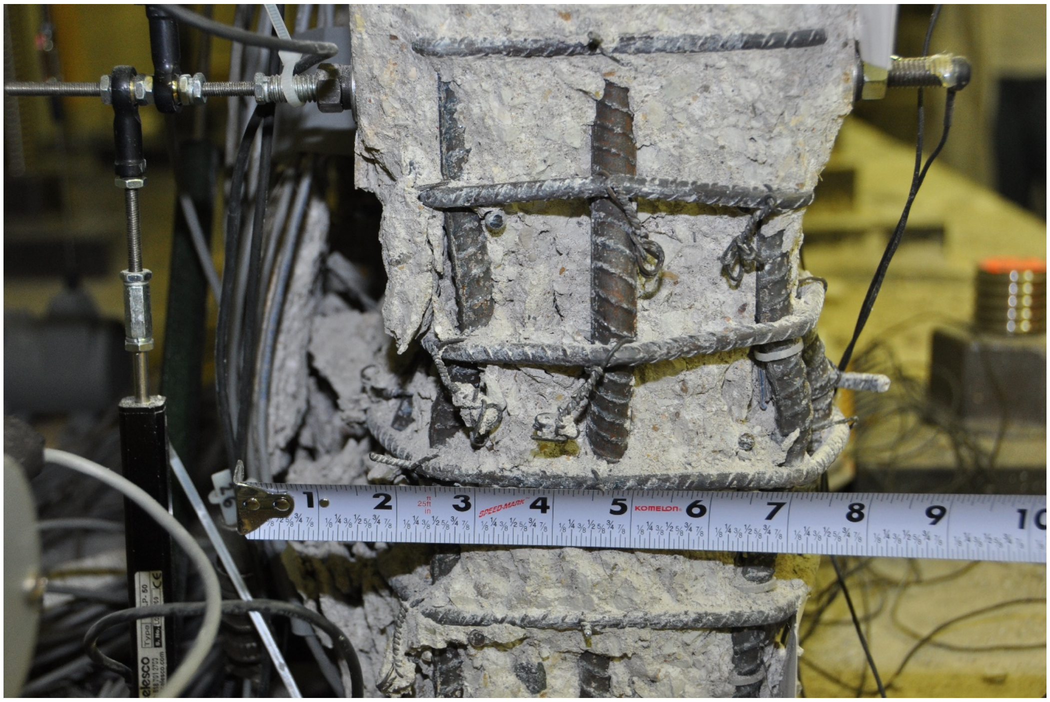

Figure 4.39: West facing edge of WWP at W- peak (2.25% D.C. (A), Step 1003)

Figure 4.40: Close-up of WWP buckled rebar at W- peak (2.25% D.C. (A), Step 1003)

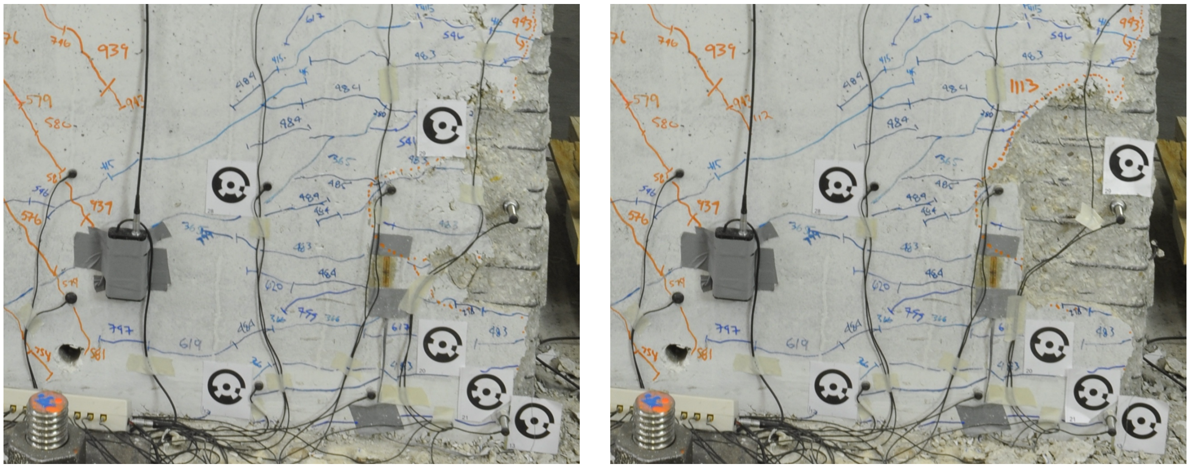

(a) 1.80% (Step 950)

(b) 2.00% (Step 952)

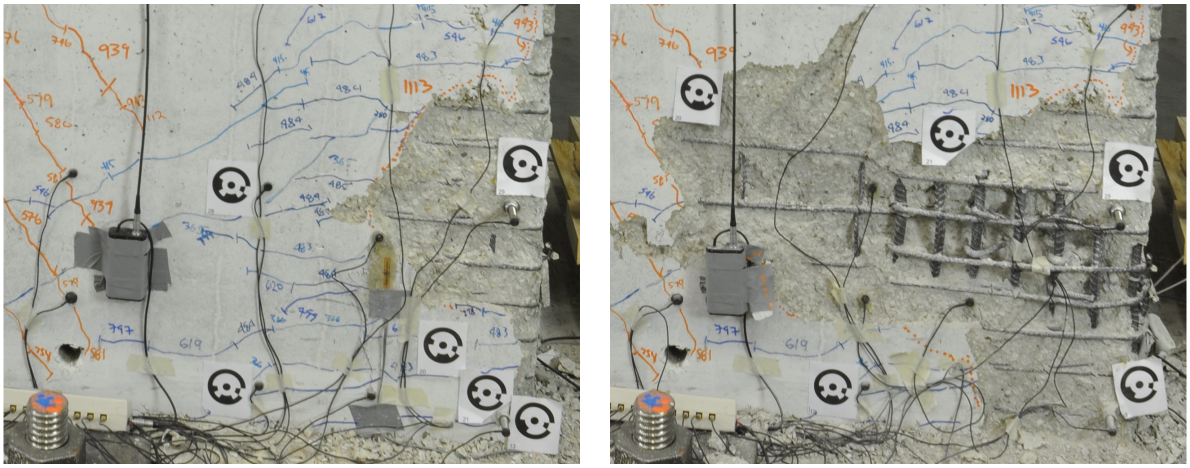

(c) 2.20% (Step 954)

(d) 2.27% (Step 955)

Figure 4.41: Failure sequence at 2.25% E+ peak

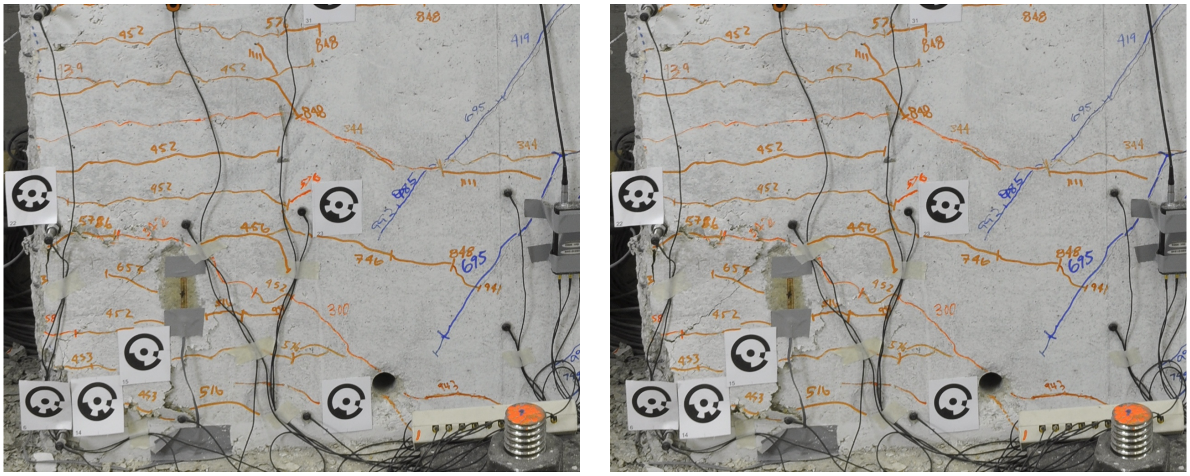

(a) -2.00% (Step 1000)

(b) -2.10% (Step 1001)

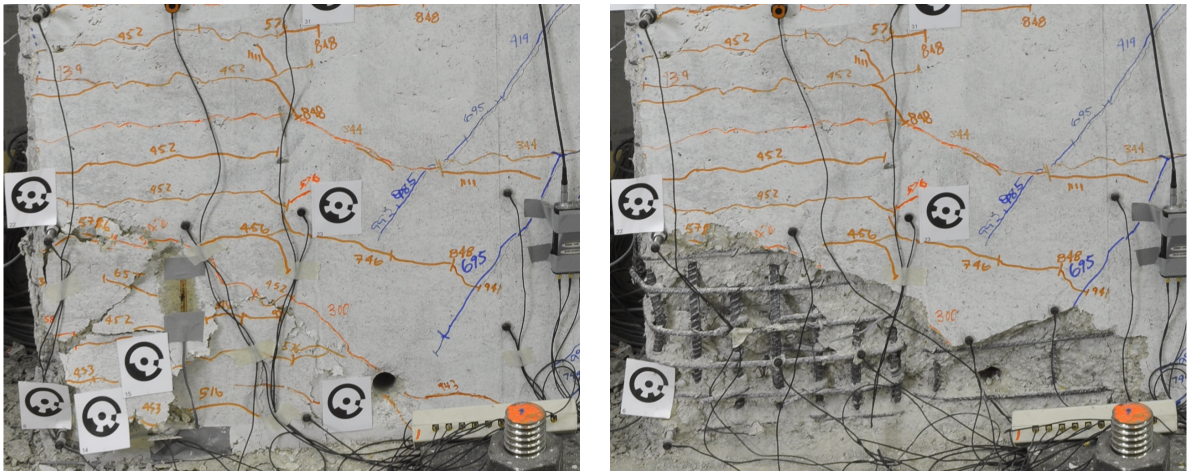

(c) -2.20% (Step 1002)

(d) -2.27% (Step 1003)

Figure 4.42: Failure sequence at -2.25% W- peak

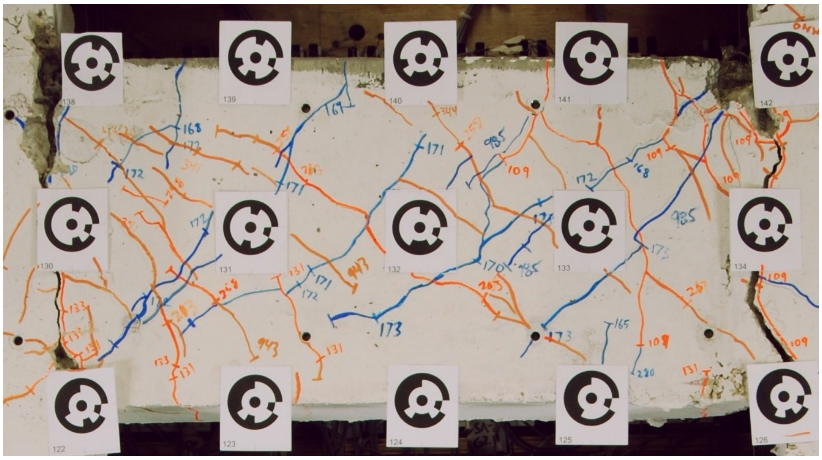

(a) Coupling beam 3

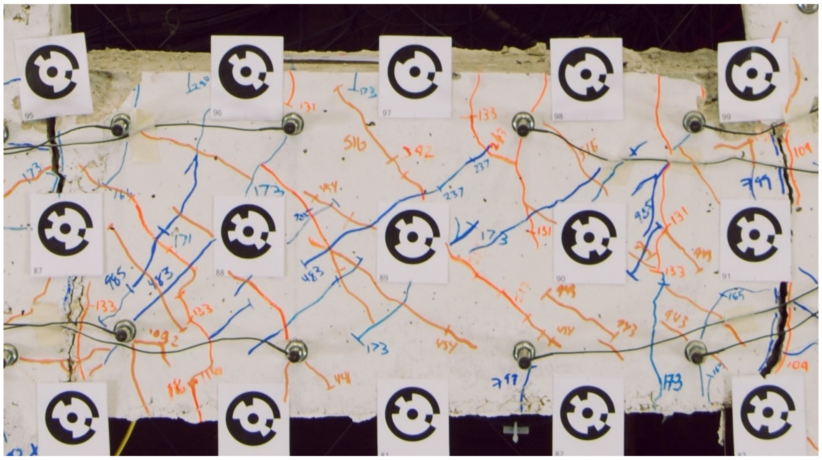

(b) Coupling beam 2

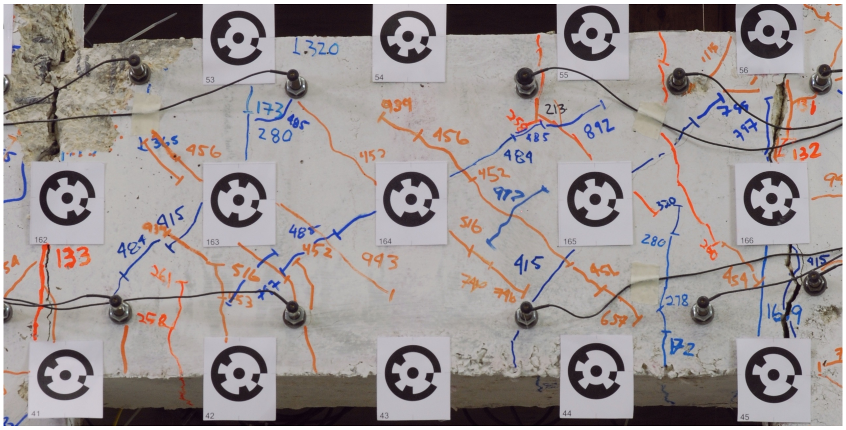

(c) Coupling beam 1

Figure 4.43: Coupling beam damage at the end of the test (-2.25% Step 1003)

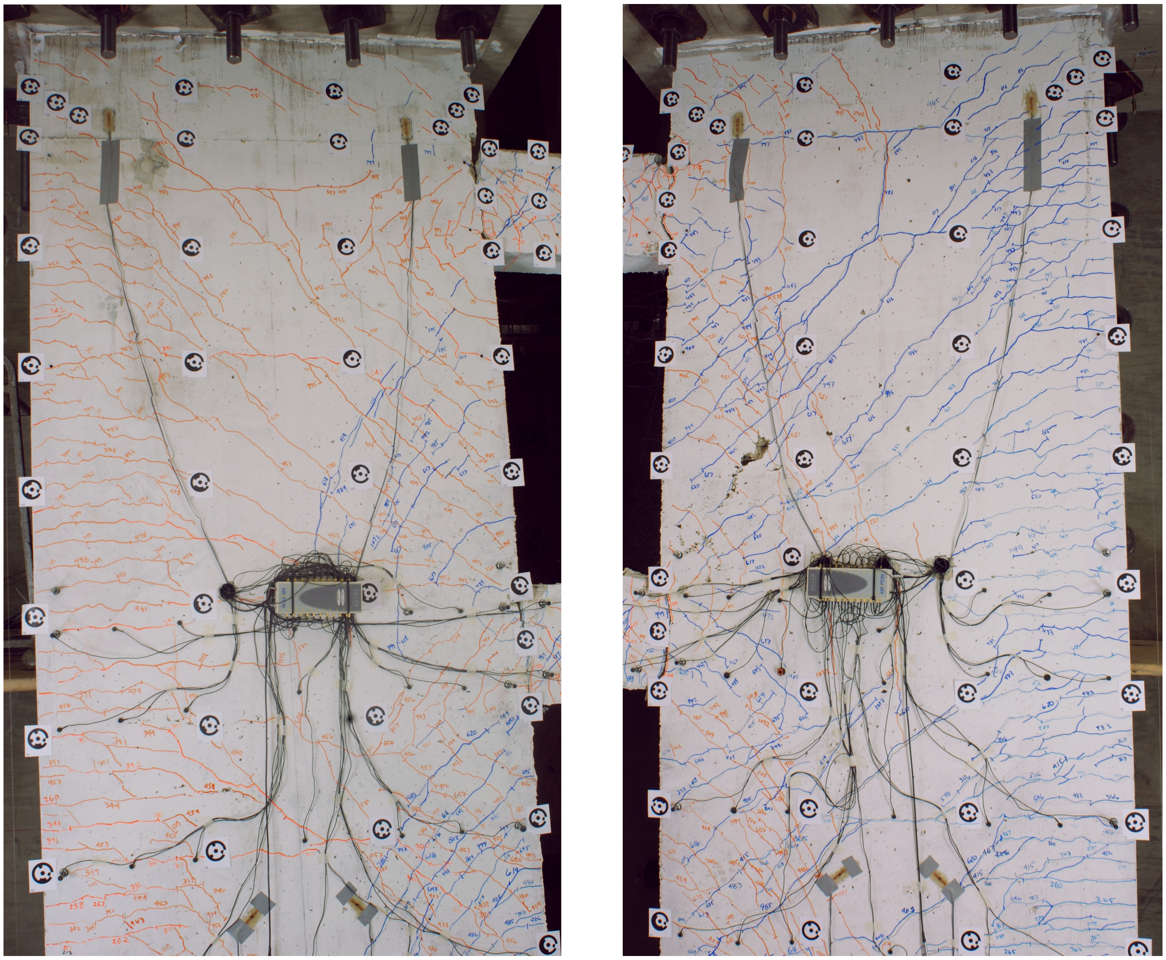

(a) WWP: Top

(b) EWP: Top

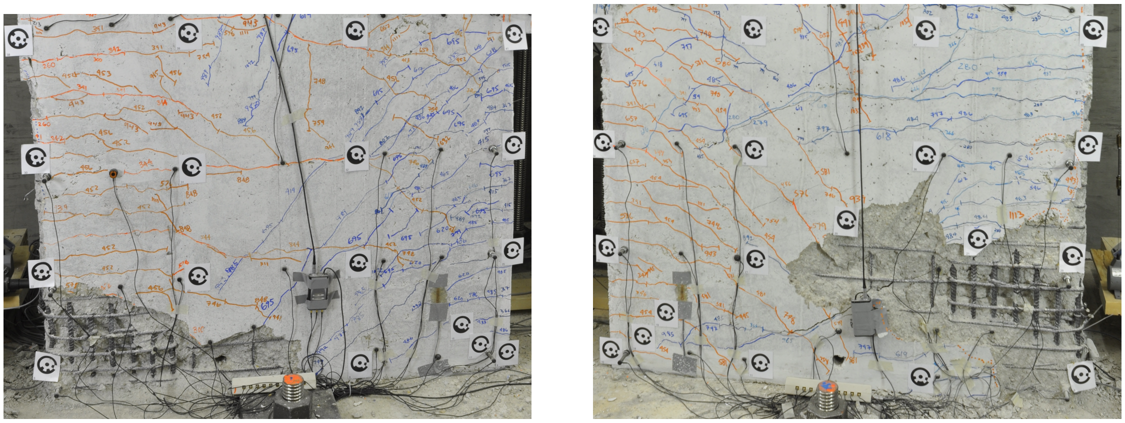

(c) WWP: Base

(d) EWP: Base

Figure 4.44: Wall pier damage at the end of the test (-2.25% Step 1003)

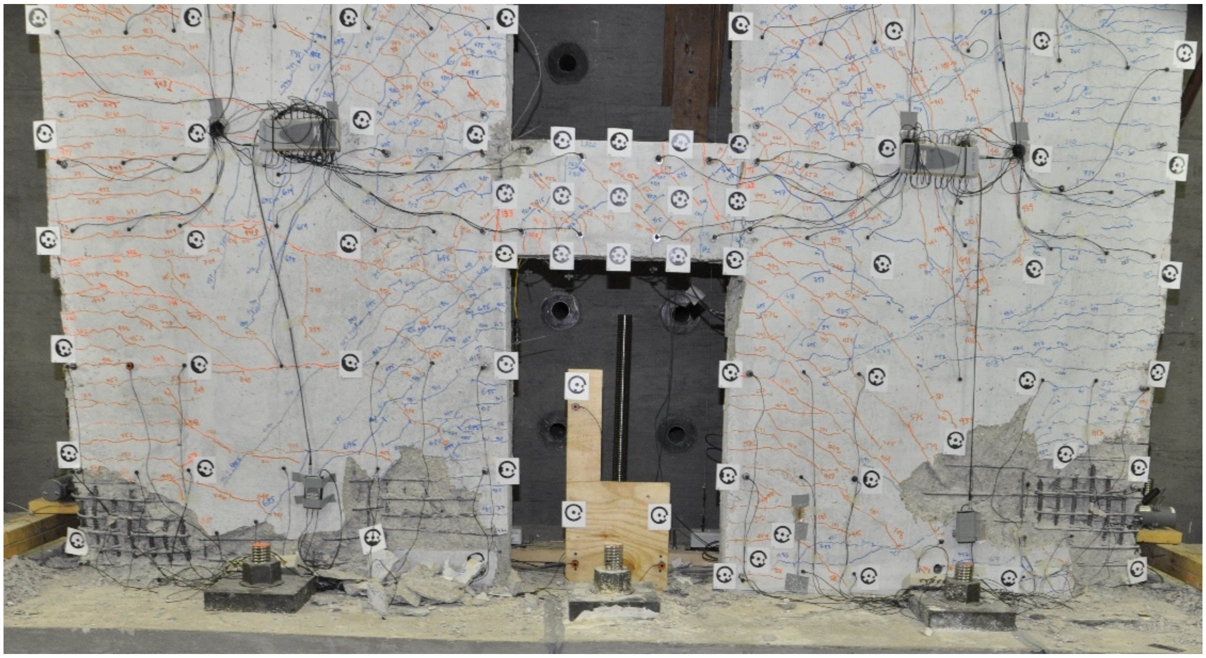

(a) Base of CW1

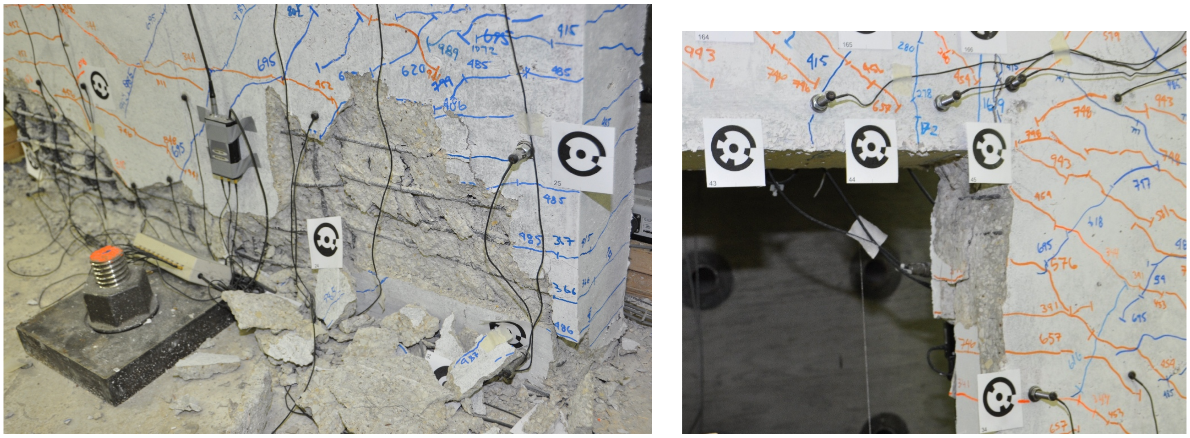

(b) Close up of the IBE of the WWP

(c) Close-up of the BEC of CB1

Figure 4.45: Damage to CW1 after axial loading to -1380 kips

Chapter 5

DETAILED INVESTIGATION OF BEHAVIOR

In Chapter 4 the load-displacement response and progression of damage for the coupled wall specimen are discussed. These results provide a general understanding of performance. A more in depth understanding of behavior was developed using data from non-contact, internal and external instruments. In this chapter experimental data are used to investigate the progression of yielding, internal force demands, local deformation mechanisms and coupling beam rotations. The results of these investigations are used to improve the understanding of coupled wall behavior.

5.1 Strain Guage Data

In Chapter 4, initial yielding of reinforcement is discussed in characterizing global response. Here steel strain gage data are evaluated in more detail to provide understanding of the progression and distribution of nonlinearity throughout the structure. The layout of vertical, horizontal and diagonal steel reinforcing strain gauges are shown in Figures 3.16, 3.17 and 3.18, respectively. Steel material properties were determined from uniaxial material tests as discussed in Section 3.1.6. To fully asses steel response, strain data were converted to stress data using steel material data and a cyclic stress-strain model.

Material testing established the strain at which yielding occurs, ϵ_y, the stress at which yielding occurs, f_y and the strain at which strain-hardening initiates, ϵ_{sh}, in tension. These stress/strain magnitudes were assumed to be appropriate for compression as well. Because under cyclic loading, steel may reach the compressive yield strength, $-f_y$, prior to reaching the compression yield strain, $-\epsilon_y$, the steel strain gauge histories were converted to stress histories using the hysteric stress–strain reinforcement model, developed by Hoehler and Stanton (2006). Using the stress and strain histories for each gauge and material test data, the load step at which tension and compression yielding initiated was determined.

While investigating reinforcement stress-strain response, it was noticed certain reinforcing bars reached their respective yield strain but did not experience strain significantly in excess of the yield strain and thus did not exhibit much plastic deformation. Therefore, an additional strain limit was introduced to indicate significant plastic behavior of a reinforcing bar. Steel experiencing strains in excess of the strain-hardening strain, ϵ_{sh}, was considered to experience significant plastic behavior. Figure 5.1 shows the difference in inelastic behavior of a two reinforcing bars measured in CW1.

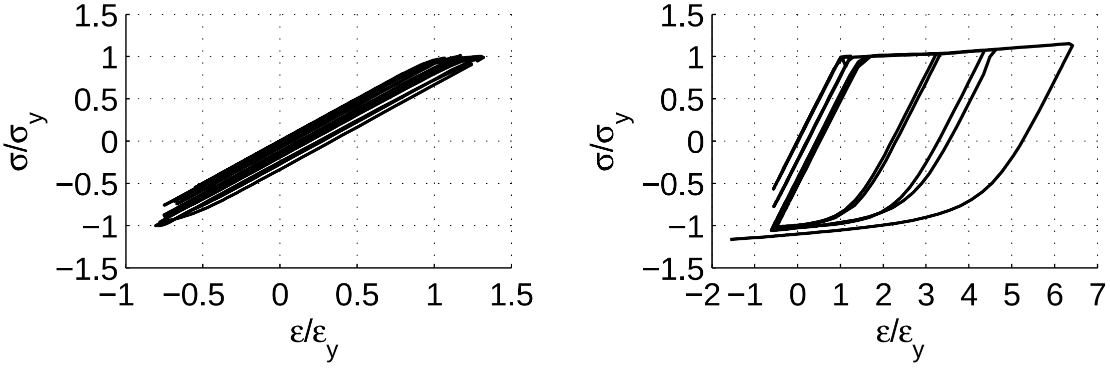

(a) Initial yield

(b) Plastic behavior

Figure 5.1: Typical stress-strain behavior for CW1 reinforcement

Figures 5.2 through 5.6 show the results of the strain gauge data analysis. In each figure, the subfigure on the left shows strain gauge yielding in tension and the onset of plastic behavior in tension, while the subfigure on the right shows similar data for compression. Note that the subfigure showing yielding in compression also identifies locations at which yielding in compression occurred following yielding in tension at strains that were larger than the negative compressive yield strain due to cycle loading.

The extent of yielding after cycling to 0.75% drift level is shown in Figure 5.2. While only reinforcing bars yielded in compression at only a few locations, at this drift level, yielding of reinforcement had initiated in tension in a lot of locations. The coupling beams at the second and third floor reached their plastic behavior limit and reached the compressive strength on the reverse cycle. The damage observed in CB2 and CB3 at this point in the test (Figure 4.18) is consistent with the strain gauge data indicating significant plastic behavior.

Figure 5.3 shows the extend of yielding following cycling at 1.0% drift. The data in Figure 5.3 shows that some of the reinforcing bars in the OBE of both wall piers exhibited plastic behavior and yielding up the first story in the IBEs occurred. This behavior is shown in Figure 5.3. Additionally, horizontal reinforcing bars yielded in both wall piers during this drift level.

Figure 5.4 shows the extent of yielding following cycling to 1.5% drift. These data show that yielding of horizontal bars at the top of the first story and in the second and third stories. At the end of this drift level, plastic behavior at the ends of all the coupling beams and at the base of the wall piers is clearly seen.

Figures 5.5 and 5.6 show respectively, the extent of yielding after the first half cycle to +2.25% drift and the end of other the test, following another half-cycle of loading to -2.25% drift. After the first half-cycle to 2.25% drift, the horizontal reinforcement in the first story reached its yield strain in both piers. It is clear from this figure the reinforcement in both wall piers exhibit plastic behavior from the base of the walls up to approximately 36 inches above the foundation. This equates to plastic behavior of over a height equal to $0.75l_w$. Finally, two time-lapse movies illustrating the tensile and compressive yield behavior for CW1 are available online at `http://www.youtube.com/user/NEESRWallProject`.

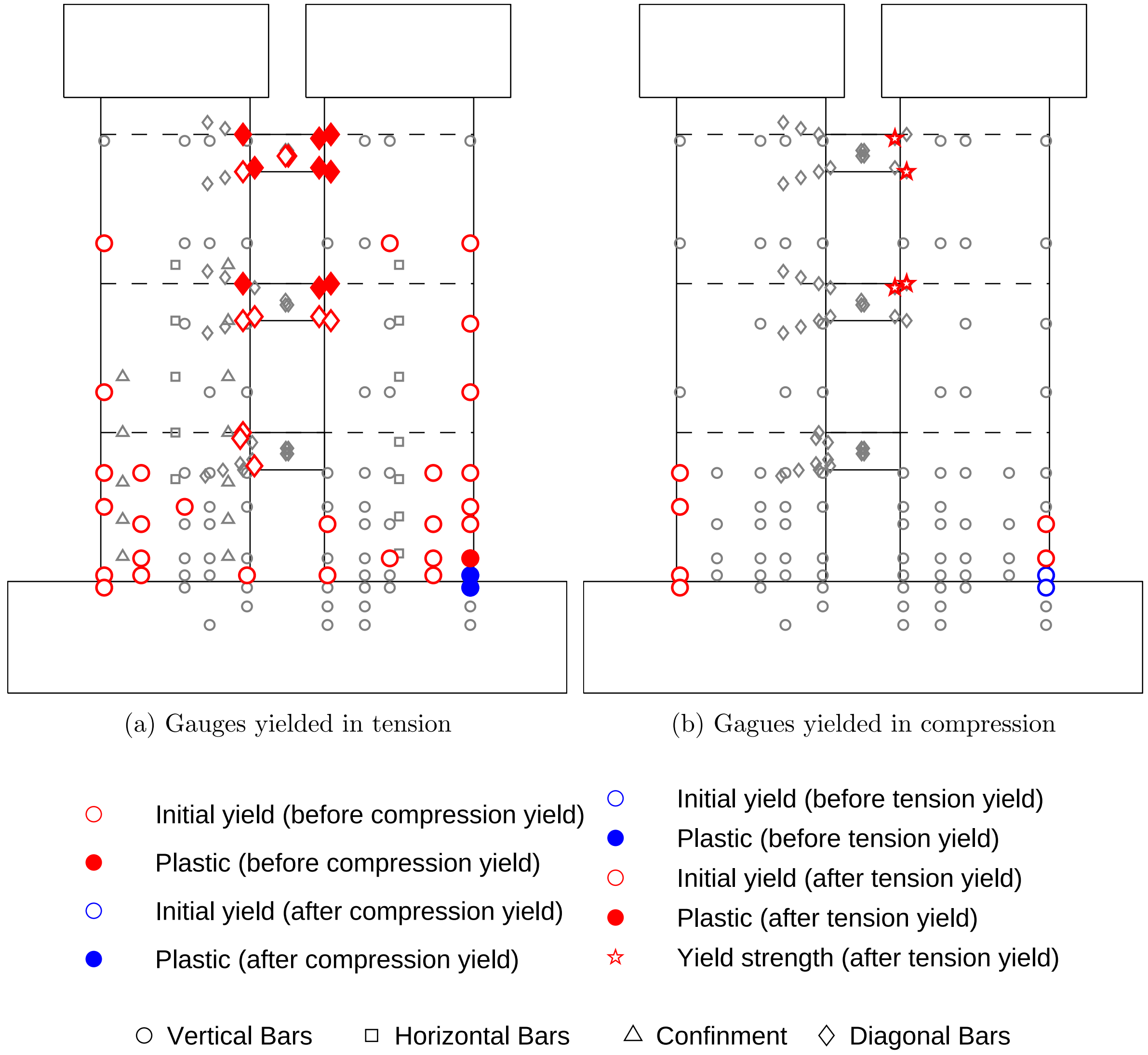
(a) Gauges yielded in tension

(b) Gagues yielded in compression

Figure 5.2: Yielded strain gauges at the end of the 0.75% drift level

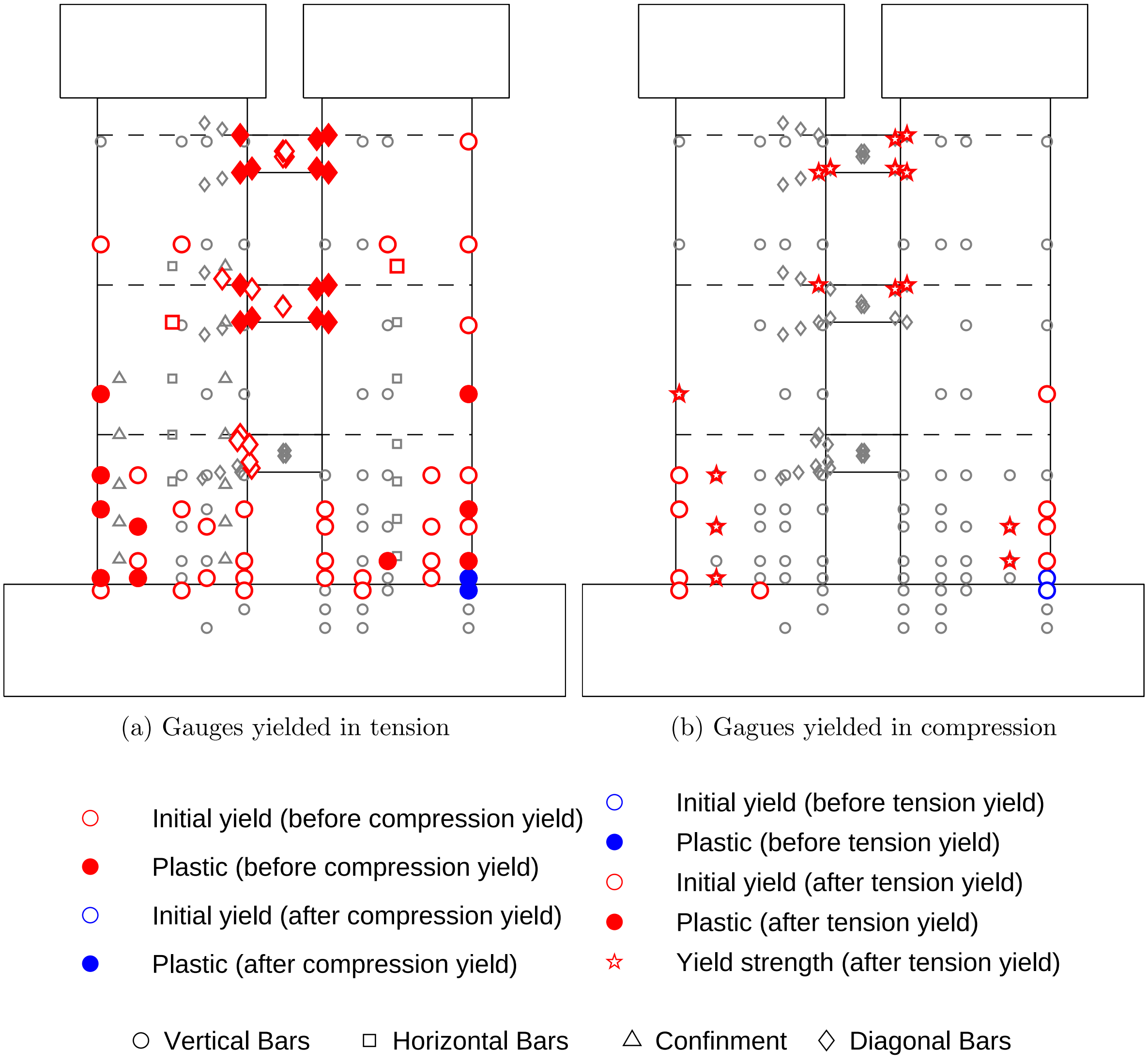
(a) Gauges yielded in tension

(b) Gagues yielded in compression

Figure 5.3: Yielded strain gauges at the end of the 1.00% drift level

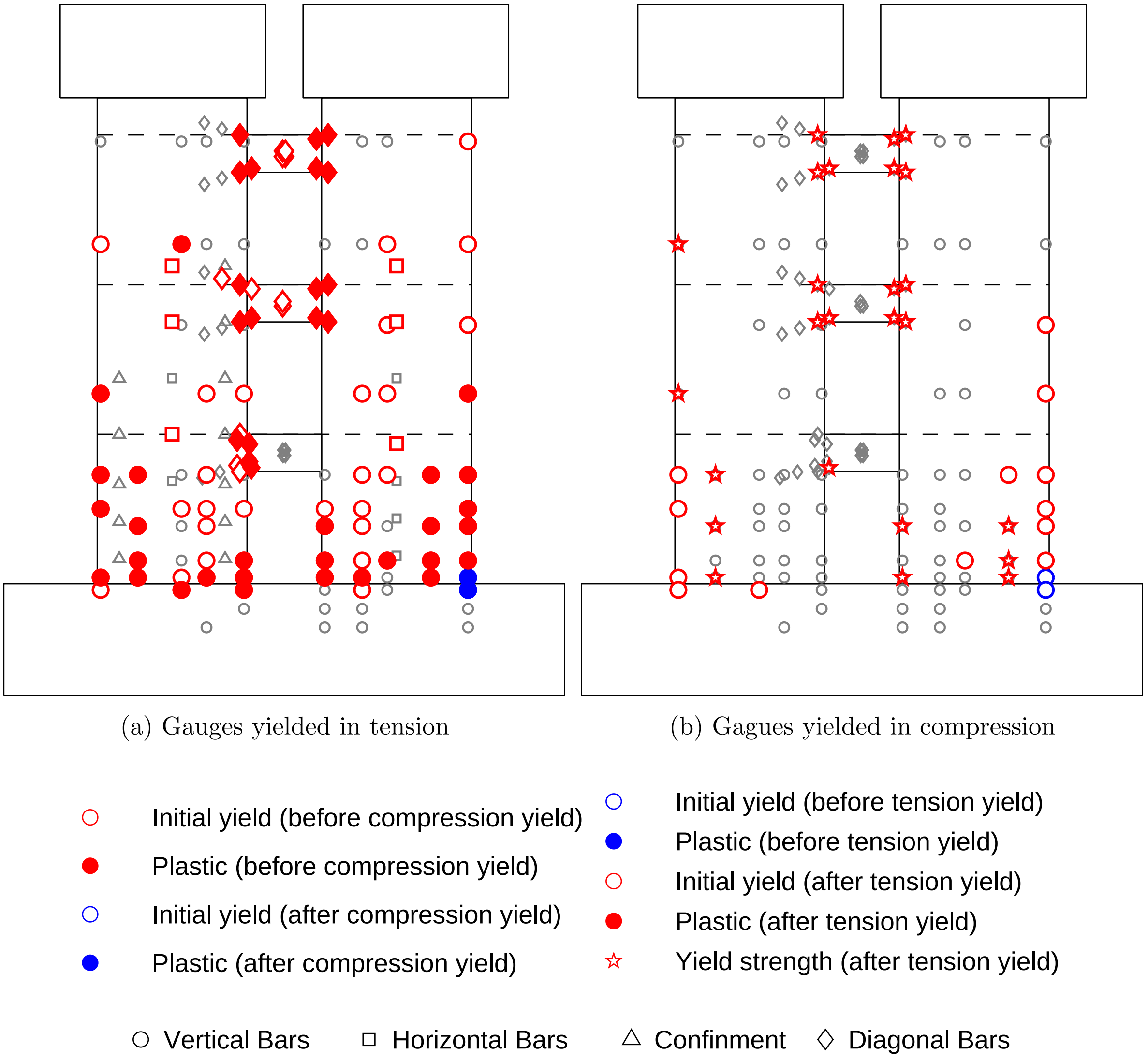

(a) Gauges yielded in tension

(b) Gagues yielded in compression

Figure 5.4: Yielded strain gauges at the end of the 1.50% drift level

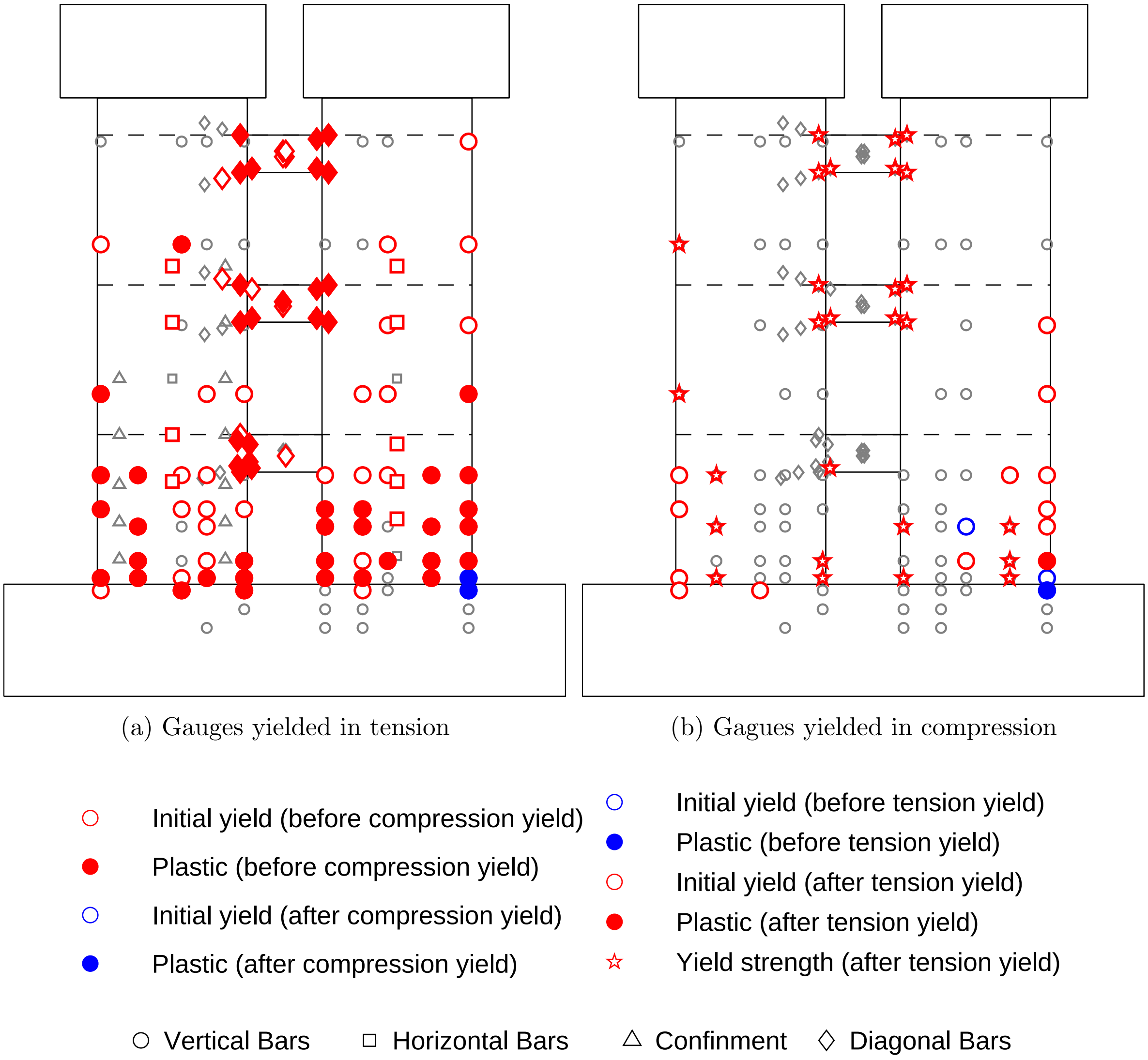
(a) Gauges yielded in tension (b) Gagues yielded in compression

Figure 5.5: Yielded strain gauges at the end of the +2.25% drift half cycle

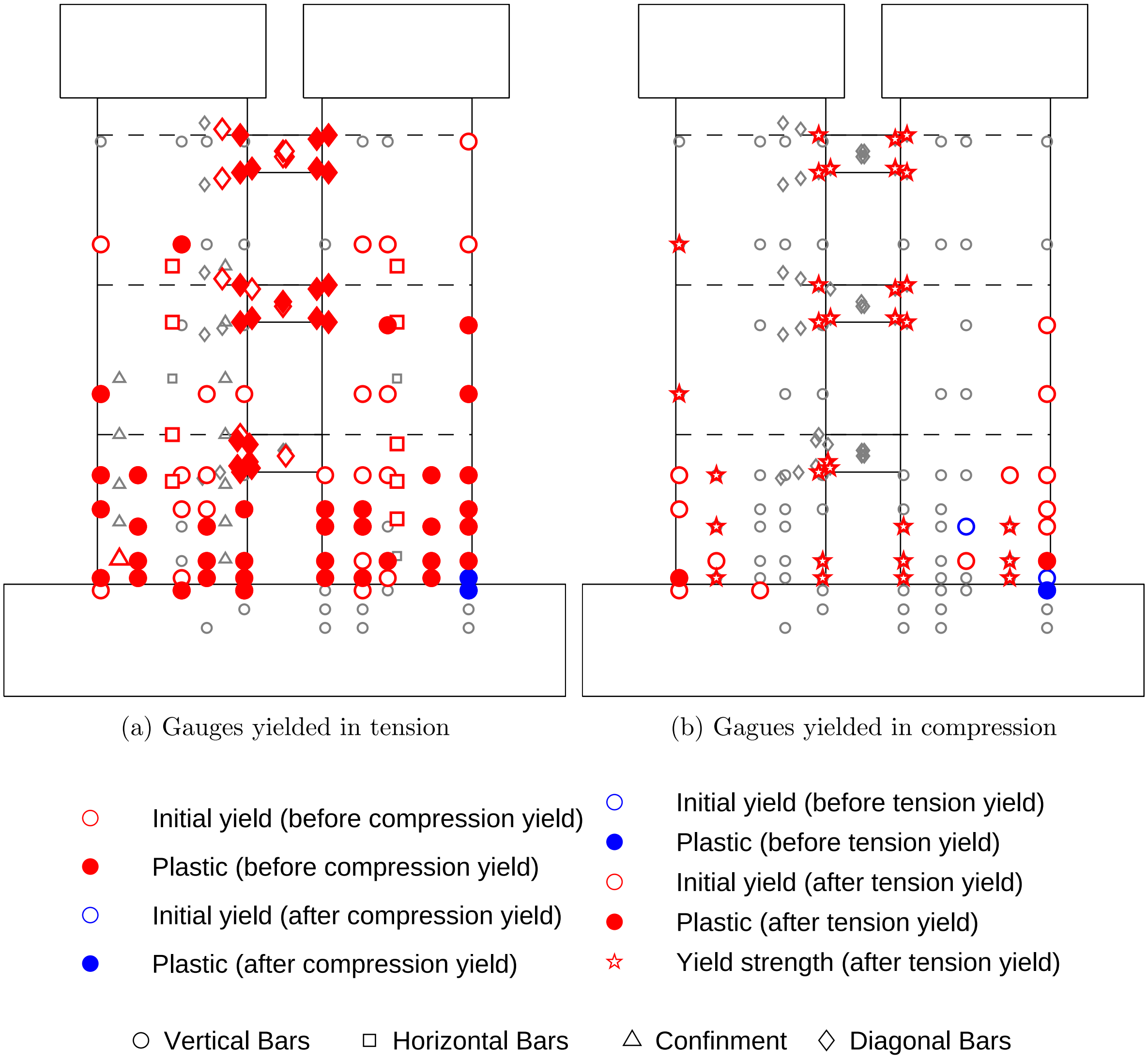

(a) Gauges yielded in tension

(b) Gagues yielded in compression

Figure 5.6: Yielded strain gauges at the end of the test

5.2 Coupling Beam Forces

While the performance of coupling beams has been well established by experimental component testing and numerical simulations, it is important to verify the performance of coupling beams in an actual a coupled-wall structure. This is challenging because the internal forces in the coupling beams cannot be calculated directly using equilibrium as the coupled wall subassemblage is statically indeterminate. However, using the steel stresses computed from the steel strain gauges at the ends of the coupling beams, the tension and compression forces in the diagonal reinforcement can be estimated (recall from Section 5.1 that the steel stresses were computed from steel strain gauge data using the Hoehler–Stanton model). The relationship between the diagonal reinforcement stresses, f_s, and the internal forces, T_s and C_s, is shown in Figure 5.7a, and expressed in Equation 5.1:

$$T_s = C_s = A_{vd} f_s \tag{5.1}$$

By summing the forces at the at the beam-to-wall interface, Equations 5.2 and 5.3 are derived; the definitions of the variables in these equations are provided in Figure 5.7b, where A_{vd} is the total area of one diagonal reinforcement bundle:

$$V_{cb} = 2T_s sin(\alpha) = 2A_{vd} f_s sin(\alpha) \tag{5.2}$$

$$M_{cb} = A_{vd} f_s cos(h - 2d') \tag{5.3}$$

The estimated shear demands in each coupling beam are shown in Figures 5.8 and 5.9. The coupling beam shear stress demands never exceed $10\sqrt{f'_c}$ (psi), which is used in ACI 318-08 as an upper limit to prevent sliding action. In these figures, the right axis shows shear demand normalized by the ACI nominal shear strength, V_n (Eq. 3.1). This calculation is based on the actual yield strength of the reinforcing bar as reported in

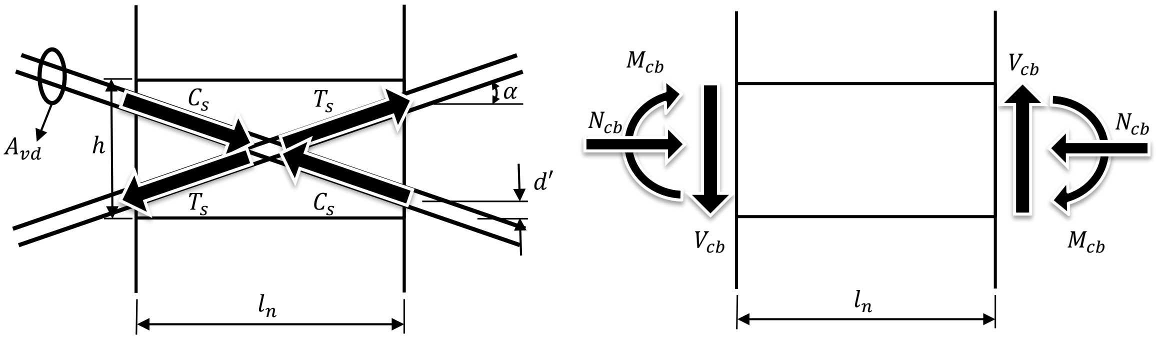

(a) Tension and compression (b) Shear and moment

Figure 5.7: Coupling beam force equilibrium

Chapter 3. When the specimen was loaded to the east, the data suggests the shear in CB3 exceeded the nominal strength by more than 30%; loading to the west resultsin in nominal strength being exceeded by almost 50%. This over strength exceeds the recommendation of $1.25f_y$ used to calculate M_{pr} in the ICC (2007) plastic analysis procedures discussed in Section 2.2.

For loading towards the east and west, an intermediate data point was added between the points for the 1.5% and 2.25% peaks. These data points are one load step prior to dailure in the respective directions. These data points were added to quantify the demands at the point of max base shear, in each direction, and are repeated in other data analysis plots and tables throughout this chapter.

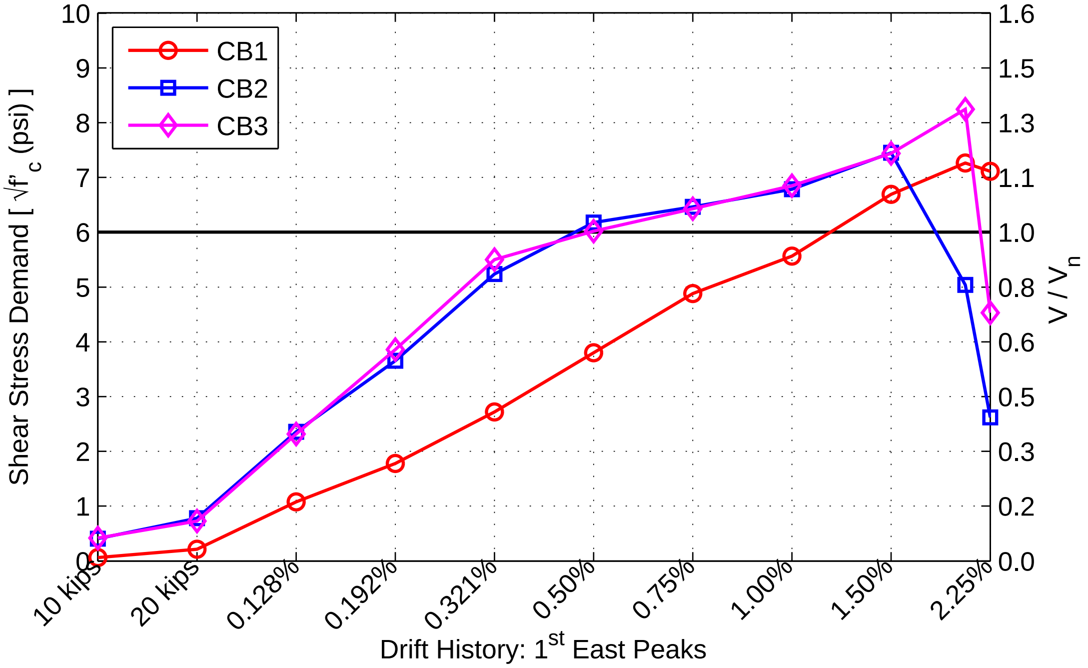

Figure 5.8: East peak coupling beam shear demands using steel strain gauges

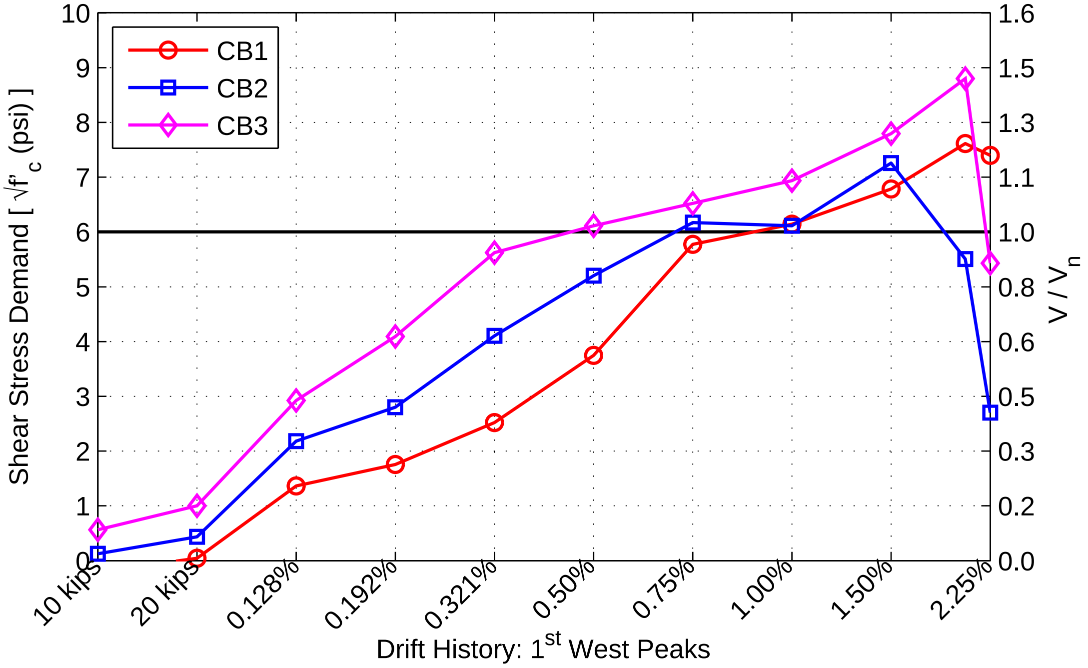

Figure 5.9: West peak coupling beam shear demands using steel strain gauges

5.3 *Wall Pier Axial Forces*

In a coupled wall, the internal shear forces in the coupling beams impose axial compressive and tensile load demands on the wall piers at each floor. Using the coupling beam shears estimated in the previous section and the measured axial force applied to the piers above the third floor, the axial forces in the wall piers in each story can be calculated. These forces are shown in Figures 5.10 – 5.13. In Figures 5.10 and 5.11, the right axis shows axial force, N, normalized by the tensile yield capacity of the wall pier, $\sum A_s f_y$ where, A_s and f_y are the nominal area and yield strength of an individual reinforcing bar. In Figures 5.12 and 5.13, the right axis shows axial force normalized by the compressive capacity of the wall pier, $A_g f'_c$ where, A_g is the gross area of the wall pier.

Calculated axial forces at the base of each wall pier at key damage states are tabulated in Table 5.1. These key damage states (DS) are defined on the basis of wall pier damage:

DS0 *Diagonal cracking* of the wall piers (0.321% drift level)

DS1 *Yielding* of vertical reinforcement in the OBE of the wall piers (0.50% drift level)

DS2 *Initial spalling* of the wall pier concrete cover (1.00% drift level)

DS3 *Moderate spalling* of the wall pier concrete cover that exposes the longitudinal reinforcement (1.50% drift level)

DS4 *Bar buckling and core crushing* in the OBE of each wall pier (2.25% drift level)

In Figures 5.10 and 5.11, the axial force in the WWP and EWP are plotted for the first east and west peaks, respectively. The data in these figures represents when the wall pier is increasing in axial tension due to the overturning moment; a wall pier subjected to this type of increasing demand is commonly referred to as a “tension wall.” A wall pier subjected to increasing compressive demands, as shown in Figures 5.12 and 5.13, is referred to as a “compression wall.” This nomenclature is used throughout this chapter.

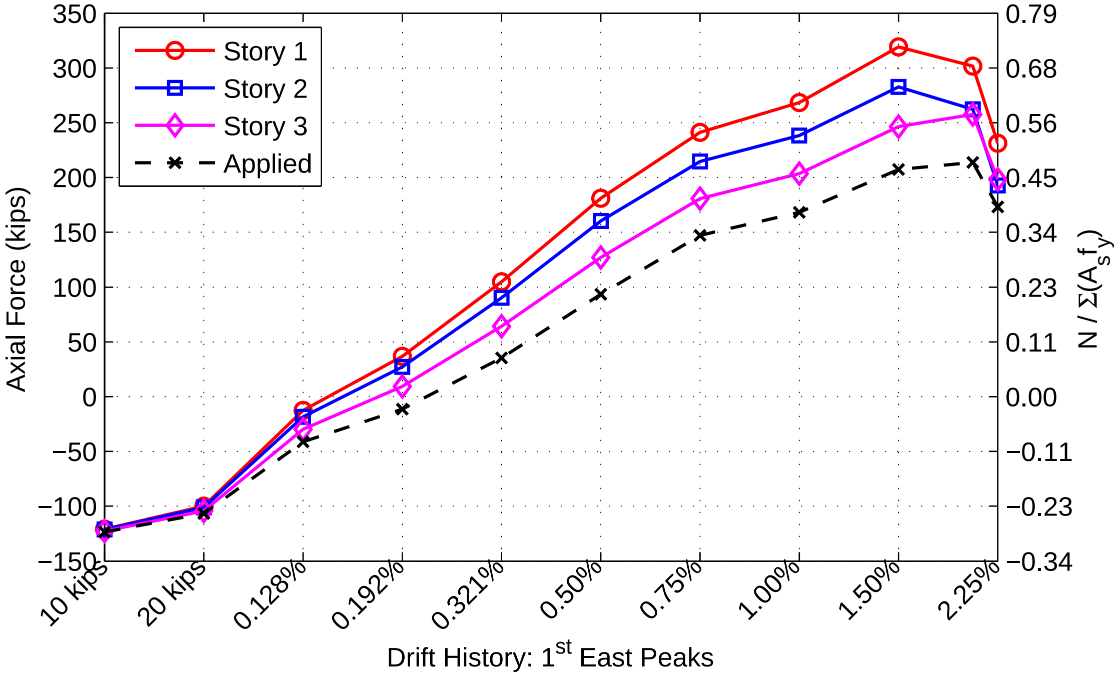

Figure 5.10: West wall pier axial force demand during first east peaks

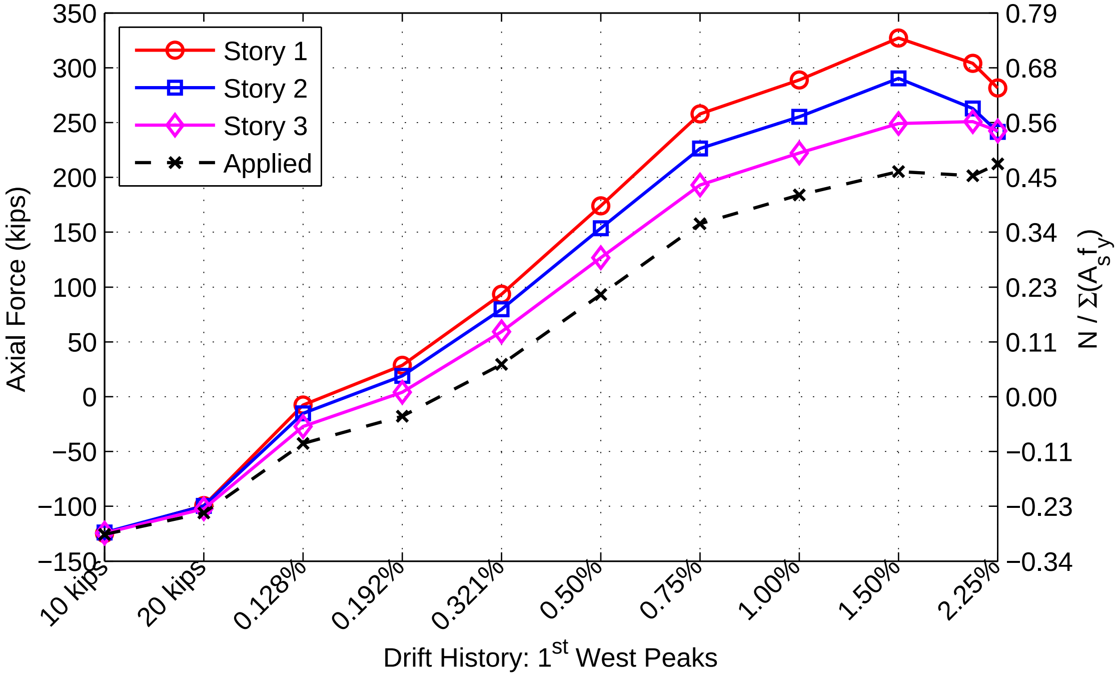

Figure 5.11: East wall pier axial force demand during first west peaks

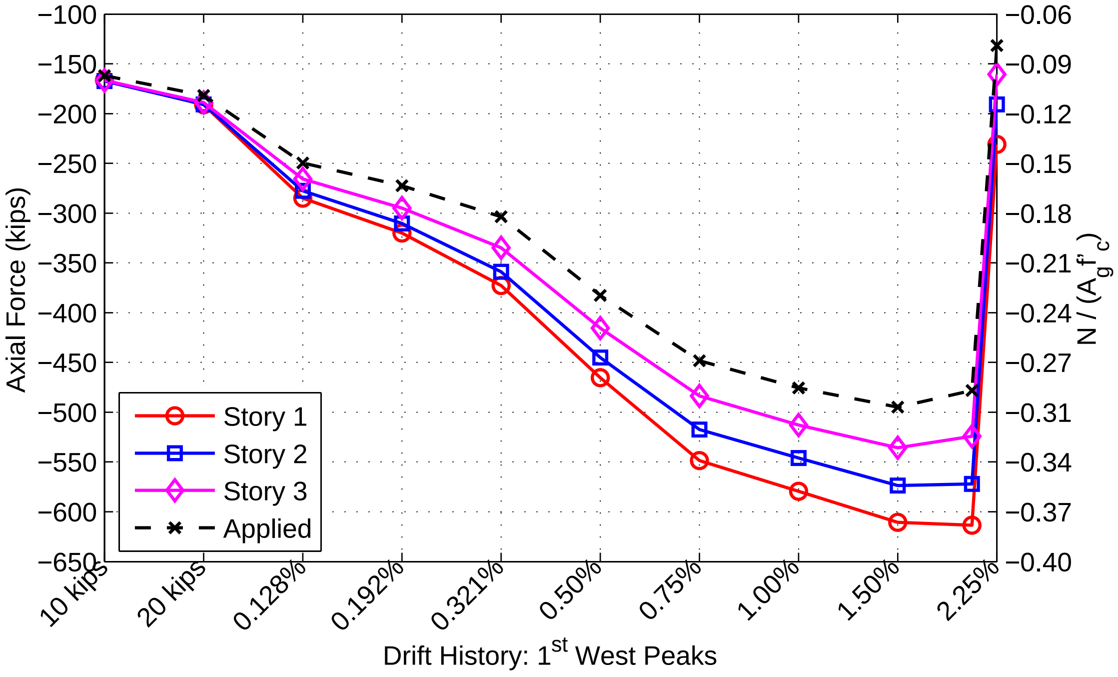

Figure 5.12: West wall pier axial force demand during first west peaks

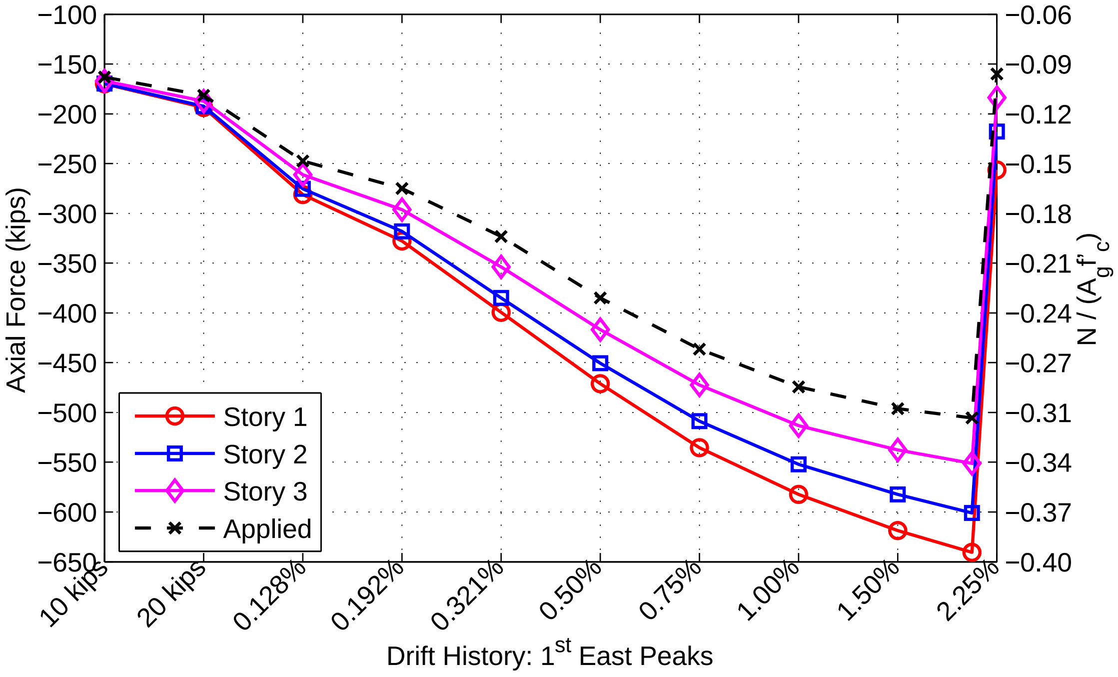

Figure 5.13: East wall pier axial force demand during first east peaks

Table 5.1: Axial load demands estimated at the base of each wall pier

		First East Peak (E+)				First West Peak (W-)			
		WWP		**EWP**		**WWP**		**EWP**	
DS	**Drift**	N_e	$\frac{N_e}{\sum(A_s f_y)}$	N_e	$\frac{N_e}{A_g f_c'}$	N_e	$\frac{N_e}{A_g f_c'}$	N_e	$\frac{N_e}{\sum(A_s f_y)}$
[+0.1in]	(%)	(kips)		(kips)		(kips)		(kips)	
DS0	0.321%	105	0.24	-400	-0.24	-373	-0.23	93.5	0.21
DS1	0.50%	181	0.41	-471	-0.29	-465	-0.28	174	0.39
DS2	1.00%	268	0.61	-582	-0.36	-579	-0.35	289	0.65
DS3	1.50%	319	0.72	-619	-0.38	-610	-0.37	327	0.74
DS4	2.20%*	302	0.68	-641	-0.39	-613	-0.37	304	0.69

* One step prior to peak drift

Researchers at UC-Berkeley Ozselcuk (1989) recommend that coupled walls be designed so that axial forces resulting from gravity and lateral forces do not cause tension in the wall piers. However, the data Figures 5.10 and 5.11 show that the axial force at the base of the wall the EWP and WWP overcomes the gravity load ($0.1f_c'A_g$) during the 0.192% drift level and that the axial loads applied to the top of each wall pier overcome the gravity loads during the 0.321% drift level. These results suggest that it is not practical to design a modern mid-rise coupled-wall system in which the tension wall never goes into tension (i.e. the tension demands from the coupling beams never exceed the gravity load).

As discussed earlier, on the right side of Figures 5.10 and 5.11, the axial forces are normalized by the tensile yield capacity of an individual wall pier; this ratio is the DCR_{axial} defined in Section 6.1. This design parameter may be used to relate the potential tensile demand associated with all the coupling beams yielding up the height of the building to the tensile yield capacity of the wall pier. The maximum DCR_{axial} for the test specimen was estimated to be 0.43; this value was achieved in the test during the 0.5% drift level where initial yielding occurred in both wall piers and in coupling beams 2 and 3. However, at 1.5% drift the maximum DCR_{axial} of 0.72 in the WWP during the E+ peak and

0.74 in the EWP during the W- peak was achieved.

The DCR_{axial} provides important info for design, establishing that wall pier tensile capacity will not limit coupling beam yielding up the entire height of the structure. Axial compression demand (ACD) in the wall piers is also important, potentially affecting when failure of the wall piers occurs. In Figures 5.12 and 5.13, wall pier axial compressive forces are plotted verse drift. The maximum axial compressive force in the wall piers was -641 kips (-$0.39f'_cA_g$) one step prior to failure of the EWP. During the reverse half-cycle the axial compression was -613 kips (-$0.37f'_cA_g$) one step prior to failure of the WWP. These axial demands are relatively high when one considers the axial-moment interaction diagram (Figure 5.14). At the respective failures in the test, the axial forces in the compression piers were approximately at the balanced axial force condition (i.e. the tensile reinforcement reaches the yield strain at the same instant the extreme compressive fiber reaches -0.003), and this resulted in compressive type failures in both wall piers.

In design (Section 6.1), the expected axial demand in the compression wall pier was estimated at -$0.29f'_cA_g$. During the test, this demand was reached in both wall piers at the ±0.50% peaks. Furthermore, the axial load was 22% larger than the predicted value, at 1.00% drift. This is when the concrete cover spalled in the OBE of the EWP. At failure, the amount of force redistribution within the specimen is illustrated when comparing the drops in axial force between the tension wall and the compression. The EWP dropped 60% of its compressive load in one step while the tension wall (WWP) only dropped 23% of its tension force during the same step.

The predicted DCR_{axial} and ACD are based on the nominal shear strength of the coupling beams (i.e. yielding of the diagonally steel), while the actual axial demands estimated in the wall pier accounts for additional factors which increase the coupling beam flexural strength or the resulting shear force in the coupling beam. As discussed in the previous section, the shear forces measured in the coupling beams were much larger than the expected nominal shear strengths of the coupling beams, thus resulting in a higher measured axial forced compared to the predicted values.

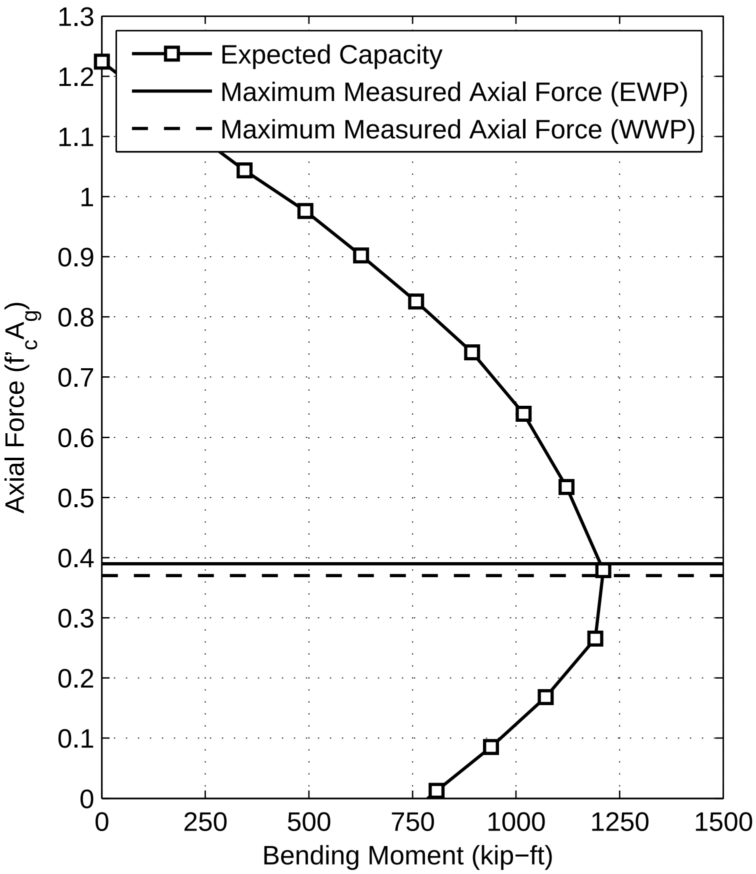

Figure 5.14: CW1 P-M interaction and maximum measured axial forces for the compression wall piers

Using the axial forces computed for the wall piers in this section, the degree of coupling (DOC) as defined by Harries (2001) was calculated as a function of the drift history using the following equation:

$$DOC = \frac{N \times L}{M_{y,total}} \times 100\% \tag{5.4}$$

where, L is the horizontal distance between the centroids of the wall piers and $M_{y,total}$ is the known overturning moment measured from the experiment (Section 3.5). The measured degree of coupling (DOC) is shown in Figures 5.15 for the east and west peaks. The predicted DOC determined during the design of the coupled-wall specimen (Section

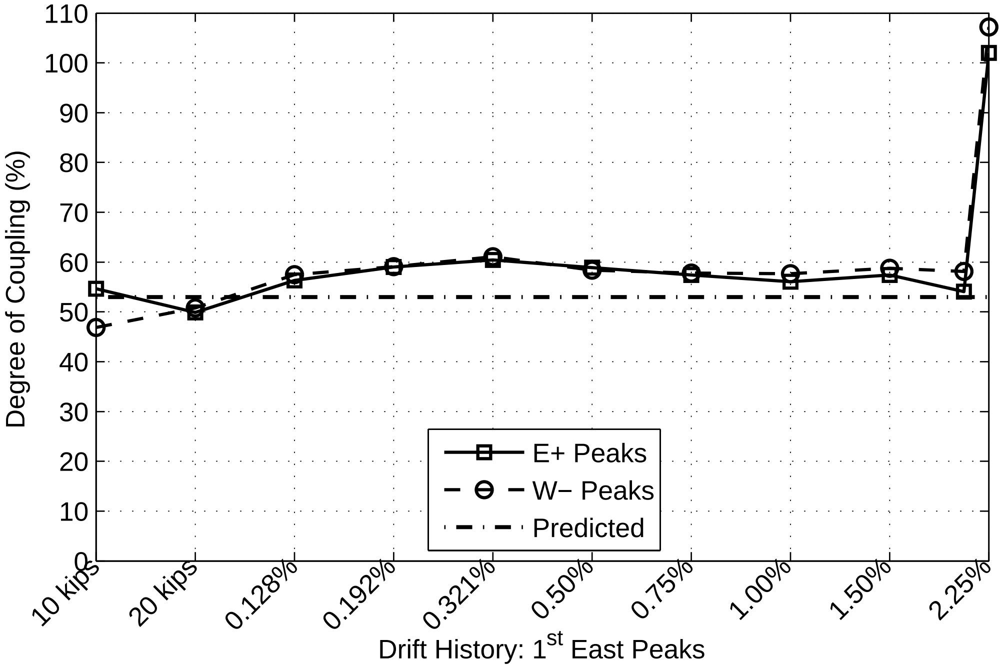

Figure 5.15: Measured degree of coupling (DOC) at the base of CW1

6.1) is also included in this figure. Throughout the drift history, the measured DOC values were within 7% error compared to the predicted value calcualted using Equaction 2.1.

5.4 Wall Pier Axial Deformations

The axial forces in the wall piers provide interesting and important results regarding the behavior of the coupling action in the specimen, in order to really assess the axial stiffness differences between the tension and compression wall, the axial deformations were calculated at each story as well as over the total height of the specimen. To properly assess these deformations, traditional instrumentation, which is presented in Section 3.4, was used to measure the axial deformation of each wall pier.

To begin, the axial deformations at each story were calculated using LVDTs fixed vertically along the outer and inner edges of each wall pier. These instruments were attached to the north face of the coupled wall and are shown in Figure 3.15. For a vertical line of LVDTs on a given wall edge, the deformations per story were summed up the height of the story and then averaged with the adjacent line of LVDTs. This calculated axial deformation is the average story deformation of a given wall pier. Finally, three vertical in-plane transducers connected to the top of the foundation and strung to the bottom of a given wall pier concrete cap were used to determine the average vertical deformation along the entire height of the specimen. The layout of these instruments are shown in Figure 3.14. The wall pier axial deformations for each wall pier are shown in Figures 5.16 – 5.19, and the deformation measured over the total height of the wall, using in-plane transducers, is referred to as the "total" deformation.

More specifically, the axial deformation in the tension wall is shown in Figures 5.16 – 5.17. As shown in both piers approximately 50% of the total axial deformation happened in the first floor. On the other hand, the axial deformation in the compression piers are shown in Figures 5.18 – 5.19. The axial deformations in the compression wall are not as clear as in the tension wall. For example, the deformations on average along the first and second stories are actually increasing with more compressive demand. Because the wall pier in question is actually in elongating substantially in tension during the reverse half cycle, there is large amount plastic strain accumulating in the reinforcing steel due to inelastic behavior. This accumulative deformation is never overcome when the specimen is reversed and the wall contracts in compression. Additionally, the severity of shortening in the first story of the wall piers due to bar buckling and core crushing is quite clear at the end of the test.

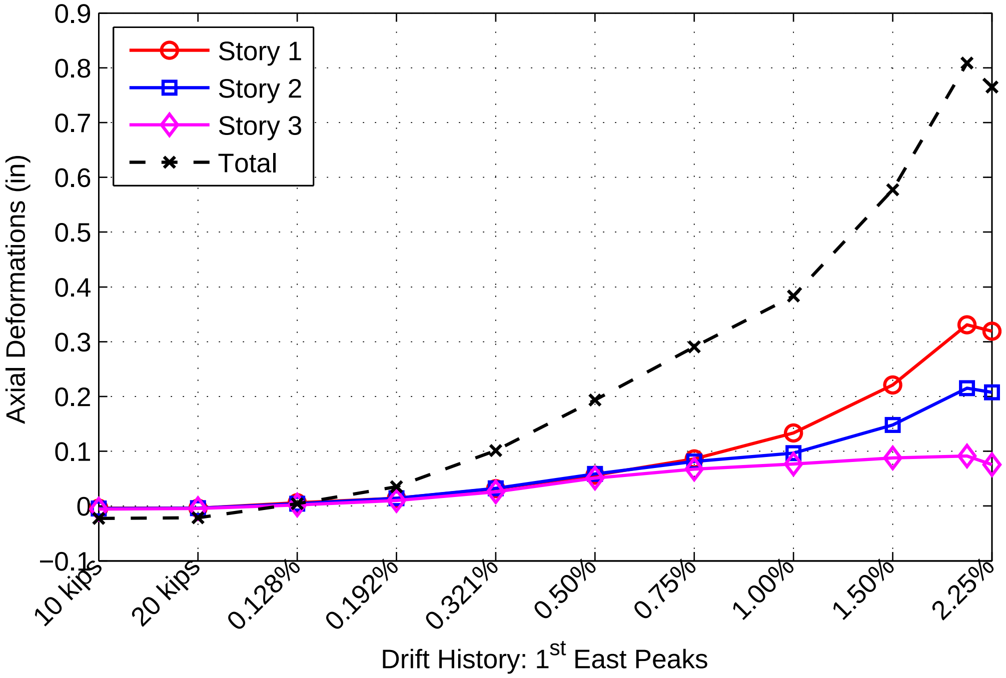

Figure 5.16: Axial deformations of west wall pier for increasing axial tension demand

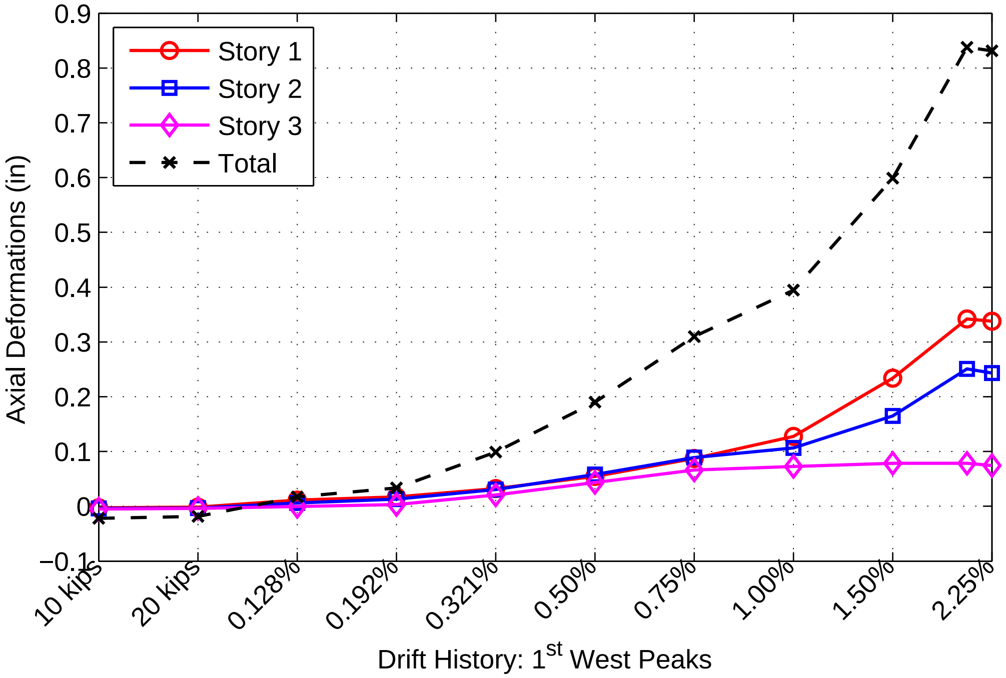

Figure 5.17: Axial deformations of east wall pier for increasing axial tension demand

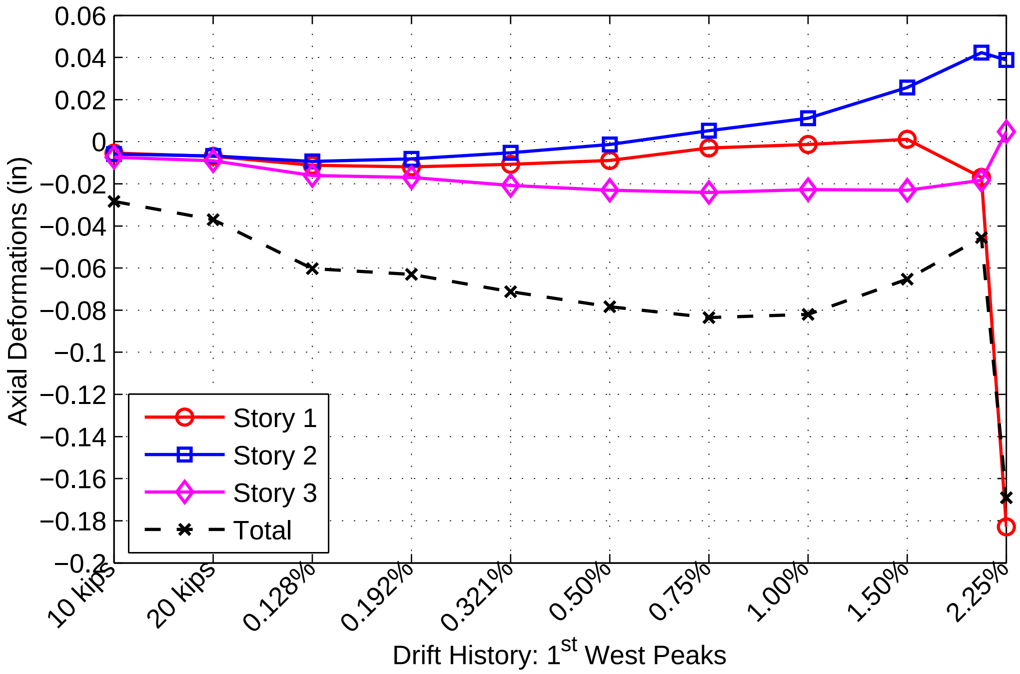

Figure 5.18: Axial deformations of west wall pier for increasing axial compressive demand

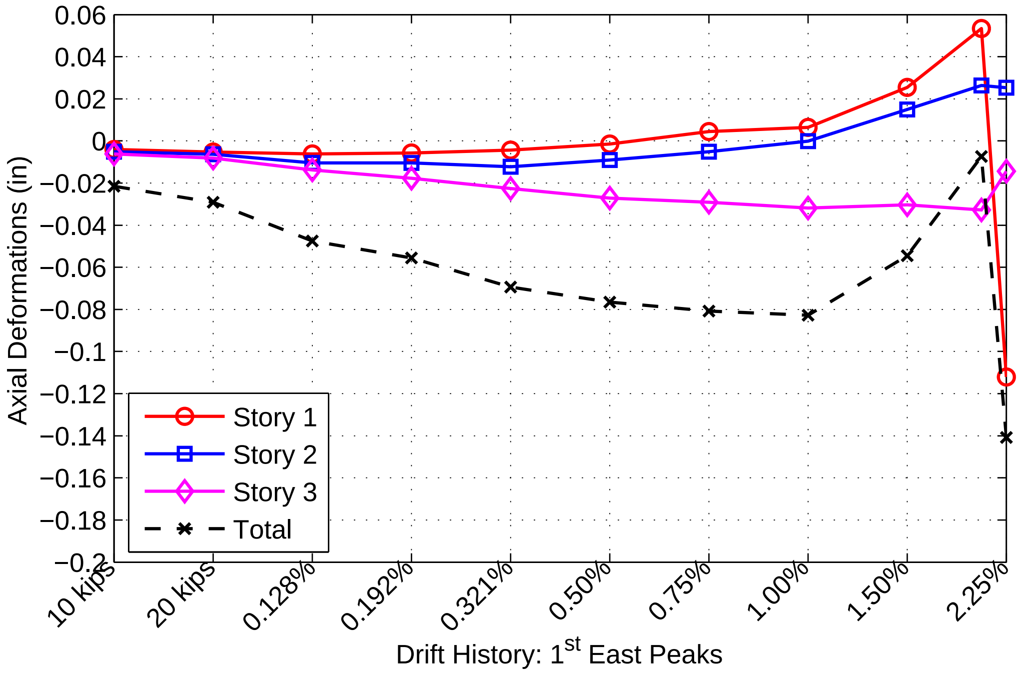

Figure 5.19: Axial deformations of east wall pier for increasing axial compressive demand

5.5 *Wall Pier Axial Stiffness*

With the axial forces and deformations estimated for each story known, the axial stiffness was be approximated using the secant stiffness method. At zero lateral force, the axial load in each wall pier was simply $-0.1 f'_c A_g$. Taking the difference in axial force between the peak lateral step and the zero force step, the change in axial force, ΔN, was calculated. Similarly, the change in axial deformation, Δ_{axial}, was calculated using the same approach. Figure 5.20 illustrates the definition of the axial secant stiffness for a given half cycle in the loading history where, α is the ratio of the axial load in a story over the gross axial section properties. Furthermore, using the calculation for the story axial secant stiffness, the "total" axial deformation was used with the applied axial load to estimate an average pier stiffness over the entire height of one wall pier.

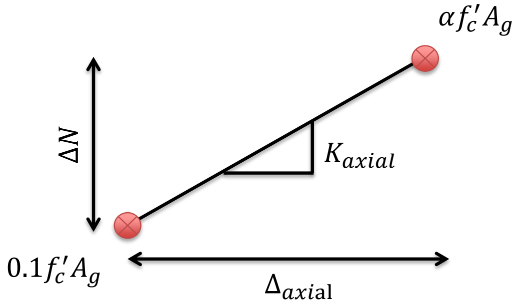

Figure 5.20: Definition for wall pier axial secant stiffness

Figures 5.21 and 5.22 show the calculated axial stiffness values for the east and west wall piers when the peak axial force is in tension. Note the significant degradation in the axial stiffness depending on level of demand. In general, design codes usually recommend modeling a component, such as a wall, with an effective axial stiffness of $1.0 E'_c A_g$; however, based on these results, this design assumption is grossly overestimated. The axial tensile stiffness in both wall piers is approximately $0.2 E_c A_g$ when the tension wall begins to yield. The reduction in the stiffness based on the walls gross properties at the end of the test was more than 90%. This degradation in stiffness due to large axial tension demands significantly affects the shear and flexural strength and stiffness of the tension wall. The loss of stiffness in the tension wall increases the shear and moment demands on the compression wall which changes its behavior dramatically (Ozselcuk, 1989).

In addition to the axial stiffness normalized by the gross cross-sectional properties, the right-hand side of the figures provides the secant stiffness normalized by the elastic stiffness of the total area of vertical reinforcement in the wall pier. Note for all the stories except story three, the axial stiffness is softer than the elastic reinforcement stiffness past the 1.5% drift level. This is mostly attributed by the large amount of yielding occurring in the bottom two stories of the tension wall.

The estimated axial stiffness of the compression walls are shown in Figures 5.23 and 5.24. The level of stiffness degradation in the compression piers is less pronounced than the tension wall, but after spalling occurs during the 1.0% drift level, a reduction in the axial stiffness is seen clearly. Investigating the average axial stiffness estimated over the entire height of the specimen, suggests the average estimated axial stiffness of the east and west wall pier is approximately $0.43E_cA_g$ with a standard deviation of $0.131E_cA_g$ and $0.53E_cA_g$ with a standard deviation of $0.122E_cA_g$, respectively.

Additionally, Figures 5.25 and 5.26 show the axial stiffness of the compression wall only at each peak drift for the entire drift cycle. The difference between the cycle A and cycle B results for the WWP are small. However, the loading path of the specimen always results in the EWP being loaded in axial compression first. When the loading is reversed, the EWP is loaded into tension and flexural and diagonal cracks open up. At higher drifts, yielding of the vertical reinforcement occurs which accumulates plastic strain, so the wall expands along its length. On the walls return to compression (cycle B), all the large deformations due to the high tension demand are much harder to overcome. This dependence on loading direction results in an axial stiffness reduction, which is clearly seen after 0.321% drift when significant cracking in the EWP has occurred.

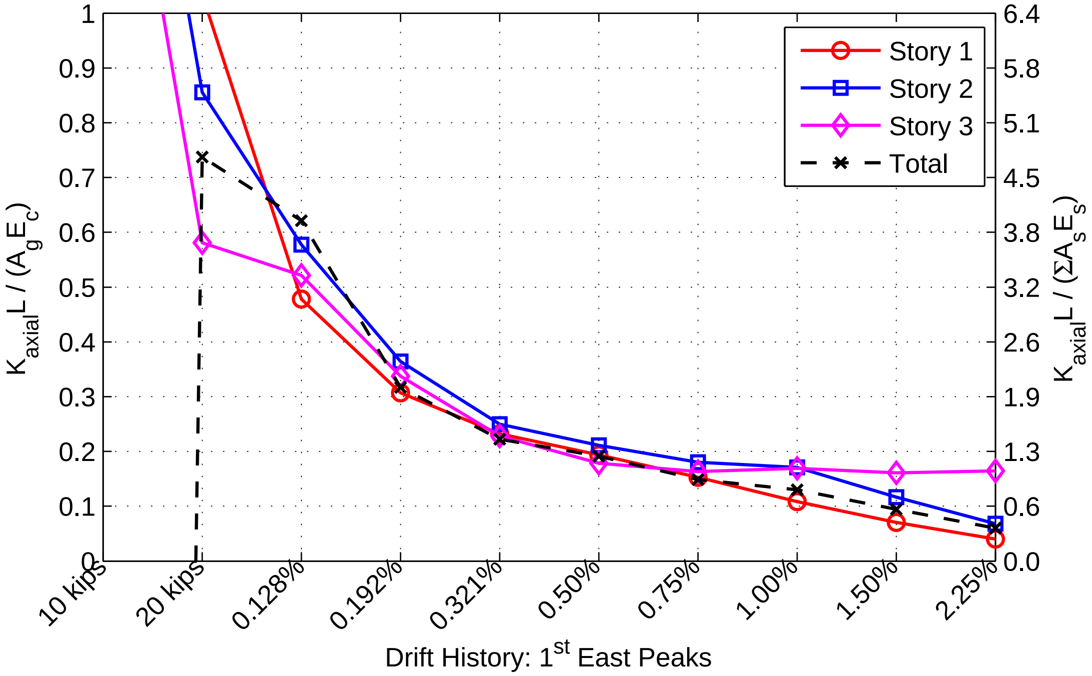

Figure 5.21: Axial stiffness of west wall pier for increasing axial tension demand

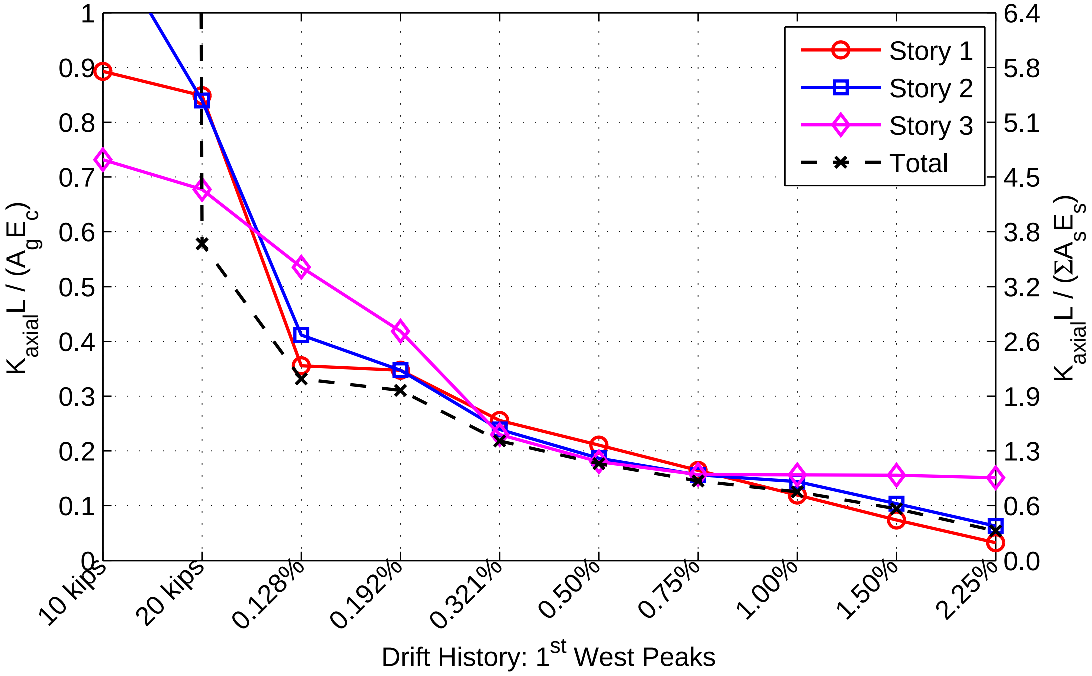

Figure 5.22: Axial stiffness of east wall pier for increasing axial tension demand

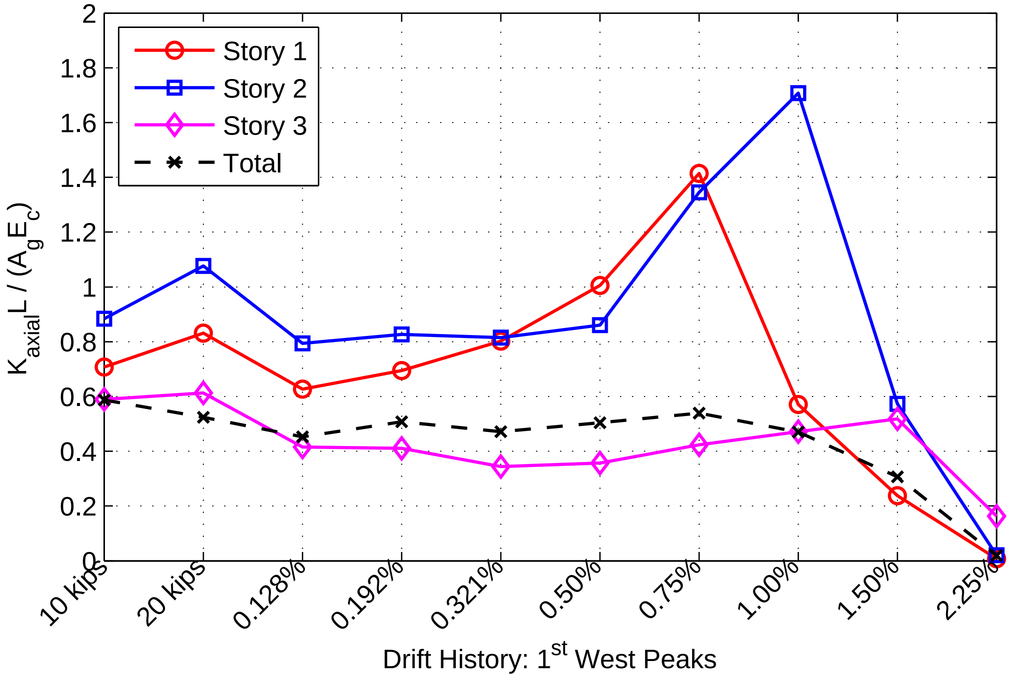

Figure 5.23: Axial stiffness of west wall pier for increasing axial compressive demand

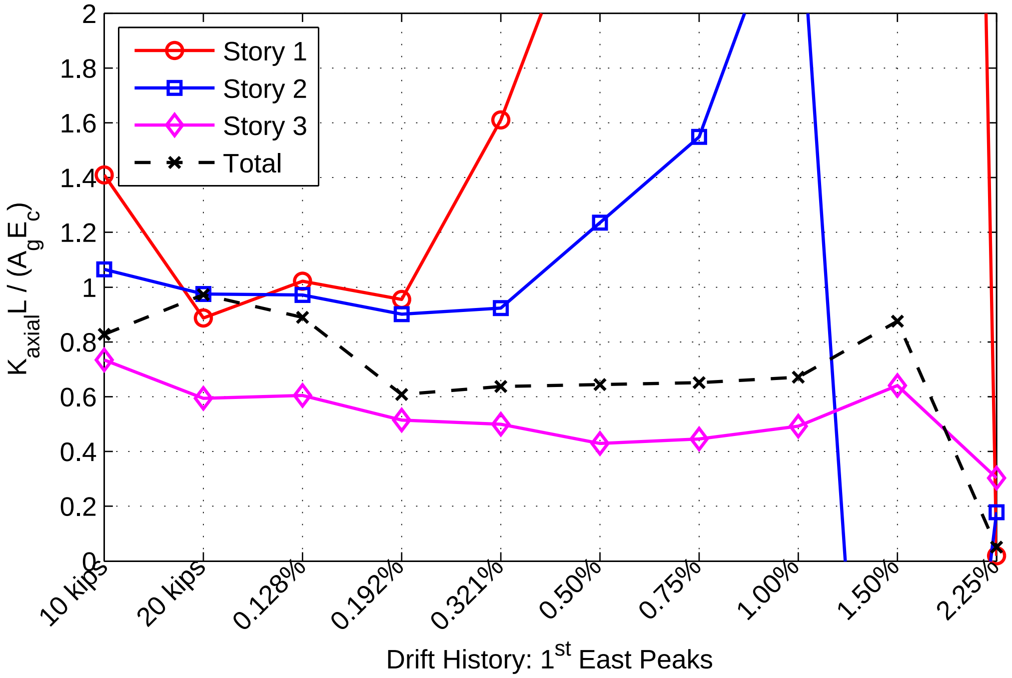

Figure 5.24: Axial stiffness of east wall pier for increasing axial compressive demand

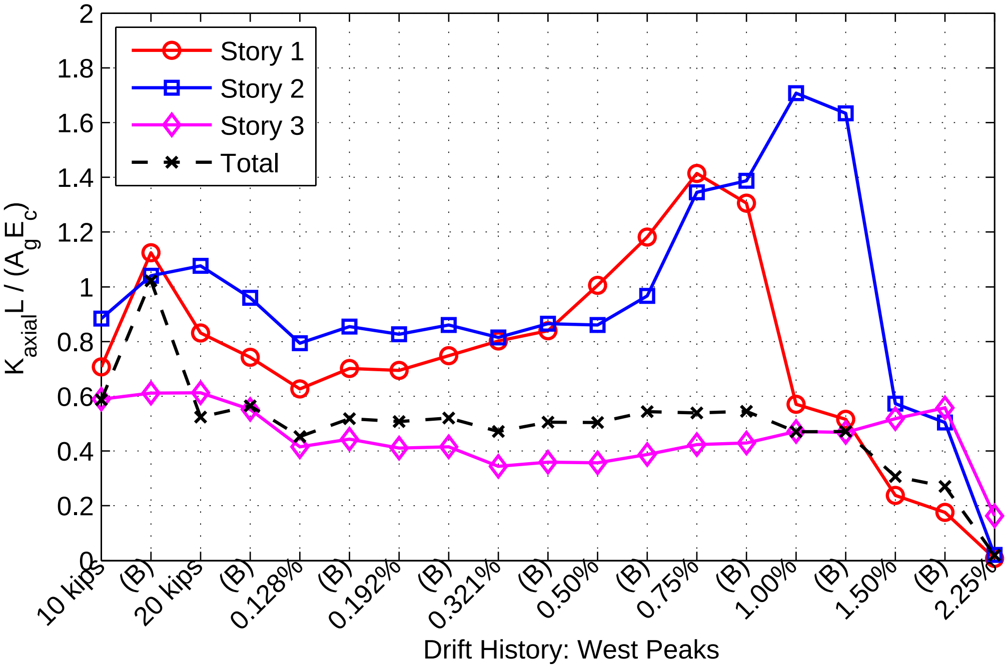

Figure 5.25: West wall pier compressive axial stiffness at peak cycles A and B

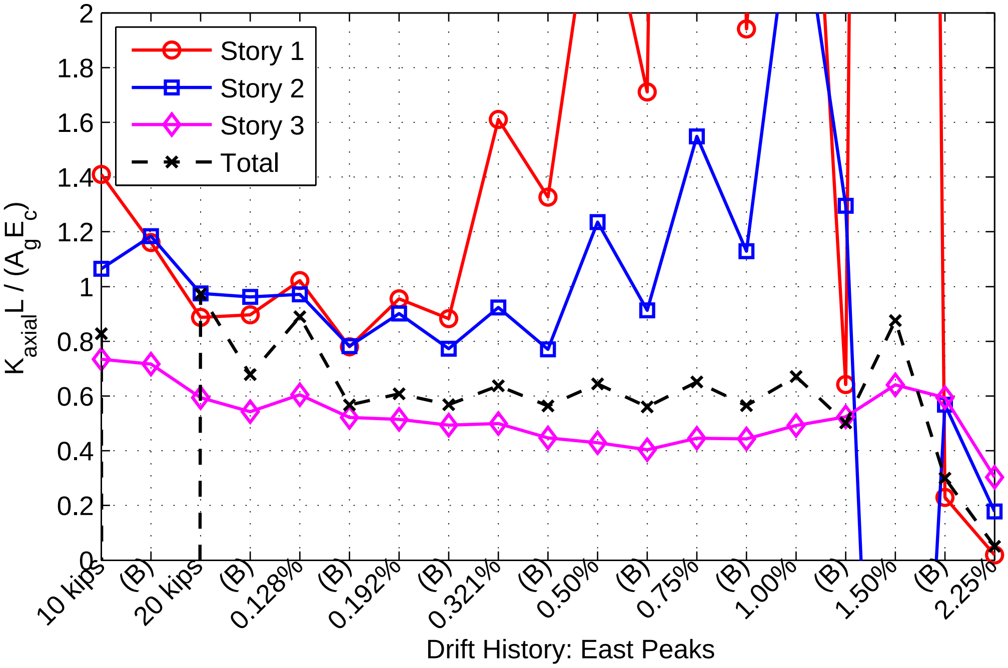

Figure 5.26: East wall pier compressive axial stiffness at peak cycles A and B

5.6 Wall Pier Flexural Stiffness

AA significant loss in axial stiffness in the tension wall was calculated for CW1 at levels prior to yield, and this loss plays a key role in the flexural behavior of the wall piers. The interaction axial forces and the flexural stiffness of the wall piers are investigated in this section. The axial forces in the wall piers were estimated in Section 5.3. However, the moment and shear distribution between the tension and compression wall is challenging to predict using the experimental data due to the indeterminacy associated with the test setup. Therefore, using the results of the VecTor2 nonlinear finite element analyses discussed in Section 3.5, the distribution of shear and moments at the base of the wall was approximated (Figures 5.27 and 5.28). These results were then used with the experimental deformation data to estimate the flexural stiffness of the wall piers.

In order the estimate the reactions at the base for the wall, the base reaction from the

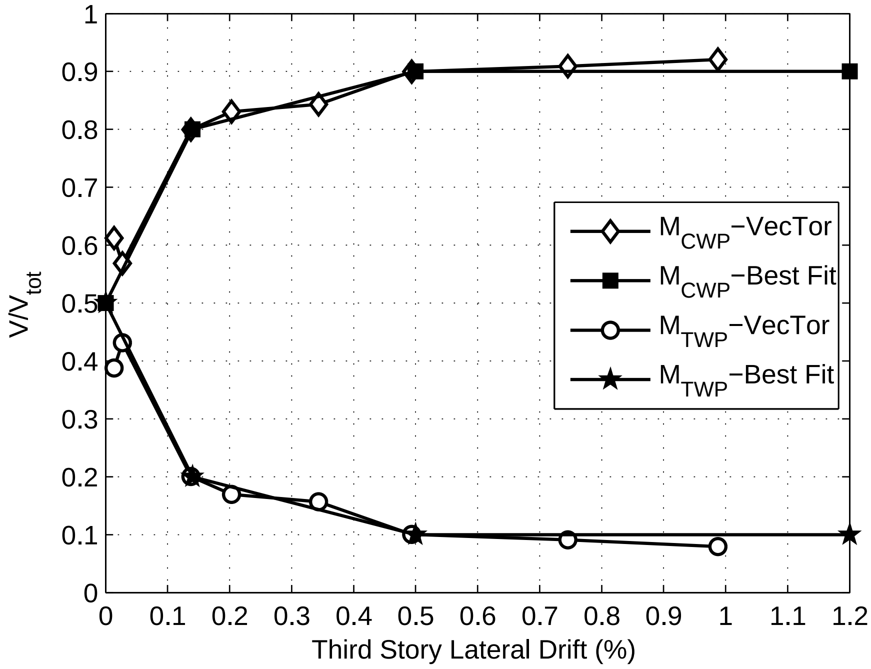

Figure 5.27: VecTor2 base shear distribution vs. drift results

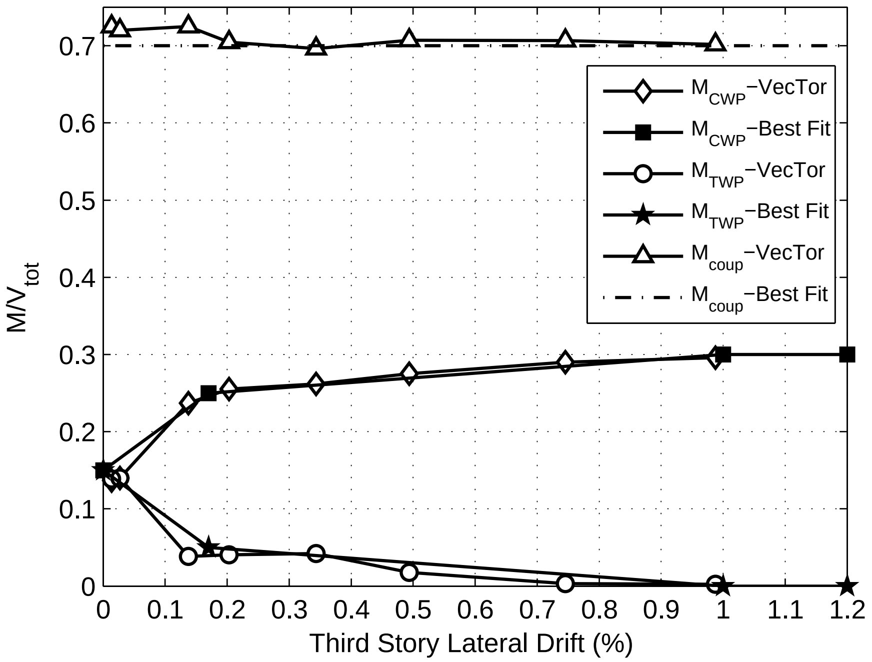

Figure 5.28: VecTor2 base moment distribution vs. drift results

10-story prototype model were fit with a quad-linear relationship. Based on the vector results, the coupling moment was assumed to be equal to 70% of the total overturning moment. Using the experimental total moment and shear for a given drift, the shear and moment distribution at the base of each wall pier was estimated using these best fit relationships. For a given wall pier, a linear fit to the Metris LED vertical displacement data, 38 inches above the foundation (Figure 3.11), was used to calculate the rotation, θ, just below the coupling beam. The rotation at the base for the wall was assumed as fixed, which was consistent with the experimental data taken at the base of the foundation block. The effective flexural stiffness, EI_{eff}, in the first story of each wall pier was calculated using the following equation derived from the moment-curvature equation:

$$EI_{eff} = \frac{h_1}{\theta}\left(M_e - \frac{V_e h_1}{2}\right) \tag{5.5}$$

where, h_1 is defined as the vertical distance from the top of the foundation to the row of LEDs. V_e and M_e are the shear and moment estimated for an individual wall pier.

The estimated flexural stiffness of the wall piers is shown in Figures 5.29 and 5.30. Each figure includes the tension wall pier axial load plotted verse the drift. The flexural stiffness of the tension wall was approximately $0.2EI_g$ at the same drift when the axial load in the tension wall overcomes the gravity force. On the other hand, the flexural stiffness in the compression pier was approximately $0.60EI_g$ at the same drift. When the wall piers yield, 0.50% drift, the flexural stiffness of the tension and compression wall was approximately $0.1EI_g$ and $0.40EI_g$, respectively. Addtionally, the flexural stiffness estimated for the compression wall piers, plotted with its respecitve axial load, are shown in Figures 5.31 and 5.32.

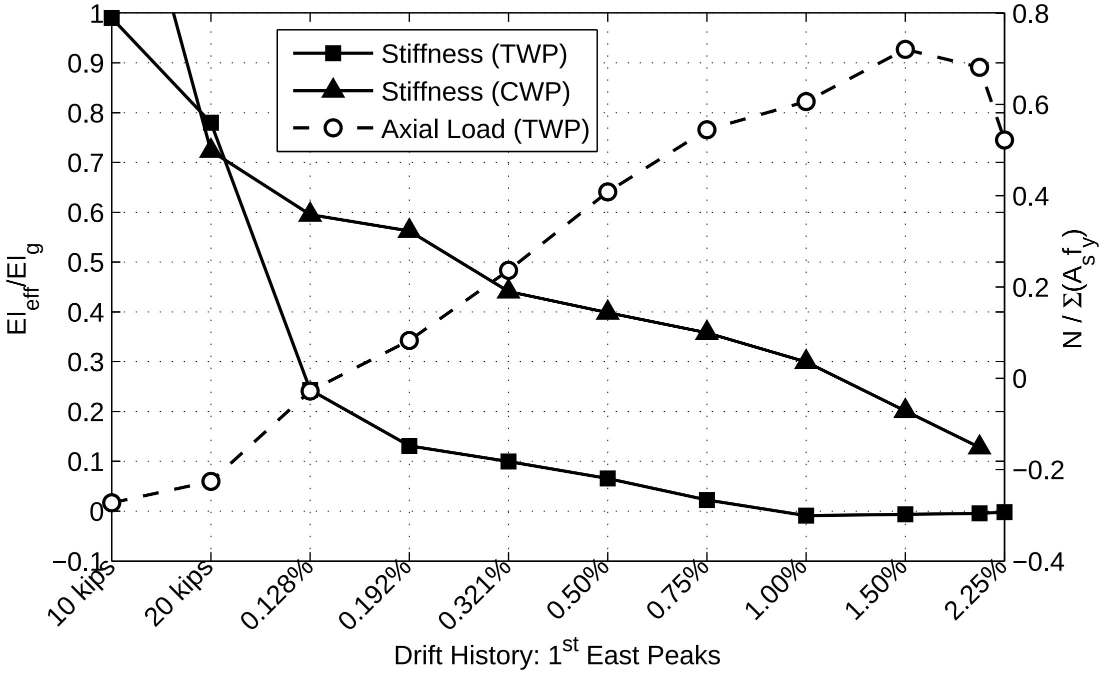

Figure 5.29: Flexural stiffness of wall piers plotted with TWP axial force (E+ Peaks)

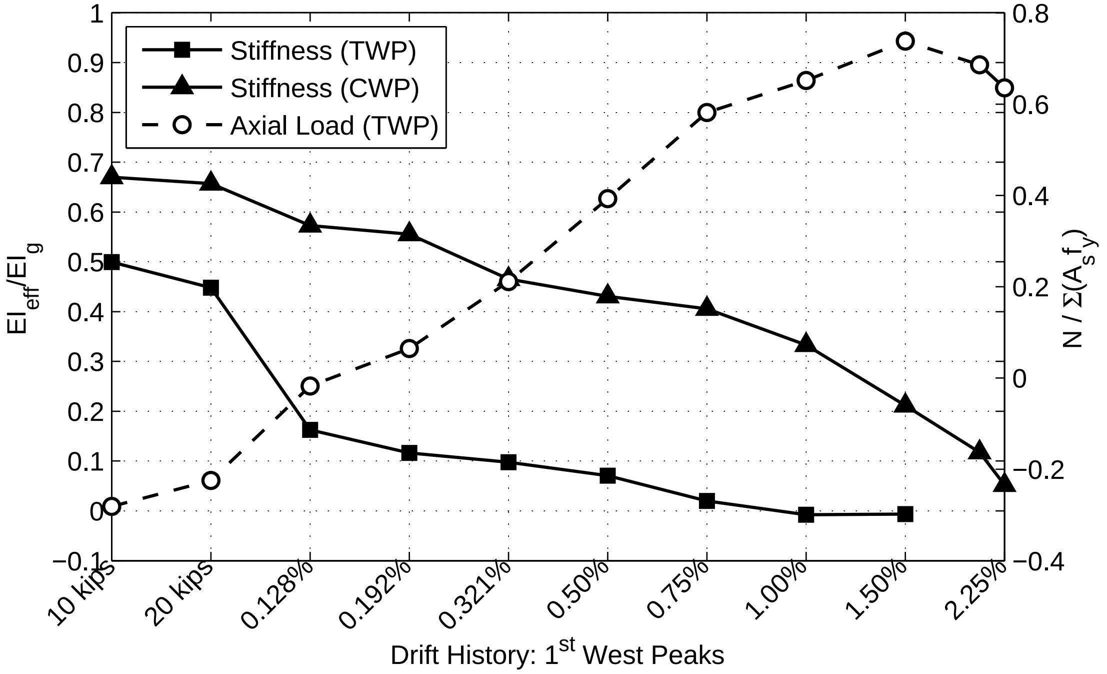

Figure 5.30: Flexural stiffness of wall piers plotted with TWP axial force (W- peaks)

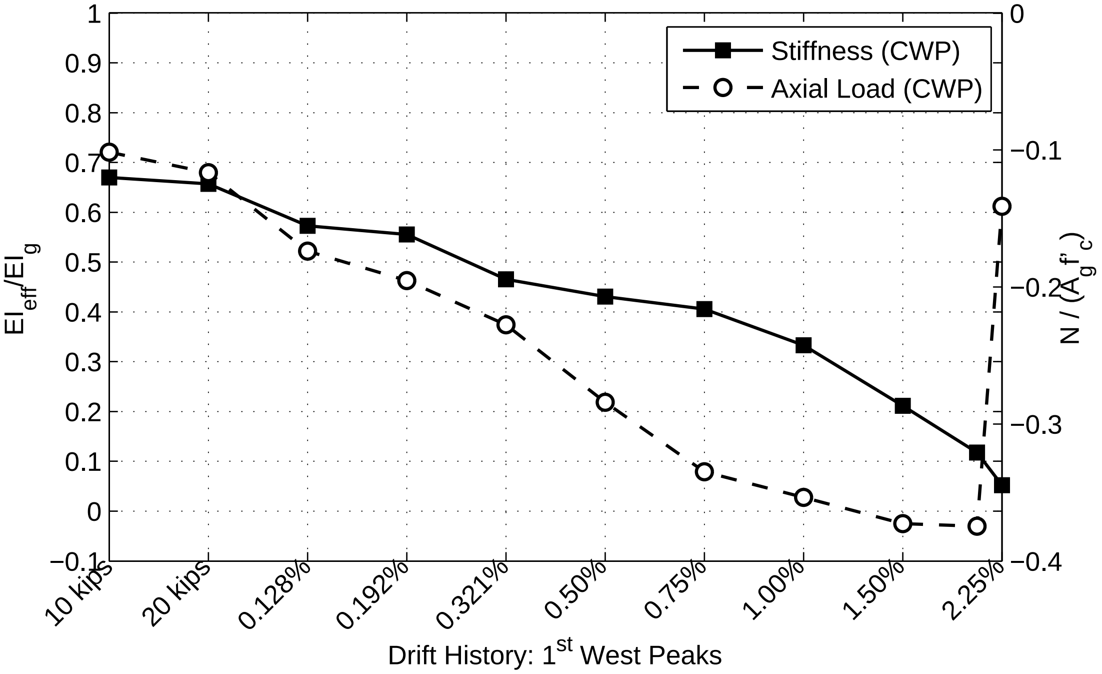

Figure 5.31: Flexural stiffness of WWP for increasing axial compressive demand

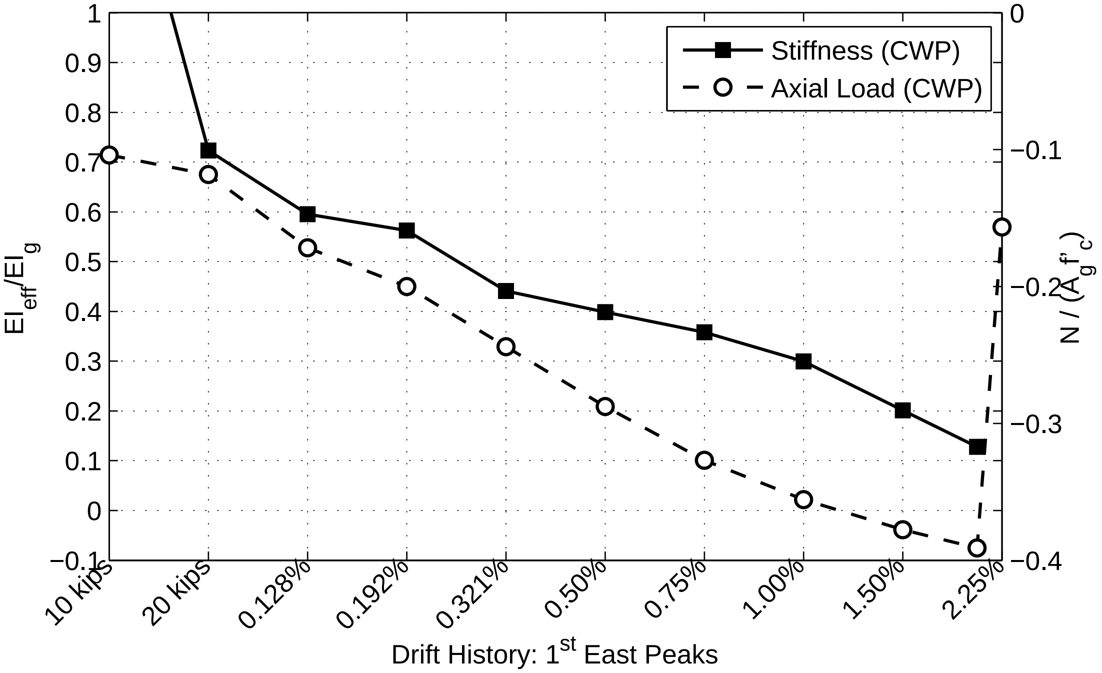

Figure 5.32: Flexural stiffness of EWP for increasing axial compressive demand

5.7 Wall Pier Demands

Due to the coupling behavior of the system, the axial, moment and shear demands in the compression wall can be quite significant. As the axial force in the tension pier increases due to the coupling moment, large cracks form and longitudinal reinforcement yields degrading the flexural and shear stiffness of the pier. As a result, the compression wall pier demands (i.e. moment and shear) increase in order to satisfy force equilibrium for a given horizontal displacement. However, in a typical coupled wall design, the shear is assumed to be equally distributed over each wall pier, and the and axial and shear stress demands are typically calculated using gross section properties. These calculations may be misleading in the sense that the axial and shear stress is most likely distributed over the the compression region of the compression wall pier (i.e. the area bounded by the neutral axis and the thickness of the wall). Thus, a more detailed analysis is needed to estimate the local axial and shear stress demands in a compression wall. In the following section a procedure is proposed to estimate the axial and shear demands for the compression wall pier at failure.

In design, the internal force demands in a concrete coupled wall structure are typically estimated using an equivalent elastic analysis or in special cases a nonlinear analysis. However, estimating the internal force demands in CW1 becomes more challenging due to the order of indeterminacy associated with the test setup. Therefore, the axial loads at the base of the wall were estimated using the results of Section 5.3. A typical free-body diagram used to determine the distribution of internal forces at the base of a given wall pier is shown in Figure 5.33a. For this study, the shear demand in the compression pier was estimated two ways. First, the axial forces in the specimen coupling beams were assumed to be equal to zero, so shear at the base of the compression pier is equal to the compression pier applied horizontal force, F_{x2}. As previously mentioned this assumption is quite un-conservative because a redistribution of shear force is common even during the cracking damage state. Second, the shear distribution between the two wall piers was

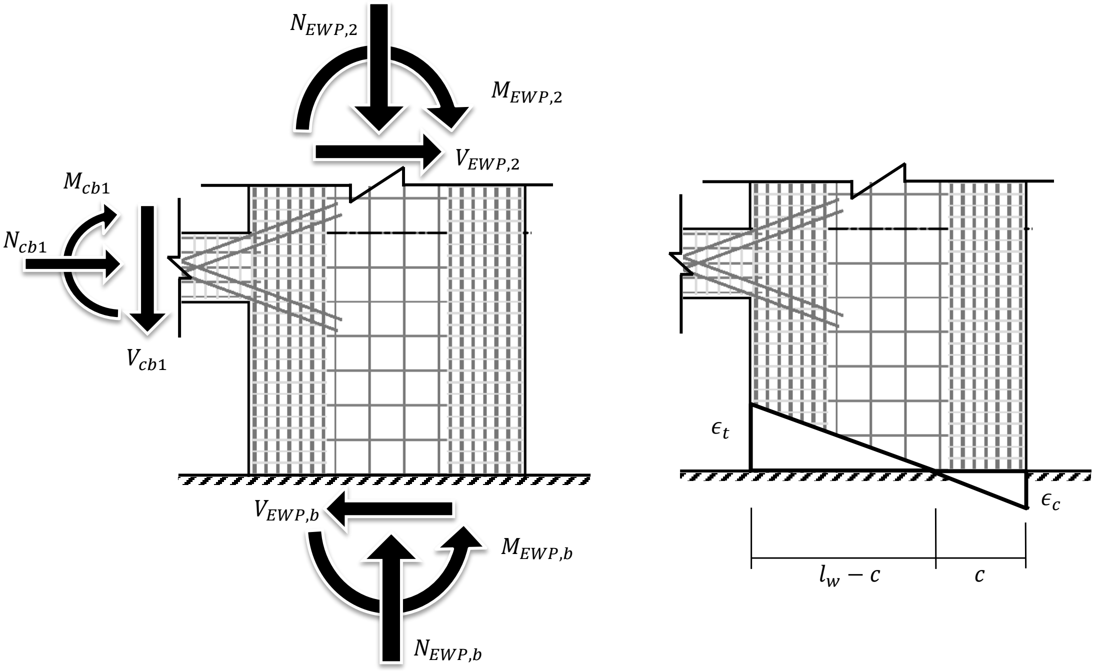

(a) Free-body diagram (b) Strain profile

Figure 5.33: Equilibrium and the assumed linear strain profile used to determine the stress demands at the base of the compression pier

approximated using the estimated shear demands from the VecTor2 analyses (Section 5.6). In these analyses, the shear in the compression wall at the end of the simulation approximated as 90% of the total base shear, V_b. This provides a better estimate of the shear demand at the base of the compression wall pier.

With the force demands known for the base of the wall pier, the neutral axis approximately 7.5 inches above the foundation was estimated using two rows of LED targets. Using the vertical strain profile of the LED data, a linear fit of these strains was performed to estimate the neutral axis location of the compressive wall pier on step prior to failure. In addition to the LED data, steel strain gauges approximately 7.5 inches above the foundation were used to determine the vertical strain profile and a linear fit of the data was used to estimate the neutral axis location. However, an engineer could simply estimate the neutral axis depth of the critical section using a moment-curvature program. The neutral axis calculated from moment-curvature analysis includes the estimated estimated axial compressive load at failure. The strain profiles for these three procedures as well as the linear fit of the Metris and strain gauge data is shown in Figures 5.34 and 5.35. Note in this study, only the neutral axis calculated using the Metris system and the moment-curvature was used because the strain gauge data does not estimate the neutral axis particular well due to the accumulation of plastic strain. While accumulated plastic strains are present in the LED data, the total strain is averaged over a length of 10.5 inches; whereas, the strain gauge measurements are local and affect the estimation of the neutral axis more.

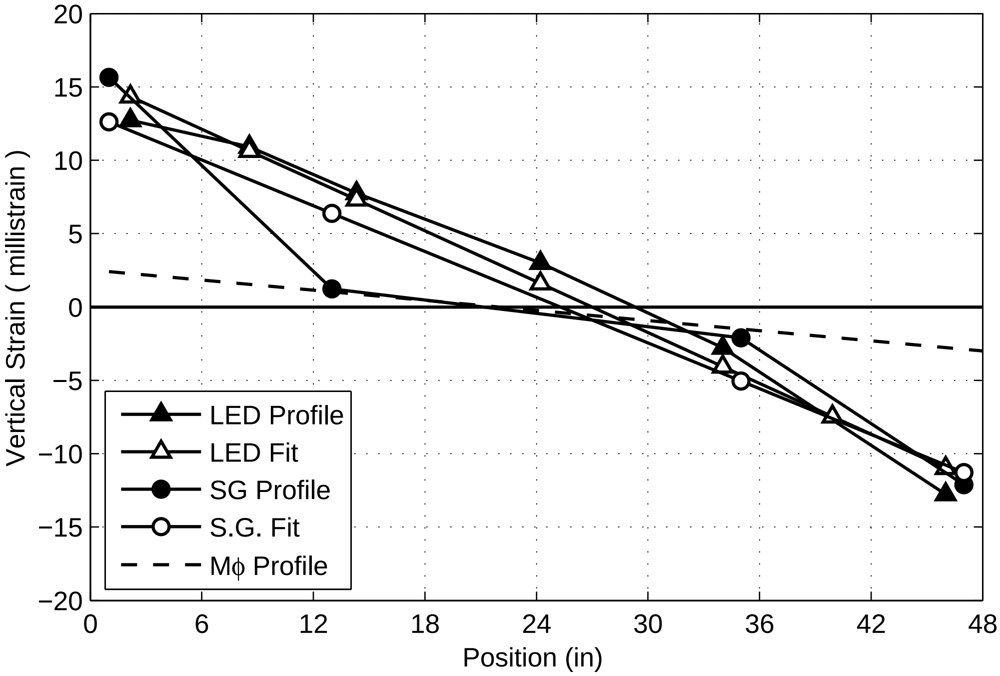

Figure 5.34: Vertical strain profile for the EWP at failure ≈ 7.5 inches above the base

Using the section geometry and the estimated neutral axis, the area over which the section carries compression and shear stress was calculated assuming all the associated force demands are only transferred through this reduced area. Furthermore, the section

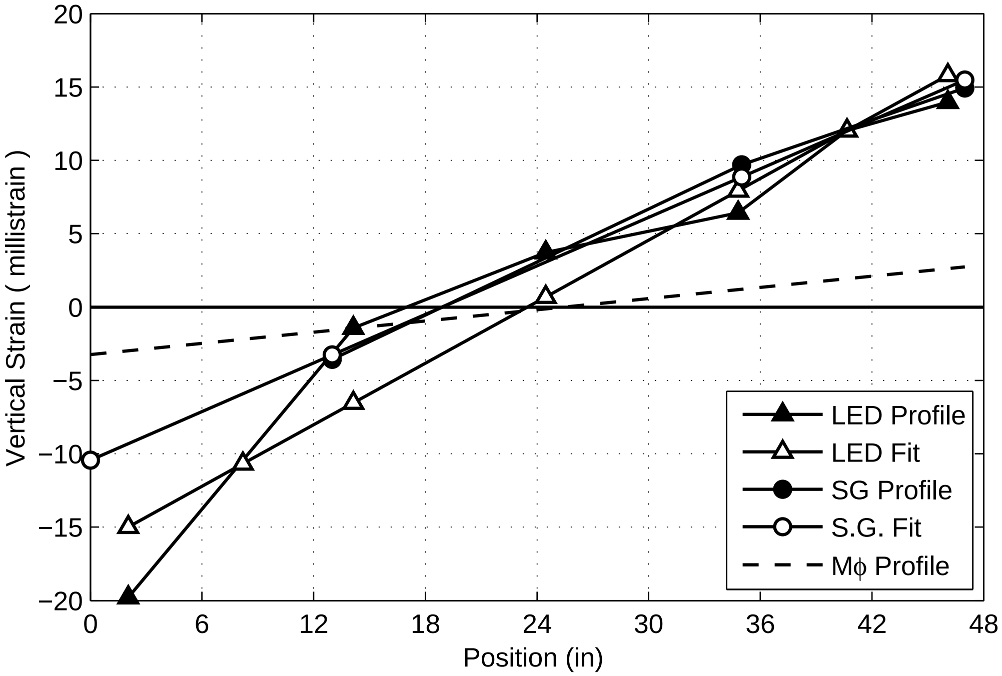

Figure 5.35: Vertical strain profile for the WWP at failure ≈ 7.5 inches above the base

loss due to spalling of the all concrete cover was included in this study to represent the approximate condition of the wall pier at failure. In addition to assuming demands are carried over these two defined areas, the area of the boundary element concrete core was used to estimate demands in the boundary element region only. Finally, the axial and shear stress demands were calculated, and the results of each study are shown in Tables 5.2 and 5.3. Estimating the stress demands using this procedure sheds light on the high demands estimated at failure during the test. Because the demands in the wall piers are not simply pure axial or pure shear demands but rather a combination of the two plus bending, there is a need to predict the force demands over a more accurate area rather than simply using the gross properties.

Table 5.2: Estimated demands in each wall pier at failure using Metris system

Demands	**WWP (-2.20%)**		**EWP (2.20%)**	
c	23.5 in		21.0 in	
A_c	$0.49A_g$		$0.44A_g$	
$A_{c,core}$	$0.40A_g$		$0.36A_g$	
$A_{BE,core}$	$0.23A_g$		$0.23A_g$	
N_e	-614 kips		-641 kips	
N_{gross}	$-0.37f'_cA_g$		$-0.39f'_cA_g$	
N_c	$-0.77f'_cA_g$		$-0.89f'_cA_g$	
$N_{c,core}$	$-0.94f'_cA_g$		$-1.10f'_cA_g$	
$N_{BE,core}$	$-1.66f'_cA_g$		$-1.73f'_cA_g$	
	$V_{cw} = F_{x2}$	$V_{cw} = 0.90V_b$	$V_{cw} = F_{x2}$	$V_{cw} = 0.90V_b$
V_e	95.5 kips	146 kips	102 kips	158 kips
V_{gross}	$4.4\sqrt{f'_c}A_g$	$6.7\sqrt{f'_c}A_g$	$4.7\sqrt{f'_c}A_g$	$7.3\sqrt{f'_c}A_g$
V_c	$9.0\sqrt{f'_c}A_g$	$13.7\sqrt{f'_c}A_g$	$10.8\sqrt{f'_c}A_g$	$16.6\sqrt{f'_c}A_g$
$V_{c,core}$	$11.0\sqrt{f'_c}A_g$	$16.8\sqrt{f'_c}A_g$	$13.2\sqrt{f'_c}A_g$	$20.4\sqrt{f'_c}A_g$
$V_{BE,core}$	$19.5\sqrt{f'_c}A_g$	$29.7\sqrt{f'_c}A_g$	$20.8\sqrt{f'_c}A_g$	$32.1\sqrt{f'_c}A_g$

Table 5.3: Estimated demands in each wall pier at failure using moment-curvature

Demands	**WWP (-2.20%)**		**EWP (2.20%)**	
c	26.6 in		26.1 in	
A_c	$0.55A_g$		$0.54A_g$	
$A_{c,core}$	$0.45A_g$		$0.44A_g$	
$A_{BE,core}$	$0.23A_g$		$0.23A_g$	
N_e	-614 kips		-641 kips	
N_{gross}	$-0.37f'_cA_g$		$-0.39f'_cA_g$	
N_c	$-0.68f'_cA_g$		$-0.72f'_cA_g$	
$N_{c,core}$	$-0.83f'_cA_g$		$-0.88f'_cA_g$	
$N_{BE,core}$	$-1.66f'_cA_g$		$-1.73f'_cA_g$	
	$V_{cw} = F_{x2}$	$V_{cw} = 0.90V_b$	$V_{cw} == F_{x2}$	$V_{cw} = 0.90V_b$
V_e	95.5 kips	132 kips	102 kips	139 kips
V_{gross}	$4.4\sqrt{f'_c}A_g$	$6.7\sqrt{f'_c}A_g$	$4.7\sqrt{f'_c}A_g$	$7.3\sqrt{f'_c}A_g$
V_c	$7.9\sqrt{f'_c}A_g$	$12.1\sqrt{f'_c}A_g$	$8.7\sqrt{f'_c}A_g$	$13.3\sqrt{f'_c}A_g$
$V_{c,core}$	$9.7\sqrt{f'_c}A_g$	$14.8\sqrt{f'_c}A_g$	$10.6\sqrt{f'_c}A_g$	$16.3\sqrt{f'_c}A_g$
$V_{BE,core}$	$19.5\sqrt{f'_c}A_g$	$29.7\sqrt{f'_c}A_g$	$20.8\sqrt{f'_c}A_g$	$32.1\sqrt{f'_c}A_g$

5.8 Strain Fields

Displacement fields in finite continuum software provide engineers with a qualitative and quantitative way to determine the local deformation demands throughout their component. Therefore, to validate these types of analyses, there is a need to calculate these measurements using experimental data. One of the main advantages of non-contact measuring devices such as the Metris system or the photogrammetry system, is the ability provide an accurate displacement field for a grid of targets just like a continuum software. These systems were previously discussed in more detail in Section 3.4. In the following section, the strain fields for CW1 were calculated using both the Metris system for the first and second stories and the photogrammetry system for all three stories. While strain field results for CW1 are presented in detail below, additional time-lapse strain field movies are provided at `http://www.youtube.com/user/NEESRWallProject`.

The geometric grid of targets used to capture the displacement field using these two non-contact systems are shown in Figures 3.11 and 3.12. Each target measured the x, y and z global displacements, so a “zero” step was taken before the start of the test in order to accurately determine the location of the target without applied forces. Then knowing the displacement of the target thereafter, the relative displacements of the target could be calculated throughout the test. First a series of elements composed of four or five nodes were determined for both systems. With the locations and deformations of the element nodes defined, an isoparametric formulation was used to determine the approximate strain field of the element (Zienkiewicz and Taylor, 2005). In general, the grid of targets is broken up into four-node quadrilateral elements. However, in the case of the photogrammetry system, on the wall piers near the wall-to-beam interface, there is a mesh discontinuity due to the refined coupling beam mesh. This issue is addressed by using a five-node quadrilateral element. In Figure 5.36 an illustration of the isoparametric mapping for the five-node quadrilateral is shown.

For a given element, the strains at each node were calculated using the formulation

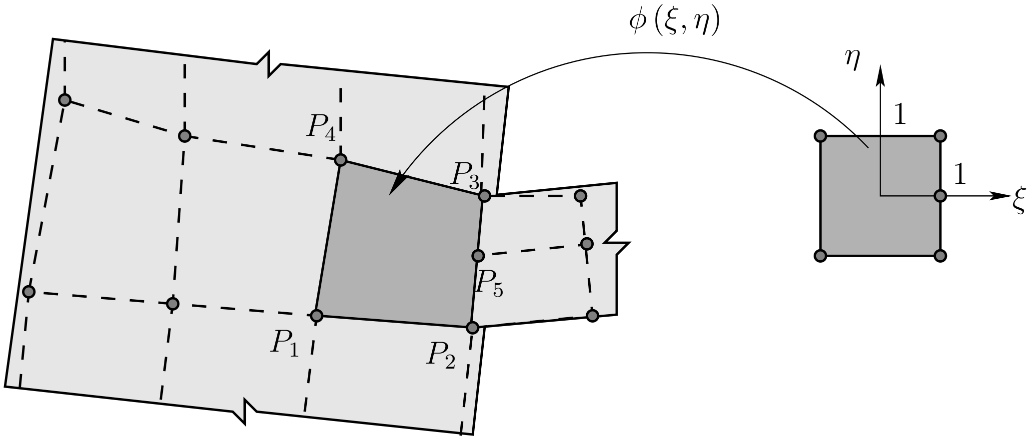

Figure 5.36: Example of five-node quadrilateral element used in strain calculation

discussed in the last paragraph. Consequently, calculating the strains at each node for each element in the wall specimen, results in multiple values of a given strain type associated to one node. This is not consistent with typical continuum finite element software where a strain or stress field would be "smoothed" over the entire mesh. Therefore, the strain fields for the specimen were smoothed at all the nodes connecting two of more elements. The smoothing process is a weighted average of the strain at a particular node for a given a number of adjacent elements. Using this procedure, the strain fields were determined to better understand the local deformation behaviors of CW1.

5.8.1 Principal Compressive Strains, ϵ_2

Figures 5.37 – 5.41 show the principal compressive strains for CW1 at drift levels which are associated with key wall pier damage states. Because many of the LEDs or photogrammetry targets are attached to the concrete directly, targets are lost during the test due to concrete cover spalling. Additionally, problems with the strain measurements due targets being damage or moving out of the capture window, as in the case of the Metris CCD camera, occur throughout the test. In order to distinguish the differences in the displacement field, each nodal displacement was amplified by a factor of 10. Note the strain concentrations occurring at the tops of the wall piers in Figures 5.37c and 5.37d. This is an anomaly in the strain calculation, and it is caused because there are only three camera used to calculated the top row of nodal displacements. Whereas, the other nodal measurements are calculated using five or more cameras which drives up the accuracy of the measurement. Finally, due to the loss of targets after the failure of the EWP, the strain fields calculated at 2.00 and 2.20% drift are shown in Figure 5.41 rather than the peak drift of 2.27%.

The principal compressive strain during the 0.321% drift level is roughly -1000 $\mu\epsilon$, and during this drift level the damage in the wall piers is associated to horizontal and diagonal cracking in the tension wall and minor horizontal cracking of the IBE of the compression wall. At initial spalling (1.00% drift) the principal compressive strain in the EWP 24 inches above the foundation (i.e. location of spalling and splitting) reached -3090 $\mu\epsilon$, and principal compressive strain in the WWP 2 inches above the foundation (i.e. location of spalling and splitting) reached 3120 $\mu\epsilon$. Each strain exceeds the strain value, -0.003, associated with nominal moment strength, according to ACI 318-08. When moderate spalling occurs in both wall piers at 1.50%, a majority of the concrete cover up to approximately 34 inches above the WWP foundation and 40 inches above the EWP foundation, had spalled. The respective principal compressive strains, measured two inches above the foundation, at this damage states were -4220 $\mu\epsilon$ and -4700 $\mu\epsilon$ for the WWP and EWP, respectively. Finally, due to concrete spalling in the last cycle on the south face of the EWP base, most of the LEDs and photogrammetry targets were erroneous, and this loss in the strain results due to spalling can be seen in Figures 5.41c and 5.41d. However, the principal compressive strain calculated two inches above the EWP foundation at 2.00% drift measured -6280 $\epsilon\mu$, and similarly the compressive strain calculated 12 inches above the WWP foundation measured -5120 $\epsilon\mu$ at -2.00% drift.

5.8.2 Shear Strains, γ

Principal compressive strain is important to engineers because concrete constitutive models developed in finite element software typically use this deformation measure to calculate concrete stresses of an element. In addition to the principal compressive strains, the shear strains were calculated for key damage states during the test. In Figures 5.42 – 5.46, the smoothed shear strain values are plotted at drift levels associated with damage. While, the magnitude of the shear strains are small during the 0.321% drift level, the deformations approximately double in the tension wall when yielding starts to initiate (i.e. 0.50% drift). These increasing shear deformations in the second and third story tension wall highlights the degradation of stiffness which results in “shedding” of the internal shear forces from the tension wall to the compression wall via the coupling beams. After the coupling beams and tension wall pier yields in the 0.50% drift cycle, the global stiffness is reduced and the redistribution of internal forces increases the demand on the compression wall. Consequently, diagonal cracks in the IBE of the compression wall form and an increase of shear deformation during the 1.00 and 1.50% drift levels results. This behavior is clearly seen in Figures 5.44 and 5.45. In the steps prior to failure, Figure 5.46, the shear strains in the tension wall are in excess of 6000 $\mu\epsilon$.

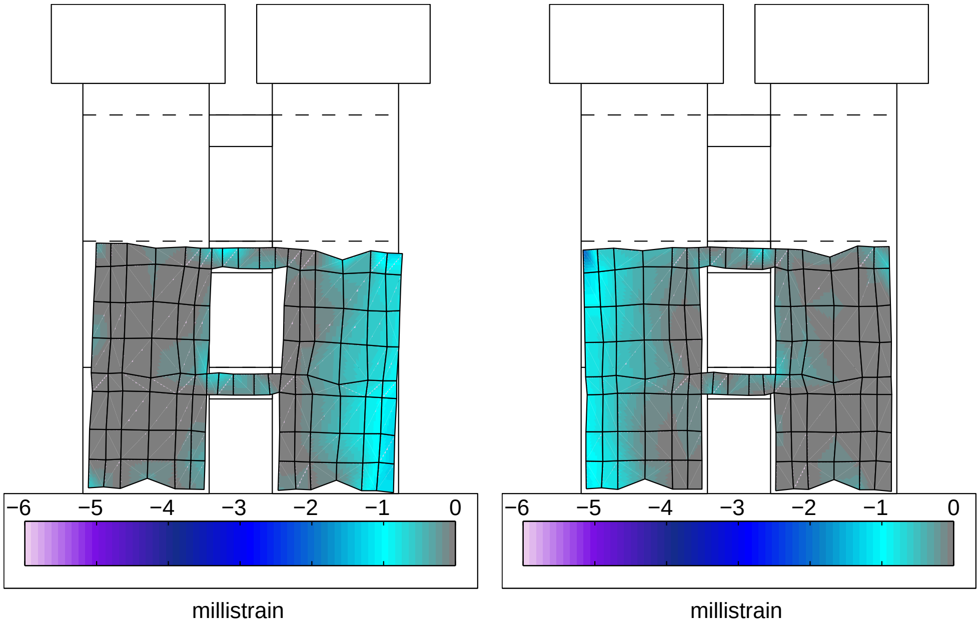

(a) 0.321% (Metris)

(b) -0.321% (Metris)

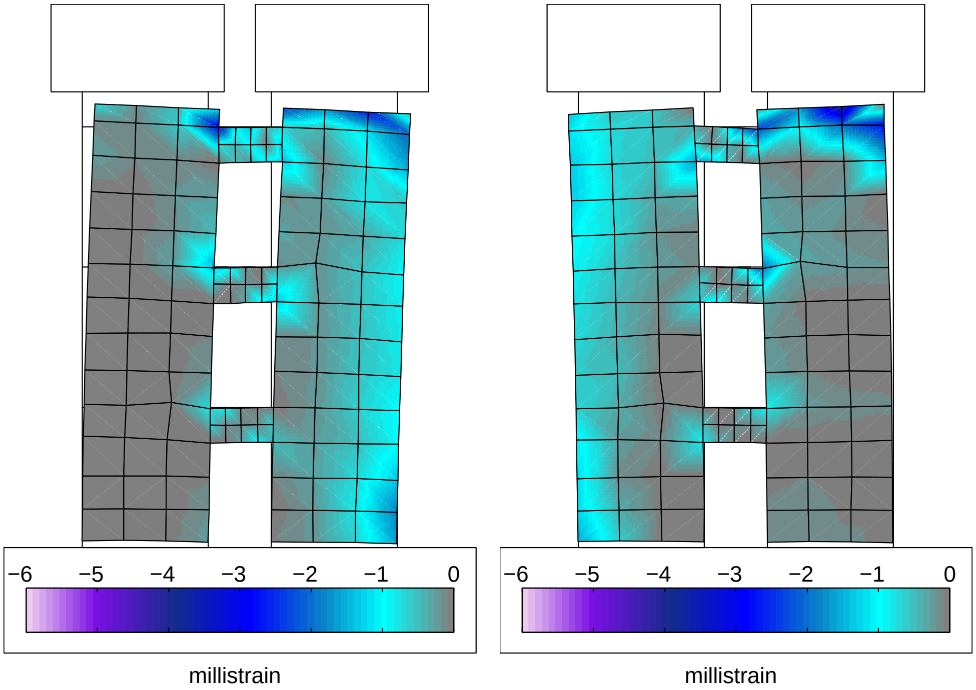

(c) 0.321% (Photogrammetry)

(d) -0.321% (Photogrammetry)

Figure 5.37: ϵ_2 field at ± 0.321% (A) (diagonal cracking)

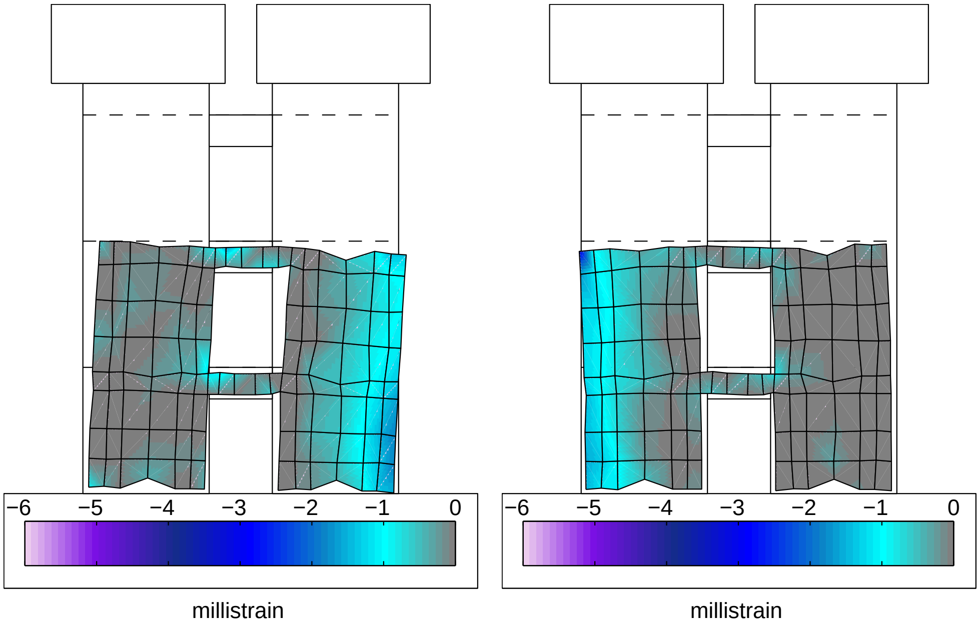

(a) 0.50% (Metris)

(b) -0.50% (Metris)

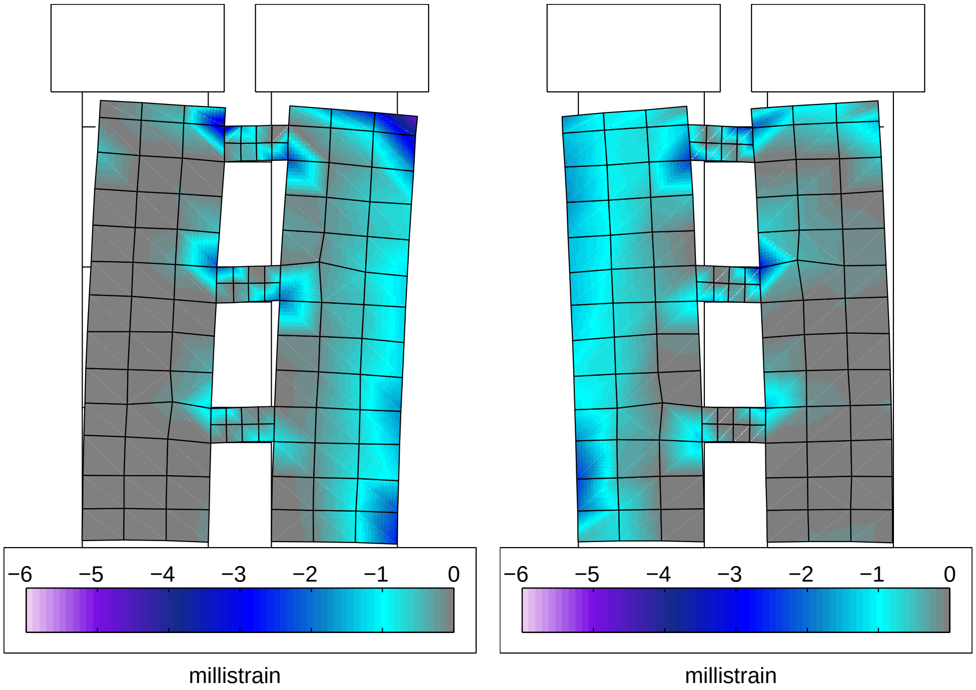

(c) 0.50% (Photogrammetry)

(d) -0.50% (Photogrammetry)

Figure 5.38: ϵ_2 field at ± 0.50% (A) (yielding)

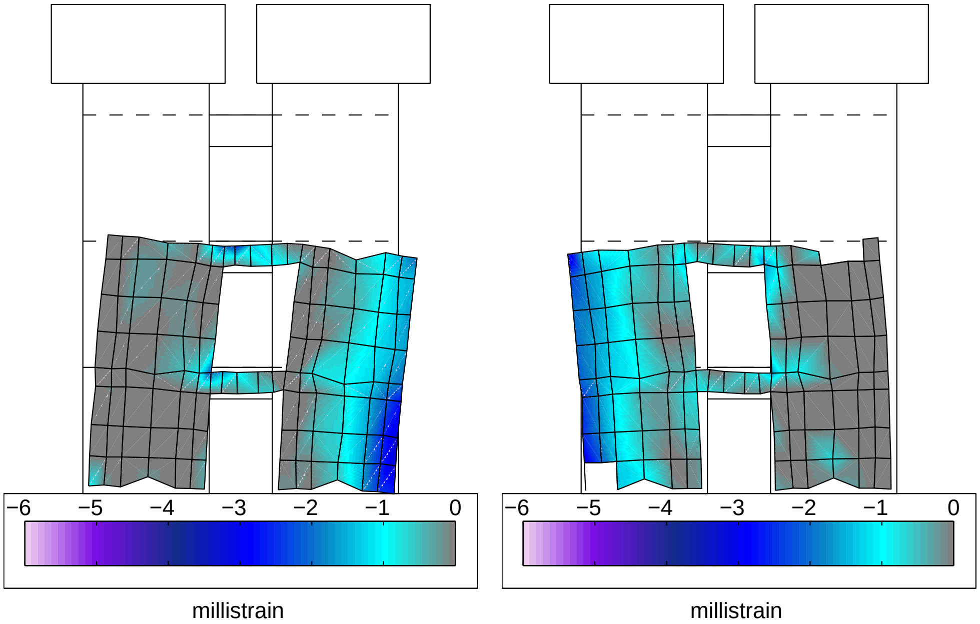

(a) 1.00% (Metris) (b) -1.00% (Metris)

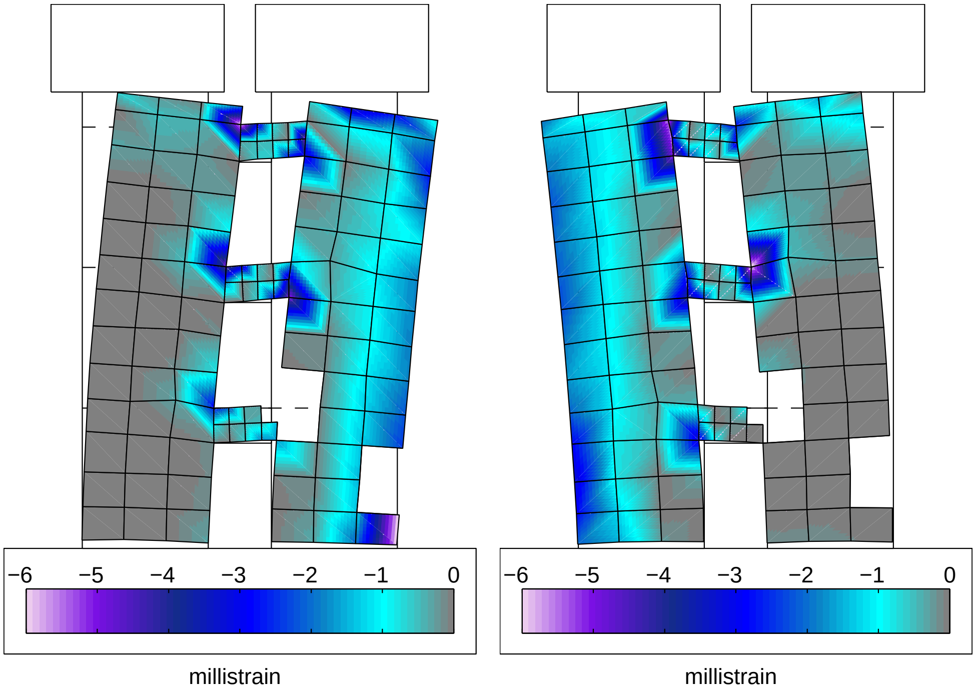

(c) 1.00% (Photogrammetry) (d) -1.00% (Photogrammetry)

Figure 5.39: ϵ_2 field at ± 1.00% (A) (initial spalling)

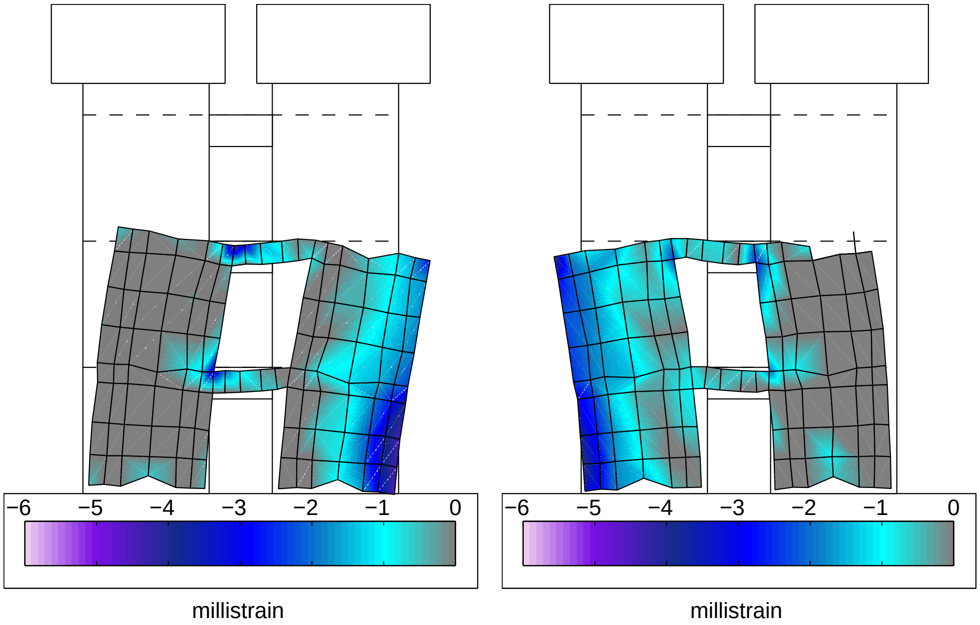

(a) 1.50% (Metris)

(b) -1.50% (Metris)

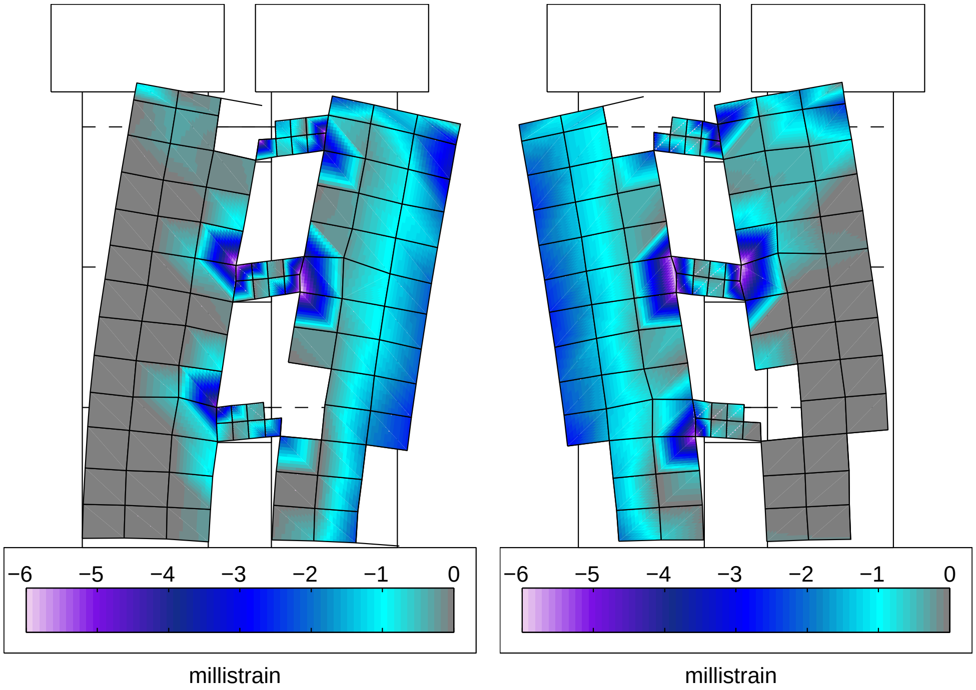

(c) 1.50% (Photogrammetry)

(d) -1.50% (Photogrammetry)

Figure 5.40: ϵ_2 field at ± 1.50% (A) (moderate spalling)

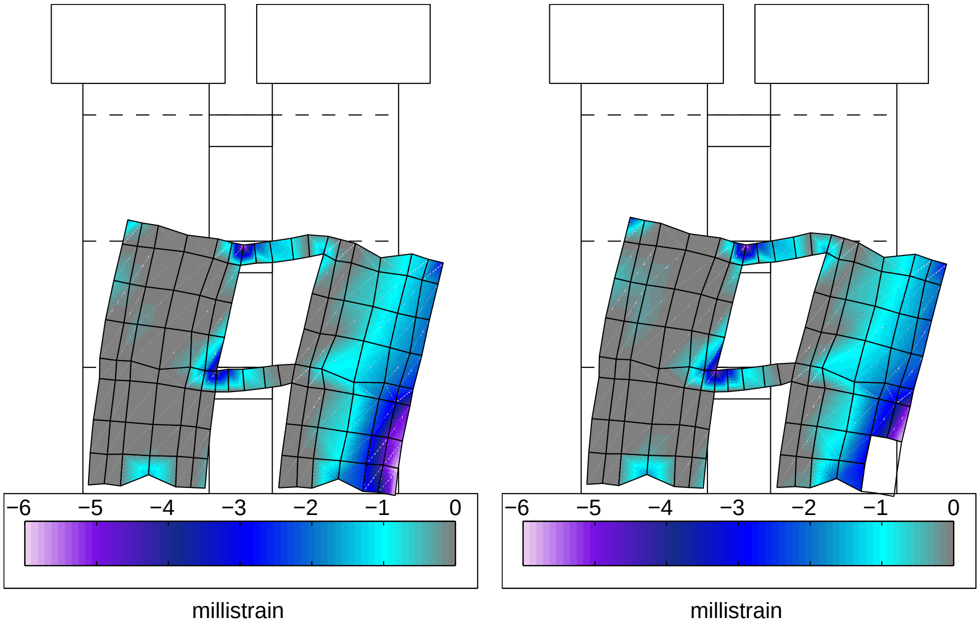

(a) 2.00% (Metris) (b) 2.20% (Metris)

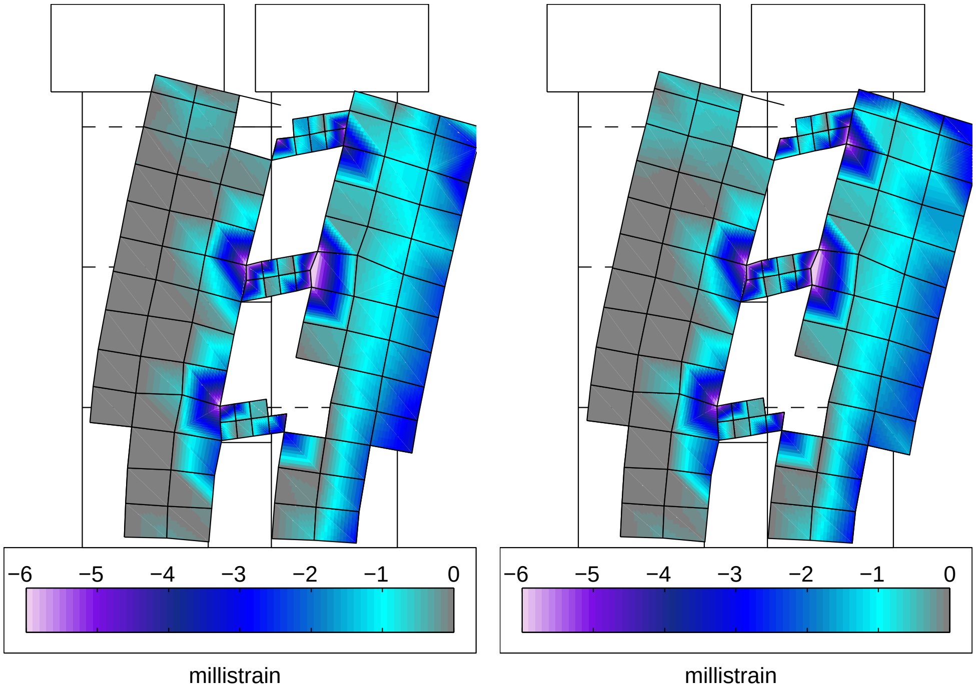

(c) 2.00% (Photogrammetry) (d) 2.20% (Photogrammetry)

Figure 5.41: ϵ_2 field near failure of the east wall pier (2.25% E+ drift level)

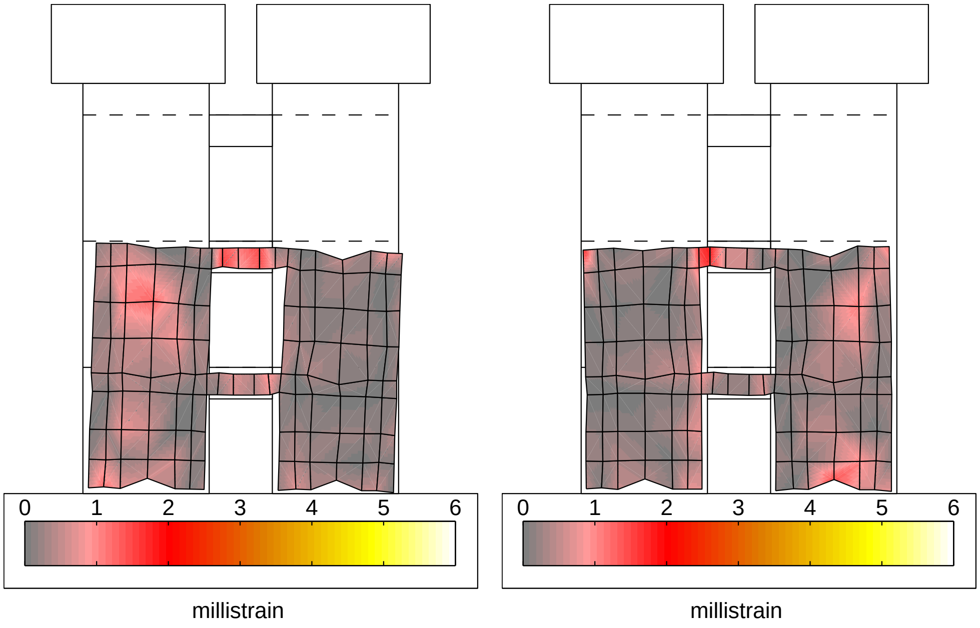

(a) 0.321% (Metris) (b) -0.321% (Metris)

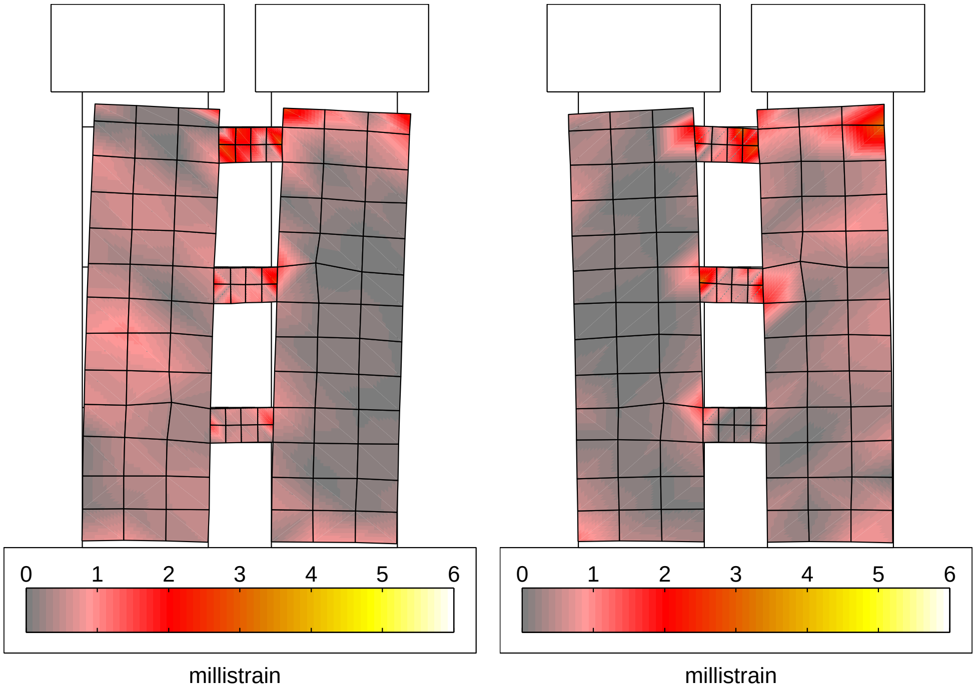

(c) 0.321% (Photogrammetry) (d) -0.321% (Photogrammetry)

Figure 5.42: γ field at ± 0.321% (A) (diagonal cracking)

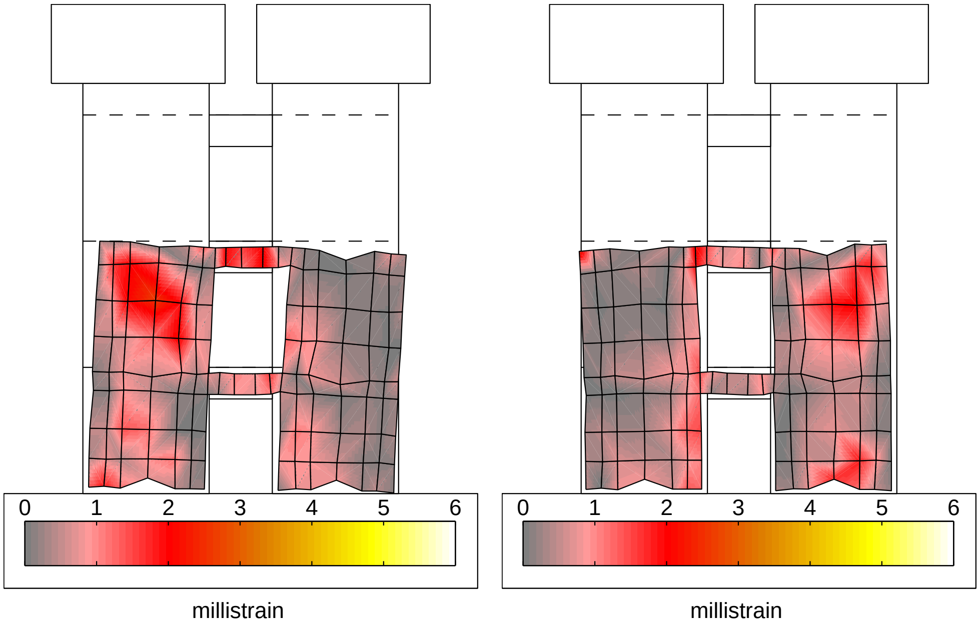

(a) 0.50% (Metris)

(b) -0.50% (Metris)

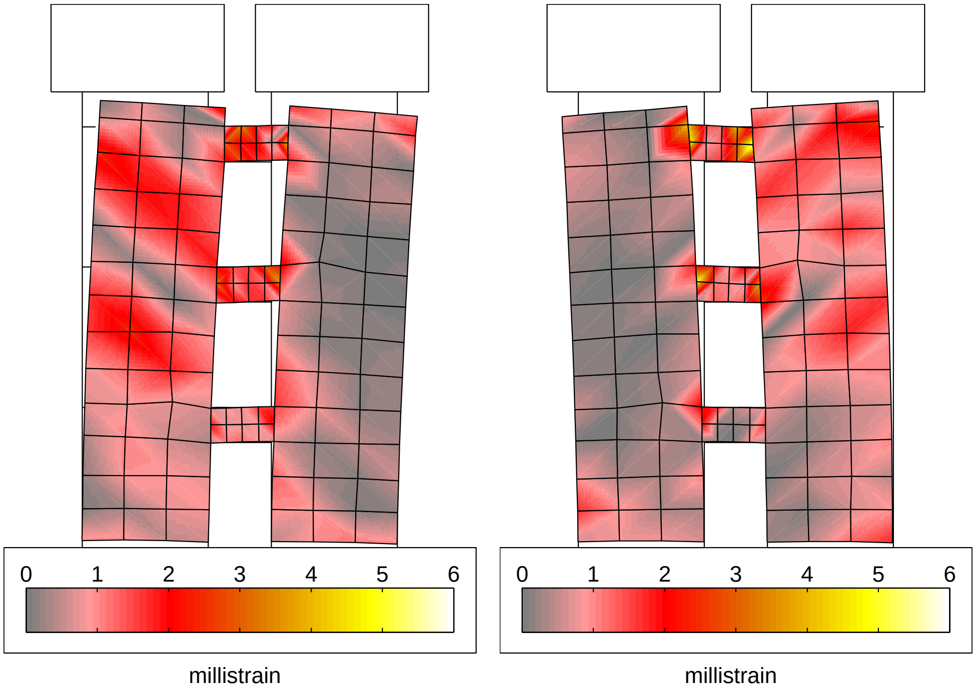

(c) 0.50% (Photogrammetry)

(d) -0.50% (Photogrammetry)

Figure 5.43: γ field at ± 0.50% (A) (yielding)

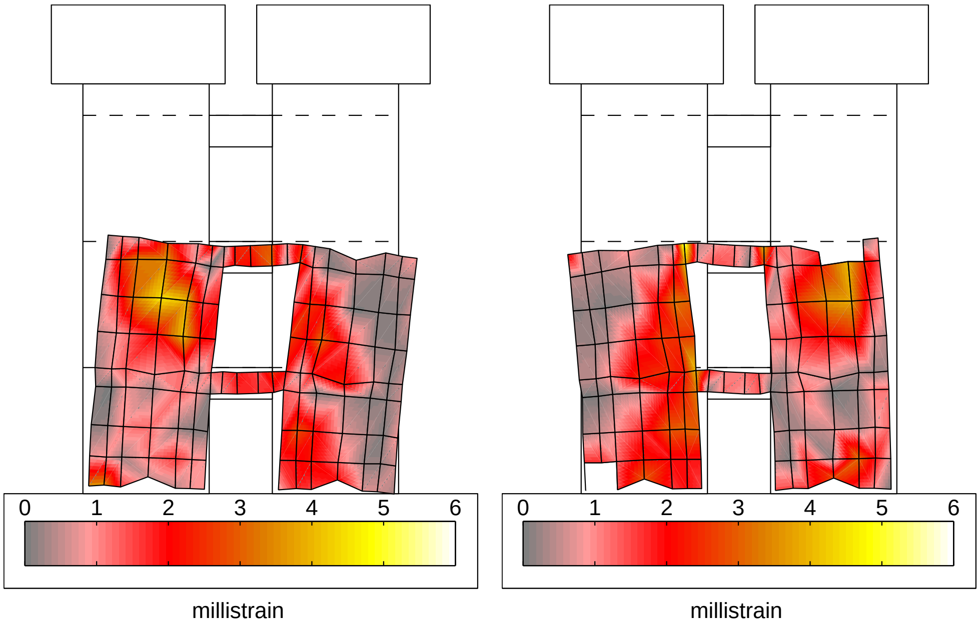

(a) 1.00% (Metris) (b) -1.00% (Metris)

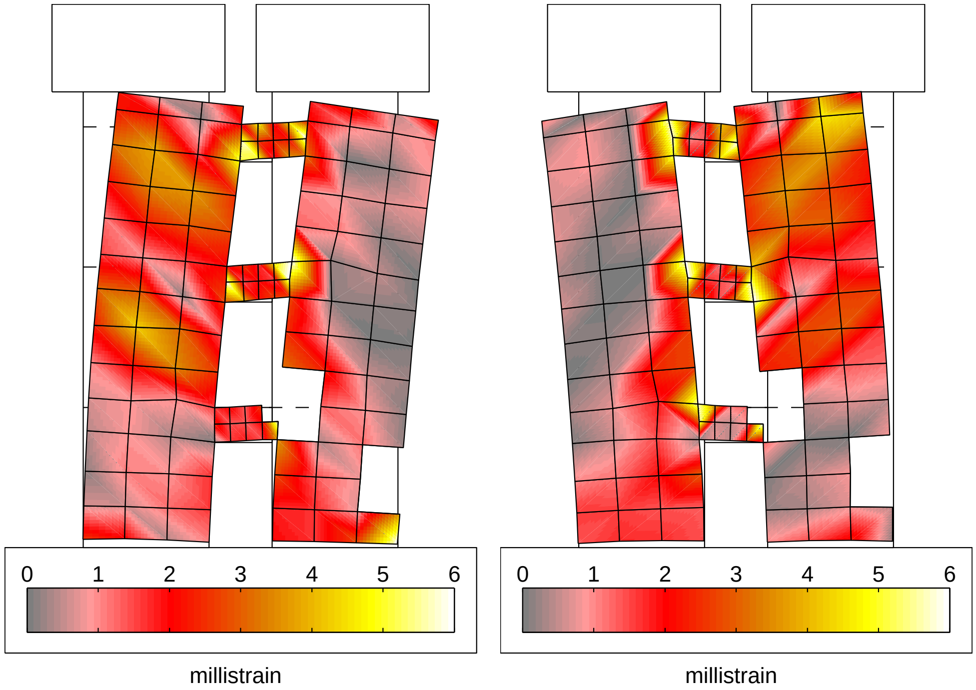

(c) 1.00% (Photogrammetry) (d) -1.00% (Photogrammetry)

Figure 5.44: γ field at ± 1.00% (A) (initial spalling)

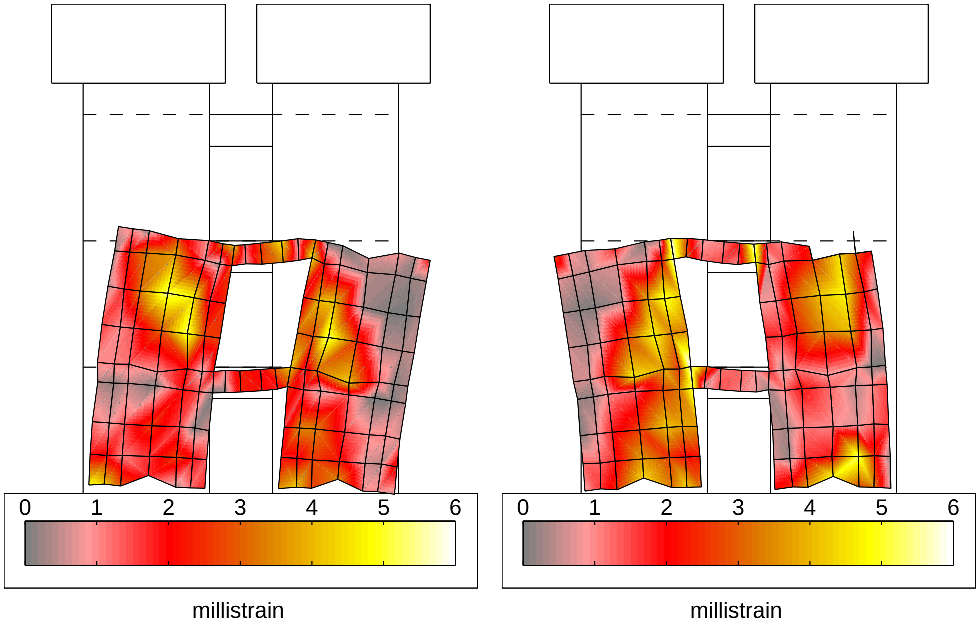

(a) 1.50% (Metris) (b) -1.50% (Metris)

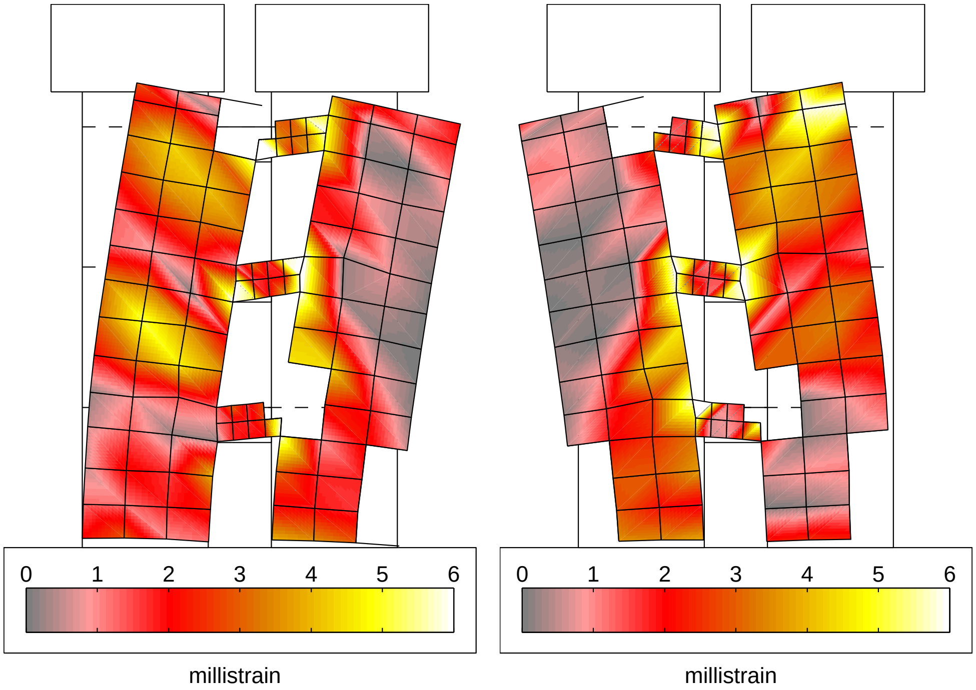

(c) 1.50% (Photogrammetry) (d) -1.50% (Photogrammetry)

Figure 5.45: γ field at ± 1.50% (A)(moderate spalling)

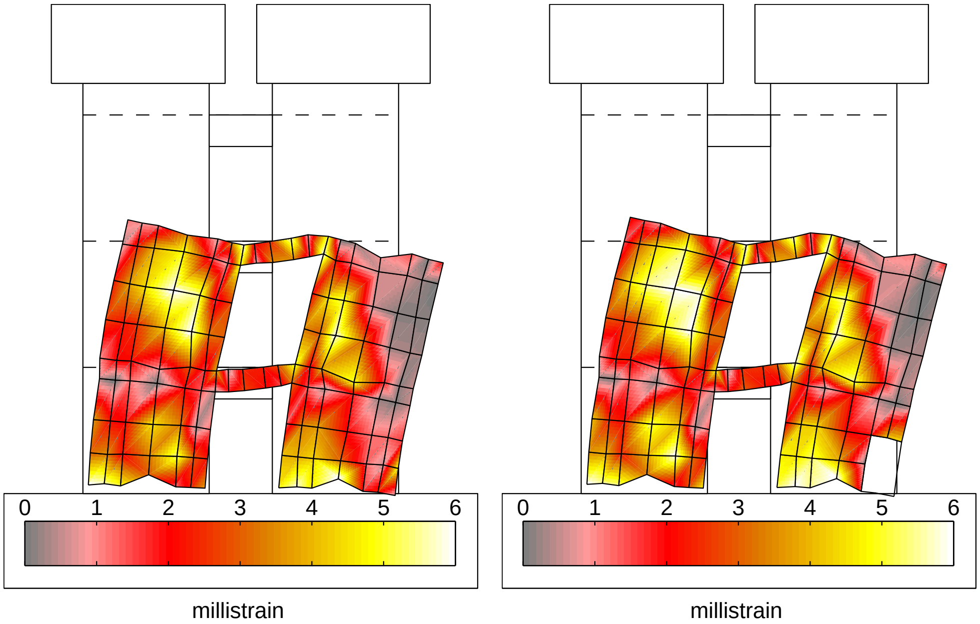

(a) 2.00% (Metris) (b) 2.20% (Metris)

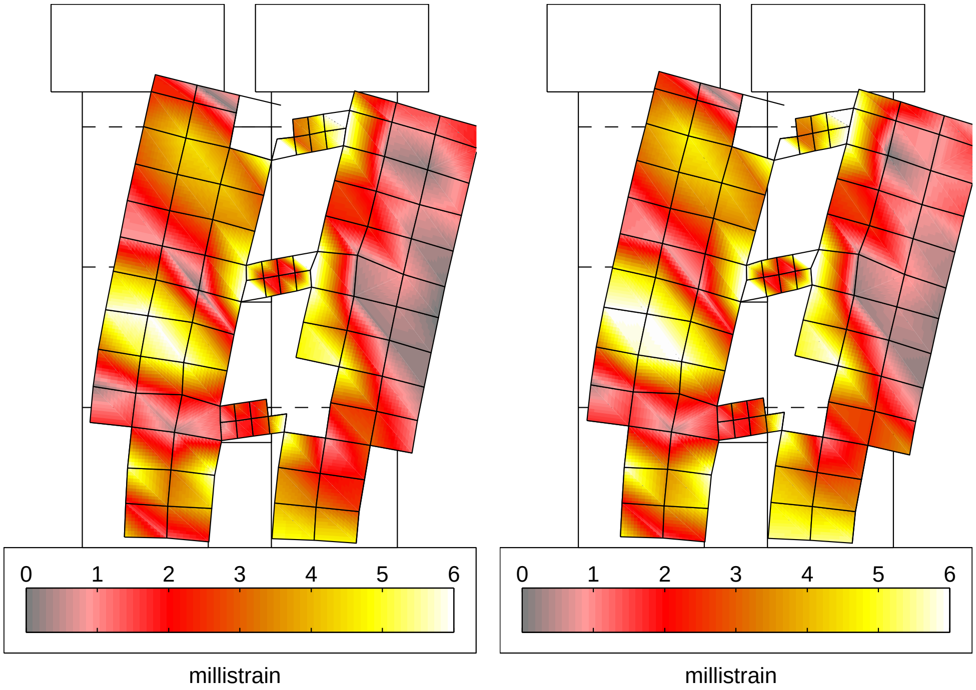

(c) 2.00% (Photogrammetry) (d) 2.20% (Photogrammetry)

Figure 5.46: γ field near failure of the east wall pier (2.25% E+ drift level)

5.8.3 Vertical Strains, ϵ_z

Due to the loss of targets during the higher drift levels, vertical strain results at the toe of each wall pier was calculated using the single column of LEDs that were glued to the embedded rods used to anchor LVDTs; these LEDs were not affected by the loss of concrete cover. These instruments were aligned vertically, two inches in from the edge of the IBE and the OBE of both wall piers. For the inner and outer edges of each wall pier, the vertical strain was calculated using two LEDs positioned approximately 12.5 inches and 2.0 inches above the foundation block. The locations of the LEDs used in the calculation of these vertical strain measurements for the WWP are shown in Figure 5.47.

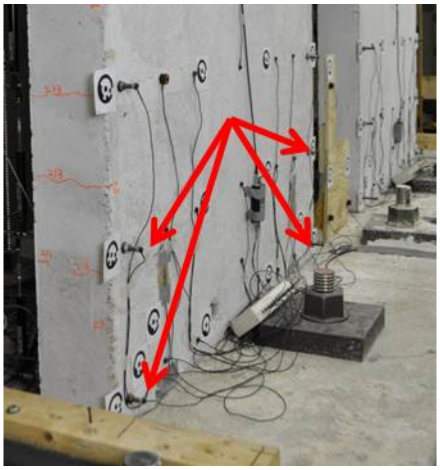

Figure 5.47: Location of WWP LEDs used to calculate vertical strain values

Table 5.4 provides the results of the vertical strain measurements, calculated from the single column of LED targets, at key damage states for the four regions specified above; strains calculated using the isoparametric formulation are included for comparison in Appendix C. Both results stemming from loading in the E+ and W- directions are included in this table. Note: bold face text indicates the average vertical strain over the given region (≈10.5 inches) has reached the tensile yield strength of the longitudinal reinforcement. Also note under DS3, two additional drift levels were included to capture the specimen behavior prior to failure. Some data are not provided for the last three drift levels because crushing results in loss of the gauge anchor rod.

The data in Table 5.4 suggests the base of the WWP and EWP fully yield in during the 2.0% and 1.5% drift level, respectively. Yielding accross the entire wall pier results in a lot of energy dissipation in the tension wall pier and ideally the response of theis wall is very ductile. On the other hand, the magnitude of tensile strain to compressive strain in the compression wall pier suggests the flexural reposne is more constant with an isolated wall under a large amount of compression force. Large vertical strains in the compression pier near the moment of crushing and bar buckling (i.e. 2.20% - 2.27% drift) are consistant with the damage seen in the base of the wall piers.

Table 5.4: Vertical strain, ϵ_z, measurements at base of each wall pier ($\mu\epsilon$)

		First East Peak (E+)				**First West Peak (W-)**			
		WWP		**EWP**		**WWP**		**EWP**	
DS	**Drift**	**OBE**	**IBE**	**IBE**	**OBE**	**OBE**	**IBE**	**IBE**	**OBE**
DS0	0.321%	1410	103	633	-1170	-1050	817	60.0	1700
DS1	0.50%	**2340**	114	833	-1560	-1410	1330	426	**2350**
DS2	1.00%	**6910**	919	2200	-2680	-2360	**2590**	568	**6340**
DS3	1.50%	**9990**	1260	**7554**	-4740	-3290	**7440**	**2850**	**10700**
	2.00%*	**14000**	**3470**	**11400**	-6350	-9210	**12600**	**4680**	–
	2.20%*	**14700**	**3590**	**12700**	-12800	-19800	**14000**	**4510**	–
DS4	2.27%	**14600**	**2853**	**11900**	-47600	-35800	**12600**	**3990**	–

Bold face: $\epsilon_z \geq \epsilon_y$
* Not a peak drift

5.8.4 Use of ϵ_z to assess if wall is compression-controlled per ACI 318-08

During the design of the CW1 wall piers, adequate longitudinal reinforcement was appropriated to the wall section to provide sufficient moment strength while still maintaining the strain condition requirements for a tension-controlled cross-section. The strength reduction factor, ϕ, accounts for the following effects on sectional strength of a reinforced concrete member (ACI, 2008):

- Uncertainty in strength due to variability in material properties and dimensions
- Design equation inaccuracies

Figure 5.48 provides the definition of the strength reduction factor as defined by ACI 318-08. When the section is tension-controlled the factor is 0.9, and when the section is compression-controlled the factor is 0.65. Between the two limits the strength reduction factor is linearly interpolated. The reduction in the factor for a compression-controlled section is intended to account for i) the loss in ductility of a compression-control section, ii) that these members are usually supporting larger areas of load and iii) a compression-controlled section typically has a higher sensitivity to the variations in concrete strength. Based on the results of Table 5.4, the strain conditions for a tension-controlled sections were checked for the compression wall using the vertical strain measurements presented above.

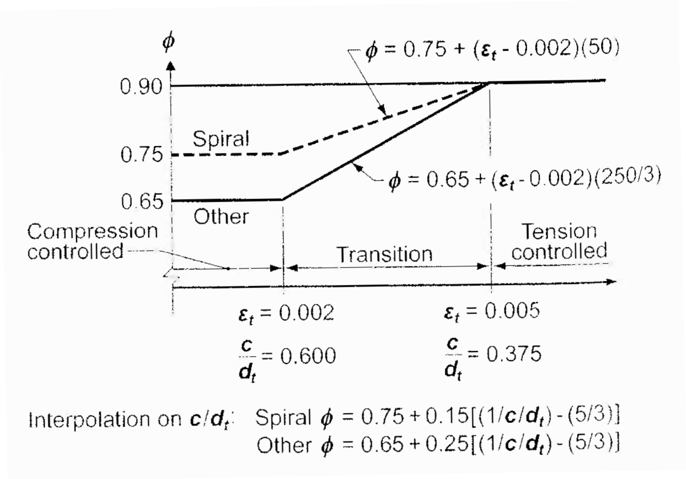

Figure 5.48: Variation of ϕ with net tensile strain, ϵ_t (ACI, 2008)

$P = \sum 1.25V_n, cb + 0.1 f'_c A_g$ The results of this study are presented in Table 5.5 and by ACI's definition, the EWP behaved in the transition zone between a tension-controlled

Table 5.5: Tension-controlled verification of compression wall piers using measured strains

	WWP (W-)				**EWP (E+)**			
Strain Condition	**Step**	**Drift**	**Strain**	ϕ	**Step**	**Drift**	**Strain**	ϕ
ϵ_t @ $\epsilon_c \approx -0.003$	832	-1.50%	0.0070	0.9	787	-1.12%	0.0029	0.725
ϵ_c @ $\epsilon_t \approx 0.005$	829	-1.27%	-0.0023	0.9	790	-1.35%	-0.0040	<0.9

and a compression-controlled section; however, the wall piers were designed to act in a tension-controlled manner as defined by ACI. In the design, the flexural strength of the wall piers were determined using the factored moment and axial demands resulting from an elastic analysis where the design forces resulted from the ASCE 7-05 lateral load distribution.

To identify the differences between the design assumptions and an actual behavior shown in Table 5.5, a similar study was completed using moment-curvature analysis. Two cases were identified as an upper and lower bound on the compressive axial load in the wall pier. First a moment-curvature analysis on the wall pier cross-section was completed with an axial force equal to the gravity load applied to the wall piers (-$0.1A_gf'_c$). Next the axial compression was increased to $-0.37f'_cA_g$ to accounts for the additional accumulation of axial force as a result of the coupling beams reaching their probable shear strength, $1.25V_{n,cb}$. This is consistent with the axial force that would be calculated using the ICC (2007) recommendation for a plastic analysis. The resulting axial load applied to the wall pier cross-section was $P = \sum 1.25V_{n,cb} + 0.1f'_cA_g$. The design material properties were used in this calculation to give the ideal difference between design and actual wall pier response.

The results of this study are shown in Table 5.6. While the gravity load provides a tensile strain representative of tension-controlled behavior, the strain profile in the wall pier under the upper-bound axial force would mean the strength reduction factor, ϕ, would need to be reduced to 0.70.

Table 5.6: Tension-controlled verification of compression wall pier using moment-curvature analysis and design material strengths (i.e. $f_y = 60$ ksi and $f'_c = 5$ ksi)

Strain Condition	**Axial Load**	**Strain**	ϕ
ϵ_t @ $\epsilon_c \approx -0.003$	$-0.1 f'_c A_g$	0.00865	0.9
ϵ_t @ $\epsilon_c \approx -0.003$	$-0.37 f'_c A_g$	0.00255	0.7

5.9 Deformation Components

The local strain field data provide a quantitative view of deformations at key areas in the wall piers and coupling beams. However, from the strain field data, it is difficult to understand the impact. To assess this impact, the contribution of local deformation mechanisms to the total lateral displacement at the third story of each wall pier was computed. Local deformation mechanisms considered included base rotation, base slip, flexure and shear. Researchers have developed techniques using different configurations of instruments to capture these deformation mechanisms, and a detailed study of the use of these techniques are discussed in Birely (2011). On the basis of these, Birely (2011) proposes a technique for measuring the source of wall deformation for four planar walls that are a part of this research program. The following section applies the deformation contribution techniques developed by Birely (2011), to calculate the total contribution of each deformation mechanism for the CW1 specimen.

The lateral movement of each wall pier was measured using the photogrammetry system and absolute displacement transducers. The lateral displacement as measured by the photogrammetry system was computed as the average horizontal displacement of top row of targets. The layout of photogrammetry targets is shown in Figure 3.12; the vertical location of the top row of targets was approximately 150 inches above the foundation. In Figures 5.49 and 5.50, the lateral drift of each wall pier using the photogrammetry system is plotted against the lateral drift measured using the in-plane transducers, which are attached to the center wall piers approximately 154 inches above the foundation (Figure

3.14). The data is Figures 5.49 and 5.50 show there is very little noticeable difference between each measurement system. Ultimately, lateral displacements of each wall pier was determined using the photogrammetry system.

The Metris and photogrammetry systems are ideal for computing the contributions to the total lateral drift of different response mechanisms because they provide a denser displacement field than is provided by traditional LVDTs. The Metris system provides more accurate measurement of displacement as discussed in Section 3.4. However, following failure of the EWP, there was an unnoticed break in communication between the LEDs on the second story of the EWP and the CCD camera, and these displacement data were not recorded for these targets for the remainder of the test. Therefore, in computing deformations resulting from various response mechanisms, Metris data for the bottom three rows of LED targets were used and the data for the photogrammetry system targets were used for the rest of the wall pier. To be consistent, this method was also used on the WWP, even though Metris data were available. The layout of the LED and photogrammetry targets are shown in Figures 3.11 and 3.12. Figure 5.51 shows a close up of the Metris and photogrammetry targets used to calculate deformations.

The line of Metris LEDs located two inches above the base of each wall pier (Figure 5.51) were used to calculate the fixed-end or base rotation of each wall pier as well as horizontal translation or “slip” that occurred between the base of each wall pier and the foundation block. The vertical and horizontal movements of the foundation block were assumed to be equal to zero, and this was verified by LVDTs measuring foundation-block slip and rotation with respect to the strong floor.

To compute the contribution of flexural deformation to total lateral deformation, the change in rotation between two rows of Metris or Photogrammetry targets was used. For a given row of LED or photogrammetry targets, a linear fit was performed to the vertical displacement data for all the targets in that row. Then, the wall pier angle of rotation, with respect to the horizontal axis, was calculated for that row. Finally, the change in rotation, $\Delta\theta_l$, between two adjacent rows of targets was calculated using the following

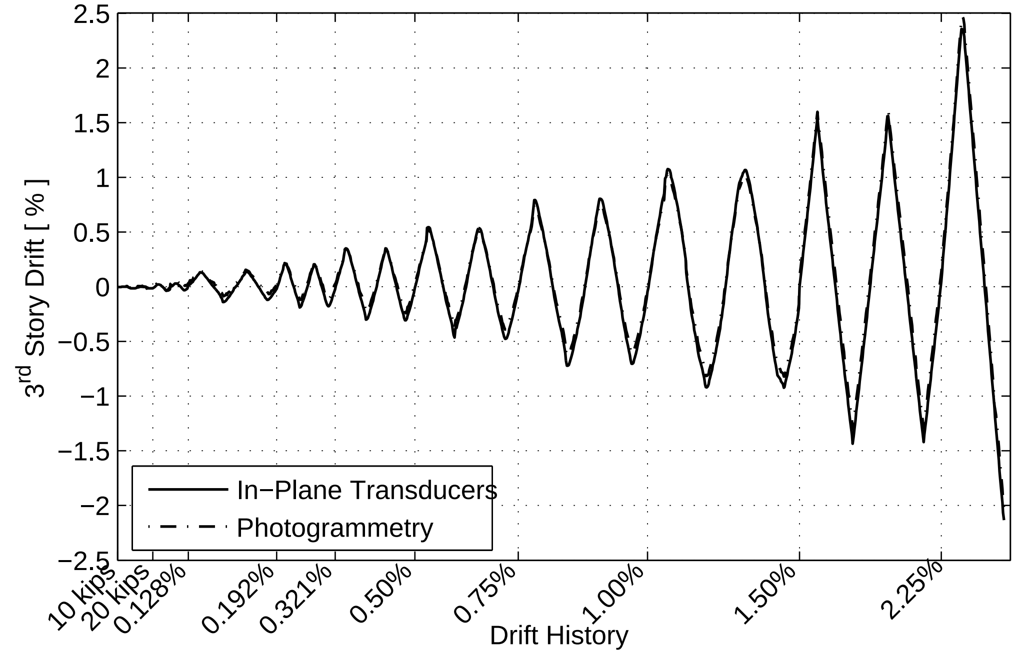

Figure 5.49: Lateral third story drift history for EWP

equation:

$$\Delta\theta_l = \theta_t - \theta_b \tag{5.6}$$

where, the rotations are defined in Figure 5.52a and the subscript l refers to a "layer" of the wall which is the vertical segment of wall between two rows of targets. Assuming flexural deformation is uniformly distributed between the two rows of targets, the contribution to the total lateral displacement at the top of the pier (height = 150 in) due to flexural deformation between the two rows of Metris/Photogrammetry targets is calculated using the following equation:

$$\delta_{\theta,l} = (h_3 - h_l)\tan(\Delta\theta_l) \tag{5.7}$$

where, h_3 is the height of the top of the wall pier, 150 in, and h_l is the mid-height of the two rows of targets. In the case of the base rotation, only the row of LEDs two inches

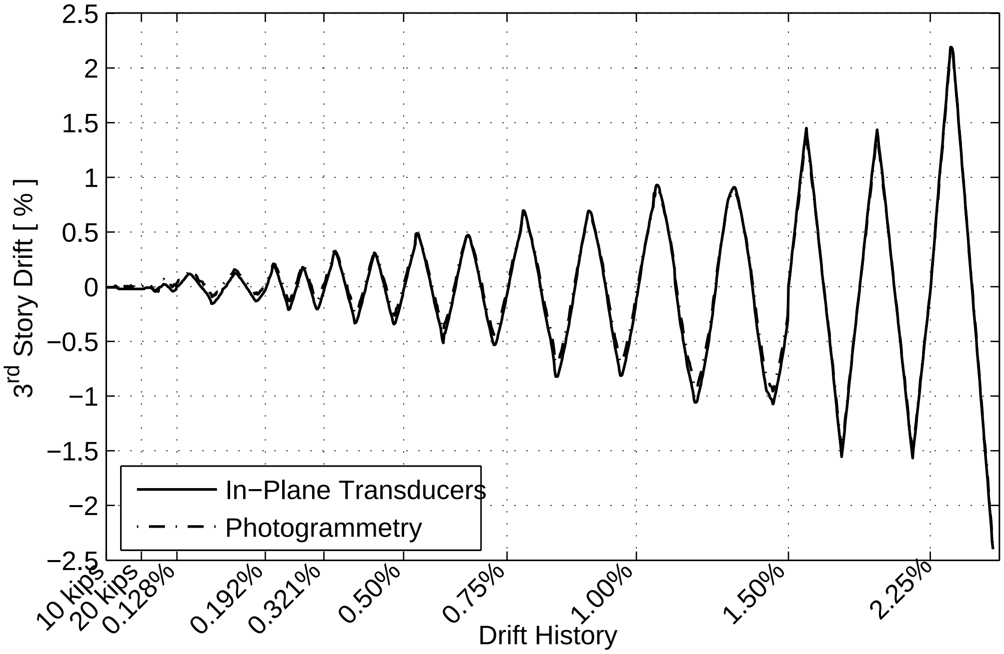

Figure 5.50: Lateral third story drift history for WWP

above the foundation is used to calculate the drift contribution because the foundation rotation is assumed to be equal to zero; therefore, the elevation of this layer, h_l, is equal to one inch. The procedure described above is repeated for each layer up the entire height of the wall pier.

The contribution to total lateral displacement of shear deformations is computed using the average shear strain from the layer of wall between two rows of Metris or photogrammetry targets. In Section 5.8 the procedure for computing the γ field for wall pier is presented; the grids of LED and photogrammetry targets are divided into 4- or 5-node elements and strains are computed using the isoparametric formulation employed by the finite element method. To compute the contribution to total lateral displacement of shear deformation, the shear strain at the center of each element is computed. For the first two layers in each wall pier, each layer comprises six elements made up of LEDs. For the layers above the third row of Metris and/or photogrammetry targets (Figure 5.51),

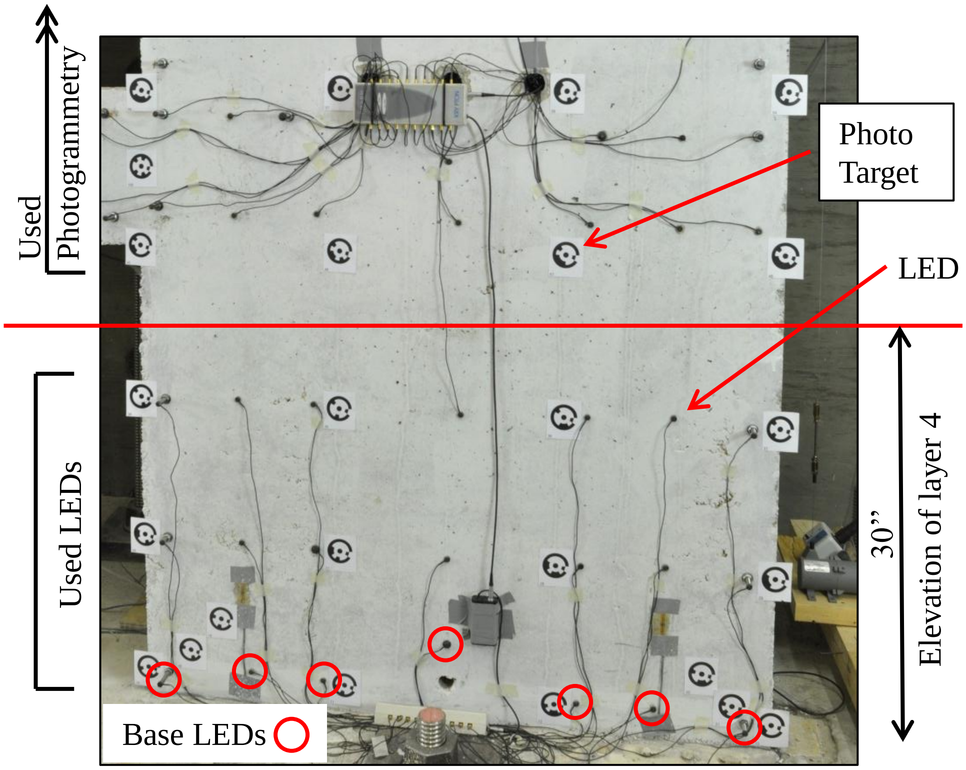

Figure 5.51: Layout of EWP instrumentation used to calculate drift contributions

each layer comprises three elements made up of photogrammetry targets. The shear deformation for each element, $\delta_{\gamma e}$, was calculated using the following equation:

$$\delta_{\gamma,e} = \Delta_{ze} \tan\left(\gamma_{center}\right) \tag{5.8}$$

where each variable is defined in Figure 5.52b. Then, each shear deformation was averaged across the width of the wall pier to estimate an average shear deformation for a given layer, $\delta_{\gamma,l}$.

The total contribution to total lateral displacement of each deformation mechanism throughout the history of the experiment is shown in Figure 5.53; deformation contributions for layers were summed to get the story-wise contribution shown in the figure. The

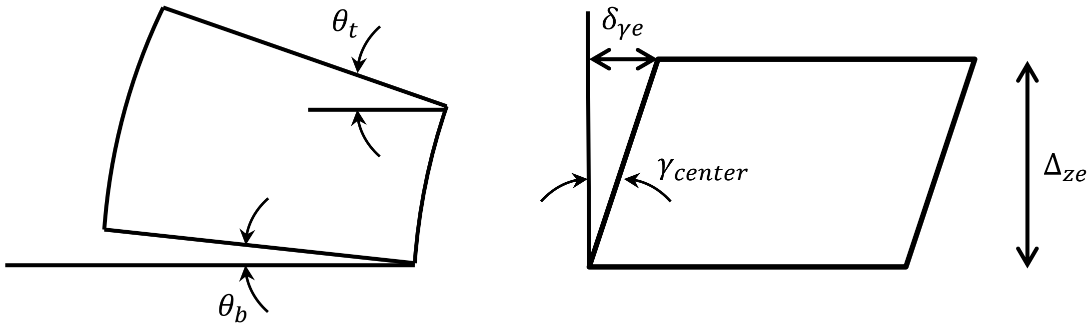

(a) Flexural deformation

(b) Shear deformation

Figure 5.52: Wall pier deformation mechanisms for a typical element

drift contribution results for the WWP at the east and west peaks are shown in Figures 5.53a and 5.53c, and the results for the EWP at the east and west peaks are shown in Figures 5.53b and 5.53d. Contributions are not shown for the drift cycles before 0.321% because the instruments used were not particularly accurate at small displacements.

Overall, each wall pier is deforming predominately in flexure, and most of the total third-story lateral drift is occurring due to first floor flexure and base rotation. After spalling occurred during the 1.00% drift level, the contribution of first floor flexure increases significantly and continues to increase throughout the remainder of the test. While the contribution of second story flexure and base rotation began to decrease. This is attributed to spreading of plasticification up the height of the wall. For the tension wall pier, the relative contribution to total drift of the deformation mechanisms change very little through the test. The data in Figure 5.53 provide significant insight into wall response. The shear deformations in the tension walls (Figures 5.53a and 5.53d) were on average larger than the deformation in the compression piers. This difference is attributed to the tension wall having much lower shear stiffness (rather than higher shear demand) than the compression wall due to open concrete cracks and longitudinal steel yielding. For the tension wall pier, the shear deformation in the third story of is larger than in the first or second story; while for the compression wall shear deformation is largest at the base. This is attributed to the redistribution of shear forces between the tension and compression walls via the coupling beams at each floor. In Figure 5.53d, the percentage of total drift is under 100% at the end of the test. This occurred because after buckling of the EWP during the E+ loading direction, the flexural contribution in that region is negative in magnitude due to the residual deformations created by shortening of the OBE.

Figures 5.54–5.58 provide a more detailed look at the percentage of total drift coming from each of the deformation mechanisms discussed. Each figure shows the drift contributions at key damage states discussed earlier previously (Section 5.3).

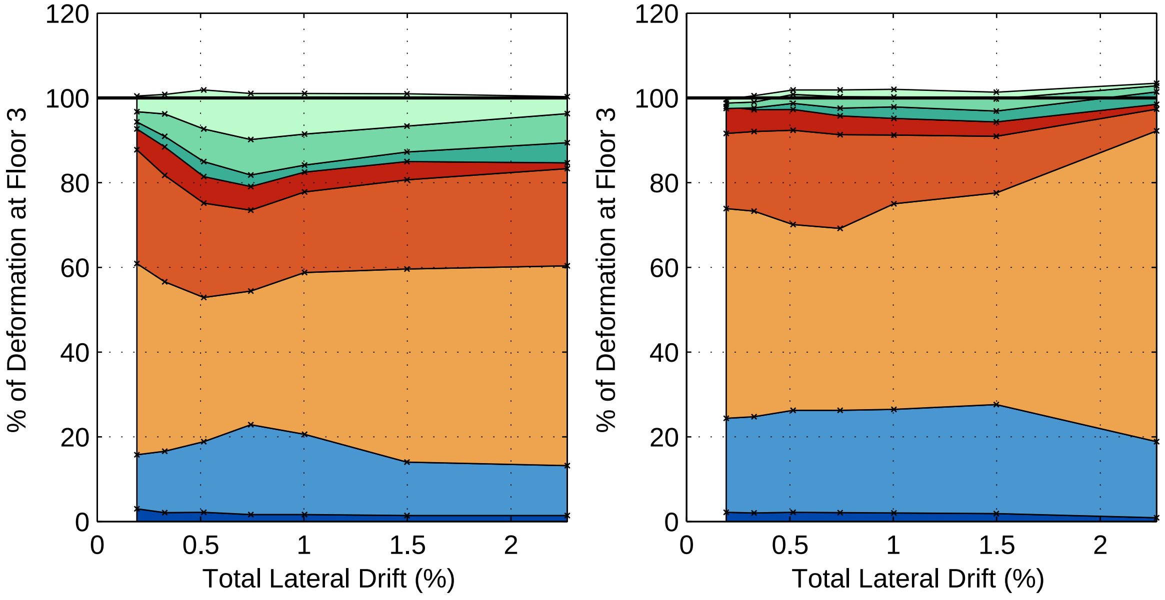

(a) WWP - East Peaks

(b) EWP - East Peaks

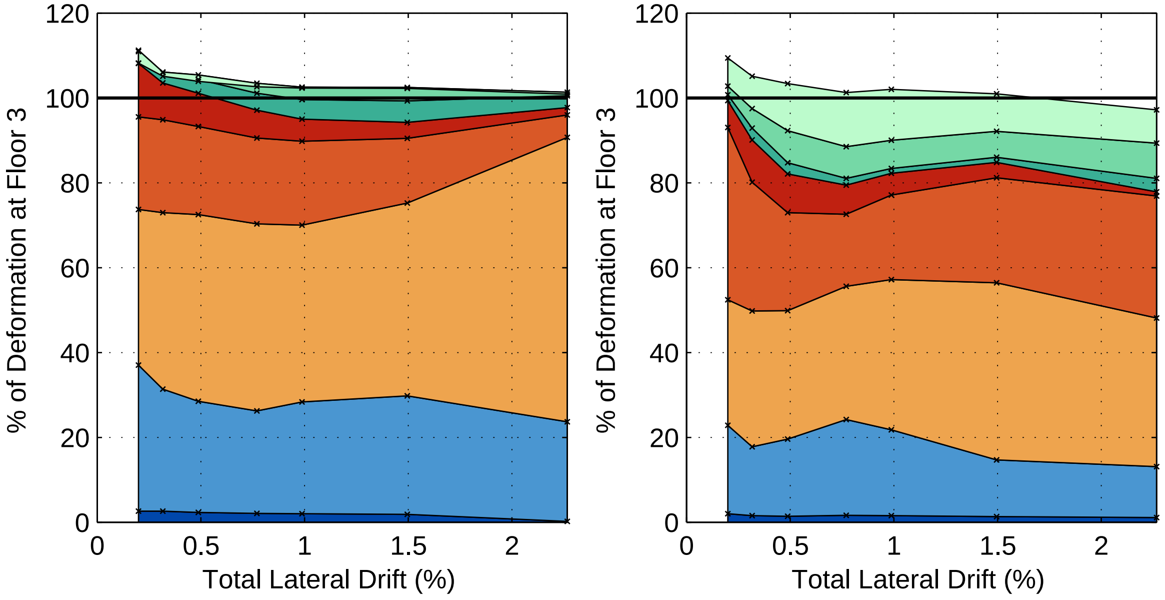

(c) WWP - West Peaks

(d) EWP - West Peaks

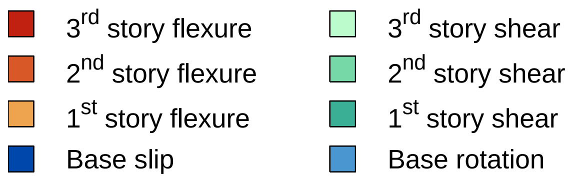

Figure 5.53: Contribution to total drift from different response mechanisms

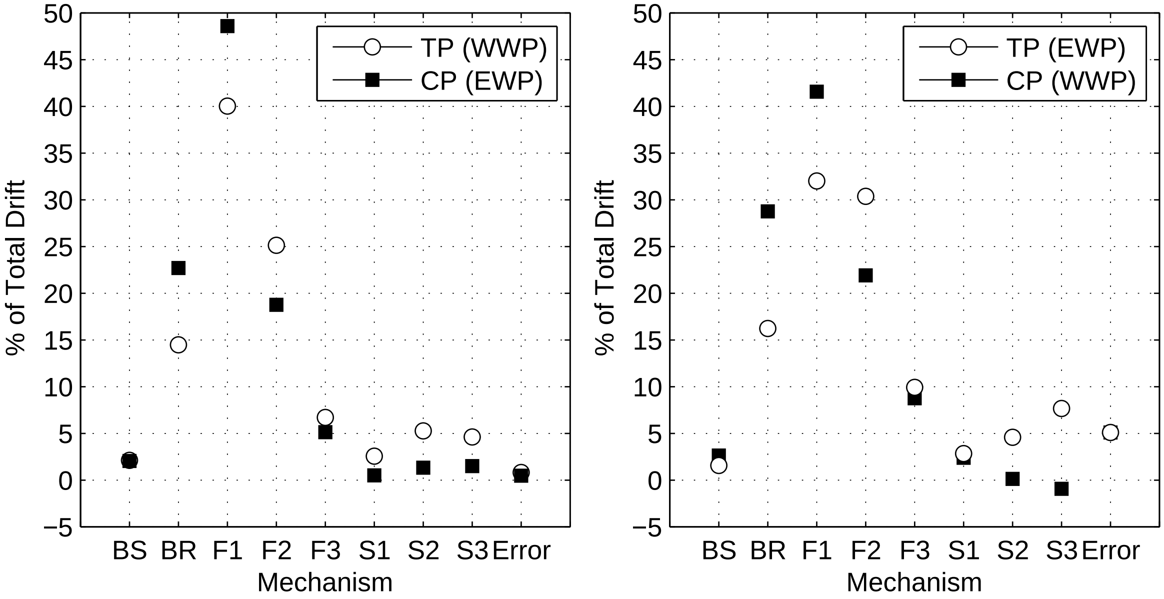

(a) 0.321% E+ Peaks (b) -0.321% W- Peaks

Figure 5.54: Contributions to total drift during 0.321% drift level (diagonal cracking)

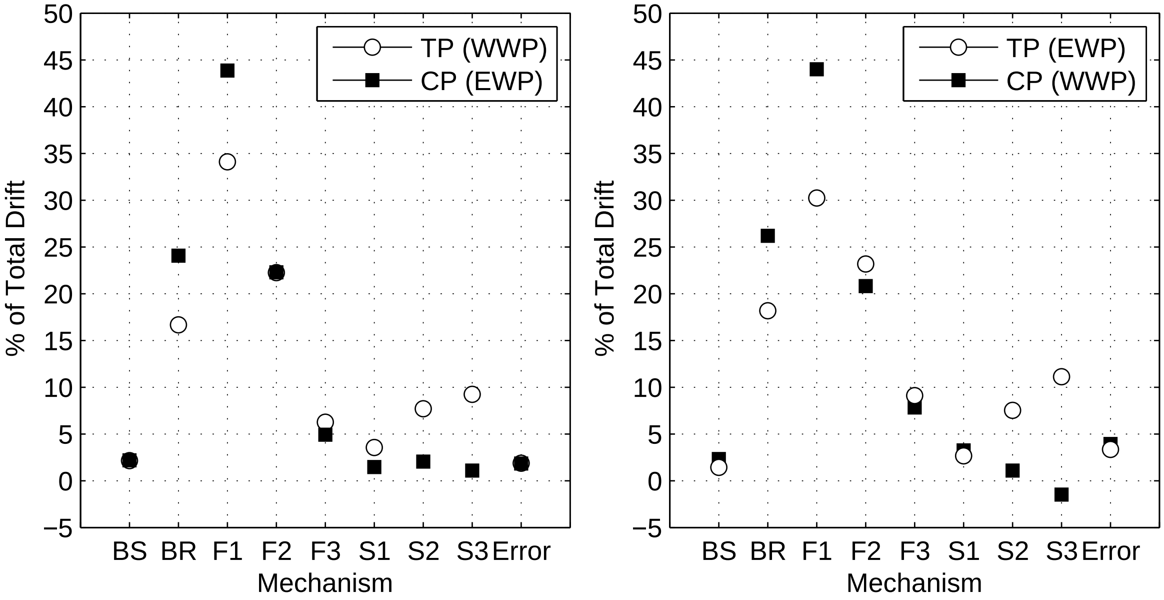

(a) 0.50% E+ Peaks (b) -0.50% W- Peaks

Figure 5.55: Contribution to total drift during 0.50% drift level (yielding)

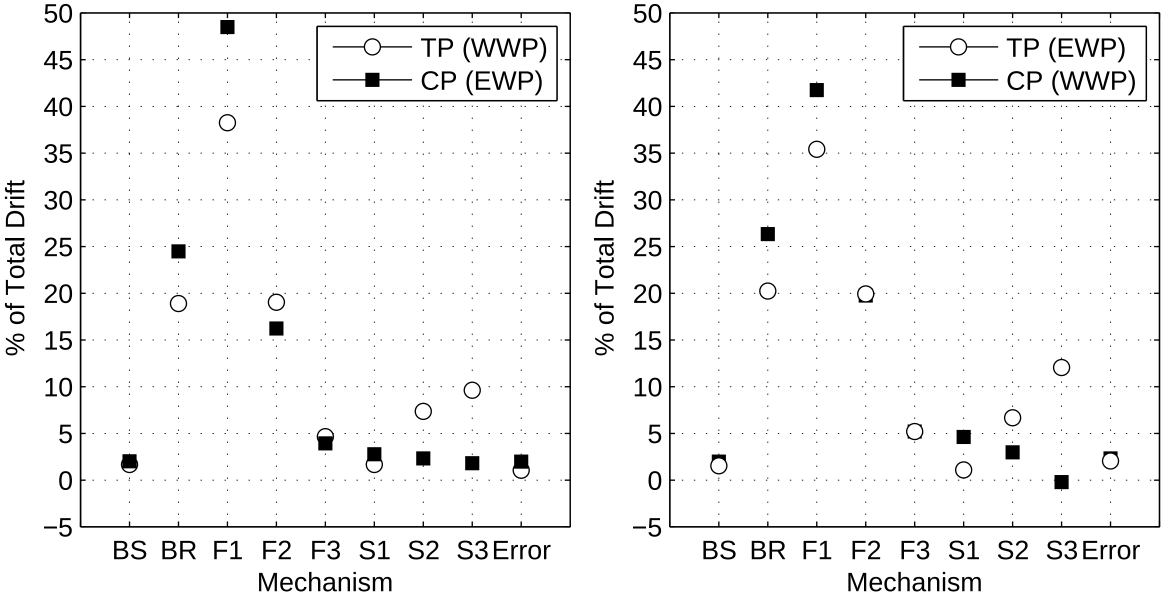

(a) 1.00% E+ Peaks (b) -1.00% W- Peaks

Figure 5.56: Contribution to total drift during 1.00% drift level (initial spalling)

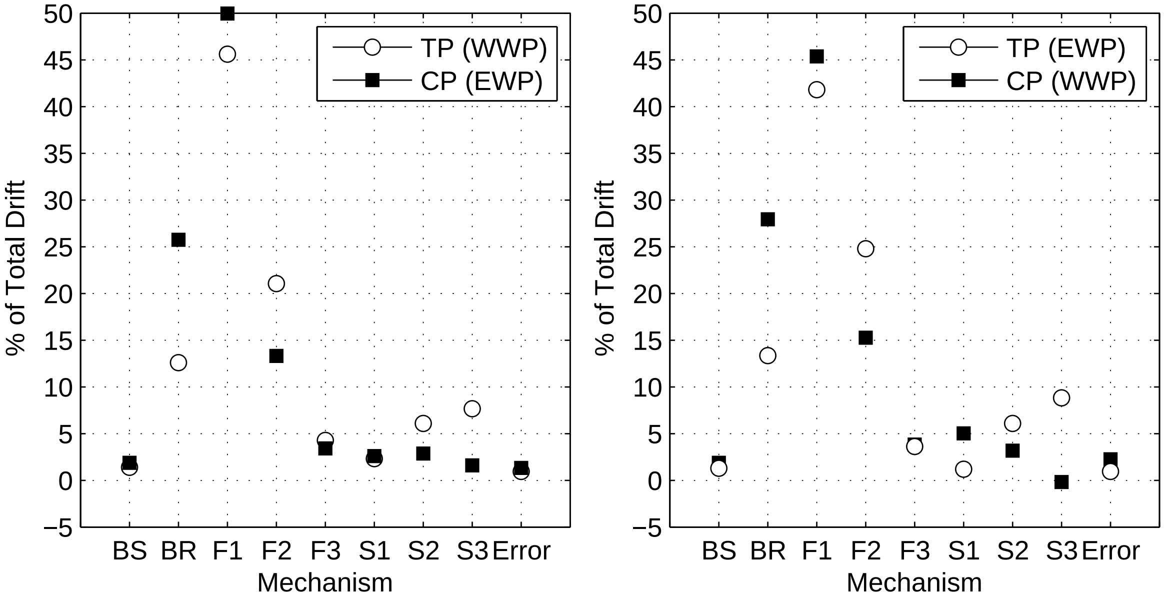

(a) 1.50% E+ Peaks (b) -1.50% W- Peaks

Figure 5.57: Contribution to total drift during 1.50% drift level (moderate spalling)

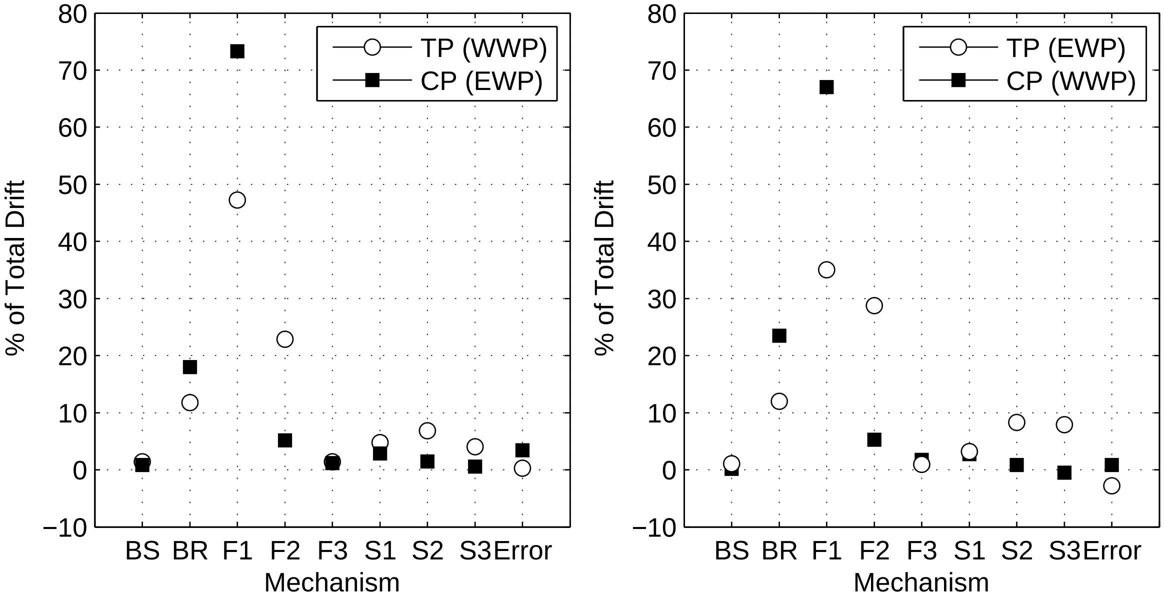

(a) 2.25% E+ Peaks (b) -2.25% W- Peaks

Figure 5.58: Contribution to total drift during 2.25% drift level (failure)

where,

TP	Tension pier
CP	Compression pier
BS	Base slip
BR	Base rotation
F1,F2,F3	Flexure at stories 1, 2 and 3
S1,S2,S3	Shear at stories 1, 2 and 3
Error	100% - $\sum$(% of Total Drift)

5.10 Coupling Beam Rotations

The deformation contributions discussed in the previous section provide an understanding of the wall pier deformation behavior; here coupling beam rotational deformation is discussed. Recent coupling beam component experiments (Naish et al., 2009) have shown coupling beams with modern detailing can experience rotational demands on the order of 6-8% with little or no strength loss. While, simplifying assumptions about coupled wall response can be used to estimate coupling beam rotation demands in a real system, there is a need to evaluate these simply models using data from coupled wall test results. Here, the rotation demands of the CW1 coupling beams are calculated using two different techniques.

First, the rotation for each end of the coupling beams was calculated using the following two equations:

$$\theta_{cbe,w} = \theta_{WWP} + \beta \tag{5.9a}$$

$$\theta_{cbe,e} = \theta_{EWP} + \beta \tag{5.9b}$$

where, variables are defined in Figure 5.59. The rotation of each wall pier as well as the chord rotation, β, was determined using the Metris system for CB1 and CB2 and the photogrammetry system for CB3.

Figures 5.60 and 5.61 show the coupling beam end rotations for the E+ and W- peak drifts. When comparing both of the figures, the end rotations along the compression wall-to-beam interface are much larger than the end rotations along the tension wall-to-beam interface. This difference is more apparent after the 0.321% drift level and can be attributed to the differences in the loading conditions, stiffness and deformation mechanism between the two wall piers. The maximum rotations for CB2 and CB3 occurred one step prior to failure of the EWP occurred on the east side of the coupling beam; whereas, the maximum rotation of CB1 occurred at the E+ peak on the east

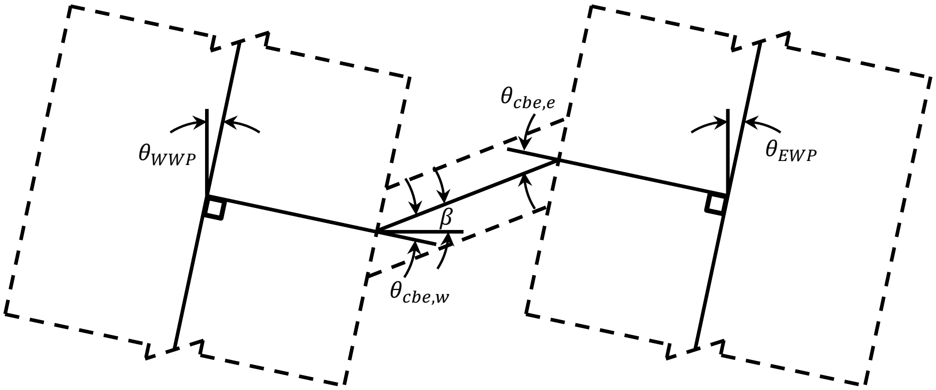

Figure 5.59: Definition of coupling beam end rotation

side of the coupling beam. The end rotations for CB1, CB2 and CB3 measured 0.0367, 0.0443 and 0.0472 radians, respectively. During the next reverse half cycle, the maximum rotations for CB2 and CB3 occurred one step prior to failure of the WWP on the west side of the coupling beam; whereas, the maximum rotation of CB1 occurred at the W-peak on the west side of the coupling beam. The end rotations for CB1, CB2 and CB3 measured -0.0315, -0.0388 and -0.0425 radians, respectively. While these rotations are large at the end of the test, damage to the coupling beams was relatively minor compared with damage at the base of the wall piers even with estimated shear stress demands in the coupling beams ranging from $6\sqrt{f'_c} - 9\sqrt{f'_c}$. As mentioned in the preceding chapter, diagonal cracking and spalling on the coupling beams was minor compared to damage observed in previous coupled wall experiments suggesting the coupling beams in CW1, which utilize modern detailing, performed as expected.

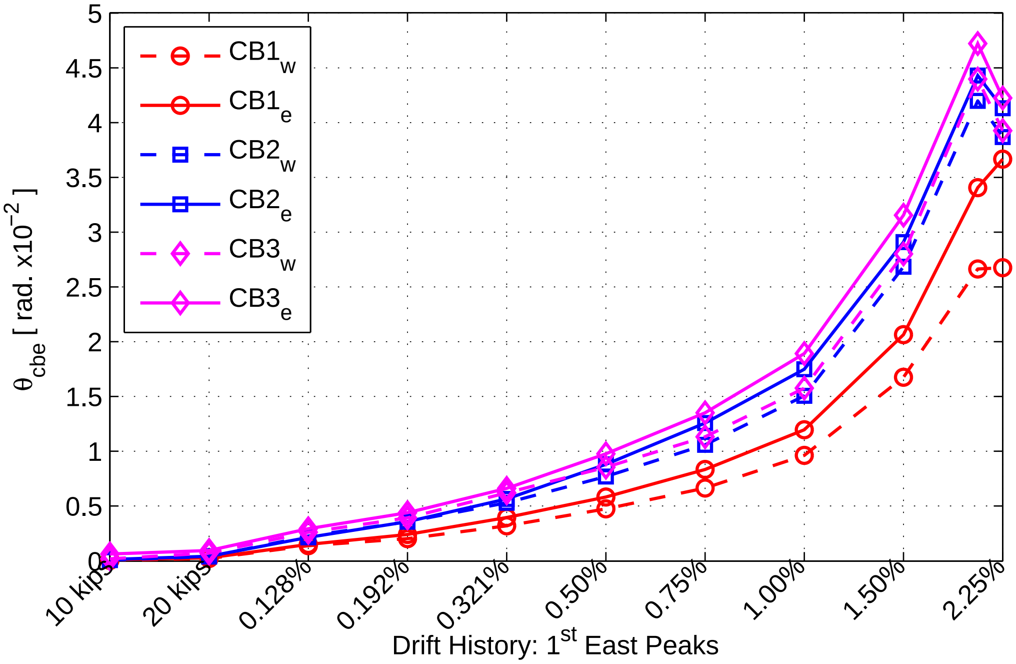

Figure 5.60: East peak coupling beam rotation

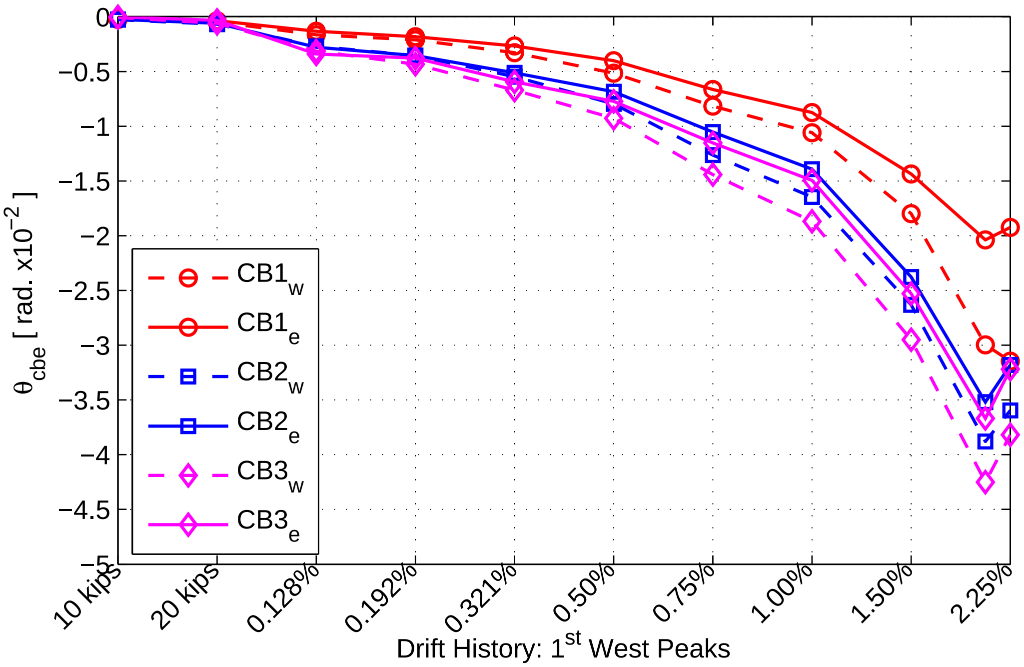

Figure 5.61: West peak coupling beam rotation

In design, coupling beam rotations are typically predicted using the wall pier rotations and an assumed geometric relation between the, the center-to-center distance spanning the wall piers and an effective coupling beam length. Assuming the joint region between the centroidal axes of the wall piers and the beam-to-wall interface is completely rigid, the following coupling beam rotation equation is derived:

$$\theta_{cb} = \frac{L}{l_n}\theta_w \tag{5.10}$$

where, the notation used is defined in Figure 5.62.

Additionally, Wight and MacGregor (2009) suggest the effective coupling beam length is not equal to the clear-span length of the beam, but rather includes some additional length to account for loss in stiffness at the beam-to-wall interface. Their assumption is to move the connection point between the coupling beam and the wall a distance $h_b/2$ into each wall pier. This relationship is expressed in the following equation and is also illustrated in Figure 5.62b.

$$\theta_{cb} = \frac{L}{l_n + h_b}\theta_w \tag{5.11}$$

Both of these assumptions assume the wall piers rotate about their centroidal axes; another plausible model is to assume that the wall piers wall piers rotate about their neutral axes (Paulay, 2002). In the CW1 experiment, the resulting deformation behavior of the compression wall is quite different than the tension wall, and even, early on in the loading history, the neutral axis of the tension wall moved closer and closer to the compression wall as the tensile force and bending moment increased. On the other hand, the neutral axis of the compression wall did not vary much beyond the centriodal axis location due to the increasing compressive axial force. This third rotation relationship between coupling beam rotation and wall rotation, shown in Figure 5.62c and expressed in Equation 5.12, was used to modify the distance between the wall pier points of rotation. It was assumed the tension wall rotates about its bottom inside corner (i.e. $c_{tw} = 0$) and the compression wall rotates about its neutral axis, c_{cw}, which was assumed to be

21 inches from the OBE face as calculated in Section 5.7.

$$\theta_{cb} = \frac{L_{mod}}{l_n + h_b}\theta_w \quad \text{where, } L_{mod} = c_{tw} + l_n + (l_w - c_{cw}) \tag{5.12}$$

Using the measured experimental results and dividing the coupling beam end rotation by the wall rotation for each coupling beam end, the observed rotation relationship was determined. These results are shown for both directions of loading in Figures 5.63 and 5.64. Included in these results are the three theoretical rotation relationships defined by Equations 5.10–5.12. The coupling beam-to-wall rotation relationship, θ_{cb}/θ_w, calculated by manipulating Equations 5.10, 5.11 and 5.12 was equal to 3.0, 2.0 and 1.42 for CW1, respectively. Similar to results in the coupled wall experiments tested by Lequesne (2011), the relationship between the coupling beam and wall pier rotations for CW1 were on average lower than the ratios predicted using Equations 5.10 and 5.11. While the rigid assumption is grossly over-predicting the rotation relationship between the coupling beam and the wall piers, Equation 5.11 and 5.12 provide a reasonable upper and lower bound to the data.

The second method for calculating the rotations of the coupling beams utilizes instrumentation that spans each beam-to-wall interface. These measured rotations are referred to as the hinge rotations. At the first and second floors LED targets were used to calculate total rotation of the coupling beam. The four targets show in Figure 5.65a were used to determine the lateral deformation of the top and bottom corners of the coupling beam. These deformations are measured relative to the rotated axis A' as shown in Figure 5.65. This reference axis is used to remove rigid body translations for a set of LEDs. With the deformations defined, the coupling beam hinge rotation was calculated using the following equation:

$$\theta_{cbh} = \tan^{-1}\left(\frac{\Delta_t' - \Delta_b'}{\Delta_z}\right) \tag{5.13}$$

where, the notation and location of the instrumentation is shown in Figure 5.65. Because no LEDs were used on the third story coupling beam, traditional instrumentation was needed to calculate the hinge rotation. LVDTs were used to determine the horizontal deformations along the top and bottom of CB3. The layout of instruments a the third story is shown in Figure 3.15. The measurements along the top and bottom beam-to-wall interface are relative displacements, so they were directly defined as Δ_t' and Δ_b', respectively. The average vertical distance between each LVDT anchor was determined using the know coordinates of the LVDT anchors. Using Equation 5.13, the hinge rotations at each end of the third story coupling were calculated.

The results of the hinge rotations for all the coupling beams are shown in Figure 5.66. In addition to the hinge rotations, the coupling beam end rotations are included in Figure 5.66 as a comparison. In general, the hinge rotations are smaller in magnitude than the end rotations, but they are similar in the sense that the end of the coupling beam connected to the compression wall is rotating more than the end connected to the tension wall.

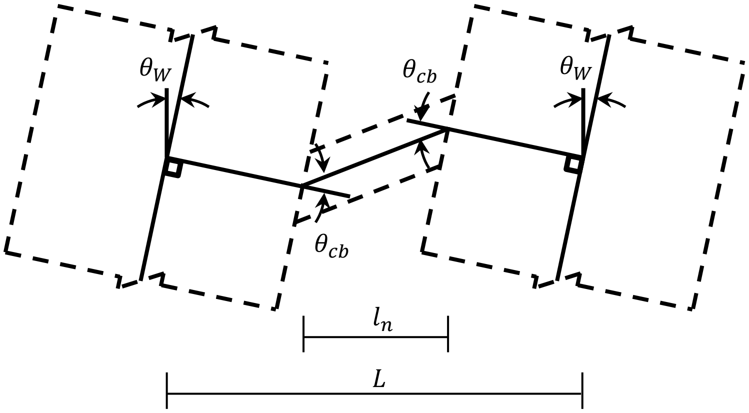

(a) Rigid assumption

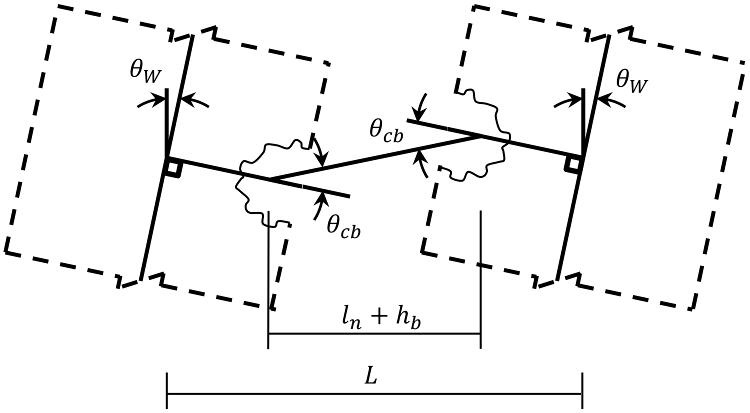

(b) Wight and MacGregor (2009) assumption

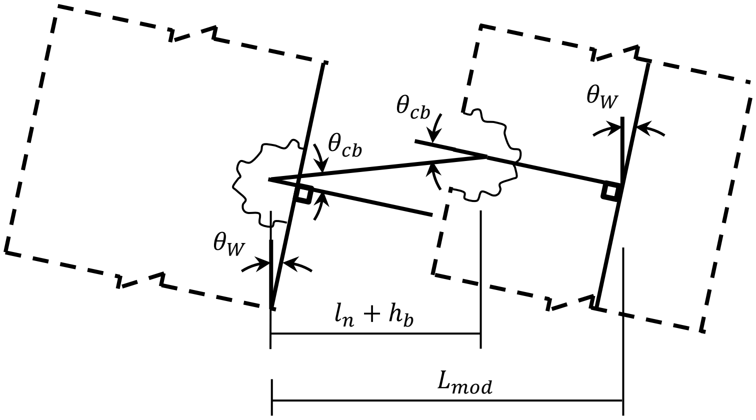

(c) Modified assumption

Figure 5.62: Wall pier and coupling beam rotation relationship

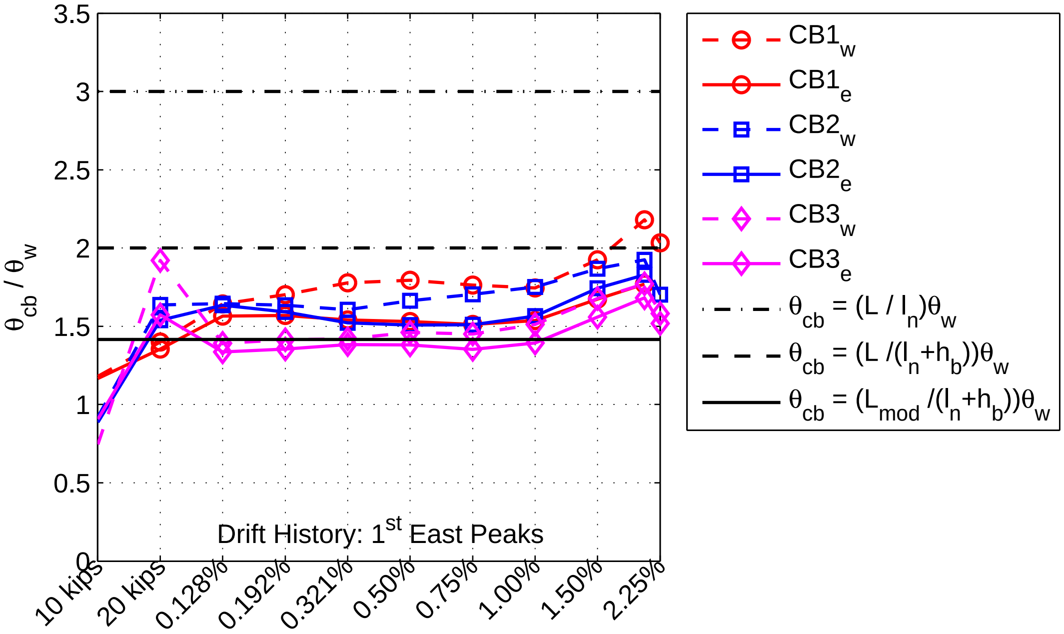

Figure 5.63: Ratio of wall pier and coupling beam rotations for east peaks

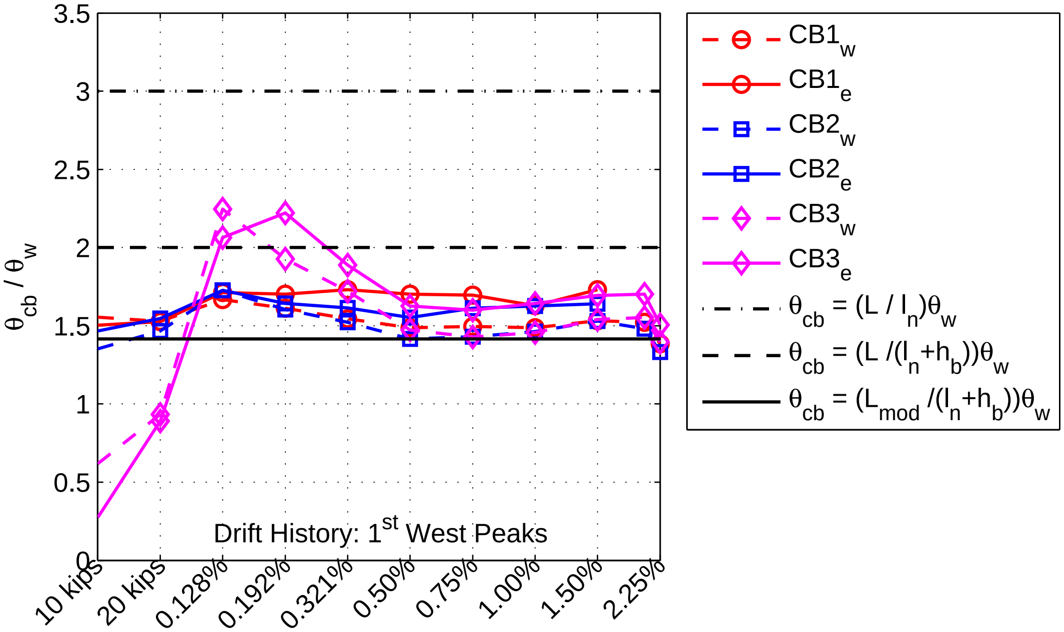

Figure 5.64: Ratio of wall pier and coupling beam rotations for west peaks

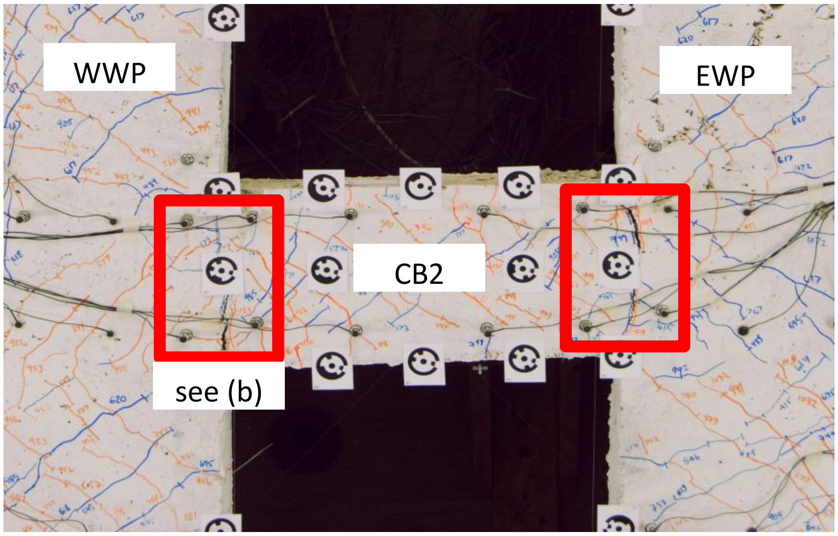

(a) LED locations (note LEDs are small black targets located near the corners of the boxes)

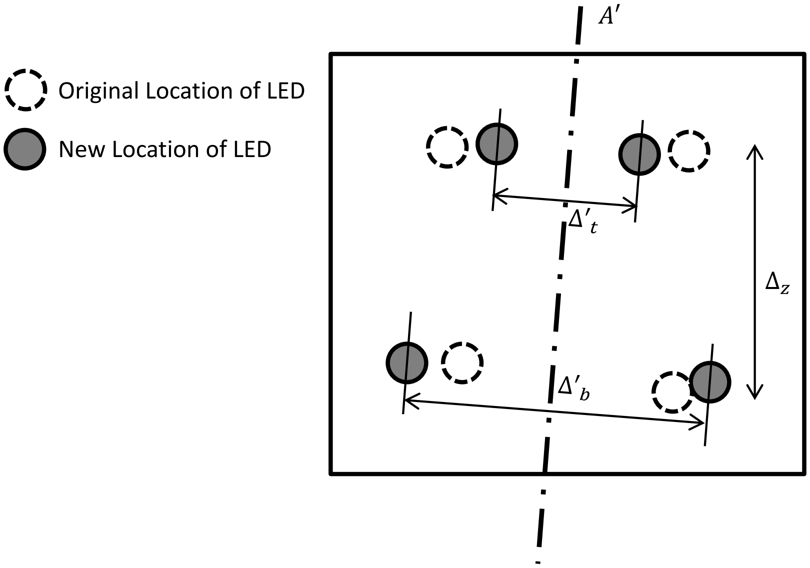

(b) Rotation notation

Figure 5.65: Hinge rotation instrumentation and notation for CB1 and CB2. (Note that A’ defines the interface between the coupling beam and the wall pier)

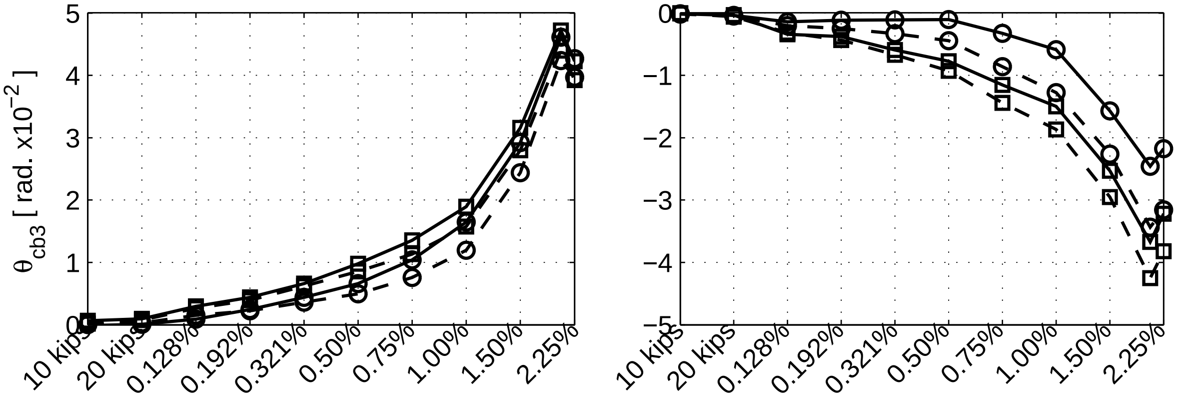

(a) CB3, E+ drift (b) CB3, W- drift

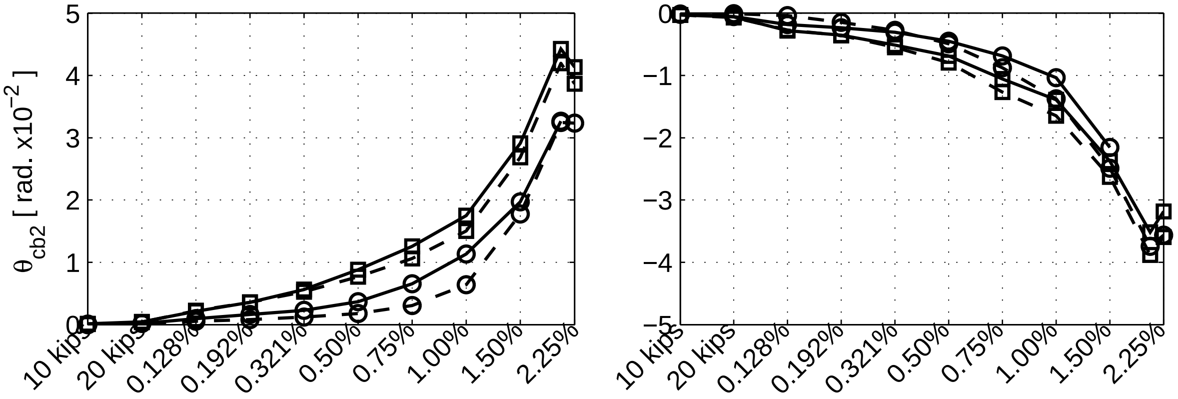

(c) CB2, E+ drift (d) CB2, W- drift

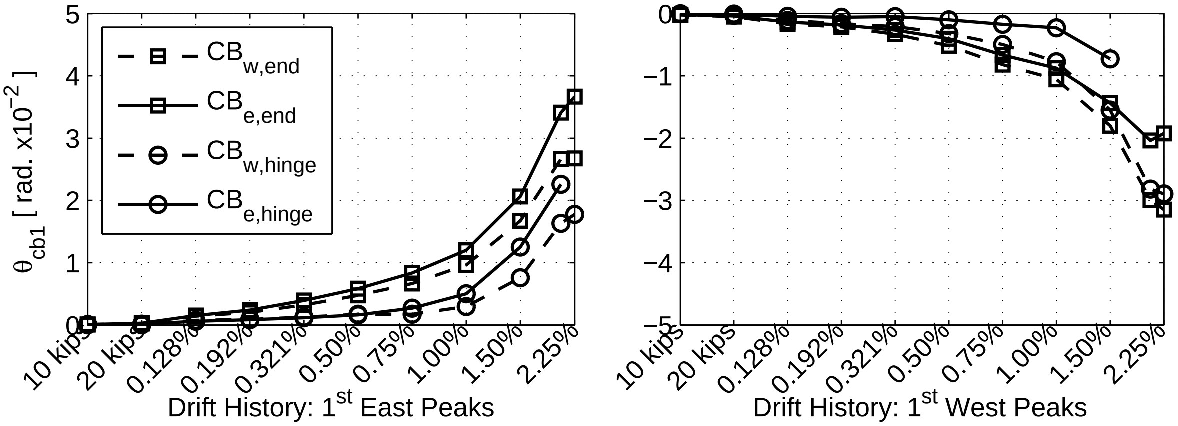

(e) CB1, E+ drift (f) CB1, W- drift

Figure 5.66: Comparison between experimental end and hinge rotational measurements

Chapter 6

COUPLED WALL PERFORMANCE AND DAMAGE EVALUATION

The behavior of the coupled wall specimen, CW1, was discussed in detail in the preceding two chapters. Experimental observations were made regarding concrete damage, spallling and failure of the wall piers. Additionally, a thorough investigation of wall pier and coupling beam force and deformation behavior on a global and local scale all contributed to a better understanding of coupled wall performance. In the design CW1, the specimen followed a recommended design procedure that is typical in code-based design of coupled wall systems. However, other performance criterion developed by past researchers was also used to better predict the seismic performance of CW1. These design measures were compared to the previously tested coupled wall specimens as well as the building inventory (Stringer, 2007). Furthermore, the progression of damage for a set of previously tested coupled wall experiment was categorized and compared to Specimen CW1. The comparison of design parameters and damage highlight differences between the assumptions made in design and the observed behavior of a coupled wall structure subjected to earthquake level forces.

6.1 Performance Evaluation Parameters

Stringer (2007) developed a procedure for predicting the seismic performance of core wall systems (Section 2.1) and where used to predict the performance of 13 mid- to high-rise coupled shear wall buildings. While, some of these design parameters were utilized in the design of CW1, the performance procedure developed by Stringer (2007) was used in this section to predict design quantities such as the degree of coupling (DOC) and the wall pier demand capacity ratios for a set of previously tested coupled-wall specimens as well as Specimen CW1.

The specimen geometries, reinforcement details, loading conditions and measured material strengths were used to predict the force demands resulting from the development of a flexural mechanism (Stringer, 2007). This mechanism assumes all the coupling beam ends and the wall pier bases develop hinges. The degree of coupling was calculated using Equation 2.1. Additionally, the axial tension demand capacity ratio, DCR_{axial}, was calculated using Equation 2.2. Equation 2.3 was used to estimate the shear demand capacity ratio at the base of the wall piers, DCR_{shear}. In order to quantify the compressive demand in the compression pier due to coupling action, the axial compression demand (ACD) resulting from the coupling action (Figure 2.2) was also calculated. The results of this performance analysis for the coupled-wall dataset is shown in Table 6.1. In the table, the base shear stress demand, v_p, from the plastic analysis is reported, and the predicted base shear demand, V_p, is compared to the maximum base shear demand, V_{max}, measured during the experiment (Table 2.9).

Table 6.1: Performance analysis results

Specimen Name	$v_{\mathbf{p}}$ ($\sqrt{f'_c}$)	V_{max}/V_p	DCR_{shear}	DCR_{axial}	**ACD** (f'_cA_g)	**DOC** (%)
CW1	3.08	1.30	0.41	0.43	0.29	52.68
Santhakumar WallA	4.15	1.14	0.52	0.46	0.30	50.64
Santhakumar WallB	4.44	1.21	0.54	0.52	0.33	52.74
Shiu CS1	3.42	1.03	0.41	0.09	0.02	9.31
Shiu RCS1	5.66	0.94	0.68	0.64	0.18	42.75
Ozselcuk 1C	7.17	1.00	0.93	0.93	0.35	64.18
Lequesne CW1	5.18	1.13	0.91	0.04	0.13	37.98
Lequesne CW2	5.14	1.31	0.64	0.04	0.13	38.24

The results presented in Table 6.1 for each coupled wall specimen is combined with the results of the building inventory performance analysis developed by Stringer (2007).

These performance evaluations parameters are plotted against the building/specimen height (i.e. number of stories) and presented in Figures 6.1 – 6.6.

While no discernible tends were found with respect to the axial compression demand (Figure 6.1), a trend is shown in Figure 6.2 where the axial demand capacity ratio of the tension wall increases with building height. Additionally, axial DCRs larger than one were calculated suggesting a less desirable mechanism would form (e.g. only a portion of the coupling beams yield before the tension wall reaches its yield capacity).

The base shear demand/DCR results are shown in Figures 6.3 and 6.4. The shear DCR for three building inventory case studies was larger than 1.0 and four data points including two specimens were calculated above 0.8. Specimen Lequesne CW1 failed due to vertical reinforcement fracture in the wall piers and coupling beams and Ozselcuk 1C failed due to crushing of concrete in the web. The base shear demands used in these calculations were based on the fact that the wall piers each carried half the shear demand. Based on the results from CW1 as well as results presented in the literature, this assumption seems to be too conservative. It was estimated in these tests that 75 to 90% of the base shear was carried by the compression wall after the axial force in the tension wall overcame gravity. These observations suggest the data presented in Figure 6.4 are under predicted.

Finally, the degree of coupling data suggests there is a strong correlation between the building height and degree of coupling. In Section 2.1 limits on the degree of coupling were recommended by Harries (2001) for both diagonally (D) reinforced coupling beams (DOC=55%) and conventionally (C) reinforced coupling beams (DOC = 50%). These limits are included in Figure 6.5. The trend seems to show it would be very difficult for a building over 30 stories to achieve the recommendation without a significant reduction in coupling beam strength or an increase in the moment strength of the wall piers. Recall, the predicted DOC for Specimen CW1 was designed to be below this recommendation.

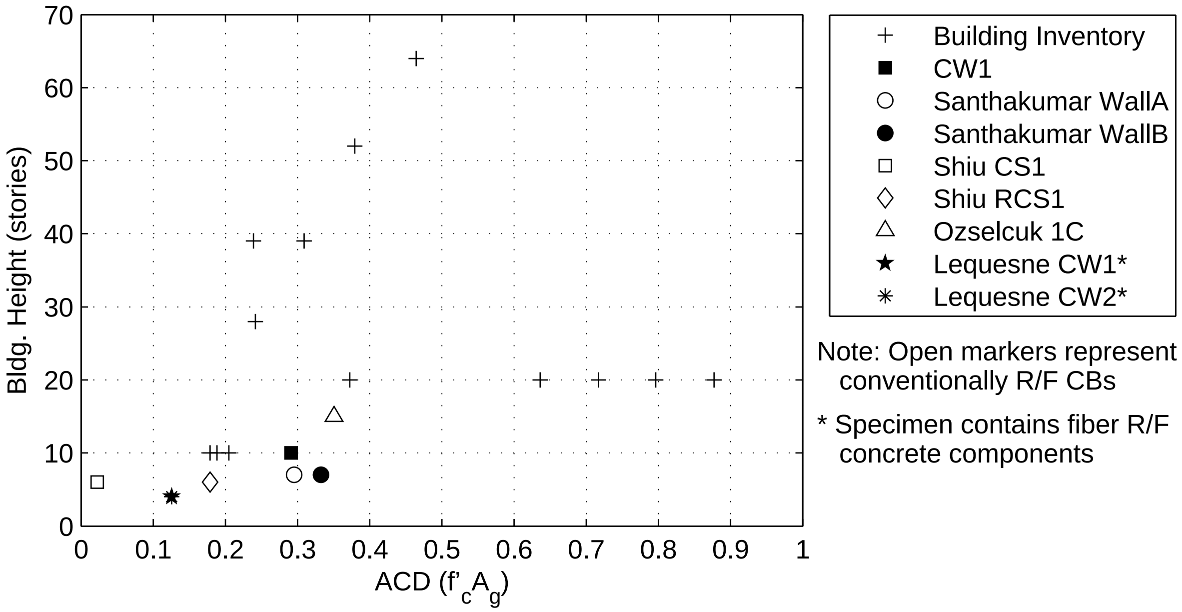

Figure 6.1: Story height vs. axial compression demand (ACD)

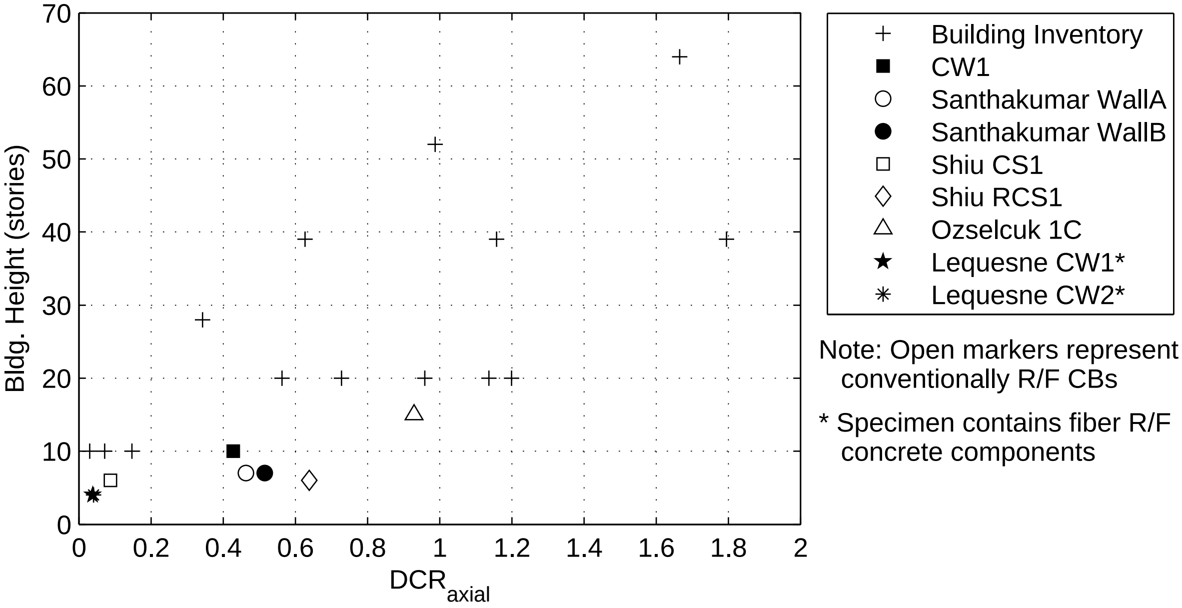

Figure 6.2: Story height vs. axial demand capacity ratio of the tension wall, DCR_{axial}

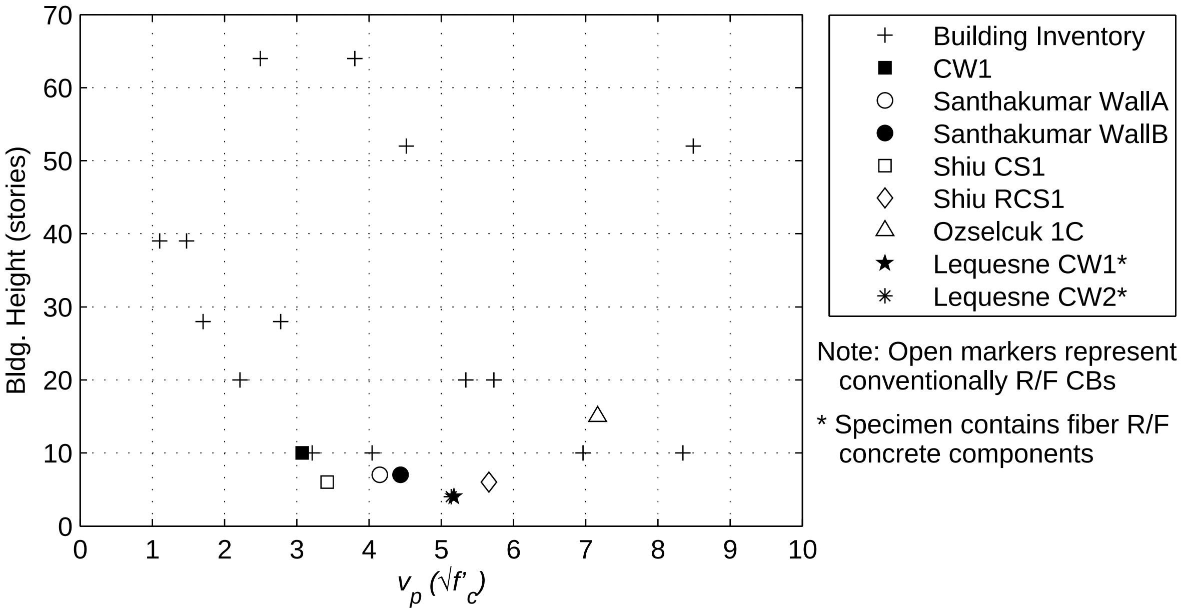

Figure 6.3: Story height vs. plastic base shear stress demand, v_p

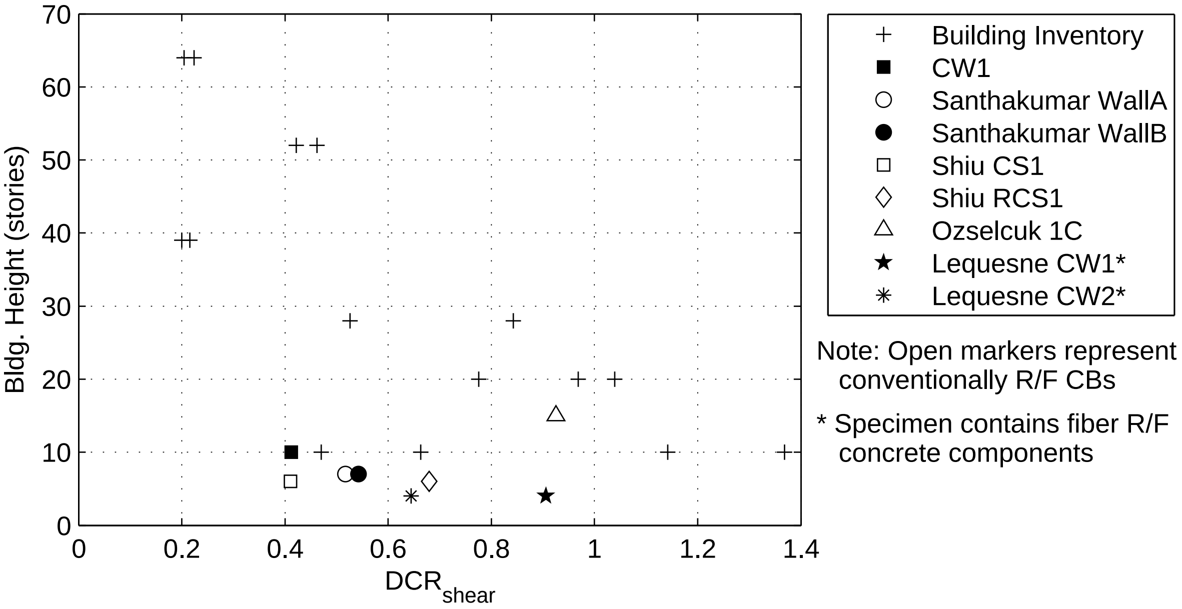

Figure 6.4: Story height vs. base shear demand capacity ratio, DCR_{shear}

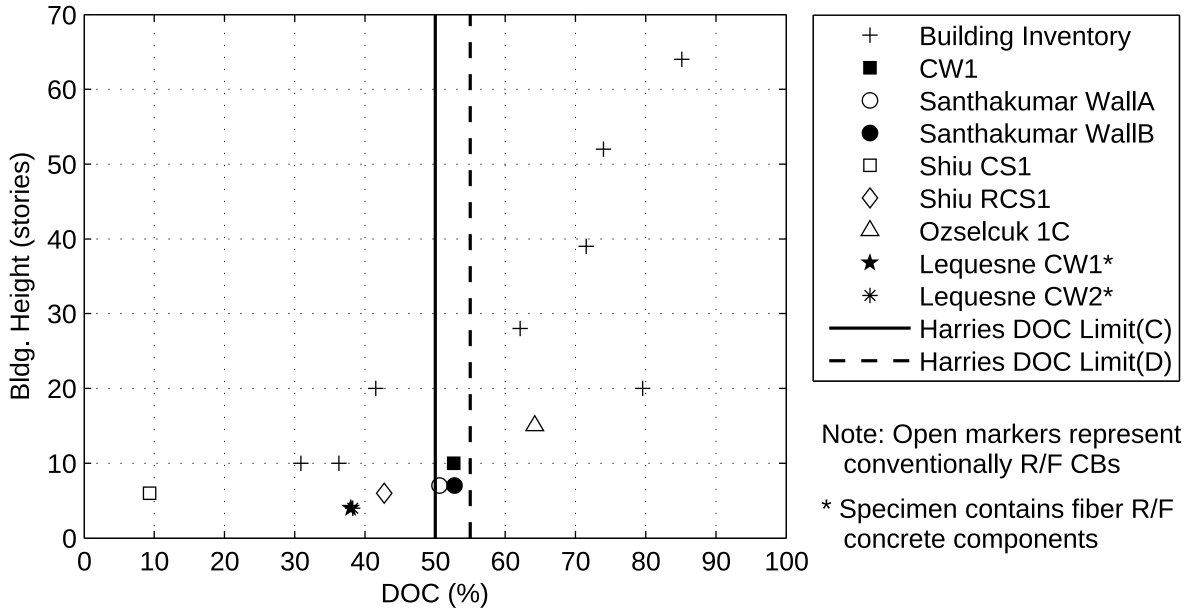

Figure 6.5: Story height vs. degree of coupling (DOC)

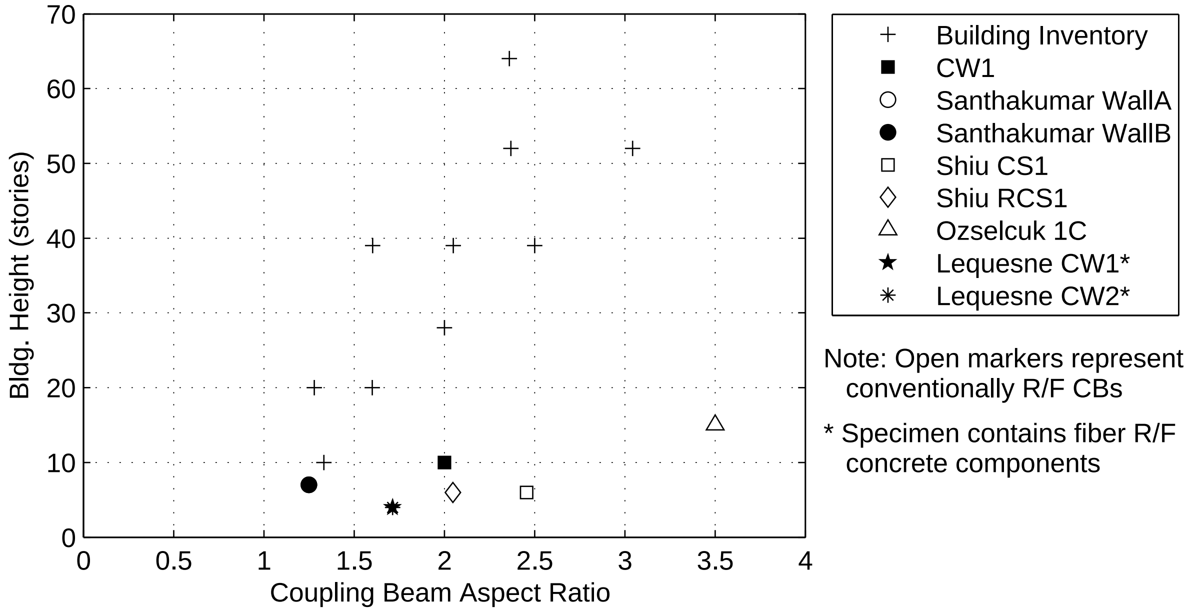

Figure 6.6: Story height vs. coupling beam aspect ratio (AR)

6.2 Comparison of Coupled Wall Damage

In Chapter 5, a brief description of key damage stages (DS) was used in order to highlight observed behavior of Specimen CW1 at various drift levels throughout the experiment. These damage states were particular useful to distinguish general damage such as cracking and yielding for Specimen CW1. However, to better quantify observed damage and compare these damage states between a set of previously tested coupled wall systems, a more detailed set of damage states was developed. In general, damage states are used to define the progression of damage in a structural component; therefore, the damage states developed for this study were separated into wall pier and coupling beam damage states. The establishment of the damage states used in this study was guided by the results of previous research on reinforced concrete components (Brown and Lowes, 2007), (Gulec et al., 2010) and (Birely, 2011). Table 6.3 and 6.4 provides a summary of the damage states used to quantify and compare the observed wall pier and coupling beam damage for a set of previously tested coupled wall tests including Specimen CW1.

Reported damage observations for the previously tested coupled wall experiments was extracted from the literature and in the case of CW1, damage observations presented in Section 4.2 were also used. The damage was then categorized using the damage states defined in Tables 6.3 and 6.4. The observed damage progression of these experiments are shown in Figures 6.7 – 6.14. Note the coupling beam notation was the same notation defined in Chapter 4; however, the wall piers were labeled as either the right wall pier (RWP) or left wall pier (LWP) in order to stay consistent among specimens. In many cases, the final damage state of a particular test specimen was not reported, so hatching was used to indicate that damage past the last identified damage state was unknown. Additional notation notation is defined in Table 6.2. Finally, a comparison of the damage progression for all the specimens is shown in Figure 6.15.

Table 6.2: Notation used in Figures 6.7 – 6.14

DCR_{axial}	Axial demand capacity ratio of the tension pier (Eq. 2.2)
DCR_{shear}	Wall pier shear demand capacity ratio (Eq. 2.3)
ACD	Axial compression demand in the compression pier
DOC	Degree of coupling (Eq. 2.1)
Wall Shape	R - Rectangular, B - Barbell, T - T-shaped
CB R/F Layout	C - Conventionally reinforced, D - Diagonally reinforced
WP X-Sec AR	Cross-sectional aspect ratio of wall pier, l_w/t_w (Table 2.5)
CB-AR	Coupling beam span-to-depth ratio, l_n/h_b (Table 2.5)
p	Positive peak ID
n	Negative peak ID

Table 6.3: Wall pier damage states

Damage State	Description
DS1a	Initiation of cracking
DS1b	Initiation of wall pier horizontal cracking
DS1c	Initiation of wall pier diagonal cracking
DS1d	Maximum measured wall pier horizontal crack widths less than 1/16 in
DS1e	Maximum measured wall pier diagonal crack widths less than 1/16 in
DS1f	Initiation of tension yielding in vertical boundary element reinforcement
DS1g	Initiation of compression yielding in vertical boundary element reinforcement
DS1h	Initiation of yielding in horizontal boundary element reinforcement
DS1i	Initiation of yielding in vertical web reinforcement
DS1j	Initiation of yielding in horizontal web reinforcement
DS2a	Maximum measured wall pier horizontal crack widths greater than 1/16 in but less than 1/8 in
DS2b	Maximum measured wall pier diagonal crack widths greater than 1/16 in but less than 1/8 in
DS2c	Spalling of wall pier concrete cover that does not expose longitudinal reinforcement
DS3a	Spalling of wall pier concrete cover that exposes longitudinal reinforcement
DS4a	Maximum measured wall pier horizontal crack widths greater than 1/8
DS4b	Maximum measured wall pier diagonal crack widths greater than 1/8
DS4c	Buckling of wall pier boundary element vertical reinforcement
DS4d	Buckling of wall pier web element vertical reinforcement
DS4e	Initiation of sliding
DS4f	Vertical reinforcement fracture
DS4g	Confinement hoop reinforcement fracture
DS4h	Widespread crushing of concrete
DS4i	Shear failure
DS4j	Out-of-plane buckling of wall pier
DS4k	Severe loss of lateral load caring capacity in wall pier

Table 6.4: Coupling beam damage states

Damage State	Description
DS1a	Initiation of cracking
DS1b	Initiation of coupling beam vertical cracking
DS1c	Initiation of coupling beam diagonal cracking
DS1d	Maximum measured coupling beam vertical crack widths less than $^1/_{16}$ in
DS1e	Maximum measured coupling beam diagonal crack widths less than $^1/_{16}$ in
DS1f	Initiation of yielding in beam longitudinal reinforcement
DS1fMIN	Lower bound on initiation of yielding in beam longitudinal reinforcement
DS1g	Initiation of yielding in beam transverse reinforcement
DS2a	Maximum measured coupling beam vertical crack widths greater than $^1/_{16}$ in but less than $^1/_8$ in
DS2b	Maximum measured coupling beam diagonal crack widths greater than $^1/_{16}$ in but less than $^1/_8$ in
DS2c	Maximum measured coupling beam vertical crack widths greater than or equal to $^1/_8$ in
DS2d	Spalling of coupling beam concrete cover that does not expose longitudinal reinforcement
DS3a	Spalling of coupling beam concrete cover that exposes longitudinal reinforcement
DS4a	Maximum measured coupling beam diagonal crack widths greater than or equal to $^1/_8$ in
DS4b	Buckling of coupling beam longitudinal reinforcement
DS4c	Initiation of sliding at beam-to-wall interface
DS4d	Longitudinal reinforcement fracture
DS4e	Severe loss of flexural or shear capacity in beam

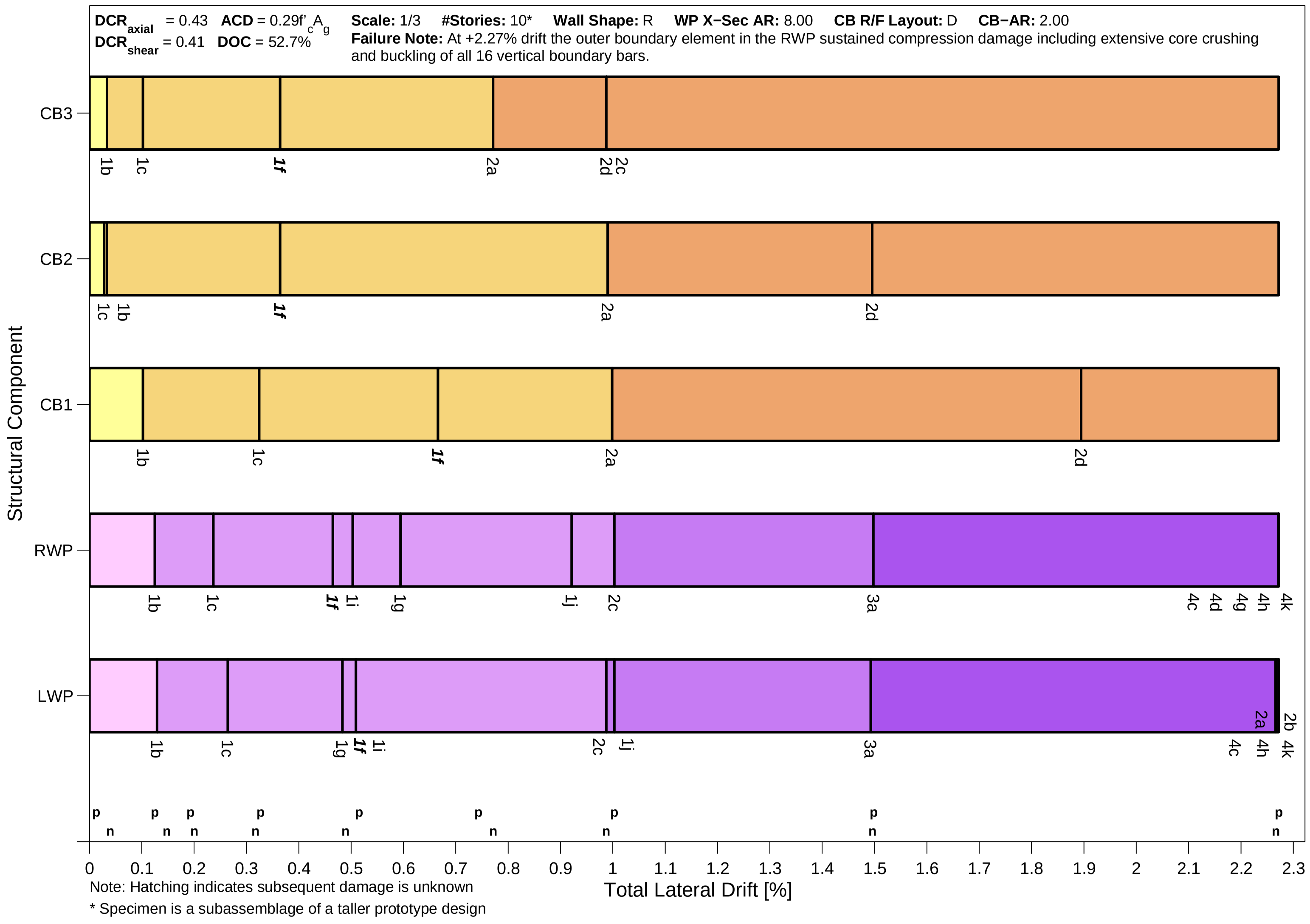

Figure 6.7: Damage sequence chart for CW1

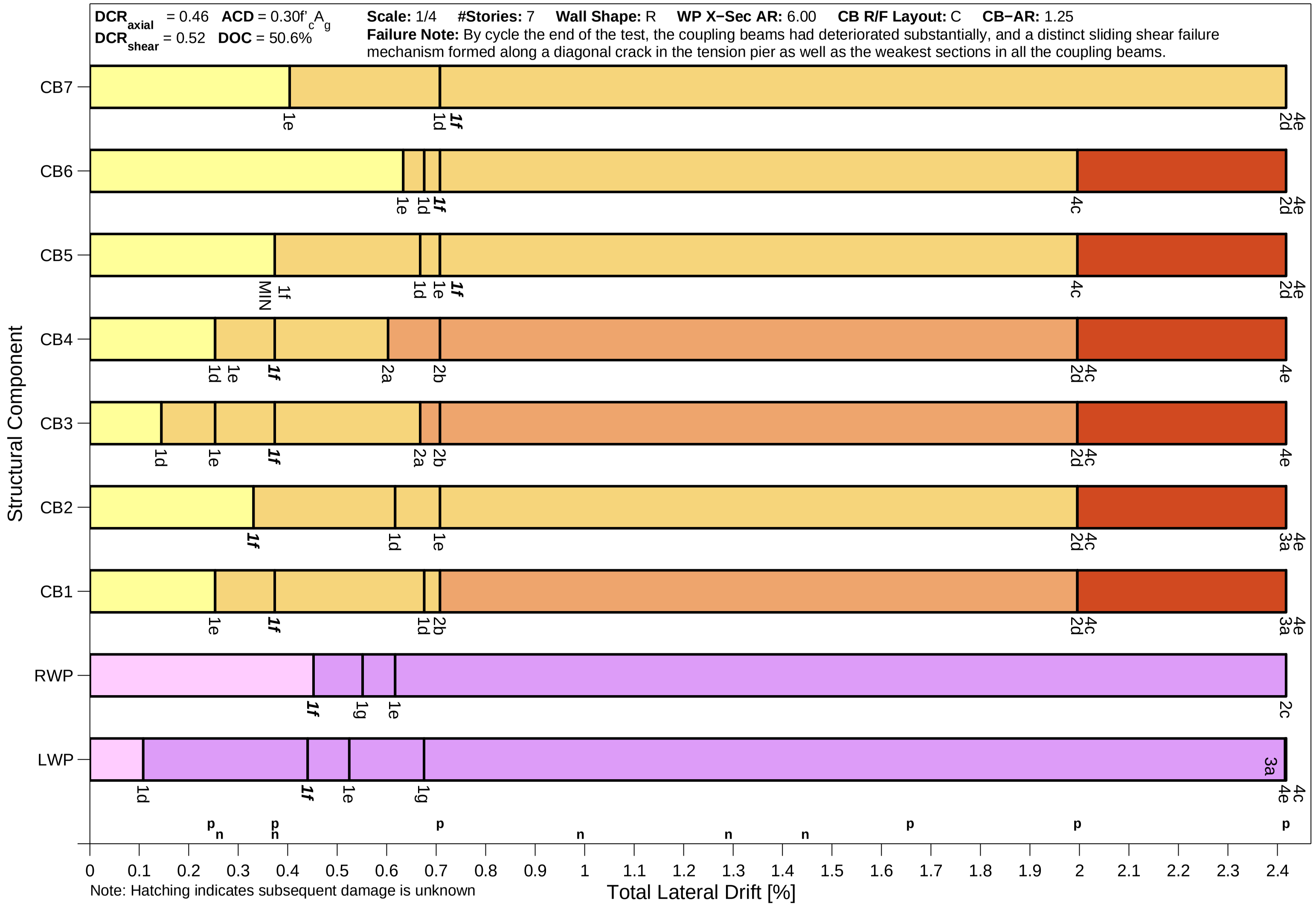

Figure 6.8: Damage sequence chart for Santhakumar WallA

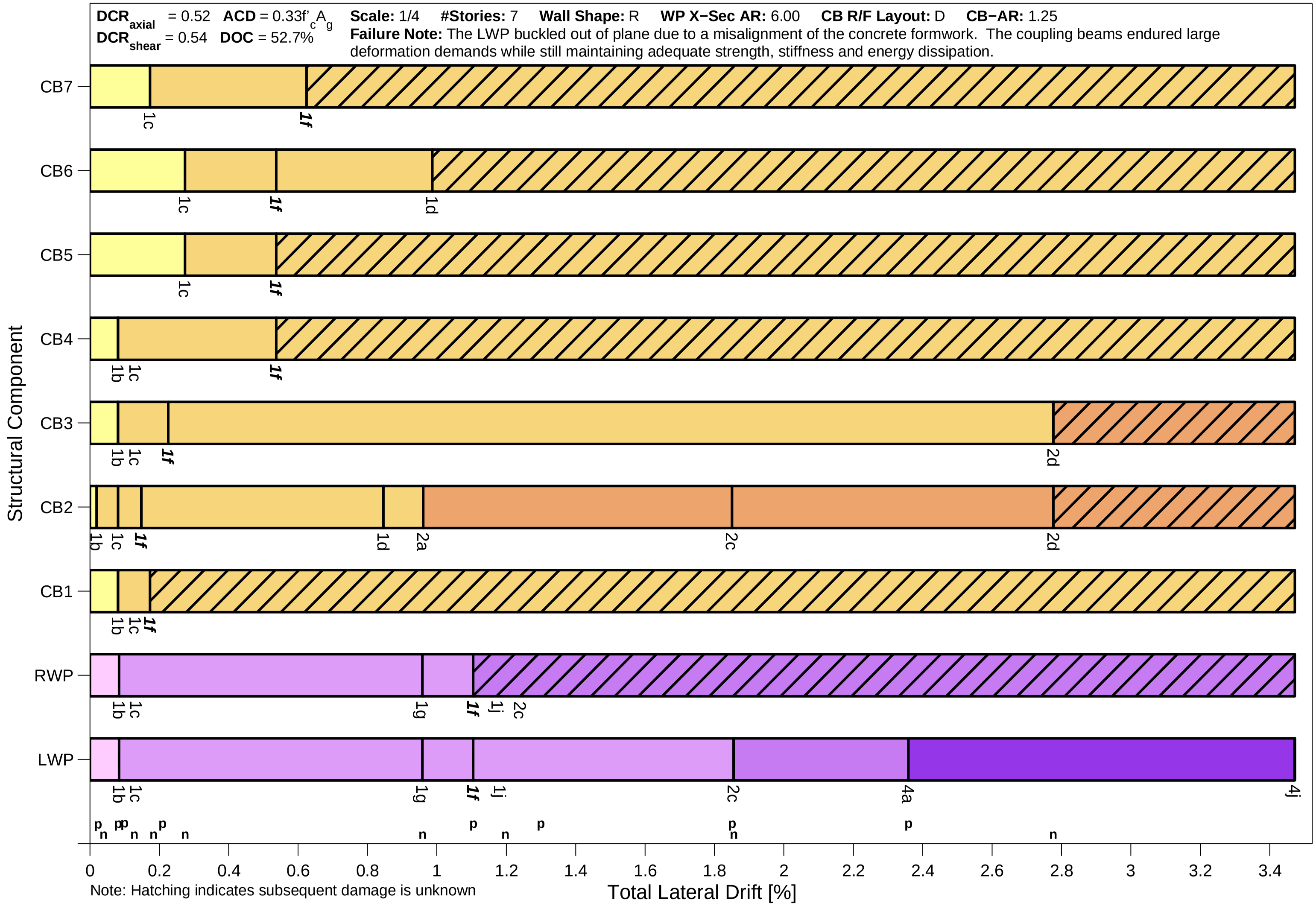

Figure 6.9: Damage sequence chart for Santhakumar WallB

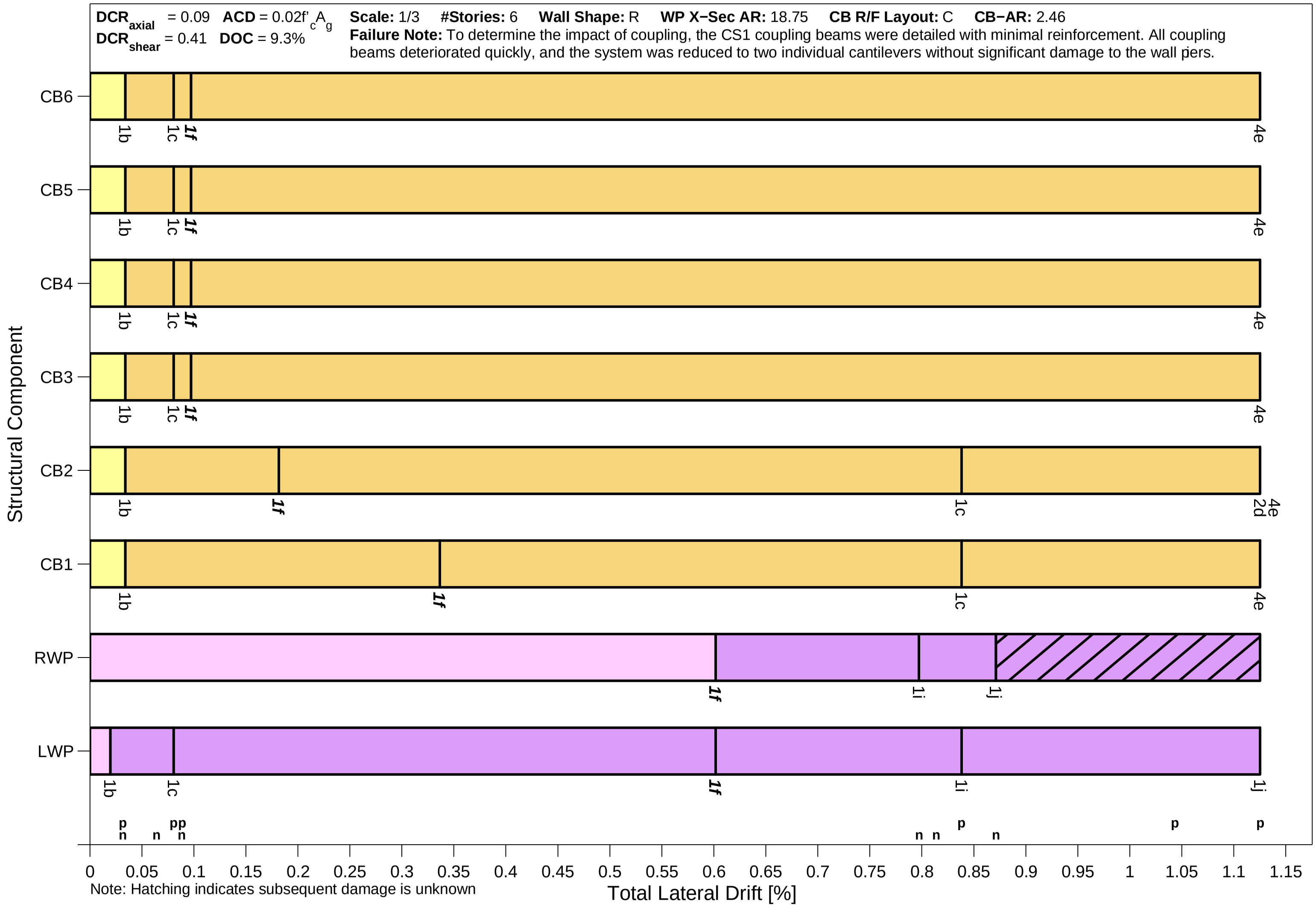

Figure 6.10: Damage sequence chart for Shiu CS1

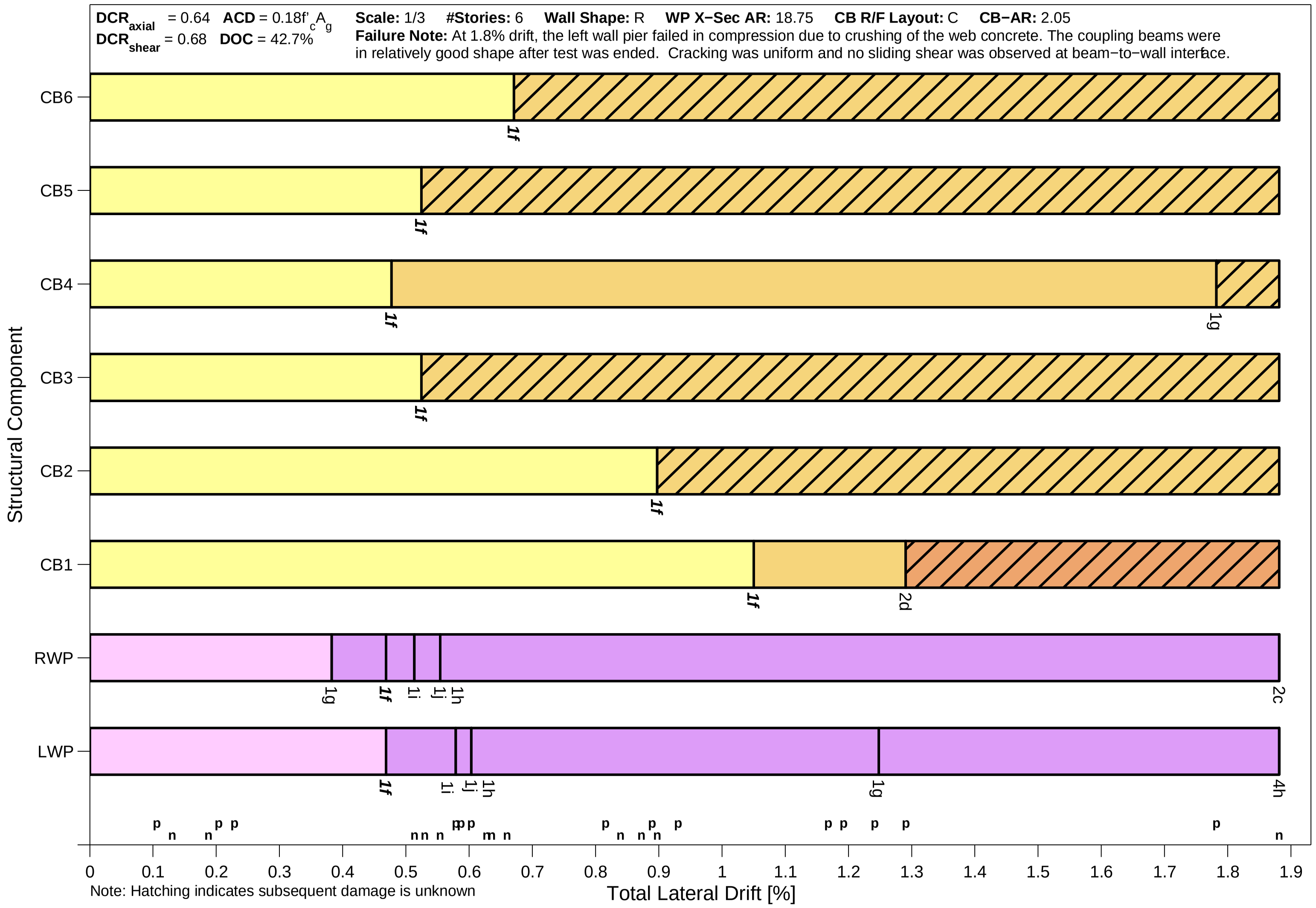

Figure 6.11: Damage sequence chart for Shiu RCS1

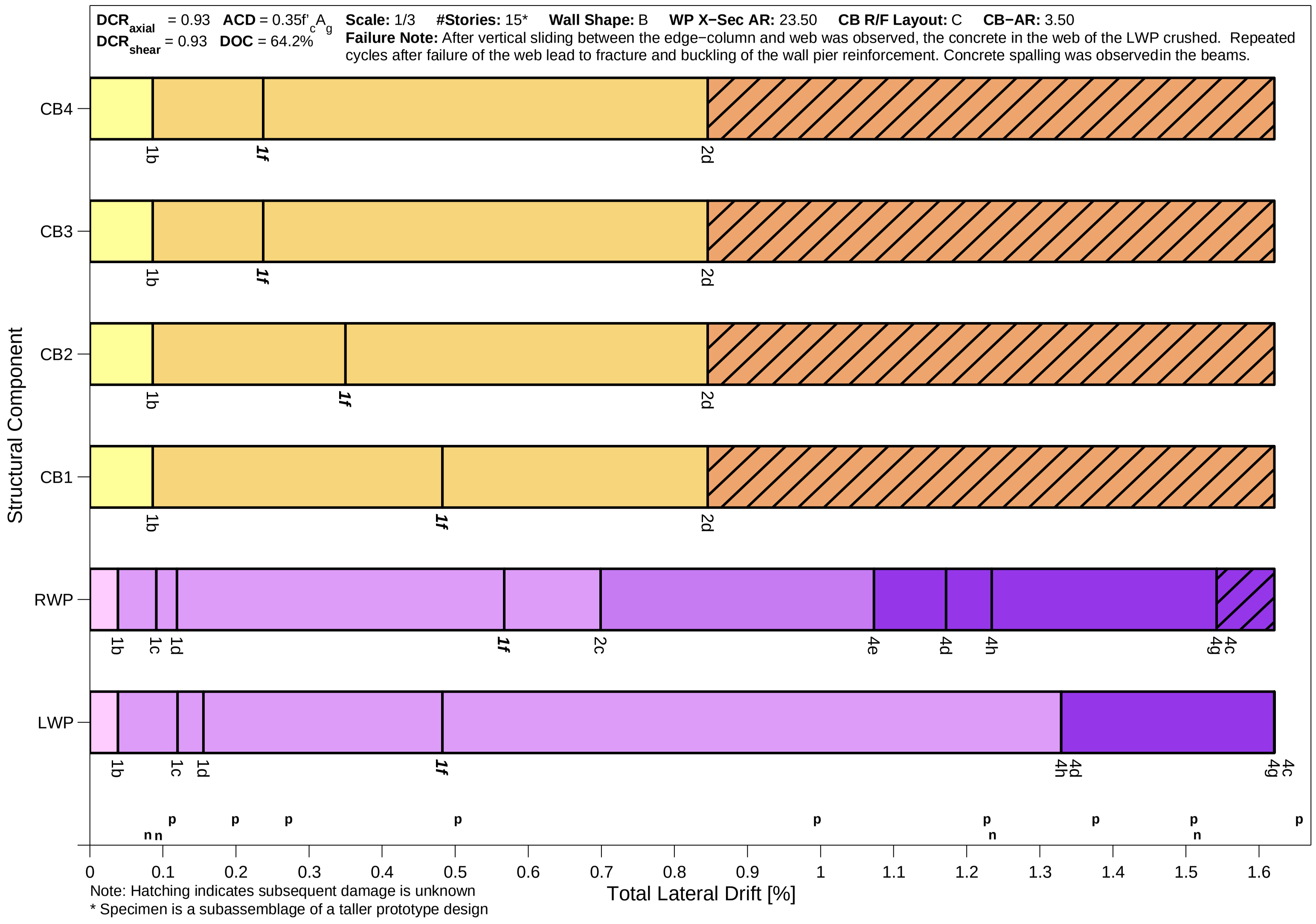

Figure 6.12: Damage sequence chart for Ozselcuk 1C

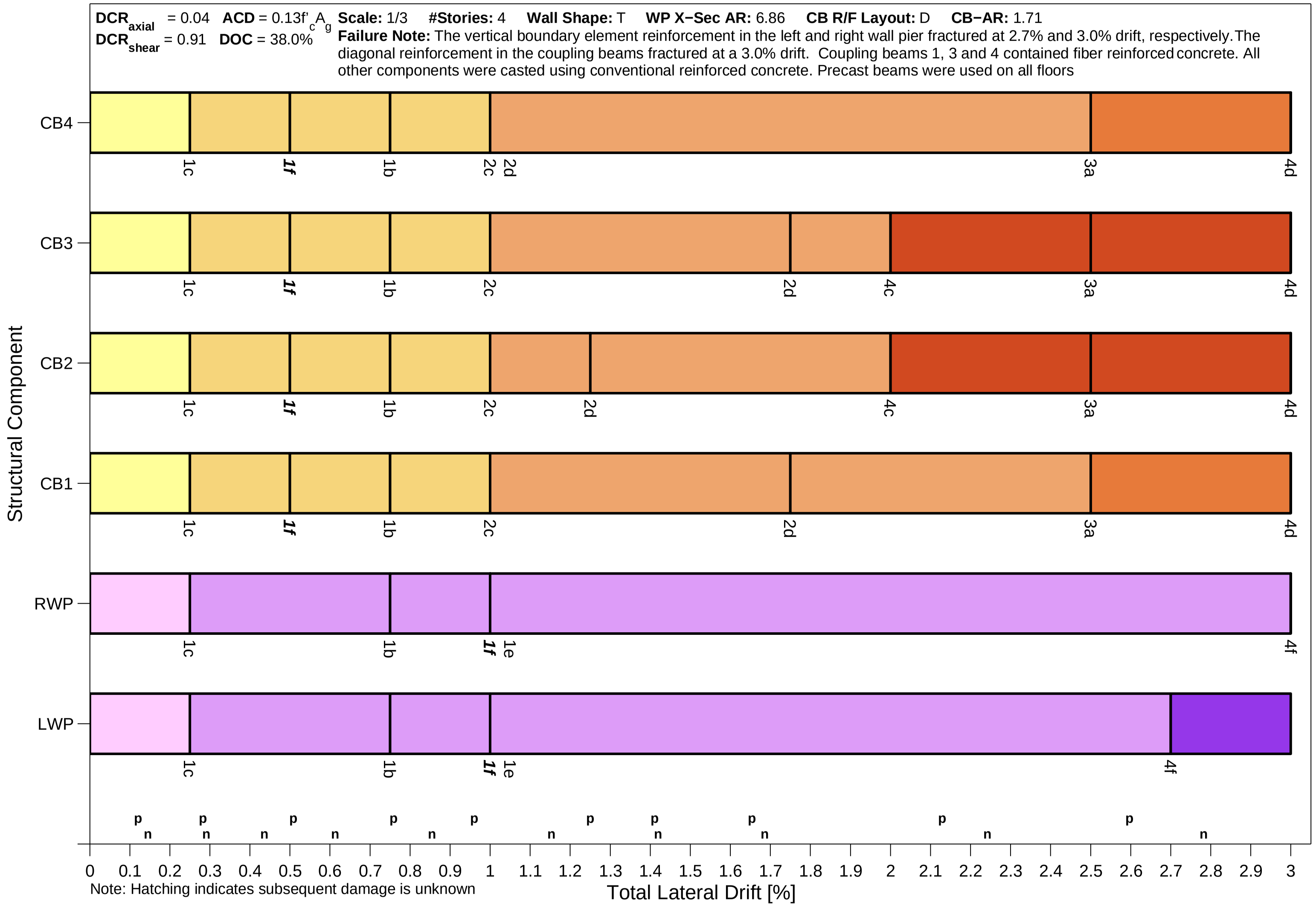

Figure 6.13: Damage sequence chart for Lequesne CW1

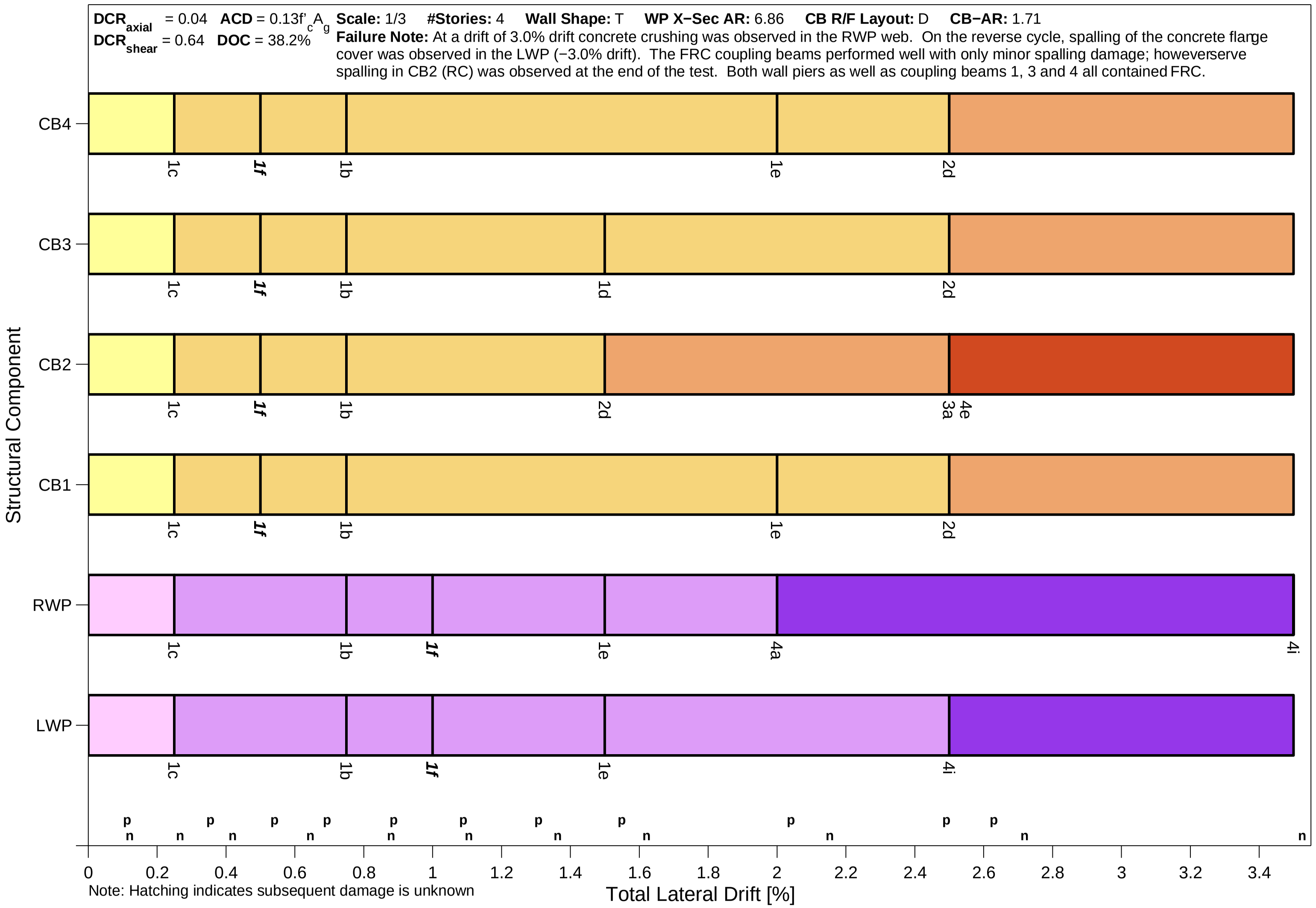

DCR$_{axial}$ = 0.04 **ACD** = 0.13f'$_c$A$_g$ **Scale:** 1/3 **#Stories:** 4 **Wall Shape:** T **WP X−Sec AR:** 6.86 **CB R/F Layout:** D **CB−AR:** 1.71

DCR$_{shear}$ = 0.64 **DOC** = 38.2%

Failure Note: At a drift of 3.0% drift concrete crushing was observed in the RWP web. On the reverse cycle, spalling of the concrete flange cover was observed in the LWP (−3.0% drift). The FRC coupling beams performed well with only minor spalling damage; howeverserve spalling in CB2 (RC) was observed at the end of the test. Both wall piers as well as coupling beams 1, 3 and 4 all contained FRC.

Note: Hatching indicates subsequent damage is unknown

Figure 6.14: Damage sequence chart for Lequesne CW2

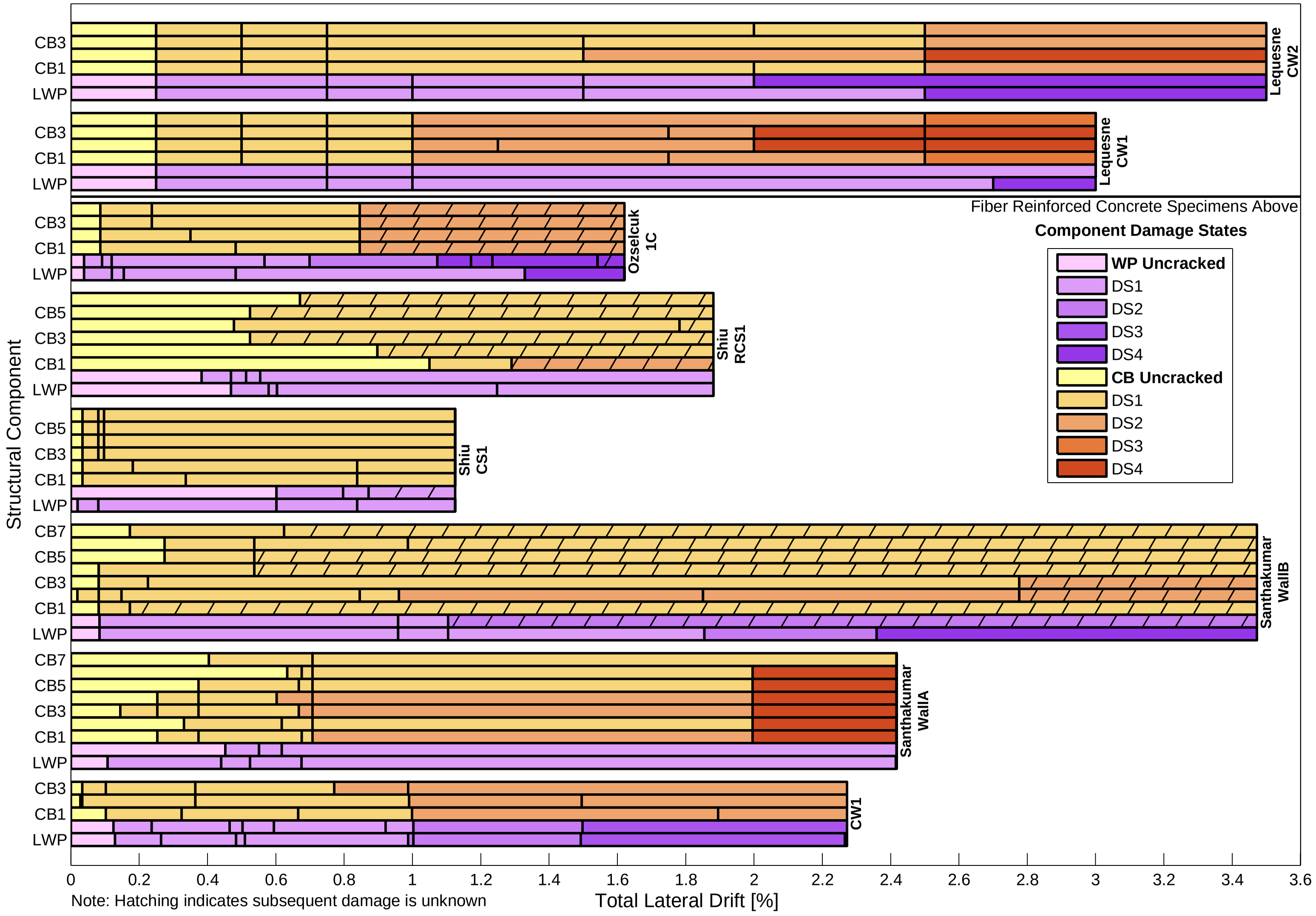

Figure 6.15: Comparison of coupled wall damage states

6.3 Drift Capacity based on Damage States

Drift capacity of a structure is an important engineering demand parameter (EDP) used in design to predict the behavior of a structure during a large seismic event. In performance-based design, an accurate prediction of this EDP is crucial when assessing the structure for the “near collapse” performance level. Based on the force-displacement results for the set of previously tested coupled wall systems, the drift capacities were estimated when the total base shear of the system reach 90% of its maximum base shear (i.e. after the peak was reached (Table 2.9)). In the study presented in the last section, DS4 is typically used to refer to observed damage where the method of repair would lead to replacement of that particular structural component. Therefore, using the damage progression results above, a new set of drift capacities were determined when observed damage reached DS4. The results of the two methods are tabulated in Table 6.5.

Table 6.5: Coupled wall experimental drift capacity comparison

Specimen Name	**CB-R/F Layout**	D_{DS} (%)	**DS at Failure**	$D_{V_{90}}$ (%)	$\frac{D_{DS}}{D_{V_{90}}}$
CW1	D	2.27	WP: DS4c	2.21	1.02
Santhakumar WallA	C	1.45	CB: DS4c	1.93	0.75
Santhakumar WallB	D	2.36	WP: DS4a	3.50	0.67
Shiu CS1	C	1.13	CB: DS4e	0.86	1.31
Shiu RCS1	C	1.88	WP: DS4h	1.60	1.18
Ozselcuk 1C	C	1.07	WP: DS4e	1.34	0.80
Lequesne CW1	D	2.00	CB: DS4c	2.43	0.82
Lequesne CW2	D	2.00	WP: DS4a	1.87	1.07

Chapter 7

ELASTIC ANALYSIS OF COUPLED WALL EXPERIMENTS

Seismic demand analysis requires a structural model of a building stiffness typically modeled using beam-column and/or multi-spring elements. For low-to-mid rise concrete building systems (e.g. less than 240 feet), the seismic design base shear may be determined using the equivalent lateral force procedure (ELF) or a modal response spectrum analysis, as defined in ASCE 7-10 (ASCE, 2010). The prescribed lateral force distribution is used to conduct an elastic analysis to determine the demands in the wall piers and coupling beams and to determine the elastic drift limits. These demands are compared with the corresponding strength and displacement limits.

In order to reasonably predict force and deformation demands at yield in a reinforced concrete building structure subjected for earthquake force demands, engineers have to determine appropriate reduced stiffness parameters to account for concrete cracking and other damage. One interest is to evaluate appropriate stiffness values using coupled walls. Experimental results of the data set includes Specimen CW1 and seven coupled wall specimens presented in Section 2.5. These specimens were analyzed using recommended effective stiffness values from the literature and the research of walls and coupling beams. For each specimen, seven analysis cases were conducted for each recommended set of stiffness values. The predicted global engineering demand parameters at yield were compared with the measured parameters to quantify error and variability. The following sections give overview to the elastic model, a review of the recommended stiffness values and the results of the analyses.

7.1 Overview of Elastic Model in OpenSees

The analyses were performed using the open-source platform analysis program OpenSees (McKenna et al., 2000). A static pushover analysis was performed to determine the elastic response for a set of concrete coupled wall configurations. Each coupled wall was modeled using a two-dimensional equivalent frame. An example is shown in Figure 7.1. The wall piers and coupling beams were modeled using linear elastic beam-column elements. Each line elements was connected by nodes at the intersection of the centriodal axes of the wall piers and coupling beams. The horizontal distance between the centroid of both wall piers is noted L in Figure 7.1. Rigid offsets were used to form the element simulating the coupling beam. The offset started at the intersection of the wall and beam element and spans the width of the wall pier for both ends of the beam element. This rigid offset simulated the flexural and axial rigidity of the wall pier relative to the flexibility of the coupling beam.

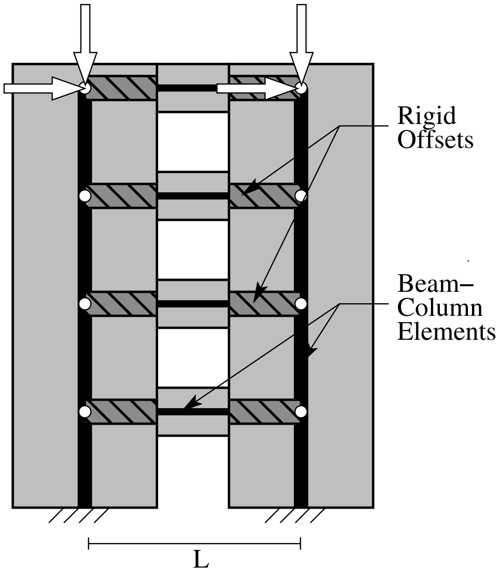

Figure 7.1: Equivalent frame model for an elastic analysis of a coupled wall specimen

Appropriate gravity and lateral loads were applied to simulate the loading conditions used in the experimental. In all cases the boundary conditions at the base were assumed fixed (i.e. all three DOFs were constrained). To account for shear deformations, γ, in the wall piers and coupling beams, a linear shear-deformation model was used. It was independent of the axial and flexural deformations. The shear-deformation model is given by Equation 7.1.

$$V = \frac{G_c A_{cv}}{f_s}\gamma \tag{7.1}$$

where G_c is the effective shear modulus of the concrete component, A_{cv} is the gross area bounded by the thickness of the web and the length of the wall section in the case of the wall piers or bounded by the thickness of the beam web and the height of the coupling beam. The coefficient, f_s, is the shape factor for shear which accounts for nonuniform distribution of shear stress on the section. The shape factor for a rectangular cross section is 1.2. For each set of recommended stiffness values if an effective shear stiffness value was provided, the shear-deformation model described above was included in the analysis.

7.2 Review of Recommended Effective Stiffness values

Recommendations for effective stiffness values are present in design codes and the technical literature. The following provides a review of frequently used methods and current recommendations. Table 7.1 and Figure 7.2 summarize typical effective stiffness values used to model walls and coupling beams in a concrete coupled wall building systems.

Table 7.1: Summary of effective stiffness values for coupled wall elements

	Case A	**Case B1**	**Case B2**	**Case C**	**Case D**	**Case E**	**Case F**
Source	**ASCE 41**	**ACI 318**	**ACI 318**	**CSA A23.3**	**NZS 3101**	**ATC 72**	**Birely/Mohr**
Compression Wall Pier							
Flexure	$0.50E_cI_g$	$0.70E_cI_g$	$0.35E_cI_g$	$0.80E_cI_g$	$0.45E_cI_g$	$0.45E_cI_g$	$0.35E_cI_g$
Shear	$1.00GA_{cv}$	$1.00GA_{cv}$	$1.00GA_{cv}$	—	—	$0.10GA_{cv}$	$0.15GA_{cv}$
Axial	$1.00E_cA_g$	$1.00E_cA_g$	$1.00E_cA_g$	$0.80E_cA_g$	$1.00E_cA_g$	$1.00E_cA_g$	$1.00E_cA_g$
Tension Wall Pier							
Flexure	$0.50E_cI_g$	$0.70E_cI_g$	$0.35E_cI_g$	$0.60E_cI_g$	$0.28E_cI_g$	$0.20E_cI_g$	$0.35E_cI_g$
Shear	$1.00GA_{cv}$	$1.00GA_{cv}$	$1.00GA_{cv}$	—	—	$0.10GA_{cv}$	$0.15GA_{cv}$
Axial	$1.00E_cA_g$	$1.00E_cA_g$	$1.00E_cA_g$	$0.60E_cA_g$	$1.00E_cA_g$	$1.00E_cA_g$	$1.00E_cA_g$
Conventionally Reinforced Coupling Beams							
Flexure	$0.30E_cI_g$	$0.35E_cI_g$	$0.35E_cI_g$	$0.40E_cI_g$	$\alpha_c 0.4E_{40}I_g^*$	$0.15E_cI_g$	$0.041E_cI_g$
Shear	$1.00GA_{cv}$	$1.00GA_{cv}$	$1.00GA_{cv}$	$0.15GA_{cv}$	—	$0.25GA_{cv} - 1.0GA_{cv}$	$0.15GA_{cv}$
Axial	$1.00E_cA_g$	$1.00E_cA_g$	$1.00E_cA_g$	$1.00E_cA_g$	$1.00E_cA_g$	$1.00E_cA_g$	$1.00E_cA_g$
Diagonally Reinforced Coupling Beams							
Flexure	$0.30E_cI_g$	$0.35E_cI_g$	$0.35E_cI_g$	$0.25E_cI_g$	$0.60E_cI_g$	$0.15E_cI_g$	$0.044E_cI_g$
Shear	$1.00GA_{cv}$	$1.00GA_{cv}$	$1.00GA_{cv}$	$0.45GA_{cv}$	GA_{shear}‡	$0.25GA_{cv} - 1.0GA_{cv}$	$0.15GA_{cv}$
Axial	$1.00E_cA_g$	$1.00E_cA_g$	$1.00E_cA_g$	$1.00E_cA_g$	$1.00E_cA_g$	$1.00E_cA_g$	$1.00E_cA_g$

* If beam has flanges, substitute 0.40 for 0.35 and α_c accounts for diagonal cracking and ranges from 1.0 – 0.25 depending on the shear span ratio

‡ A_{shear} ranges from $0.20A_g$ – $0.05A_g$ and is defined in Section 7.2.4

[ht!]

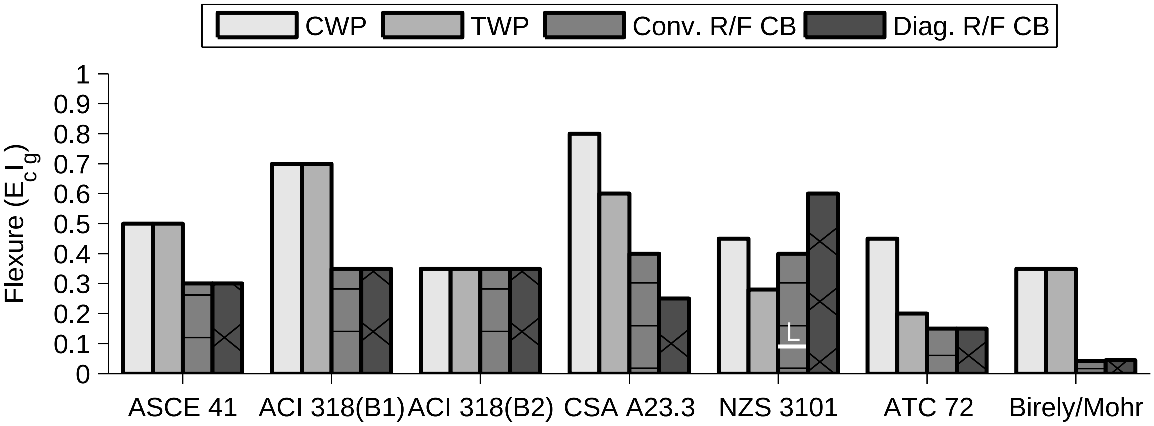

(a) Effective flexural stiffness

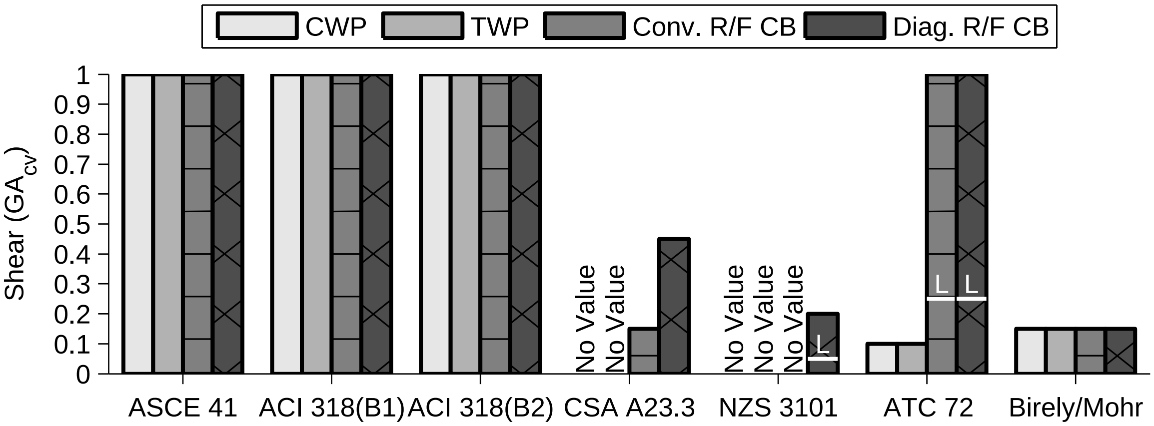

(b) Effective shear stiffness

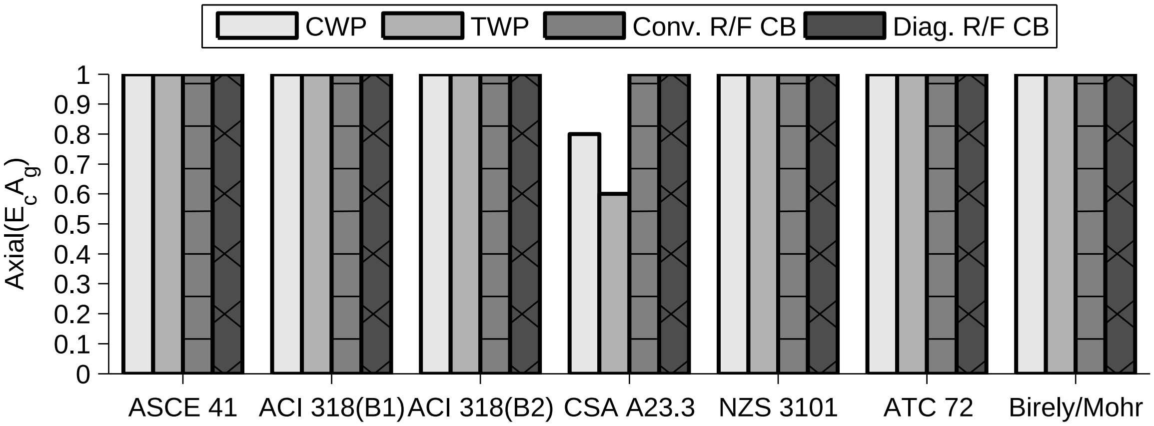

(c) Effective axial stiffness

Figure 7.2: Effective stiffness values (L - Lower bound value)

7.2.1 ASCE/SEI 41-06

ASCE/SEI 41-06 (ASCE, 2007a) provides recommended effective stiffness values for modeling reinforced concrete wall piers and coupling beams. Table 7.2 summarizes the effective stiffness values recommended in the ASCE/SEI 41-06 *Supplement No. 1* (ASCE, 2007b). These effective stiffness values are intended to be used in the design of structures using linear analysis methods and correspond to secant stiffness values up to yield of the structural element.

Table 7.2: Effective stiffness values for coupled wall components (ASCE, 2007b)

Component	**Flexural Rigidity**	**Shear Rigidity**	**Axial Rigidity**
Beams-nonprestressed	$0.3E_cI_g$	$0.4E_cA_{cv}$	$1.0E_cA_g$
Walls-uncracked	$0.8E_cI_g$	$0.4E_cA_{cv}$	$1.0E_cA_g$
Walls-cracked	$0.5E_cI_g$	$0.4E_cA_{cv}$	$1.0E_cA_g$

In general, the effective shear stiffness values for both coupling beams and wall piers are taken as the gross section properties. Using uncracked concrete properties, the shear stiffness is provided as follows:

$$G_cA = \frac{E_c}{2(1+\nu)}A_{cv} = 0.4E_cA_{cv} \tag{7.2}$$

where E_c, A_{cv} and ν are the modulus of elasticity of concrete, the cross-sectional area of the web and Poisson's ratio, respectively. For uncracked concrete ν is taken as 0.2. The effective flexural stiffness for structural walls is categorized by either uncracked or cracked. It is recommended in ASCE/SEI 41-06 that all of the structural walls in a building be modeled either assuming uncracked or cracked stiffness in order to maintain a reasonable distribution of lateral forces. Diagonally and conventionally reinforced coupling beams are given the same stiffness guidelines and do not address differences in behavior that are differentiated in other building codes.

7.2.2 ACI 318-08

Similar to ASCE/SEI 41-06, the American Concrete Institute (ACI, 2008) provides recommendations for the effective moment of inertia and cross-sectional area depending on a structural member. As long as the assumptions stay consistent throughout an analysis, ACI states an engineer may use a reasonable set of assumptions when computing effective stiffness values for structural members. More specifically, calculating the lateral deflections of a reinforced concrete building system using an elastic analysis may be computed using section properties defined in ACI §10.10.4.1(a) through (c) or by simply using 50% of the gross stiffness values. In general, ACI commentary provides justification to use the prescribed effective stiffness values in §10.10.4.1 citing a correlation to experimental and analytical results.

If an elastic analysis is performed using uncracked moments of inertia for the wall members and the wall factored moments and shears indicate cracking based on the modulus of rapture, the analysis should be repeated using the cracked properties in the stories where cracking is present. In addition to modeling the flexural stiffness of a given member, it is also permissible to assume a shear modulus of $0.4E_c$ when calculating a shear stiffness.

Two cases, B1 and B2, were used in this study to represent both an upper and lower bound on the effective stiffness values for cracked and uncracked wall piers. Case B1 was used to simply demonstrate an upper-bound and did not follow the commentary suggestions to identify cracking regions and iterate on the analysis. The recommend ACI values coupled wall components are shown in Table 7.1.

7.2.3 CSA A23.3-04

In the *Design of Concrete Structures* published by the Canadian Standard Association (CSA, 2004), reduced section properties are used to determine deflections and force demands. The effective section properties are reduced as a fraction of the gross properties similar to the procedure in ACI 318-08. The CSA makes a distinction between the stiffness of a reinforced beam and a ductile coupling beam. A ductile coupling beam needs to meet the requirements of §21.6.8.5 – S21.6.8.7 which includes a span-to-depth ratio greater than or equal to 2.0. Furthermore, the flexural stiffness assigned to a coupling beam with diagonal reinforcement is less than a coupling beam without diagonal reinforcement, but the shear stiffness assigned to a diagonally reinforced coupling beam is higher than a conventionally reinforced beam. The recommended effective stiffness values are included in Table 7.1.

To determine the effective flexural stiffness in the wall piers, a procedure that accounts for the axial load in the wall. The CSA procedure adopted an upper-bound limit on flexural stiffness for an individual wall as proposed by Adebar et al. (2007). The following equations are recommended to calculate the effective properties of the wall piers.

$$I_e = \alpha_w I_g \tag{7.3}$$

where, I_e is the effective moment of inertia and α_w is defined as follows:

$$\alpha_w = 0.6 + \frac{P_s}{f_c' A_g} \leq 1.0 \tag{7.4}$$

where P_s is the axial load at the base of the wall from factored loads. Additionally, the axial load may be averaged between each wall pier in a coupled wall system. In this study, however, α_w in the tension wall and the compression wall were individually calculated. The procedure described above is also used to define the effective axial cross sectional area, Axe, of the wall piers (Equation 7.5).

$$A_{xe} = \alpha_w A_g \tag{7.5}$$

Additionally, the shear flexibility was not addressed in the CSA guidelines.

7.2.4 NZS 3101-06

The *Concrete Structures Standard*, published by Standards New Zealand (NZS, 2006), provide a procedure for determining the effective stiffness properties used in elastic analysis. The effective section properties separated into ultimate and serviceability limit state recommendations. The ultimate limit state recommendations corresponds to sectional properties which are used in elastic analyses of structures subjected to seismic demands and correspond to member stiffness properties at first yield. On the other hand, the serviceability limit state corresponds to a level of demand in which the structure becomes unfit for its intended use. This limit state was not included as a part of this study.

The effective moment of inertia recommendations are shown in Table 7.3 for coupled wall components at the ultimate limit state (i.e. yield). When calculating the coupling beam effective moment of inertia from Table 7.3, a linear interpolation using the exact yield strength of the reinforcement should be performed. On the other hand, when calculating the wall pier effective moment of inertia, a bilinear interpolation should be performed between the yield strength of the longitudinal reinforcement and the factored axial load in the wall pier.

To account for the decrease in shear stiffness resulting from to diagonal tension cracking in conventionally reinforced with short span-to-depth ratios, I_e from Table 7.3 is multiplied by a reduction factor, α_c (Table 7.4). This effect can be ignored if the nominal shear stress in the beam is less than $0.25\sqrt{f'_c}$. Table 7.4 provides the relationship between the inverse of the shear span to depth ratio, ${}^{M}\!/_{Vd}$ and α_c. Values between the given ${}^{M}\!/_{Vd}$ ratios are linearly interpolated in order to accurately capture stiffness reduction.

Because Table 7.3 tends to underestimate the flexural stiffness for conventionally reinforced coupling beams with reinforcement ratios exceeding 0.8% for Grade 500 reinforcement and 1.1% for Grade 300 reinforcement, the effective second moment of inertia may be calculated using Equation 7.6. However, the values recommended in Table 7.3 were sufficient for this study due to the low reinforcement ratios in the conventionally

Table 7.3: Effective second moment of inertia values, I_e, for coupled wall components (NZS, 2006)

	Ultimate limit state	
Type of Member	f_y **= 300 MPa**	f_y **= 500 MPa**
Conventionally Reinforced Beams		
Rectangular	$0.4I_g$‡	$0.32I_g$‡
T and L beams	$0.35I_g$‡	$0.27I_g$‡
Walls		
$N^*/A_g f'_c = 0.2$	$0.48I_g$	$0.42I_g$
$N^*/A_g f'_c = 0.1$	$0.40I_g$	$0.33I_g$
$N^*/A_g f'_c = 0.0$	$0.32I_g$	$0.25I_g$
Diagonally Reinforced Coupling Beams		
$0.6I_g$ for flexure		
A_{shear} as defined in text		

‡use with E_{40} only

N*	design axial load at ultimate limit state
A_g	gross cross-sectional area
I_g	gross second moment of inertia
f'_c	compressive strength of concrete
f_y	yield strength of concrete longitudinal reinforcement
E_{40}	modulus of elasticity for 40 MPa concrete

Table 7.4: NZS stiffness reduction to account for diagonal cracking in beams

$\frac{M}{Vd}$	≤ 0.5	0.75	1.0	1.5	2.0
α_c	0.25	0.38	0.5	0.75	1.0

reinforced coupling beams.

$$I_e = (0.32 + 40(\rho - 0.0075))I_g \geq \begin{cases} 0.32 & \text{for Grade 500 reinforcement} \\ 0.40 & \text{for Grade 300 reinforcement} \end{cases} \tag{7.6}$$

The reinforcement ratio, ρ, is the defined as $A_s/b_w d$ where A_s is the area of the tension reinforcement, b_w is the width of the beam web and d is the depth measured from the top of the beam to the tension reinforcement. If the beam includes flanges, the width of the beam is $1.1b_w$, and this width is used to calculate the reinforcement ratio.

The flexural stiffness values provided in Table 7.3 indicate higher values for a diagonally reinforced coupling beam. However, the effective shear stiffness is modified to provide additional flexibility due to diagonal cracking. The modification includes reducing the shear area, A_{shear}, using the following procedure.

Because a diagonally reinforced coupling beam typically deforms in shear, the NZS 3101 requires the pairing of a flexural stiffness and shear stiffness. The shear stiffness is based on the shear demand in the coupling beam when yield is reached in the diagonal reinforcement, and this demand is defined as:

$$V_y = 2A_{vd}f_y sin(\alpha) \tag{7.7}$$

where A_{vd} is the total area of a bundle of diagonal reinforcement and α is the diagonal reinforcement angle of inclinations with respect to the horizontal axis of the beam. The shear deformation, δ_y at first yield is calculated using Equation 7.8, and this equations accounts for the additional deformation due to the development of the diagonal reinforcement yield strength, f_y.

$$\delta_y = \left(\frac{l_n}{cos(\alpha)} + \frac{f_y d_b}{15}\right)\frac{f_y}{E_s} \tag{7.8}$$

The clear span of the coupling beam is given as l_n and d_b is the diameter of the diagonal reinforcement.

Next, the stiffness of the diagonal reinforcement and concrete (i.e. the compression strut) is assumed to be 20% of the tension reinforcement reiforcemetn stiffness; therefore, the shear deflection, δ_v, can be calculated using Equation 7.9.

$$\delta_v = \frac{1.2\delta_y}{2sin(\alpha)} \tag{7.9}$$

Finally, the effective shear area can be calculated using:

$$A_{shear} = \frac{V_y}{0.4E_c l_n \delta_y} A_g \tag{7.10}$$

Modification factors to estimate the flexural stiffness of the wall piers are given in Table 7.3. These factors are a function of the design axial load, N*, estimated for the ultimate limit state (Table 7.3). No requirements are given for wall pier shear stiffness values; however, it is recommended the effective cross-sectional area of the wall piers be taken as the gross area.

7.2.5 PEER/ATC-72-1

The seismic design of tall buildings has been investigated through a partnership with the Pacific Earthquake Engineering Research Center (PEER) and the Applied Technology Council (ATC), named the PEER Tall Buildings Initiative (PEER/ATC-72-1, 2010). The study provided recommended effective stiffness values for modeling reinforced concrete shear walls, including coupled walls.

In comparison to current reference codes and standards, effective stiffness values derived from coupling beam tests are low (Paulay and Binney (1974); Barney et al. (1980); Tassios et al. (1996); Galano and Vignoli (2000); Kwan and Zhao (2002); Naish et al. (2009)). Using these experimental results an effective flexural stiffness $E_cI_e \approx 0.15E_cI_g$ is recommended. Effective shear stiffness values for coupling beams depend on the span-to-depth ratio, l_n/h. For decreasing the span-to-depth ratios, the deformation mode in a coupling beam changes from flexure to shear which results in additional nonlinear behavior. As a results, ATC recommends using an effective shear modulus of, $G_c = 0.40E_c$

for coupling beams with $l_n/h \geq 2.0$ and $G_c = 0.10E_c$ for coupling beams with $l_n/h \leq 1.4$. The effective shear stiffness is linearly interpolation between the span-to-depth ratio limits.

The relationship for the wall piers up to the point of yield and when axial load demands are on the order of $P \approx 0.10f'_cA_g$, appropriate effective flexural stiffness for walls range from $0.40E_cI_g$ and $0.5E_cI_g$. Equation 7.11, developed by Adebar et al. (2007), is used to estimate the wall flexural stiffness and is a function of the axial load. The upper-bound equation is appropriate for uncracked walls (i.e. the maximum roof displacement is less than or equal to 20% of the yield displacement). The lower-bound equations is appropriate for displacements at or above the yield drift. Furthermore, ATC recommends using Equation 7.11b only for axial loads less than $0.1f'_cA_g$ because they state there is insufficient test data available to suggest an increase in the effective flexural stiffness for higher axial stress demands.

$$I_e = \left(0.6 + \frac{P}{f'_cA_g}\right) I_g \leq I_g \text{ Upper-bound} \tag{7.11a}$$

$$I_e = \left(0.2 + 2.5\frac{P}{f'_cA_g}\right) I_g \leq 0.7I_g \text{ Lower-bound} \tag{7.11b}$$

For a wall with a shear strength of $5\sqrt{f'_c}A_{cv}$ or greater, ATC recommends an effective shear modulus at yield of $G_c/20$. This value was derived using the assumption that the shear strain at yield is twice the principal strain (e.g. approximately 0.002 for Grade 60 reinforcement). Furthermore, typical walls in new construction have shear strengths on the order of $10\sqrt{f'_c}A_{cv}$ and in that case $G_c/10$ is recommended for the effective shear modulus value. In addition, it is recommended that the effective shear stiffness values be parameterized in order to capture the sensitivity of the analysis with respect to cracking and axial load.

7.2.6 Mohr, 2007

Mohr (2007) evaluated nonlinear finite element models to estimate the response of reinforced concrete coupling beams. A database was established of prior experimental test programs including tests by Galano and Vignoli (2000), Kwan and Zhao (2002) and Tassios et al. (1996). Specimens ranged in aspect ratio, reinforcement ratio, level of confinement and reinforcement layout (conventional or diagonal).

This experimental data was used to derive an effective flexural stiffness which was calculated for each experiment using Equation 7.17. The following procedure utilizes the experimental data and Timoshenko beam theory (Timoshenko and Goodier, 1970) to calculate an effective flexural stiffness of a given coupling beam at yield assuming an effective shear stiffness. The following procedures is similar to techniques used by Birely (2011) in Section 7.2.7. Equations 7.12 and 7.13 are given by the Timoshenko beam theory.

$$\frac{d\theta}{dx} = \frac{M\left(x\right)}{EI} \tag{7.12}$$

$$\frac{\partial u}{\partial x} = \theta - \frac{1}{\kappa AG}\frac{\partial}{\partial x}\left(EI\frac{\partial \theta}{\partial x}\right) \tag{7.13}$$

The Timoshenko beam theory requires the moment distribution along the length of the beam. Typically, a single point load was applied to one end of the beam and the rotational degrees of freedom where fixed in order to capture equal end moments. This loading and boundary conditions results in a constant shear force, V(x)=V, and a linear bending moment, M(x), along the beam. The moment at any point along the beam is defined as:

$$M(x) = V\left[\frac{l_n}{2} - x\right] \tag{7.14}$$

The rotation along the length of the beam, $\theta\left(x\right)$, is derived below by integrating Equation

7.12, applying the boundary condition $\theta(x = 0) = 0$ and substituting in Equation 7.14.

$$\theta(x) = \frac{Vx}{2EI}\left(l_n - x\right) \tag{7.15}$$

Integrating Equation 7.13, applying the boundary condition $u(x = 0) = 0$ and substituting in Equation 7.15 results in the following expression of the displacement of the coupling beam along its length, $u(x)$:

$$u(x) = \frac{Vx^2}{12EI}\left(3l_n - 2x\right) + \frac{Vx}{\kappa GA} \tag{7.16}$$

The measured yield displacement, δ_y, and strength, V_y, are used. Rearranging terms and substituting in these measured values into Equation 7.16 results in the following expression to estimate the effective flexural stiffness, E_cI_e, at yield:

$$E_cI_e = \frac{V_y l_n^3}{12}\left(\frac{\kappa G_c A_{cv}}{\kappa G_c A_{cv}\delta_y - V_y l_n}\right) \tag{7.17}$$

where κ is simply the inverse of the shape factor for shear, f_s as defined in Section 7.1.

To calculate the experimental effective flexural stiffness for a coupling beam test using Equation 7.17, an effective shear stiffness, $\kappa G_c A_{cv}$ at yield needs to be assumed. Based on recommendations made by Saatcioglu et al. (1983), Paulay (1971) the effective shear modulus of 0.15G was assumed. The results indicate the mean effective flexural stiffness for a conventionally reinforced coupling beam is $E_cI_e = 0.041E_cI_g$ and for diagonally reinforced coupling beams $E_cI_e = 0.044E_cI_g$. The standard deviations for these results were $0.0284E_cI_g$ and $0.0246E_cI_g$, respectively.

7.2.7 Birely

Using the the test results for the four planar wall tests that were completed as part of this research program to derive effective flexural and shear stiffness results. These results are shown in Figure 7.3.

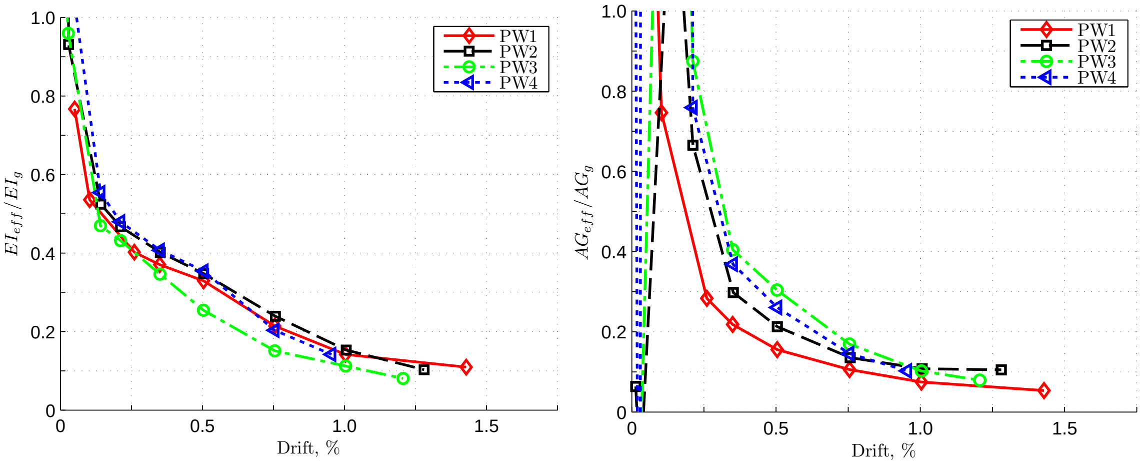

(a) Effective flexural stiffness, E_cI_e (b) Effective shear stiffness, G_cA_{cv}

Figure 7.3: Effective stiffness values derived from experimental results (Birely, 2011)

The effective stiffness values were derived using Timoshenko beam theory and measurements including the horizontal displacements and rotations along the height of the planar wall specimens. The effective flexural and shear stiffness values were calculated at different drift levels through the experiment. Using these results at yield, the effective flexural and shear stiffness at yield were determined as $0.35I_g$ and $0.15GA_{cv}$, respectively. These results were derived for experiments with axial load demands of approximately $0.1f'_cA_g$.

7.2.8 Summary of model variations

A summary of the current code specified and researched based methods for determining effective stiffness coefficients for coupled wall components are presented here. The following model cases were used to estimate the elastic behavior of previously coupled wall specimens:

Case A ASCE/SEI 41-06 (ASCE, 2007a)

Case B1 ACI 318-08 where the wall piers are considered uncracked (ACI, 2008)

Case B2 ACI 318-08 where the wall piers are considered cracked (ACI, 2008)

Case C CSA A23.3-04 (CSA, 2004)

Case D NZS 3101-06 (NZS, 2006)

Case E PEER/ATC-72-1 (PEER/ATC-72-1, 2010)

Case F Combination of results from Mohr (2007) and Birely (2011)

The effective stiffness values for each test specimen used in the evaluation of previous coupled wall experiments are presented in Tables D.1 to D.7 located in Appendix D.1. Results of analyses for seven coupled wall specimens using multiple stiffness methods are discussed in the next section.

7.3 Comparisons of Elastic Analysis Results

To evaluate each set of modeling parameters, elastic models where developed for each test specimen presented in Tables D.1 to D.7. Each set of effective stiffness parameters described previously were used. The models were evaluated based on the variability of the predicted engineering demand parameters including the stiffness, base reactions and elastic story drift.

7.3.1 Force-Displacement Results

Figures 7.4–7.9 are analytical force-drift results for model cases A-F as well as the experimental force-drift envelope. The total lateral drift is the lateral displacement relative to (or normalized by) the vertical distance to the location of measured displacement. The total lateral drift for each model cooresponded to the node representing the location of measured drift for each experiment. Tables 7.5 –7.7 present the predicted drift, base shear and secant stiffness at yield for each specimen.

Yield was determined for the elastic analysis when the moment in either a coupling beam or a wall pier reached its respective yield strength. Furthermore, the yield moment for a wall pier was estimated using moment-curvature results with zero axial load applied to the section. Additionally, the yield strength of diagonally reinforced coupling beams was estimated using the moment demand when the beam reaches its nominal shear strength as defined in Chapter 21 of ACI 318-08. The yield strength for a conventionally reinforced coupling beam was estimated as 85% of the nominal moment strength.

Table 7.5: Summary of predicted drift at yield for linear elastic analyses (%)

		Santhakumar		**Shiu**	**Ozselcuk**	**Lequesne**	
	CW1	**WallA**	**WallB**	**CS1**	**1C**	**CW1**	**CW2**
ASCE 41 (A)	0.112	0.090	0.121	0.047	0.095	0.101	0.101
ACI 318 (B1)	0.105	0.090	0.119	0.047	0.095	0.098	0.098
ACI 318 (B2)	0.109	0.090	0.117	0.047	0.082	0.095	0.095
CSA A23.3 (C)	0.127	0.164	0.164	0.052	0.113	0.110	0.110
NZS 3101 (D)	0.178	0.095	0.190	0.045	0.068	0.185	0.179
ATC 72 (E)	0.246	0.200	0.259	0.082	0.252	0.335	0.277
Birely/Mohr (F)	0.362	0.281	0.362	0.120	0.378	0.364	0.350
Mean	**0.177**	**0.144**	**0.190**	**0.063**	**0.155**	**0.184**	**0.173**
Std. Dev.	**0.096**	**0.074**	**0.091**	**0.028**	**0.116**	**0.118**	**0.102**
Measured	**0.364**	**0.331**	**0.148**	**0.097**	**0.237**	**0.500**	**0.500**

The ACI 318 uncracked(B1) and crack(B2) cases predict yield at essentially the same drift and base shear; however, the secant stiffness is much larger than the experiments. Further investigation into Tables 7.5 and 7.6 reveals the drift and base shear at which the cracked model yields are a bit lower on average than the uncracked model. In a model of a single component (i.e. a wall) reducing the effective stiffness increased the yield drift. In a typical coupled wall system, the relative and total stiffness values mater. If the coupling beam controls the behavior, reducing the effective stiffness of the wall pier does not directly translate into an improved estimate of the yield displacement. For 90% of the analyses the initial yield displacement cooresponds to one (or more) coupling beams reaching their yield strength.

Analyses where the wall piers yield first are noted in Table 7.5; however, the experimental specimens did not exhibited this behavior. The tension wall in three of the analyses yields first for cases where the coupling beam stiffness is low (Birely/Mohr). This is a result of more forces being distributed to the wall piers. The other instance occurs in a barbell shaped wall with an effective flexural stiffness of $0.95E_cI_g$ (CSA) which is high compared to the coupling beam stiffness ($0.40E_cI_g$), so it is reasonable that this component yields first. These four analyses are for tests with flanged specimens which have much stiffer wall components relative to the coupling beams.

Table 7.6: Summary of predicted base shear at yield for linear elastic analyses (kips)

		Santhakumar		**Shiu**	**Ozselcuk**	**Lequesne**	
	CW1	**WallA**	**WallB**	**CS1**	**1C**	**CW1**	**CW2**
ASCE 41 (A)	71.3	19.6	25.5	26.1	193	195	195
ACI 318 (B1)	75.8	20.9	26.7	32.2	231	216	216
ACI 318 (B2)	64.8	18.9	23.6	21.6	147	171	171
CSA A23.3 (C)	83.0	26.3	30.0	33.2	319	232	232
NZS 3101 (D)	74.4	19.5	28.0	19.6	146	214	212
ATC 72 (E)	68.0	20.4	25.9	19.1	154	177	179
Birely/Mohr (F)	87.7	25.1	31.9	32.7	278	232	223
Mean	**75.0**	**21.5**	**27.4**	**26.4**	**210**	**205**	**204**
Std. Dev.	**8.10**	**2.93**	**2.83**	**6.36**	**69.0**	**25.1**	**23.0**
Measured	**94.3**	**34.6**	**34.0**	**42.0**	**242**	**265**	**265**

The impact of stiffness recommendations for coupling beams can be seen in the experiments conducted by Santhakumar (1974). As discussed in the literature, the only difference between WallA and WallB is the coupling beam reinforcement layout (i.e Wall A was conventionally reinforced and Wall B was diagonally reinforced). This coupling beam parameter only affects the results of Case C and D where a distinction is made between the types of coupling beam reinforcement layout. The CSA model predicts the same yield drift for Specimens WallA and WallB. Differences between the stiffness

Table 7.7: Summary of predicted secant stiffness at yield for linear elastic analyses (kip/in)

		Santhakumar		**Shiu**	**Ozselcuk**	**Lequesne**	
	CW1	**WallA**	**WallB**	**CS1**	**1C**	**CW1**	**CW2**
ASCE 41 (A)	412.4	104.7	97.2	256.7	1055	1069	1069
ACI 318 (B1)	468.1	111.9	103.9	317.5	1267	1223	1223
ACI 318 (B2)	387.1	101.1	93.9	212.7	941.6	994.2	994.2
CSA A23.3 (C)	425.0	77.3	84.6	297.3	1465	1174	1174
NZS 3101 (D)	272.2	99.1	68.2	203.3	1120	641.5	657.2
ATC 72 (E)	179.2	49.2	46.2	107.5	316.9	293.0	359.3
Birely/Mohr (F)	157.2	43.2	40.9	126.3	383.9	354.7	354.8
Mean	**328.7**	**83.8**	**76.4**	**217.3**	**935.5**	**821.2**	**832.9**
Std. Dev.	**125.2**	**27.8**	**25.2**	**80.1**	**433.0**	**388.5**	**372.7**
Measured	**168.1**	**50.6**	**106.2**	**199.8**	**530.8**	**294.0**	**294.0**

and base shear at yield are relatively small. It is possible there is enough balance between the effective flexural and shear stiffness depending on the type of coupling beam reinforcement layout.

However, the NZS model is much stiffer for WallA than WallB. The New Zealand Standard recommends a model to account for the shear deformations for diagonally reinforced coupling beams and an expression to account for the reduction of the flexural stiffness that is a function of the shear span-to-depth ratio of the beam.

In general, the elastic analyses of the specimens modeled with effective stiffness values recommended by design codes and standards (Case A-D) were stiffer than the experimental results, while Case E and F provided a lower bound to the experimental data.

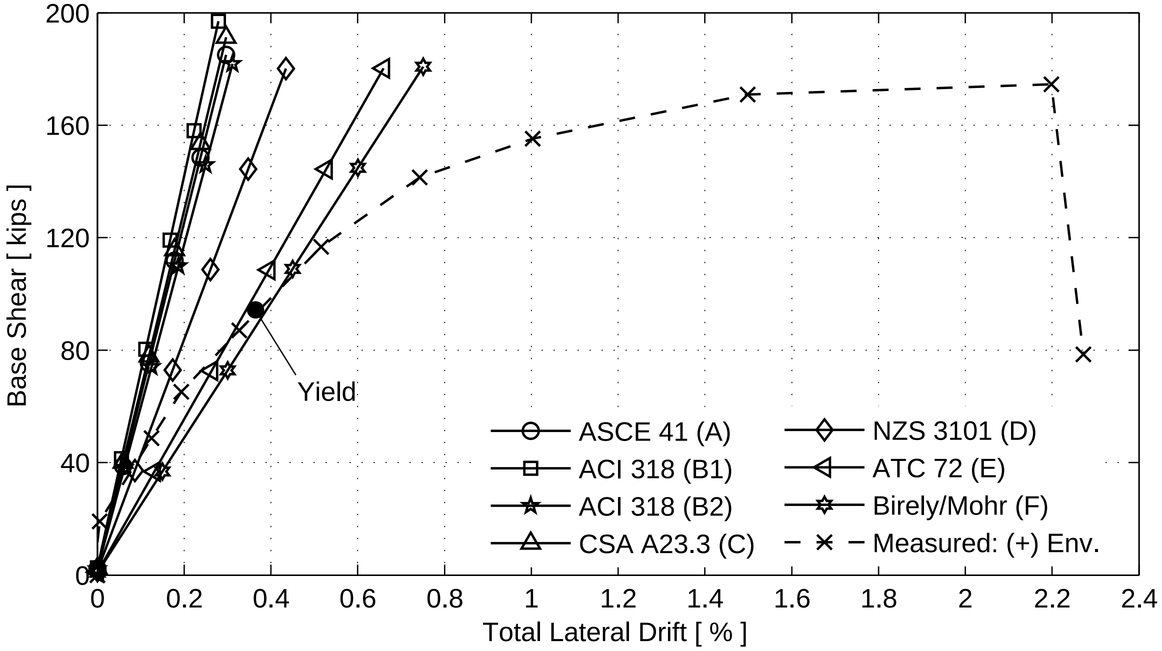

Figure 7.4: Predicted and measured responses for CW1

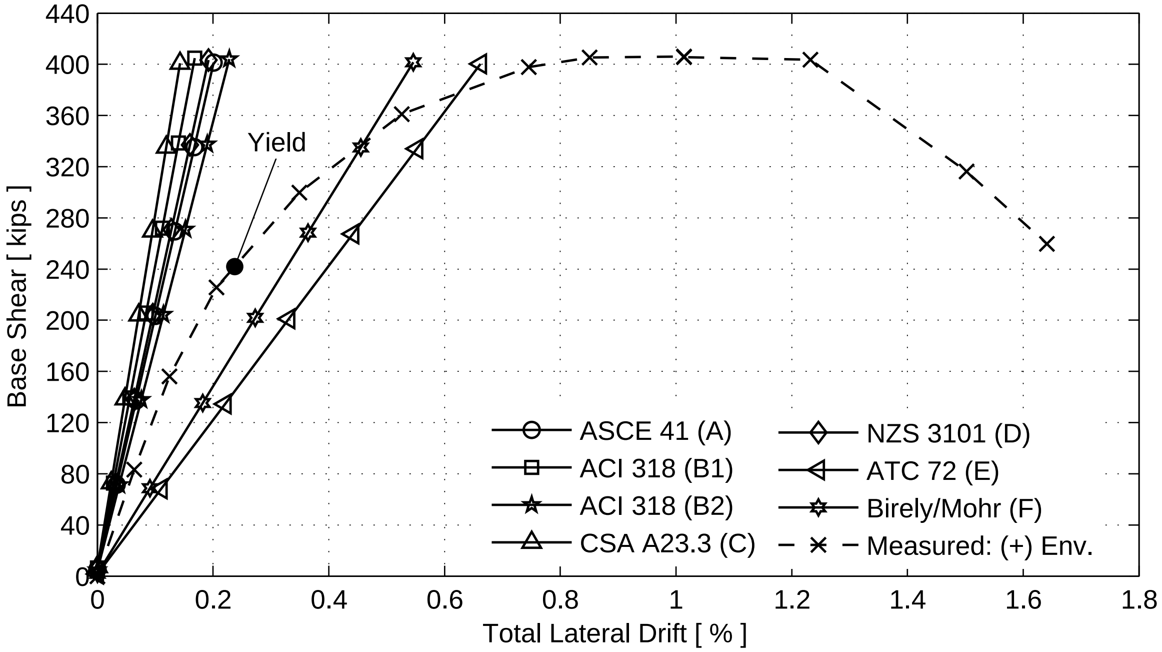

Figure 7.5: Predicted and measured responses for Ozselcuk 1C

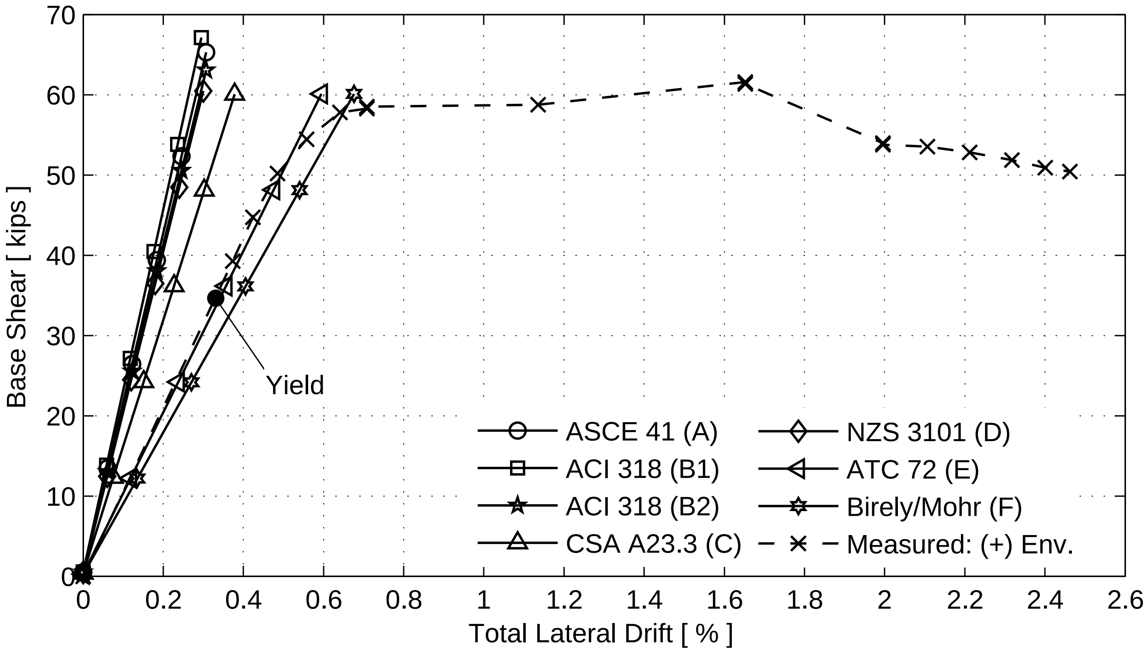

Figure 7.6: Predicted and measured responses for Santhakumar WallA

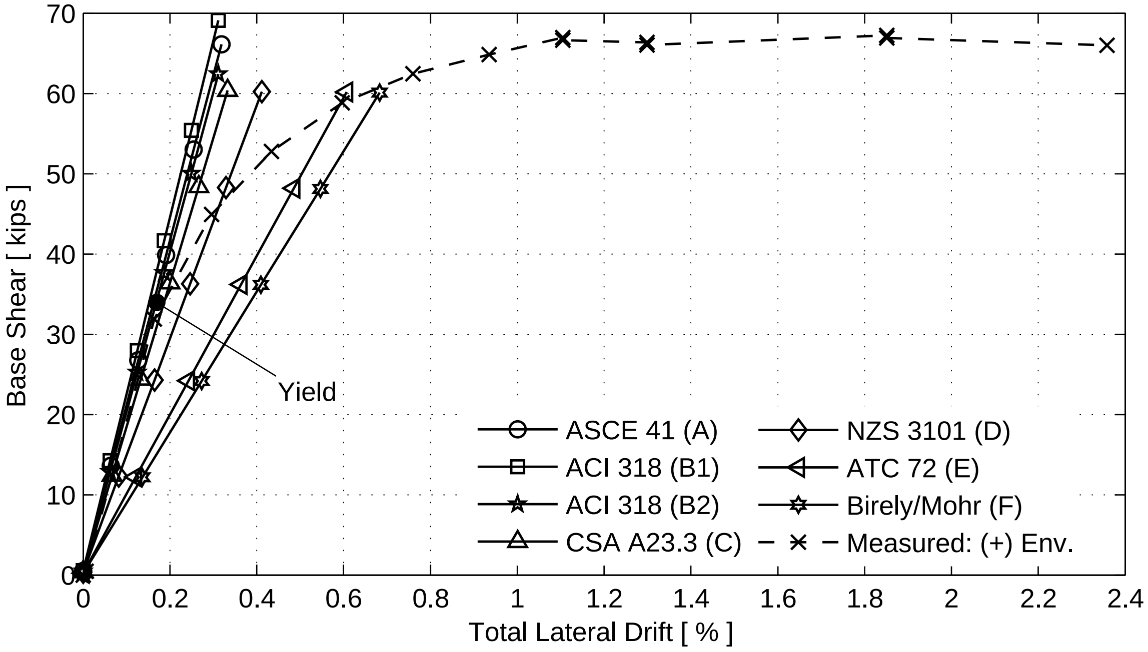

Figure 7.7: Predicted and measured responses for Santhakumar WallB

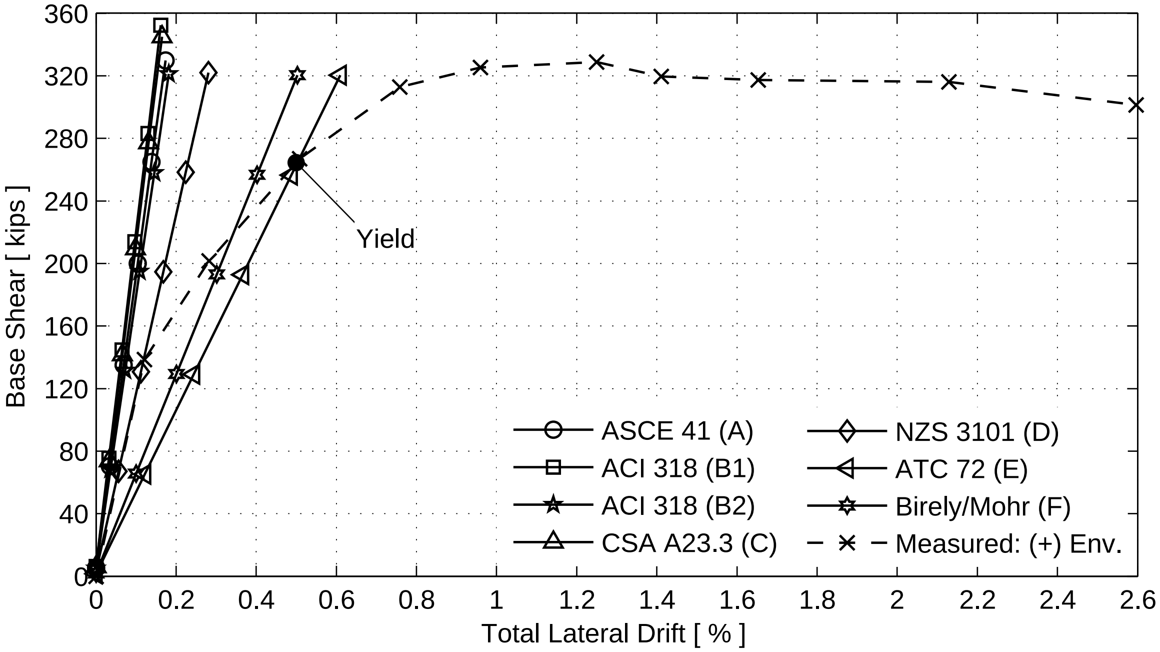

Figure 7.8: Predicted and measured responses for Lequesne CW1

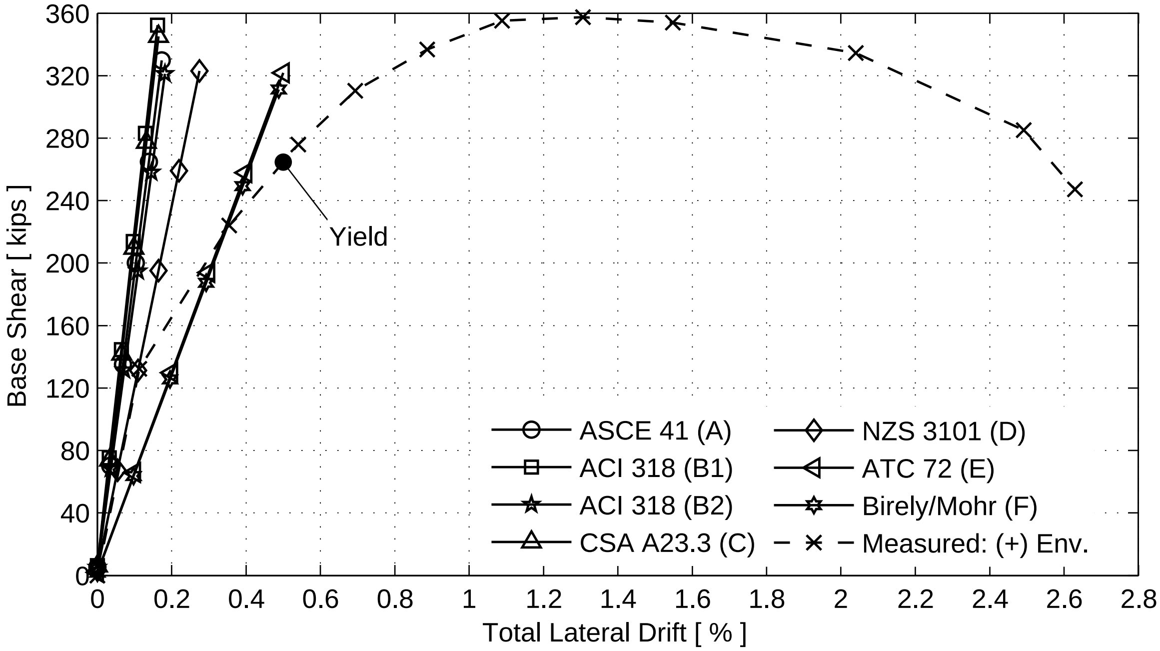

Figure 7.9: Predicted and measured responses for Lequesne CW2

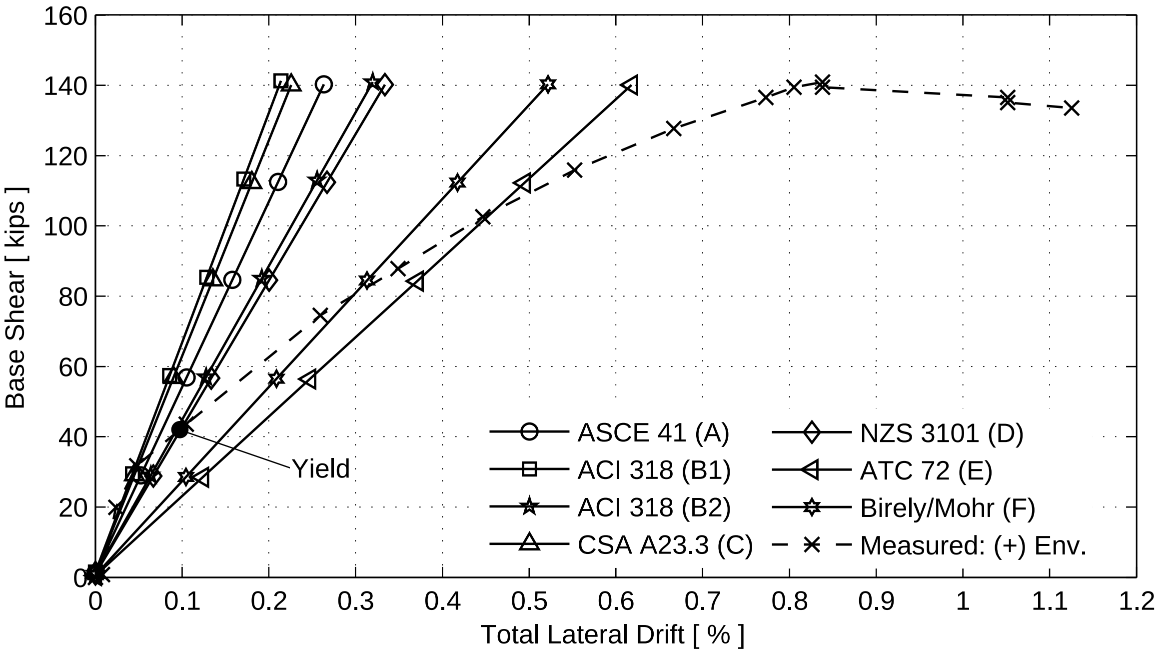

Figure 7.10: Predicted and measured responses for Shiu CS1

7.3.2 Variability of Elastic Analysis

The results were used to evaluate the effective stiffness recommendations. Equation 7.18, provides the error expression where, χ is a response parameter such as drift, shear force, stiffness or axial load. A positive error indicates the predicted response quantity exceeds the measured response. The experimental results at yield are reported in Section 2.5.

$$Error = \left\{ \frac{|\chi_{model}| - |\chi_{measured}|}{|\chi_{model}|} \right\} \times 100\% \tag{7.18}$$

The error defined above is presented in Tables 7.8–7.10. The drift and base shear at yield were, on average, under predicted for all the analysis cases with the exception of the drift from the Birely/Mohr model. Additionally, Cases B2-D over predict the secant stiffness at yield by more than 30% and Cases A, B1 and C by more than 50%. On the other hand, Cases E and F under predict the secant stiffness at yield by more than 20%. Cases B2 produced the results with the most drift and base shear error due to the high shear stiffness and coupling beam flexural stiffness. Ignoring Case B1 because its only function was to provide an upper bound on the stiffness, the CSA A23 model produces the highest yield stiffness error; however, it predicts the base shear at yield better than all the other procedures. Furthermore, the Birely/Mohr model predicts the experimental drift and stiffness at yield with the least amount of error.

For the Lequesne CW1, ATC 72 model, does a particular good job predicting the yield stiffness (-0.34% error), but the Lequesne CW2, ATC 72 model, is 18.2% stiffer than the experimental results. Additionally, comparing the ATC 72 predicted stiffness values between each experiment in Table 7.7, CW2 is substantially stiffer than CW1. Recall, that one of the main differences between these two specimens is CW2 includes fiber reinforced concrete (FRC) at the wall pier bases. Traditional reinforced concrete is typically assumed to have a concrete shear strength of $2\sqrt{f'_c}A_{cv}$, but the authors state FRC concrete increases this strength to $4\sqrt{f'_c}A_{cv}$ (Lequesne et al., 2010). The procedure in ATC 72 to calculate the effective shear stress is dependent on the nominal shear strength of the wall, and therefore, the shear stiffness was increased for CW2 resulting in a stiffer system behavior as seen in Figure 7.8.

Table 7.8: Elastic analysis drift error at yield (%)

Specimen Name	Case A ASCE 41	Case B1 ACI 318	Case B2 ACI 318	Case C CSA A23.3	Case D NZS 3101	Case E ATC 72	Case F Birely/Mohr
CW1	-224	-247	-235	-187	-105	-47.9	-0.55
Santhakumar WallA	-266	-266	-266	-102	-248	-65.6	-17.9
Santhakumar WallB	-22.1	-24.5	-27.1	9.77	22.2	42.9	59.1
Shiu CS1	-107	-107	-107	-88.2	-118	-18.3	18.8
Ozselcuk 1C	-150	-150	-191	-109	-251	5.94	37.1
Lequesne CW1	-394	-409	-424	-355	-170	-49.2	-37.3
Lequesne CW2	-394	-409	-424	-355	-179	-80.2	-43.0
Mean	**-225**	**-233**	**-240**	**-177**	**-153**	**-33.38**	**0.81**
Std. Dev.	**124**	**129**	**131**	**122**	**85.98**	**38.31**	**33.83**

Table 7.9: Elastic analysis base shear error at yield (%)

Specimen Name	Case A ASCE 41	Case B1 ACI 318	Case B2 ACI 318	Case C CSA A23.3	Case D NZS 3101	Case E ATC 72	Case F Birely/Mohr
CW1	-32.2	-24.5	-45.6	-13.7	-26.8	-38.8	-7.54
Santhakumar WallA	-76.9	-65.5	-83.2	-31.9	-77.6	-70.2	-38.1
Santhakumar WallB	-33.3	-27.2	-43.6	-13.3	-21.1	-31.3	-6.37
Shiu CS1	-61.1	-30.3	-94.4	-26.4	-114	-120	-28.4
Ozselcuk 1C	-25.6	-4.61	-64.2	24.2	-66.2	-57.5	13.1
Lequesne CW1	-36.0	-22.3	-55.0	-14.0	-23.8	-49.7	-13.8
Lequesne CW2	-36.0	-22.4	-55.0	-14.1	-24.8	-47.5	-18.5
Mean	**-36.17**	**-21.87**	**-54.68**	**-7.61**	**-41.55**	**-50.49**	**-7.75**
Std. Dev.	**23.80**	**22.61**	**26.57**	**20.32**	**36.43**	**32.37**	**19.35**

Table 7.10: Elastic analysis secant stiffness error at yield (%)

Specimen Name	**Case A** **ASCE 41**	**Case B1** **ACI 318**	**Case B2** **ACI 318**	**Case C** **CSA A23.3**	**Case D** **NZS 3101**	**Case E** **ATC 72**	**Case F** **Birely/Mohr**
CW1	59.2	64.1	56.6	60.4	38.2	6.15	-6.95
Santhakumar WallA	51.7	54.8	50.0	34.6	49.0	-2.79	-17.2
Santhakumar WallB	-9.21	-2.13	-13.0	-25.6	-55.7	-130	-160
Shiu CS1	22.2	37.1	6.08	32.8	1.73	-85.8	-58.2
Ozselcuk 1C	49.7	58.1	43.6	63.8	52.6	-67.5	-38.3
Lequesne CW1	72.5	76.0	70.4	75.0	54.2	-0.34	17.1
Lequesne CW2	72.5	76.0	70.4	74.9	55.3	18.2	17.1
Mean	**50.23**	**56.25**	**45.70**	**50.79**	**34.19**	**-25.26**	**-23.61**
Std. Dev.	**27.29**	**25.19**	**29.65**	**32.88**	**38.42**	**54.94**	**58.38**

7.3.3 Axial load comparison

Based on the severity of the failure mode during the CW1 experiment, the prediction of the axial loads at yield using an equivalent frame elastic analysis needed to be investigated to better understand how these models are predicting internal forces. The results for all of the modeling cases are presented in Table 7.11, and on average all the analyses under predict the axial load at the base of the tension and compression wall. The measured axial forces at the base of the test specimen were approximated using the procedure explained in Section 5.3.

Additionally, the axial loads at yield in Specimen 1C were reported by Ozselcuk (1989). The researchers used load cells at mid span of the each coupling beam to reduced the degree of indeterminacy. These results are presented in Table 7.12. In general, all the analyses are under predicting the axial load in both wall piers, but the error associated with the axial load in the tension wall is much higher than the compression wall. This behavior was also apparent in the CW1 results, but not as staggering.

Table 7.11: Wall pier analytical axial force results for CW1

	Tension Wall		**Compression Wall**	
	$\frac{N_{y,tw}}{\sum(A_s f_y)}$	**Error (%)**	$\frac{N_{y,cw}}{\sum(A_g f'_c)}$	**Error (%)**
ASCE 41 (A)	0.23	-74.4	-0.24	-20.2
ACI 318 (B1)	0.24	-71.6	-0.24	-19.7
ACI 318 (B2)	0.21	-91.0	-0.23	-23.0
CSA A23.3 (C)*	0.25	-63.7	-0.24	-18.2
NZS 3101 (D)	0.24	-71.5	-0.24	-19.7
ATC 72 (E)	0.22	-83.3	-0.24	-21.8
Birely/Mohr (F)	0.27	-52.6	-0.25	-15.8
Mean	**0.24**	**-72.6**	**-0.24**	**-19.8**
Std. Dev.	**0.018**	**12.5**	**0.005**	**2.35**
Measured	**0.41**	–	**-0.29**	–

* Requires axial stiffness reduction to account for axial load

Table 7.12: Wall pier analytical axial force results for Ozselcuk 1C

	Tension Wall		**Compression Wall**	
	$\frac{N_{y,tw}}{\sum(A_s f_y)}$	**Error (%)**	$\frac{N_{y,cw}}{\sum(A_g f'_c)}$	**Error (%)**
ASCE 41 (A)	0.19	-235	-0.21	-39.3
ACI 318 (B1)	0.28	-130	-0.23	-29.0
ACI 318 (B2)	0.08	-681	-0.19	-54.7
CSA A23.3 (C)*	0.48	-33.8	-0.27	-10.3
NZS 3101 (D)	0.07	-799	-0.19	-56.4
ATC 72 (E)	0.08	-708	-0.19	-55.2
Birely/Mohr (F)	0.32	-101	-0.24	-24.7
Mean	**0.22**	**-383.9**	**-0.22**	**-38.5**
Std. Dev.	**0.156**	**330.3**	**0.030**	**17.99**
Measured	**0.65**	–	**-0.29**	–

* Requires axial stiffness reduction to account for axial load

As explained in Section 2.2, the overturning moment is dependent on the moment in the tension wall, moment in the compression wall and axial forces in each wall pier, so these results are complex in the sense that for a given lateral load, the overturning of the structure is related to the axial and flexural stiffness of each wall pier. No one stiffness procedure predicts the axial tension force relatively well, and the procedures using gross axial stiffness and low flexural stiffness values (NZS 3101 and ATC 72) are nowhere close to the measure axial force.

Based on the CSA model and axial stiffness results presented in Section 5.3, it is possibly to conceive that the axial stiffness needs to be reduced in the tension wall in order to better match the measured results, but the results presented in Table 7.13 suggests the axial loads in the model are not sensitive to the axial stiffness properties. Comparing both ACI 318 models, where only the flexural stiffness is different, suggests the axial loads are more dependent on the flexural stiffness of the wall piers because they have a signification impact on the coupling beam deformations (i.e. the yielding elements in most cases).

Table 7.13: Axial stiffness study for Mohr/Birely model (Case F)

	Tension Wall		**Compression Wall**	
	$\frac{N_{y,tw}}{\sum(A_s f_y)}$	**Error (%)**	$\frac{N_{y,cw}}{\sum(A_g f_c')}$	**Error (%)**
CW1				
Measured	0.41	–	-0.29	–
$1.0E_cA_g$ Both Walls	0.27	-52.6	-0.25	-15.8
$0.6E_cA_g$ Both Walls	0.27	-53.5	-0.25	-16.0
$0.2E_cA_g$Ten. & $1.2E_cA_g$ Compr.	0.27	-51.5	-0.25	-15.6
Ozselcuk 1C				
Measured	0.65	–	-0.29	–
$1.0E_cA_g$ Both Walls	0.32	-101	-0.24	-24.7
$0.6E_cA_g$ Both Walls	0.31	-110	-0.23	-26.2
$0.2E_cA_g$Ten. & $1.2E_cA_g$ Compr.	0.31	-111	-0.23	-26.3

7.3.4 Recommendations

Based on the results presented for equivalent frame elastic analyses, engineers need to use good judgment when selecting effective stiffness terms. The results suggest the stiffness of the coupling beams have a significant impact on the response of the system, and this is truer for coupling beams with aspect ratios near or below two. In order to achieve reasonable shear stress demands in the coupling beams, engineers commonly reduce the stiffness of the coupling beam, and based on the research presented by Mohr (2007) and this study, it seems conceivable to use a coupling beam effective flexural stiffness values as low as $0.15E_cI_g$ to $0.05E_cI_g$.

Overall, the analysis using the Birely/Mohr recommendations produce the most accurate results, and are within 1% error with regards to the total lateral drift at yield. Table 7.14 presens the effective stiffness values recommended to be used in an equivalent frame elastic analysis of a concrete coupled wall system. Furthermore, these recommendations are based on experimental data of structural components designed using modern details. This method seems to predict the axial forces in the wall piers within a reasonable amount of error which is good in design because the axial loads have a large effect on the moment strength of the wall. Finally, while this method produces a more flexible response (i.e. larger yield drift), all the results satisfy allowable limits on story drift set by ASCE 7-05 (ASCE, 2010).

Table 7.14: Recommended effective stiffness values for coupled wall components

Component	**Flexural Rigidity**	**Shear Rigidity**	**Axial Rigidity**
Wall Piers	$0.35E_cI_g$	$0.15GA_{cv}$	$1.0E_cA_g$
Coupling Beams	$0.05E_cI_g$	$0.15GA_{cv}$	$1.0E_cA_g$

Chapter 8

NONLINEAR ANALYSIS OF COUPLED WALLS

Elastic analyses were performed using a set of effective stiffness values determined from code-based as well as experimental research recommendations. These models were evaluated in the previous chapter in order to determine a recommended set of stiffness values for accurately predicting the first yield of a coupled wall system. While these analyses address the response of coupled wall systems up to yield, in order to capture a more accurate distribution of forces post yield, nonlinear analyses are needed.

The fiber-hinge beam-column element or typically referred to as a lumped plasticity element (LPE) is more common in structural engineering because it is readily available in most finite element packages. One drawback of this element is the hinge length over which nonlinear curvatures are calculated needs to be assumed, and in a concrete structure, effective stiffness values also need to be assigned. On the other hand, the force-based beam column-element, also known as a distributed plasticity element (DPE), is attractive to engineers because its formulation incorporates sectional nonlinearity along the length of the element. Thus, there is no need to define a plastic hinge length, and the stiffness of the element is calculated at each section along the length of the element so effective properties do not need to be assumed. The results of each analysis was investigated and compared against experimental and design parameters in order to quantify the distribution of shear, moment and axial loads between the tension and compression wall piers.

8.1 Overview of Nonlinear Model in OpenSees

The analyses were performed using the open-source platform analysis program OpenSees (McKenna et al., 2000). A static pushover analysis was performed to determine the nonlinear response for a set of concrete coupled wall configurations. Each coupled wall was modeled using a two-dimensional equivalent frame which was explained in Chapter 7. Furthermore, the boundary and loading conditions as well as the shear-deformation model in the nonlinear models were similar to the equivalent elastic frame models presented in Chapter 7. Finally, two different types of force-based nonlinear finite-element beam-column elements where used to represent the wall piers and coupling beams.

8.1.1 Nonlinear Elements

The components in the lumped plasticity model (LPM) were modeled as lumped plasticity elements and the components in the distributed plasticity model (DPM) were modeled as distributed plastic elements with one exception discussed later. Additionally, the specific names of the LPE and the DPE used in this study are implemented in OpenSees and titled as the "Beam With Hinges" element and the "Force-Based Beam-Column" element. Gauss-Lobatto quadrature was used as the integration scheme for the forced-based elements because the two outer-most quadrature points are placed at the ends of the element. This was convenient in the case of a coupled wall because the bending moments are the largest at the ends of the coupling beams and wall piers.

These elements are capable of capturing nonlinear material behaviors using fiber sections modeled at the ends of the element in the case of the LPE and at each quadrature point in the case of the DPE. For example, the fiber sections used to define the wall pier and coupling beam cross-sections are shown in Figure 8.1. Each material model uses a uni-axial response to represent its specific behavior (i.e. reinforcing steel, unconfined and confined concrete). The area of a single fiber representing a diagonal reinforcing bars was set equal to $A_s cos\alpha$ in order to account for the inclination of the bar. A_s and α are equal to the area and inclination of the reinforcing bar. The plastic hinge length, L_p, of the LPE was based on half the depth of the structural component as recommended by Paulay and Priestley (1992). This plastic hinge length was equal to $l_w/2$ for the wall pier and $h_b/2$ for the coupling beams. For all the elements, hinges were assigned to both ends of the element to capture plasticity on both ends of the coupling beams as well as any spreading of plasticity up the height of the wall piers.

While the LPE uses two fiber cross sections at the end of the element, the remaining portion of the element needs to be assigned elastic flexural and axial stiffness properties.

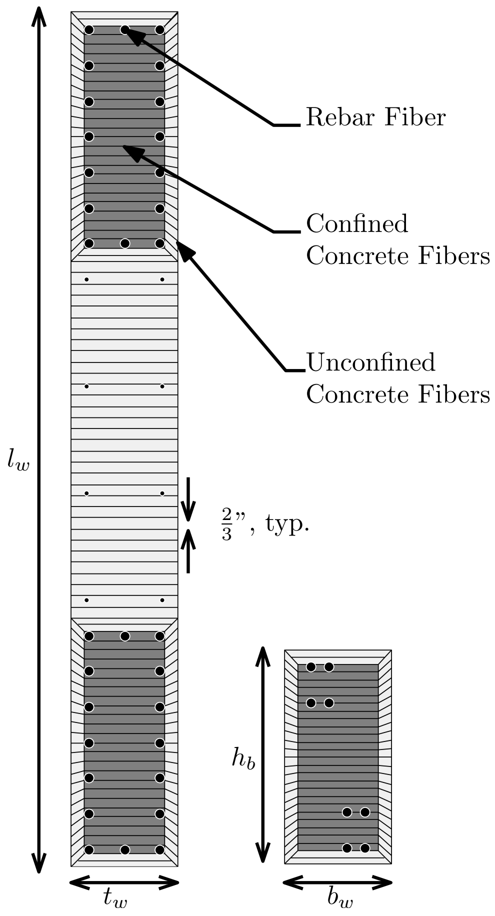

Figure 8.1: Fiber cross-section for CW1

In some cases where the element aspect ratios was roughly one or smaller, the plastic hinge length of the element was assigned such that one inch of the length of the element is proportioned to the elastic region of the element. In the case of the LPM, the effective flexural stiffness was assumed to be proportional to the cracked moment of inertia, I_{cr}, which was calculated from first principals (Table 8.1). The axial stiffness properties were taken as the gross axial stiffness (E_cA_g). The effective shear stiffness was assumed to be $0.15G_cA_{cv}$ as discussed in Chapter 7.

Table 8.1: Cracked flexural stiffness properties for LPM

	I_{cr}/I_g				
Specimen Name	**TWP**	**CWP**	**CB, avg**	**CB, min**	**CB, max**
CW1	0.39	0.39	0.40	–	–
Santhakumar WallA	0.93	0.86	0.36	–	–
Santhakumar WallB	0.94	0.88	0.43	–	–
Shiu CS1	0.43	0.43	0.13	0.12	0.14
Ozselcuk 1C	0.29	0.29	0.27	0.12	0.37
mean	**0.60**	**0.57**	**0.32**		
min	**0.29**	**0.29**	**0.13**		
max	**0.94**	**0.88**	**0.43**		

In the case of the DPM, when an odd number of sections are defined using Gauss-Lobatto quadrature, the middle section is placed at the center of the element. For the elements simulating diagonal coupling beams, the reinforcing bar fibers in the center section are positioned near the center of the cross-section, and this may lead to convergence issues within the element if the moment distribution leads to even a small amount of moment at the midspan of the beam. To mitigate this potential problem, diagonal reinforced coupling beams in the DPM where modeled using LPEs.

8.1.2 Constitutive Models

The coupling beam cross-sections were first discretized into concrete fibers repenting unconfined and confined regions of the section. The sections were discretized vertically into a number of slices in order to accurately capture the behavior of the section. In general, fibers were discretized so their thickness was typically 2/3 of an inch. The stress-strain relation for the concrete material was modeled using the "Concrete01" constitutive model developed in OpenSees. This model has zero tensile strength and has a post-peak softening behavior. To account for the cracked condition of the concrete, no tensile strength was modeled. While this may not be the best approximations at service level drifts, there was no interest in capturing that portion of the force-displacement curve for this study. A typical stress-strain behavior of this concrete model is shown in Figure 8.2b. The monotonic envelope curve of this model uses the modified Kent and Park stress-strain relation (Park et al., 1982), which is an extension of the model developed by Kent and Park (1971). The unconfined and confined concrete parameters were determined using procedures address in (Park et al., 1982), and the volumetric reinforcement ratios as well as effective core geometries were calculated using equations from Mander et al. (1982).

Steel fibers were modeled using a uni-axial stress-strain relationship shown in Figure 8.2a. The response of the steel is defined by a tri-linear curve with a linear-elastic, strain-hardening and maximum stress behavior. In the first iterations of the analyses, coupling beam reinforcement was modeled with a bilinear curve, which accounted for strain hardening. However, due to large deformation demands on the coupling beams, moment and shears in the coupling beams reached erroneous strengths due in most part to a well confined core and an infinitely increasing strain-hardening behavior. As a result, the model was changed to the "Hysteric" material model in OpenSees, which accommodates a tri-linear stress-strain response. This model was chosen in order to limit the amount of strain hardening occurring in the coupling beams during a particular analysis. The elastic modules, yield strength, strain-hardening ratio and ultimate strength are model

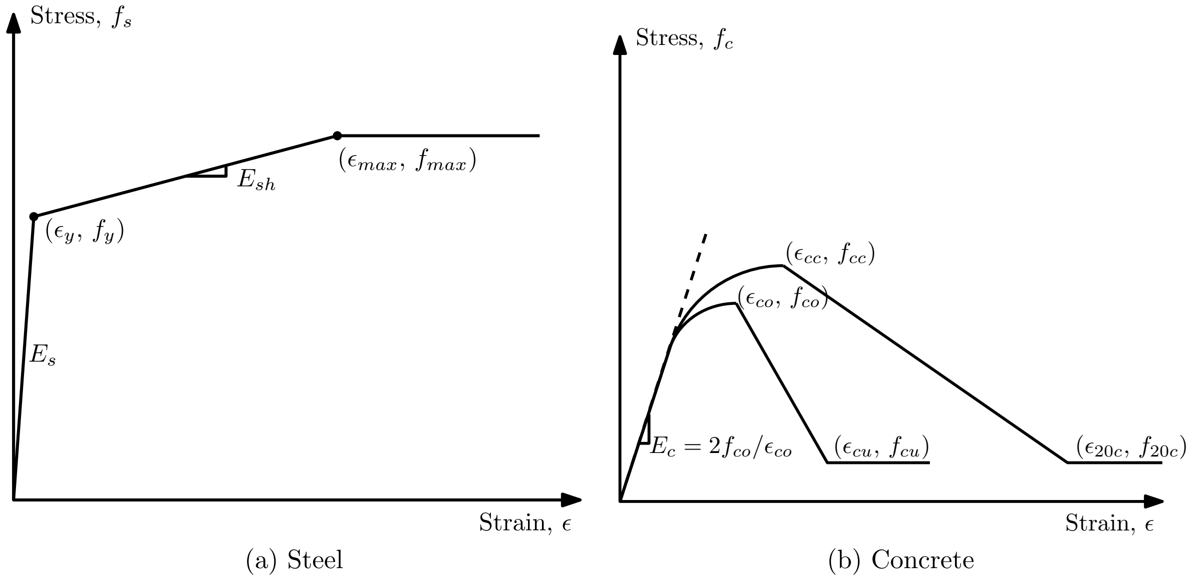

(a) Steel (b) Concrete

Figure 8.2: Steel and concrete constitutive models (“Hysteretic” and “Concrete01”)

using parameters presented in the literature. Furthermore, strain penetration and bar slip was not considered in these models.

8.1.3 Selection of Quadrature Points

Reinforced concrete components modeled using distributed plasticity elements tend to loss objectivity at the element and sectional level as a result of strain localization at a particular quadrature point. This occurs when the section response of the element is exhibiting a softening or perfectly-plastic behavior. When this occurs, the nonlinear response of the element localizes at the end section(s) of the elements (Coleman and Spacone, 2000). The length over which the curvatures are integrated, L_{IP} is equal to the weight of the end quadrature point times the length of the element ($\omega_i l_n$). However, this plastic hinge length based purely on the Gauss-Lobatto integration scheme is smaller on average than a plastic hinge length, L_p, computed using half the depth of the element as defined by Paulay and Priestley (1992). The number of quadrature points was selected by picking the number that provided a L_{IP} similar to the length calculated by half the element depth. The results of this study for the wall pier and coupling beam elements are presented in Tables 8.2 and 8.3. As a result of this study, three quadrature points were selected along the length of the distributed plastic elements for both the wall piers and coupling beams.

Table 8.2: Wall pier element quadrature point selection

Specimen Name	# Gauss Points	L_{IP}/l_w	L_{IP} (in)	L_p (in)	L_{IP}/L_p
CW1	3	0.15	7.0	24.0	0.29
Santhakumar WallA	3	0.21	5.0	12.0	0.42
Santhakumar WallB	3	0.21	5.0	12.0	0.42
Shiu CS1	3	0.07	5.4	37.5	0.15
Ozselcuk 1C	3	0.07	6.7	47.0	0.14

Table 8.3: Coupling beam element quadrature point selection

Specimen Name	# Gauss Points	L_{IP}/h_b	L_{IP} (in)	L_p (in)	L_{IP}/L_p
CW1*	–	–	–	6.0	–
Santhakumar WallA	3	0.21	2.5	6.0	0.42
Santhakumar WallB*	–	–	–	6.0	–
Shiu CS1	3	0.41	2.7	3.3	0.81
Ozselcuk 1C	3	0.58	9.3	8.0	1.16

* Model uses lumped plasticity elements

where,

L_{IP}	plastic hinge length associated with Gauss-Lobatto integration scheme
L_p	plastic hinge length defined as $l_w/2$ (wall pier) or $h_b/2$ (coupling beam)
l_w	length of the wall pier
h_b	height of the coupling beam

8.2 Results and Comparisons of Nonlinear Analysis

In this section, the results of the nonlinear static analyses for multiple concrete coupled wall specimens are presented and discussed. For each specimen two models are presented, the lump plasticity model (LPM) and the distributed plasticity model (DPM). The objective of the study was to assess equivalent frame nonlinear finite element models developed in OpenSees by comparing force-drift results with experimental data. Additionally, results of presenting distribution of shear forces and moments at the base of the coupled wall structure are presented and compared to experimental data where applicable. Finally, the axial force verse drift results for both models are compared and evaluated using experimental data where applicable. All the results are above are compared to the coupled wall performance evaluation parameters discussed in Chapter 6.

8.2.1 Force-Drift Response

The force-drift results are shown in Figures 8.3 – 8.7. Both the LPM and the DPM are shown along with the experimental force-drift envelope and the predicted plastic shear demand resulting from a plastic analysis using the procedure discussed in Section 2.2. A deviation from the recommended procedure was used to better represent the actual experimental behavior of the specimen. Because the measured material properties were known, M_{pr} for the coupling beams was calculated using $1.1f_y$ rather than $1.25f_y$. Additionally, the probable moments of the wall piers was calculated using moment-curvature analyses where the steel model utilized measured yield and strain hardening properties of the steel; therefore, there was no need to apply any additional factor to the yield strength of the steel. The positive and negative axial loads resulting from the accumulation of beam shear up the height of the specimen were also included to the moment-curvature analysis.

First yield of the analysis was determined when the strain in any longitudinal reinforcing fiber in either the wall piers or coupling beam reached its respective yield strain.

This occurs in the coupling beam elements for all the analyses and these results are tabulated in Table 8.4. In addition to yield, a plastic limit state was determined when the total base shear in the analysis reached the predicted base shear demand determined from the plastic analysis discussed above. These two limits states are used here out to discuss moment, shear and axial force demands in the wall piers.

Table 8.4: Drift results for LPM and DPM at critical limits states

	Yield		**Plastic**	
Specimen Name	**LPM** (%)	**DPM** (%)	**LPM** (%)	**DPM** (%)
CW1	0.18	0.20	0.70	0.62
Ozselcuk 1C	0.20	0.26	0.65	0.69
Santhakumar WallA	0.20	0.22	0.66	0.68
Santhakumar WallB	0.24	0.26	0.59	0.62
Shiu CS1	0.06	0.07	0.74	1.13

In general, the results of the set of four preciously tested coupled wall specimens were fairly consistent with the experimental force-drift results. The comparison between the lumped plasticity and distributed plasticity model results for this particular set of analyses show almost identical response behavior between the two models. All of the models reach their respective base plastic shear demand. The initial stiffness of the Sanathakumar WallA analyses is over-predicted, but this is mostly likely due to an accidental loading of the specimen prior to the actual test (Section 2.5).

The observed failure of the wall pier in the CW1 experiment occurred at 2.27% drift when concrete crushing and bar buckling was observed. In the nonlinear analyses of this specimen, the loss in sectional capacity occurs at a much earlier drift. Because the initial response of both models grossly over predicted the stiffness compared to the experiment, the axial force and moment demands at the base of the wall were reached at a lower drift than they would have if the response was less stiff. At the maximum recorded base shear, a majority of the concrete core fibers in the compression wall pier element for both models reached compressive strains beyond ϵ_{20c}. This resulted in a large loss of axial and flexural capacity of the base compression wall section which led to a redistribution of forces to the other elements (i.e. the tension wall elements). This redistribution is discussed in more detail the sections below. The DPM analysis was unable to recover after the peak was reached and simply did not converge on a global solution; however, the LPM was able to recover, but was limited to a mechanism where the base tension wall element as the primary load-resisting member.

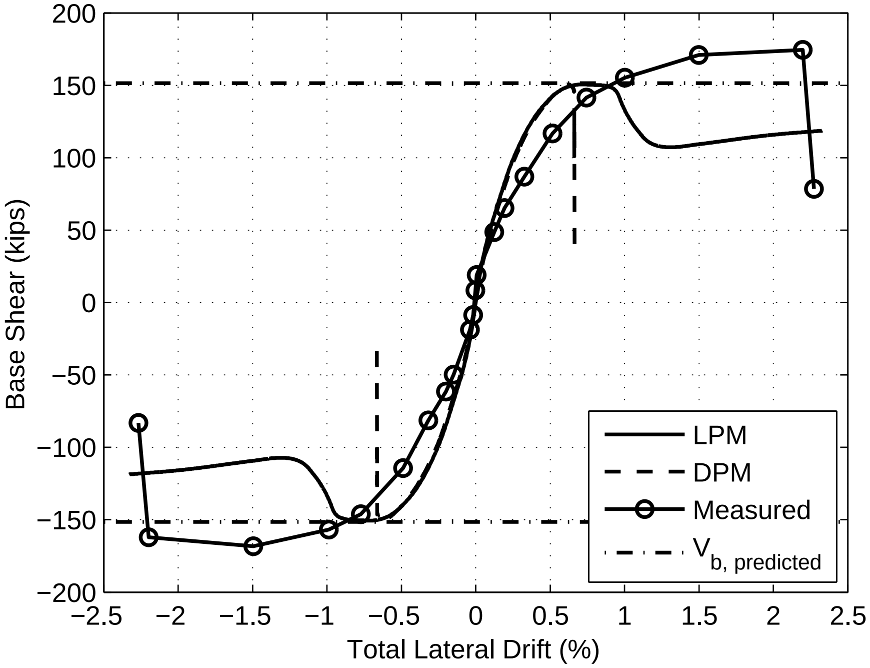

Figure 8.3: Nonlinear analysis CW1 force-drift response

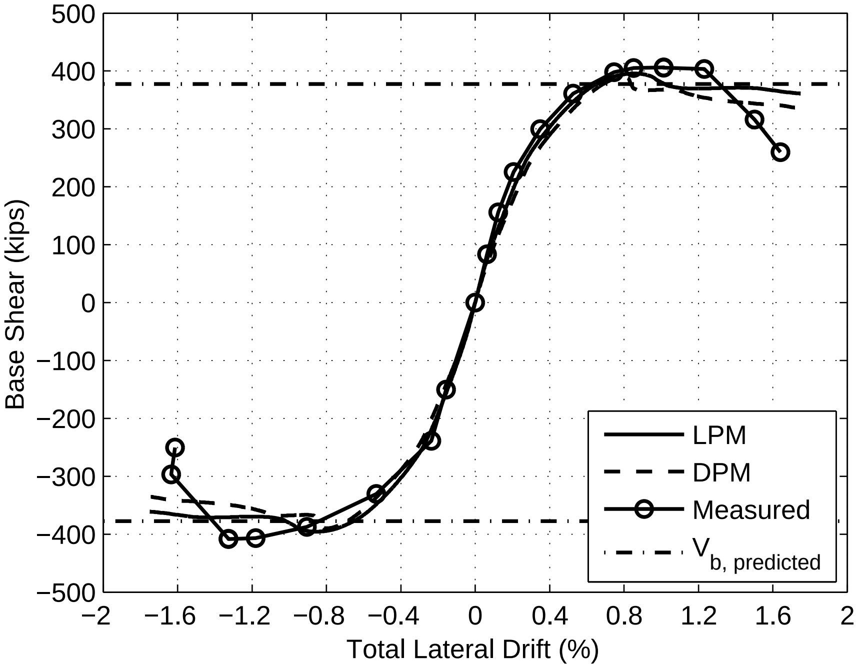

Figure 8.4: Nonlinear analysis Ozselcuk 1C force-drift response

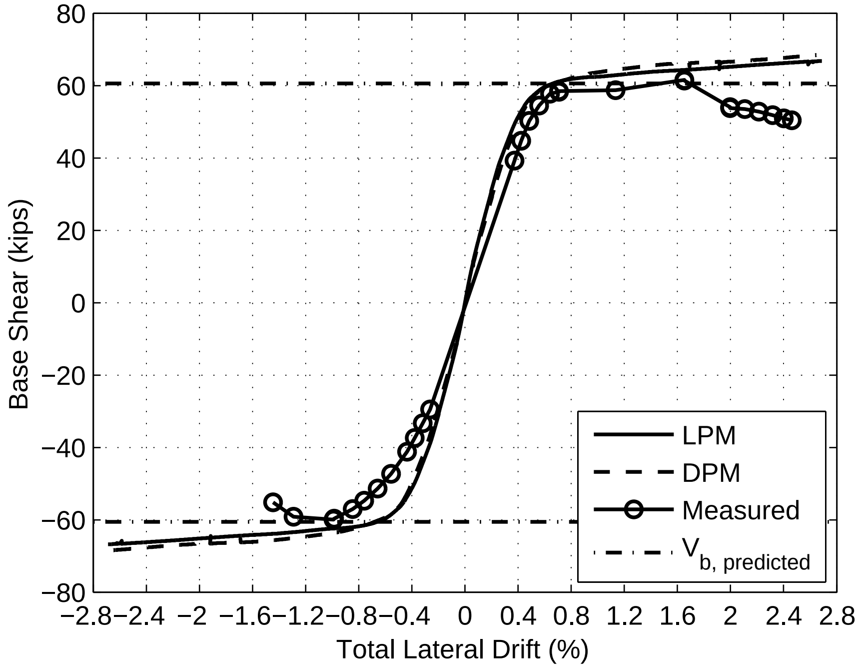

Figure 8.5: Nonlinear analysis Santhakumar WallA force-drift response

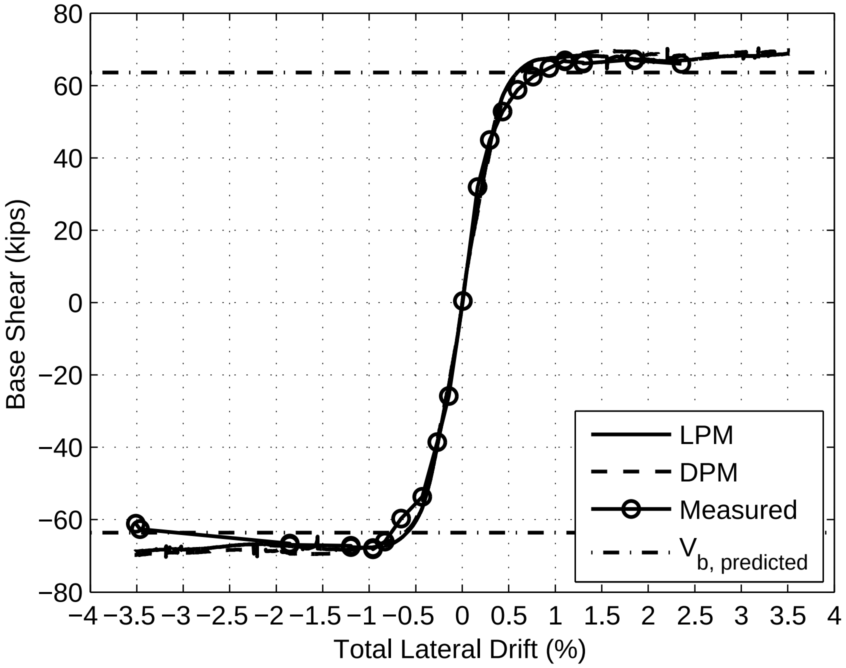

Figure 8.6: Nonlinear analysis Santhakumar WallB force-drift response

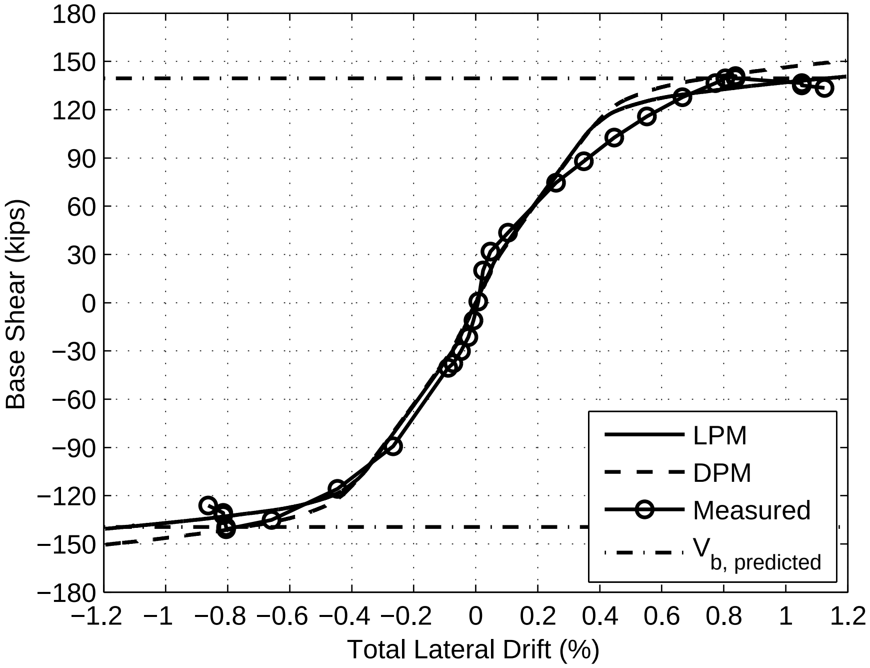

Figure 8.7: Nonlinear analysis Shiu CS1 force-drift response

8.2.2 Base Shear Distribution

The redistribution of shear demand from the tension wall to the compression wall has shown to affect the behavior of the coupled wall system especially the deformation capacity of the compression pier. This redistribution is a consequence of a low stiffness in the tension wall due to the effects of the axial tensile demand. On the other hand, the compression pier is subjected to increasing axial compressive demand which reduces or eliminates cracking resulting in a stiffer component. One caveat of this behavior is the compression demand also endures more shear and moment demand due to the differences in wall pier stiffness. Using the nonlinear analysis results of each model, the redistribution of shear demand between the two wall piers is shown in Figures 8.8 – 8.17.

The shear distribution for all the analyses with the exception of Shiu CS1 resulted in a greater redistribution of shear to the compression wall in the LPM. On average, the redistribution in the LPM predicted 5 to 8% more distribution between the tension and compression wall than the DPM. Additionally, the analytical shear stress demands in each wall pier are tabulated in Table 8.5. Yield was determined when the strain in a reinforcing fiber reached its respective yield strain. This occurs in the coupling beam elements for all the analyses and is indicated by a star in the figures. The plastic limit state is determined when the total base shear in the analysis reaches the predicted base shear demands determined from the plastic analysis. On average, the compression wall carries approximately 60% of the total base shear demand at yield and 78% of the total base shear demand when the plastic strength is met. Recall, the base shear demand is assumed to be distributed equally between each wall pier in a plastic analysis (50/50). However, the nonlinear analyses predict shear demands in the compression pier approximately 1.6 times the 50/50 distribution assumption.

The CW1 analyses in particular yielded the following results. When the distributions of shear to the compression wall were at their respective maxima, the compression pier shear demand was approximately 80% of the total base shear in the LPM and 75%

Table 8.5: Nonlinear analysis wall pier base shear stress demands

	Tension Wall				**Compression Wall**			
	Yield		**Plastic**		**Yield**		**Plastic**	
Specimen Name	LPM $(\sqrt{f'_c})$	DPM $(\sqrt{f'_c})$	LPM $(\sqrt{f'_c})$	DPM $(\sqrt{f'_c})$	LPM $(\sqrt{f'_c})$	DPM $(\sqrt{f'_c})$	LPM $(\sqrt{f'_c})$	DPM $(\sqrt{f'_c})$
CW1	1.22	1.52	1.60	1.60	2.47	2.27	5.35	5.35
Ozselcuk 1C	2.26	3.03	1.14	2.12	4.59	4.55	12.0	11.1
Santhakumar WallA	2.06	2.25	2.33	2.98	2.74	2.54	7.00	6.34
Santhakumar WallB	2.53	2.60	2.71	3.21	3.22	3.18	7.33	6.83
Shiu CS1	0.40	0.56	1.39	1.32	0.85	0.81	5.57	5.64

of the total base shear in the DPM. As discussed in the prior section, the capacity of the compression pier reached its limit at approximately 0.65% drift, and this when the shear demand in the tension wall started to increase and compensate for the damaged compression pier (Figure 8.8).

The redistribution of shear demand to the compression wall and back to the tension wall were observed in the Oszelcuk 1C and Santhakumar WallB analyses. This observation may led one to believe a failure occurred in the compression pier similar to CW1; however, further investigation into the model suggest this behavior was caused by a different mechanism. In the case of Oszelcuk 1C, both the LPM and the DPM the moment-curvature response of the bottom section in the compression pier element softened approximately 10%. However, the main reason for the increase in tension wall shear demand occurred because the tension wall force-displacement response began to harden due to strain hardening of the reinforcing steel. The redistribution of shear demands back to the tension wall for the Santhakumar WallB model occurred because the moment-displacement response of the lower six coupling beams began to softened at approximately 1.2% drift. As a consequence, the axial load in the wall piers decreased. This increased the moment/shear demands in the tension pier and decreased the moment/shear demand in the compression wall.

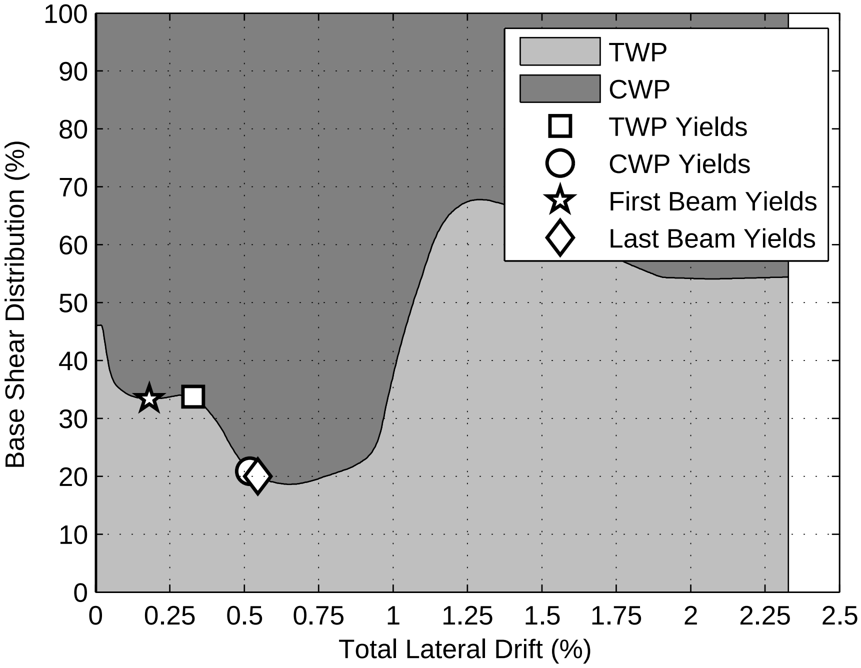

Figure 8.8: LPM model distribution of shear at base of CW1

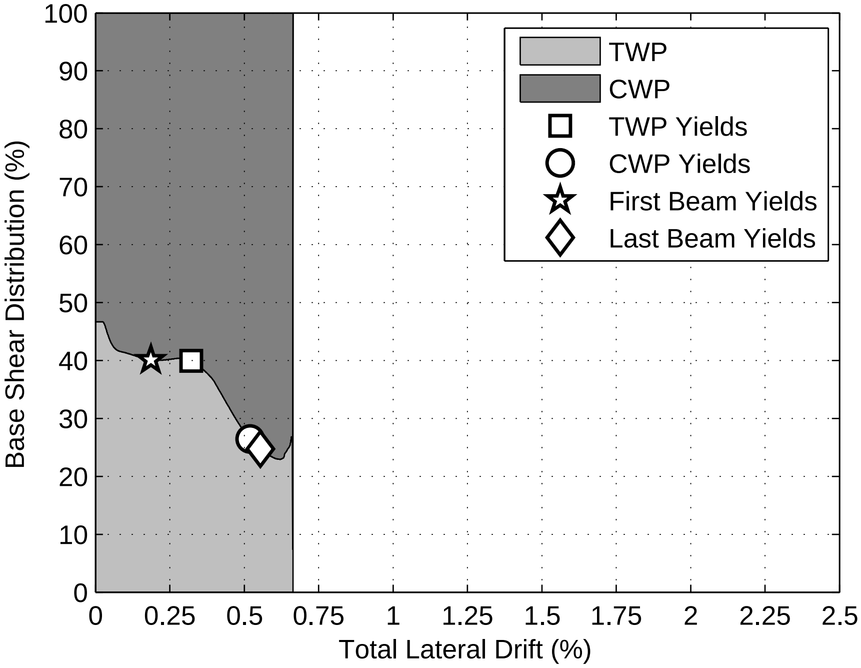

Figure 8.9: DPM model distribution of shear at base of CW1

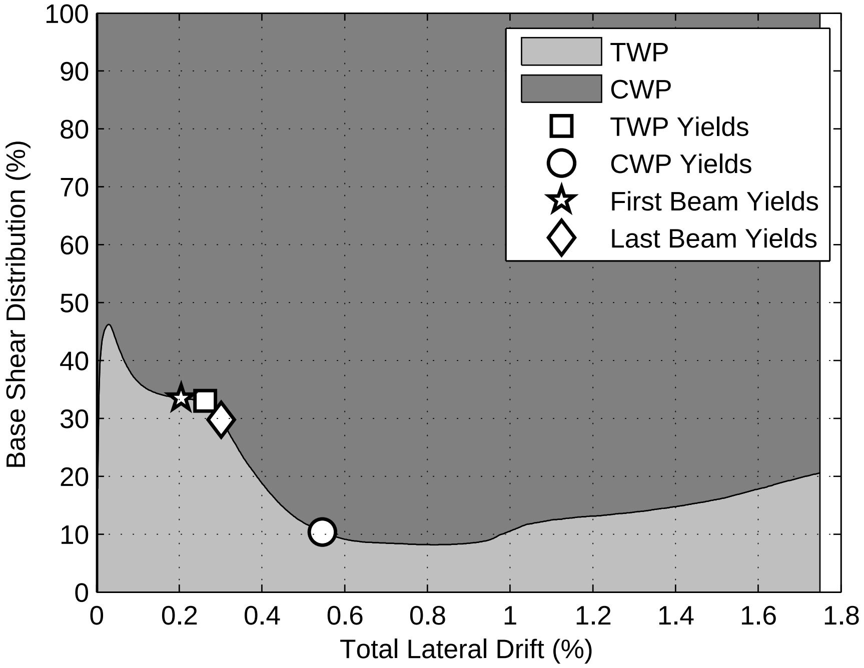

Figure 8.10: LPM model distribution of shear at base of Ozselcuk 1C

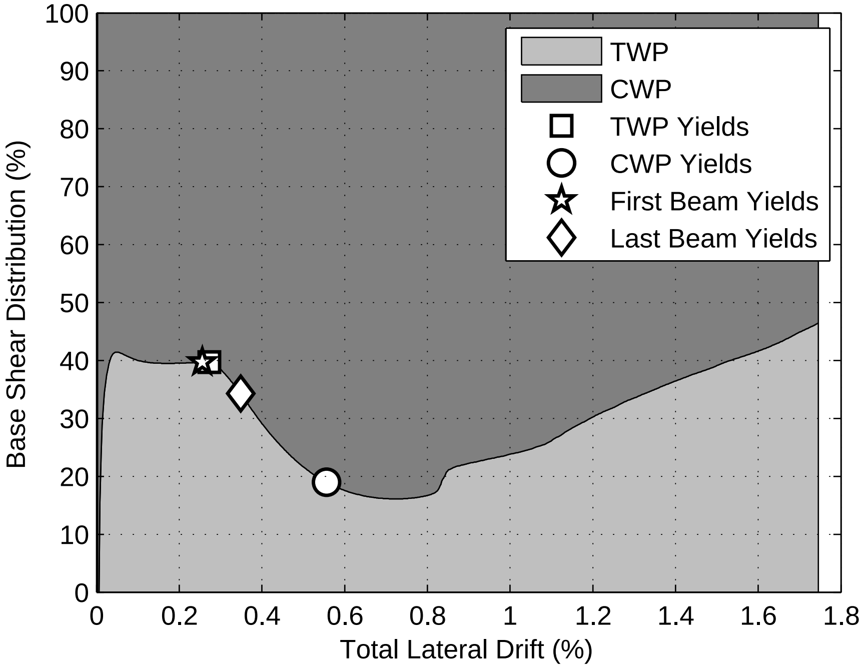

Figure 8.11: DPM model distribution of shear at base of Ozselcuk 1C

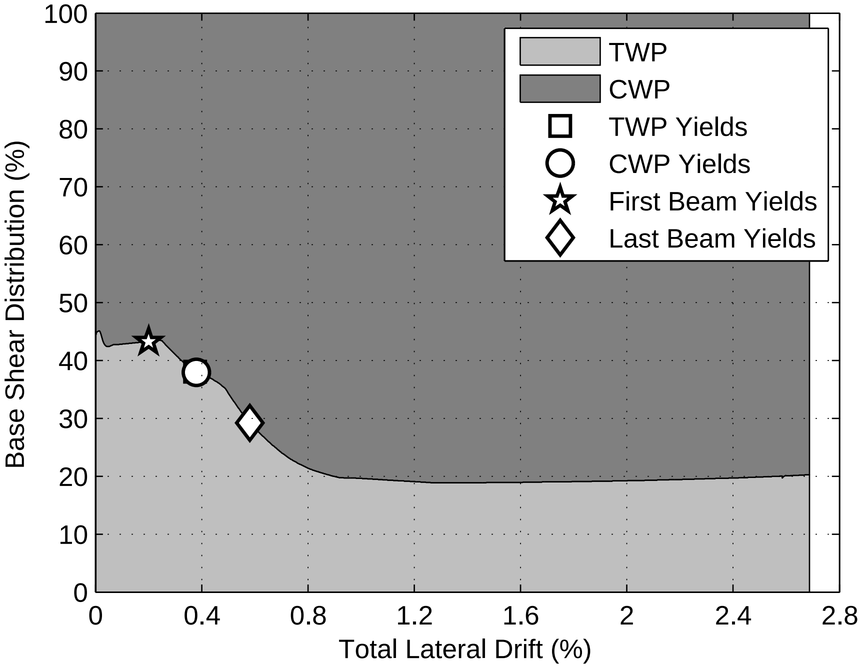

Figure 8.12: LPM model distribution of shear at base of Santhakumar WallA

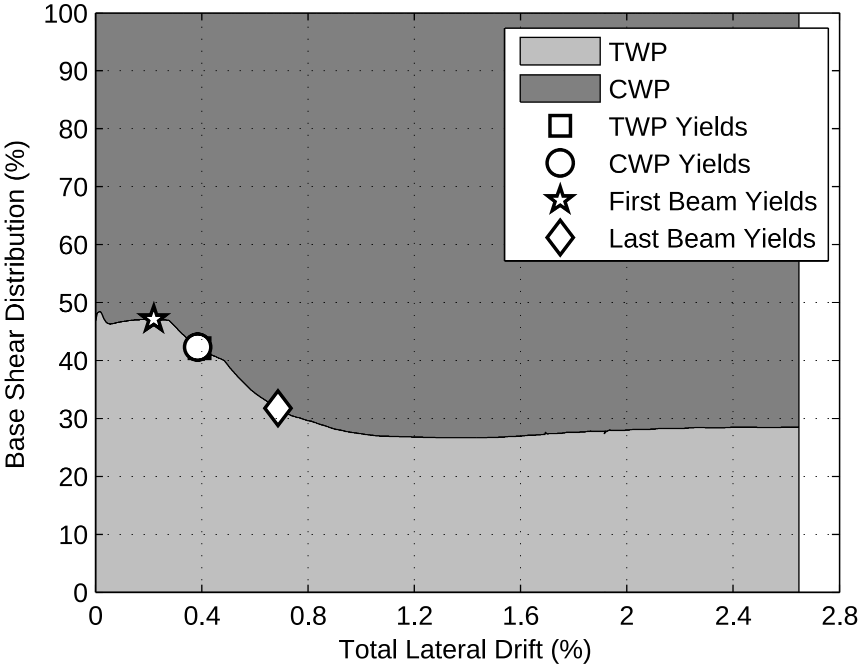

Figure 8.13: DPM model distribution of shear at base of Santhakumar WallA

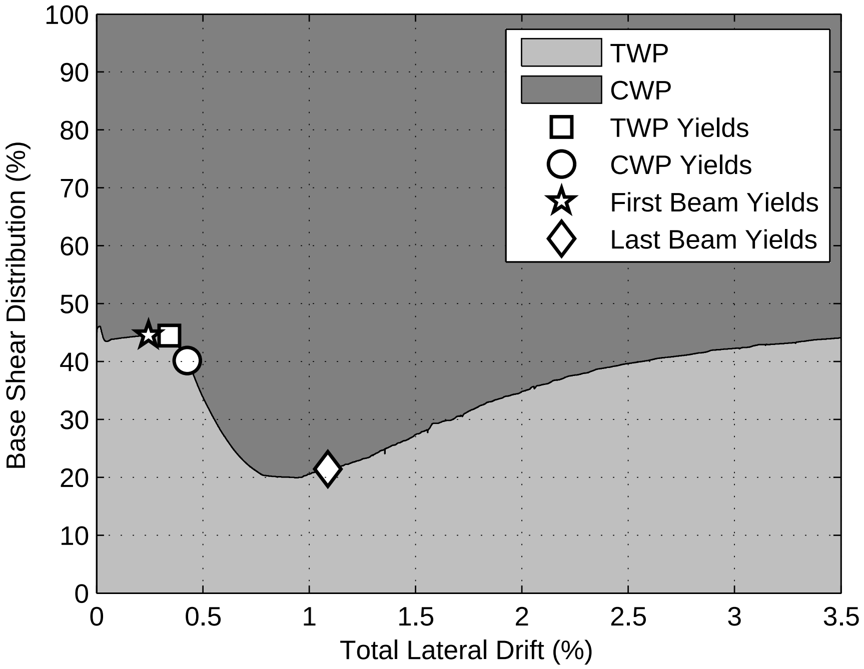

Figure 8.14: LPM model distribution of shear at base of Santhakumar WallB

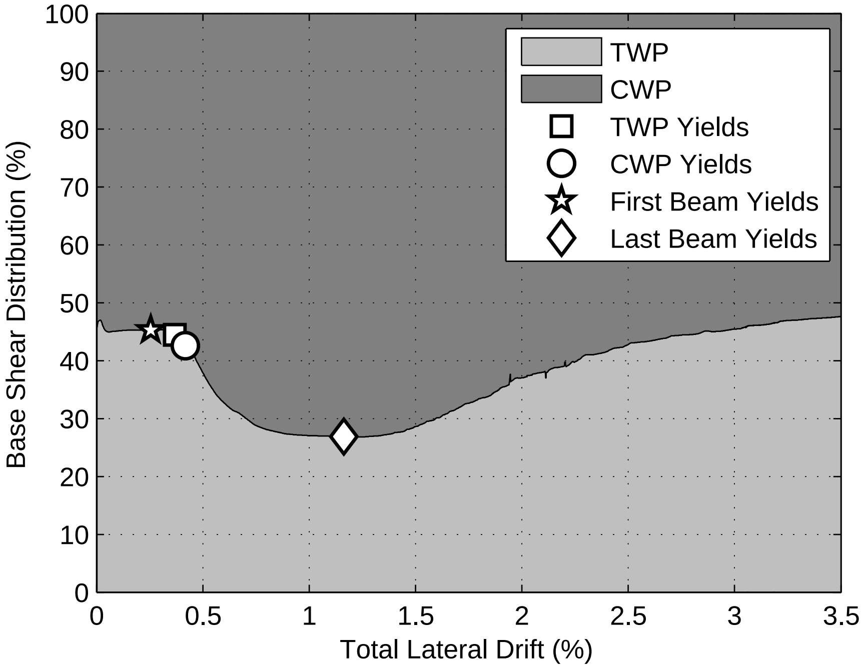

Figure 8.15: DPM model distribution of shear at base of Santhakumar WallB

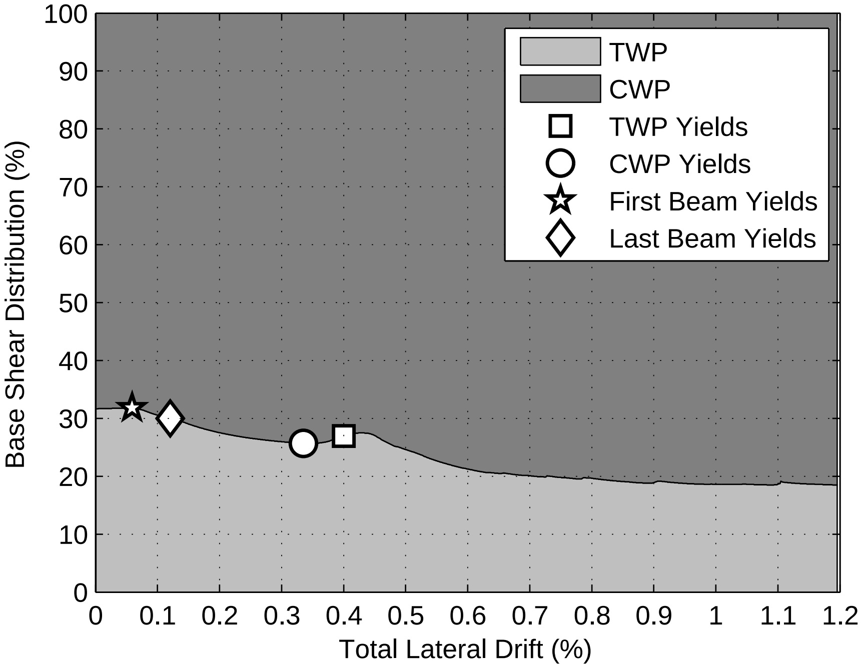

Figure 8.16: LPM model distribution of shear at base of Shiu CS1

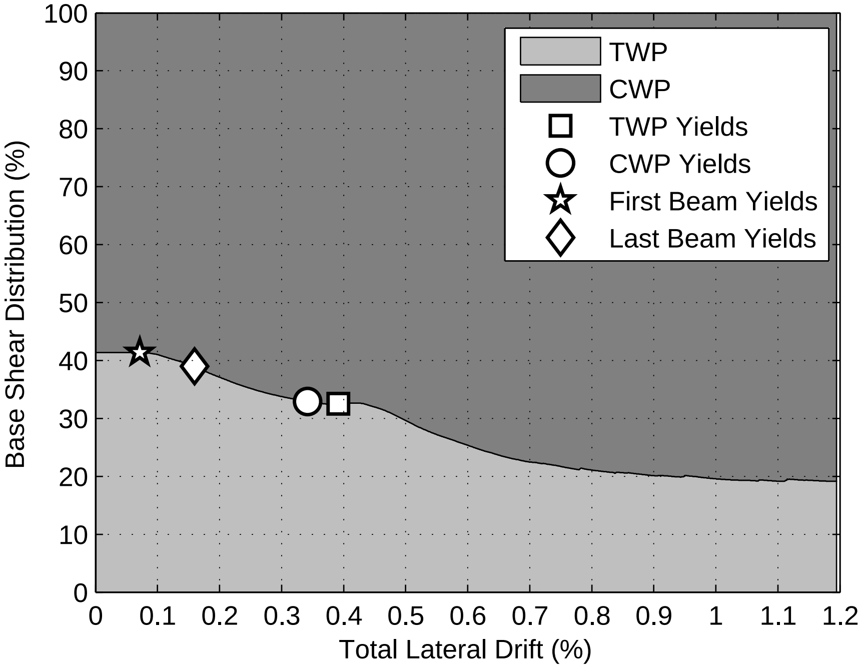

Figure 8.17: DPM model distribution of shear at base of Shiu CS1

8.2.3 Base Moment Distribution

The degree of coupling (DOC) design parameter discussed in Section 2.1, provides an effective way to predict the distribution of total overturning moment between the individual wall pier moments and the “coupling” moment. The coupling moment affects axial loads in the wall piers, which in turn changes the distribution of wall pier moments between the TWP and the CWP. The distribution of moments across the base of the coupled wall models are shown in Figures 8.18 – 8.27. The analytical results were compared to the predicted DOC calculated in Chapter 6, as well as the experimental DOC values for the CW1 and the Ozselcuk (1989) coupled wall tests. Additionally, the analytical moment distribution results for each model are tabulated in Tables 8.6 and 8.7. Results of each model were chosen based on the same limit states used in Table 8.5.

With the exception of two specimens, the DOC from the nonlinear analyses remains somewhat constant throughout the experiment. One exception is the DOC for the CW1 LPM model increases from approximately 65% to roughly 81% simply due redistribution of forces as a result of the loss in capacity of the CWP element. The other being, the DOC in both Shiu CS1 models rapidly degraded from approximately 0.06% drift (first yield) to 0.4% drift (CWP yield). The LPM and DPM degree of coupling at first yield was 43% and 37.4%, respectively. By the time the models reached their respective plastic strength, the DOC had decreased to 17.1% in the LPM and 15.3% in the DPM. This behavior is a result of the coupling beam elements losing a significant amount of strength at each floor which reduces the axial forces in the wall piers.

The percent difference between the DOC results for the lumped and distributed plastic models are smaller than 5% suggesting the DOC is not sensitive to the type of nonlinear element formulation. In general, the analytical results over-estimate the DOC when compared to the predicted DOC based on a plastic mechanism. This over-prediction is attributed to more hardening occurring at the ends of the coupling beam sections in the nonlinear analyses. Additionally, when the shear demands at the ends of the coupling beams are calculated to determine the predicted DOC values, no axial load is assumed to be in the coupling beam. This assumption is inaccurate in a real system and can result in an under-prediction of the coupling beam moment/shear demands. Axial loads in the coupling beams for all the nonlinear models ranged from $0.01f'_cA_g$ to $0.12f'_cA_g$, which was not trivial.

Like the distribution of shear demand from the tension wall to the compression wall, the moment distribution is important to quantify the amount of force demands localizing at the base of the compression pier. On average, the moment in the compression wall was approximately twice the moment demand in the tension wall when the analyses reached their respective plastic shear strength. At yield, this difference was on the order of 1.7, on average.

Table 8.6: LPM wall pier base moment distributions

Specimen Name	**Yield**			**Plastic**			**Predicted**
	$\frac{TL}{M_{tot}}$ (%)	$\frac{M_{tw}}{M_{tot}}$ (%)	$\frac{M_{cw}}{M_{tot}}$ (%)	$\frac{TL}{M_{tot}}$ (%)	$\frac{M_{tw}}{M_{tot}}$ (%)	$\frac{M_{cw}}{M_{tot}}$ (%)	**DOC** (%)
CW1	68.4	7.0	24.6	63.4	5.9	30.7	52.7
Ozselcuk 1C	66.0	11.6	22.4	66.6	3.0	30.4	64.2
Santhakumar WallA	63.3	15.8	20.9	60.4	15.8	23.8	50.6
Santhakumar WallB	63.1	16.3	20.6	63.1	13.7	23.2	52.7
Shiu CS1	43.0	18.8	38.2	17.1	35.3	47.6	9.3

Table 8.7: DPM wall pier base moment distributions

Specimen Name	**Yield**			**Plastic**			**Predicted**
	$\frac{TL}{M_{tot}}$ (%)	$\frac{M_{tw}}{M_{tot}}$ (%)	$\frac{M_{cw}}{M_{tot}}$ (%)	$\frac{TL}{M_{tot}}$ (%)	$\frac{M_{tw}}{M_{tot}}$ (%)	$\frac{M_{cw}}{M_{tot}}$ (%)	**DOC** (%)
CW1	67.8	8.0	24.2	62.5	6.8	30.7	52.7
Ozselcuk 1C	63.1	13.5	23.4	64.0	5.6	30.4	64.2
Santhakumar WallA	61.4	16.4	22.2	60.6	16.6	22.8	50.6
Santhakumar WallB	62.5	15.8	21.7	62.3	14.7	23.0	52.7
Shiu CS1	37.4	23.8	38.8	15.3	34.9	49.8	9.3

where,

TL	moment due to coupling action (a.k.a the coupling moment, M_{coup})
M_{tw}	moment at the base of the TWP element
M_{cw}	moment at the base of the CWP element
M_{tot}	total overturning moment at the base of the coupled wall system

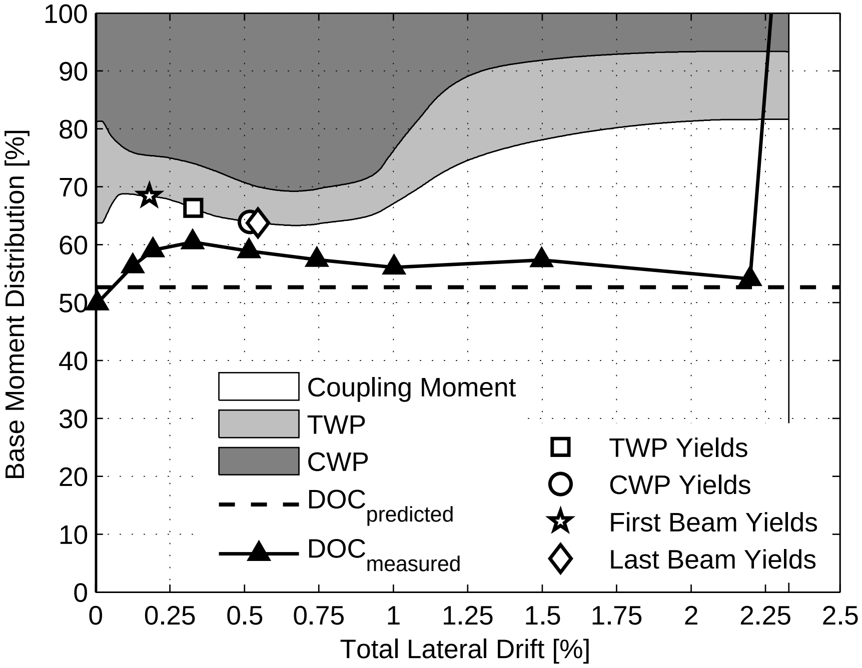

Figure 8.18: LPM model distribution of moment at base of CW1

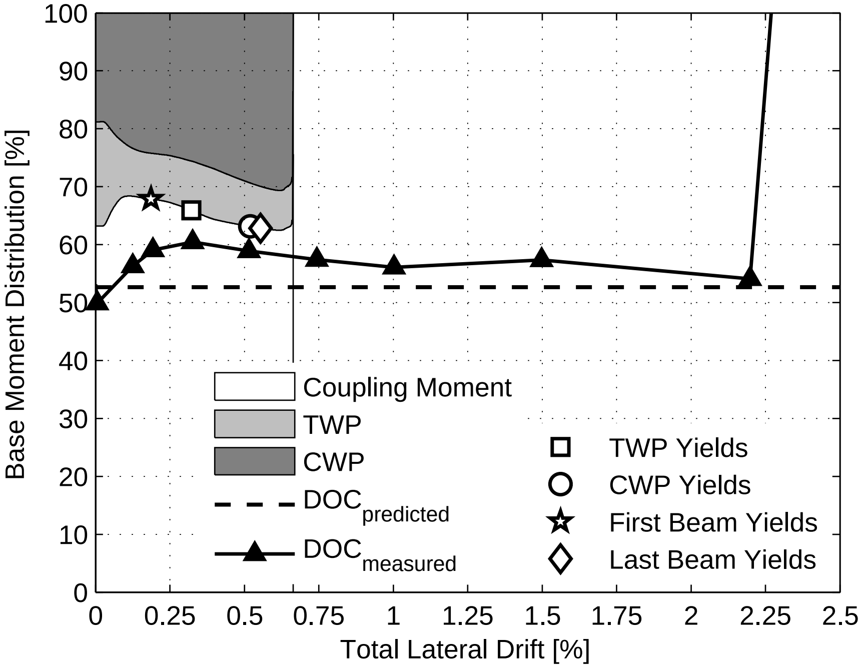

Figure 8.19: DPM model distribution of moment at base of CW1

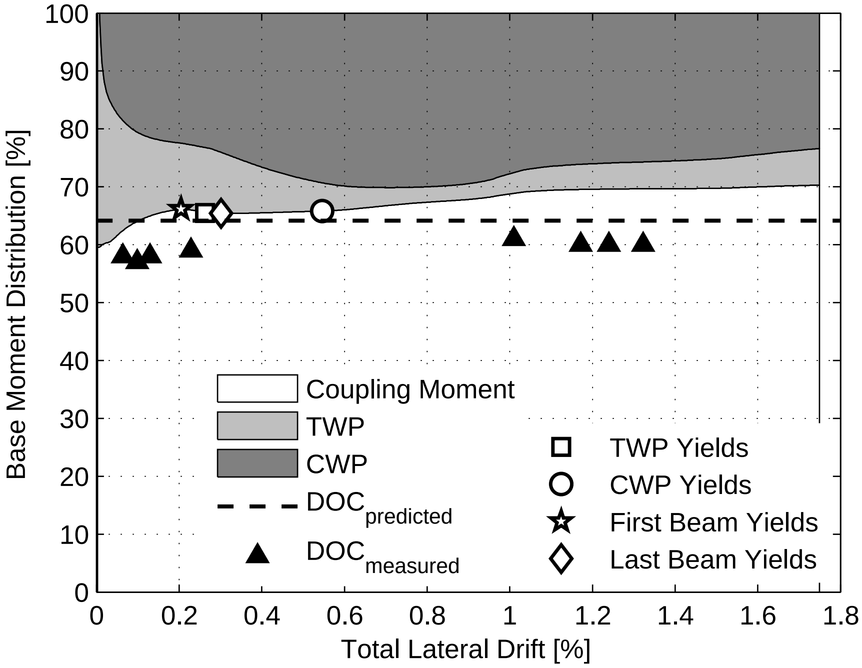

Figure 8.20: LPM model distribution of moment at base of Ozselcuk 1C

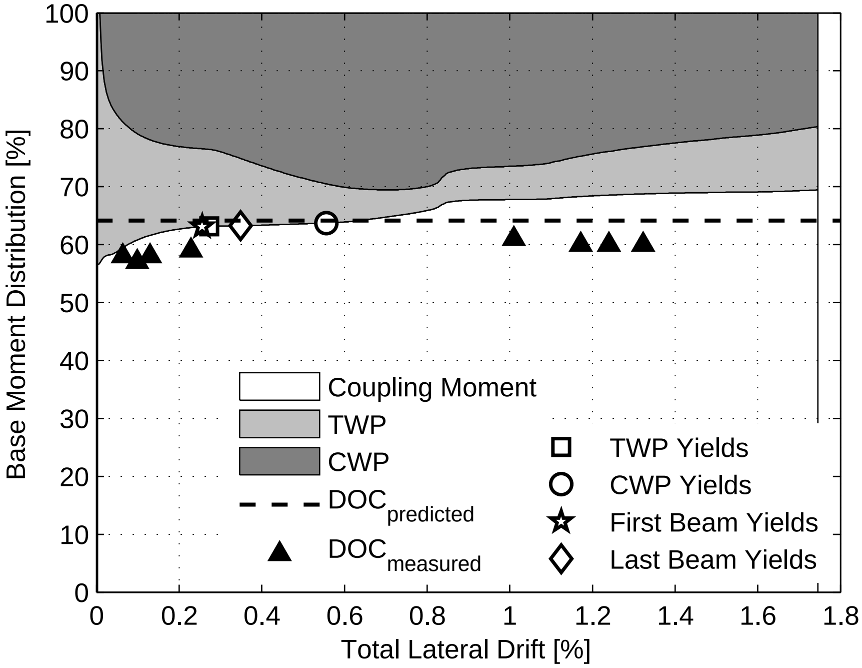

Figure 8.21: DPM model distribution of moment at base of Ozselcuk 1C

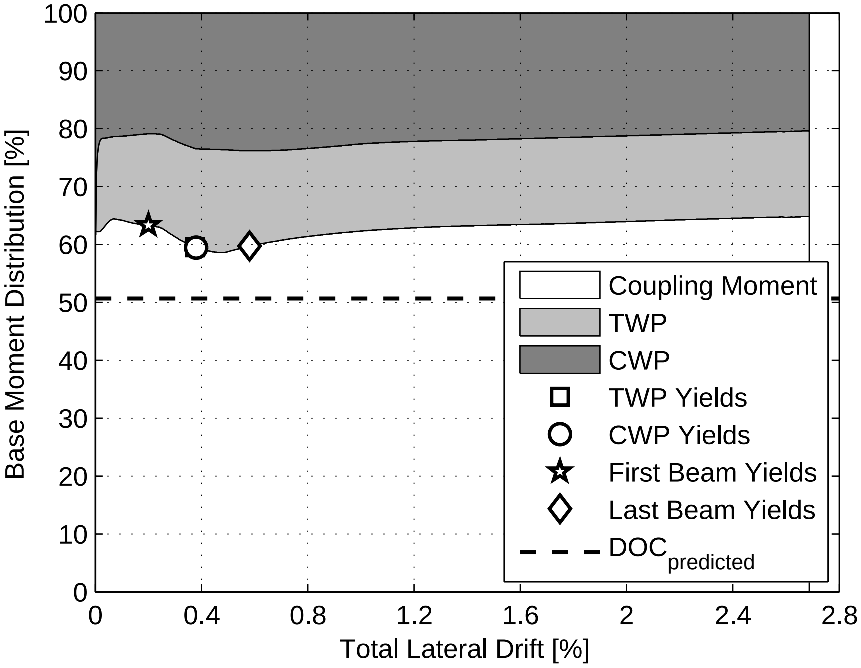

Figure 8.22: LPM model distribution of moment at base of Santhakumar WallA

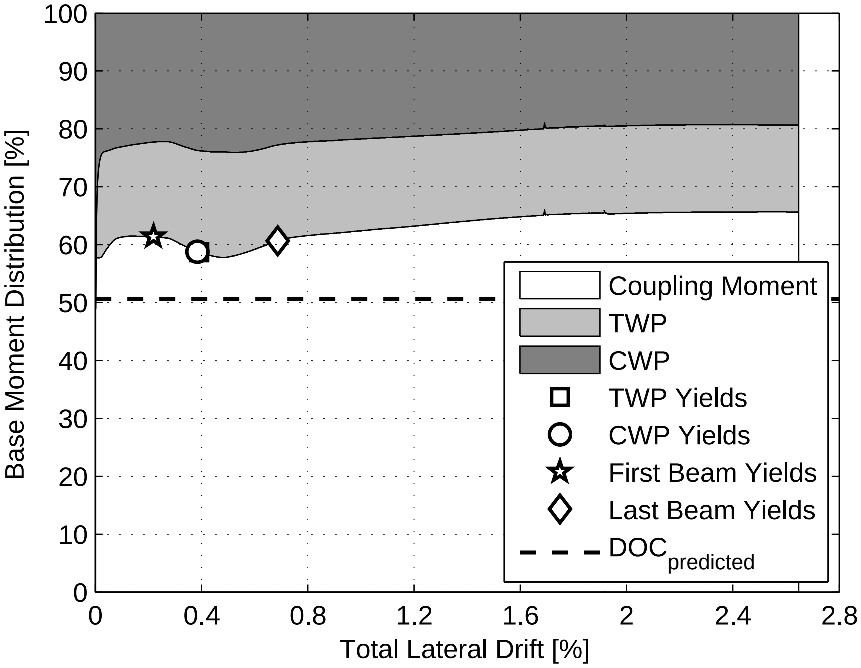

Figure 8.23: DPM model distribution of moment at base of Santhakumar WallA

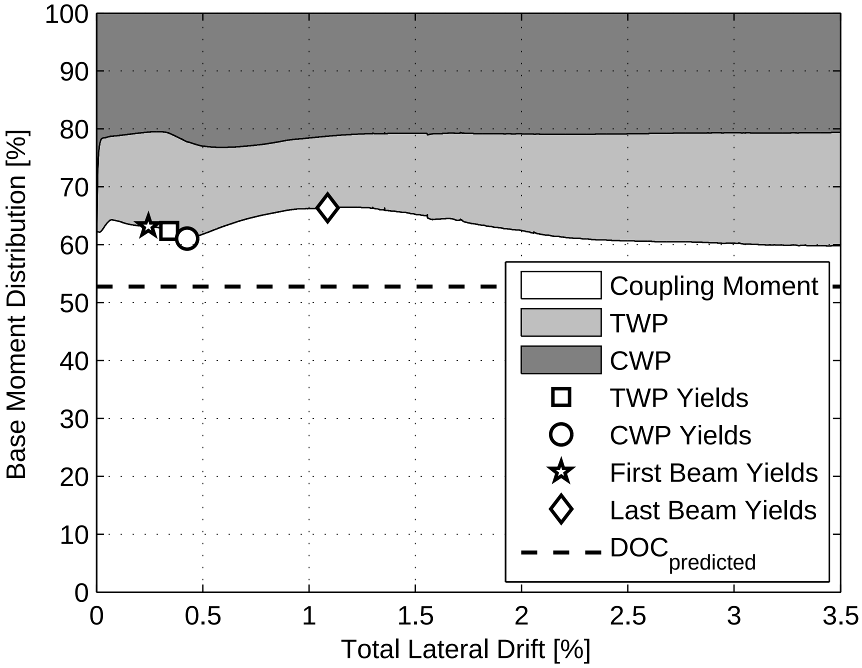

Figure 8.24: LPM model distribution of moment at base of Santhakumar WallB

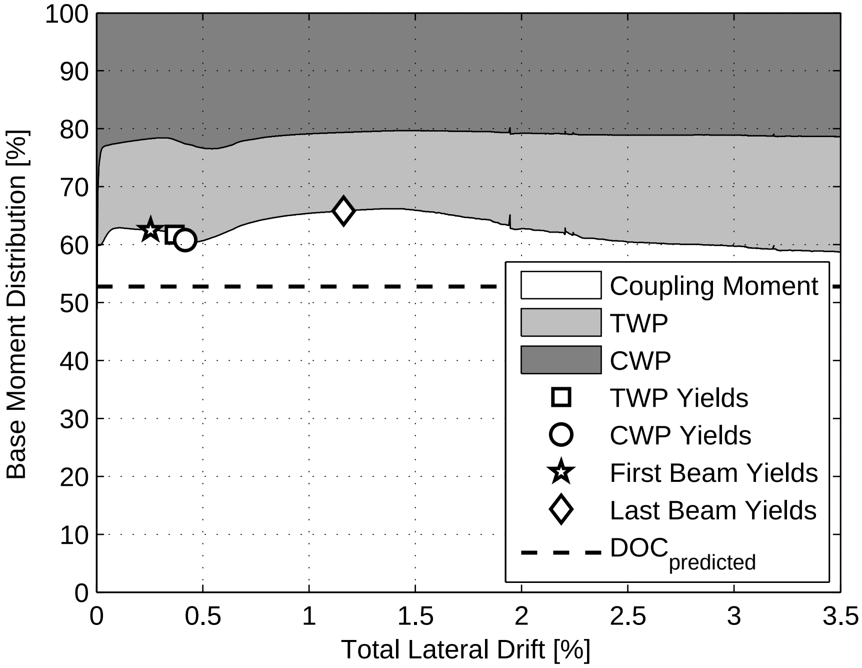

Figure 8.25: DPM model distribution of moment at base of Santhakumar WallB

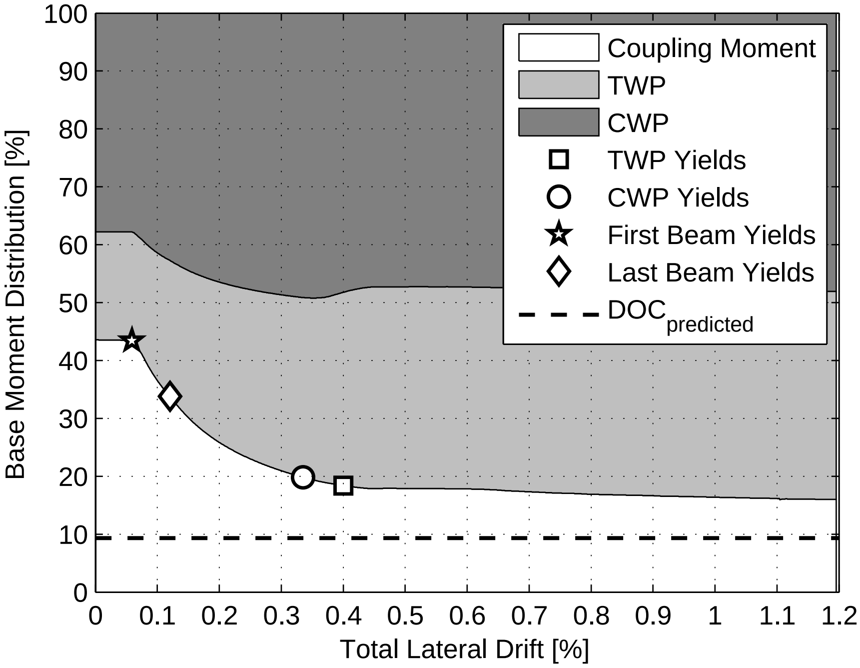

Figure 8.26: LPM model distribution of moment at base of Shiu CS1

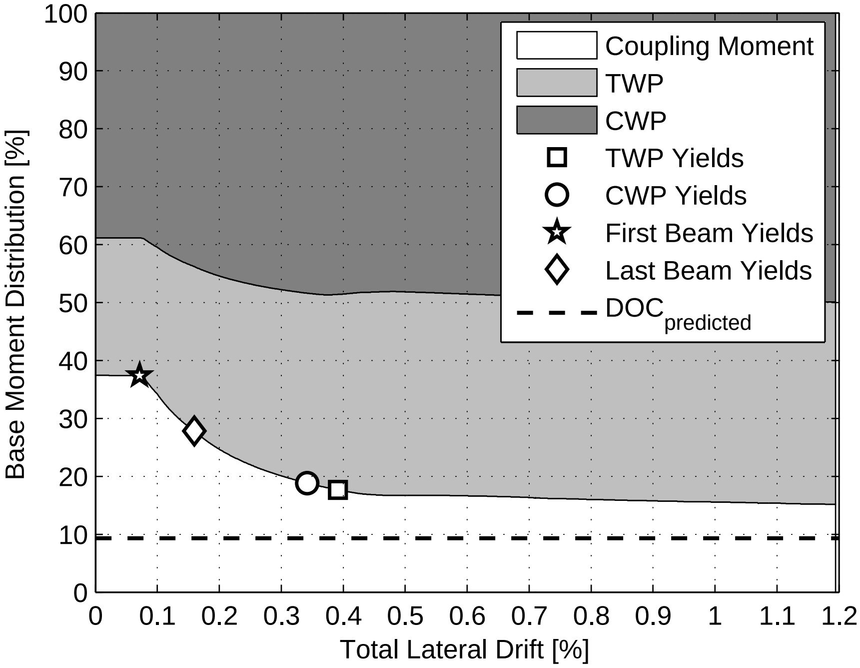

Figure 8.27: DPM model distribution of moment at base of Shiu CS1

8.2.4 Axial Forces

The axial loads in the wall piers have a significant influence of the wall pier axial and flexural stiffness, and as a consequence, moment and shears at the base of the wall piers are redistributed predominately to the compression wall pier. This behavior not only effects the overall deformation and strength of a coupled wall system, but for many cases, it limits the drift capacity of a coupled wall to the overstressed compression pier. The axial force verse drift results for the tension and compression wall piers are shown in Figures 8.29 – 8.38. The analytical results for the tension wall were compared to the predicted axial tension demand capacity ratio (DCR_{axial}) which was calculated in Chapter 6, and the results for the compression wall were compared to the predicted axial compression demand (ACD) which was also calculated in Chapter 6. In addition to these comparisons, the experimental axial force results were compared to the analytical results for the CW1 and the Ozselcuk (1989) coupled wall tests. The axial force results for all the analyses at the two critical limit states are presented in Tables 8.8 and 8.9. These results were chosen based on the same limit states (i.e. first yield and plastic strength) used in the previous two subsections.

Table 8.8: Tension wall pier axial results for LPM and DPM

	Yield		**Plastic**		**Predicted**
Specimen Name	$\frac{N_{LPM}}{\sum(A_s f_y)}$	$\frac{N_{DPM}}{\sum(A_s f_y)}$	$\frac{N_{LPM}}{\sum(A_s f_y)}$	$\frac{N_{DPM}}{\sum(A_s f_y)}$	DCR_{axial}
CW1	0.24	0.26	0.67	0.65	0.43
Ozselcuk 1C	0.20	0.26	0.83	0.80	0.93
Santhakumar WallA	0.30	0.28	0.67	0.68	0.46
Santhakumar WallB	0.37	0.37	0.75	0.74	0.52
Shiu CS1	0.07	0.07	0.14	0.14	0.09

All the analyses, except for the two Ozselcuk 1C models, over-estimate the axial forces in the tension wall pier when compared to the predicted DCR_{axial}. On average,

Table 8.9: Compression wall pier axial results for LPM and DPM

	Yield		**Plastic**		**Predicted**
Specimen Name	$\frac{N_{LPM}}{A_g f'_c}$	$\frac{N_{DPM}}{A_g f'_c}$	$\frac{N_{LPM}}{A_g f'_c}$	$\frac{N_{DPM}}{A_g f'_c}$	**ACD** $(A_g f'_c)$
CW1	-0.24	-0.24	-0.36	-0.35	-0.29
Ozselcuk 1C	-0.21	-0.22	-0.33	-0.33	-0.35
Santhakumar WallA	-0.23	-0.23	-0.38	-0.38	-0.30
Santhakumar WallB	-0.27	-0.27	-0.43	-0.43	-0.33
Shiu CS1	-0.02	-0.02	-0.04	-0.04	-0.02

the axial tensile load in the wall pier for the lumped and distributed plasticity models at the plastic limit state were approximately 38% larger than their predicted DCRs. The Ozselcuk 1C models are not reaching their respective DCRs, but are by far the most accurate. Figure 8.35, the LMP nearly reaches the DCR_{axial} at approximately 0.88%. Additionally, the difference in error between the Ozselcuk 1C models and the predicted demand capacity ratios at the plastic limit state was approximately 11% (LPM) and 15% (DPM). Measured experimental axial force data was compared to the models as well, and the LPM and DPM result in a particularly good upper and lower bound on the experimental results at larger drifts.

On the other hand, the CW1 axial force-drift response for both models, up until failure of the compression pier, is much stiffer than the experimental results, which were estimated in Section 5.3. Just prior to failure of the compression pier in the analyses, the plastic limit state was reached at 0.93% and the axial force in the tension wall was approximately 12% larger than the experimental results. This additional demand in the tension pier is attributed to the over-prediction of shear demand in the coupling beams up the height of the 10-story model. For example, a comparison between the analytical and experimental shear demand results for the second floor coupling beam is shown in Figure 8.28. When the second floor coupling beam reaches its respective maximum

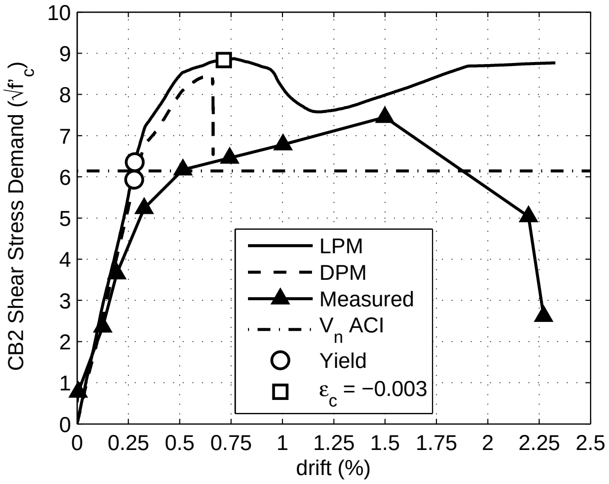

Figure 8.28: Shear stress demand in CB2 for CW1 models

in the nonlinear model, the shear demand was nearly 40% larger than the estimated experimental demand, and almost 50% larger than the nominal shear strength of the coupling beam as defined by ACI (Equation 3.1).

The axial load results of the compression wall pier for all the analyses except the Ozselcuk 1C models were over-predicted when compared to the ACD calculated in Chapter 6. On average, the axial compression demand in the wall pier for the lumped and distributed plasticity models at the plastic limit state were approximately 30% larger than the predicted demands. Similar to the TWP results, the Oszelcuk 1C models under predict the axial demand by approximately 5% (LPM) and 7% (DPM) when compared to the predicted ACD calculated in Chapter 6. These models reasonable bound the experimental data at larger drifts. The same over-strength noted for the CW1 coupling beams (Figure 8.28) increased the axial demands in the CWP for Specimen CW1. This behavior is clearly seen in Figure 8.36 where the axial compression load reaches its maximum at a lower drift than the experimental results. In the analyses, this behavior combined with the moment in the CWP leads to a large loss in lateral capacity. Thus, the ductility capacity of the coupled wall system is truly dependent capacity of the compression pier.

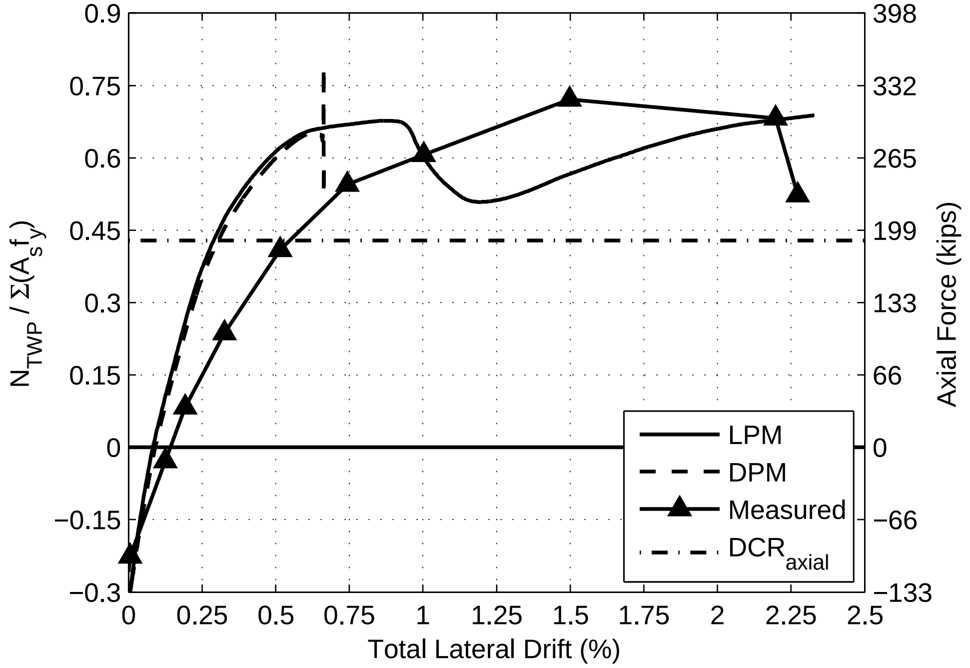

Figure 8.29: Tension wall pier axial load caparison, CW1

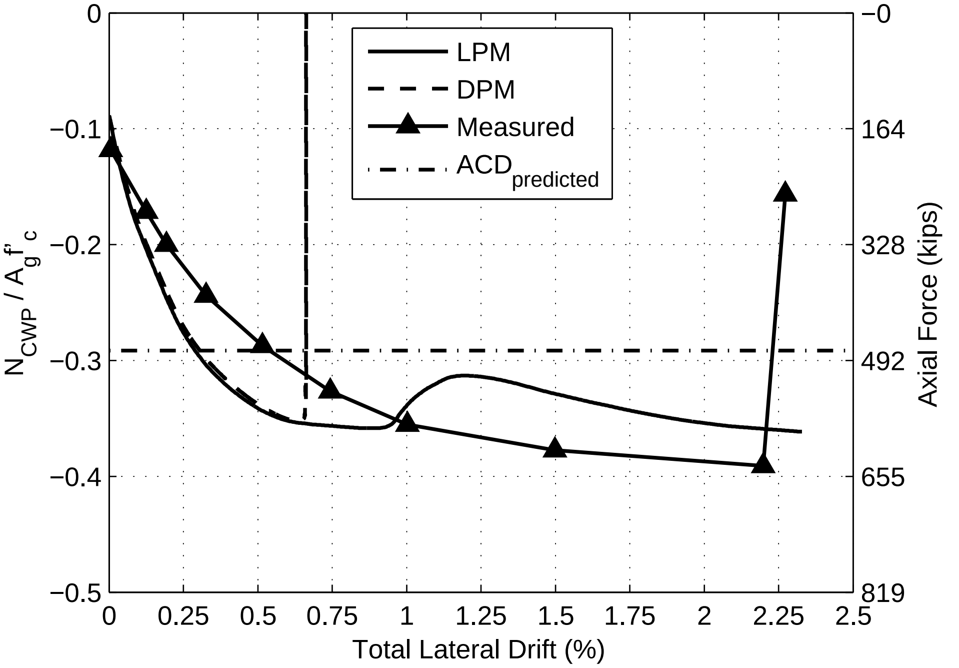

Figure 8.30: Compression wall pier axial load caparison, CW1

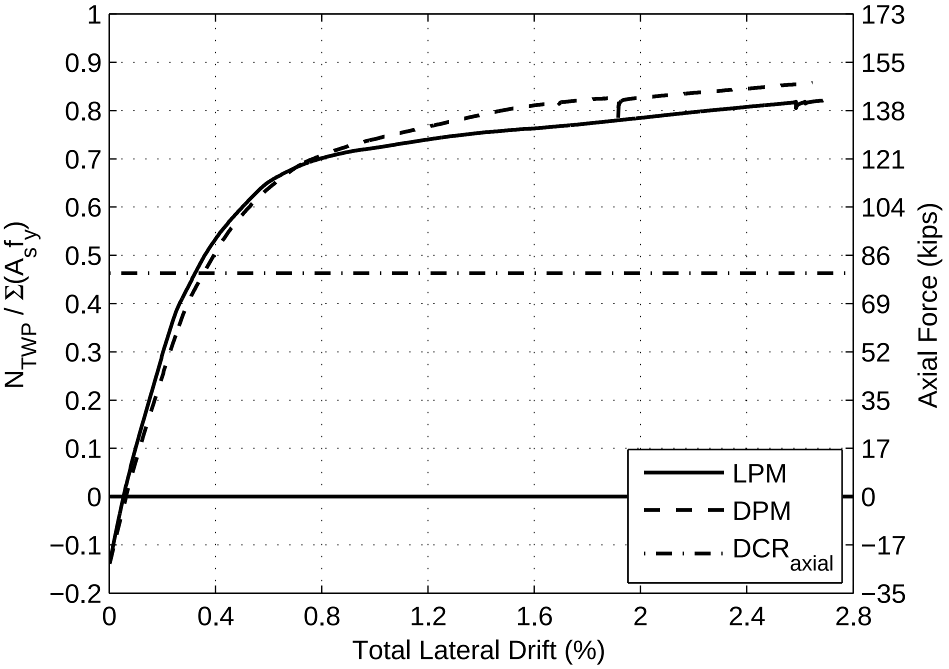

Figure 8.31: Tension wall pier axial load caparison, Santhakumar WallA

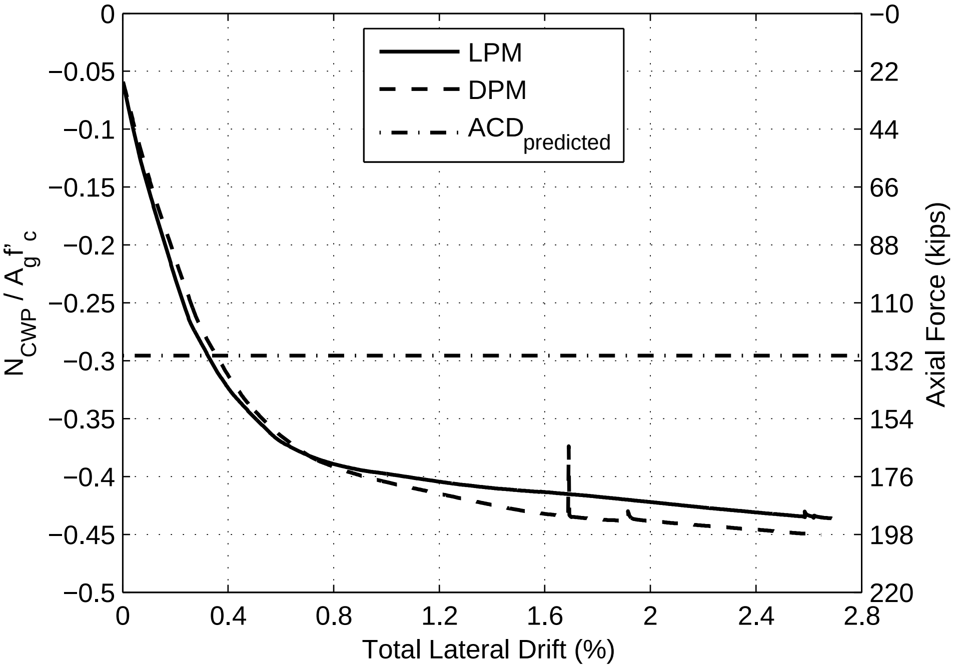

Figure 8.32: Compression wall pier axial load caparison, Santhakumar WallA

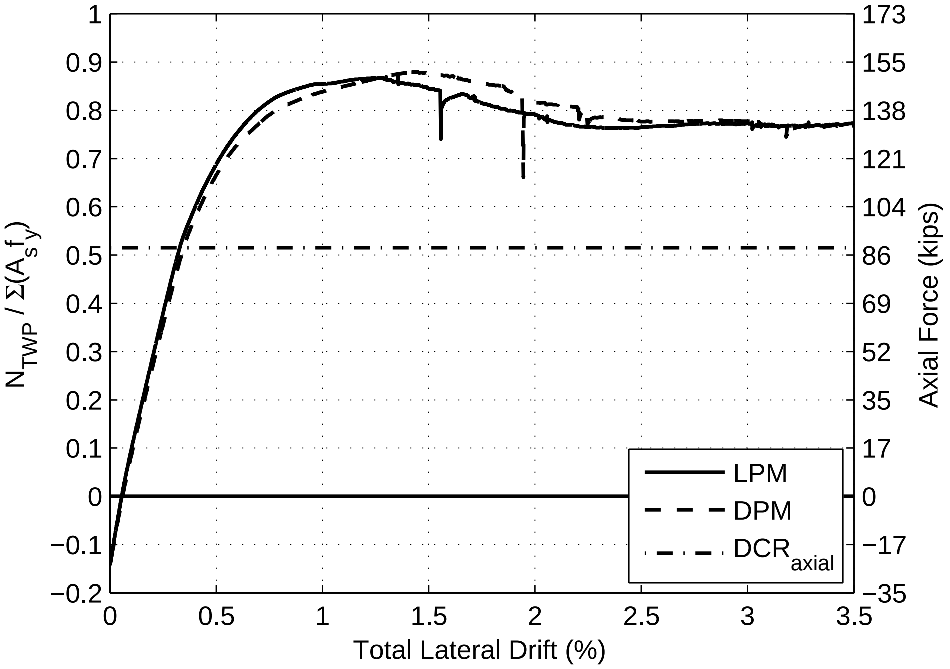

Figure 8.33: Tension wall pier axial load caparison, Santhakumar WallB

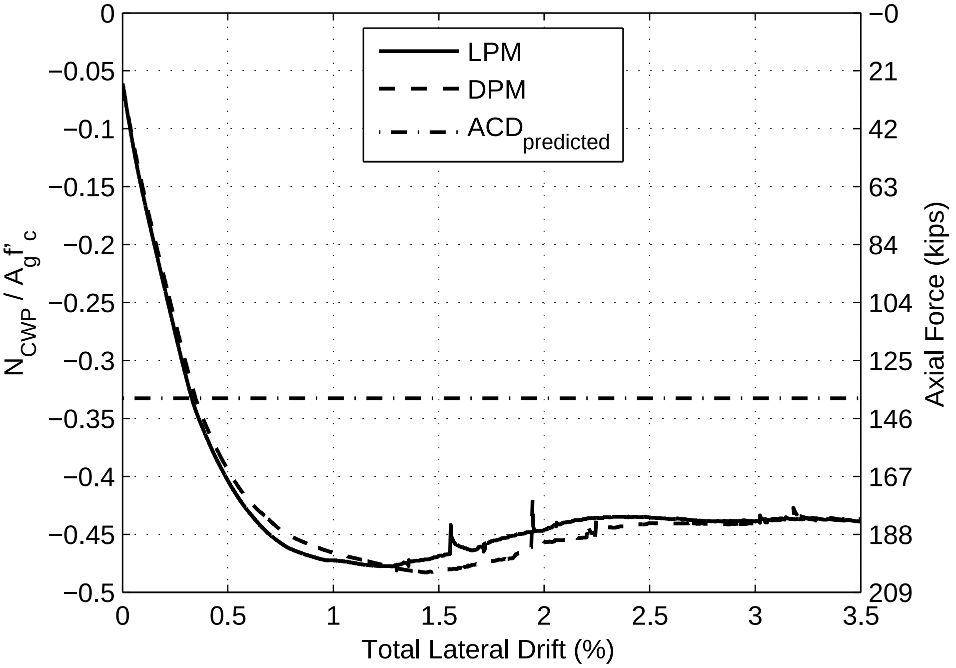

Figure 8.34: Compression wall pier axial load caparison, Santhakumar WallB

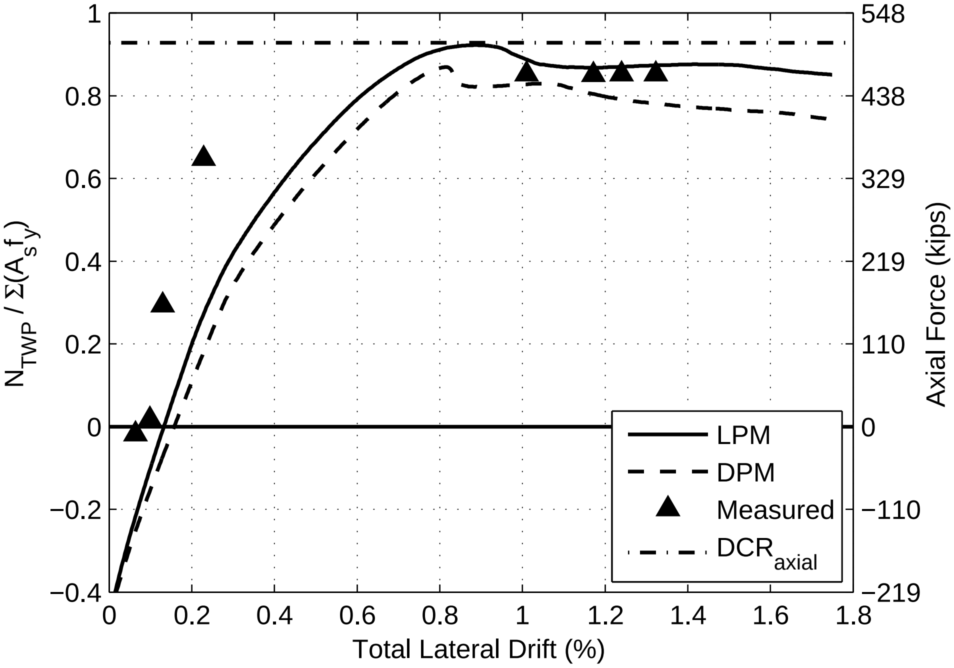

Figure 8.35: Tension wall pier axial load caparison, Ozselcuk 1C

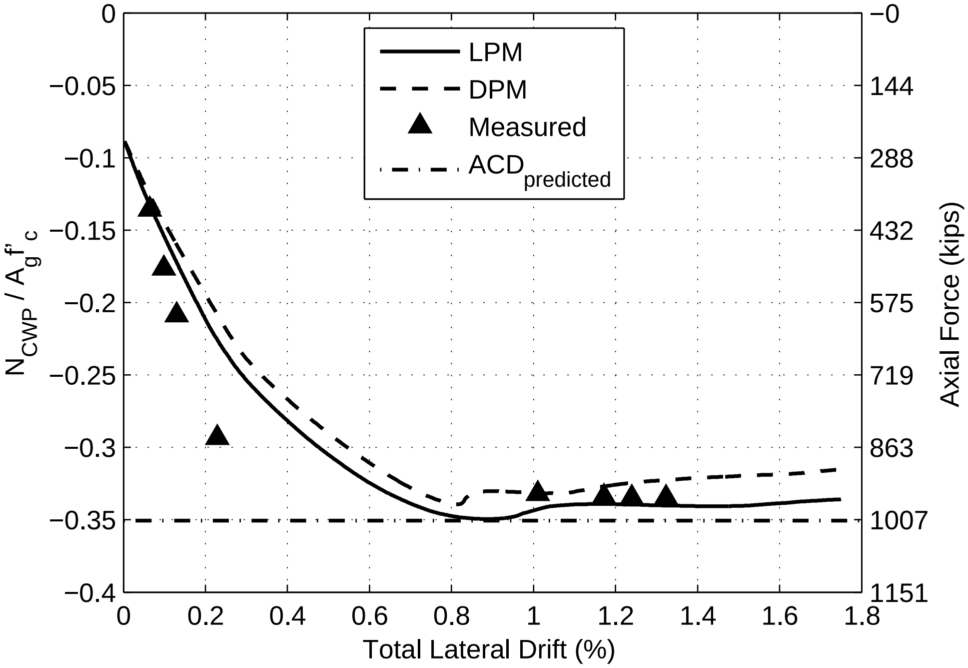

Figure 8.36: Compression wall pier axial load caparison, Ozselcuk 1C

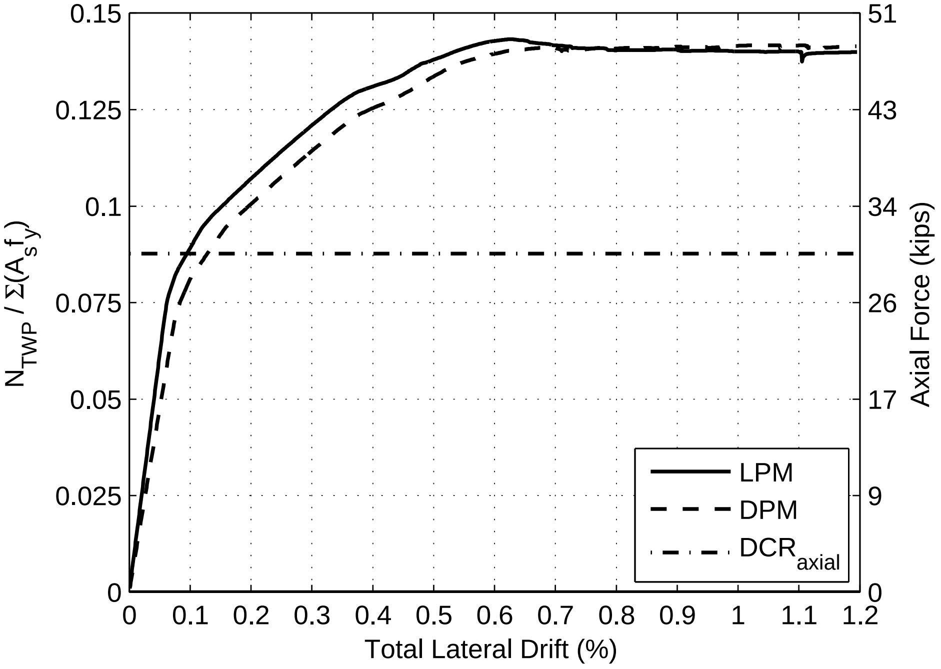

Figure 8.37: Tension wall pier axial load caparison, Shiu CS1

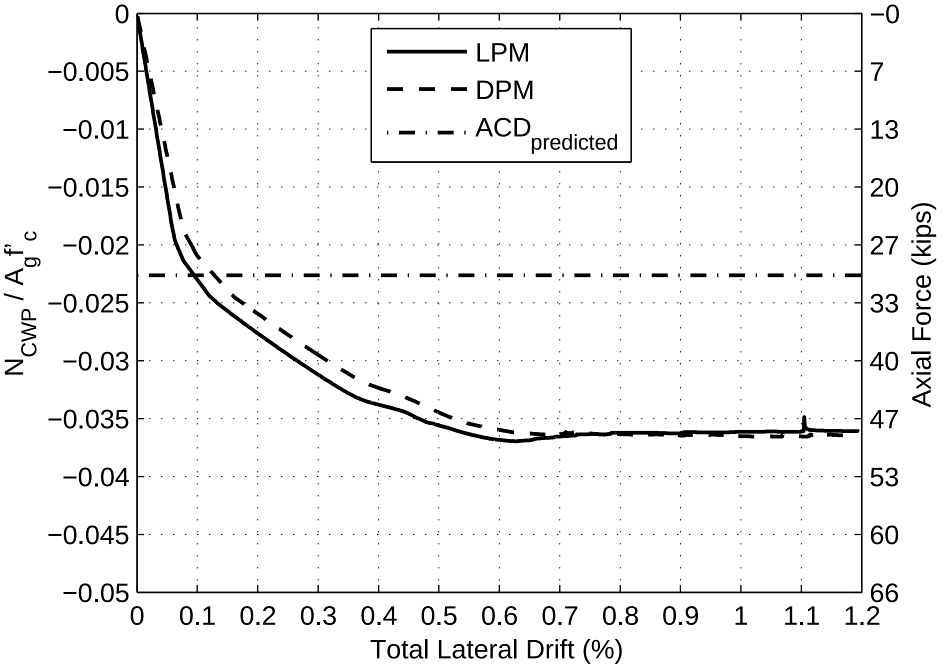

Figure 8.38: Compression wall pier axial load caparison, Shiu CS1

Chapter 9

DESIGN RECOMMENDATIONS

In a coupled wall system, the individual components and their intended interaction must be given careful consideration throughout the design process. In particular, the relative strengths, geometries and stiffness of the coupling beams and wall piers are important. These properties determine the force transfer among these elements, which determined the design demands. A design method that accounts for this force transfer with attention to the system properties is required.

The prior research results are combined with Specimen CW1, discussed herein, to develop recommended design expressions for coupled wall systems. First, target values of moment, shear and axial ratios are provided, where the ratios are target values to distribute the loading between the coupling beams and the wall piers or are target values for the compression wall pier. As demonstrated by this research and prior experimental studied, under overturning action, the compression wall pier is stiffer and attracts larger shear. In addition, large compressive stress demands in the wall can result in compression failure of the pier. These issues are addressed in Section 9.1.

The accuracy of a demand analysis of a coupled wall is strongly influenced by the effective stiffness values used for the wall piers and coupling beams, as indicated in Chapter 7. Those results are combined and recommended values are provided in Section 9.2

The final sections of the chapter address best practice design recommendations for the compression wall pier (Section 9.4) coupling beams (Section 9.3)

9.1 *Initial Design of a Coupled Wall*

Recommendations for the preliminary phase of coupled wall design are presented here. Typically due to architectural constraints, the length of the wall pier and aspect ratio of the coupling beams are known at the start of preliminary design. Therefore, the thickness and strength of the wall piers and coupling beams should be proportioned using the following procedure:

1. Choose a target degree of coupling within the range of 20% to 50%.

2. Calculate the total coupling beam shear demand up the height of the building (Equation 9.1) from the targeted DOC and the total seismic overturning moment, $M_{o,ASCE}$, which is known from the total design lateral force calculated from ASCE 7 and the moment-to-shear ratio resulting from the ASCE 7 procedure.

$$\sum V_{u,cb} = \frac{M_{o,ASCE}}{L} \times DOC \tag{9.1}$$

3. Size the each wall pier to meet the axial stress limit (i.e. $\sum V_{u,cb} + P_D = 0.2f'_c A_g$), where P_D is the axial force from dead load

4. Size the each wall pier to meet a shear stress limit of $7\sqrt{f'_c}$ (psi) assuming 100% of the total design lateral force calculated from ASCE 7 is carried by that wall pier

5. Select the wall size which results in the larger of (3) or (4)

6. Resize thickness of coupling beams to have the same thickness as the wall

7. Find an estimate of the coupling beam longitudinal reinforcement to meet the total coupling beam shear demand, $\sum V_{u,cb}$, using the vertical distribution of coupling beams shear forces determined from demand analysis discussed in next section

8. Find an estimate of the wall pier longitudinal reinforcement to meet the flexural demands resulting from DOC

The recommendations presented above are primarily based on previously tested coupled wall tests including the test of CW1. These data were combined in Chapter 6, and performance evaluation parameters (i.e. degree of coupling, wall pier demand capacity ratios, etc.) were calculated. Here, these parameters are compared to the respective experimental drift capacities for the combined dataset. The drift capacity of the specimen was taken from its force-displacement envelope when the specimen reached 90% of the maximum measured base shear, V_{max}. In particular, the drift was chosen after the specimen reached the peak base shear and continued to softened to 90% of V_{max} (Table 6.5). The results of this study are shown in Figures 9.1–9.3.

The degree of coupling (DOC) range was selected using the data presented in Figure 9.1, which suggest there is no performance advantage in proportioning the strength of the wall piers and coupling beams, such that, the DOC is greater than 55%. On the other

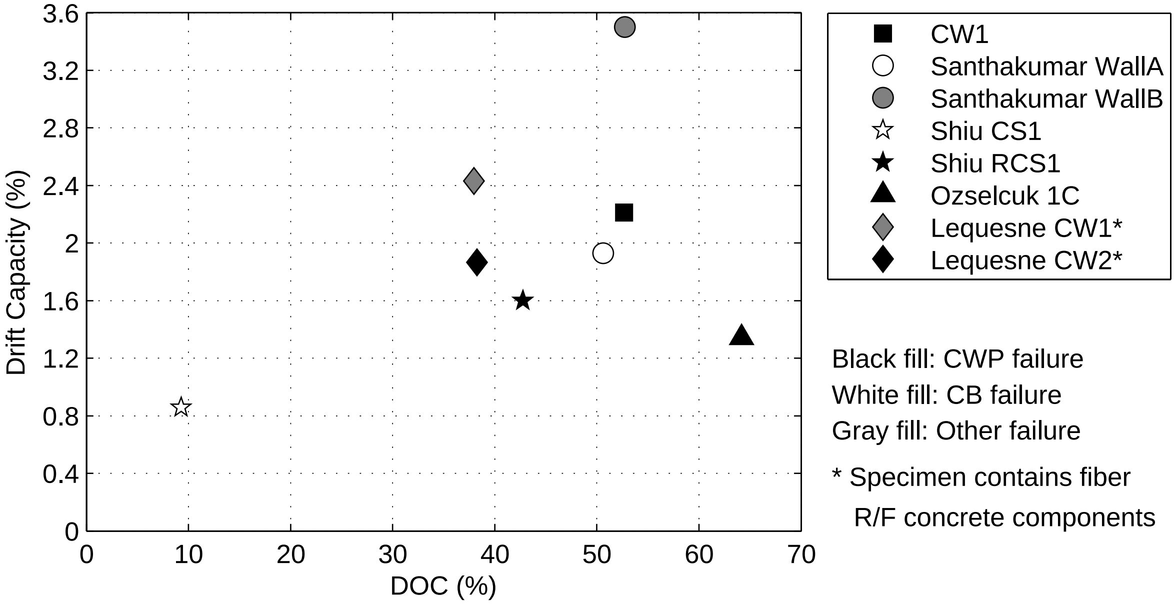

Figure 9.1: Drift capacity vs. degree of coupling (DOC)

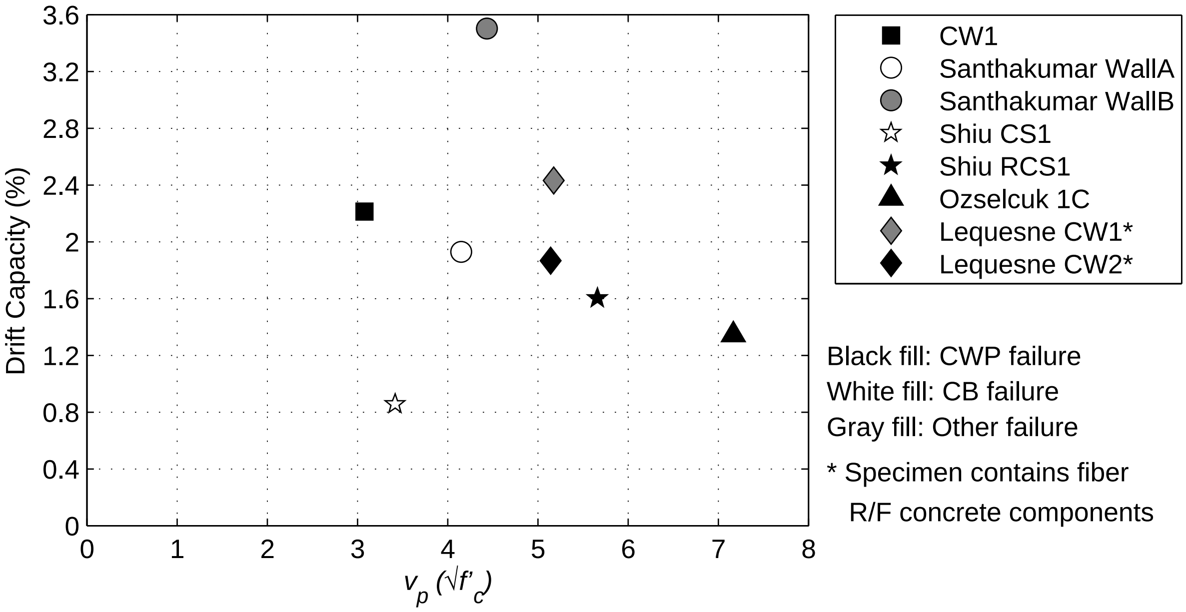

Figure 9.2: Drift capacity vs. plastic base shear stress demand, v_p

hand, the results of Shiu et al. (1981) suggests a low degree of coupling (10%) negatively impacts the performance of coupled walls with conventionally reinforced coupling beam. For the data available, the highest drift capacities are reached for degrees of coupling in the range of 35% – 53%. Note, there is currently no degree of coupling data available between 10% and 35%.

Figure 9.2 indicates the shear stress demand, which is distributed evenly across the base of both wall piers, and was calculated assuming a plastic mechanism (Figure 2.1). Here it is evident that increased shear reduces the drift capacity of the system even without a shear failure. Similar results are noted for planar walls (Birely, 2011). Because results of experimental and analytical research presented in this research has shown a strong disproportion of shear forces between the tension wall and compression wall, the shear stress in the compression pier corresponding to a plastic moment should be limited to $10\sqrt{f'_c}$ (psi). For initial design the shear strength is proportioned by the strength reduction factors for elastic (0.6 ACI 318-08) and plastic design (0.85 ACI 318-08). The limiting shear stress demand recommended for initial design of an individual wall piers is $0.6/0.85 \times 10\sqrt{f'_c} = 7\sqrt{f'_c}$.

The axial compression demand resulting from the accumulation of all the coupling beams yielding up the height of the wall piers and the applied gravity force are plotted in Figure 9.3 verse the drift capacity of the coupled wall specimen. These results are related to the shear stress demand results shown in Figure 9.2 because high axial and shear demands in the compression wall piers is typically linked to compressive type damage. For wall piers with ratios larger than $0.3f'_cA_g$, the drift capacity is limited. This is expected since this axial stress ratio is widely assumed to approximately provided balanced response, and therefore axial stress ratios larger than this value will limit tensile yielding in the compression wall and thereby limit drift capacity. For **initial** design, however, the axial stress demand in the compression wall pier should be limited to $0.2f_c$ in order to a provide a sufficient factor of safety related to over-strength in the coupling beam flexural capacity which cause additional axial stress demand in the wall piers.

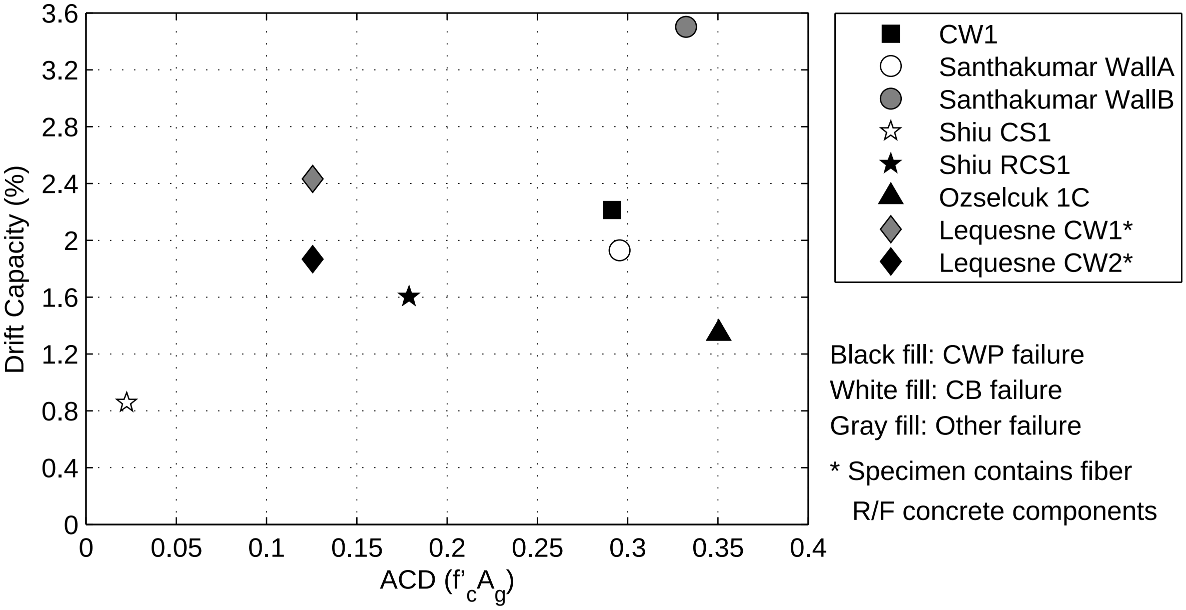

Figure 9.3: Drift capacity vs. axial compression demand (ACD)

9.2 Demand Analysis

In order to determine the distribution of internal forces within a coupled wall, an elastic analysis should be performed. The stiffness of the wall piers and coupling beams are modeled with effective stiffness values in order to capture the elastic response of a coupled wall up to yield. Based on the results presented in Chapter 7, effective stiffness recommendations for elastic analysis provided by the ACI, ASCE, CSA and NZS design codes do not provided accurate prediction of response to yield of the system. In general the response of these models are in general too stiff. Simulation of system behavior is very sensitive to the flexural stiffness of the coupling beams as well as the shear stiffness of the both the coupling beams and wall piers and the design codes recommend stiffness values that are too large.

In general, the elastic analysis results indicate that recommendations by Birely (2011) and Mohr (2007) for the wall piers and coupling beams, respectively, provide the best estimate of the yield. Of the recommendations reviewed, those by Birely (2011) and Mohr (2007) provide the most accurate and precise prediction of response. From these results the effective stiffness values presented in Table 9.1 are recommended for modeling the elastic response of coupling beams and coupled walls.

Table 9.1: Recommended effective stiffness values for coupled wall components

Component	**Flexural Rigidity**	**Shear Rigidity**	**Axial Rigidity**
Wall Piers	$0.35E_cI_g$	$0.15GA_{cv}$	$1.0E_cA_g$
Coupling Beams	$0.05E_cI_g$	$0.15GA_{cv}$	$1.0E_cA_g$

9.3 Coupling beams

In order to accurately predict probable axial forces and shear demands in the wall piers at the ultimate strength of the coupled wall, a plastic analysis needs to be performed.

This should employ expected plastic strength of coupling beams, which is a function of strain-hardening of the tension reinforcement, axial force present in the coupling beam, reinforced concrete slab and the contribution of concrete confinement. Results show this expected plastic strength may exceed 140% of the expected nominal strength (i.e. measured material properties). Research by Naish et al. (2009) suggests there is a similar over-strength in expected plastic strength due to the presence of a reinforced concrete slab. Therefore, it is recommended, that for a plastic analysis, the coupling beam expected plastic shear strength be calculated as $1.4V_{n,cb}$, as a minimum.

9.4 Wall Piers

When the coupling beams are strong relative to the wall piers (i.e. a high DOC), large axial demands develop in the wall piers. The development of large a tensile force in the tension wall pier results in a reduction in the stiffness. As a consequence, the majority of the moment and shear shared between the wall piers must be carried by the compression pier. Because the compression wall pier attracts most of the forces in the system, it is the design of each wall pier in compression that is most likely to control; here, the design of the wall piers in compression for shear and axial demands are discussed.

9.4.1 Shear

Based on the nonlinear analyses results presented in Chapter 8, the CWP resisted approximately 78% (average of LPM and DPM) of the total base shear demand when the base shear reached the plastic strength of the system (Table 9.2). In addition to the OpenSees analyses, the results of VecTor2 analyses for Specimen CW1 suggest 90% of the total base shear was resisted by the CWP by the time the plastic base shear strength was achieved in the system. These results are discussed in Chapter 3 as a part of the loading protocol development.

The results of the two coupled wall experiments tested by Ozselcuk (1989) also showed the distribution of shear demand on the compression wall pier were roughly 80-90% of

Table 9.2: Percentage of total base shear resisted by CWP at plastic strength (LPM Results, Chapter 8)

Specimen Name	V_{cw} **(kips)**	$\frac{V_{cw}}{V_p}$	$V_{n,cw}$ **(kips)**	$\frac{V_{cw}}{V_{n,cw}}$
CW1	116	0.77	162	0.72
Ozselcuk 1C	344	0.91	222	1.55
Santhakumar WallA	45.5	0.75	52.1	0.87
Santhakumar WallB	46.4	0.73	51.8	0.90
Shiu CS1	111	0.80	166	0.67
Average	–	**0.79**	–	**0.94**
Std. Dev.	–	**0.071**	–	**0.355**

where,

V_{cw}	base shear demand in CWP
V_p	total base shear demand at plastic strength
$V_{n,cw}$	nominal shear strength of CWP per ACI 318-08 (Equation 3.2)

the total base shear when the vertical reinforcement in the wall piers reached yield. Due to the special test setup discussed in Chapter 2, the demands at the base of the wall piers were directly calculated. Both of the wall pier shear reinforcement was detailed to resist the shear demands resulting from a plastic analysis. However, the failure of these specimens was caused by crushing of web concrete in the compression wall pier.

In design however, this distribution of shear force is assumed to be equal among each wall pier because the design forces are computed using an elastic analysis. Furthermore, if the shear strength of the wall piers are designed as a result of a plastic analysis recommended by ICC (2007), the base shear demand is assumed to be distributed equally to each wall pier. Therefore, there is no current design standard recommending the nominal shear strength of an individual wall pier be designed to withstand a larger shear demand than half the total base shear.

The results of the OpenSees and VecTor2 analyses as well as experimental tests by Ozselcuk (1989) suggest that an individual compression pier carries at least 80 to 90% of the total shear demand. The results of Table 9.3 assume all of the maximum base shear recorded for the previous coupled wall experiments was resisted by the compression wall pier only. From these results, CW1 has a demand capacity ratio for shear that is 1.08 at maximum base shear, and no sliding shear failure was observed in the CWP.

As a result, it is recommended that the compression pier be design such that the total base shear demand of the coupled wall be resisted by the CWP alone in order to properly avoid a shear failure in the wall pier.

Table 9.3: Maximum experimental base shear demand capacity ratio assuming all shear is resisted by CWP

Specimen Name	V_{max} **(kips)**	$V_{n,cw}$ **(kips)**	$\frac{V_{max}}{V_{n,cw}}$
CW1	175	162	1.08
Ozselcuk 1C	409	222	1.84
Ozselcuk 2C	338	220	1.54
Santhakumar WallA	61.6	52.1	1.18
Santhakumar WallB	68.2	21.8	1.32
Shiu CS1	141	166	0.85
Shiu RCS1	213	166	1.28
Lequesne CW1	329	161	2.04
Lequesne CW2	379	224	1.69
Average	–	–	**1.42**
Std. Dev.	–	–	**0.385**

where,

V_{max}	maximum base shear reached in experiment (Table 2.9)
$V_{n,cw}$	nominal shear strength of CWP (Equation 3.2)

9.4.2 Moment-Axial Force Interaction

The interaction between the axial force and moment in the compression pier wall may limit the deformation capacity of the coupled wall system. Compiled axial and moment results are presented in Tables 9.4 and 9.5 for the analyses discussed in Chapters 7 and 8 as well as the predicted results using expected strengths calculated in Chapter 6. The axial demands in the CWP at the plastic limit state were roughly 50 to 60% larger than the axial loads in the CWP at yield. This is a significant amount of axial demand on the compression pier especially at the plastic limit state because the coupling beams are designed to be at their probable moment strength.

In Table 9.5, the moment demand in the compression wall was normalized by the total moment resisted by the two wall piers. In a coupled wall system once a majority of yielding has occurred, the degree of coupling remains essentially constant as long as the coupling beams do not substantially degrade in strength. However, moment is transferred from the tension wall to the compression wall due to the changing axial loads in the wall piers. For a typical elastic analysis, this distribution is 50/50 between each wall pier. The

Table 9.4: Compression wall pier axial results at yield and plastic strength

	Yield			**Plastic**		**Predicted**
Specimen Name	$\frac{N_{EA}}{A_g f'_c}$*	$\frac{N_{LPM}}{A_g f'_c}$	$\frac{N_{DPM}}{A_g f'_c}$	$\frac{N_{LPM}}{A_g f'_c}$	$\frac{N_{DPM}}{A_g f'_c}$	**ACD** $(A_g f'_c)$
CW1	-0.25	-0.24	-0.24	-0.36	-0.35	-0.29
Ozselcuk 1C	-0.24	-0.21	-0.22	-0.33	-0.33	-0.35
Santhakumar WallA	-0.21	-0.23	-0.23	-0.38	-0.38	-0.30
Santhakumar WallB	-0.27	-0.27	-0.27	-0.43	-0.43	-0.33
Shiu CS1	-0.02	-0.02	-0.02	-0.04	-0.04	-0.02
Shiu RCS1	-0.12	–	–	–	–	-0.18
Lequesne CW1	-0.11	–	–	–	–	-0.13
Lequesne CW2	-0.11	–	–	–	–	-0.13

* Results are from Birely/Mohr elastic analysis (EA) model Case F

Table 9.5: Ratio of CWP moment, M_{cw}, to total moment resisted by both wall piers, $M_{tw} + M_{cw}$

	Yield			**Plastic**		**Predicted****
Specimen Name	**EA***	**LPM**	**DPM**	**LPM**	**DPM**	$\frac{M_{n,cw}}{M_{n,tw} + M_{n,cw}}$
CW1	0.50	0.78	0.75	0.84	0.82	0.70
Ozselcuk 1C	0.50	0.66	0.63	0.91	0.84	0.76
Santhakumar WallA	0.50	0.57	0.58	0.60	0.58	0.49
Santhakumar WallB	0.50	0.56	0.58	0.63	0.61	0.50
Shiu CS1	0.50	0.67	0.62	0.57	0.59	0.52
Shiu RCS1	0.50	–	–	–	–	0.67
Lequesne CW1	0.50	–	–	–	–	0.54
Lequesne CW2	0.50	–	–	–	–	0.53

* Results are from Birely/Mohr elastic analysis (EA) model Case F

** Nominal moment strengths calculated with axial loads (Stringer, 2007)

nonlinear elements, on the other hand, were assigned fiber cross-sections which capture the axial-moment interaction in the element; therefore, the nonlinear analyses were able to capture the moment transfer between the tension wall and compression wall at yield.

An elastic analysis using beam-column elements to estimate seismic design forces is not sufficient. The actual behavior a coupled wall system distributes large moment, shear and axial forces to the compression wall piers. While the strength and stiffness of the CWP will be increased due to this increase in axial load, the elastic analysis cannot predict these forces, and in the case of CW1, the axial-moment interaction in the CWP at the plastic strength limit state is undesirable. For example, the results of the elastic analyses, nonlinear analyses, measured/estimated experimental results and predicted results for Specimen CW1 are plotted with the expected axial-moment interaction diagram (P-M) in Figure 9.4.

For the elastic analysis results, the axial force and moment are plotted at yield for the different model cases (A-F) discussed in Chapter 7. The measure axial load results

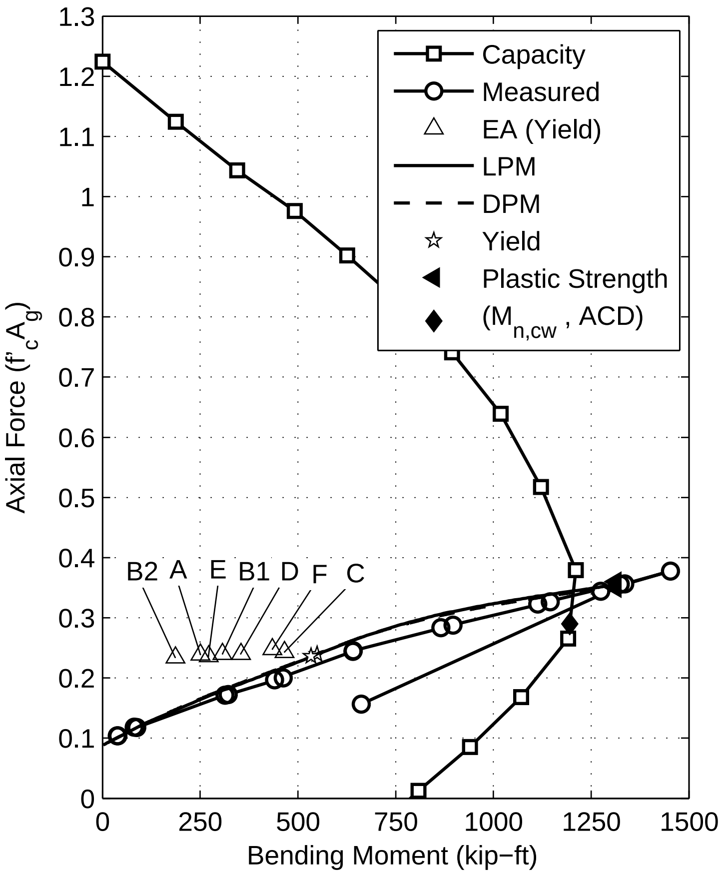

Figure 9.4: CW1 P-M interaction and analysis results for the compression wall pier

for CW1 were discussed in Section 5.3, and the moment in the CWP pier was estimated using the VecTor2 results discussed in Section 5.6. While the results of the elastic analysis at yield are within the frame-work of the expected P-M interaction capacity of the compression pier, the axial load in the analyses are more the double the assumed gravity load of $0.1f'_cA_g$.

For example, when a coupled-wall system, similar to CW1, is subjected to seismic demands beyond yield, these results suggest the compression pier may have an undesirable compressive failure. This may occur because the axial load in the compression pier is going to increase from the current limit state (yield) to a much higher force due to coupling. Additionally, forces at the base of compression wall pier will increase due to the redistribution of shear and moment from the tension wall to the compression wall. The result of this undesirable behavior are shown on the interaction diagram for the nonlinear analyses and measured response. When the analyses reach the plastic limit state (i.e. the black triangle in Figure 9.4) the axial force is near the balance axial force and the moment is beyond its expected nominal moment strength. Additionally, the experimental data suggests at failure of the compression pier, the axial load and moment where outside of the expected P-M interaction.

The plastic analysis recommendations provided by the ICC (2007) only calls for the wall piers to be detailed against the additional shear demand as a result of a plastic mechanism. The axial and moment interaction is not checked for the wall pier because the accumulation of shear forces from the coupling beams are not assumed to contribute to the probable moment calculation of the wall pier. However, an engineer should be able to gauge where the wall pier design falls on the P-M interaction from the elastic analysis results by determining the proximity of the axial force to balanced axial force. While, the moment strength defined by ACI 318-08 may still be considered tension-controlled at yield (as was the CW1 wall pier design), the axial loads at the plastic limit state may result in the wall pier design that is classified as a compression- or transition-controlled component. At the plastic limit state, the axial load in the CWP for CW1 was 1.5 times larger than the axial load at yield.

9.4.3 Design Recommendation for Wall Piers

As a result of this study, the following design recommendations presented to adequately design the wall piers (i.e. compression pier) for the axial, shear and moment forces unique to coupled wall behavior.

1. Proportion the wall using the initial design procedure (Section 9.1)

2. Conduct a demand analysis of the coupled wall system to determine the shear and

total moment resisted by each wall pier (i.e. $M_{tw} + M_{cw}$).

3. Using the demands from (2), design the wall piers such that when in compression, the wall piers sustains 80% of the shear force and 70% of the moment shared by the tension and compresion pier ($M_{tw} + M_{cw}$).

4. Perform a plastic analysis using the plastic mechanism shown in Figure 2.1 (ICC, 2007). This should employ the expected plastic strength of coupling beams as discussed in Section 9.3 (i.e. $V_{pr,cb}$ may be taken as $1.4V_{n,cb}$ or greater).

5. From the resulting plastic analysis, determine the compression demand in the wall pier ($\sum V_{pr,cb} + P_D$) and if the resulting axial stress is greater than $0.3f'_c$, resize the wall pier.

6. From the resulting plastic analysis, determine the plastic base shear and assume total shear is carried solely by the compression pier. Ensure the wall shear stress demand does not exceed $10\sqrt{f'_c}$ (psi) with the appropriate strength reduction factor (0.85 in ACI 318-08)

Chapter 10

SUMMARY AND CONCLUSIONS

The test setup, experimental observations and data analysis results for the NEESR coupled wall specimen reported in Chapters 3 through 5 are summarized in this chapter. In addition, a summary is provided of the analysis results for this specimen and the set of previously tested coupled wall specimens that is presented in Chapter 2. Conclusions based on this work as well as recommendations for future work provided.

10.1 Summary

10.1.1 Summary of UW-UIUC Coupled Wall Test

As part of a larger research program focused on advancing performance-based design of structural concrete walls, a one-third scale model of a modern coupled wall was tested at the NEES MUST-SIM facility at the University of Illinois, Urbana-Champaign. This specimen was designed and constructed using geometries and details that are representative of current practice for mid-rise coupled-wall buildings along the West Coast, including diagonally reinforced coupling beams with an aspect ratio of 2. The specimen tested in the laboratory represented the bottom three stories of a 10-story building; axial, moment and shear forces were applied at the top of the specimen to simulate the seismic loads developed in the upper stories of the wall. Loads were applied to generate a quasi-static cyclic lateral displacement hist at the top the specimen and maintain a constant axial load equal to 10% of the concrete gross section strength. Multiple instrumentation systems were used to monitor response: i) a Metris photogrammetric system employing LED targets and infrared cameras and an ad-hoc photogrammetric system employing high-contrast paper targets and high resolution still cameras were used to monitor the displacement of the wall at a grid of points, ii) absolute displacement trasducers measured displacements of the wall at multiple locations relative to the strong wall and floor, iii) relative displacement transducers measured deformations of the wall, iv) concrete and steel strain gauges were used and v) load cells measured the applied loads.

The following summarizes the key observations and results of the NEESR coupled wall test:

1. The coupled wall specimen exhibited significant loss of lateral load-carrying capacity, due to explosive compressive failure of the compression region of the compression wall, at a third-story drift demand of 2.27% in both loading directions. The drift capcity of the coupled wall specimen was larger than that of comparable planar wall specimens (Birely, 2011).

2. A maximum base shear of 175 kips was reached at 2.20% drift; this exceeded the shear capacity determined from a plastic analysis.

3. The progression of yielding was as follows: yielding of the coupling beam diagonal reinforcement in stories two and three (0.36% drift) followed by yielding of the wall pier longitudinal reinforcement (0.50% drift) and, finally, by yielding of the first-story coupling beam diagonal reinforcement (0.67% drift).

4. The progression of yielding and damage at the base of the wall piers and the ends of the coupling beams was consistent with the assumed plastic mechanism illustrated in Figure 2.1.

5. At the peaks of the 1.00% drift cycles, spalling of concrete cover occured on the outer boundary element of both wall piers as well as the corner of the third floor coupling beam. At the peaks of the 1.50% drif cycles, more extensive spalling occurred on the outer boundary elements of the wall piers and initial spalling occured at the second floor coupling beam.

6.

7. Unlike the progression of damage observed up to 2.20% drift, which was considred to be moderate in nature, the observed failure mode of the compression wall pier (i.e. concrete crushing and bar buckling) at 2.27% drift was sudden and unexpected.

8. The primary response mechanism of the coupled wall was flexure. Third-story drift was due primarily to flexural deformation in the first story and secondarily to the second-story flexural deformation.

9. The contribution of each mechanism to the drift (i.e, first story flexure, base rotation, shear in each story) in the tension pier were similar throughout the drift history. The drift contributions in the compression pier changed significantly with initial damage in the concrete (i.e. spalling during the 1.0% drift level). More extensive concrete damage thereafter translated into more significant first-story flexural contributions.

10. The degree of coupling (DOC) computed from the experimental data ranged between 50 and 60% and was consistent with the theoretical DOC (53%)

11. The axial compressive stresses over the entire east and west wall pier cross-sectional area reached -0.39f'_c and -0.37f'_c, respectively.

12. The axial stresses in the compression region of the compression pier were estimated to be between 0.8 (full cover) and 1.1 (no cover) of the concrete compressive strength. If the core of the boundary element was assumed to carry all the axial stress, the estimated stresses in this region exceeded 1.5f'_c.

13. The axial compressive stresses over the entire east and west wall pier cross-sectional area reached -0.39f'_c and -0.37f'_c, respectively.

14. Assuming the entire compression pier carries 100% of the the total base shear at failure, the shear stress demand over the entire east and west wall pier cross-sectional area was $8.1\sqrt{f_c'}$ and $7.9\sqrt{f_c'}$, respectively.

15. The shear stress demand in the compression region of the compression pier were estimated to be between $9\sqrt{f_c'}$ (full cover) and $20\sqrt{f_c'}$ (no cover) depending on distribution of base shear between the tension and compression wall piers.

16. Once yielding occurred in the tension wall pier, its axial and flexural stiffness reduced significantly. Analytical and previous test results suggests the loss of stiffness in the tension wall leads to a shift in shear and moment demands from the tension wall to the compression wall. With the presence of large axial forces, this shift ultimately resulted in a shear-moment-axial interaction that was in excess of the compression pier capacity. This behavior limits the ductility and drift capacity of the coupled wall system solely on the drift capacity of the compression wall pier, which is not consistent with current design philosophy.

17. The damage patterns in the coupling beams at the end of the lateral test included modest spalling and vertical cracking along the beam-to-wall interface. Diagonal cracks widths in the coupling beams did not exceed 1/16 of an inch.

18. The coupling beams endured plastic rotations in the range of 4 to 5% while maintaining shear stress demands in the range of 7 to $9\sqrt{f_c'}$ (psi). The damage pattern at the end of the beams and the measured plastic strains in the diagonal reinforcement suggests the coupling beams acted as the energy dissipating components they were designed to be.

19. At the end of the test both wall piers had sustained severe damage in the first-story portion of the OBE. The damage consisted of extensive concrete crushing and buckling of all longitudinal reinforcement in the OBE of both wall piers.

20. The post-damage axial capacity was $0.42A_gf'_c$.

The results from the coupled wall tests conducted as part of this study were combined with prior experimental tests of large-scale coupled walls to compare the observed damage patterns and assess coupled wall design. For this combined dataset, six of nine specimens exhibited compressive type failures in the compression wall pier (i.e. concrete crushing in the web and/or boundary element). Two of nine specimens (Santhakumar WallA and Shiu CS1) exhibited significant damage to the coupling beams and significant loss of lateral strength due to coupling beam failure. The final specimen in the dataset (Lequesne CW1) failed due to fracture of the steel reinforcing bars in the wall piers and coupling beams. The damage patterns and progression of yielding observed in all of the coupled wall tests were consistent with the desired plastic mechanism defined in Figure 2.1.

The coupled wall experimental dataset was used to assess existing effective stiffness recommendations for elastic analyses provided by ACI, ASCE, CSA, NZS, ATC, Birely (2011) and Mohr (2007). Recommendations were assessed on the basis of the accuracy and precision with which drift, base shear and stiffness were computed. In general, the code-based recommendations are too stiff; while the recommendations made based on experimental research (ATC 72 and Birely/Mohr) predict the yield stiffness and drift more accurately.

The coupled wall dataset was used also to assess the accuracy and precision of nonlinear analysis using the lumped and distributed plasticity elements available in the OpenSees platform. Models were evaluated by comparing simulated and measured and observed initial stiffness, strength, progression of yielding and drift capacity and failure mechanism. The tensile strength of the concrete was ignored in the concrete constitutive model in order to match the cracked stiffness of the system. In general, when the initial stiffness of the system was simulated well compared to the experimental coupled wall stiffness (i.e. all the specimens but CW1), the measured ultimate strength of the system was met. In the case of CW1, the stiffness and strength of the simulated diagonally reinforced coupling beams was crossly over estimated by the force-based beam-column elements with fiber cross-sections. This resulted in a coupled wall force-displacement response that was too stiff. The resulting error in the coupling beam stiffness and strength resulted in an increase in axial demand in the compression pier, which caused premature failure in the CWP compared to the measured response.

Nonlinear analysis results provide understanding of the distribution of shear, moment and axial load that cannot be obtained from the instrumentation used typically in coupled wall tests. Results of these analyses show that there is significant amount of shear and moment redistribution from the tension wall to the compression wall; the shear demand in the compression wall was, on average, 78% of the total base shear once the plastic shear was reached and the compression pier carried 70% more moment demand than the tension pier, on average.

In comparison with plastic analysis in which coupling beam strength is defined entirely by coupling beam steel and concrete strength, the nonlinear analysis coupling beams carry axial force that increase the moment capacity and thus resulting shear demand, which intern increased the compression demand in the CWP and increases the DOC. On average the simulated compression demands are 30% larger than the plastic analsyiss and the simulated DOC is 26% larger than the plastic analysis.

Finally, experimental data and analytical results were complied and used to develop a set of design recommendations for improved the performance of coupled wall systems.

10.2 Conclusions

Conclusions are presented addressing i) coupled wall behavior, ii) elastic and nonlinear analyses and iii) current design and evaluation procedures for coupled wall systems.

10.2.1 Experimental Coupled Wall Behavior

The section describes the conclusion made for the combined dataset of previous coupled wall tests as well as Specimen CW1, which was tested as a part of this research.

- The degree of coupling (DOC) has a significant role in the behavior of the coupled wall system. A high DOC is associated with high axial forces in the tension and compression pier. These high axial forces significantly impact the wall pier behavior and performance. Furthermore, as the net axial tension demands in the tension wall pier overcome the gravity force and/or yielding occurs in the tension wall, the axial and flexural stiffness of the tension pier is significantly reduced. Consequently, the loss in stiffness in the tension pier places large shear and moment demands on the compression pier. This increase in axial, moment and shear demands has been shown to limit the deformation capacity of the compression pier, which ultimately limits the ductility of the coupled wall system.

- The results of the test specimens that exhibited compressive type failures suggest for a given displacement step, the increase in axial, moment and shear demand in the compression pier, if not accounted for in design, may lead to an undesirable failure in the wall pier. However, the current design guides do not address the axial-moment interaction at the ultimate limit state (i.e. plastic analysis).

- Experimental tests by Ozselcuk (1989) and nonlinear analyses conducted as part of this study show that the compression pier carries 80% to 90% of the total shear demand. In current design (ICC, 2006), shear demand is assumed to be equally distributed between the wall piers.

10.2.2 Analysis of Coupled Wall Systems

- Recommended effective stiffness values for elastic analysis provided by the ACI, ASCE, CSA and NZS design codes do not provided accurate prediction of response to yield of the system (the error associated with displacement at yield ranged from -150% to -230% and the error associated with stiffness up to yield ranged from 30% to 55%). Simulation of system behavior is very sensitive to the flexural stiffness of the coupling beams and the design codes recommend stiffness values that are too large. Another critical parameter on the response of an elastic analysis is the effective shear stiffness; for example elements with low aspect ratios deform more in shear, so it is important incorporate this behavior into an elastic model. Currently, ACI and ASCE do not recommend reducing the shear stiffness for the wall piers and coupling beams and these analysis results tend to dramatically over predict the stiffness and under-predict the yield drift compared to the coupled wall test results.

- Of the recommendations reviewed, those by Birely/Mohr provide the most accurate and precise prediction of response (0.8% error in displacement at initial yield, with a standard deviation of 33.8% for the 7 wall dataset). This is attributed to the use of effective stiffness values for the wall piers and coupling beams that are based on experimental data. More specifically, the coupling beam flexural stiffness used in the models was approximately $0.04EI_g$. Additionally, an effective shear stiffness of $0.15GA_{cv}$ was used for the wall piers and coupling beams. These reductions provided additional flexibility, which improved the overall response.

- Elastic analysis cannot simulate the redistribution of shear and moment from the tension wall to the compression wall; elastic analysis significantly under predicts the wall pier axial tension and compression load compared to experimental results.

- Nonlinear analysis using line-element models with fiber cross-sections provides accurate prediction of initial stiffness and ultimate strength compared to experimental test data (on average for the 5 specimens the error was within 5% for the initial stiffness up to yield and ultimate strength). However, the nonlinear analysis results for Specimen CW1 indicate that simulating diagonally reinforced coupling beams using force-based beam-column elements with fiber cross-sections results in a shear-displacement response that is too stiff and too strong. For Specimen CW1, this results in over prediction of system stiffness as well as over prediction of compression wall pier compression demand and, as a result, under prediction of CWP drift capacity.

10.2.3 Design Recommendations for Coupled-Wall Systems

- The wall pier and coupling beam strengths should be initially portioned such that the degree of coupling (DOC) does not exceed 50%, the axial compression stess from the targeted DOC does not exceed $0.2f_c$ and the shear stress in an individual wall pier does not exceed $7\sqrt{f_c'}$ (psi) assuming 100% of the total design lateral force carried by that wall pier.

- If elastic analysis results are used for design, recommendations by Birely (2011) and Mohr (2007) (Table 9.1) for the wall piers and coupling beams effective stiffnesses should be used.

- A plastic analysis needs to be performed to determine axial forces and shear. This should employ expected plastic strength of coupling beams, which is a function of strain-hardening of the tension reinforcement, axial force present in the coupling beam, reinforced concrete slab and the contribution of concrete confinement. Results show this expected plastic strength may be 140% of the expected nominal strength (i.e. measured material properties).

- To ensure the axial force in the compression pier never exceeds balanced axial force, the wall piers should be designed such that the axial compression stress calculated from the plastic analysis is less than $0.3f_c'$.

- To ensure adequate shear resistance, each wall pier should be designed to resist the entire base shear demand resulting from a plastic analysis (ICC, 2007). Redistribution of shear force will result in the compression pier carrying at least 80% of the base shear.

- Wall piers should be designed for the axial forces resulting from a plastic analysis.

- Coupled walls should be designed to achieve a DOC less that 50% and greater than 20%. Specimen CW1 was designed to have a DOC of 53% but exhibited a flexural compression failure indicating compression forces due to the high DOC were too large. The coupled walls tested by Ozselcuk (1989) also support this conclusion. The coupled wall tested by Shiu et al. (1981) was designed to have a DOC of 10% and exhibited coupling beams failure due to conventionally reinforced coupling beams that were too weak. A more precise recommendation for the DOC cannot be made at this time due to limited data.

10.3 Future Work

The results of this study indicate the following gaps in knowledge to be addressed by future research.

1. Recommend a range of DOC to ensure that compression wall pier does not see excessive compression force demands (DOC too high), coupling beans are not subjected to severe deformation demands (DOC too low) and the coupled-wall system remains an efficient lateral load resisting system.

2. Impact of coupled wall geometry (i.e. couping of C- and T-shaped walls) on system response including the DOC and redistribution of shear.

3. The typical distribution of coupling beam yielding up the height of the coupled wall and, thus the true DOC and axial force demands, that develop in coupled walls in

mid- and high-rise buildings.

4. An improved nonlinear model for coupling beams that is appropriate for use with line element models

Research to eliminate these gaps in knowledge includes numerical modeling. For items 1-3 above, suites of coupled wall systems of varying height, DOC and wall geometry could be designed and analyzed for a range of ground motion demands; data from these analyses could be mined to address the issues. Item 4 requires model development using existing experimental data. To supplement results of numerical modeling and further improve understanding of CW response the results of numerical analysis could be use to identify the best set of specimens for laboratory testing to address items 1 and 2 above.

BIBLIOGRAPHY

ACI (2008). *Building Code Requirements for Structural Concrete (ACI 318-08) and Commentary*. American Concrete Institute, Farmington, IL.

Adebar, P., Ibrahim, A. M. M., and Bryson, M. (2007). Test of high–rise core wall: Effective stiffness for seismic analysis. *ACI Structural Journal*, 104(5):549–559.

Aktan, A. E., Bertero, V. V., and Piazza, M. (1982). Prediction of the seismic reponses of R/C frame-coupled wall structures. UCB/EERC-82/12, University of California, Berkeley, CA.

ASCE (2007a). *Seismic Rehabilitaion of Existing Buildings*. ASCE Standard ASCE/SEI 41-06, American Society of Civil Engineers, Reston, VA.

ASCE (2007b). Supplement No. 1 to ASCE 41. `http://content.seinstitute.org/publications/ASCE41supplement.html`. Visited January 2011.

ASCE (2010). *Minimum Design Loads for Buildings and Other Structures*. ASCE Standard ASCE/SEI 7-10, American Society of Civil Engineers, Reston, VA.

Barney, G. B., Shiu, K. N., Rabbit, B. G., Fiorato, A. E., Russell, H. G., and Corley, W. G. (1980). Behavior of coupling beams under load reversals. Research and Development Bulletin RD068.01B, Construction Technology Laboratories, A Division of Portland Cement Association, Stokie, IL.

Birely, A. C. (2011). *Seismic Performance of Slender Reinforced Concrete Walls*. Ph.d. dissertation proposal document, University of Washington, Seattle, WA.

Brown, P. and Lowes, L. (2007). Fragility functions for modern reinforced concrete beam-column joints. *Earthquake Spectra, EERI*, 23(2):263–289.

Canbolat, A. B., Parra-Montesinos, G., and Wight, J. K. (2005). Experimental study on seismic behavior of high-performance fiber-reinforced cement composite coupling beams. *ACI Structural Journal*, 102(1):159–166.

Carr, A. J. (2001). *RUAUMOKO.* Inelastic Dynamic Analysis Computer Program, University of Canterbury.

Coleman, J. and Spacone, E. (2000). Localization issues in force-based frame elements. *Journal of the Structural Division, ASCE*, 127(11):1257–1265.

CSA (2004). *Design of Concrete Structures (CSA A23.3-04).* Standards Council of Canada, Toronto, Ontario, Canada (reaffirmed 2010).

CSI (2001). *ETABS Nonlinear Version 7.24-Extended 3D Analysis of Building Systems.* Computers and Structures, Inc, Berkeley, CA.

CSI (2006). *Perform 3-D Nonlinear Analysis and Performance Assessment for 3D Structures Version 4*. Computers and Structures, Inc, Berkeley, CA.

Fry, A. J., Hooper, J. D., and Klemencic, R. (2010). Core wall case study design for pacific earthquake engineering research/seismic safety commission tall building design case study 2. *The Structural Design of Tall and Special Buildings*, 19(1-2):61–75.

Galano, L. and Vignoli, A. (2000). Seismic behavior of short coupling beams with different reinforcement layouts. *ACI Structural Journal*, 97(6):876–885.

Ghodsi, T. and Flores Ruiz, J. A. (2010). Pacific earthquake engineering research/seismic safety commission tall building design case study 2. *The Structural Design of Tall and Special Buildings*, 19(1-2):197–256.

Gulec, C., Whittaker, A., and Hooper, J. (2010). Fragility functions for low aspect ratio reinforced concrete walls. *Engineering Structures*, 32:2894–2901.

Harries, K. A. (1999). Ductility and deformability of coupling beams in reinforced concrete coupled walls. In *8th Canadian Conference on Earthquake Engineering*, pages 475–478, Vancouver, B.C.

Harries, K. A. (2001). Ductility and deformability of coupling beams in reinforced concrete coupled walls. *Earthquake Spectra, EERI*, 17(3):457–478.

Hart, C. R. (2011). *Tensile Response of Reinforced Concrete Structural Walls under Reversed Cyclic Loading*. Ph.d. dissertation, University of Illinois at Urbana-Champaign, Champaign, IL.

Hoehler, M. S. and Stanton, J. F. (2006). Simple phenomenological model for reinforcing steel under arbitrary load. *Journal of the Structural Division, ASCE*, 132(7):1061–1069.

ICC (2006). *2006 International Building Code*. International Code Council, Falls Church, VA.

ICC (2007). *2006 IBC Structural/Seismic Design Manual*, volume 3. International Code Council, Falls Church, VA.

Kent, D. C. and Park, R. (1971). Flexural members with confined concrete. *Journal of the Structural Division, ASCE*, 97(7):1969–1990.

Klemencic, R., Fry, A. J., Hooper, J. D., and Morgen, B. G. (2007). Performance-based design of ductile concrete core wall buildings–issues to consider before detailed analysis. *The Structural Design of Tall and Special Buildings*, 16(5):583–597.

Kwan, A. K. H. and Zhao, Z. Z. (2002). Cyclic behaviour of deep reinforced concrete coupling beams. *Structures & Buildings*, 152(3):283–293.

LATBSDC (2005). *An Alternative Procedure for Seismic Analysis and Design of Tall Buildings Located in the Los Angeles Region.* Los Angeles Tall Buildings Structural Design Council (LATBSDC), Los Angeles, CA.

LATBSDC (2008). *An Alternative Procedure for Seismic Analysis and Design of Tall Buildings Located in the Los Angeles Region.* Los Angeles Tall Buildings Structural Design Council (LATBSDC), Los Angeles, CA.

Lequesne, R. D. (2011). *Design and Behavior of High-Performance Fiber-Reinforced Concrete Coupling Beams and Coupled-Wall Systems.* Ph.d. dissertation proposal document, University of Michigan, Ann Arbor, MI.

Lequesne, R. D., Parra-Montesinos, G. J., and Wight, J. K. (2009). Test of a Coupled Wall with High-Performance Fiber-Reinforced Concrete Coupling Beams. *Thomas T. C. Hsu Symposium: Shear and Torsion of Concrete Structures*, SP-265, American Concrete Institute, Farmington Hills, MI.

Lequesne, R. D., Wight, J. K., and Parra-Montesinos, G. J. (2010). Seismic detailing and behavior of coupled-wall systems with high-performance fiber-reinforced concrete. In *Proceedings of the 9th U.S. National and 10th Canadian Conference on Earthquake Engineering*, Toronto, Ontario, Canada.

Lowes, L. N., Lehman, D. E., Birely, A. C., Pugh, J., Kuchma, D., Hart, C. R., and Marley, K. P. (2009). Investigation of the seismic response of slender planar concrete walls. In *SEAOC 2009 Convention Proceedings*, San Diego, CA. Structural Engineers Association of California (SEAOC).

Mander, J. B., Priestley, M. J. N., and Park, R. (1982). Theoretical stress–strain model for confined concrete. *Journal of the Structural Division, ASCE*, 108(4):929–950.

Marley, K. P. (2011). *Evaluation of Concrete Compressive Models Applied to Large-*

Scale Structural Walls. Ph.d. dissertation, University of Illinois at Urbana-Champaign, Champaign, IL.

McKenna, F., Scott, M. H., Fenves, G. L., and Jeremic, B. (2000). *Open System for Earthquake Engineering Simulation (OpenSees)*. Pacific Earthquake Engineering Research Center, University of California, Berkeley.

McNeice, D. S. and Harries, K. A. (2004). Performance based design of a 30-story coupled wall structure. CE/ST 31, University of Pittsburgh, Pittsburh, PA.

Mohr, D. S. (2007). Nonlinear analysis and performance based design methods for reinforced concrete coupled shear walls. Master's thesis, University of Washington, Seattle, WA.

Naish, D., Wallace, J., Fry, J. A., and Klemencic, R. (2009). Reinforced concrete link beams: Alternative details for improved construction. UCLA-SGEL 2009/06 Report to National Science Foundation, University of California, Los Angeles, CA.

NZS (2006). *Concrete Structures Standard, Part 1 – The Design of Concrete Structures, Part 2 – Commentary on the Design of Concrete Structures (3101:2006)*. Standards Council, Wellington, New Zealand.

Oyen, P. E. (2006). Evaluation of analytical tools for determining the seismic response of reinforced concrete shear walls. Master's thesis, University of Washington, Seattle, WA.

Ozselcuk, A. R. (1989). *Experimental and Analytical Studies of Coupled Wall Structures*. Ph.d. dissertation, University of California, Berkeley, CA.

Park, R., Priestley, M. J. N., and Gill, W. D. (1982). Ductility of squared–confined concrete columns. *Journal of the Structural Division, ASCE*, 108(4):929–950.

Paulay, T. (1971). Coupling beams of reinforced concrete shear walls. *Journal of the Structural Division, ASCE*, 97(3):843–861.

Paulay, T. (2002). The displacement capacity of reinforced concrete coupled walls. *Engineering Structures*, 24:1165–1175.

Paulay, T. and Binney, J. R. (1974). Diagonally Reinforced Coupling Beams of Shear Walls. *Shear in Reinforced Concrete*, SP-42, American Concrete Institute, Detroit, MI.

Paulay, T. and Priestley, M. J. N. (1992). *Reinforced Concrete Structures*. Wiley & Sons, New York.

PEER/ATC-72-1 (2010). Modeling and acceptance criteria for seismic design and analysis of tall buildings. Task 7 Report for the Tall Buildings Initiative, Pacific Earthquake Engineering Research Center and the Applied Technology Council, Richmond, CA.

Powell, G. H. (1973). Drain-2d user's guide. EERC-73/22, University of California, Berkeley, CA.

Pugh, J. (2012). *Analytical Modeling Recommendations for Squat and Slender Reinforced Concrete Walls*. Ph.d. dissertation, in progress, University of Washington, Seattle, WA.

Saatcioglu, M., Derecho, A. T., and Corley, W. G. (1983). Modeling hysteretic behavior of coupled walls for dynamic analysis. *Earthquake Engineering and Structural Dynamics*, 11(4):711–726.

Salas, M. C. (2008). Modeling of tall reinforced concrete wall buildings. Master's thesis, University of California, Los Angeles, CA.

Santhakumar, A. R. (1974). *The Ductility of Coupled Shear Walls*. Ph.d. dissertation, University of Canterbury, Christchurch, New Zealand.

Shiu, K. N., Aristizabal-Ochoa, J. D., Barney, G. B., Fiorato, A. E., and Corley, W. G. (1981). Earthquake resistant structural walls – coupled wall tests. Report to National Science Foundation, Construction Technology Laboratories, A Division of Portland Cement Association, Stokie, IL.

Stringer, S. (2007). Preliminary investigation into the seismic performance of mid to high-rise reinforced concrete coupled shear wall buildings. Interdepartmental Document, University of Washington, Seattle.

Tassios, T. P., Moretti, M., and Bezas, A. (1996). On the behavior and ductility of reinforced concrete coupling beams of shear walls. *ACI Structural Journal*, 93(6):711–720.

Timoshenko, S. and Goodier, J. N. (1970). *Theory of Elasticity*. McGraw-Hill, New York.

Wight, J. K. and MacGregor, J. G. (2009). *Reinforced Concrete Mechanics and Design*. Pearson Education, Inc., New Jersey.

Wilson, E. L. and Dovey, H. H. (1972). Three dimensional analysis of building systems. EERC-72/8, University of California, Berkeley, CA.

Wong, P. S. and Vecchio, F. J. (2002). *VecTor2 & Formworks User's Manual*. University of Toronto, Toronto, ON.

Zekioglu, A., Willford, M., Jin, L., and Melek, M. (2007). Case study using the los angeles tall buildings structural design council guidelines: 40-storey concrete core wall building. *The Structural Design of Tall and Special Buildings*, 16(5):583–597.

Zienkiewicz, O. C. and Taylor, R. L. (2005). *The Finite Element Method for Solid and Structural Mechanics*. Elsevier Ltd., Burlington, MA, 6th edition.

Appendix A

LIST OF SYMBOLS

A_s	area of tension reinforcement
A'_s	area of compression reinforcement
A_{vd}	area of diagonal reinforcement in bundle
A_{vd}	area of vertical skin reinforcement in a coupling beam
b	breath of coupling beam
b_w	breath of coupling beam web
d	distance from extreme compression fiber to centroid of longitudinal tension reinforcement
d'	distance from extreme compression fiber to centroid of longitudinal compression reinforcement
f'_c	average compressive strength of concrete determined from compressive cylinder tests
l_w	length of wall pier
N_g	applied gravity load for each test specimen
t_w	thickness of wall pier

Appendix B

CW1 EXPERIMENTAL INFORMATION

B.1 CW1 Instrumentation Errors

Table B.1: Record of SimCor step numbers where instruments did not record data

Instrument Name	**SimCor Step Numbers**
Data Acquisition System	280, 487–489 & 778
Metris Krypton LED System	32, 71–72, 487–489, & 1151–1156
Photogrammetry System	487–489
Photography System	
BackCenter	487–489
BackEastBottom	431 & 487–489
BackEastTop	431 & 487–489
BackWestBottom	487–489 &
BackWestTop	487–489 & 1154
CouplingBeam1	487–489
CouplingBeam2and3	487–489
FrontEastBottom	431, 487–489 & 1059–1060
FrontEastTop	431 & 487–489
FrontWestBottom	487–489 & 1154
FrontWestTop	487–489 & 1154

B.2 CW1 Peak Drift Information

Table B.2: CW1 peak drift steps

Load Step	SimCor Step	Drift Cycle	Drift (%)	V_b (kips)
6	16	10 kips (A)	-0.003	8
16	26	10 kips (A)	-0.017	-9
26	36	10 kips (B)	-0.010	9
36	46	10 kips (B)	-0.018	-9
46	56	20 kips (A)	0.006	19
56	66	20 kips (A)	-0.040	-19
66	87	20 kips (B)	0.026	20
76	97	20 kips (B)	-0.038	-20
94	147	0.128% (A)	0.125	49
120	174	0.128% (A)	-0.148	-50
146	213	0.128% (B)	0.129	50
170	241	0.128% (B)	-0.125	-42
190	263	0.192% (A)	0.193	65
207	284	0.192% (A)	-0.200	-62
223	304	0.192% (B)	0.191	62
239	324	0.192% (B)	-0.191	-58
259	344	0.321% (A)	0.327	87
282	369	0.321% (A)	-0.317	-81
304	393	0.321% (B)	0.329	87
326	416	0.321% (B)	-0.324	-82
352	456	0.50% (A)	0.515	117
382	486	0.50% (A)	-0.489	-114
409	516	0.50% (B)	0.504	112
439	546	0.50% (B)	-0.503	-112
472	581	0.75% (A)	0.743	141
509	620	0.75% (A)	-0.771	-146
546	657	0.75% (B)	0.748	137
582	695	0.75% (B)	-0.758	-140
623	757	1.00% (A)	1.00	155
666	802	1.00% (A)	-0.988	-157
710	848	1.00% (B)	0.988	149
754	892	1.00% (B)	-0.999	-154
792	945	1.50% (A)	1.50	171
832	992	1.50% (A)	-1.50	-168
872	1032	1.50% (B)	1.50	163
912	1072	1.50% (B)	-1.49	-163
955	1117	2.25% (A)	2.27	79
1003	1165	2.25% (A)	-2.27	-83

B.3 CW1 Testing Notes

Table B.3: Log of testing comments

SimCor Step	Load Step	Comments	Roam Start	Roam End
1	—	most instruments are zeroed at this step in post analysis	—	—
11	1	Start of 10 kip elastic cycle	—	—
31	21	Start of 10 kip elastic cycle x2	—	—
51	41	Start of 20 kip elastic cycle	—	—
71	—	Instruments (adv03f0c, adv12f0c, inip03f3f, inip12f3f, inip05f1h) where added to experiment, zeroed in post analysis, 5 inch gauge length string pots (adh03f3f, adh12f3f) replaced 20 inch, rezeroed at this step in post analysis, 2 inch gauge length string pots (adv05f0c, adv10f0c) replaced 10 inch, rezeroed at this step in post analysis	—	—
82	61	Start of 20 kip elastic cycle x2	—	—
109	—	Initiation of flexural cracks in the top right corner of CB3, crack along beam/wall interface	—	—
116	—	Initiation of flexural crack in bottom left corner of CB2, 5 inches in from wall. Lost connection to OM and had to back off axial load to shut down.	—	—
120	81	Start of 0.2 inch cycle	—	—
131	92	Initiation of cracking in the right corner of CB1, initiation of diagonal crack is CB3	—	—
132	93	CB1 crack extended	—	—
133	—	Cracks forming in the bottom left corner of CB1	—	—
134	—	Start of lateral force plateau	—	—
147	94	Force Plateau ended	—	—
165	112	Flexural cracking in bottom right corner of CB2 and CB3	—	—
166	113	Flexural cracking in top left corner of CB2	—	—
168	115	Flexural cracking in the top left corner of CB2	—	—
169	116	Flexural Cracking in the bottom right corner of CB1	—	—
170	117	Cracks Measures	—	—
171	118	Initiation of diagonal cracking in CB3	—	—
172	119	Flexural cracking in the top left corner of CB1	—	—
173	—	Hydraulics surge, switch from global to local caused an out of plane torque of 0.8 inches out of plane. The force limits tripped at 10 kips and the hydraulics locked. Concrete surface strain gauges spiked to about 75 micro strain in (NBWI) west pier and 40 micro strain in east pier....Diagonals cracking in CB2	—	—

continued

Table B.3: continued

SimCor Step	**Load Step**	**Comments**	**Roam Start**	**Roam End**
174	120	After error, Ken loaded new log file, so we dont have to do constant force peak movement. OM link problems, so we have an additional zero step	—	—
190	—	End of Day5	—	—
200	133	Start of 0.2 inch cycle x2	—	—
213	146	Roaming camera photo board says 27, but it should have said 72, initiation of flexural cracking on the outer west wall pier, Diagonal cracks on CB3 (minimal diagonal on CB2)	79	82
237	—	Flexural cracking in the outside of the east pier	84	89
252	181	Start of 0.3 inch cycle	—	—
258	187	Cracking Marked	91	91
260	189	Cracking Marked	93	96
261	—	Cracking Marked	—	—
262	—	Cracking Marked	—	—
272	199	Krypton froze, see plugin errors	—	—
273	200	Krypton didn't fire, see plugin errors	—	—
278	205	Flexural crack across the east pier are elongating and forming inside the web.	100	100
279	206	Cracks marked	102	104
280	—	Cracks marked, flexural crack in web is measureable, DAQ did not receive step 280, but it did get 281 which is a zero step, so use 281 for the Peak	106	108
281	—	Zero step, start of lateral force plateau	—	—
282	—	We had an error message with the DAQ with no signs of DAQ issues. 280 was completed	—	—
285	208	End of constant force plateau steps, heading back down	—	—
292	215	Start of 0.3 inch cycle x2	—	—
300	—	Cracks marked, larger crack developing on inside of CB1 top left.	110	114
301	—	Zero step, start of lateral force plateau	—	—
303	—	Ended plateau, took 2 303 steps in the DAQ	—	—
317	236	2 DAQ Recorded steps	—	—
320	—	Cracks marked and measured	116	116
321	—	Lateral force plateau started	—	—
324	239	End force plateau	—	—
332	247	Start of 0.5 inch cycle	—	—
341	256	East Inner pier flexural crack, cracking marked, cracks in third story	118	123

continued

Table B.3: continued

SimCor Step	**Load Step**	**Comments**	**Roam Start**	**Roam End**
342	257	Shear crack in the web of the west pier at the second floor	125	132
344	259	Diagonal shear crack in 2nd story web is 0.01 inches, vertical cracks in the east wall pier around the location of diagonal beam reinforcement termination. This is probably a result of the boundary condition at the top of the wall. Cracks Marked	133	137
357	272	DAQ is duplicating steps at a number of different displacements notes are incomplete on this error from here out.	—	—
365	280	Marked cracks, flexural-shear crack in the lower story of the east pier	138	141
366	281	Marked cracks, flexural crack on the inner west wall pier	143	148
367	—	Marked and measure cracks, more cracking on inner west pier	150	157
368	—	zero step plateau	—	—
380	293	Start of 0.5 inch cycle x2	—	—
391	—	Marked cracks, measured cracks. We are switching to marking cracks after the pictures are taken at the peak because the forces in the LBCBs drop to while it holds the displacements. Therefore, we wanted to get the instrument data first before the layover due to crack drawing.	159	164
392	—	Plateau step that changed axial loads and redistributed some of the moments	—	—
415	—	Cracks marked, larger cracks in the coupling beams, 3rd story beam is on the order of 1/32 of an inch. Diagonal Cracks in CB1	166	173
416	326	Plateau step, communication break, but seems like step was executed successfully	—	—
427	—	End of cycle, take off axial load	—	—
430	—	End of day 6	—	—
431	—	start of test day 7, BackEastBottom, BackEastTop, FrontEastBottom and FrontEastTop Cameras DID NOT TRIGGER	—	—
440	337	Start of 0.5% drift cycle	—	—
452	349	Cracks marked, the west pier diagonal crack in the second story is now at 0.02 inches. Diagonal Cracking on CB1	176	182
453	350	Cracks marked and measured. Diagonal cracks in the west pier are still opening up.	190	193

continued

Table B.3: continued

SimCor Step	**Load Step**	**Comments**	**Roam Start**	**Roam End**
454	—	We dropped 20 kips of shear force in the east pier, (compression) shear force on the way to this step. We heard a small noise and a sudden drop in force. We were able to climb back up to 100 kips. Horz string pots did not move. Cracks marked. There was a lot of diagonal cracks starting in the east wall pier at the first story. The third story west pier is developing a lot of diagonal cracks in the web. The diagonal strut through the second story beam is starting to show well in the form of diagonal cracks in the third story west pier and first story east pier. A majoring of the cracking developed in and around CB2	198	204
455	351	This was essentially a zero step. We plan to move to the peak on the next step	—	—
456	352	Shear crack in the west wall pier has now doubled. Cracks marked. The CB3 crack is now 0.04”	207	212
483	379	Cracks marked, diagonal cracks starting to progress through the web of the east pier through the coupling beams	217	222
484	380	cracks marked	224	229
485	381	cracks marked, continuing to see more diagonal cracks show up in the tension pier (east). There is also developments of flexural cracks along the inner west wall at the 2nd story level.	231	235
486	382	cracks marked and measured, peak. Diagonals starting to open up in the east pier	238	244
487	—	DID NOT TRIGGER (NO STEP DATA RECORDED)	—	—
488	—	DID NOT TRIGGER (NO STEP DATA RECORDED)	—	—
489	—	DID NOT TRIGGER (NO STEP DATA RECORDED)	—	—
501	394	Start of 0.5% drift cycle x2	—	—
516	409	Cracks marked at the peak, more flexural cracks on the outer west wall are filling in at tighter crack spacing. CB3 upper right diagonal jumped from yield to 0.05. First bar to see significant straining in the west pier (Bar - A)	246	252
546	439	Cracks marked, CB3 crack to 0.5, diagonal and web flex crack in east pier increased.	254	261
561	454	Start of 0.75% drift cycle	—	—

continued

Table B.3: continued

SimCor Step	**Load Step**	**Comments**	**Roam Start**	**Roam End**
576	—	Cracks marked, CB3 is starting to hinge and cracks seem to be opening up. Seeing plastic strains in the strain gauges. CB2 is starting to see the same behavior. Two 586 steps in the DAQ	263	269
579	470	cracks marked and measured. The left most bar (A03) is reaching larger strains, 5 milli strain. Coupling beams CB3 and CB2 are seeing plastic strains and seem to be starting to hinge	275	283
580	471	Flaking in the top right corner of CB3. (tension corner), measureable cracks at the base of west wall. The strain gauge at this location is showing 5 millistrain.	284	294
581	472	Outer edge of west wall is yielding. Each story in the west wall has a well established diagonal crack. Crack in CB1 opened to 0.03 inches (see roaming camera shot 299)	295	299
601	490	measured residual cracks	—	—
616	505	cracks marked and measured	—	—
617	506	cracks marked and measured, more diagonals are starting to show in the inner west pier. (compression). A crack on the top west corner of CB1 is starting to open up. The cracks up the height are starting to form with uniform crack spacing of about 2.5 inches	302	309
618	507	cracks mark and measured, took a roaming camera picture of crack spacing on the outer east wall pier. More diagonals are forming on the tension wall and the inner edge of the 2nd story of the west (compr) pier	310	317
619	508	cracks marked and measured, good diagonals showing up on both wall piers	319	328
620	509	we had to manual trigger the krypton it was step 188. Peak cracks marked and measured. Continue to notice a lot of diagonal cracks forming through the coupling beams. Hit yield strain in coupling beam diagonals.	331	339
621	510	krypton failed to trigger, manual trigger and named it step 189.	—	—
639	528	Measured residual cracks, start of 0.75% drift cycle x2	—	—
657	546	cracks marked and measured, diagonal cracks are continuing to develop. Note: cracks are starting to show in the walls where we believe the diagonal bars in tension are developing. The pattern is seen in the roaming camera. It is a strutting mechanism due to anchorage developing.	341	354
677	564	residual cracks taken, 0.04 in CB3	—	—

continued

Table B.3: continued

SimCor Step	**Load Step**	**Comments**	**Roam Start**	**Roam End**
695	582	Cracks Marked and measured. No new measurements. Continuing to see the anchorage type cracking around all coupling beam diagonal bars	356	368
696	—	Krypton had an error, manual trigger.	—	—
704	589	Noticed that the continuous data was sampling at 1.6 seconds instead of 1.5 secs	—	—
714	599	Krypton Error, start up K Link and take manual trigger. It was named 284	—	—
715	—	Measured residual cracks	—	—
718	—	End of day 7	—	—
719	—	Start of day 8, Start of LinearPot being multiplied by excitation voltage	—	—
727	600	Start of the 1.00% drift cycle	—	—
746	619	cracks marked	—	—
747	—	cover on east pier spalled, 1.5 feet above base. Stiffness dropped. We are yielding all the vertical bars in the tension wall in the first story. Took pictures of spalling. There is a significant drop in the tension wall stiffness that has made it hard for the control plugin to converge. Based on the total shear force a total moment is calculated. Then 80% of that moment is applied in the coupling moment. Then, the tension wall is asked to take a moment of 0.5%Mt, but it is having a hard time converging on that tension moment.	370	376
748	—	The notes are not lining up now.	378	391
754	—	spalling more concrete at the location of spalling in step 747. Picture taken. Cracks were marked and measured. Spalling on outer east wall in the back corner.	393	405
755	622	Ken tried to take 748 and it appended to krypton as 748. The cameras did not take pictures for 748, but DAQ will have an additional log step for 748 appended after 754.	—	—
757	623	peak chosen by control SPs	—	—
767	633	Took a manual krypton trigger.	—	—
777	643	residuals measurements taken	—	—
778	—	DAQ DID NOT TRIGGER (NO STEP DATA RECORDED)	—	—
797	662	cracks marked	407	418
799	664	cracks marked, diagonals are starting to flatting at the base of the tension wall.	420	426

continued

Table B.3: continued

SimCor Step	**Load Step**	**Comments**	**Roam Start**	**Roam End**
800	—	initiation of spalling, back corner of outer west wall base, visual no photos	—	—
802	666	The peak. Measure cracks, marked cracks. Vertical cracks in coupling beams are continuing to open up. Shear cracks in the compression wall are starting to open to 0.02 inches. The shear cracks in the 3rd and 2nd story of the east wall pier are opening to 0.035 to 0.04 inches. Took pictures of spalling in the outer corner of the east wall. Transverse reinforcement is not showing.	428	437
823	685	Measured residual cracks	—	—
824	686	Start of the 1.00% drift cycle x2	—	—
844	706	More spalling on the outer east pier, horz string gauge data may be funny here. Transverse reinforcement is exposed	—	—
848	710	cracks marked and measured. Spalling on CB3 on last peak. The cover is popping out as cracks reopened. Vertical bars on inner wall pier are exposed. No diagonal steel is exposed at this time. CB2 is starting to flake at the upper right corner	444	456
867	729	measured residual cracks	—	—
872	734	Reattached top left CB1 photo target	—	—
882	744	More spalling on the outer west end. Still no transverse r/f exposure	—	—
892	754	cracks marked and measured, spalling on upper left corner of CB3 (happened prior peak but falling out here). upper left photo target was reglued. Vertical BE bars are exposed in the inner piers but no diagonal bars are exposed. Outer wall pier has spalled.	457	465
910	—	residual cracks measures. We took off the axial load and locked the actuators. We need to increase the gauge length of the horizontal control string pots. The loading protocol is changing to horizontal displacement control of each wall pier. The moments will be resolved in force control. Loading protocol is similar to the protocol devised in the first week of testing. End of test day 8	—	—
911	—	Switching to mix-mode control. Controlling the Dx, and applying Fz, My in force control. Start of new test day	—	—

continued

Table B.3: continued

SimCor Step	**Load Step**	**Comments**	**Roam Start**	**Roam End**
912	—	Adding axial load, and resetting the horizontal position to zero. We had to switch out horizontal string pots from 5 inch to 10 inch gauge length. This resulted in an offset of out horizontal displacement when the actuators were locked.	—	—
920	—	Michael fix OM bug	—	—
922	—	Manual Krypton Trigger	—	—
923	—	First movement to zero out	—	—
925	772	Start of the 1.5% drift cycle, 10 inch gauge length string pots (adh03f3f, adh12f3f) replaced the 5 inch gauge for additional length. rezeroed at this step in post analysis. As seen in the target displacements, the first acutall zero posistion in terms of horizontal displacement is at this step. Axial load was applied well before this, but it should not effect horizontal drift too much.	—	—
939	786	cracks marked. We had spalling occur on the outer east pier (inside corner at the base). Diagonal cracks in the east (compr) pier are starting to move in a more vertical inclination. We are putting 0.5f'cAg in the compression wall at the 3rd floor. Spalling has continued to fall off on the tension pier as it opens up. Transverse reinforcement is showing at the base of the wall. Diagonal cracks are starting to show up again in all the coupling beams	519	527
941	788	Spalling occurred mid step. It happened at peak as well. Spalling has moved from base of wall at each cover to 40 inches above base. Cracks continue to angle in a more vertical orientation. Yielding into the inner boundary element.	529	538
942	789	Inner r/f yielding in the inner face of the east (compression pier). Spalling on the outer compression face continues to occur through sub steps.	—	—
943	790	More spalling, cracks marked. Diagonals continue to orientate in a vertical direction through the first floor level.	540	548
				continued

Table B.3: continued

SimCor Step	**Load Step**	**Comments**	**Roam Start**	**Roam End**
945	792	Peak, cracks marked and measure, a small amount of spalling. Flexural cracks in the boundary element of the west (tension) wall are starting to develop again between other uniformly spaced cracks. The diagonals and web cracks in the tension wall are starting to open up more and more. CB1 is starting to flake a small amount in the top left corner. CB2 has yet to spall, but seeing 3% Strain. CB3 has spalling in both corners and the cracks are starting to open to 0.2 inches. The diagonal steel has also seen 0.1% strain in one bar. On our way to 946 we lost communication with plugging, so we needed to lock boxes. There was 100 lbs of axial force change throughout the unlocking phase. This is impressive	554	576
946	—	zero step, stringpots agree	—	—
947	—	zero step, string pots agree	—	—
959	804	Hit 0 force, measured cracks	—	—
976	821	After we hit the zero displacement step, the plug-in was calculating a dF target with the opposite sign. This was putting 10 - 15 more kips of shear into the tension wall then the compression wall. A trigger disconnect was performed and then the plugin bug was corrected.	—	—
985	826	cracks marked. Shear cracks are starting to form again in the coupling beams. The shear cracks in the west (compression) wall are starting to orientate in a vertical direction.	578	587
987	828	cracks marked. On the west wall the outer cover is fell off. The middle vertical bar in the outer row is showing. This damage state would have occurred in the last positive peak.	589	601
988	829	Spalling on the outer east pier	—	—
989	830	cracks marked, Spalling on the outer east pier. Spalling (flaking) starting to occur in bottom right corner and top left corner of CB2. We killed the plugin with a force trip limit. Need to restart.	602	608
990	—	zero step	—	—
992	832	peak, cracks measured and marked. Larger cracks are starting to develop well up the height of the outer east wall pier in the BE. Some skin steel is showing in the spalled region of the 2nd and 3rd beam. No diagonal reinforcement is showing yet.	610	631
1005	845	Residual cracks measured	—	—

continued

Table B.3: continued

SimCor Step	**Load Step**	**Comments**	**Roam Start**	**Roam End**
1012	852	Start of the 1.5% drift cycle x2	—	—
1032	872	cracks marked and measured. CB2 is spalling more in the upper right corner and up the wall pier because it spalled last peak and is opening up. Cracks are starting to stay open up the entire depth of the coupling beam. A lot more spalling on the west pier has fallen off. spalling on the west pier is now up to 40” from the base. No vertical bars are exposed. More spalling on the top right of CB3. Note: did not take straight on pictures of the ends of CB2 and CB3 with roaming camera. The last two pictures in this step are the under side of CB2	633	654
1059	899	FrontEastBottom Camera DID NOT TRIGGER	—	—
1060	900	FrontEastBottom Camera DID NOT TRIGGER	—	—
1072	912	More spalling on CB3. No diagonal bars are showing but cracks are increasing greatly. Cover on the east pier outer face has lost more of the cover that was spalled in the positive displacement peak. 2 vertical r/f bars are now exposed at the base. The middle bar and the back corner bar are exposed.	656	675
1092	932	Start of the 2.25% drift cycle	—	—
1109	947	Discovered the slip issue in the test setup	—	—
1111	949	marked cracks and took pictures. There was some spalling on the outer east wall pier. Length of spalling did not grow.	682	690
1113	951	Spalling continues up the height of the outer east wall pier. The top left corner of the CB1 spalled. Longitudinal bars in the west wall are now exposed from spalling at the last peak.	692	708
1114	952	The bottom left corner is opening up on the CB3 and letting concrete fall. It has spalled on the last negative peak	—	—
1115	953	reglued 3 led’s on bottom east side.	710	721
1116	954	Going to move in small increments to 1117	—	—
9990	—	A major portion of the outer east pier wall spalled. It seems like there was crushing of the interior, but it is hard to tell. Took a manual trigger of the Krypton and Cameras. StepTest02	723	737

continued

Table B.3: continued

SimCor Step	**Load Step**	**Comments**	**Roam Start**	**Roam End**
9991	—	Moving a bit farther in as we tried to converge on 1117, we had a compression failure in through the whole B.E. All 16 bars buckled over a length of 6 inches vertically. Extensive core crushing. More spalling in the top left corner of coupling beams 3 - 1. As the tension corners of CB3-2 open up the concrete that spalled from last neg peak fell out. Did a Vamp step (99999→1117m1 in cameras). Cracks marked and measured	738	803
1117	955	zero step	—	—
1122	960	Started doing axial cycles, 288	—	—
1123	961	We are zero	—	—
1125	963	End of axial test, put back on 288	—	—
1142	980	zero displacements	—	—
1151	989	Krypton did not fire	—	—
1152	990	Krypton did not fire	—	—
1153	991	Krypton did not fire	—	—
1154	992	Krypton did not fire, FrontWestTop, FrontWestBottom, BackWestTop Cameras DID NOT TRIGGER	—	—
1155	993	Krypton did not fire, BackCenter, BackWestBottom, FrontWestTop, BackWestTop Cameras DID NOT FIRE. A manual trigger, "Test01," was taken and renamed 1155	—	—
1156	994	Krypton did not fire	—	—
1157	995	Krypton did not fire, took a manual trigger	—	—
1165	1003	Took a Vamp step 99999. East outer B.E. failed in compression. The core crushed and the vertical reinforcement buckled in a similar manner to the east pier. This should be called step 1165	934	973
9992	—	We took lateral load to zero and increased the total axial load to just shy of 1.4 million pounds. There was a continuation of crushing up to peak axial load. The inner west pier B.E crushed and the vertical bars buckled at the peak axial load of 1400 kips. There was not trigger, but continuous data was taken.	977	986

B.4 CW1 Crack Widths

Table B.4: Log of measured crack widths

SimCor Step	Load Step	Crack Width (in)											
		West Pier (Wall 1)			East Pier (Wall 2)			CB1		CB2		CB3	
		Flexure		Shear	Flexure		Shear	Flex.	Shear	Flex.	Shear	Flex.	Shear
		B.E.	Web		B.E.	Web							
109 (M)	—	—	—	—	—	—	—	—	—	—	—	0.015	—
116 (M)	—	—	—	—	—	—	—	—	—	0.005	—	0.015	—
131 (M)	92	—	—	—	—	—	—	0.005	—	0.005	—	0.015	—
132 (M)	93	—	—	—	—	—	—	0.005	—	0.005	—	0.015	—
133 (P)	—	—	—	—	—	—	—	0.005	—	0.005	—	0.015	—
165 (M)	112	—	—	—	—	—	—	0.005	—	0.005	—	0.015	—
166 (M)	113	—	—	—	—	—	—	0.005	—	0.005	—	0.015	—
168 (M)	115	—	—	—	—	—	—	0.005	—	0.005	—	0.015	—
169 (M)	116	—	—	—	—	—	—	0.005	—	0.005	—	0.015	—
170 (M)	117	—	—	—	—	—	—	0.005	—	0.005	—	0.015	—
171 (M)	118	—	—	—	—	—	—	0.005	—	0.005	—	0.015	0.005
172 (M)	119	—	—	—	—	—	—	0.005	—	0.005	—	0.015	0.005
173 (P)	—	—	—	—	—	—	—	0.005	—	0.005	0.005	0.015	0.005
213 (P)	146	0.005	—	—	—	—	—	0.005	—	0.005	0.005	0.015	0.005
237 (P)	—	0.005	—	—	0.005	—	—	0.005	—	0.005	0.005	0.015	0.005
258 (M)	187	0.005	—	—	0.005	—	—	0.005	—	0.005	0.005	0.015	0.005

P - Peak Drift Level, M - Mid Drift Level, R - Residual Crack Measurement

Table B.4: continued

SimCor Step	**Load Step**	**West Pier (Wall 1)**			**East Pier (Wall 2)**			**CB1**		**CB2**		**CB3**	
		Flexure		**Shear**	**Flexure**		**Shear**	**Flex.**	**Shear**	**Flex.**	**Shear**	**Flex.**	**Shear**
		B.E.	**Web**		**B.E.**	**Web**							
260 (M)	189	0.005	—	—	0.005	—	—	0.005	—	0.005	0.005	0.015	0.005
261 (M)	—	0.005	—	—	0.005	—	—	0.005	—	0.005	0.005	0.015	0.005
262 (P)	—	0.005	—	—	0.005	—	—	0.005	—	0.005	0.005	0.015	0.005
278 (M)	205	0.005	0.005	—	0.005	0.005	—	0.005	—	0.005	0.005	0.015	0.005
279 (M)	206	0.005	0.005	—	0.005	0.005	—	0.005	—	0.005	0.005	0.015	0.005
280 (P)	—	0.005	0.005	—	0.005	0.005	—	0.005	—	0.005	0.005	0.015	0.005
300 (P)	—	0.005	0.005	—	0.005	0.005	—	0.005	—	0.005	0.005	0.015	0.005
320 (P)	—	0.005	0.005	—	0.005	0.010	—	0.005	—	0.005	0.005	0.015	0.005
341 (M)	256	0.005	0.005	—	0.005	0.010	—	0.005	—	0.005	0.005	0.015	0.005
342 (M)	257	0.005	0.005	0.005	0.005	0.010	—	0.005	—	0.005	0.005	0.015	0.005
344 (P)	259	0.005	0.005	0.015	0.005	0.010	0.005	0.005	—	0.010	0.005	0.025	0.005
365 (M)	280	0.005	0.005	0.015	0.005	0.010	0.005	0.005	—	0.010	0.005	0.025	0.005
366 (M)	281	0.005	0.005	0.015	0.005	0.010	0.005	0.005	—	0.010	0.005	0.025	0.005
367 (P)	—	0.005	0.005	0.015	0.005	0.010	0.005	0.005	—	0.010	0.005	0.025	0.005
391 (P)	—	0.005	0.005	0.015	0.005	0.010	0.005	0.010	—	0.010	0.005	0.025	0.005
415 (P)	—	0.005	0.005	0.015	0.005	0.015	0.005	0.010	0.005	0.020	0.005	0.030	0.005
452 (M)	349	0.005	0.005	0.020	0.005	0.015	0.005	0.010	0.005	0.020	0.005	0.030	0.005

P - Peak Drift Level, M - Mid Drift Level, R - Residual Crack Measurement

Table B.4: continued

SimCor Step	**Load Step**	**West Pier (Wall 1)**			**East Pier (Wall 2)**			**CB1**		**CB2**		**CB3**	
		Flexure		**Shear**	**Flexure**		**Shear**	**Flex.**	**Shear**	**Flex.**	**Shear**	**Flex.**	**Shear**
		B.E.	**Web**		**B.E.**	**Web**							
453 (M)	350	0.005	0.005	0.025	0.005	0.015	0.005	0.010	0.005	0.020	0.005	0.035	0.005
454 (M)	—	0.005	0.005	0.025	0.005	0.015	0.005	0.010	0.005	0.020	0.005	0.035	0.005
456 (P)	352	0.005	0.005	0.030	0.005	0.015	0.005	0.010	0.005	0.020	0.005	0.040	0.005
483 (M)	379	0.005	0.005	0.030	0.005	0.015	0.005	0.010	0.005	0.020	0.005	0.040	0.005
484 (M)	380	0.005	0.005	0.030	0.005	0.015	0.005	0.010	0.005	0.020	0.005	0.040	0.005
485 (M)	381	0.005	0.005	0.030	0.005	0.015	0.005	0.010	0.005	0.020	0.005	0.040	0.005
486 (P)	382	0.005	0.005	0.030	0.005	0.015	0.015	0.015	0.005	0.020	0.005	0.040	0.005
516 (P)	409	0.005	0.005	0.035	0.005	0.015	0.015	0.015	0.005	0.020	0.005	0.040	0.005
546 (P)	439	0.005	0.005	0.035	0.005	0.020	0.020	0.015	0.005	0.020	0.005	0.050	0.005
576 (M)	—	0.005	0.005	0.035	0.005	0.020	0.020	0.015	0.005	0.020	0.005	0.050	0.005
579 (M)	470	0.005	0.005	0.035	0.005	0.020	0.020	0.015	0.005	0.025	0.005	0.050	0.015
580 (M)	471	0.010	0.005	0.035	0.005	0.020	0.020	0.015	0.005	0.025	0.005	0.050	0.015
581 (P)	472	0.010	0.005	0.035	0.005	0.020	0.020	0.030	0.005	0.040	0.005	0.060	0.015
601 (R)	490	closed	closed	0.010	closed	closed	0.005	0.005	closed	0.025	closed	0.035	0.005
616 (M)	505	0.010	0.005	0.035	0.005	0.020	0.020	0.030	0.005	0.040	0.005	0.060	0.015
617 (M)	506	0.010	0.005	0.035	0.005	0.020	0.020	0.030	0.005	0.040	0.005	0.060	0.015
618 (M)	507	0.010	0.005	0.035	0.005	0.020	0.020	0.030	0.005	0.040	0.005	0.060	0.015

P - Peak Drift Level, M - Mid Drift Level, R - Residual Crack Measurement

Table B.4: continued

SimCor Step	Load Step	West Pier (Wall 1)			East Pier (Wall 2)			CB1		CB2		CB3	
		Flexure		Shear	Flexure		Shear	Flex.	Shear	Flex.	Shear	Flex.	Shear
		B.E.	Web		B.E.	Web							
619 (M)	508	0.010	0.005	0.035	0.005	0.020	0.020	0.030	0.005	0.040	0.005	0.060	0.015
620 (P)	509	0.010	0.005	0.035	0.010	0.010	0.030	0.030	0.005	0.060	0.005	0.075	0.015
639 (R)	528	closed	closed	closed	closed	0.005	0.005	0.010	closed	0.030	closed	0.005	0.040
657 (P)	546	0.010	0.005	0.035	0.010	0.010	0.030	0.035	0.005	0.060	0.005	0.075	0.015
677 (R)	564	0.005	0.005	0.015	closed	closed	0.005	0.010	closed	0.030	closed	0.040	0.005
695 (P)	582	0.010	0.005	0.035	0.010	0.010	0.030	0.035	0.005	0.060	0.005	0.075	0.015
715 (R)	—	closed	closed	0.010	closed	0.005	0.010	0.010	closed	0.035	closed	0.050	0.005
746 (M)	619	0.010	0.005	0.035	0.010	0.010	0.030	0.035	0.005	0.060	0.005	0.075	0.015
747 (M)	—	0.010	0.005	0.035	0.010	0.010	0.030	0.035	0.005	0.060	0.005	0.075	0.015
754 (P)	—	0.010	0.005	0.035	0.010	0.010	0.030	0.035	0.005	0.075	0.005	0.100	0.015
777 (R)	643	0.005	0.005	0.010	closed	closed	0.010	0.020	closed	0.060	closed	0.075	0.005
797 (M)	662	0.010	0.005	0.035	0.010	0.010	0.030	0.035	0.005	0.075	0.005	0.100	0.015
799 (M)	664	0.010	0.005	0.035	0.010	0.010	0.030	0.035	0.005	0.075	0.005	0.100	0.015
802 (P)	666	0.010	0.005	0.035	0.020	0.020	0.040	0.050	0.005	0.100	0.005	0.125	0.015
823 (R)	685	closed	0.005	0.010	0.005	0.005	0.010	0.025	closed	0.060	0.010	0.075	0.005
848 (P)	710	0.010	0.005	0.035	0.020	0.020	0.040	0.050	0.005	0.100	0.005	0.125	0.015
867 (R)	729	0.005	0.005	0.010	closed	closed	0.015	0.025	0.005	0.075	0.005	0.100	0.005

P - Peak Drift Level, M - Mid Drift Level, R - Residual Crack Measurement

Table B.4: continued

SimCor Step	Load Step	West Pier (Wall 1)			East Pier (Wall 2)			CB1		CB2		CB3	
		Flexure		Shear	Flexure		Shear	Flex.	Shear	Flex.	Shear	Flex.	Shear
		B.E.	Web		B.E.	Web							
892 (P)	754	0.010	0.005	0.035	0.020	0.040	0.040	0.075	0.005	0.150	0.005	0.188	0.015
910 (R)	—	closed	closed	0.010	0.005	0.005	0.015	0.035	0.005	0.075	0.005	0.100	0.005
939 (M)	786	0.010	0.005	0.035	0.020	0.040	0.040	0.075	0.005	0.150	0.005	0.188	0.015
941 (M)	788	0.010	0.005	0.035	0.020	0.040	0.040	0.075	0.005	0.150	0.005	0.188	0.015
943 (M)	790	0.010	0.005	0.035	0.020	0.040	0.040	0.075	0.005	0.150	0.005	0.188	0.015
945 (P)	792	0.020	0.060	0.060	0.020	0.040	0.050	0.075	0.005	0.150	0.005	0.200	0.015
959 (R)	804	0.010	0.020	0.015	0.005	0.005	0.025	0.100	0.005	0.150	0.005	0.150	0.005
985 (M)	826	0.020	0.060	0.060	0.020	0.040	0.050	0.075	0.005	0.150	0.005	0.200	0.015
987 (M)	828	0.020	0.060	0.060	0.020	0.040	0.050	0.075	0.005	0.150	0.005	0.200	0.015
989 (M)	830	0.020	0.060	0.060	0.020	0.040	0.050	0.075	0.005	0.150	0.005	0.200	0.015
992 (P)	832	0.025	0.060	0.060	0.035	0.050	0.050	0.100	0.005	0.250	0.005	0.250	0.015
1005 (R)	845	closed	closed	0.015	0.010	0.015	0.020	0.100	0.005	0.150	0.005	0.150	0.005
1032 (P)	872	0.025	0.060	0.060	0.035	0.050	0.050	0.100	0.005	0.250	0.005	0.250	0.015
1072 (P)	912	0.025	0.060	0.060	0.035	0.050	0.050	0.150	0.010	0.250	0.005	0.250	0.015
1111 (M)	949	0.025	0.060	0.060	0.035	0.050	0.050	0.150	0.010	0.250	0.005	0.250	0.015
1117 (P)	955	0.025	0.100	0.075	0.035	0.050	0.050	0.150	0.010	0.400	0.005	0.300	0.015

P - Peak Drift Level, M - Mid Drift Level, R - Residual Crack Measurement

Appendix C

CW1 DATA ANALYSIS

C.1 Vertical Strain Fields

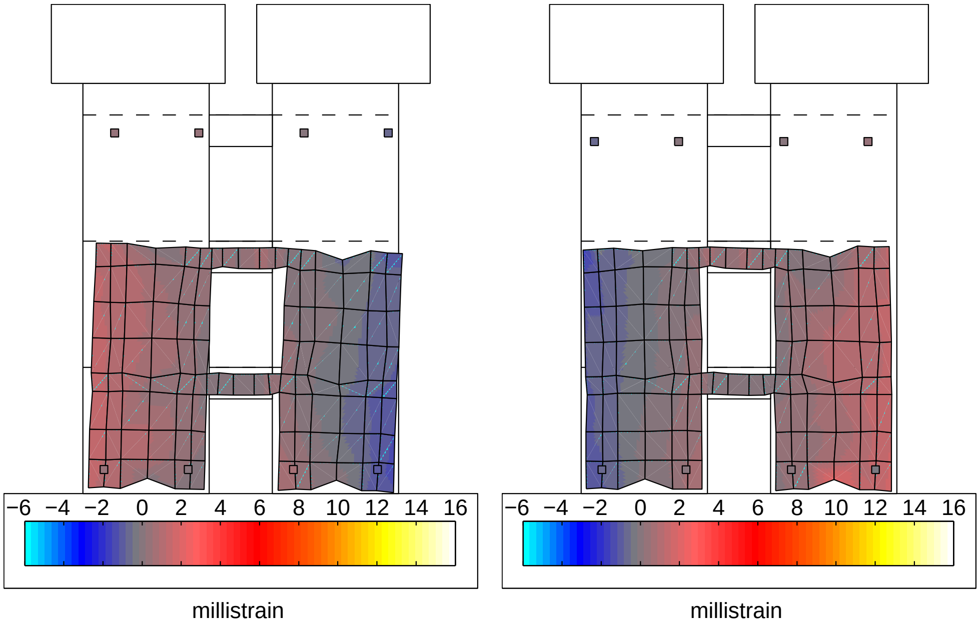

(a) 0.321% (Metris) (b) -0.321% (Metris)

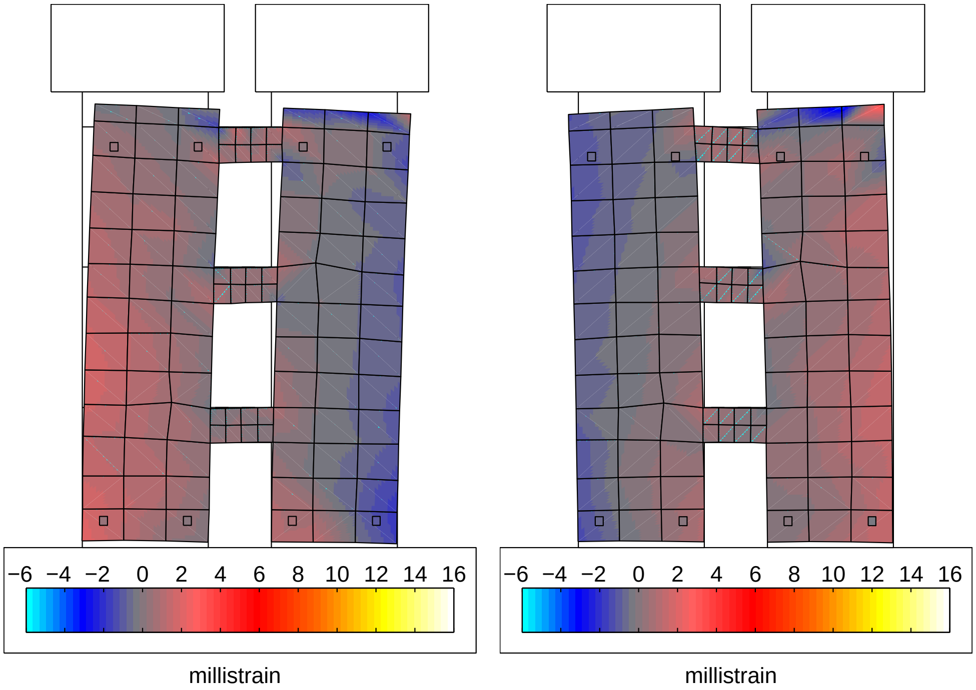

(c) 0.321% (Photogrammetry) (d) -0.321% (Photogrammetry)

Figure C.1: ϵ_z field at ± 0.321% (A) (diagonal cracking)

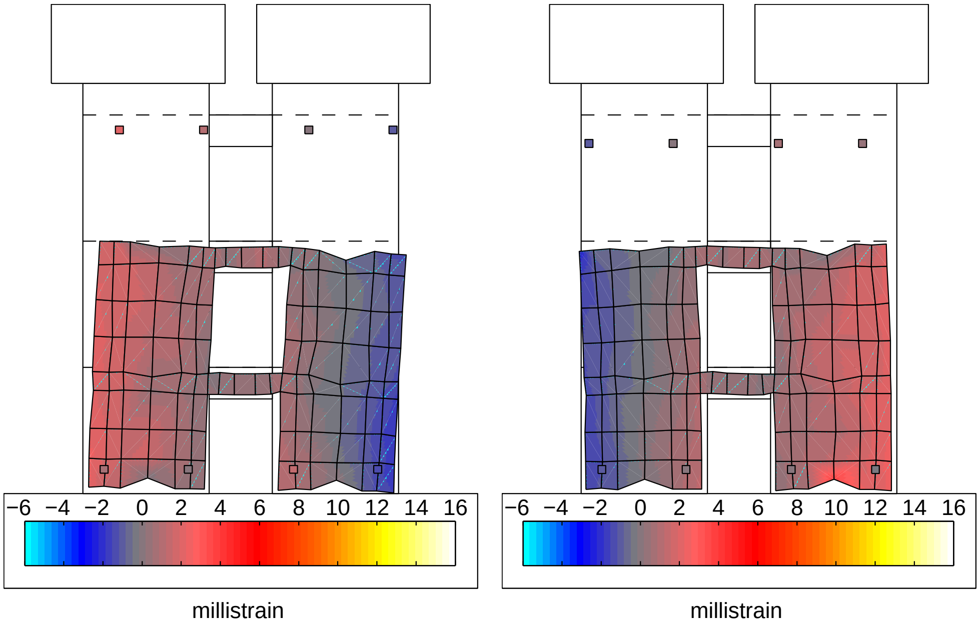

(a) 0.50% (Metris) (b) -0.50% (Metris)

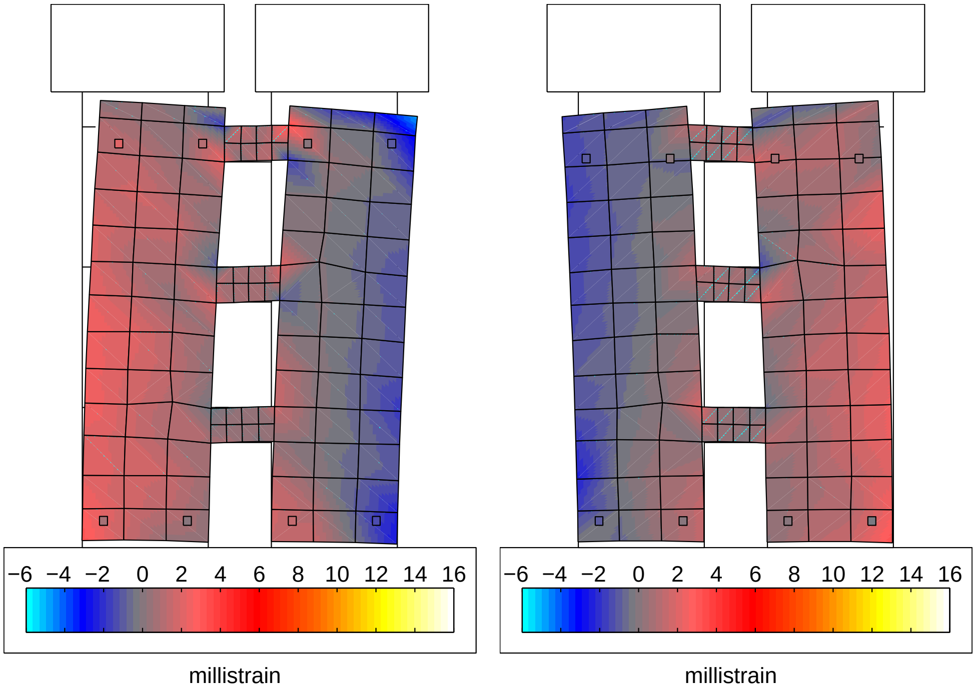

(c) 0.50% (Photogrammetry) (d) -0.50% (Photogrammetry)

Figure C.2: ϵ_z field at ± 0.50% (A) (yielding)

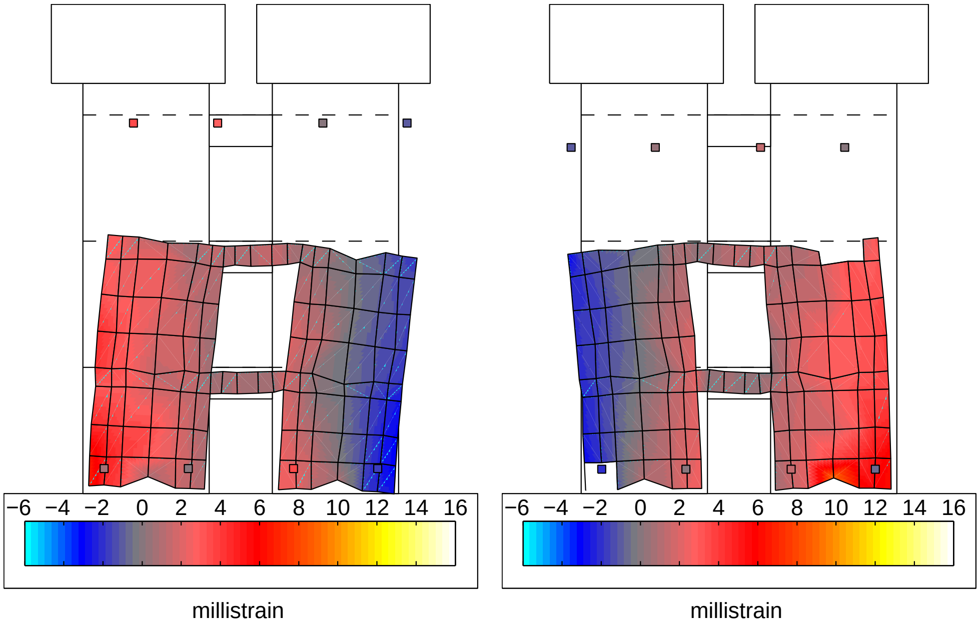

(a) 1.00% (Metris)

(b) -1.00% (Metris)

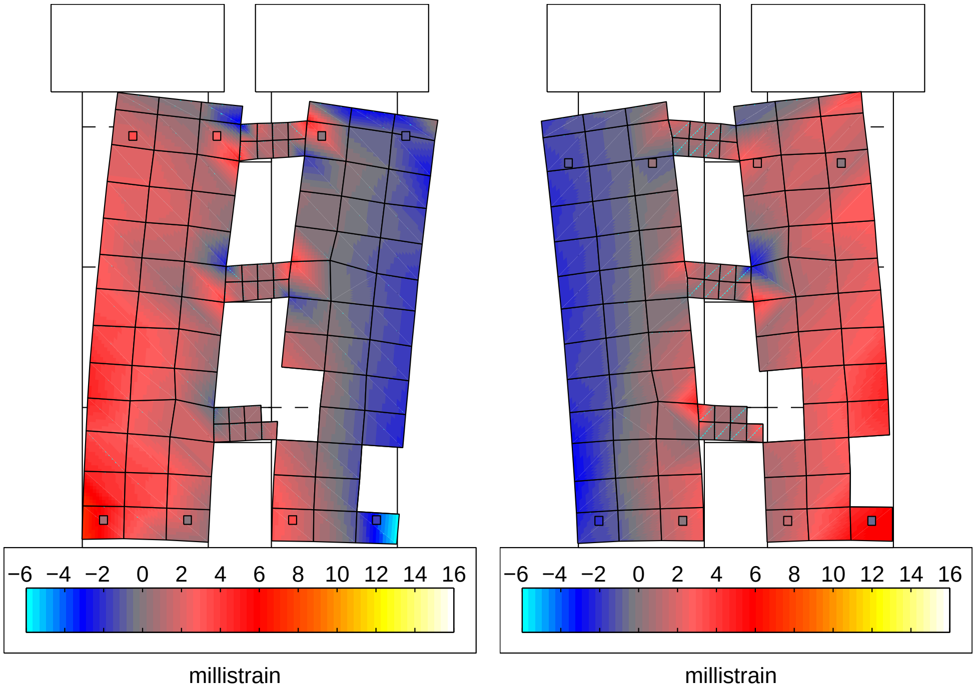

(c) 1.00% (Photogrammetry)

(d) -1.00% (Photogrammetry)

Figure C.3: ϵ_z field at ± 1.00% (A) (initial spalling)

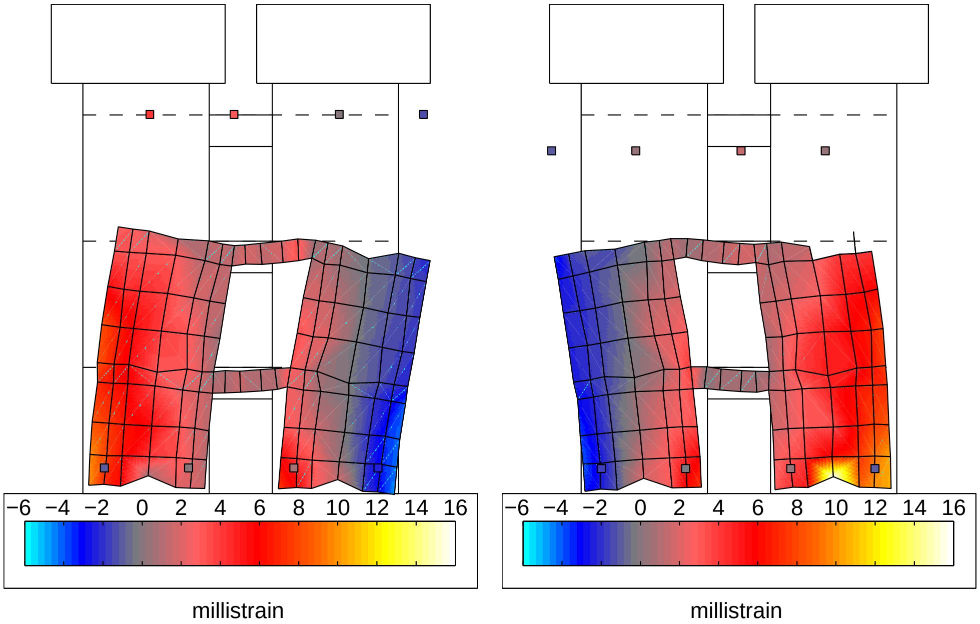

(a) 1.50% (Metris) (b) -1.50% (Metris)

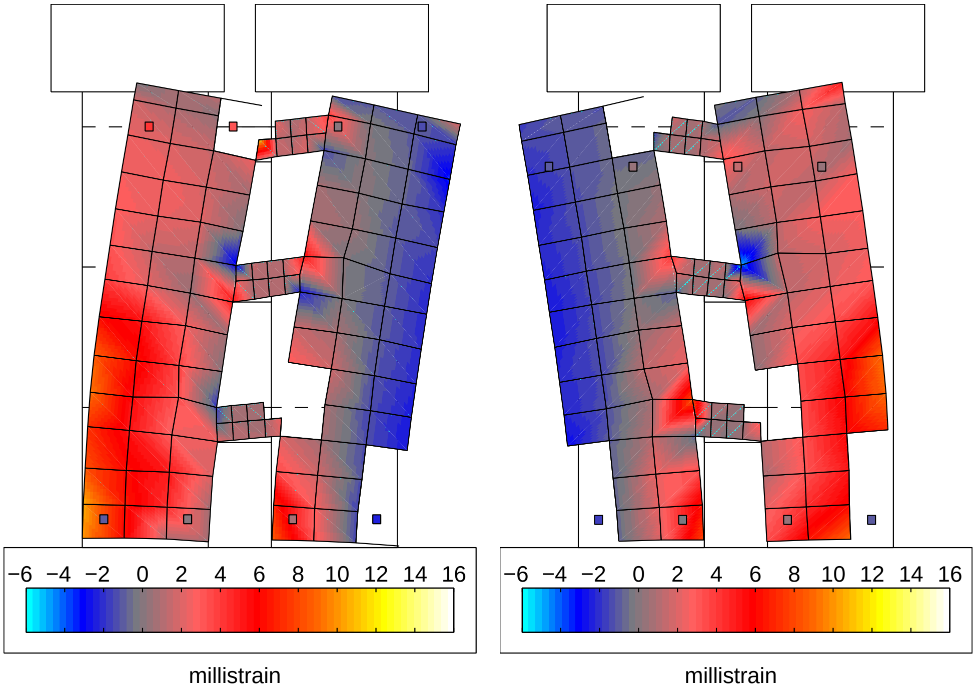

(c) 1.50% (Photogrammetry) (d) -1.50% (Photogrammetry)

Figure C.4: ϵ_z field at ± 1.50% (A)(moderate spalling)

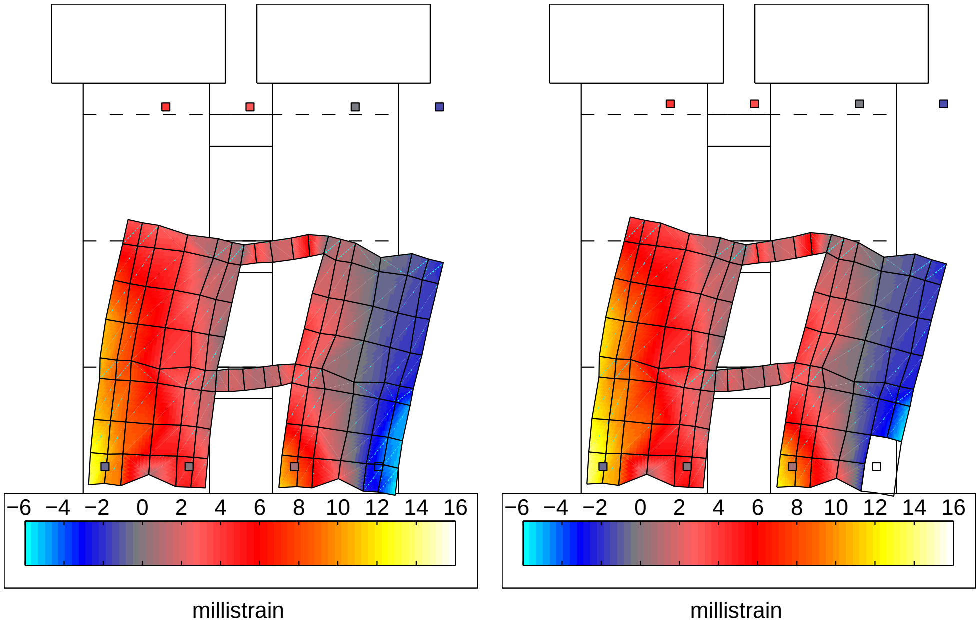

(a) 2.00% (Metris)

(b) 2.20% (Metris)

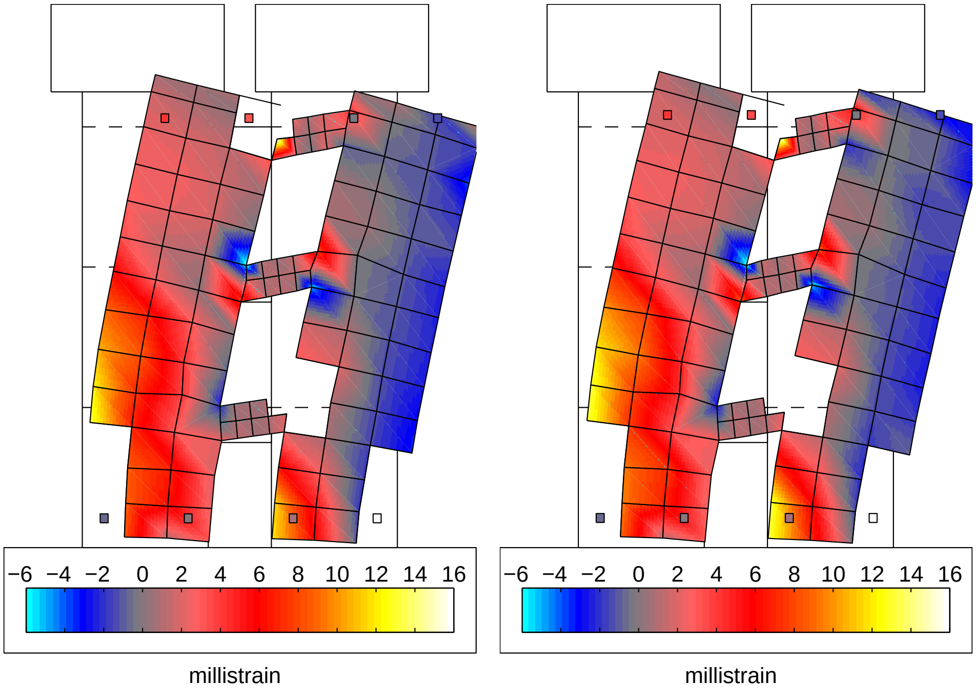

(c) 2.00% (Photogrammetry)

(d) 2.20% (Photogrammetry)

Figure C.5: ϵ_z field near failure of the east wall pier (2.25% E+ drift level)

Appendix D

ELASTIC ANALYSIS OF COUPLED WALL EXPERIMENTS

D.1 Effective stiffness values used in each model

Table D.1: CW1 effective stiffness values used in linear elastic analysis

	Case A	**Case B1**	**Case B2**	**Case C**	**Case D**	**Case E**	**Case F**
Source	**ASCE 41**	**ACI 318**	**ACI 318**	**CSA A23.3**	**NZS 3101**	**ATC 72**	**Birely/Mohr**
Compression Wall Pier							
Flexure	$0.50E_cI_g$	$0.70E_cI_g$	$0.35E_cI_g$	$0.89E_cI_g$	$0.43E_cI_g$	$0.45E_cI_g$	$0.35E_cI_g$
Shear	$1.00GA_{cv}$	$1.00GA_{cv}$	$1.00GA_{cv}$	—	—	$0.07GA_{cv}$	$0.15GA_{cv}$
Axial	$1.00E_cA_g$	$1.00E_cA_g$	$1.00E_cA_g$	$0.89E_cA_g$	$1.00E_cA_g$	$1.00E_cA_g$	$1.00E_cA_g$
Tension Wall Pier							
Flexure	$0.50E_cI_g$	$0.70E_cI_g$	$0.35E_cI_g$	$0.60E_cI_g$	$0.27E_cI_g$	$0.20E_cI_g$	$0.35E_cI_g$
Shear	$1.00GA_{cv}$	$1.00GA_{cv}$	$1.00GA_{cv}$	—	—	$0.07GA_{cv}$	$0.15GA_{cv}$
Axial	$1.00E_cA_g$	$1.00E_cA_g$	$1.00E_cA_g$	$0.60E_cA_g$	$1.00E_cA_g$	$1.00E_cA_g$	$1.00E_cA_g$
Diagonally Reinforced Coupling Beams							
Flexure	$0.30E_cI_g$	$0.35E_cI_g$	$0.35E_cI_g$	$0.25E_cI_g$	$0.60E_cI_g$	$0.15E_cI_g$	$0.04E_cI_g$
Shear	$1.00GA_{cv}$	$1.00GA_{cv}$	$1.00GA_{cv}$	$0.45GA_{cv}$	$0.07GA_{cv}$	$1.00GA_{cv}$	$0.15GA_{cv}$
Axial	$1.00E_cA_g$	$1.00E_cA_g$	$1.00E_cA_g$	$1.00E_cA_g$	$1.00E_cA_g$	$1.00E_cA_g$	$1.00E_cA_g$

Table D.2: Santhakumar WallA effective stiffness values used in linear elastic analysis

	Case A	**Case B1**	**Case B2**	**Case C**	**Case D**	**Case E**	**Case F**
Source	**ASCE 41**	**ACI 318**	**ACI 318**	**CSA A23.3**	**NZS 3101**	**ATC 72**	**Birely/Mohr**
Compression Wall Pier							
Flexure	$0.50E_cI_g$	$0.70E_cI_g$	$0.35E_cI_g$	$0.90E_cI_g$	$0.48E_cI_g$	$0.45E_cI_g$	$0.35E_cI_g$
Shear	$1.00GA_{cv}$	$1.00GA_{cv}$	$1.00GA_{cv}$	—	—	$0.08GA_{cv}$	$0.15GA_{cv}$
Axial	$1.00E_cA_g$	$1.00E_cA_g$	$1.00E_cA_g$	$0.90E_cA_g$	$1.00E_cA_g$	$1.00E_cA_g$	$1.00E_cA_g$
Tension Wall Pier							
Flexure	$0.50E_cI_g$	$0.70E_cI_g$	$0.35E_cI_g$	$0.60E_cI_g$	$0.32E_cI_g$	$0.20E_cI_g$	$0.35E_cI_g$
Shear	$1.00GA_{cv}$	$1.00GA_{cv}$	$1.00GA_{cv}$	—	—	$0.08GA_{cv}$	$0.15GA_{cv}$
Axial	$1.00E_cA_g$	$1.00E_cA_g$	$1.00E_cA_g$	$0.60E_cA_g$	$1.00E_cA_g$	$1.00E_cA_g$	$1.00E_cA_g$
Conventionally Reinforced Coupling Beams							
Flexure	$0.30E_cI_g$	$0.35E_cI_g$	$0.35E_cI_g$	$0.40E_cI_g$	$0.13E_{40}I_g$	$0.15E_cI_g$	$0.04E_cI_g$
Shear	$1.00GA_{cv}$	$1.00GA_{cv}$	$1.00GA_{cv}$	$0.15GA_{cv}$	—	$0.25GA_{cv}$	$0.15GA_{cv}$
Axial	$1.00E_cA_g$	$1.00E_cA_g$	$1.00E_cA_g$	$1.00E_cA_g$	$1.00E_cA_g$	$1.00E_cA_g$	$1.00E_cA_g$

Table D.3: Santhakumar WallB effective stiffness values used in linear elastic analysis

	Case A	**Case B1**	**Case B2**	**Case C**	**Case D**	**Case E**	**Case F**
Source	**ASCE 41**	**ACI 318**	**ACI 318**	**CSA A23.3**	**NZS 3101**	**ATC 72**	**Birely/Mohr**
Compression Wall Pier							
Flexure	$0.50E_cI_g$	$0.70E_cI_g$	$0.35E_cI_g$	$0.93E_cI_g$	$0.48E_cI_g$	$0.45E_cI_g$	$0.35E_cI_g$
Shear	$1.00GA_{cv}$	$1.00GA_{cv}$	$1.00GA_{cv}$	—	—	$0.08GA_{cv}$	$0.15GA_{cv}$
Axial	$1.00E_cA_g$	$1.00E_cA_g$	$1.00E_cA_g$	$0.93E_cA_g$	$1.00E_cA_g$	$1.00E_cA_g$	$1.00E_cA_g$
Tension Wall Pier							
Flexure	$0.50E_cI_g$	$0.70E_cI_g$	$0.35E_cI_g$	$0.60E_cI_g$	$0.32E_cI_g$	$0.20E_cI_g$	$0.35E_cI_g$
Shear	$1.00GA_{cv}$	$1.00GA_{cv}$	$1.00GA_{cv}$	—	—	$0.08GA_{cv}$	$0.15GA_{cv}$
Axial	$1.00E_cA_g$	$1.00E_cA_g$	$1.00E_cA_g$	$0.60E_cA_g$	$1.00E_cA_g$	$1.00E_cA_g$	$1.00E_cA_g$
Diagonally Reinforced Coupling Beams							
Flexure	$0.30E_cI_g$	$0.35E_cI_g$	$0.35E_cI_g$	$0.25E_cI_g$	$0.60E_cI_g$	$0.15E_cI_g$	$0.04E_cI_g$
Shear	$1.00GA_{cv}$	$1.00GA_{cv}$	$1.00GA_{cv}$	$0.45GA_{cv}$	$0.11GA_{cv}$	$0.25GA_{cv}$	$0.15GA_{cv}$
Axial	$1.00E_cA_g$	$1.00E_cA_g$	$1.00E_cA_g$	$1.00E_cA_g$	$1.00E_cA_g$	$1.00E_cA_g$	$1.00E_cA_g$

Table D.4: Shiu CS1 effective stiffness values used in linear elastic analysis

	Case A	**Case B1**	**Case B2**	**Case C**	**Case D**	**Case E**	**Case F**
Source	**ASCE 41**	**ACI 318**	**ACI 318**	**CSA A23.3**	**NZS 3101**	**ATC 72**	**Birely/Mohr**
Compression Wall Pier							
Flexure	$0.50E_cI_g$	$0.70E_cI_g$	$0.35E_cI_g$	$0.62E_cI_g$	$0.30E_cI_g$	$0.26E_cI_g$	$0.35E_cI_g$
Shear	$1.00GA_{cv}$	$1.00GA_{cv}$	$1.00GA_{cv}$	—	—	$0.08GA_{cv}$	$0.15GA_{cv}$
Axial	$1.00E_cA_g$	$1.00E_cA_g$	$1.00E_cA_g$	$0.62E_cA_g$	$1.00E_cA_g$	$1.00E_cA_g$	$1.00E_cA_g$
Tension Wall Pier							
Flexure	$0.50E_cI_g$	$0.70E_cI_g$	$0.35E_cI_g$	$0.60E_cI_g$	$0.27E_cI_g$	$0.20E_cI_g$	$0.35E_cI_g$
Shear	$1.00GA_{cv}$	$1.00GA_{cv}$	$1.00GA_{cv}$	—	—	$0.08GA_{cv}$	$0.15GA_{cv}$
Axial	$1.00E_cA_g$	$1.00E_cA_g$	$1.00E_cA_g$	$0.60E_cA_g$	$1.00E_cA_g$	$1.00E_cA_g$	$1.00E_cA_g$
Conventionally Reinforced Coupling Beams							
Flexure	$0.30E_cI_g$	$0.35E_cI_g$	$0.35E_cI_g$	$0.40E_cI_g$	$0.21E_{40}I_g$	$0.15E_cI_g$	$0.04E_cI_g$
Shear	$1.00GA_{cv}$	$1.00GA_{cv}$	$1.00GA_{cv}$	$0.15GA_{cv}$	—	$1.00GA_{cv}$	$0.15GA_{cv}$
Axial	$1.00E_cA_g$	$1.00E_cA_g$	$1.00E_cA_g$	$1.00E_cA_g$	$1.00E_cA_g$	$1.00E_cA_g$	$1.00E_cA_g$

Table D.5: Ozselcuk 1C effective stiffness values used in linear elastic analysis

	Case A	**Case B1**	**Case B2**	**Case C**	**Case D**	**Case E**	**Case F**
Source	**ASCE 41**	**ACI 318**	**ACI 318**	**CSA A23.3**	**NZS 3101**	**ATC 72**	**Birely/Mohr**
Compression Wall Pier							
Flexure	$0.50E_cI_g$	$0.70E_cI_g$	$0.35E_cI_g$	$0.95E_cI_g$	$0.45E_cI_g$	$0.45E_cI_g$	$0.35E_cI_g$
Shear	$1.00GA_{cv}$	$1.00GA_{cv}$	$1.00GA_{cv}$	—	—	$0.08GA_{cv}$	$0.15GA_{cv}$
Axial	$1.00E_cA_g$	$1.00E_cA_g$	$1.00E_cA_g$	$0.95E_cA_g$	$1.00E_cA_g$	$1.00E_cA_g$	$1.00E_cA_g$
Tension Wall Pier							
Flexure	$0.50E_cI_g$	$0.70E_cI_g$	$0.35E_cI_g$	$0.60E_cI_g$	$0.28E_cI_g$	$0.20E_cI_g$	$0.35E_cI_g$
Shear	$1.00GA_{cv}$	$1.00GA_{cv}$	$1.00GA_{cv}$	—	—	$0.08GA_{cv}$	$0.15GA_{cv}$
Axial	$1.00E_cA_g$	$1.00E_cA_g$	$1.00E_cA_g$	$0.60E_cA_g$	$1.00E_cA_g$	$1.00E_cA_g$	$1.00E_cA_g$
Conventionally Reinforced Coupling Beams							
Flexure	$0.30E_cI_g$	$0.35E_cI_g$	$0.35E_cI_g$	$0.40E_cI_g$	$0.31E_{40}I_g$	$0.15E_cI_g$	$0.04E_cI_g$
Shear	$1.00GA_{cv}$	$1.00GA_{cv}$	$1.00GA_{cv}$	$0.15GA_{cv}$	—	$1.00GA_{cv}$	$0.15GA_{cv}$
Axial	$1.00E_cA_g$	$1.00E_cA_g$	$1.00E_cA_g$	$1.00E_cA_g$	$1.00E_cA_g$	$1.00E_cA_g$	$1.00E_cA_g$

Table D.6: Lequesne CW1 effective stiffness values used in linear elastic analysis

	Case A	**Case B1**	**Case B2**	**Case C**	**Case D**	**Case E**	**Case F**
Source	**ASCE 41**	**ACI 318**	**ACI 318**	**CSA A23.3**	**NZS 3101**	**ATC 72**	**Birely/Mohr**
Compression Wall Pier							
Flexure	$0.50E_cI_g$	$0.70E_cI_g$	$0.35E_cI_g$	$0.73E_cI_g$	$0.37E_cI_g$	$0.45E_cI_g$	$0.35E_cI_g$
Shear	$1.00GA_{cv}$	$1.00GA_{cv}$	$1.00GA_{cv}$	—	—	$0.06GA_{cv}$	$0.15GA_{cv}$
Axial	$1.00E_cA_g$	$1.00E_cA_g$	$1.00E_cA_g$	$0.73E_cA_g$	$1.00E_cA_g$	$1.00E_cA_g$	$1.00E_cA_g$
Tension Wall Pier							
Flexure	$0.50E_cI_g$	$0.70E_cI_g$	$0.35E_cI_g$	$0.60E_cI_g$	$0.26E_cI_g$	$0.20E_cI_g$	$0.35E_cI_g$
Shear	$1.00GA_{cv}$	$1.00GA_{cv}$	$1.00GA_{cv}$	—	—	$0.06GA_{cv}$	$0.15GA_{cv}$
Axial	$1.00E_cA_g$	$1.00E_cA_g$	$1.00E_cA_g$	$0.60E_cA_g$	$1.00E_cA_g$	$1.00E_cA_g$	$1.00E_cA_g$
Diagonally Reinforced Coupling Beams							
Flexure	$0.30E_cI_g$	$0.35E_cI_g$	$0.35E_cI_g$	$0.25E_cI_g$	$0.60E_cI_g$	$0.15E_cI_g$	$0.04E_cI_g$
Shear	$1.00GA_{cv}$	$1.00GA_{cv}$	$1.00GA_{cv}$	$0.45GA_{cv}$	$0.08GA_{cv}$	$0.64GA_{cv}$	$0.15GA_{cv}$
Axial	$1.00E_cA_g$	$1.00E_cA_g$	$1.00E_cA_g$	$1.00E_cA_g$	$1.00E_cA_g$	$1.00E_cA_g$	$1.00E_cA_g$

Table D.7: Lequesne CW2 effective stiffness values used in linear elastic analysis

	Case A	**Case B1**	**Case B2**	**Case C**	**Case D**	**Case E**	**Case F**
Source	**ASCE 41**	**ACI 318**	**ACI 318**	**CSA A23.3**	**NZS 3101**	**ATC 72**	**Birely/Mohr**
Compression Wall Pier							
Flexure	$0.50E_cI_g$	$0.70E_cI_g$	$0.35E_cI_g$	$0.73E_cI_g$	$0.37E_cI_g$	$0.45E_cI_g$	$0.35E_cI_g$
Shear	$1.00GA_{cv}$	$1.00GA_{cv}$	$1.00GA_{cv}$	—	—	$0.08GA_{cv}$	$0.15GA_{cv}$
Axial	$1.00E_cA_g$	$1.00E_cA_g$	$1.00E_cA_g$	$0.73E_cA_g$	$1.00E_cA_g$	$1.00E_cA_g$	$1.00E_cA_g$
Tension Wall Pier							
Flexure	$0.50E_cI_g$	$0.70E_cI_g$	$0.35E_cI_g$	$0.60E_cI_g$	$0.26E_cI_g$	$0.20E_cI_g$	$0.35E_cI_g$
Shear	$1.00GA_{cv}$	$1.00GA_{cv}$	$1.00GA_{cv}$	—	—	$0.08GA_{cv}$	$0.15GA_{cv}$
Axial	$1.00E_cA_g$	$1.00E_cA_g$	$1.00E_cA_g$	$0.60E_cA_g$	$1.00E_cA_g$	$1.00E_cA_g$	$1.00E_cA_g$
Diagonally Reinforced Coupling Beams							
Flexure	$0.30E_cI_g$	$0.35E_cI_g$	$0.35E_cI_g$	$0.25E_cI_g$	$0.60E_cI_g$	$0.15E_cI_g$	$0.04E_cI_g$
Shear	$1.00GA_{cv}$	$1.00GA_{cv}$	$1.00GA_{cv}$	$0.45GA_{cv}$	$0.08GA_{cv}$	$0.64GA_{cv}$	$0.15GA_{cv}$
Axial	$1.00E_cA_g$	$1.00E_cA_g$	$1.00E_cA_g$	$1.00E_cA_g$	$1.00E_cA_g$	$1.00E_cA_g$	$1.00E_cA_g$